به نام خدا

مرکز دانلود رایگان
مهندسی متالورژی و مواد

www.Iran-mavad.com

Duplex Stainless Steels

Duplex Stainless Steels

Edited by
Iris Alvarez-Armas
Suzanne Degallaix-Moreuil

ISTE
WILEY

First published in Great Britain and the United States in 2009 by ISTE Ltd and John Wiley & Sons, Inc.

ISTE Ltd
27-37 St George's Road
London SW19 4EU
UK

www.iste.co.uk

John Wiley & Sons, Inc.
111 River Street
Hoboken, NJ 07030
USA

www.wiley.com

Library of Congress Cataloging-in-Publication Data

Duplex stainless steels / edited by Iris Alvarez-Armas, Suzanne Degallaix-Moreuil.
p. cm.
Includes bibliographical references and index.
ISBN 978-1-84821-137-7
1. Duplex stainless steel. I. Alvarez-Armas, Iris. II. Degallaix-Moreuil, Suzanne.
TN757.C5D87 2009
672--dc22

2009026201

British Library Cataloguing-in-Publication Data
A CIP record for this book is available from the British Library
ISBN: 978-1-84821-137-7

Printed and bound in Great Britain by CPI/Antony Rowe, Chippenham and Eastbourne.

Table of Contents

Preface

Duplex stainless steels (DSSs) are chromium-nickel-molybdenum-iron bi-phased alloys in which the proportions of the constituent elements enable the optimization of the balance of the volume fractions of austenite and ferrite. Due to their ferritic-austenitic bi-phased microstructure, they possess higher mechanical strength and better corrosion resistance than standard austenitic stainless steels. Nowadays, the applications and markets for DSSs are increasing continuously, due to their outstanding properties and their relatively low cost.

The use of DSS has drastically grown in the last 10 years, particularly in the oil and gas, the pulp and paper, and chemical industries, and in chemical tankers. In all these examples, properties, such as welding, corrosion resistance, and mechanical strength, are crucial. Recent publications have also emphasized the importance of the fabrication process, as well as the effect of aging, on fracture and long-term mechanical properties, such as fatigue of DSSs; a subject that is hardly dealt with in Gunn's[1] book.

Since the edition of the book by Robert Gunn, there have been important advances in the knowledge of the DSSs, as revealed by the extensive research in the scientific literature on a wide range of topics relating to DSSs. The significance of the DSSs is reflected by the fact that the International Conference DUPLEX 2007 is the fourth conference on the subject since the publication of Gunn's book, in a series of seven since the first St Louis, USA, in 1982.

The intention of the present book is to review the most updated progress achieved in the last 10 years regarding the microstructure, corrosion resistance, and mechanical strength properties of DSSs, as well as highlighting the industrial

1 Gunn R.N., Ed., *Duplex Stainless Steels, Microstructure, Properties and Applications*, Abington publishing, Cambridge, 1997.

applications as a result of the development of new grades. The different subjects are developed in chapters written by world-renowned experts among the industrial and scientific communities:

Chapter 1 analyzes the impact of different microstructural variables on the hot workability of DSSs.

Chapter 2 focuses on corrosion-resistance properties and in-service properties of standard and newly developed duplex grades.

Chapter 3 describes the phase transformations that take place from the liquid state down to subzero temperatures, related microstructures, and their influence on mechanical and corrosion properties.

Chapter 4 analyzes the effect of thermal histories induced by welding processes on the austenitic-ferritic microstructure, as well as the secondary-phase precipitations. It is also proposed a guideline regarding the choice of material, process, and filler metal, in order to obtain sound welds, both in terms of corrosion resistance and mechanical properties.

Chapter 5 provides general information related to the elaboration of cast DSS and a review of the mechanisms of embrittlement occurring during aging in the temperature range 300-500°C and the consequences on fracture mechanical properties. Models of the heterogenity and size effects on the fracture result scatter are also provided.

Chapters 6 and 7 describe the cyclic plastic behavior and the dislocation structure evolution in DSSs tested under cyclic uniaxial (tension-compression) and multiaxial (tension-compression-torsion) cyclic loading at room temperature.

Chapter 8 discusses the cyclic accommodation mechanisms in a DSS from AFM measurements of the surface topography created in the two phases. It highlights the role played by each phase – austenite and ferrite – on the macroscopic behavior and provides an explanation of how they interact.

Chapter 9 discusses the modeling on different scales of monotonic and cyclic plastic behavior at room temperature observed in a hot-forged DSS.

Chapter 10 studies and compares the cyclic plastic behavior, the fatigue lifetimes, and the dislocation structures of different generations of DSSs in the as-received and aged conditions between 20 and 500°C.

Chapter 11 concisely summarizes the basics of the industrial production of DSSs and their effects on crystallographic and microstructural properties leading to differences in fatigue resistance.

Chapter 12 presents the large variety of application fields of different DSS grades and, in particular, the new DSSs.

Finally, an appendix summarizes the chemical composition of the different families of DSSs, including both cast and wrought austenitic and DSSs, and provides the designations from the different nomenclatural systems.

The Editors are grateful to all the authors who have kindly contributed to this book, especially for their effort and personal time invested in the writing of their contribution.

Iris ALVAREZ-ARMAS
Suzanne DEGALLAIX-MOREUIL

Chapter 1

Process: Hot Workability

1.1. Introduction

The advantageous performance of duplex stainless steels in many applications, when compared with other stainless steels, is directly related to their austeno-ferritic microstructure [FLO 68, SOL 83, BER 91, COM 91, NIL 92A, NIL 92B]. However, the biggest difficulties in processing duplex stainless steels arise during hot working as a direct consequence of this same austeno-ferritic microstructure [IZA 07]. In general, duplex stainless steels have poor hot workability, which consequently leads to a relatively narrow processing window. This raises difficulties during their industrial processing and the severity of the problem often produces defects seen immediately in the hot rolled material or only detected in the finished product.

The different metallurgical factors behind the hot workability of duplex stainless steels are reviewed in this paper.

1.2. As-cast microstructure

In general, duplex stainless steels of practical interest solidify to δ-ferrite, leading to the primary as-cast pattern shown schematically in Figure 1.1a in which a shell of small equiaxed grains in contact with the cast surface is followed by several

---

Chapter written by Isabel GUTIERREZ and Amaia IZA-MENDIA.

Duplex Stainless Steels Edited by Iris Alvarez-Armas and Suzanne Degallaix-Moreuil

millimeter long columnar grains and finally coarse equiaxed grains at the center of the cast.

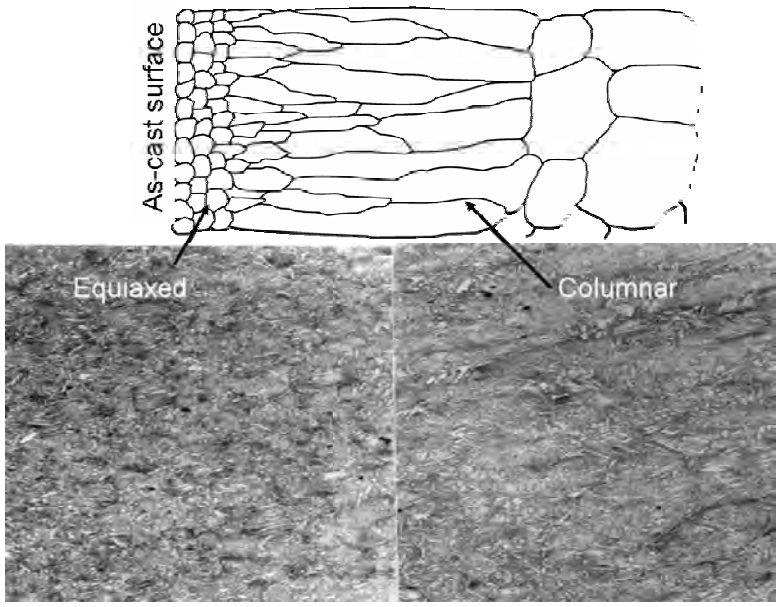

Figure 1.1. *a) Diagram showing standard as-cast grain distribution across the section and b) resultant duplex as-cast microstructure after cooling [GAR 03]*

Duplex as-cast microstructures form during the cooling as a consequence of solid state precipitation of austenite ridges at δ prior grain boundaries and Widmanstätten microstructure inside the δ-ferrite grains, as seen in Figure 1.1b. The result is a distribution of plate-like austenite monocrystals oriented in space almost at random within a polycrystalline ferrite matrix, as seen in Figure 1.2a.

Widmanstätten austenite, like its homonymous ferrite, involves a combination of some diffusive and displacive transformations [OHM 95]. This kind of solid-state transformation imposes an orientation relationship of the type Kurdjumov-Sachs (K-S) or Nishiyama-Wasserman (N-W) between the new austenite and the parent ferrite [SOL 83, IZA 97A, IZA 98], as seen in Figure 1.3, lead to semi-coherent interphase boundaries [POR 92] due to lattice plane correspondences:

$$\text{K-S: } (\mathbf{011})_{\text{Ferrite}} // (\mathbf{111})_{\text{austenite}} \text{ and } [\mathbf{11\bar{1}}]_{\text{Ferrite}} // [\mathbf{10\bar{1}}]_{\text{austenite}}$$

from which N-W can be generated by a rotation of 5.26° about $[011]_{\text{Ferrite}}$.

The austenite ridges at ferrite grain boundaries maintain this same type of orientation relationship with one of the ferrite grains while the other interphase boundary is incoherent.

The isothermal kinetics of the austenite precipitation can be expressed by an Avrami-type equation [SOU 80]. However, under non-isothermal conditions, the cooling rate has a great effect on the morphology and amount of precipitated austenite. Widmanstätten-type growth takes place below 1,000°C [OHM 95] and it has been reported that it can be suppressed in a deformed microstructure when cooling at a rate higher than 2°C/s. However, in the absence of deformation high cooling rates enhance such types of transformation [KAU 93].

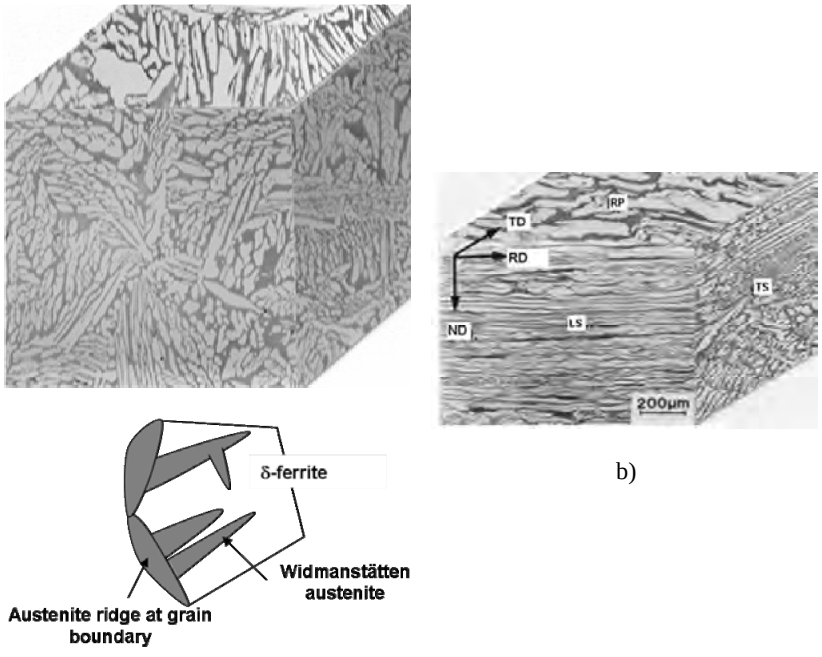

Figure 1.2. *3D reconstruction made from optical images of the a) equiaxed region of as-cast microstructure and diagram showing the austenite morphology and b) wrought microstructure after 77% hot reduction of the same duplex stainless steel. The rolling plane (RP), longitudinal section (LS) and transverse section (TS) [PIÑ 97] are also indicated*

Atamert and King [ATA 92] devised an equation for welding by relating the volume fraction of austenite to the difference between Cr_{eq} and Ni_{eq} and the cooling time between 1,250 and 800°C. Similar approaches or continuous cooling-phase

transformation models allow us to predict the fraction of austenite after continuous/ingot casting [GOB 07]. However, it should be noted that, when the as-cast material is cooled and subsequently reheated at a high temperature before hot working, the relevant microstructure is the actual structure present at this stage and evolving throughout the whole process.

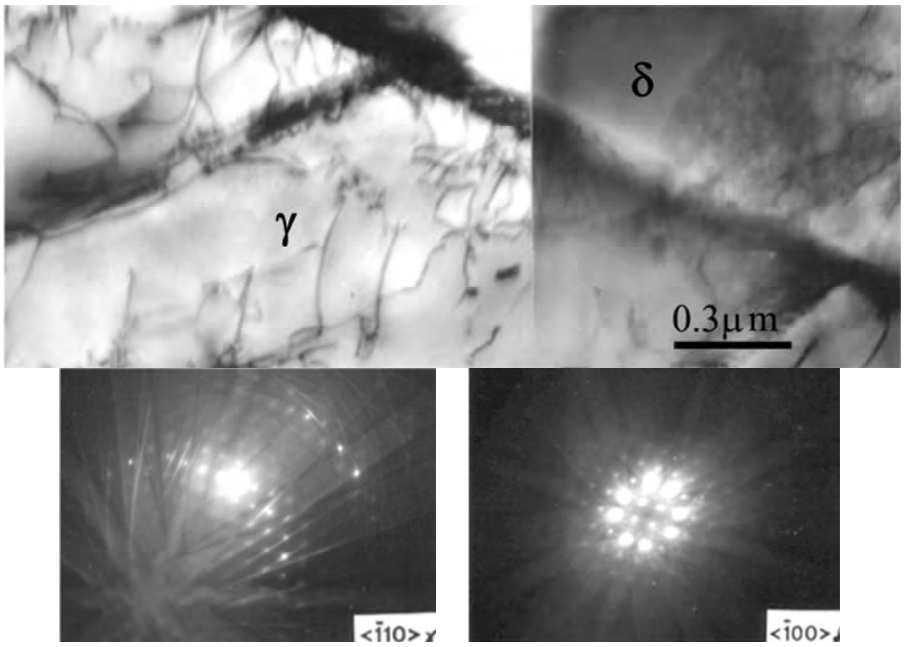

Figure 1.3. *K-S orientation relationship between austenite and parent δ-ferrite in the as-cast microstructure [IZA 99]*

1.3. Microstructural evolution during hot working

The process of industrial hot rolling begins with a reheating stage at around 1,250°C [BOT 96, DUP 02A]. This stage acts as a solution treatment leading to a certain phase balance depending on the steel composition, as seen in Figure 1.4. However, given that an important fraction of austenite remains undissolved at reheating temperatures for commercial compositions, the as-cast microstructure is preserved to some extent. Increasing the holding time has been reported to induce a degree of globulization of the austenite phase [GOB 07].

Hot rolling transforms this microstructure to a planar linear configuration, as illustrated in Figure 1.2b. After a 70% hot rolling reduction, the microstructure has a

fibrous appearance throughout the longitudinal section: long austenite stringers distributed in a ferritic matrix. In other sections, the austenite appears more dispersedly distributed. The size of the austenite stringers and the separation between them vary from region to region. Additionally, at certain locations, some units lose the general alignment and/or present a blocky aspect. Lower rolling reductions produce microstructures that are midway between as-cast and the wrought one shown in Figure 1.2b.

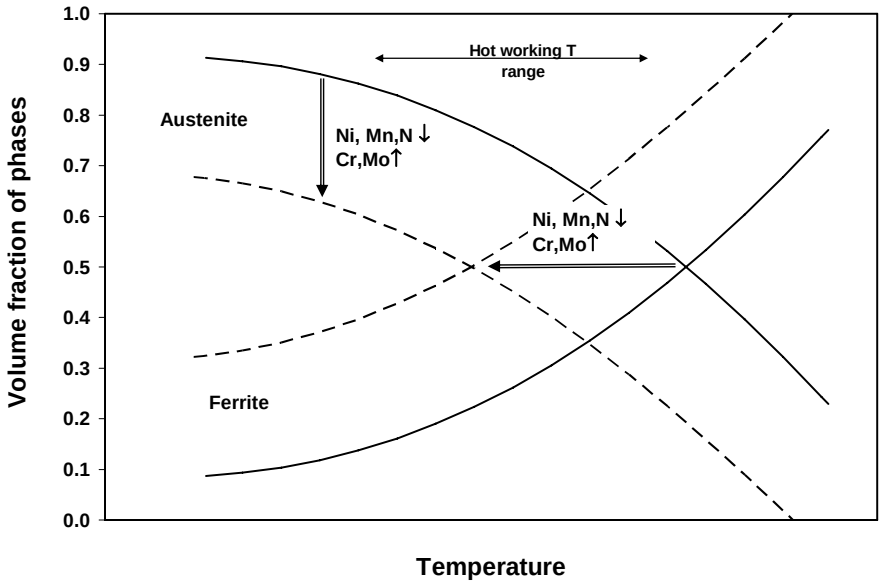

Figure 1.4. *Diagram showing the effect of temperature and steel composition on the phase balance*

Although the development of an oriented microstructure is the most evident microstructural change produced by hot rolling, a detailed analysis of the evolution of a duplex microstructure requires at least three different levels:

– distribution, shape, volume fraction, and phase size;

– interphase boundaries and eventual orientation relationships;

– grain microstructure within each phase and associated textures and/or mesotextures.

1.3.1. *Changes in morphology and distribution of the dispersed γ phase*

The use of marked specimens to perform thermomechanical simulations in the laboratory, followed by microstructural observations [PIÑ 99, PIÑ 00A] enabled the identification of several mechanisms that modify the shape and distribution of the austenite. Some of the mechanisms listed in Figure 1.5 account for plastic deformation, whereas others are the result of strain partitioning, strain localization, some phase accommodation, and microstructural changes towards equilibrium.

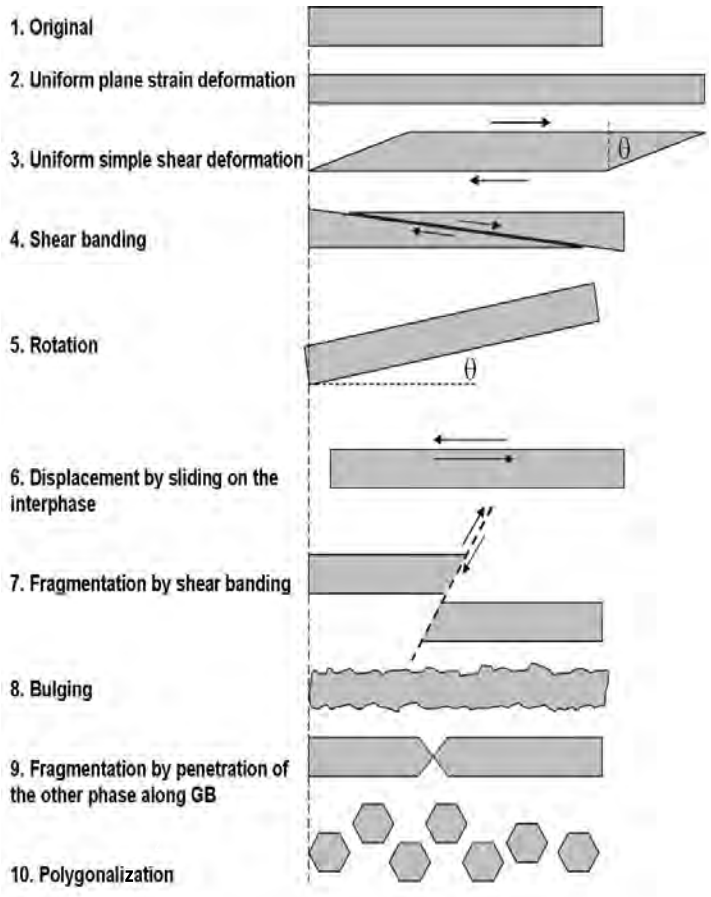

Figure 1.5. *Mechanisms acting on the disperse phase that are responsible for the morphological and distribution changes undergone by the austenite during hot working of austeno-ferritic stainless steels (grain boundary)*

1.3.2. *Plastic deformation*

Plane strain and pure shear are the only mechanisms that account for the uniform plastic deformation of both ferrite and austenite. The microstructural evolution taking place during hot working within both phases in a duplex microstructure can significantly differ from that observed in single-phase materials. This is because, in addition to their respective high (ferrite) and low (austenite) stacking fault energies, other factors, such as relative strength, morphology, and strain partitioning, also play an important role.

Ferrite: Ferritic stainless steels undergo dynamic recovery [SEL 76, MCQ 96, URC 87, EVA 91, LOM 81] and develop a well-defined subgrain microstructure quite early that remains equiaxed and of constant size once a steady state is reached. In an austeno-ferritic microstructure, dynamic recovery is the primary softening mechanism activated in ferrite [IZA 97B, CIZ 06, DEH 07], see subgrains in Figure 1.6. The ferrite substructure becomes more polygonalized at higher deformations and low strain rates. However, the interphase boundary imposes some restrictions and, as the strain increases, ferrite becomes partially entrapped between γ stringers. The thickness of ferrite (distance between γ stringers) decreases with increasing strain, until it becomes comparable with the ferrite subgrain size.

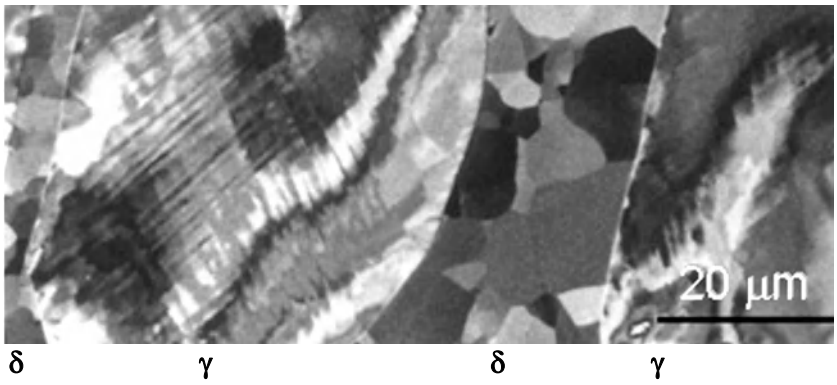

Figure 1.6. *Scanning electron microscopy backscattered electron image of as-cast 2304 duplex stainless steel deformed at 1,000°C and $1s^{-1}$ to a strain $\varepsilon=1$ [IZA 99]*

This is a quite heterogenous process that leads to a bamboo-type structure, as illustrated in Figure 1.7, forming narrow bands of ferrite, limited laterally by the interphase boundaries and subdivided by a mixture of low and high-angle ferrite-ferrite boundaries. The mechanism responsible for the formation of high-angle homophase boundaries in ferrite has been attributed to continuous dynamic

recrystallization [IZA 97B, DEH 07], geometric dynamic recrystallization [EVA 04], or extended dynamic recovery [CIZ 06].

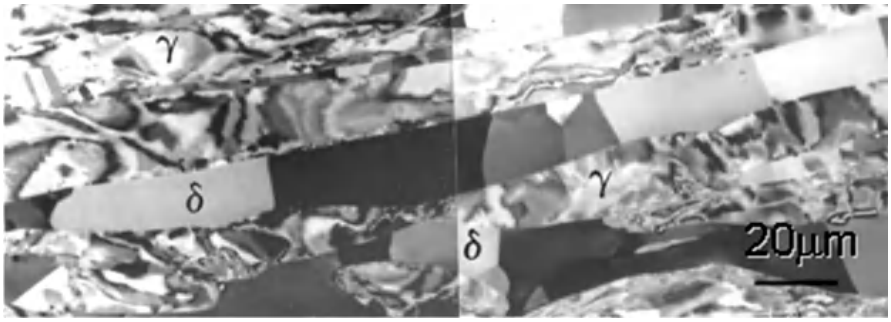

Figure 1.7. *Scanning electron microscopy backscattered electron image showing δ with bamboo-type structure. As-cast 2205 steel deformed by plane strain compression (PSC) at 1,000°C and $1s^{-1}$ to ε=1.2 [IZA 99]*

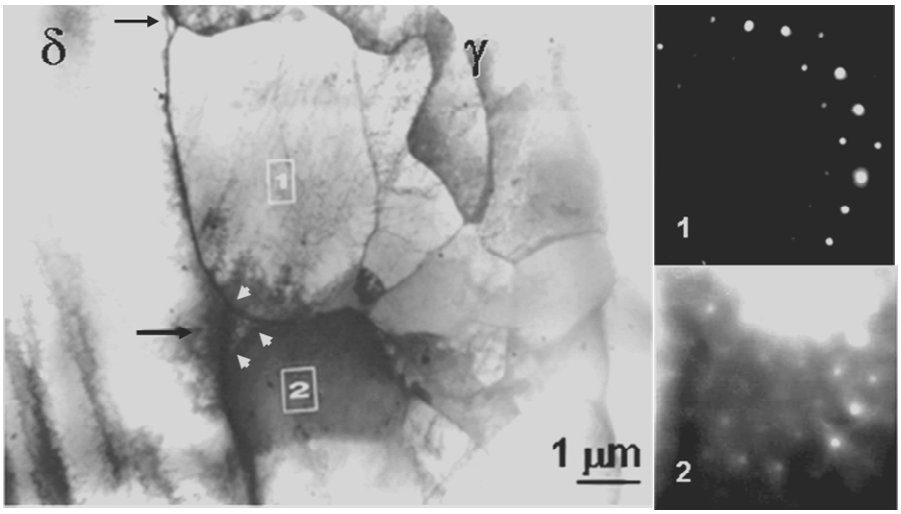

Figure 1.8. *Transmission electron microscopy image and diffraction patterns corresponding to two subgrains in austenite. Steel 2205 deformed at 1,200°C and $1s^{-1}$ to ε=1.76 [IZA 99]*

Austenite: Due to their low stacking fault energy, austenitic steels undergo significant work hardening before the onset of dynamic recrystallization at hot working temperatures [MCQ 75, BAR 79, AHL 82, RYA 90, VEN 94, JOR 05]. The flow curves of the duplex stainless steel frequently exhibit a strain-hardening stage, and then reach a peak followed by some softening [IZA 97A]. Such behavior

has sometimes been attributed to the occurrence of dynamic recrystallization of the austenite. However, microstructural observations prove otherwise. Misorientation analysis shows that, even at high deformation temperatures, dynamic recrystallization does not occur even at strains well beyond the peak [IZA 97A, IZA 98]. Furthermore, when it is observed it reaches negligible volume fractions [DEH 07]. The level of the dynamic recovery in γ-phase increases with rising temperature and decreasing strain rate. In fact, when deforming an austeno-ferritic microstructure at temperatures around 1,000°C, the austenite remains structureless at low strains and progressively develops a tangled microstructure as the strain increases, as illustrated in Figure 1.6.

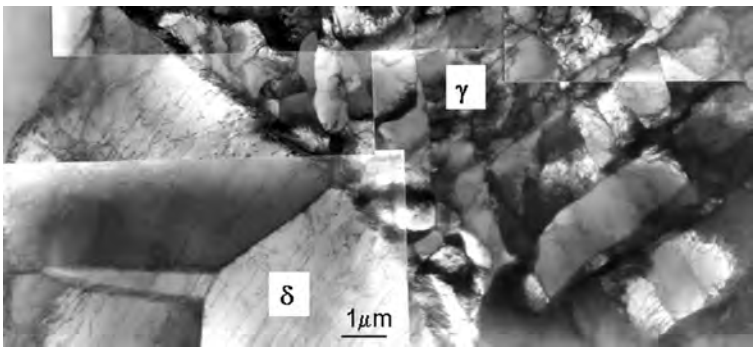

Figure 1.9. *Transmission electron microscopy image showing different degrees of recovery in ferrite and in austenite. Wrought 2304 steel with a globular structure deformed at 1,000°C $1s^{-1}$ to a strain ε=1.4 [IZA 99]*

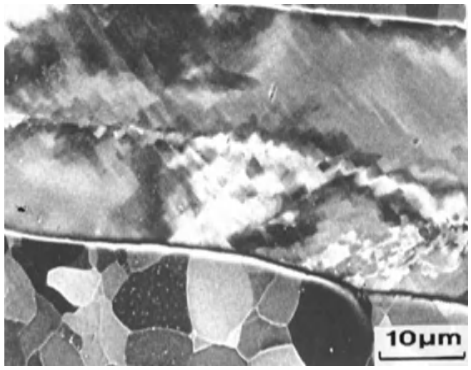

Figure 1.10. *Scanning electron microscopy backscattered electron image showing a micro shear band in austenite. As-cast 2304 steel deformed at 1,000°C and $1s^{-1}$ to a strain ε=1.6 [IZA 99]*

At 1,100°C and above, cells and subgrains form within the austenite. An example of well-developed subgrain within an austenite stringer is shown in the transmission electron microscopy (TEM) image in Figure 1.8. Independently of deformation conditions, the degree of recovery during hot working is always higher in δ than in γ: austenite always exhibits cells/subgrains smaller in size than ferrite subgrains, as depicted in Figure 1.9. The strain distributes quite heterogenously from place to place. A degree of microshear banding is often observed within austenite units at the transition between regions in which different slip systems have activated, as seen in Figure 1.10.

Interphase boundary coherency: The development of high-angle boundaries in ferrite involves some lattice rotations that significantly change the character of the ferrite-austenite interphase boundaries, as illustrated in Figure 1.11 [IZA 99]. The channeling contrast image shows a ferrite unit located between two austenite grains. The central part of ferrite in the image has a zone axis close to $<359>_{\delta}$ and maintains the K-S orientation within a deviation of 3-6° with austenite at each side. The upper part of the ferrite in the image has developed subgrains with a zone axis close to $<111>_{\delta}$. The lattice rotation between the two ferrite zone axes can be described approximately by 24° around a $<122>_{\delta}$ axis. As a result of such rotation the initial K-S orientation relationship present in the as-cast microstructure between ferrite and austenite is lost locally and random interphase boundary segments have developed.

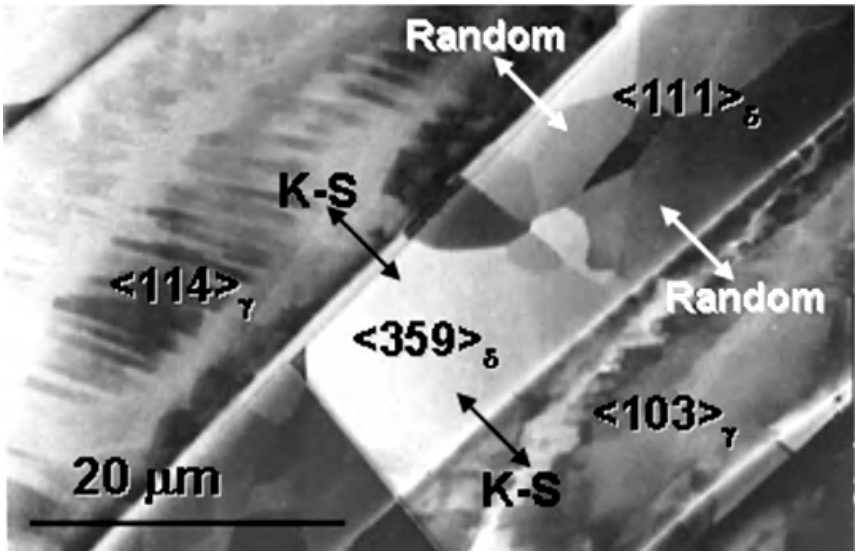

Figure 1.11. *STEM channeling image and crystallographic orientation analysis. As-cast 2304 steel deformed at 1,000°C and $1s^{-1}$ to a strain ε=1.6 [IZA 99]*

Interphase boundary mobility: When deforming at 1,000°C or even at lower temperatures, the interphase boundary remains perfectly flat, as illustrated in Figure 1.11. However, as the deformation temperature increases, the interphases become mobile and bulges develop. The perturbations of the interphase take place on a small scale (fractions of micron) and lead to some interpenetration of both ferrite in austenite or austenite in ferrite. The TEM image in Figure 1.8 illustrates how two γ subgrains bulge (point 8 in Figure 1.5) from austenite and produce a sharp triple point formed by the common subgrain boundary and the interphase (see arrows). This example is a clear exponent of the fact that bulging is not related to dynamic recrystallization in an austeno-ferritic microstructure in contrast to what happens in austenitic steels. Sharp triple points also form at the intersection between the interphase boundary and ferrite-ferrite single-phase grain boundaries, which are almost perpendicular to it, as shown in Figure 1.12 (point 9 in Figure 1.5).

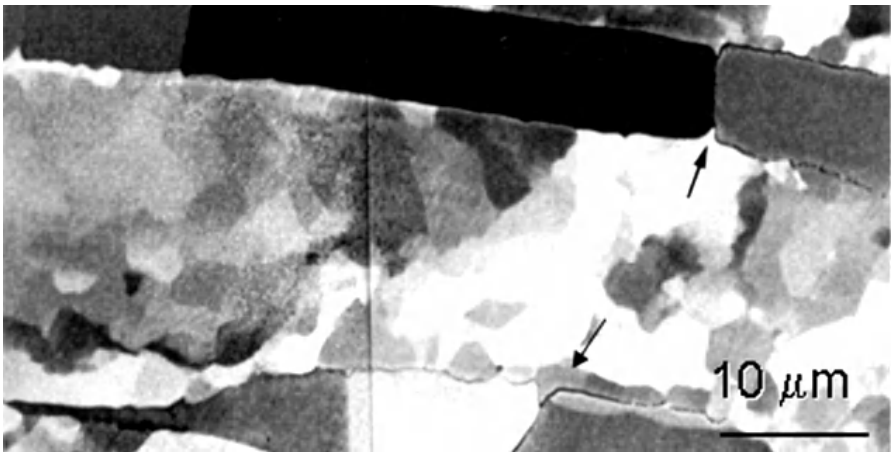

Figure 1.12. *Scanning electron microscopy backscattered electron image showing irregularities at austenite-ferrite interphases. As-cast 2304 steel deformed at 1,200°C and $1s^{-1}$ to a strain ε=1.6 [IZA 99]*

1.3.3. *Rotation*

Apart from the lattice rotations taking place on a substructural scale, such as those illustrated in Figure 1.12, marked specimens reveal macroscopic phase rotations (point 5 in Figure 1.5). The marks in Figure 1.13 clearly illustrate that the austenite in the middle of the image has rotated as a whole within the ferrite matrix, which has simultaneously experienced intense local shearing [PIÑ 03].

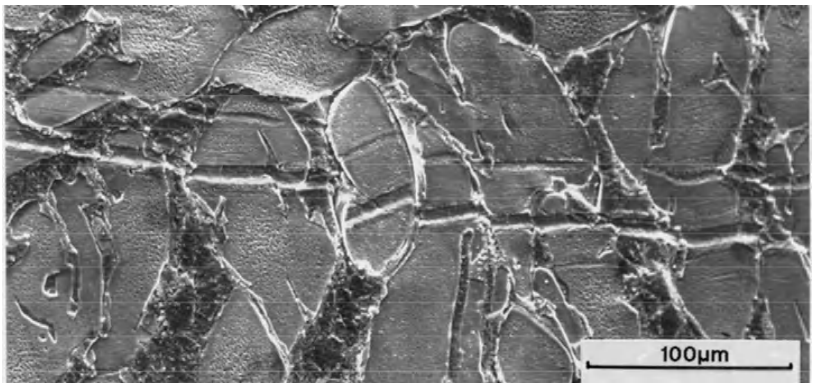

Figure 1.13. *SEM image showing the rotation of an austenite unit outlined by the displacement of the scratch markers at the specimen surface. As-cast material deformed by torsion at 1,000°C and 1s^{-1} to a strain of 1.6 [PIÑ 03]*

1.3.4. *Interphase boundary sliding*

Sliding involves the translation of a grain with respect to another by a shear movement parallel to their common boundary [ALD 67, MUR 75] (point 6 in Figure 1.5). Sliding has been identified in hot-worked, as-cast and wrought duplex stainless specimens, aided by metallographic characterization after deformation of pre-polished and marked specimens [PIÑ 00A].

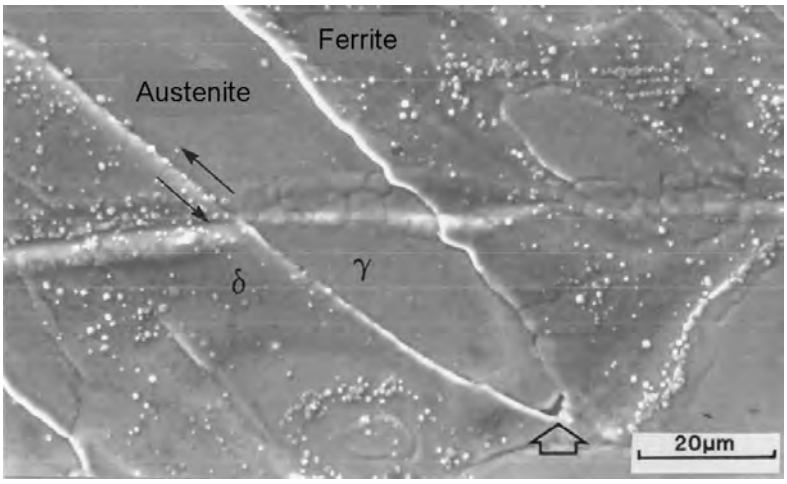

Figure 1.14. *A clear example of interphase boundary sliding leading to some damage formation [PIÑ 99]*

The SEM image in Figure 1.14 is a clear example of this phenomenon. It shows the sliding displacement of the scratch marker on one of the austenite-ferrite interphases and some resultant damage nucleated at the austenite block tip. Sliding concentrates at the interphase but does not happen at α-α or γ-γ boundaries. This finding supports earlier results on ferrite-austenite diffusion-bonded couples loaded parallel to the longitudinal axis of the interface, showing that sliding is easier (higher sliding rate) on interphase than on single-phase boundaries [HAS 94].

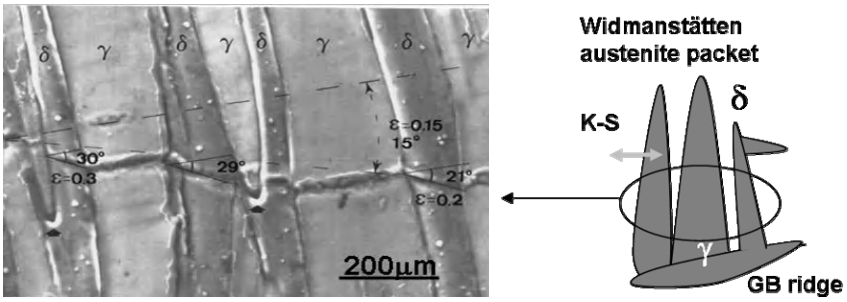

a) as-cast microstructure

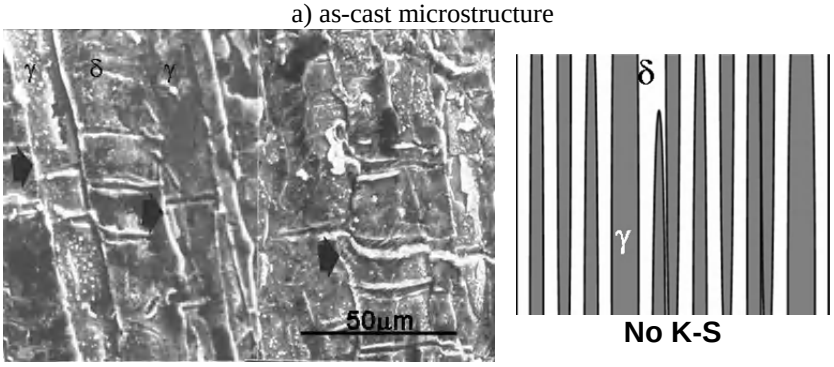

b) wrought material

Figure 1.15. *SEM micrographs showing the surfaces of two marked pre-polished specimen surfaces: a) δ/γ packet in the as-cast and b) wrought 77% hot-rolled 2304 steel. Deformation by torsion at 1,000°C and 1 s^{-1} to a strain of about 0.17 [PIÑ 00A]*

The ease of sliding depends on the character of the boundary [SHE 84]: coherent and semi-coherent interfaces being less apt for sliding than incoherent boundaries [MUR 75]. This can be extended to hot-worked duplex stainless steels for which the crystallographic character of the interphase has been demonstrated to be a key parameter in controlling their sliding ability [PIÑ 00A]. Deformation applied to marked as-cast and wrought duplex specimens has shown that sliding at the interface between ferrite and austenite is not possible while the two lattices at each side share a K-S type orientation relationship. In a Widmanstätten microstructure, the scratch

markers are slightly deflected at each interphase boundary, but do not lose continuity, as seen in Figure 1.15a. On the contrary, in a wrought, hot-rolled microstructure, such as that seen in Figure 1.15b, the scratch markers prove the occurrence of intense sliding. This last scenario produces relative displacements of the marks over several microns at interphase boundaries.

1.3.5. *Shear banding*

Laboratory testing, modeling, and observation of industrially deformed austeno-ferritic stainless steels have shown that these materials have a high tendency towards strain localization and shear band formation. Finite element modeling applied to duplex microstructures deformed under plane strain compression (PSC) shows the development of shear stresses not present in a single-phase material [TEL 97] and microstructural predictions in agreement with experiment, as can be seen when Figure 1.16 is compared with the micrographs shown in Figure 1.17. This micrograph has been obtained in the central part of a region below the tools and relatively close to the surface of a specimen deformed by PSC. The application of microgrid techniques has also revealed that shear banding occurs during PSC of duplex structures with equiaxed ferrite and austenite phase morphology [HER 06]. The presence of two phases with significantly different mechanical strengths can be considered here, as the primary cause for shear band formation, which is, as mentioned, not exclusive to laboratory tests, but is also observed in hot-rolled materials [IZA 07].

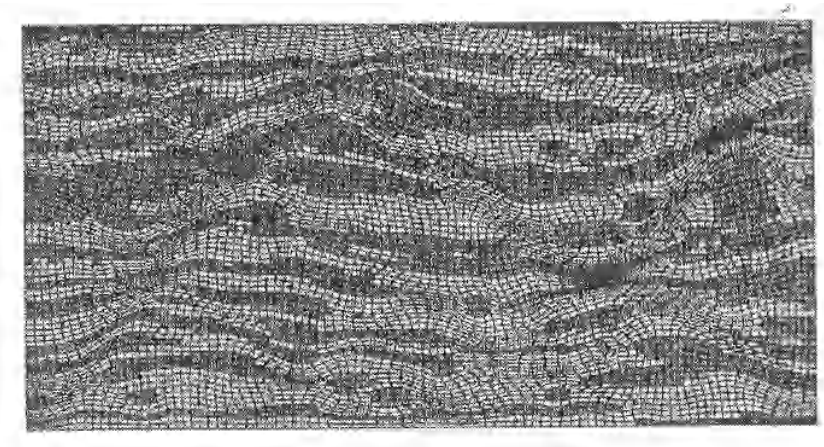

Figure 1.16. *Deformed mesh obtained via finite element modeling after codification of an actual wrought, hot-rolled microstructure [TEL 97]*

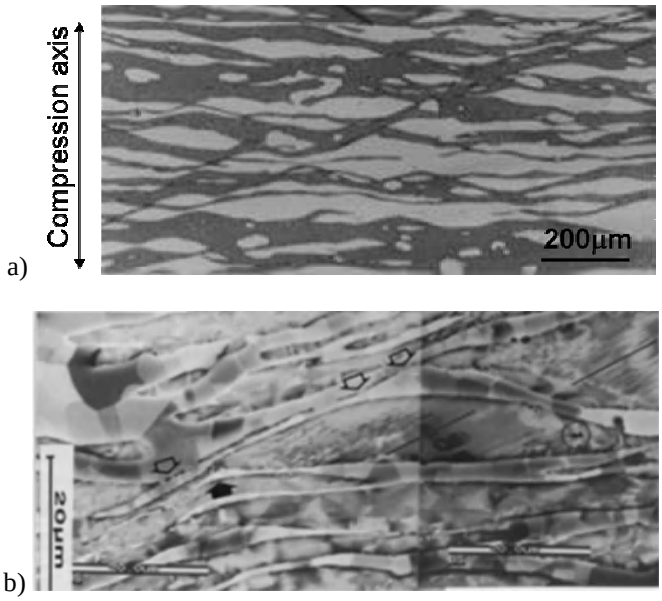

Figure 1.17. *a) Optical and b) backscattered electron images showing the formation of shear bands in a plane strain compressed specimen deformed at 915°C and a strain rate of $1s^{-1}$ to ε=1. Wrought, hot-rolled 2304 steel [PIÑ 99]*

1.3.6. *Fragmentation*

Some microstructural fragmentation has been observed to take place in combination with deformation at both high and low deformation temperatures. However, the mechanism behind this is essentially different in each case [IZA 99]. At around 1,000°C and below, shear bands crossing the interphase boundary can produce some fragmentation of the austenite by shearing, as seen in Figure 1.17a (point 7 in Figure 1.5).

At deformation temperatures above 1,100°C, interphase mobility is high enough to produce some bulging and some local scale rearrangements in the microstructure. For example, deformation at high temperatures produces some fragmentation of the initial microstructure through the following mechanisms: interphase boundary bulging, formation of sharp triple points at the intersection between the interphase boundary and both γ-γ boundaries and δ-δ grain boundaries of bamboo-type ferrite, as seen in Figure 1.12. Bulging out of austenite into ferrite and some penetration of ferrite through austenite single-phase boundaries lead, at the limit, to fragmentation of austenite stringers into individual crystallites, as depicted in Figure 1.18 (points 9 and 10 in Figure 1.5).

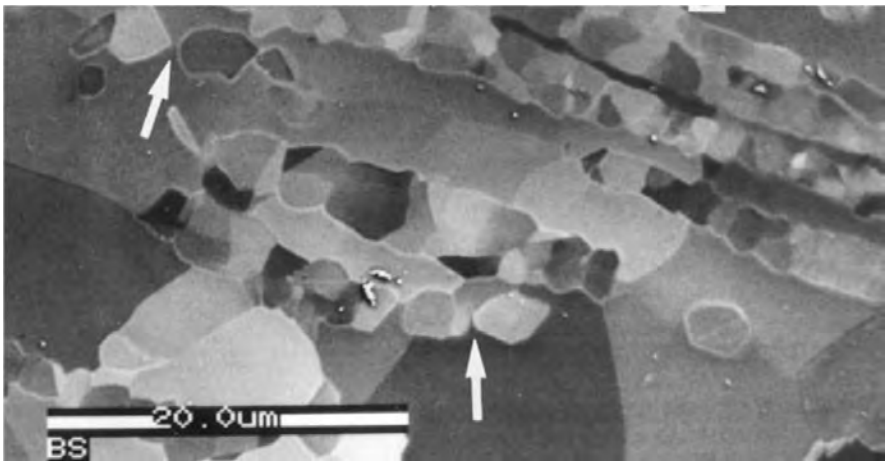

Figure 1.18. *SEM channeling image showing bulging of austenite and its fragmentation into individual crystallites. As-cast 2205 steel deformed at 1,200°C and $1s^{-1}$ to $\varepsilon = 1.75$ [IZA 99]*

The fragmentation taking place at high temperature requires both deformation and thermal activation and takes place both dynamically during deformation and statically during holding at high temperatures. It is driven by the tendency to an equilibrium polygonal or microduplex microstructure, minimizing the total interfacial energy. However, reaching equilibrium microstructures requires extensive periods of annealing [KEI 03]. Fragmentation and, at the limit, polygonalization of the phases produced during hot working is very locally and heterogenously distributed. However, it is enhanced to some extent by multipass sequences in which deformation and holding stages alternate at high temperatures.

1.4. Mechanical behavior under hot working

Any attempt aimed at producing models applicable to hot working requires constitutive equations relating stress to deformation conditions (temperature and strain rate) as a function of the composition. Research and modeling efforts devoted to stainless steels have mainly concentrated on austenitic compositions, while quantitative data are far scarcer concerning ferritic and duplex steels.

Alongside the normal difficulties encountered when working with single-phase materials, austeno-ferritic microstructures, problems associated with the presence of two phases with different mechanical behaviors and a broad range of possible microstructural arrangements also occur (section 1.3).

1.4.1. *Constitutive equations*

The application of equation [JON 69]:

$$\dot{\varepsilon}\exp\left(\frac{Q_{Hw}}{RT}\right) = A[\sinh(\alpha\sigma)]^n \qquad [1.1]$$

(with $\dot{\varepsilon}$ being the strain rate, σ the stress, Q_{HW} the hot working activation energy and α and n constants) to the data obtained from hot deformation tests allows for the estimation of the effect of temperature and strain rate on the stress required to deform the material.

Ref.	n	α	A (s)	Q_{HW} (kJ/mol)	Material	Def. mode
[IZA 98]	4.2	0.0139	$7.12\ 10^{16}$	450	23Cr-4.8Ni-0.22Mo-0.095N: 77% hot rolled	PSC
	4	0.0143	$6.2\ 10^{21}$	578		T
[BOT 96, PAU 93]	3.85	0.008	$3.54\ 10^{14}$	380	22Cr-5.6Ni-3Mo-0.136N : As-cast	PSC
[CAB 03]	6.9	0.009	$1,5\ 10^{22}$	569	22Cr-5.5Ni-3Mo-0.13N: bar	UC
	4	0.007	$2.3\ 10^{16}$	438	25Cr-7Ni-3.8Mo-0.26N : bar	
[DUP 02C]				425	22.6 Cr-5.9Ni-3.1Mo-0.16N: 80% hot rolled	T
[EVA 04]	5.63	0.012	$1.0\ 10^{20}$	525	23Cr-4Ni-0.29Mo-0.1N: hot rolled	T
	3.8		$1.0\ 10^{15}$	394	22Cr-5.5Ni-3Mo-0.12N: hot rolled	
[VER 91]	4.18	0.01	$3.95\ 10^{15}$	400	27.6Cr-4.25Ni-1.3 Mo-0.14N : bar	T
[CAR 01]	3.77	0.0115	$2.68\ 10^{16}$	447	25Cr-7Ni-3.7Mo-0.17N : bar	T
[BAL 00]	4.07	0.015	$2.04\ 10^{19}$	488	26.5Cr-4.9Ni-1.63Mo-0.04N	T
[ROB 07]	4.9	0.014	8.410^{14}	430	22Cr-5.3Ni-3.43Mo-0.168N: forged bar	Ten
[PAU 93]	5,8	0.0091	$3.19\ 10^{15}$	450	Austenitic-304*	PSC
[SEL 76]	3,1	0,0115		261	Ferritic	PSC

*more data in [RYA 90]; PSC=plane strain compression; T=Torsion; UC=Uniaxial compression, Ten=tension.

Table 1.1. *Values reported by different authors for the significant parameters in equation [1.1]*

The results reported by different authors for the coefficients in this equation are shown in Table 1.1. The activations energies reported in the 578-380 kJ/mol range depend on the steel and are not directly comparable because they correspond to different α values. However, they fall within the composition-dependent energy range reported for austenitic steels [RYA 90].

1.4.2. *Fraction of phases and strength ratio*

The graph in Figure 1.19 shows the evolution of the microhardness of ferrite and austenite phases with temperature.

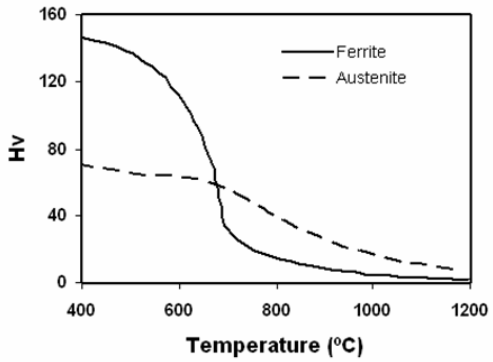

Figure 1.19. *Microhardness of the phases as a function of temperature in ferrite-austenite bicrystals [HAS 94]*

Within the hot working temperature range, ferritic stainless steels are between two and three times softer than austenitic [SHE 87, EVA 04]. However, the actual strength ratio in austeno-ferritic steels depends on the steel composition and element partitioning.

The fraction of austenite is a strong function of composition and temperature, as illustrated in Figure 1.4, but also depends on the history of the material. The holding time at reheating temperatures before deformation can have a crucial effect on the phase balance [BAL 00]. In consequence, when analyzing the data in Table 1.1, the fact that temperature dependence of hot strength includes the variation of phase balance should be taken into consideration. In fact, Al-Jouni and Sellars [ALJ 03] showed that the activation energy for deformation and the hot strength of steels with duplex microstructures vary systematically with the δ-ferrite content, but not simply as a weighted average of the values for single-phase steels.

1.4.3. *Composition and element partitioning*

Changes in composition modify the hot strength of both austenitic and ferritic stainless steels through solute strengthening. The composition also contributes to the hot strength of austeno-ferritic steels in a more complex way. Element partitioning takes place and, in addition to the intrinsic contribution of the solutes, the fact that composition also modifies phase balance must be taken into account.

McQueen and Ryan analyzed the effect of the solute content on the hot strength of austenitic stainless steels, [MCQ 91, MCQ 93, MCQ 02] concluding that equation [1.1] is widely suitable to relate the peak stress to the deformation temperature and strain rate with average n values of 4.3 and Q_{HW}(kJ/mol) = 13.5x(total metallic solute). These authors also deduced a logarithmic linear relation between the peak stress and the weight percent of metallic solute content (in the range 26.9 to 37.9%) leading to a slope of 0.625 for a broad range of deformation conditions. Peak stress rises with increasing chromium (Cr) and molybdenum (Mo) content, but nickel (Ni) causes little strengthening. Nitrogen (N) has been reported to induce a planar dislocation structure detrimental to the cell or subgrain substructure and also to contribute to the hot strength by about 25 MPa by 0.1% of N in a 18% Cr 9% Ni austenitic steel [TEN 01]. This last relation between flow stress and N is maintained independently of the temperature and strain rate.

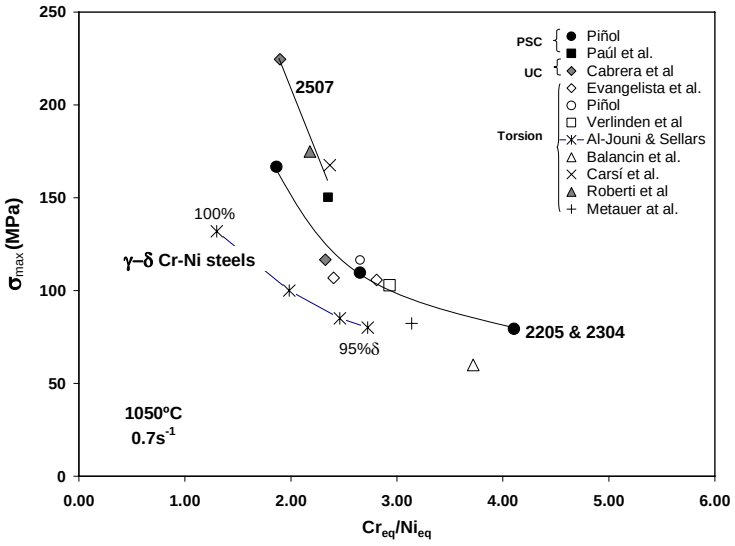

Figure 1.20. *Maximum stress calculated for the indicated deformation temperature and strain rate from equation [1.1] and the data in Table 1.1, as a function of the relation between* $Cr_{eq}=Cr+Mo+1.5Si$ *and* $Ni_{eq}=Ni+30(N+C)+0.5Mn$

For ferritic stainless steels, the addition of about 0.9% Mo increases the stress between 10 and 20 MPa [MCQ 02]. The increase of about 5.5% Cr when passing from 409 to 430 ferritic stainless steels, leads to an increase of around 10 to 30 MPa. Both contributions depend inversely on deformation temperature and, consequently, cannot be entirely attributed to solution strengthening.

The effect of N on the hot strength of duplex stainless steels has been estimated in 27 MPa for each 0.1 wt% of N that can be attributed to both increasing of the volume fraction of austenite and solution strengthening [VER 91].

Equation [1.1] and the data in Table 1.1 can be used to compare the stress levels in different austeno-ferritic steels. Selecting a temperature of 1,050°C and a strain rate of $0.7s^{-1}$, yields results that can be compared to those obtained from Cr-Ni steels with a different phase balance [ALJ 03]. The maximum stress has been plotted as a function of the Cr_{eq}:Ni_{eq} ratio in Figure 1.20. Three different groups of data can be differentiated: highest stresses belong to superduplex compositions, followed by 2205 and 2304 duplex, and finally the softest grades correspond to laboratory Cr-Ni alloys. Within each group of steels, the stress decreases systematically with an increasing Cr_{eq} to Ni_{eq} ratio, due partially to the decrease of the volume fraction of austenite and to differences in chemical phase composition.

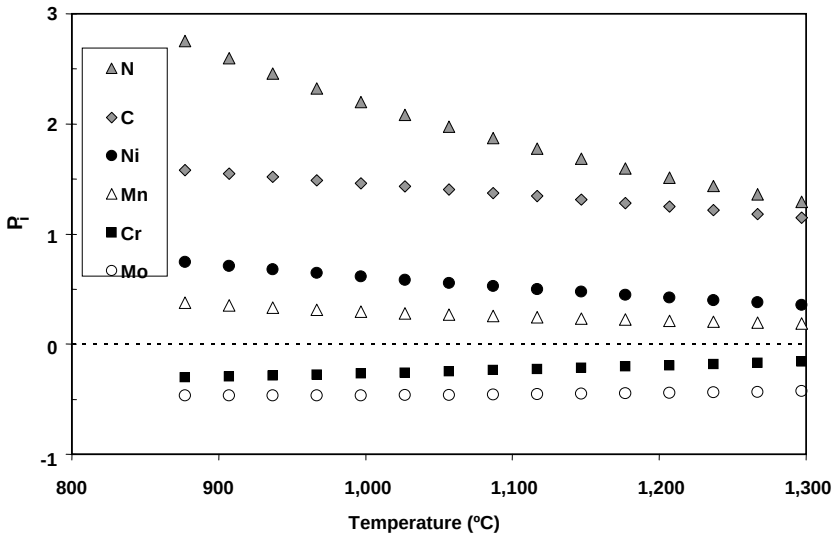

Figure 1.21. *Mass-percentage natural partitioning coefficient, P_i, defined [COR 91] as the natural logarithm of the ratio between the element concentrations in austenite and in ferrite, plotted as a function of temperature. Predictions made using ThermoCalc under equilibrium conditions*

The temperature variation of element partitioning between ferrite and austenite estimated while assuming equilibrium conditions is shown in Figure 1.21 for a 2304 duplex stainless steel. At both extremes, Mo is the element that exhibits the highest partitioning to ferrite, while carbon (C) and N exhibit the lowest. Mo concentration decreases, but N and Ni increase in both ferrite and austenite with increasing temperature. At the same time, the concentration of Cr remains constant in austenite, but decreases in ferrite. For a given composition, the concentration of metallic elements in austenite remains almost independent of temperature. In agreement with this, the main temperature variation of austenite strength could be attributed to N and C. In ferrite, the increase of Cr and Mo content with decreasing temperature should produce some strengthening, which partially compensates the softening associated with the decrease in N.

Changes in element partitioning with varying temperature contribute to differences in hot deformation behavior between the start and the end of hot rolling. The higher the temperature, the more uniform the element partitioning is between the phases [COR 91, ATA 91, CHE 01]. Nevertheless, actual conditions during processing can significantly deviate from equilibrium. Such deviations can affect all the material or happen on a local scale. In fact, microanalyses performed by TEM reveal some local concentration gradients in the neighborhood of the ferrite-austenite interphase boundaries [IZA 99].

1.4.4. *The two-phase rule*

The mechanical behavior of an alloy constituted by two ductile phases depends on their morphology and distribution, mechanical properties, and the interaction between them. The macroscopic stress (σ_{Mix}) and strain (ε_{Mix}) of a duplex microstructure, as illustrated in Figure 1.22, can be expressed as a function of the stresses σ_1 and σ_2, strains ε_1 and ε_2 in each of the two phases and the volume fraction, f_1, of the softest one according to [VER 92]:

$$\begin{cases} \sigma_{Mix} = f_1\sigma_1(\varepsilon_1) + (1 - f_1)\ \sigma_2(\varepsilon_2) \\ \varepsilon_{Mix} = f_1\ \varepsilon_1 + (1 - f_1)\ \varepsilon_2 \end{cases} \quad [1.2]$$

Simple solutions to the above equation system can only be obtained for both ideal phase distributions with respect to the direction of material flow shown in Figure 1.23. When phases are distributed like continuous fibers parallel to the direction of tensile stress, the strain is distributed uniformly and the contribution of ferrite and austenite to the overall stress is proportional to their volume fraction.

Other configurations concerning continuous fibers or disperse hard phase in a soft matrix involve some strain partitioning.

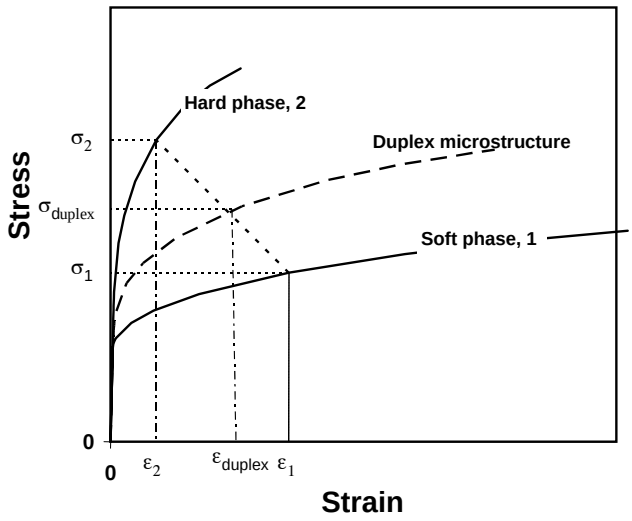

Figure 1.22. *Stress and strain partitioning among the phases and resultant macroscopic σ_{Mix} and ε_{Mix} for a duplex microstructure [TOM 92]*

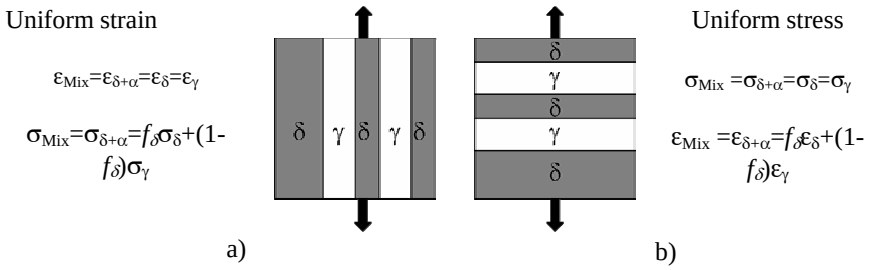

Figure 1.23. *Representation of particular solutions to the law of mixtures when applied to an idealized, wrought, rolled austeno-ferritic microstructure [VER 92]*

1.4.5. *Strain partitioning*

Some examples taken from different authors demonstrate the occurrence of strain partitioning in hot-worked duplex microstructures. Evidence of strain partitioning can be found in the micrograph in Figure 1.24, which was taken of as-cast steel after hot deformation to a strain ε=0.4. Ferrite shows a well-developed

subgrain microstructure, but the majority of austenite units appear to be structureless, with the exception of a few planar dislocation configurations [IZA 97A].

Wrought microstructures behave differently, depending on their particular phase configuration. Al-Jouni and Sellars [ALJ 03] obtained rods with an equiaxed austeno-ferritic microstructure after extrusion of as-cast material and heat treatments. Subsequent rolling in a direction parallel to the initial extrusion axis produces almost uniform strain, but which is less than the macroscopic strain.

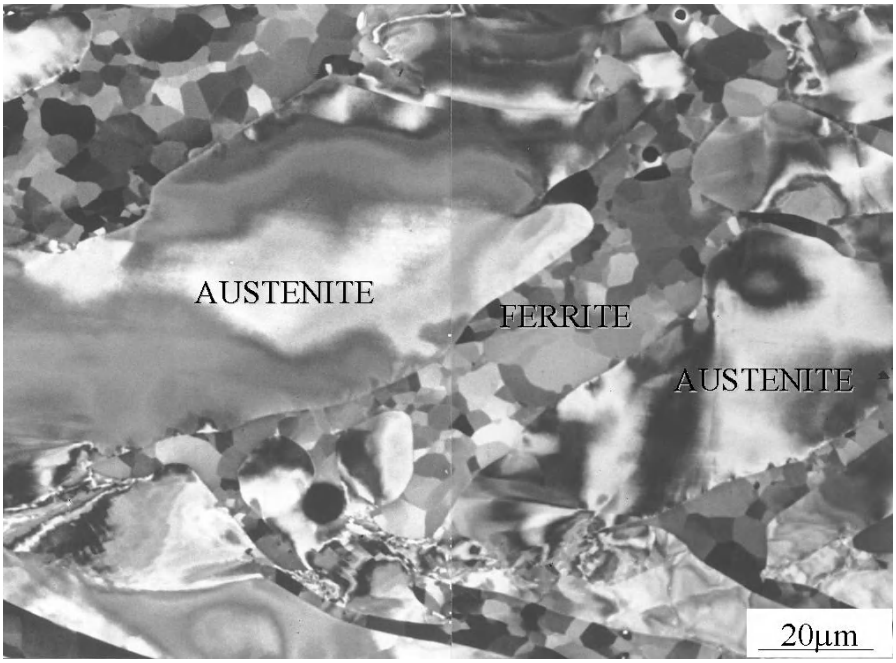

Figure 1.24. *SEM backscattered electron image. As-cast duplex steel deformed at 1,000°C and 1 s^{-1} to a strain of 0.4 [IZA 97A]*

In the research conducted by Duprez *et al.* [DUP 02B], laboratory hot rolling was performed in a direction normal to the original industrial rolling direction. Due to this 90° rotation, the austenite appeared in the form of discrete and almost equiaxed blocks in the longitudinal section before the last rolling. Under these conditions, distinct strain partitioning was observed, with the austenite accommodating only a fraction of the applied strain.

Piñol-Juez *et al.* [PIÑ 97, PIÑ 99] applied PSC to hot deform two previously hot-rolled duplex stainless steels (75 and 50% γ) with well-defined planar-linear distribution of the phases (f-b). The load was applied perpendicularly to the original rolling plane and the material flow was parallel to the original rolling direction, as illustrated in Figure 1.25. Under these conditions, the strain taken by each phase is approximately the same (uniform plastic strain), though it was at least 20% lower than macroscopic strain.

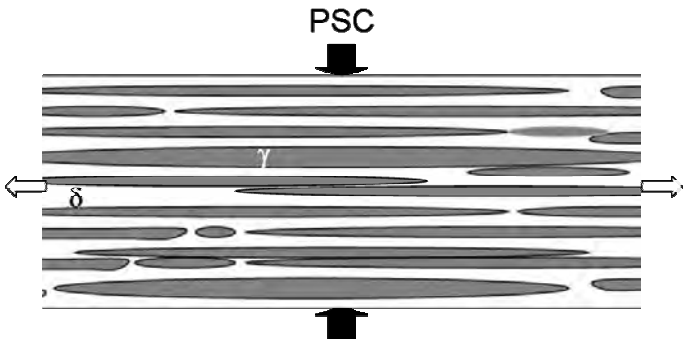

Figure 1.25. *Schematic representation of the PSC performed on a wrought duplex microstructure in [PIÑ 97, PIÑ 99]*

These two last examples clearly show that similar wrought microstructures with elongated distribution of the phases, subjected to comparable deformation modes (hot rolling or PSC) behave quite differently depending on the relative orientation of the phases with respect to the direction of flow during deformation. With a configuration like that in Figure 1.25, the material must flow parallel to the elongated "austenite fibers," as schematized in Figure 1.23a, which leads to uniform strain. However, if the direction of compression is rotated 90°, the material approaches the uniform stress configuration, as illustrated in Figure 1.23b, which matches the observed strain partitioning in [DUP 02B].

Duplex microstructures can behave differently with respect to strain partitioning, but various authors unanimously agree on the fact that the plane strain taken on by the phases is lower than the macroscopic strain. This means that other mechanisms, such as some of those listed in Figure 1.5, account for part of the macroscopic deformation.

1.4.6. *Deformation mode and phase morphology*

The mechanical behavior of an austeno-ferritic microstructure exhibits a high degree of anisotropy. The stress-stain curves fall between those corresponding to ferritic and austenitic stainless steels, but their shape and the stress levels depend on both the deformation mode and the phase morphology and orientation, as can be seen in Figure 1.26. These curves belong to the same 2304 duplex stainless as-cast and wrought, hot-rolled microstructures deformed in PSC and pure shear mode at 1,000°C and 1 s^{-1}.

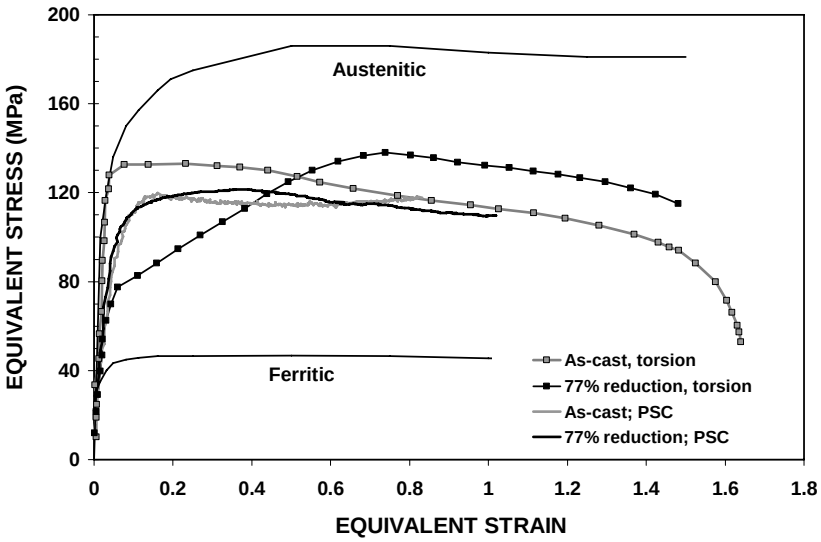

Figure 1.26. *Effect on the stress-strain curves of the prior morphology of the phases and of the deformation mode [IZA 98] for 2304 steel. Calculated curves for ferritic and austenitic 304 steels are also shown for comparison [SEL 76, BAR 79]. Deformation temperature=1,000°C and strain rate=1 s^{-1}*

Single-phase as-cast and wrought microstructures tend to behave differently, but the differences are far more pronounced in austeno-ferritic microstructures and low strains. As-cast material deformed under PSC produces a flow curve with a peak strain of about 0.17, whereas the peaks occurs even earlier under pure shear (torsion mode; $\varepsilon_p < 0.1$). However, it reaches higher stress values under torsion and is followed by a more pronounced continuous decrease of stress than during compression. The two curves converge for equivalent strains $\varepsilon \cong 1$ [PIÑ 97]. The flow curves of as-cast and wrought microstructures are quite similar when obtained

under PSC. Nevertheless, the curves for a wrought, hot-rolled material deformed in pure shear mode are extremely sensitive to the phase morphology.

1.4.7. *Axially oriented microstructures deformed in pure shear*

Wrought, hot-rolled, duplex austenite-ferrite microstructures exhibit a planar-linear phase configuration that, when deformed in pure shear mode, behave quite differently depending on the degree of phase alignment with respect to the torsion axis, as illustrated in Figure 1.27. In particular, when the two-phase microstructure is aligned with the torsion axis (specimens machined with the axial direction lying on the rolling plane parallel to the rolling direction) [IZA 98, PIÑ 99, DUP 02C] the shear stress-shear strain curves show peculiar slope changes. Very different two-phase materials with an axially oriented lamellar structure also show this type of particular behavior when deformed at room temperature [GIL 08].

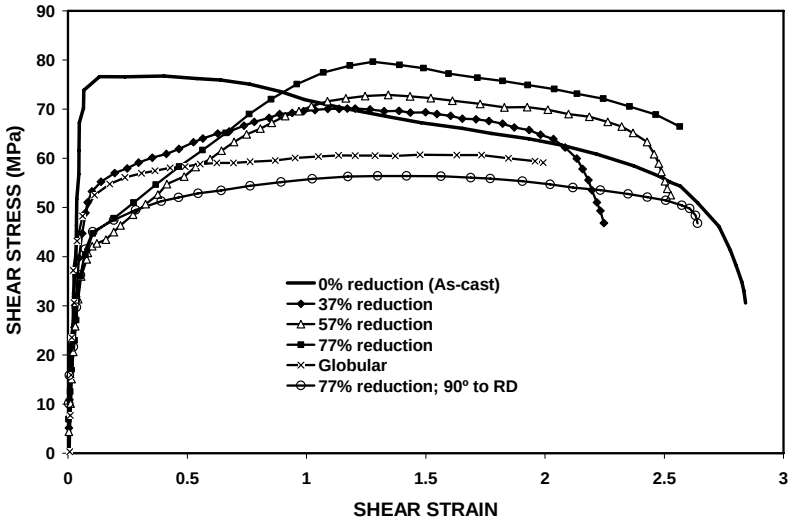

Figure 1.27. *Shear stress-shear strain curves obtained by torsion at 1,000°C, $1s^{-1}$ on wrought, hot-rolled, duplex stainless steels with different levels of hot rolling reductions with the torsion axis parallel to RD or perpendicular to RD and as-cast and globular microstructures [IZA 98, PIÑ 99]*

The effect of hot-rolling reduction and hence the effect of the degree of phase alignment on shear stress-strain curves is shown in Figure 1.27, for 37%, 57% and 77% reductions. A parabolic strain hardening is observed to reach a small plateau at low strains, followed by a peaking high hardening stage (constant slope of a near-

yield stress value). Yielding occurs at lower stress values for higher reductions and peak stress increases progressively up to a 77% reduction. Ductility also increases with reduction percentage, therefore with alignment of microstructure. The peak happens for equivalent shear strains between 1 and 1.3, which gives way to some softening before final fracture.

The same trend is observed when other deformation temperatures or strain rates are applied [IZA 97A]. The increase of the deformation temperature produces a decrease of the slope of the linear part of the curve (constant hardening rate), while the increase of the phase aspect ratios (increase of the rolling reduction) has the opposite effect [PIÑ 99]. This particular behavior is absent from the torsion test of the as-cast or globularized (austenite particles embedded in ferrite) non-oriented duplex structures and from torsion tests of the hot-rolled structure performed with the axis normal to the rolling plane.

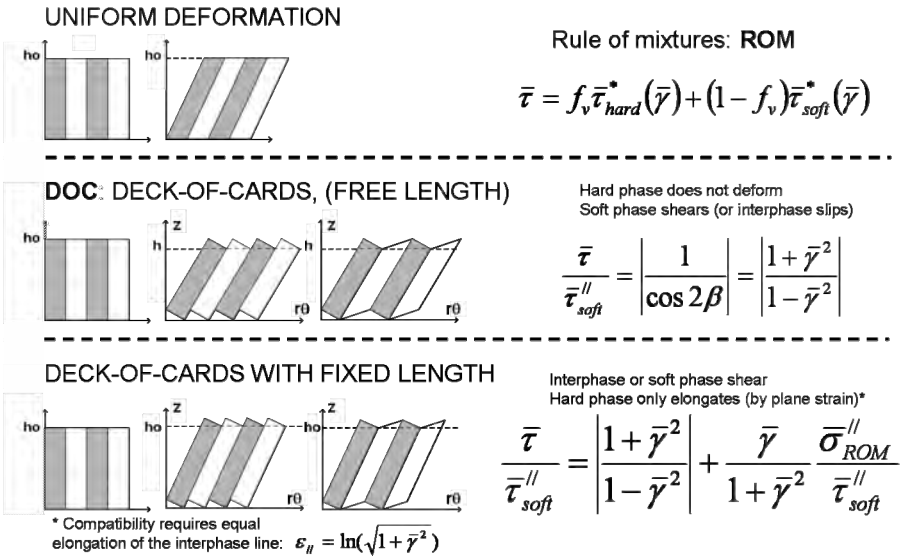

Figure 1.28. *Summary of the admissible deformation fields for macroscopic simple shear of axially oriented two-phase material: uniform deformation (iso-strain); deck-of-cards mode of shear deformation for free and fixed-length torsion. For these two last cases there are two possibilities: 1) only interphase sliding, both phases remaining undeformed and 2) uniform shear of the soft phase, parallel to the interphase [GIL 08]*

The above facts can only attribute to the axial alignment of the microstructure with the direction of maximum shear stress [PIÑ 97]. Compatible co-deformation without the delamination of lamellar structures imposes equal longitudinal

deformation components in the current lamellar plane. Because of the orientation relationship of the microstructure and the simple shear geometry of the torsion test, the structure will start to deform in a deck-of-cards mode at the elastic limit, as shown in Figure 1.28. This will involve plastic yielding of the softest phase or alternatively interfacial shear, if this mode is the softest one under the actual strain rate and temperature conditions. These solutions are addressed to perfectly continuous oriented microstructures and are only approximate for high aspect-ratio discontinuous lamellar structure like that of the hot-rolled duplex stainless steels, as illustrated in Figure 1.2b.

1.5. Static softening

Both static and dynamic softening processes have been extensively studied in austenitic and ferritic stainless steels [BAR 79, LOM 81, RYA 90, EVA 91, EVA 04]. Static softening after hot deformation of the duplex stainless steel can be mainly attributed to the static recovery of the ferrite [IZA 97B] and to the static recrystallization of the austenite [PIÑ 95]. In general, the recrystallization of the ferrite requires more time. The micrograph in Figure 1.29 shows well-recovered ferrite and partially recrystallized austenite.

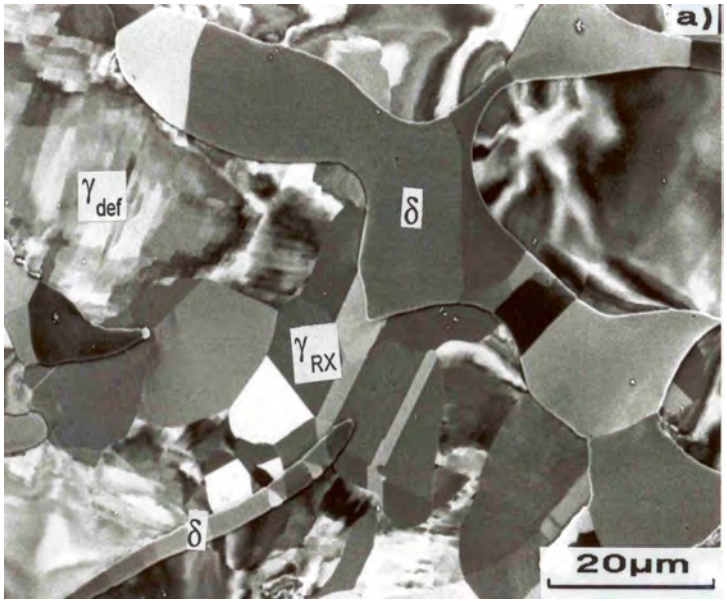

Figure 1.29. *SEM back-scattered electron image showing partially recrystallized austenite. As-cast 2205 deformed at 1,000°C and 1 s^{-1} to ε =0.5 and annealed during 2 min at 1,000°C [IZA 99]*

The data in Figure 1.30 show the time it takes to reach 50% recrystallization, $t_{0.5}$, of δ-ferrite and austenite as a function of the volume fraction of ferrite in different austeno-ferritic Cr-Ni [ALJ 03] steels and a 2304 [PIÑ 99] steel. The presence of a second phase produces an important delay of recrystallization because growth of freshly recrystallized grains is stopped by interphase boundaries. Inherent microstructural heterogenity of the hot-worked material also contributes to an irregular progress of recrystallization. Planar dislocation substructures in austenite can be annealed out through static recovery or produce isolated recrystallized grains exhibiting stepped γ-γ interfaces, while cellular regions undergo static recrystallization [IZA 97B]. Nucleation of recrystallized grains in austenite takes place at the δ/γ interphase boundary and eventually at transition bands formed inside this phase [IZA 97B]. Complete recrystallization is rarely observed, even after long annealing. Applied strain significantly modifies the recrystallization kinetics of as-cast microstructures, but only moderately affects that of wrought, hot-worked material, as in Figure 1.31.

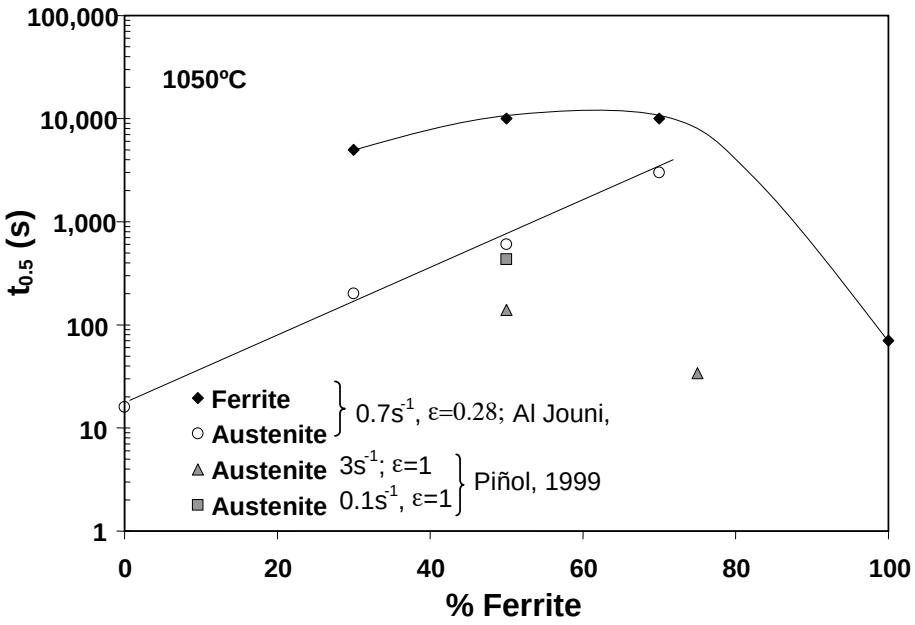

Figure 1.30. *Time to 50% recrystallization, $t_{0.5}$ for ferrite and austenite, as a function of the volume fraction of ferrite. Deformation and annealing at 1,050°C [PIÑ 99, ALJ 03]*

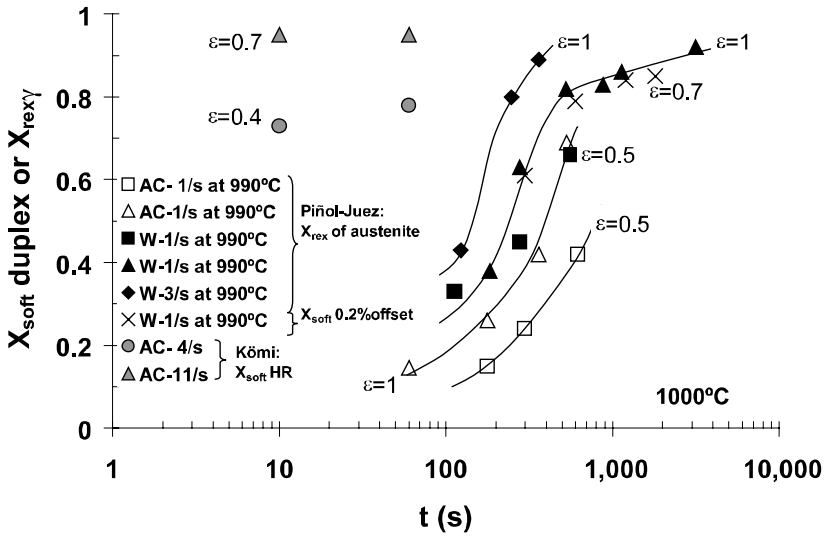

Figure 1.31. *Fractional softening from laboratory rolling tests (HR) as-cast 2205 steel [KÖM 02], and from double hit PSC tests (0.2% offset method) wrought, rolled 2304 steel [PIÑ 95] and fraction of recrystallized austenite 2304 [IZA 97B]*

Both the high fraction of interphase boundaries that remain coherent in a moderately strained as-cast microstructure and strain partitioning explain the delayed nucleation (combination of scarce nucleation sites and low driving energy). As the applied strain increases, the coherence of the interphase is progressively lost and as-cast microstructure morphology approaches that of the wrought material and uniform strain conditions. This explains why the recrystallization kinetics in both the as-cast and wrought microstructures finally converges at high strains, as seen in Figure 1.31. The fractional softening curve approximately superposes with the one for γ recrystallization. Increasing the strain rate significantly reduces the recrystallization time. The following equation has been reported to relate $t_{0.5}$ for austenite to the Zener-Hollomon parameter and temperature, T_a [PIÑ 99, IZA 97B]:

$$t_{0.5} = BZ^{-0.35} \exp\left(\frac{232000}{RT_a}\right) \qquad [1.3]$$

in which B decreases one order of magnitude when passing from 50% δ to 75% δ. Softening times deduced from laboratory hot-rolling tests in a 2205 steel [KÖM 02] are significantly lower than those obtained from PSC double hit tests in a 2304 steel [PIÑ 95]. These differences cannot yet be explained.

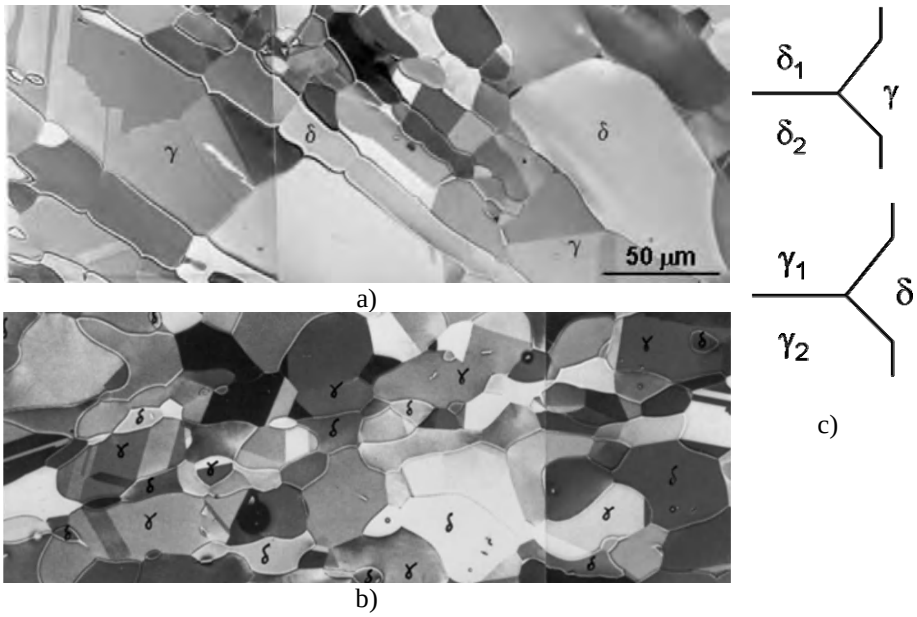

Figure 1.32. *Same deformed material as that shown in Figure 1.7, but after a) 1 h and b) 4 h at 1,100°C. Diagrams showing boundary phenomena inducing microstructural polygonalization (points 9 and 10 in Figure 1.5) [IZA 99]*

Recrystallization is not the only reaction taking place during annealing. In fact, hot-deformed microstructures, like the one in Figure 1.7, evolve progressively to a polygonalized microduplex configuration that is only reached after sufficiently long annealing times (Figure 1.32). The mechanisms responsible for this polygonalization have points in common with those described in section 1.3.6 and are shown schematically in Figure 1.32c. Initially flat interphase boundaries develop sharp triple points at the intersections with γ-γ and δ-δ single-phase boundaries, until each one of the two phases breaks up into individual crystallites.

1.6. Hot workability

The ability of a material to be hot-worked in a safe way depends on both the intrinsic material ductility and the process itself [AHL 82]. The strain to fracture or the reduction in area obtained, respectively, from torsion or tension laboratory tests are aimed to provide a measure of the material ductility. Such types of analysis allows for systematic studies that are relatively easy to perform in the laboratory and provide valuable information. However, this only partially addresses the complexity of the hot workability problem [KÖM 93, BIA 98].

In addition to heterogenities in microstructure and composition inherited from the casting, local conditions during industrial hot working can have a dramatic effect on effective hot workability. Among these factors are the chilling at the surface, the reversion of the shear strain under the rolls, and some superficial dissolution/precipitation of the austenite.

It has also to be taken into account that some defects detected after hot working can have nucleated at former stages, evolve during deformation, and can be erroneously attributed to a lack of hot ductility. For example, high N content in duplex stainless steels can produce gas pores during solidification [ARO 99, PAR 03]. Transverse cracking during continuous casting can happen under tensile strand stresses due to a temperature-dependent weakening of the material at grain boundaries. This problem can be exacerbated in the presence of columnar grains [MIN 00].

From this point on, only those factors directly related to crack formation during the hot-working process will be addressed. Some of the described microstructures and deformation conditions do not necessarily belong to optimized conditions, but help analyze damage formation mechanisms.

1.6.1. *Effect of composition*

The extent of edge cracking of duplex stainless steels increases with N content [LIO 01]. The negative effect of this element is double, because it increases the volume fraction of austenite and significantly increases its strength. The dependence of edge crack length on the alloying elements in 2205 steel has been expressed in terms of the crack sensitivity index (CSI) [LIO 01]:

$$CSI = 45.2\,C + 18.3\,N + Mo + Cu + 0.65\,Ni - 297\,B - 0.14\,Cr - 0.7\,Mn \qquad [1.4]$$

with all the element concentrations in weight percent. When the value of CSI is higher than 5.5, the stainless steel is susceptible to edge crack.

Impurities and trace elements can seriously deteriorate hot workability as segregation can produce “hot shortness” in a range of temperatures, the width of which depends on the steel composition. Among these elements the most harmful are sulfur (S) and phosphorus (P), but trace elements like lead (Pb), bismuth (Bi) and tin (Sn) [AHL 82] can also have a detrimental effect.

The work done on laboratory casts [KÖM 91] demonstrates the detrimental effect of S, due to a ductility trough at around 1,100°C leading to the formation of edge cracks during hot rolling performed at this temperature. In order to avoid this

problem, the concentration of S should be reduced to below 30 ppm or the steel should be alloyed with cerium (Ce) while the content of S is kept low. The formation of CeS sulfides prevents sulfur segregation [KÖM 91]. Alloying with calcium (Ca) has also been reported to improve hot ductility if the ratio Ca:S is 3 or higher [KAW 86]. P concentrations up to 150 ppm have no significant effect on hot ductility. Kömi *et al.* [KÖM 91] deduced that 530 ppm P is as harmful as 60 ppm S.

The hot ductility index (HDI) considers the effect of composition on phase balance (Cr_{eq} and Ni_{eq}) and grain boundary strength [LIO 01]:

$$HDI = Cr + 0.6\,Mo - 0.9\,[Ni + Cu + 1.9\,Mn + 35\,(1.5\,C + N)] + 270\,(2.5\,B - S) \quad [1.5]$$

with all the element concentrations in weight percent. The grain boundary strength is expressed as a function of the boron (B) and S contents. The higher the HDI, the better the hot ductility of the duplex stainless steel.

1.6.2. *As-cast microstructures*

In austeno-ferritic steels, the primary δ ferrite solidification microstructure shown in Figure 1.1 is preserved to some extent after reheating of the as-cast material. Specific hot deformation tests performed in the laboratory [IZA 07] demonstrated that fine equiaxed grains at the surface of the as-cast material act as a protective layer against the formation of severe surface defects. This contrasts with the easy propagation of the cracks along the columnar grain boundaries when these outcrop at the surface or close to it. As can be seen in Figure 1.33 a columnar microstructure is not by itself a source of defect.

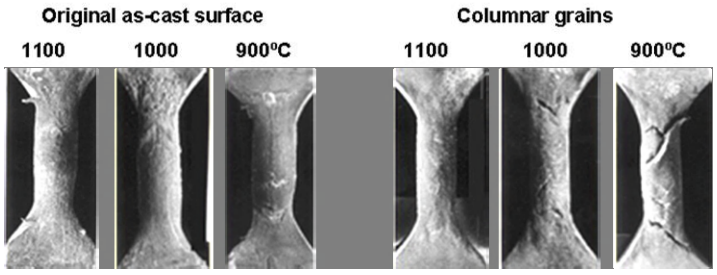

Figure 1.33. *View of both longitudinal sides (equiaxed original as-cast surface and surface resulting from cutting across the columnar region) of PSC specimens deformed at different temperatures [GAR 03, IZA 07]*

At 1,100°C, the two surfaces of the PSC appear crack-free regardless of whether equiaxed or columnar grains are below them. At lower temperatures, a ductility

trough happens and cracks nucleate at the edges of the specimens where the appropriate stress state is present. Under these conditions, the different response of equiaxed grains below the original as-cast surface and that of columnar grains becomes evident. In industry, severe cracking can result from the combinations of columnar grains, the appropriate stress state, and either hot shortness or the loss of ductility due to surface chilling.

1.6.3. *Hot ductility*

In general, duplex stainless steels have poor hot ductility, except when deformed at temperatures above or slightly lower than the austenite dissolution temperature [BAL 00, REI 00]. For most commercial compositions and industrial schedules that use reheating temperatures around 1,250°C, a significant volume fraction of austenite remains undissolved. At hot working temperatures, in general, the ductility of ferrite is better than that of austenite, but both are significantly impaired by the presence of a second phase, as shown in Figure 1.34 [IZA 07]. This produces a ductility trough for austeno-ferritic microstructures at the bottom of which are as-cast materials.

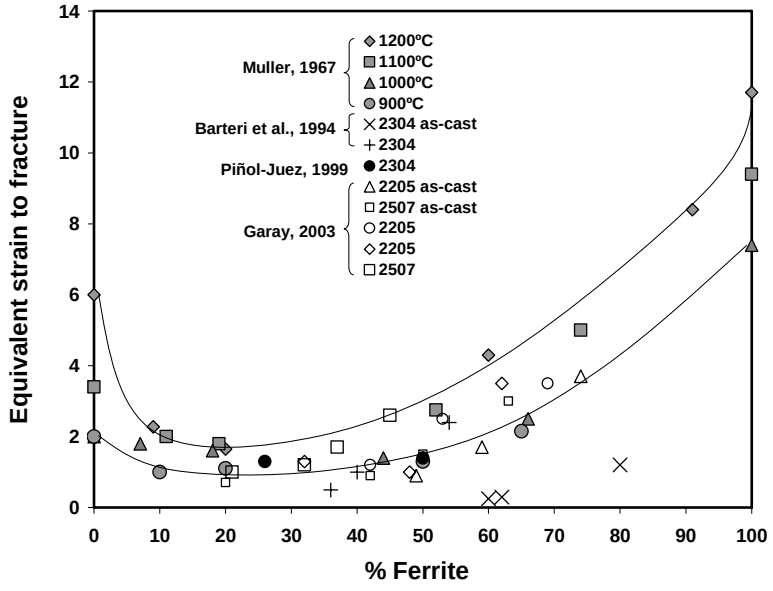

Figure 1.34. *Effect of the volume fraction and deformation temperature on the strain to fracture for different steel compositions [MUL 67, BAR 94, PIÑ 99, GAR 03, EVA 04]*

Improved hot ductility is reached in the presence of microduplex microstructures that are know to exhibit even superplastic behavior [GIB 68, SMI 76, KAS 83]. Unfortunately, the production of a microduplex structure requires operations [MAK 01] that are not suitable during the conventional hot processing of an as-cast material.

Ductility has been found to be a strong function of the Zener-Hollomon parameter [DUP 02C], but when considering temperature and strain rate separately, contradictory results can be yielded. There is general agreement regarding the beneficial effect of increasing deformation temperature [MUL 67, KÖM 93, PIÑ 99, DUP 02C, GAR 03, EVA 04]. However, some laboratory hot-rolling tests indicate the opposite [KÖM 93], with crack length increasing along with deformation temperature. According to the results in [KÖM 93], the region of low ductility disappears with decreasing strain rate (in 10-0.1s^{-1} range). In agreement with this Evangelista *et al.* and Duprez *et al.* [DUP 02C, EVA 04] indicate ductility apparently increases for temperatures above 1,100°C when the strain rate is reduced, but the strain rate has a minimal effect at low deformation temperatures.

When considering the effect that the volume fraction of the constitutive phases has on hot ductility, the research unanimously agrees, as shown in Figure 1.34 (for details see Iza-Mendia and Gutierrez [IZA 07]). The reduction in the volume fraction of ferrite has a higher negative effect on hot ductility than reducing the testing temperature, but given that the concentration of ferrite runs parallel with temperature, the two contributions cannot be separated.

1.6.4. *Sources of failure*

Damage at ferrite-austenite interphase boundaries has been identified as the main source of defects under hot working conditions in duplex stainless steels [IZA, 98, MCQ 03]. In fact, in laboratory tests, damage is often observed well before the final fracture of the material [PIÑ 00B].

Brittle intermetallic phases, such as sigma phase, are expected to play a marginal role during hot working. This type of precipitation takes place in duplex stainless steels below about 1,000°C [NIL 92A, NIL 00, SIE 07], but it generally requires relatively long holding times or cooling rates lower than roughly 0.8°C/s in the 1,000-600°C range. As a consequence, most of the time, intermetallic precipitation can easily be avoided during normal hot working processes, even though the sigma phase often precipitates during subsequent cooling to room temperature in large sections [EST 08]. In high N steels, nitride precipitation, which is faster than that of intermetallics, can occur at hot working temperatures and some care is required in order to avoid ductility problems. In laboratory tests [IZA, 98, PIÑ 99, GAR 03] no

precipitation at interphase boundaries has been observed, consequently precipitation is not the cause of failure. However, sliding on the interphase has been identified as a source of damage (Figure 1.14). Boundary sliding is an important source of damage in austenitic stainless steels, but its negative contribution is limited by dynamic recrystallization [EVA 04]. In duplex stainless steel, the dynamic recrystallization is hindered and different degrees of sliding on the interphase boundaries have been observed, depending on the material and deformation mode. Sliding contributes to strain accommodation in the austeno-ferritic steels during hot working [ALJ 83]. Strain partitioning, for example, requires some amount of sliding on the interphase boundaries in order to maintain continuity. Strain localization and disperse phase rotations (Figure 1.5) also induce some sliding. For example, the austenite block rotation shown in Figure 1.13, is accompanied by severe shearing in the surrounding soft ferrite and by damage formation at several points of the interphase boundary. The micrograph in Figure 1.35 shows some shear localization and cracking at the surface of an industrially hot-rolled duplex stainless steel. Normally, shear stresses develop close to the surface in contact with the rolls, but in duplex microstructures shear stresses also appear as a result of the presence of two phases with different mechanical properties [TEL 97, HER 06]. Additionally, under certain conditions (Figure 1.26) duplex stainless steels are softer when deformed under pure shear mode than under plane strain conditions enhancing the formation of shear bands [GIL 93].

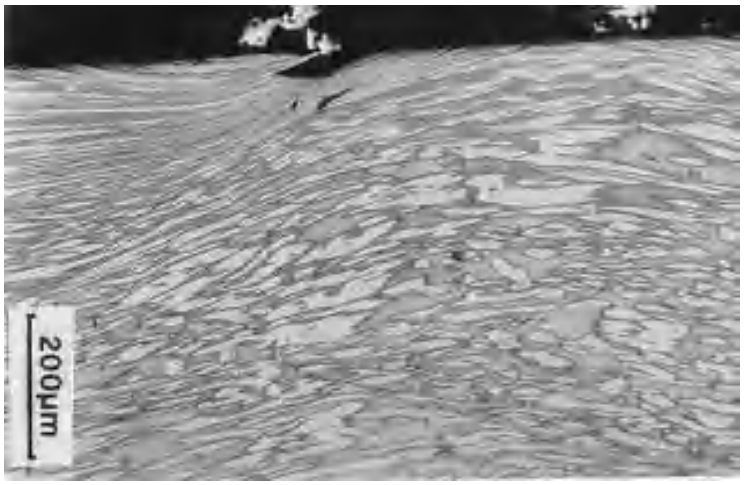

Figure 1.35. *Industrially hot-rolled material showing some shear close to the surface in contact with the rolls, leading to the formation of defects. Longitudinal section [IZA 07]*

In a wrought microstructure, sliding affects most interphase boundaries, but is not necessarily associated with damage nucleation at moderate strains under

monotonic deformation conditions (Figure 1.15b) although cyclic hot deformation significantly enhances its deleterious effect [PIÑ 03]. In as-cast microstructures, most interphase boundaries share a K-S orientation relationship. As a consequence, strain accommodation is only possible through severe localized sliding at the incoherent interphases [PIÑ 00A].

The decohesion at the incoherent interphase boundary between an austenite ridge and ferrite can clearly be observed in the SEM image shown in Figure 1.36. In order to accentuate this effect, the specimen was subjected to a strain reversal torsion test. Another example is given in Figure 1.37, in which severe displacements of the markers can be observed at the intersection between two different Widmanstätten austenite packets. A combination of preferential deformation of ferrite and interphase boundary sliding has produced damage pits roughly the size of 0.1 μm at this early deformation stage of $\varepsilon = 0.16$. In fact, observations made on as-cast microstructures deformed at 1,000°C show that at strains as low as 0.15 damage affects about 0.6% of the total length of the δ/γ interphase boundaries and this fraction increases with strain according to a potential function [PIÑ 00, PIÑ 03].

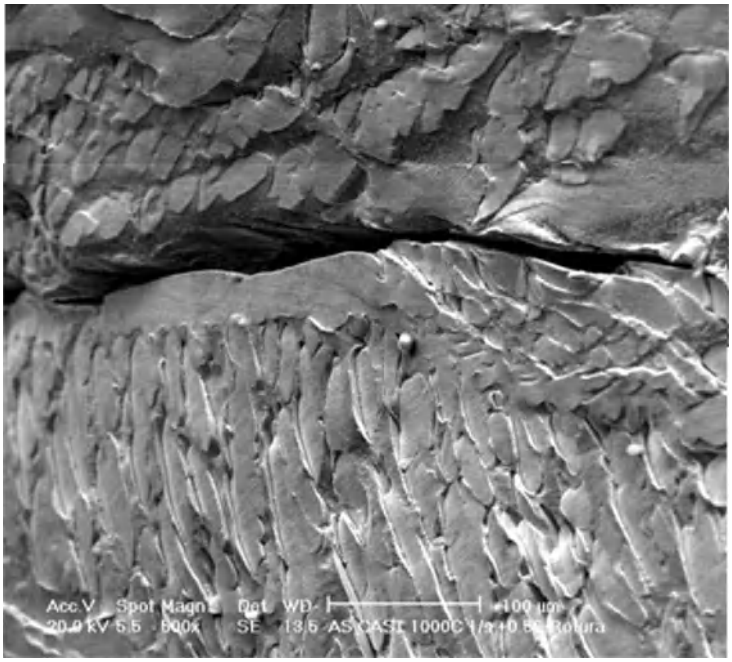

Figure 1.36. *Crack formed at the incoherent interphase boundary between an austenite ridge and ferrite matrix. As-cast duplex 2304 stainless steel deformed to fracture at 1,000°C and 1 s^{-1}. The strain was reversed at $\varepsilon = 0.56$*

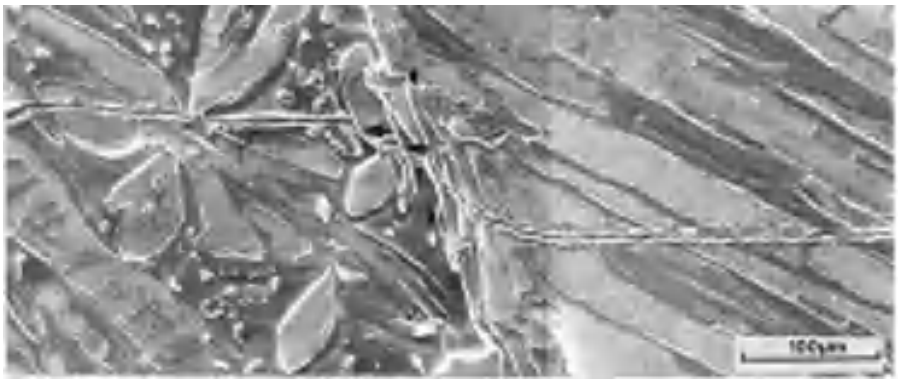

Figure 1.37. *Marks showing the combination of preferential shear of the ferrite and interphase boundary sliding at the intersection of two different Widmanstätten austenite packets. As-cast 2304 steel deformed at 1,100°C; 1s^{-1}; def=0.16*

1.6.5. *Multipass sequences*

In general, industrial processing involves several deformation passes at different temperatures and strain rates. Between the interpass periods, static softening mechanisms activate and are able to improve hot workability by isolating possible cracks nucleated at grain boundaries. Isothermal multistage deformation experiments were performed on wrought 2205 and 2304 steels, and static recrystallization of the austenite during the interpass time led to a degree of softening [EVA 04]. However, the total strain to fracture was approximately the same when deformation was applied in one or several passes. Multipass deformation sequences were performed on a 2205 steel [IZA 99] at 1,000°C and 1 s^{-1} with different interpass times ranging from 5 to 20 s. These tests showed that increasing the interpass time leads to some softening and to a slight improvement of the surface quality of the deformed specimens.

A combination of low reduction per pass and a shift to higher deformation temperatures can help in the definition of improved deformation sequences [BOT 96]. Partial dissolution of the austenite during reheating and multistage deformation at decreasing temperatures can produce some $\delta \rightarrow \gamma$ transformation induced movement of the interphase boundary. Such mechanisms coupled with static softening can have a beneficial effect on ductility because they play the same role as recrystallization in isolating damage from the interphase [IZA 99]. However, this can only be beneficial if reductions per pass are lower than a critical value 15-20% for the first passes at temperatures in the range 1,150-1,200°C and interpass times longer than 2 s [KÖM 96]. The two phases break up into individual crystallites.

1.7. Conclusions

The presence in duplex stainless steels of two ductile phases with different mechanical properties determines the complex behavior of these materials during hot working. Composition and temperature define phase balance and strength, and become key parameters for industrial processing. The mechanical behavior of as-cast and wrought microstructures is different and relates to deformation mode. Strain partitioning, rotation, and interphase boundary sliding contribute to accommodate the imposed deformation among the two phases, but can be the source of localization and defect formation.

1.8. Acknowledgments

We would like to remember Javier Urcola who pioneered a line of research on austeno-ferritic steels at CEIT and to thank Ana Piñol-Juez for her outstanding contribution in building upon it.

1.9. References

[AHL 82] AHLBLOM B., SANDSTROM R., "Hot workability of stainless steels: influence of deformation parameters, microstructural components, and restoration processes", *International Metals Reviews*, vol. 27, 1-27, 1982.

[ALD 67] ALDEN T.H., "The origin of superplasticity in the Sn-5% Bi alloy", *Acta Metallurgica*, vol. 15, 469-480, 1967.

[ALJ 83] AL-JOUNI F.E., SELLARS C.M., "Hot deformation of two-phase stainless steels", *Proceedings of the Riso International Symposium on Metallurgy and Materials Science*, in B SORENSEN, N. HANSEN, A. HORSEWELL, T. LEFFERS, H. LILHOLT, *Deformation of Multi-Phase, Particle Containing Materials*, Riso National Laboratory, Roskilde, Denmark, 131-137, 1983.

[ALJ 03] AL JOUNI F.E., SELLARS C.M., "Recrystallisation after hot deformation of two phase stainless steels", *Materials Science and Technology*, vol. 19, 1311-1320, 2003.

[ARO 99] AROLA R., WENDT J., KIVINEVA E., "Gas porosity defects in duplex stainless steel castings", *Materials Science Forum*, vol. 318-320, 297-302, 1999.

[ATA 91] ATAMERT S., KING J.E., "Elemental partitioning and microstructural development in duplex stainless steel weld metal", *Acta Metallurgica et Materialia*, vol. 39, 273-285, 1991.

[ATA 92] ATAMERT S., KING J.E., "Super duplex stainless steels. Part 1. Heat affected zone microstructures", *Materials Science and Technology*, vol. 8, 896-911, 1992.

[BAL 00] BALANCIN O., HOFFMANN W.A.M., JONAS J.J., "Influence of microstructure on the flow behaviour of duplex stainless steels at high temperature", *Metallurgical and Materials Transactions A*, vol. 31A, 1353-1364, 2000.

[BAR 79] BARRACLOUGH D.R., SELLARS C.M., "Static recrystallization and restoration after hot deformation of type 304 stainless steel", *Metal Science*, vol. 13, 257-267, 1979.

[BAR 94] BARTERI M., MECOZZI M.G., "Hot workability of some duplex stainless steels", *Proc. 4th international Conference Duplex´94 Stainless Steels*, paper 88, Abington Publishing, Glasgow, Scotland, 1994.

[BER 91] BERNHARDSSON S., "The corrosion resistance of duplex stainless steels", *Proc. Conf. "Duplex stainless steels'91'"*, Les Editions de Physique, France, 185-210, 1991.

[BIA 98] BIANCHI J., URCOLA J.J., *Development of a model for hot strip rolling of duplex and non-oriented magnetic steels with a full coupling between the thermomechanics and the kinetics of microstructural evolution*, Technical steel Research, EUR 18378EN, Office for Official Publications of the European Communities, Luxembourg, 1998.

[BOT 96] BOTELLA J., MARTOS J.L., SÁNCHEZ R., "Optimizing the hot deformability of 2205 duplex stainless steel by thermal/mechanical simultation", *Proc. Int. Congress Stainless Steel '96*, Düsseldorf/Neuss, June 3-5, 116-121, 1996.

[CAB 03] CABRERA J.M., MATEO A., LLANES L., PRADO J.M., ANGLADA M., "Hot deformation of duplex stainless steels", *Journal of Materials Processing Technology*, vol. 143-144, 321-325, 2003.

[CAR 01] CARSI M., JIMENEZ J.A., RIEIRO I., RUANO O.A., "Conformado a altas temperaturas, y su simulación por torsión, de un acero superdúplex", *III Seminario de Tecnología Metalúrgica: Aceros inoxidables*, UPC-Barcelona Tech, 105-122, 2001.

[CHE 01] CHEN T.H., YANG J.R., "Effects of solution treatment and continuous cooling on σ-phase precipitation in a 2205 duplex stainless steel", *Materials Science and Engineering A*, vol. 311, 28-41, 2001.

[CIZ 06] CIZEK P., WYNNE B.P., RAINFORTH W.M., "EBSD investigation of the microstructure and texture characteristics of hot deformed duplex stainless steel", *Journal of Microscopy*, vol. 22, 85, 2006.

[COM 91] COMBRADE O., AUDOUARD J.P., "Duplex stainless steels and localized corrosion resistance", *Proc. Conf. Duplex stainless steels '91*, France, Les Editions de Physique, 257-281, 1991.

[COR 91] CORTIE M.B., POTGIETER J.H., "Effect of temperature and nitrogen content on the partitioning of alloy elements in duplex stainless steels", *Metallurgical Transactions A*, vol. 22A , 2173-2179, 1991.

[DEH 07] DEHGHAN-MANSHADI A., BARNETT M.R., HODGSON P.H., "Microstructural evolution during hot deformation of duplex stainless steel", *Materials Science and Technology*, vol. 23, 1478-1484, 2007.

[DUP 02A] DUPREZ L., DE COOMAN B.C., AKDUT N., "Deformation behaviour of duplex stainless steel during industrial hot rolling", *Steel Research*, vol. 73, 531-538, 2002.

[DUP 02B] DUPREZ L., DE COOMAN B.C., AKDUT N., "High-temperature stress and strain partitioning in duplex stainless steel", *Zeitschrift fuer Metallkunde*, vol. 93, 236-243, 2002.

[DUP 02C] DUPREZ L., DE COOMAN B.C., AKDUT N., "Flow stress and ductility of duplex stainless steel during high-temperature torsion deformation", *Metallurgical and Materials Transactions A*, vol. 33, 1931-1938, 2002.

[EST 08] ESTEBAN M.P., IZA-MENDIA A., GUTIERREZ I., "Precipitación anisotérmica de fases intermetálicas en un acero inoxidable duplex de grado 2205", *Proc. Tratermat´2008*, Univ. Politécnica de Valencia, 377-386, 2008.

[EVA 91] EVANGELISTA E., MENGUCCI P., BOWLES J., MCQUEEN H.C., "Grain and subgrain structures developed by hot working in as-cast 434 stainless steel", in BRANDON *et al.*, *Proc. ICSMA´9*, 713-721, 1991.

[EVA 04] EVANGELISTA E., MCQUEEN H.J., NIEWCZAS M., CABIBBO M., "Hot workability of 2304 and 2205 duplex stainless steels", *Canadian Metallurgical Quarterly*, vol. 43, 339-354, 2004.

[FLO 68] FLOREEN S., HAYDEN H.W., "The influence of austenite and ferrite on the mechanical properties of two-phase stainless steels having microduplex structures", *Transactions of the American Society of Metals Quarterly*, vol. 61, 489-499, 1968.

[GAR 03] GARAY A., Optimización del conformado en caliente y tratamientos térmicos en aceros austenoferríticos, PhD Thesis, University of Navarra, 2003.

[GIB 68] GIBSON R.C., HAYDEN H.W., BROPHY J.H., "Properties of stainless steels with a microduplex structure", *Transactions of the American Society of Metals Quarterly*, vol. 61, 85-93, 1968.

[GIL 93] GIL-SEVILLANO J., "Flow stress and work hardening", Chapter 2 in H. MUGHRABI, vol. 6 *Plastic Deformation and fracture of materials*, in R.W. CAHN, P. HAASEN, E.J. KRAMER, *Materials Science and Technology*, 19-88, 1993.

[GIL 08] GIL SEVILLANO J., GUTIERREZ I., "Plastic shear stress-strain behaviour of axially oriented microstructures", in K.J. Hsia *et al.*, *Proc. of the Hael Mughraby Honorary Symposium*, The Minerals, Metals & Materials Society, 89-95, 2008.

[GOB 07] GOBERT C., ALFONSO A.D, DELAUNOIS F., DUMORTIER C., "Evolution of ferrite content of continuously cast slabs of 2205 duplex stainless steel", CD format, *Proc. Duplex 2007 International Conference and Expo*, AIM, June 18-20, Grado, Italy, 2007.

[HAS 94] HASHIMOTO S., MIYAMOTO H., MIURA S., "Role of Interphase-boundary sliding in a superplastic flow of duplex materials consisting of a soft and a hard phases", in Y. Hosoi, H. Yoshinaha, H. Oikawa, K. Maruyama, *Proc 7th JIM International Symposium on Aspects of High Temperature Deformation, Fracture in Crystalline Materials*, The Japan Institute of Metals, 115-122, 1994.

[HER 06] HERNANDEZ-CASTILLO L.E., RUPIN N., BOLDETTI C., PINNA C., BORNERT M., "Evaluation of local strain fields in hot worked stainless steel", www.carloboldetti.com/academia/photomech06.pdf

[IZA 97A] IZA-MENDIA A., PIÑOL-JUEZ A., GUTIERREZ I., URCOLA J.J., "Study of the role of the interface coherence on the hot deformation behaviour of duplex stainless steels", *Key Engineering Materials*, vol. 127-131, 1033-1040, 1997.

[IZA 97B] IZA-MENDIA A., PIÑOL-JUEZ A., GUTIERREZ I., URCOLA J.J., "Microstructural evolution on a duplex stainless steel during annealing after hot working", in T.R. McNelley, *Proc. Recrystallization, Related Phenomena*, Monterey, California, Institute of Advanced Studies, 405-412, 1997.

[IZA 98] IZA-MENDIA A., PIÑOL-JUEZ A., URCOLA J.J., GUTIERREZ I., "Microstructural and mechanical behavior of a duplex stainless steel under hot working conditions", *Metallurgical and Materials Transactions A*, vol. 29, 2975-2986, 1998.

[IZA 99] IZA-MENDIA A., Optimización del conformado en caliente de aceros inoxidables dúplex austenoferríticos. Caracterización microestructural. PhD Thesis, University of Navarra, 1999.

[IZA 07] IZA-MENDIA A., GUTIERREZ I., "Factors affecting the hot workability of duplex stainless steels", *CD Proc. Duplex 2007 International Conference and Expo*, AIM, June 18-20, Grado, Italy, 2007.

[JON 69] JONAS J., SELLARS C.M., TEGART W.J.MCG., "Strength and structure under hot working conditions", *Metallurgical Reviews*, vol. 14, 1-24, 1969.

[JOR 05] JORGE JR M.A. BALANCIN O., "Prediction of steel flow stresses under hot working conditions", *Materials Research*, vol. 8, 309-315, 2005.

[KAS 83] KASHYAP B.P., MUKHERJEE A.K., "Influence of nonsteady state behavior on superplastic deformation of a 25.7 Cr-6.6 Ni stainless steel", *Metallurgical Transactions A*, vol. 14A, 1875-1882, 1983.

[KAU 93] KAUPPI T.A., KARJALAINEN L.P., KYRÖLÄINEN A.J., "Influence of deformation and cooling rate on the $\delta \rightarrow \gamma$ transformation in low carbon AISI 430 ferritic stainless steel", *Proc. Innovation Stainless Steels*, Florence, Italy, October, 2,333-2,338, 1993

[KAW 86] KAWASAKI T., TAKADA I., OHTSUBO H., SUZUKI S., "Hot workability of austenitic stainless steels containing delta-ferrite", *Kawasaki Steel Technical Report*, no. 14, 50-60, 1986.

[KEI 03] KEICHEL J., FOCT J., GOTTSTEIN G., "Deformation and annealing behavior of nitrogen alloyed duplex stainless steels. Part II: annealing", *ISIJ International*, vol. 43, 1788-1794, 2003.

[KÖM 91] KÖMI J.I., KYRÖLÄINEN A.J., KARJALAINEN L.P., SUUTALA L.P., "Effects of sulphur, phosphorus and cerium on the hot workability of a ferritic-austenitic stainless steel", *Proc. Int. Conf. On Stainless Steel*, ISIJ, Chiba, Japan, 10-13 June 10-13, 807-814, 1991.

[KÖM 93] KÖMI J.I., KARJALAINEN L.P., "Effect of hot working parameters on hot ductility of a ferritic-austenitic stainless steel", *Proc. Processing, Materials Innovation Stainless Steel*, Florence, AIM, Milano, 2,315, 1993.

[KÖM 96] KÖMI J.I., KARJALAINEN P., "Effect of restoration kinetics on hot ductility of a ferritic-austenitic and super austenitic stainless steel", *Proc. Int. Conf. on Stainless Steels*, Düsseldorf, Germany, June, 301-302, 1996.

[KÖM 02] KÖMI J.I., KARJALAINEN L.P., "Effect of restoration on hot ductility of high alloy and duplex stainless steels", *Materials Science and Technology*, vol. 18, 563-570, 2002.

[LIO 01] LIOU H.Y., PAN Y.T., HSIEH R.I., TSAI W.T., "Effects of alloying elements on the mechanical properties and corrosion behaviors of 2205 duplex stainless steels", *Journal of Materials Engineering and Performance*, vol. 10, 231-241, 2001.

[LOM 81] LOMBRY R., ROSSARD C., THOMAS B.J., "Etude des mécanismes de déformation et d'adoucissement dynamique des aciers ferritiques Fe-Cr au cours de la déformation à chaud", Cahiers d'Informations Techniques, *Revue de Métallurgie*, vol. 78, 975-988, 1981.

[MAK 01] MAKI T., FURUHARA T., TSUZAKI K., "Microstructure development by thermomechanical processing in duplex stainless steel", *ISIJ International*, vol. 41, 571-579, 2001.

[MCQ 75] MCQUEEN H.J., JONAS J.J., "Recovery and Recrystallization during high temperature deformation", in R.J. ARSENAULT, *Treatise on Materials Science, Technology*, Academic Press, vol. 6, 393-493, 1975.

[MCQ 91] MCQUEEN H.J., RYAN N.D., "Effects of solute constitutive constants for austenitic stainless steels", in D.J. BRANDON *et al. Strength of Metals, Alloys, ICSMA 9.* Freund Publishing House, 359-366, 1991.

[MCQ 93] MCQUEEN H.J., EVANGELISTA E., RYAN N.D., "Hot and cold working of austenitic stainless steels", *Proc. Processing, Materials Innovation Stainless Steel*, Florence, AIM, Milano, 2,289-2,302, 1993.

[MCQ 96] MCQUEEN H.J., RYAN N.D., ZARIPOVA R., FARKHUTDIVOV K., "Comparison of hot working behaviour of austenitic and ferritic stainless steels", *Proc. 37th MWSP Conf., ISS*, C.E Slater Publishers, Hamilton, Ontario, Canada, vol. XXXIII, 883-894, 1996,.

[MCQ 02] MCQUEEN H.J., RYAN N.D., "Constitutive analysis in hot working", *Materials Science and Engineering A*, vol. 322, 43-63, 2002.

[MCQ 03] MCQUEEN H.J., EVANGELISTA E., RYAN N.D., "Steel hot workability dependence on austenite-ferrite mixtures", in E.J. PALMIERE, M. MAHFOUF, C. PINNA (Eds.), *Thermomechanical Processing: Mechanics, Microstructure and Control*, University of Sheffield, 359-367, 2003.

[MIN 00] MINTZ B., COWLEY A., ABUSHOSHA R., "Influence of columnar grains in dictating hot ductility of steel", *Materials Science and Technology*, vol. 16, 1-5, 2000.

[MUL 67] MULLER T.L.F., The hot deformation of duplex alloys, PhD Thesis, University of Sheffield, 1967.

[MUR 75] MURR L.E., *Interfacial Phenomena in Metals & Alloys*, Addison-Wesley, 1975.

[NIL 92A] NILSSON J.O., "Super duplex stainless steels", *Materials Science and Technology*, vol. 8, 685-700, 1992.

[NIL 92B] NILSSON J.O., WILSON A., JOSEFSSON B., THORVALDSSON T., "Relationship between pitting corrosion, toughness and microstructure for isothermally heat treated super duplex stainless steel", *Applications of Stainless Steel '92, Proc. Conf. Stainless steels'92*, Stockholm, The Institute of Materials, 280, 1992.

[NIL 00] NILSSON J.O., KANGAS P., KARLSSON T., WILSON A., Mechanical properties, microstructural stability and kinetics of σ-phase formation in 29Cr-6Ni-2Mo-0.38N superduplex stainless steel", *Metallurgical and Materials Transactions A*, vol. 31, 35-45, 2000.

[OHM 95] OHMORI Y., NAKAI K., OHTSUBO H., ISSHIKI Y., "Mechanism of Widmanstätten austenite formation in a δ/γ duplex phase stainless steel", *ISIJ International*, vol. 35, 969-975, 1995.

[PAR 03] PARK Y.H., KIM J.W., KIM S.K., LEE Y.D., LEE Z.H., "The critical amount of nitrogen on the formation of nitrogen gas pores during solidification of 25Cr-7Ni duplex stainless steels", *Metallurgical and Materials Transactions B*, vol. 34, 313-320, 2003.

[PAU 93] PAUL A., MARTOS J.L., SANCHEZ R., "Behaviour of 2205 duplex stainless under hot working conditions", *Proc. Processing, Materials Innovation Stainless Steel*, Florence, AIM, Milano, 297-302, 1993.

[PIÑ 95] PIÑOL A., IRIGOIEN D., IZA A., GUTIERREZ I., URCOLA J.J., "Static recrystallisation of duplex stainless steels after hot working", *RISO International Symposium on Material Science*, Roskilde, Denmark, 1995, 497-502, 1995.

[PIÑ 97] PIÑOL-JUEZ A., IZA-MENDIA A., GUTIERREZ I., URCOLA J.J., "Influence of phase morphology and deformation mode on the behaviour during hot working of a two-ductile phase composite", *Key Engineering Materials*, vol. 127-131, 1025-1032, 1997.

[PIÑ 99] PIÑOL-JUEZ A., Estudio de la deformabilidad en caliente de los aceros inoxidables duplex 2304: evolución microestructural, ecuaciones constitutivas y mecanismos de formación de daño, PhD Thesis, University of Navarra, 1999.

[PIÑ 00A] PIÑOL-JUEZ A., IZA-MENDIA A., GUTIERREZ I., "δ/γ interface boundary sliding as a mechanism for strain accommodation during hot deformation in a duplex stainless steel", *Metallurgical and Materials Transactions A*, vol. 31, 1671-1677, 2000.

[PIÑ 00B] PIÑOL-JUEZ A., IZA-MENDIA A., GUTIERREZ I., "Damage formation in a 2304 duplex stainless steel under hot working conditions", in M. FUENTES *et al. Proceedings of the 13th European Conference on Fracture (ECF 13)*, no. 11U.293, 2000

[PIÑ 03] PIÑOL-JUEZ A., IZA-MENDIA A., GUTIERREZ I., "Hot workability of a duplex stainless steel related to the interface sliding under different strain paths", in E.J. Palmiere *et al. Proc. "Thermomechanical Processing: Mechanics, Microstructure, Control"*, University of Sheffield, 398-404, 2003.

[POR 92] PORTER D.A., EASTERLING K.E., *Phase Transformation in Metals and Alloys*, 2nd ed, Chapman & Hall, 1992.

[REI 00] REIS G.S., JORGE A.M., BALANCIN O., "Influence of the microstructure of duplex stainless steels on their failure characteristics during hot deformation", *Materials Research*, vol. 3, 31-35, 2000.

[ROB 07] ROBERTI R., FACCOLI M., "Hot deformation behaviour of 2205 duplex stainless steel", *CD Proc. Duplex 2007 International Conference, Expo*, Associazione Italiana di Metallurgia, June 18-20, Grado, Italy, 2007.

[RYA 90] RYAN N.D., MCQUEEN H.J., "Flow stress, dynamic restoration, strain hardening and ductility in hot working of 316 steel", *Journal of Materials Processing Technology*, vol. 21, 177-199, 1990.

[SEL 76] SELLARS C.M., SAH J.P., BEYNON J., FOSTER S.R., *Plane Strain Compression Testing at Elevated Temperatures*, Report on Research Work Supported by Science Research Council Grant B/RG/1481, 81, 1976.

[SHE 84] SHERBY O.D., WADSWORTH J., "Development and characterization of fine-grain superplastic materials", in G. KRAUSS, *Deformation, Processing and Structure*, ASM, 355-389, 1984.

[SHE 87] SHEPPARD T., RICHARDS P., "Structural and substructural observations during thermomechanical processing of two ferritic stainless steels", *Journal of Materials Science*, vol. 22, 1642-1650, 1987.

[SIE 07] SIEURIN H., SANDSTRÖM R., "Sigma phase precipitation in duplex stainless steel 2205", *Materials Science and Engineering A*, vol. 444, 271-276, 2007.

[SMI 76] SMITH C.I., NORGATE B., RIDLEY N., "Superplastic deformation and cavitation in a microduplex stainless steel", *Metal Science*, vol. 10, 182-188, 1976.

[SOL 83] SOLOMON H., DEVINE T.M., "A tale of two phases", in R.A. LULA, *Duplex Stainless Steels*, ASM, 693-756, 1983.

[SOU 80] SOUTHWICK P.D., HONEYCOMBE R.W.K., "Decomposition of ferrite to austenite in 26%-5% Ni stainless steel", *Metals Science*, vol. 14, 253-261, 1980.

[TEL 97] TELLAECHE-REPARAZ M., MARTINEZ-ESNAOLA J.M., URCOLA J.J., "Numerical simulation of plane strain compression tests of a bimetallic composite", *Key Engineering Materials*, vol. 127-131, 1215-1222, 1997.

[TEN 01] TENDO M., TADOKORO Y., SUETSUGU K., NAKAZAMA T., "Effects of nitrogen, niobium and molybdenum on strengthening of austenitic stainless steel produced by thermo-mechanical control process", *ISIJ International*, vol. 41, 262-267, 2001.

[TOM 92] TOMOTA Y., UMEMOTO M., KOMATSUBARA N., HIRAMTSU A., NAKAJIMA N., MORIYA A., WATANABE T., NANBA S., ANAN G., KUNISHIGE K., HIGO Y., MIYAHARA M., "Prediction of mechanical properties of multi-phase steels based on stress-strain curves", *ISIJ International*, vol. 32, 343-349, 1992.

[URC 87] URCOLA J.J., SELLARS C.M., "Effect of changing strain rate on stress-strain behaviour during high temperature deformation", *Acta Metallurgica*, vol. 35, 2637-2647, 1987.

[VEN 94] VENUGOPAL S., MANNAN S.-L., PRASAD Y.V.R.K., "Processing maps for hot working of commercial grade wrought stainless steel type AISI 304", *Materials Science and Engineering A*, vol. A177, 143-149, 1994.

[VER 91] VERLINDEN B., CUYPERS K., AERNOUDT E., "Influence of nitrogen content, α/γ ratio and grain size on the hot strength of duplex stainless steel", in J. CHARLES, S. BERNHARDSON, *Duplex Stainless Steels*, Les Editions de Physique, vol. 2, 711-718, 1991.

[VER 92] VERNUSSE PH, MONTHEILLET F., "Etude théorique de la rhéologie à chaud d'alliages à deux phases ductiles", *Mémoires et Etudes Scientifiques Revue de Métallurgie*, vol. 89, 83-91, 1992.

Chapter 2

Corrosion Resistance Properties

2.1. Introduction

Duplex grades have become a well-established family of products, particularly suitable for corrosion-resistance applications. They have two digits yearly of tonnage growth (total production of duplex grades by the different SS manufacturers) due to their continuous development in new applications and availability in new production ranges (coils, bars, etc). Duplex stainless steels (DSS) are targeting the slow but continued replacement of the more costly 300' series, including more recently, through the development of lean duplex grades, the 304(L). Moreover, in many applications they are replacing the rusty carbon steels, which generate expensive maintenance costs during their lifetime. Furthermore, because of their high mechanical properties, it is possible to reduce thicknesses in most of the applications making them even more cost advantageous.

The main topics of the present paper concern corrosion-resistance properties and in-service properties of standard and newly developed duplex grades.

The "standard" duplex, i.e. the S32304, S32205 and S32507 (more copper, tungsten, etc.) grades have been confirmed, by more than 20 years successful in-service applications, to be very valuable grades with outstanding performances [CHA 07a].

Chapter written by Jacques CHARLES.

Duplex Stainless Steels Edited by Iris Alvarez-Armas and Suzanne Degallaix-Moreuil

New grades, including the so-called “lean duplex” having low nickel (Ni) and molybdenum (Mo) alloying elements dedicated to volume-oriented markets (possible replacement of 304/316 grades), and some “niche” grades, which are highly alloyed and are dedicated to very specific markets, are now becoming more readily available [CHA 07b].

2.2. The duplex grades and pitting resistance equivalent numbers

2.2.1. *Chemistry of some of the main commercialized duplex grades*

Table 2.1 presents the chemical analysis of most of the currently available duplex grades, as well as most of the used austenitic grades. This table also reports pitting resistance equivalent numbers (PRE = % Cr + 3.3 % Mo; PREN = % Cr + 3.3% Mo + 16%N and PRENW = % Cr + 3.3 (% Mo + 0.5% W) + 16% N). They are useful indicators to rank the corrosion resistance of the stainless steels, particularly when considering localized corrosion resistance in acidified solutions [CHA 97, CHA 00].

The PREN values of all duplex grades are much higher than that of the 304(L) – 1.4301- and even the 316 – 1.4401 austenitic grades. This clearly indicates that the duplex grades are designed to resist most of the severe corrosive conditions.

The duplex developed 20 years ago could be divided into three families:

– the lean duplex – S32304 – (1.4362) without Mo addition and having a PREN number slightly higher than the 316L(1.4401) grade;

– the “standard” duplex – S32205 – (1.44462) type with 22% chromium (Cr) and 3% Mo having a PREN value between 33 and 36 close to the 904L(N) (1.4539) grade;

– the “superduplex” – S32750, S32760 and S32520 – (1.4507) grades with a minimum of 25% Cr, 3.5% Mo and 0.2% nitrogen (N), which guarantees a PREN value higher than 40. The grades are often specified instead of the 6Mo austenitic grades.

FAMILY	USA	EURONORM	Cr	Mo	Ni	Mn	Cu	N	Others	PRE	PREN
300	304L	1.4307	18	0	9	1	0			18	18
	316L	1.4401	17	2	11	1	0			24	24
	904LN	1.4539	20	4	25	1	1.5	0.1		33	35
Standard DUPLEX (1996)	S 32304	1.4362	23	0.3	4	1		0.13		23	25
	S 32205	1.4462	22	3	6	1		0.17		32	35
	S 32750	1.4410	25	3.5	7	1		0.27		37	41
	S 32760	1.4501	25	3.8	7	1	0.7	0.27	0.7 W	38	42
	S 32520	1.4507	25	3.5	7	1	1.5	0.25		37	41
New DUPLEX (EX)	S 31500		18.5	2.7	5	1		0.1		27	29
	S 32101	1.4162	21	0.3	1.5	5		0.2		21	24
	S 32001		20	0.3	1.7	5	0.3	0.15		21	23
	S 32003		20	1.7	3.5	2		0.15		26	28
	S 31260		27	3	7	1	0.5	0.16	0.3 W	37	39
	S 39274		25	3	7	1	0.6	0.27	2 W	35	39
	S 32906	1.4362	29	2	6	1		0.4		36	42
PRE = %Cr + 3.3%Mo ; PREN = %Cr + 3.3%Mo + 16%N											

Table 2.1. *Typical chemistry of duplex stainless steels (weight %)*

More recently, new lean duplex grades were designed to substitute the 304 alloys by combining low nickel, high nitrogen, and high manganese additions. The newly developed so-called “lean duplex” family comprises cost-competitive alloys when considering their alloying element content.

Some other duplex grades where developed for specific applications, for example, some “hyperduplex” grades with extra high chromium additions combined with dedicated alloying levels in molybdenum, tungsten or copper, as well as extra high nitrogen contents (Table 2.1).

2.2.2. *The specific case of nitrogen*

Nitrogen additions are extremely important in duplex stainless steels. Nitrogen contributes to several properties, including the high temperature stability of the two-phase microstructure particularly in the welded areas. The “old” duplex stainless steels with rather low nitrogen additions had large coarsened ferritic grains in the heat-affected zone (HAZ) with often gamma 2 or nitride precipitations, which had detrimental effects on both the toughness and corrosion resistance of the welded structure [CHA 91a].

In addition, nitrogen is also known to improve the localized (pitting and crevice) resistance properties of the stainless steels. Those two major contributions of nitrogen alloying explain why the nitrogen content in the duplex grades has been continuously increased up to levels close to the solubility limit of the grades (Figure

2.1) [GAG 07, CHA 07a]. Higher chromium and molybdenum contents increase the solubility limit of nitrogen and make it possible to further increase the nitrogen content and further improve the localized corrosion behavior of the grades.

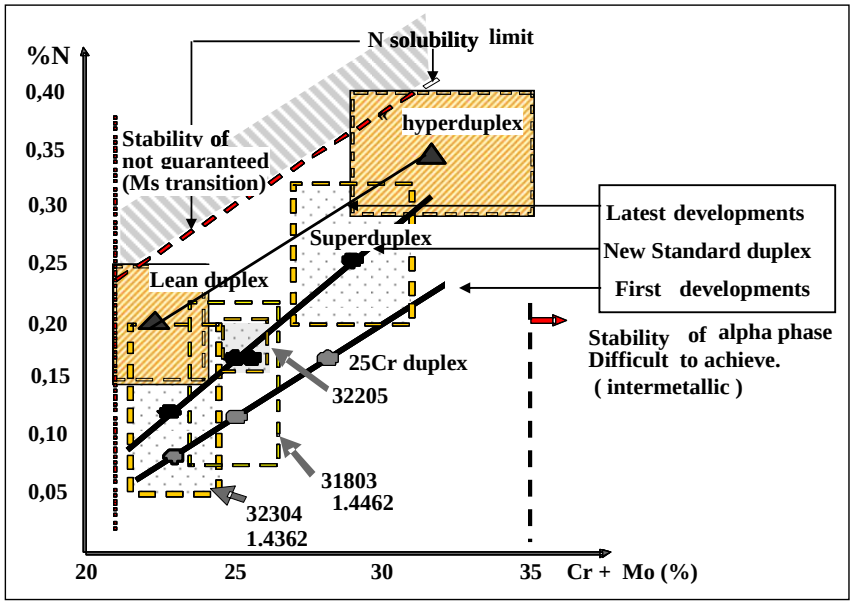

Figure 2.1. *Duplex stainless steels and nitrogen solubility*

2.3. Some fundamentals concerning stainless steel corrosion resistance

2.3.1. *General considerations*

A metal or alloy immersed in a liquid solution may convert into its oxidized form with transfer of metal ions into the solution [BAR 93]. The reaction is known as anodic dissolution, and solid metal is transformed into ions with the most stable valence under the considered conditions. Simultaneously, an electron-consuming reaction, known as the cathodic reaction, takes place at the surface of the metal.

The intensity of the reactions depends upon several factors including the difference of potential between the solution and the alloy, the pH, the temperature, the local concentration of protons, the ability of some species – oxides, hydroxides or complex species – to adsorb at the surface and form a sufficient impermeable and adherent film.

In the case of stainless steels, such a superficial film is called a “passive” film or passive layer, and can considerably reduce the anodic dissolution reaction and lead to phenomenon known as “passivation”.

The thermodynamic conditions for developing such a passive film are predicted by the so-called Pourbaix diagrams (potential/pH diagrams). Unfortunately, the protective nature of the film depends on structural and kinetic factors, which can not be interpreted by Pourbaix diagrams.

One of the best ways to investigate the corrosion-resistance behavior of stainless steels in liquid solutions is the plot of current density versus a given applied potential. Typical curves are presented in Figures 2.2 and 2.3 [BAR 93].

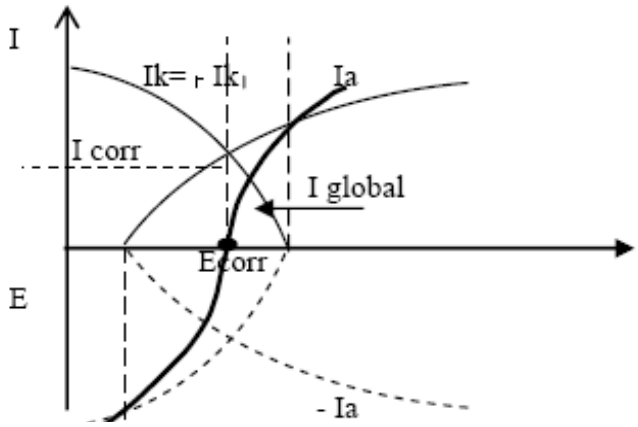

Figure 2.2. *Current density versus potential curves of the anodic (Ia) and cathodic (Ik) reactions of a given metal in a given solution. The global current Ig equal to the sum of the anodic and cathodic currents becomes zero at the corrosion potential (E=Ecorr)*

2.3.2. *Some definitions*

Ecorr: is the corrosion potential; the potential at which the anodic and cathodic currents are equal in a steady stage and as a result, the overall current “Icorr” is zero (Ig = Ia + Ik with Ia > 0 and Ik < 0 and for Ecorr Ia = -Ik).

Anodic peak: is the peak of the current generally observed for potentials higher than Ia = 0 (when the material start to be active). This peak current corresponds to an area where the dissolution of the alloy is predominant.

Ecrit: is the critical potential; the potential corresponding to the maximum of the anodic peak.

Icrit: is the critical current density; the current density corresponding to the Ecrit. Icrit has considerable practical importance, as it represents the additional cathodic current density that must be applied to the alloy to overpass the Ecrit and, as a result, move to the passive plateau. The critical current density (Icrit) depends upon in-service conditions and, particularly, the pH of the solution (lower pH, higher anodic peak). Figure 2.2 illustrates the significance of Icrit for different cathodic current densities (Ik)/cathodic curves.

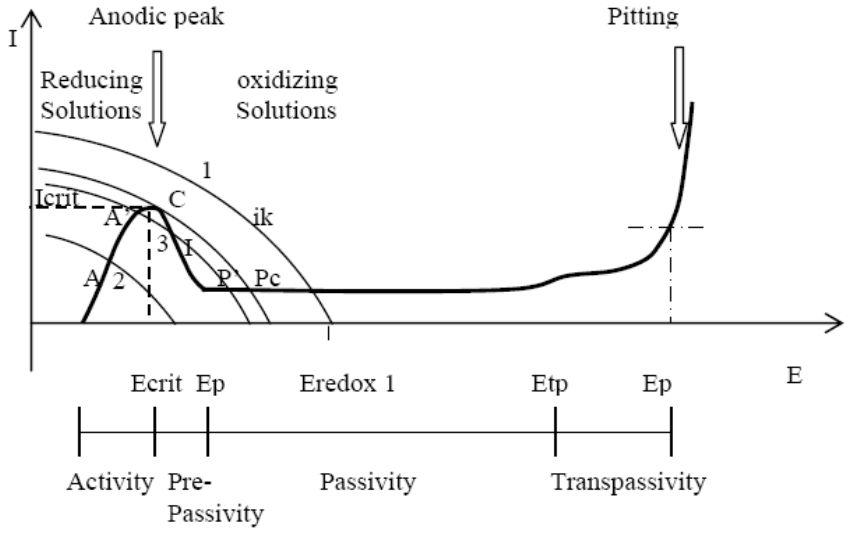

Figure 2.3. *Typical current/density curves obtained by electrochemical investigation on stainless steels for several conditions*

Passive plateau: when increasing the potential, after the anodic peak, the anodic curve may present a plateau, the so-called “passive plateau”. The current density can sharply drop and, as a result, the dissolution kinetics of the alloy is strongly reduced. The alloy is then considered to be in a passive stage, and a tightly adherent film (of a few nanometres) is formed on its surface (the so-called “passive film”). Before reaching the passive plateau, the area of the anodic peak corresponding to a decrease in the current density is often called the prepassivity area.

Transpassivity: is the area of anodic curve where the current density for potentials, higher than those of the passive plateau, starts to increase. This area may also present a kind of plateau. Under those conditions we are moving from the passive potential (Ep) to the transpassive potential (Etp) condition where the passive layer (generally an oxide layer) starts to be less protective.

Eredox: is the redox potential of the solution, which is the potential corresponding to a cathodic current equal to zero.

In case of cathodic curve 1 (Figure 2.3) – very oxidizing conditions – there is no stable active state and the passive film will be the form of quasi-equilibrium observed. In the most oxidizing conditions, the redox potential could even be in the transpassive area and as a result, the passive film could be unstable.

In case of cathodic curve 2 – very reducing conditions – there is no stable passive state, and the metal, therefore, dissolves in the active state.

In the intermediate case – cathodic curve 3 – there exists a metastable passive state (P'), a stable active state (A'), and an unstable passive state (I).

Point A' should be considered as the long-term static behavior of the alloy. We must consider in that condition that the ability of the metal to passivate naturally does not exist.

Curve C represents the limit between cases 1 and 3 and represents the critical cathodic curve leading to spontaneous passivation of the alloy in given conditions.

pHd: the pH of depassivation, which is investigated for a specific alloy composition and greatly depends upon environmental conditions. It corresponds to the pH for a given solution, above which the critical passivation current density becomes negligible, or at least of the same order of magnitude as the passive current density. The chloride and fluoride species present in the solution have a great influence on the depassivation pH as they are generally responsible for destabilization of the passive film. In a first approximation, a medium can be considered as neutral towards a stainless steel if its pH is higher than the pHd, and acid in the opposite case. Depassivation pH data are often recorded when crevice corrosion resistance of an alloy in a specific in-service condition is investigated. Furthermore, the pHd value indicates the ability of the passive film to resist local damage.

Ep: the pitting potential, it is the critical potential value, above which the passive film is unstable and local damage to the passive film occurs. In most cases, it starts around metallurgical discontinuities, such as inclusion (particularly when containing sulfur) or grain boundaries. At this potential and at higher potentials, the current

density suddenly rises to much higher values than that of the passive stage and local dissolution of the alloy starts. As a result, pits are formed in the surface of the metal investigated. The pitting potential is strongly related to the chemistry of the alloy, its cleanliness, and environmental conditions. The critical pitting temperature of an alloy in a specific condition is the critical temperature at which pitting occurs at the rest potential for that material in the defined conditions. Before reaching the Ep value polarization curves often show some current density peaks, which are related to pitting initiation followed by repassivation mechanisms.

2.3.3. *Parameters affecting the corrosion resistance of duplex grades*

2.3.3.1. *Alloying element effects*

Stainless steels – steels alloyed with a minimum level of 11.5% chromium – are known to be corrosion-resistant grades. In reality, the main property is their ability to quickly form a strong passive film in most wet oxidizing conditions in an extended range of potentials and pHs.

The adherent tinny film of several tens of Angstroms, which develops at the surface of the steel, has a low ionic permeability and as a result, the kinetics of the anodic dissolution rate drops to such a low level that the weight losses are acceptable to end users (for industrial or domestic uses). Furthermore, the passive film is uncolored and transparent. The beauty of this mechanism is that when stainless steels are damaged by, for example, scratches or abrasion phenomenon, the passive film is spontaneously restored in the passive stage. Stainless steels are self-healing or self-recover to some respect.

An increase in the chromium content enhances the strength of the passive film and as a result, drastically improves the corrosion resistance of the stainless steels (Figure 2.4).

Duplex grades have a minimal chromium content of 20%, i.e. significantly higher than most ferritic and austenitic stainless steels. Furthermore, most have the addition of complementary molybdenum, or alternatively tungsten (W) or copper (Cu) elements, which are known to be beneficial elements enhancing the corrosion resistance of the grades under most of the in-service conditions (Figure 2.5). Some synergies between those elements and chromium have been reported in the literature [AUD 93].

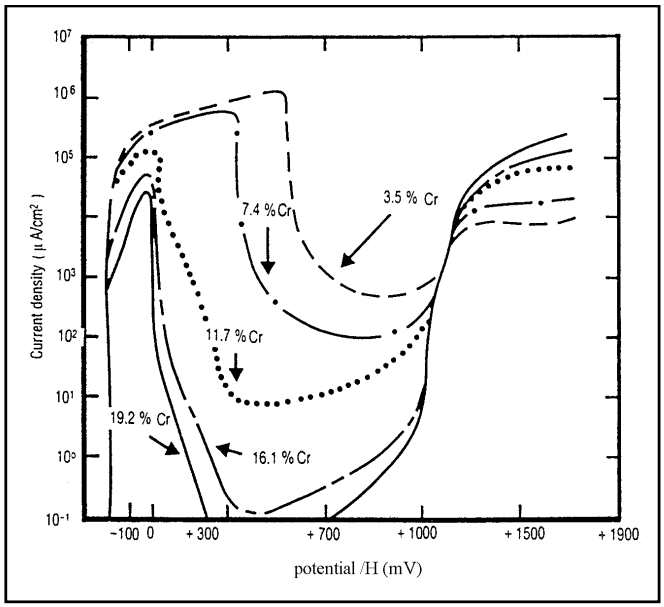

Figure 2.4. *Influence of chromium alloying on the corrosion resistance of steel in 1 M sulfuric acid (H_2SO_4) solution at 90°C*

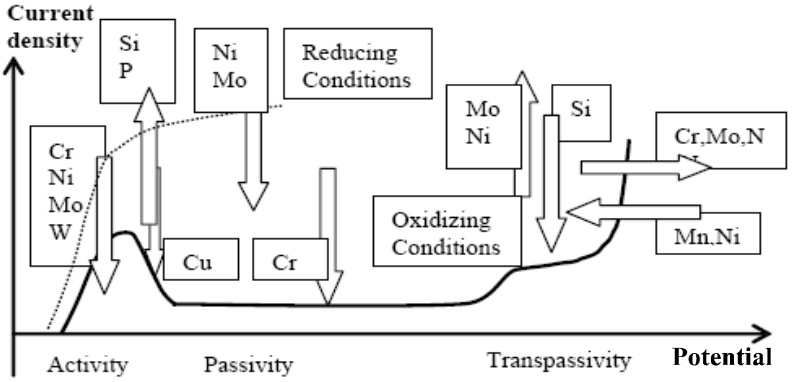

Figure 2.5. *Influence of alloying elements on the corrosion resistance*

The duplex grades are clearly designed to resist corrosion significantly better than the classical ferritic or 304/316 austenitic grades. Some duplex grades have

additional copper, which is known to have very positive effects in sulfuric acid solutions. Tungsten is known to further enhance the resistance of stainless steel to abrasion-corrosion resistance phenomena. Moreover, duplex grades have high nitrogen contents, which are known to be beneficial for localized corrosion resistance (pitting and crevice).

Among the detrimental alloying elements, sulfur has probably the worst effect. Sulfur is generally combined with manganese or several oxides to form precipitates. The worst case is a big size inclusion (a few microns) with enriched sulfur compounds on the interface inclusion/matrix, surrounded by sulfur species. Locally, the passive film is unable to resist and severe local corrosion may begin. Chromium carbides and, to some extent, nitrides are also known to reduce the corrosion resistance mainly due to the formation of dechromized areas around the precipitates, which occur mainly at grain boundaries. Duplex grades are less sensitive than austenitics regarding this phenomenon as they have a dual microstructure and ferrite transforms into a eutectoide austenite plus carbide structure. This makes it possible to firstly move the grain boundary, and secondly, speed up the chromium diffusivity by the presence of ferritic grains having a higher chromium diffusion coefficient than the austenite phase. The dechromization process is reduced [DES 93].

Manganese additions have a controversial effect. They are known to increase the nitrogen solubility and in some respect – direct or indirect effect – to stabilize the austenitic phase. Conversely, most of the localized, mainly pitting, corrosion-resistance investigations have underlined a negative effect of manganese additions.

2.3.3.2. *Metallurgical, forming, and welding effects*

Duplex stainless steels have almost a 50% austenite + 50% ferrite microstructure. Each phase has a specific electrochemical behavior and as a result, the anodic curve is the sum of both ferritic and austenitic curves. Figure 2.6 shows an example of a current density/potential plot obtained for the alloy, S32304, in a 0.5 M H_2SO_4 solution containing 10 mg/l sodium chloride (NaCl) at 70°C. The respective positions of the anodic peaks for ferrite and austenite are indicated [DES 93].

Preferential dissolution of ferritic or austenitic phases can be obtained by the appropriately selected applied potential. Fortunately, the high chromium and molybdenum contents of most of the duplex grades endow them with an exceptional capacity for passivation in most of the oxidizing industrial solutions. The relatively small differences in chemical compositions of the two phases lead to similar behavior, so that selective dissolution phenomena are, in fact, quite rare. Nevertheless, in studies of corrosion under extreme service conditions, it is essential to take into account the microanalysis of each constituent, which will depend on both alloy chemistry and heat treatment.

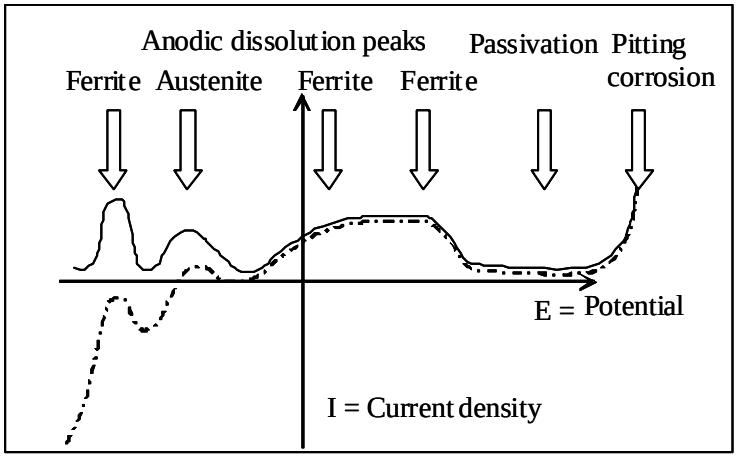

Figure 2.6. *Polarization diagram of alloy S 32304 in 0.5 M H_2SO_4 + 10 mg/l NaCl solution at 70°C. The curve presents several anodic dissolution peaks reflecting the multiphase structure*

Incorrect heat treatments obviously have a detrimental effect on the corrosion resistance of the alloy. Sigma phases, chi phase, or even gamma 2 phase precipitations by such chemical deviations are typical areas more prone to be corrosion initiation sites. Those precipitations are often observed in welded structures – HAZ and welded metal – when welding conditions are not optimized. A solution-annealing heat treatment is then recommended to restore the corrosion resistance of the duplex grade. Fortunately, in most cases the selection of appropriate welding conditions (specific heat input versus thickness and grade) and an over-alloyed filler metal make it possible to obtain acceptable corrosion resistance properties in the welds without complementary heat treatment. Welding will be free of slag inclusions and preferably pickled to avoid superficial oxidized areas. A smooth geometry is recommended to avoid possible local crevice-like configurations and optimize fatigue corrosion resistance.

Finally, stress concentration factors have to be reduced and residual stresses kept to a minimum. The ability to create smooth surfaces, which enhance the in-service properties of the grades, will once again be highlighted

2.3.3.3. *Media-related effects*

Independent of the composition of a material, the stability of the passive film depends mainly on the acidity (pH) and the oxidation-reduction or “redox” potential

of the medium, which create the metal-solution potential difference and, as a result, effects the active, passive, or transpassive dissolution state of the alloy (Figure 2.3).

Some anions like chlorides, fluorides or sulfides (mainly HS-) can disrupt the passive film due to complex and not fully elucidated processes. As a result, the passive film can be damaged and a strong anodic dissolution current may be observed (corrosion of the material). It is noteworthy that the consequences of those disturbances have different effects depending on the acidity of the media. In acid conditions, chlorides and sulfides increase the rate of uniform corrosion, whereas in neutral and oxidizing conditions they promote the appearance of the first steps of localized corrosion, which may result in further change of the rest potential and bring the metal to an active stage (Figure 2.7).

An increase of temperature enhances both the cathodic and the anodic reactions. The corrosion rate is known to be generally thermally activated. The phenomenon is generally not linear as there may be competition between the positive effect consisting of an increase in the kinetics of passivation and the negative effect consisting of the enhancement of anodic dissolution and cathodic reactions. As a result, in many cases, the temperature dependence of the corrosion rate of duplex alloys presents a kind of plateau over a quite large range of temperatures, depending mainly upon the chromium and molybdenum contents, followed by a sharp increase of the corrosion at a given temperature.

The fluid rate of the media has contradictory effects. It may contribute to an enhancement of the corrosion resistance by enhancement of the passivation kinetics and reduction of local severe corrosion, due to the agitation phenomenon that avoids some deposits, by local changes of the chemistry of the media. This is particularly the case for low-oxidizing media.

Higher fluid velocities, turbulences, and moreover, cavitation phenomena are definitively more stringent conditions and may often result in enhancing the corrosion rate of the stainless steels. Vapour bubble implosion phenomena at the surface of the steel, encountered in some cases of high velocity fluid, may mechanically destroy the passive film. Those phenomena that destroy the passive film and, thus bring the stainless grade to an active stage, are enhanced by the presence of solid particles in the fluid. The damage resulting from such abrasion-corrosion phenomena depend on the metal-medium couple, the nature of the particles (hardness, shape, density, weight, etc.), the angle of impact, the fluid rate, and the acidity [AUD 93].

The major parameters affecting the corrosion resistance of duplex stainless steels are presented in Table 2.2.

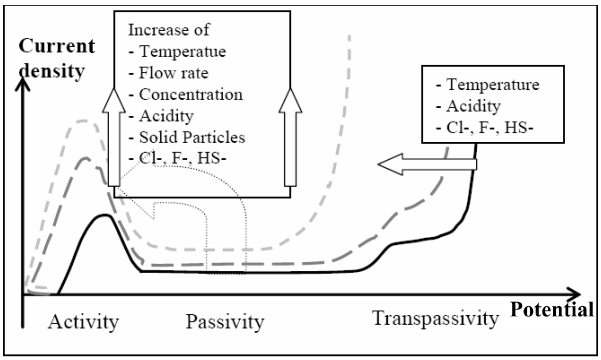

Figure 2.7. *Influence of media-related parameters (temperature, acidity, composition, and velocity of the solution) on the corrosion resistance of the polarization curves of stainless steels*

Stages	Positive effects	Negative effects
Alloying elements	Cr, Mo, W, Cu, N, Ni	S, O2, C, Mn
Metallurgy	Casting technology (magnetic bearing)	As-cast microstructure particularly when machined
Manufacturing aspects	Hot deformation + solution annealing	Inclusions particularly with S content
Improve the homogenity	Cold deformation + solution annealing	Segregated areas (machined samples)
	Solution annealed products	Inadequate heat treatment
	Water quenched products	Air cooling
		Gamma 2&3 islands/lower Cr, Mo contents/carbides
		Sigma, Chi phases with local depletion of Mo, Cr
Forming and welding	Respect of manufacturing procedures	Phase precipitations (600/1,000°C).
	Welding: use the appropriate heat input	Too high ferrite contents in HAZ.
	Welding: use overalloyed filler metals + N_2	Heavily oxidized welds/non-protective gases
	Avoid stress concentration effects	Remaining slag inclusions
	If needed: final solution annealing treatment	Lack of penetration, crevice-like configurations
	Final pickling treatment	Improper cooling rates including final treatment
Media-related aspects	Medium oxidizing conditions	Chlorides, sulfur contaminations
	Control of process conditions	Temperature rises
		Abrasion mechanisms
		Applied stresses
		Deposits, non-flowing conditions

Table 2.2. *Influence of different parameters on the corrosion resistance of duplex grades*

2.4. The different forms of corrosion

2.4.1. *General considerations*

The different kinds of corrosion encountered in industrial applications are presented in Figure 2.8. Uniform corrosion is the most frequent case but it concerns only 35% of the cases investigated [AUD 93].

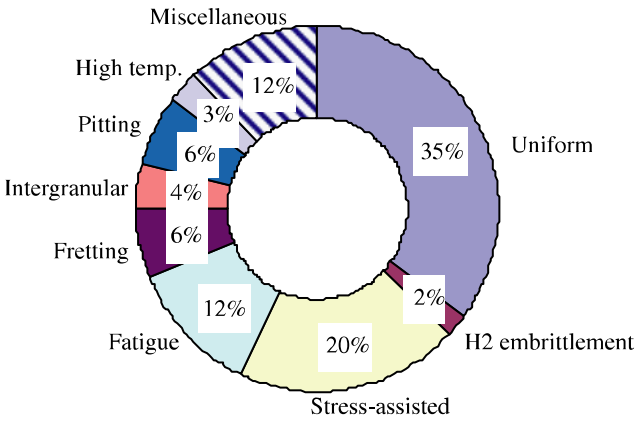

Figure 2.8. *Statistical breakdown of various forms of corrosion in industrial applications*

Stress corrosion and fatigue corrosion are, respectively, the second and third most common forms of corrosion damage. Both types of corrosion result from the combined effects of residual stresses or applied stresses and a corrosive environment. The consequences of such failures may be catastrophic as they mainly occur in non-anticipated conditions. When considering life cycle costs, design approaches are of crucial importance as they are the best way to reduce stress concentration effects. Welded joints should be carefully executed to avoid misalignments or lack of fusion. Fretting corrosion could also be considered to some extent as resulting from an “improper design” effect.

Finally, intergranular corrosion (IGC) and pitting corrosion in the case of appropriate material selection for the in-service conditions, reflects in most cases an inappropriate thermo-mechanical cycle applied during manufacturing of the alloy or the vessels. Joint boundary precipitations, such as carbides or intermetallic phases, may locally weaken the corrosion resistance of the alloy. Pitting generally occurs on inclusion sites rich in sulfur or on ferrite/austenite grain boundaries having some precipitations. The latter condition occurs mainly in more oxidizing conditions or

very corrosive conditions (increases of acidity, temperature, chloride or sulfide concentrations).

2.4.2. *General corrosion*

2.4.2.1. *"Reducing type" mineral acids: hydrochloridric acid*

Hydrochloridric acids and related industrial solutions have a high activity due to their strong reducing properties making the passivation of the duplex stainless steels unlikely despite their high chromium and molybdenum contents. Except for much diluted solutions, the alloys dissolve in the active state (Figure 2.3, cathodic curve 2). In such highly reducing conditions, the addition of some oxidizing species has a strong detrimental effect, contrary to their beneficial effects on the passivation in the low oxidizing solutions, as the anodic dissolution reaction is enhanced by a shift towards higher potential of the redox potential. Slight changes of the industrial conditions, such as air or oxidizing impurity contaminations, combined or not with local metallurgical heterogenities, such as segregation, carbide or intermetallic phase precipitations, may result in the rapid development of corrosion [AUD 93].

In such strongly reducing solutions, duplex grades are not recommended. In these cases highly nickel-alloyed grades should be recommended, if not other materials than stainless or nickel alloys. Superduplex grades could be considered only for HCL concentrations lower than 1% under boiling conditions and 2% at 60°C.

2.4.2.2. *"Non-oxidizing type" mineral acids*

2.4.2.2.1. Sulfuric acids

Pure and fairly diluted sulfuric acids are not oxidizing solutions and severe corrosion phenomena may occur if special care is not taken to material selection. The effect of oxidizing impurities is once again particularly important in a sulfuric media when considering material selection as, together with temperature and acid concentration, it clearly defines the conditions of passivation of the stainless steel grades. The presence of oxygen or reducible compounds (Fe3+, As3+, etc) in the solution displaces the cathodic curve towards more positive potentials, which corresponds to either an acceleration of the corrosion rate for the less alloyed stainless steels or conversely, to a passivation of the more noble stainless steels.

Figure 2.9 presents indicative iso-corrosion curves of several stainless steels in sulfuric acid media. Once again, the data must be considered with extreme attention as the real conditions often have a modified redox potential and possible additionally worse conditions on the stability of the passive film, such as chloride, fluoride

contamination effects, abrasion-erosion phenomena, local metallurgical heterogenities, or stress concentration effects.

When considering the effects of alloying elements in sulfuric acids, the most effective elements appear to be chromium and molybdenum. Molybdenum confers an extremely high passivity regeneration rate to the steels, regardless of the hydrodynamic conditions. It seems that the presence of molybdenum reinforces the action of chromium. Both elements are observed in the passive film [AUD 93].

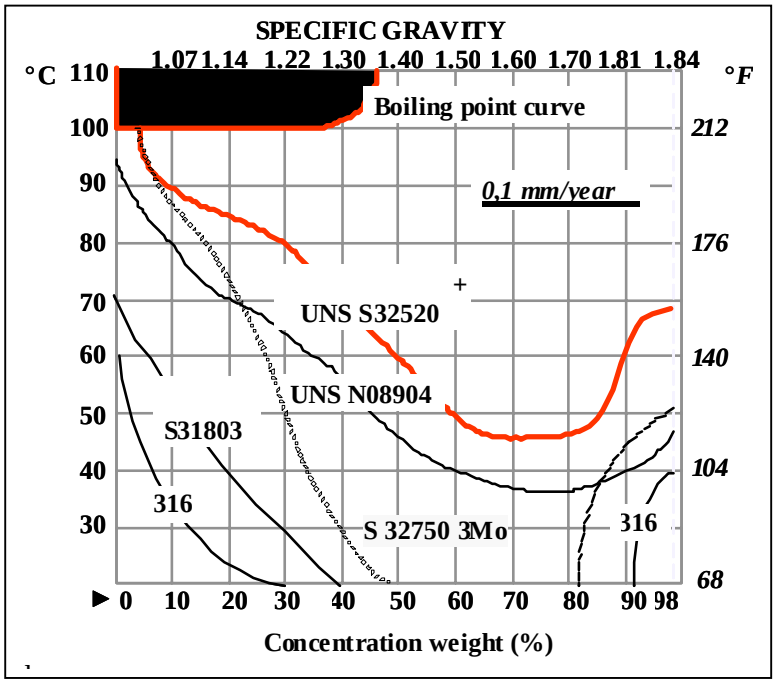

Figure 2.9. *Iso-corrosion curves of corrosion resistance of stainless steels in sulfuric acid for different levels of concentration*

Alloying stainless steels with copper notably reinforces the corrosion resistance at lower potential (close to the anodic peak between -150 and +55 mV/SHE) when chromium and molybdenum additions are not sufficient to passivate the material. In those conditions, a thin, superficial, pure metallic copper precipitation resulting from the dismutation of Cu+ and Cu+2 cations can be observed on the surface of the copper-bearing stainless steel. The film is particularly corrosion resistant in such redox potentials and provides excellent corrosion-resistance properties, even in presence of flowing fluids (heat exchangers). At higher potentials, the beneficial effects of copper addition are less obvious. Globally, copper-bearing stainless steels

are to be specified in industrial applications having more varied in-service conditions because of the wider spectrum of passivity of the stainless alloys.

Among other alloying elements, tungsten does not seem to have a positive effect on the corrosion resistance of the stainless steels in sulfuric acid solution, even in static conditions. This result is explained by the formation on the surface of powdery, non-protective WO_2 or WO_3 oxides, depending on the redox potential.

Sulfuric acid solutions are often encountered in many industrial in-service conditions. Most of the corrosion-resistance data clearly indicate that cost savings can be made when austenitic stainless steels are substituted for those of the duplex family. For the more diluted conditions 304 and even 316 grades can be substituted by lean duplexes, i.e. the S32304 grade with or without copper (Figure 2.10) and even in the less severe conditions by the S32202 grade. When the acidity and/or the temperature increase, the duplex S32205 grade is clearly a much safer choice than the 316LN and even 317LM (N) grades. This is particularly the case of diluted sulfuric acids with chlorides ions. (Concentrated sulfuric acids diluted with seawater, for example).

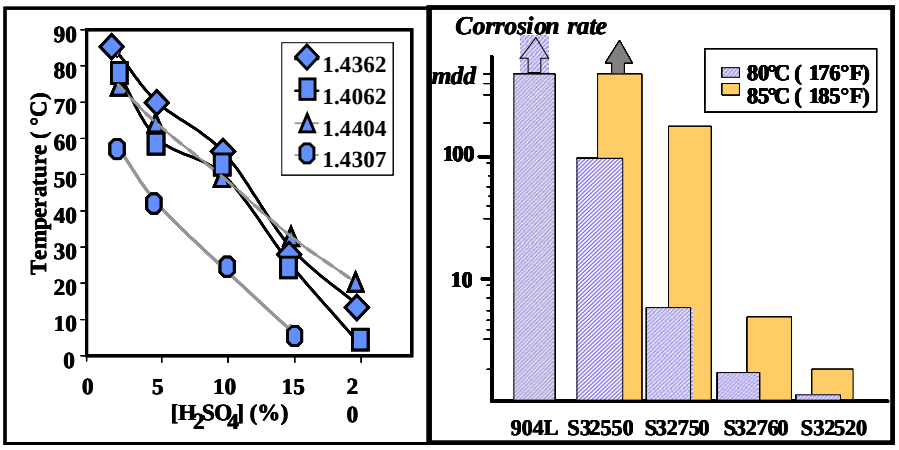

Figure 2.10. *a) Isocorrosion data determined in pure diluted H_2SO_4 (corrosion rate 0.2 mm/y). b) Weight losses (mdd) in a 10% H_2SO_4 + 500 ppm Cl^- solution (80 and 85°C)*

For the most severe conditions, “superduplex” grades and, more particularly, the grades S32520 with 25% chromium, 3.5% molybdenum, and 1.5% copper additions are considered to replace the 904L alloys (Figure 2.10a and 2.11).

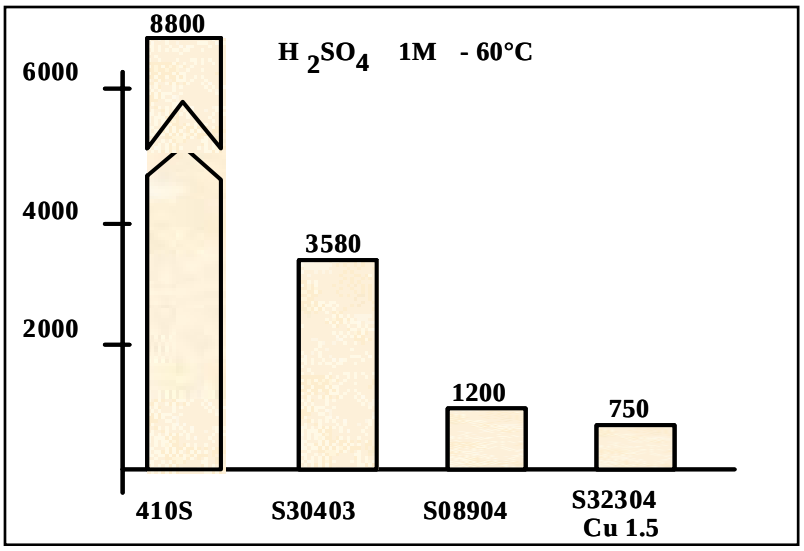

Figure 2.11. *Weight loss measurements in a 1 M H_2SO_4 solution under abrasion corrosion*

2.4.2.2.2. Phosphoric acids

Pure phosphoric acid: Phosphoric acid solutions, free of impurities, are not very aggressive solutions. Nevertheless, 17% Cr ferritic, as well as 304 austenitic, grades suffer from severe corrosion at temperatures higher than 50°C for all concentrations and should only be considered for use at low temperatures and for diluted phosphoric acid solutions.

Molybdenum addition, typically 2.5%, considerably enlarges the passivity range; 316L + 2.5Mo grade can be selected for all applications until the boiling temperature up to 50% concentration. In more concentrated, pure phosphoric acid solutions, the alloy should not be recommended for use at higher temperatures (Figure 2.11).

Again copper additions have a very positive effect on the corrosion resistance properties of stainless steels. Only 0.35% copper complementary additions to a 316L + 3Mo grade make it possible to use the grade in up to 85% H3PO4 acids at 120°C. For more concentrated acids and higher temperatures, the 904L grade, having copper additions, is generally recommended even in pure acids at temperatures up to about 180°C (Figure 2.12).

Superduplex alloy UNS 32520 with 25% Cr, 3.5% Mo, and 1.5% Cu is also to be specified in most phosphoric acid applications.

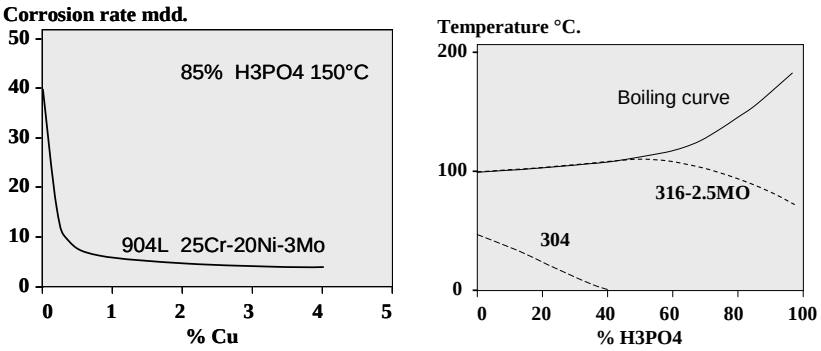

Figure 2.12. *Beneficial molybdenum and copper alloying effects of stainless steels in H_3PO_4 solutions*

Case of industrial phosphoric acids: The "wet" method is the most used method. It consists of attacking neutral tricalcium phosphates, $Ca(PO_4)_2$, with a solution of concentrated sulfuric acid at temperatures between 80 and 100°C. Impurities, such as silica (SiO2), calcium fluorides (CaF_2) or chlorides (CaCl2 and NaCl), are present. As a result, a slurry of approximately 30% P2O5 contaminated by fluoride species in the form of hydrofluoric (typical level of 0.1 - 0.2% HF) and/or fluorosilicic acid (1.5% H2SiF6), as well as chlorides (500 to 3,000 ppm), is formed. Furthermore, the slurry contains non-reactive silica particles (quartz), which cause significant abrasion phenomena.

The calcium sulfate is separated from the slurry by filtering at around 50°C. Finally, the phosphoric acid solution loaded with the remaining impurities is concentrated up to about 54% in a partial vacuum exchanger around 120°C (Figure 2.13).

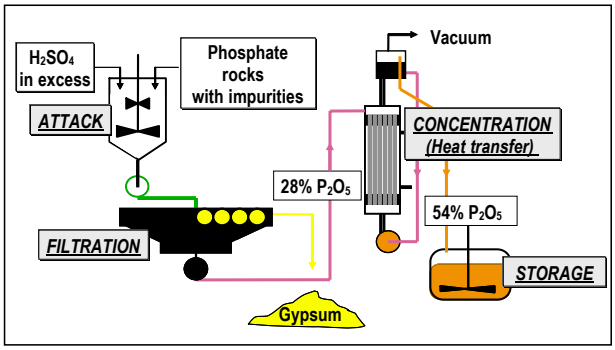

Figure 2.13. *Simplified flow diagram of phosphoric acid production*

Several corrosion-resistance investigations have determined the relative effects of alloying stainless steels, the influence of the levels of impurities, the phosphoric slurry temperature and concentration in order to better design with alloy selection the different stages of the process: phosphate attack, filtration of the slurry, and finally, the concentration of the phosphoric acid.

The main conclusions are as follows:

– the attack of natural phosphates: the abrasion corrosion conditions (presence of quartz) combined with the temperature and significant levels of HF and H2SO4 plus chlorides, requires high levels of chromium (20-25%), molybdenum (3-5%) and copper (0.5-2.5%) additions to enhance the corrosion resistance in the active stage and speed up the depassivation reactions. The best candidates are the superaustenitic grades having 25 to 35% Ni or the "superduplex" S32520 grade with 25% Cr, 3.5% Mo and 1.5% Cu (Figures 2.14 and 2.15).

Although the superduplex grade S32520 performs very well in most of the applications due to its combined abrasion resistance (higher mechanical properties) and high corrosion-resistance properties (Figures 2.14 and 2.15), the alloy, N08028, performs even better. This is probably explained by the active conditions encountered under abrasion where higher nickel contents are beneficial for the corrosion resistance.

– filtration of the slurry: lower temperatures (close to 50°C) and the absence of abrasion makes it possible to select lower alloyed stainless steels, particularly when impurities and, particularly chloride, contents are low. In this case, the 316L grade is often selected for the filters and pumps. Nevertheless, when the chloride content increases to 500-1,000 ppm, more alloyed stainless steels should be considered (superduplex S32520 or superaustenite grades). This is clearly observed in Figure 2.15.

– concentration of phosphoric acid: the filtrated 30% H_3PO_4 slurry is carried out under partial vacuum into a concentrated loop consisting of an exchanger and a circulation pump. The exchanger tubes, the most critical components of the process, are generally made of graphite due to temperature and severe corrosion conditions, particularly when an excess of sulfuric acid exists. In this case, the use of superaustenitic grades has been considered, but in most of the applications corrosion phenomena or/and calcium sulfate deposits, which reduce the heat transfer and, thus, the productivity, have been reported. Typical corrosion resistance data for 54% P2O5 solutions are presented in Figure 2.16.

Figure 2.14. *S32520 superduplex grade selected for an agitator working in an attack tank for phosphoric acid production (abrasion corrosion conditions)*

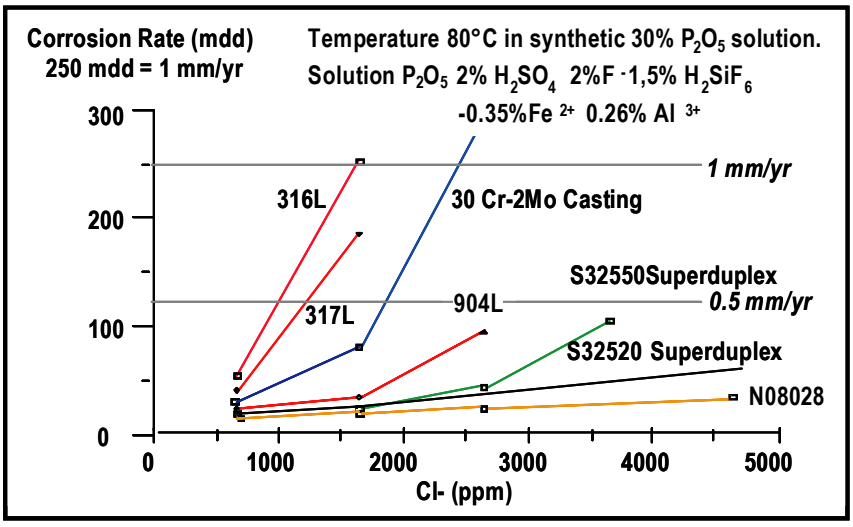

Figure 2.15. *Corrosion-resistance data determined for several stainless steels (austenitic and duplex grades) in phosphoric acid attack stage. Effects of chloride content on weight losses in a synthetic 30% P_2O_5 solution at 80°C*

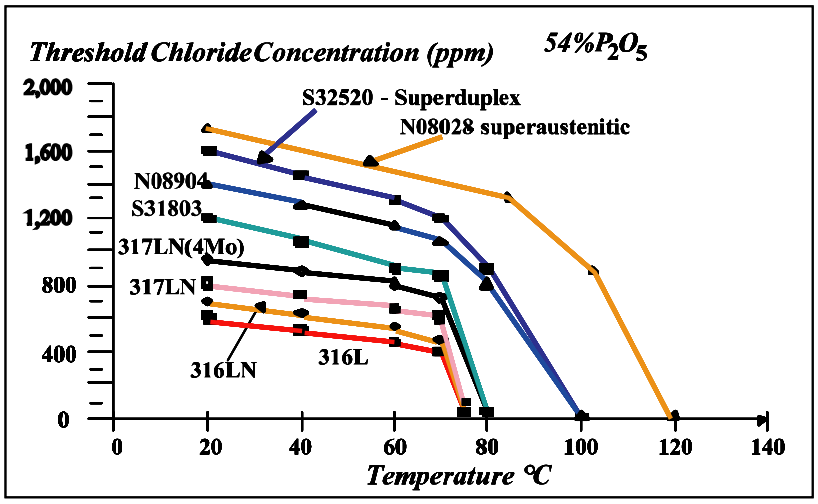

Figure 2.16. *Limit of uses of several stainless steels (austenitic and duplex grades) in phosphoric acid concentration stage or transport. Results obtained by investigating the effects of chloride concentration and temperature on the corrosion resistance behavior of several stainless steel grades (austenitic and duplex) in 54% concentrated phosphoric acid*

2.4.2.3. *Strongly oxidizing mineral acids*

The typical example of strongly oxidizing acid conditions is the nitric acid (HNO3). The acid is obtained by the catalytic oxidation of ammonia (NH_3), which forms gases (NO_2 or N_2O_4) absorbed by water. Those compounds are not very corrosive for stainless steels. When the acid concentration does not exceed 10%, 17% Cr ferritic steel or 304 austenitic stainless steels are often used in the sense that 16% Cr is enough to form a passive film at room temperature. In these extremely high redox potential, small precipitations, which are chromium rich, like carbides on the grain boundaries may lead to a very severe intergranular attack. This may occur particularly in the HAZ of the weldings. Very low carbon, as well as low silicon and phosphorus residual elements, steels are recommended. Duplex grades, including lean duplexes, can be considered as they are less prone to intergranular chromium-depletion phenomenon.

For 20-30% HNO_3 concentrations, higher chromium stainless steels are required. At a concentration of 65% HNO3, 25% Cr stainless steel is required at the boiling temperature to obtain a corrosion rate lower than 50 mdd (Figure 2.17). Silicon content appears very detrimental, and extra low silicon contents are recommended. The decrease of silicon from 1 to 0.35% reduces the corrosion rate by a factor of three.

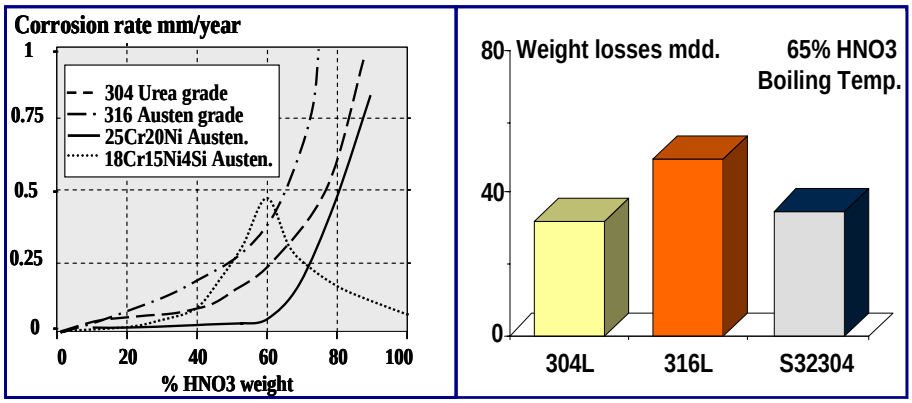

Figure 2.17. *Corrosion-resistance properties of stainless steels in HNO_3 media. S2304 grade, having high chromium and molybdenum additions, is to be considered in 65% HNO_3 solutions*

More surprisingly, molybdenum additions have a very detrimental effect on the corrosion resistance of stainless steels in boiling 65% HNO_3 solution. This results from the dissolution of molybdenum compounds in the acid; in this case molybdenum does not contribute to the strengthening of the passive film, which occurs in less oxidizing solutions, such as in sulfuric acid. As a result, in moderate corrosive conditions, the 316 alloy has a corrosion rate twice that of the 304 grade (Figure 2.17), 22% Cr and 25% Cr duplex grades having higher molybdenum contents are not considered in such media. They are very sensitive to interfacial corrosion in this environment. However, extensive testing has shown that the S32304 alloy, a 23% Cr duplex grade without Mo, has excellent corrosion resistance in nitric acid, comparable to the best 304L grades specially designed for nitric acid applications.

In 98% concentrated acid, as well as in moderately concentrated solutions containing highly oxidizing cations, for example hexavalent chromium, most of the stainless steels are subject to severe corrosion damage resulting in a particular form of localized IGC mechanism. For that particular application, a 4% Si 304 steel (S30600) has been developed.

2.4.2.4. *Strong bases (NaOH, KOH)*

2.4.2.4.1. Pure media

Caustic soda or potash solutions are negligible corrosive solutions, regardless of their concentrations. For temperatures lower than 50°C, even 17% chromium ferritic stainless steels can be selected. For temperatures up to 70°C, 17-18% Cr ferritic

steels alloyed with molybdenum are often used. Molybdenum additions seem to have a positive effect on the corrosion resistance of the alloy under such conditions.

Nickel additions have a beneficial effect on corrosion resistance in such media and this explains why 304 grade is enough to withstand significant corrosion up to about 90°C.

At higher temperatures, a minimum of 20% Cr is recommended and 25% Cr alloys are preferred as the austenitic 20% Cr are subject to undergo intergranular stress corrosion cracking (SCC) under such conditions. Their use is strictly limited to temperatures lower than 120°C in pure solutions, whereby stress concentration effects should be avoided. Aeration and concentration are also relevant parameters. Chromium and nickel additions seem to have very positive effects on the resistance to corrosion, whereas molybdenum addition seems to have a detrimental effect. The superduplex stainless steel, S32520, presents satisfactory corrosion resistance properties up to about 150°C. For higher temperatures, highly alloyed nickel grades or even pure nickel are considered for material selection.

2.4.2.4.2. Media contaminated by chlorides and/or chlorates

Industrial 50% NaOH solutions manufactured by the electrolysis of sodium chloride generally contains 1-5% NaCl and 0.1-1% $NaClO_3$. Those impurities have negligible to low corrosive effects on the austenitic stainless steels, particularly when compared to the significant risk of stress corrosion crack propagation at high temperatures in that structure. The 304 or 316 grades should not be considered at temperatures higher than 80°C.

Under those conditions, duplex grades having improved stress corrosion resistance properties are to be considered. Their use could be recommended at temperatures as high as 120°C. For the most severe conditions, nickel alloys and even low carbon content pure nickel grades are to be selected.

Once again, when considering the effects of chlorides, chlorates, or other contaminants, the redox potential should be investigated in order to determine their oxidizing power.

2.4.2.4.3. Sulfur contaminations; the specific case of the Kraft process

The Kraft process is the most common process for the manufacturing of cellulose from wood. It consists of reacting wood chips under pressure at approximately 170°C with a liquor consisting essentially of 20% caustic soda with additions of sodium sulfite (Na_2S), sodium carbonate (Na_2CO_3) and traces of sodium thiosulfate ($Na_2S_2O_3$). During the process, the solution undergoes several thermal cycles between 70°C and 170°C, and as a result, some polysulfides appear. In the

temperature range of 130°C-170°C, the corrosivity of the liquor is suddenly strongly modified and both molybdenum and nickel alloying elements play a detrimental role. The effect of molybdenum is equivalent to that observed in the pure solutions.

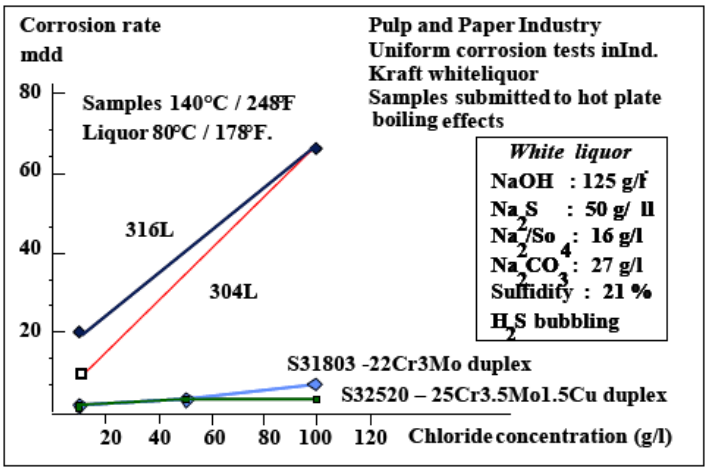

Figure 2.18. *Effects of chlorides on the corrosion-resistance properties in Kraft liquor*

The nickel effect was not expected, but under those conditions, the highly chromium-alloyed ferritic grade (26Cr-1Ni) presents the best corrosion resistance properties. Unfortunately, the grade is very difficult to produce and manufacture (welded joints with adequate corrosion resistance properties). In those circumstances, the duplex steels are the optimum choice as they combine corrosion-resistance properties and cost-savings (including weight saving when vessel design takes advantage of their high mechanical properties). Considering both general corrosion and SCC phenomena occurring in those 20% caustic soda containing chlorides, chlorates, and sulfur contents, the duplex family has experienced success stories in the pulp and paper industry (Figure 2.18).

2.4.2.5. *Organic media*

2.4.2.5.1. General considerations

Organic acids are generally less aggressive than mineral acids as they are weakly dissociated in solution. However, they can corrode the stainless steels under particular conditions, mainly at high temperature. The presence of Cl- ions substituted for hydrogen in acetyl radical considerably increases the degree of ionization and, thus, the acidity. Carboxylic acid chlorides are accordingly always more aggressive than the corresponding acids. Material selection has to take into account this evidence. Furthermore, certain manufacturing processes involve

reactions (complexations) at high temperature, which considerably increase problems regarding material selection. Some localized corrosion mechanisms may also occur at high temperature when moisture and carboxylic acids coexist.

The urea production is a typical example of the complexity of the reactions involved and as a result, specific materials, such as the S32906 grade, have been developed.

2.4.2.5.2. Acetic acid

Compared with other acids, in an aqueous solution of acetic acid the effective acidity increases rapidly with the concentration. This makes the product relatively aggressive. The material selection will depend on acid concentration, temperature, and impurities.

The 304 austenitic grades are selected in many applications where the temperature does not rise above 80°C. Almost all concentrations of acid may be considered. For concentrations lower than 20% their uses may be considered up to the boiling temperature. The 316 grades have improved corrosion-resistant properties and can be selected for almost all concentrations of acid and temperatures. Nevertheless, for the extreme conditions, boiling 99.7% acid with impurities, the 904 grade is preferred. Recently, superduplex grades have been considered as their corrosion resistance, even in boiling 99.7% industrial acetic acid, is excellent (the S32520 grade with chromium, nickel and copper additions had a corrosion rate lower than 0.02 mm/year).

2.4.2.5.3. Formic acid (HCOOH)

Formic acid is more aggressive than acetic acid. The general behavior of stainless steels can be summarized as follows:

– the 304L grade is only resistant under high temperatures when the acid concentration is less than 1% or in 100% acid;

– the 316L 2.5Mo grade has improved corrosion resistance due to the beneficial effect of molybdenum additions. It can be used up to 80°C for most concentrations;

– the duplex 2304 grade presents better corrosion resistance properties than the 316LMo grade (Figure 2.19), and is also very stable when considering phase transformations. The grade has a low nickel and high chromium content.

For higher temperatures, the selection of higher alloyed austenitic grades is not recommended as nickel additions are known to be detrimental when considering

corrosion resistance. Superferritic grades with 26% chromium and 1% nickel are very resistant but are difficult to manufacture and transform. Furthermore, they present ductile-brittle behavior for thicker gauges. The duplex family is, once again, the most appropriate choice of material, with the superduplex grades selected for the most critical conditions [BER 91, CHA 91b].

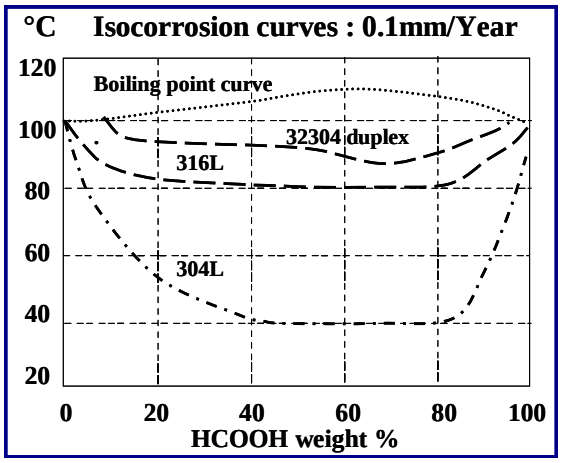

Figure 2.19. *Effect of temperature and formic acid concentration on the iso-corrosion corrosion curves of several stainless steels*

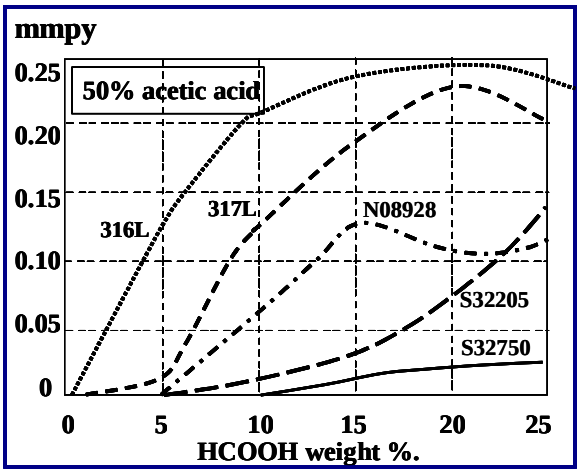

Figure 2.20. *Corrosion rate (mmpy) of several stainless steels in 50% acetic acid solution with the addition of 0 to 25% of formic acid*

2.4.2.5.4. Mixed acids: acetic + formic acids

Figure 2.20 presents iso-corrosion data obtained for several stainless steels in a 50% acetic acid containing 0 to 25% of formic acid. The exceptional behavior of duplex grades is clearly observed. More data are required to produce better material selection guidelines, including the position of the lean duplexes for use in less severe conditions.

2.4.3. *Pitting and crevice*

2.4.3.1. *Principles and similarities*

By definition, localized corrosion occurs when a significant anodic dissolution appears on a restricted zone of the steel surface with the rest of the surface remaining protected by a passive film. Therefore, local film breakdown has occurred in the absence of healing, which may eventually lead to the perforation of the metallic component.

Schematically, two main phases are discernable for both pitting and crevice mechanisms: an initiation stage, which is followed by a propagation stage. In some cases, for both pitting and crevice corrosion, a repassivation mechanism may be developed after initiation of the local corrosion process, which then terminate the process. The phenomenon may or not restart at the same area or in other place.

When considering the initiation stage, crevice formation starts by the breakdown of the passive film in the presence of occluded zones in which the acid medium progressively develops. The occluded zone may be local discontinuities or even under-deposited areas as a local galvanic coupling may form in those circumstances.

For pitting corrosion, the initiation stage occurs in the absence of either mechanical or geometrical heterogenities. The pit often initiates in weaker areas of the passive film when corrosive conditions are on the borderline of the stable passive domain. Typically, pits start on inclusion – preferably on big inclusions surrounded by sulfur species – or intergranular areas in the vicinity of chromium-rich precipitates (carbides, gamma 2, sigma, etc.). Pitting mainly occurs in oxidizing conditions.

The propagation stage for both pitting and crevice formation follows almost the same mechanism. After the start of the anodic dissolution process, local conditions are modified due to the formation of corrosion products. Local modification of the composition of the medium itself, function of the mobility of ions species, and galvanic coupling phenomenon may develop. As a result, local acidification occurs and the corrosion mechanism, including anodic dissolution, is enhanced.

Very seldomly the corrosion stops after crevice initiation; this occurs in some circumstances, such as a drop in the temperature or modification of the hydrodynamic properties of the medium. In the case of pitting corrosion, the repassivation process occurs more often and the corrosion may completely disappear or restart in the same or another place.

In summary, both pitting and crevice propagate locally and the mechanism is characterized by potential, pH, chemical gradients modified by local anodic dissolution, and properties of the steel (chemical composition, phase precipitations).

Corrosion resistance data will concern the determination of critical pH of depassivation, critical potential, critical temperature, PRE(N) numbers related to the chemistry of the alloy, all parameters defined for a given condition.

2.4.3.2. *Pitting corrosion mechanism*

The pitting corrosion mechanism is illustrated in Figure 2.21. The current potential curve i(E) is monitored, for a given stainless steel, in a potentio-kinetic mode and in a neutral chloride-containing medium. Ep is the critical pitting potential determined for a given current density, and is far higher than the current density of the passive plateau. Low redox potential, i.e. corresponding to reaction 1 leads to a stable passivity at a potential E1 lower than Ep.

For position 2, corresponding to a cathodic reaction (K2), point C2 corresponds to a potential E2 higher than Ep and pitting corrosion occurs. Curve (R) is obtained by inverting the scan of the potential to more negative values from an arbitrary K point of the i(E) curve. The Rp and Up values are determined by the crossing of curve (R) and i(E) curve. Up is called the protection potential. At potentials lower than Up, the steel has the ability to repassivate spontaneously. The Up value is related to the nature of the damages already produced by the pit.

We should also note, as already explained, that when pitting starts, the solution locally in the pit is continuously changing and acidification occurs. When free potential is recorded, we generally observe a shift from noble potentials when the pit initiates to more reducing conditions when propagation occurs. This indicates that the anodic dissolution step starts to be predominant and that locally, due to acidification, we could be in the anodic dissolution peak often observed on polarization curves determined in low pH conditions.

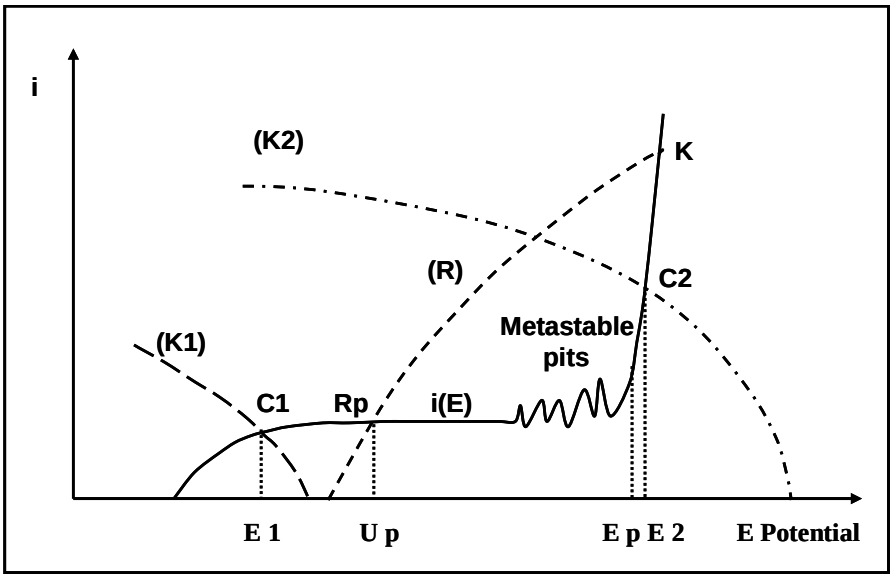

Figure 2.21. *Pitting corrosion mechanism and related current/potential curve*

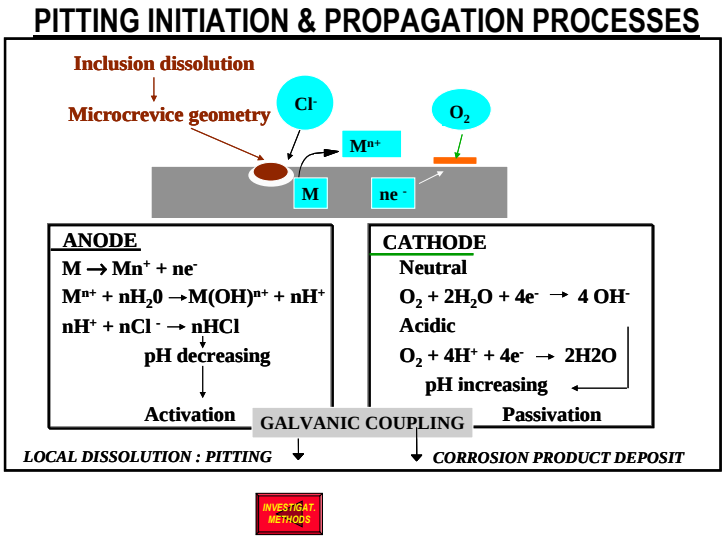

Figure 2.22. *Pitting initiation and propagation mechanisms and reactions*

It is noticeable (Figure 2.21) that before reaching the Ep potential, some discontinuities on i(E) curves are observed. In that region, metastable pits are developed. In fact, the pit is initiated and is followed by a healing mechanism of the passive film.

As the pitting phenomenon is related to a breakdown of the passive film near the area where the passive film starts to be unstable, in-service conditions (temperature, acidity, oxidizing species, and ions) are prone to reduce the strength of the passive film and play a significant role in the pitting resistance of a given alloy. Naturally, the metallurgical parameters have also their specific effects. It is important to note that the critical pitting numbers generally concerns a range of values as the Ep value changes from area to area.

Figure 2.22 illustrates the main reactions governing the pitting corrosion mechanism. Pitting starts on an inclusion and anodic dissolution is enhanced in the microcrevice geometry, which is developed after the dissolution or extraction of the inclusion. A galvanic coupling takes place with a decrease of the pH in the microcavity.

2.4.3.3. *Typical critical pitting corrosion data*

Figure 2.23 is one of the most famous testing conditions. $FeCl_3$ 6% solution (ASTM G48 A test method) is a strong oxidizing acid in excess of most of the in-service practical conditions. Nevertheless, these specific conditions are prone to pitting stainless steels. The test makes it possible to obtain a ranking between the stainless steels when considering pitting corrosion. In addition, the test is very well designed to identify some structural evolutions, such as carbides, intermetallic phase precipitations, sigma phase or chi phase, heavily segregated zones with inclusions, improper inclusion properties, particularly when sulfur content precipitations or inclusions exist. As a result, the test is particularly well suited to provide a warranty concerning the quality of the melt and thermo-mechanical treatments performed on the steel. If the steel passes the test, i.e. the recorded critical pitting temperature (CPT) is higher than the minimum value, the product is safe considering the metallurgical aspects. Naturally, for each alloy, a minimal critical temperature has been determined for standard specimens.

The test does not provide useful information concerning the real in-service conditions. For example, the 304 alloy has a CPT value close to 5°C and this does not mean that the grade cannot be selected for a specific application for temperatures higher than 5°C. On the contrary, it is know that this grade is not used in marine environments where often very oxidizing conditions and chlorides are present. In those conditions, the grade develops even at such low temperatures pits.

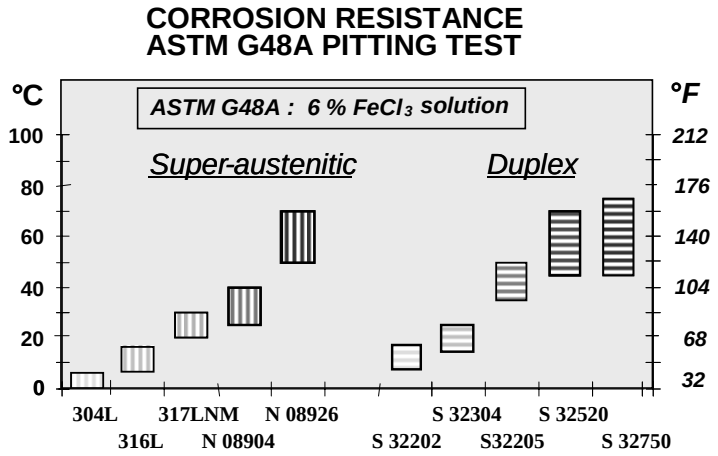

Figure 2.23. *ASTM G 48 A critical pitting temperature data for several stainless steels*

Figure 2.23 clearly shows that both families, austenitic and duplex, have CPT values related to their chemistry. Higher chromium, molybdenum, and nitrogen contents make it possible to increase the CPT. A well-know formula, PREN = % Cr + 3.3% Mo + 16% N, has been commonly agreed, although the 16 coefficient is still under question; more precisely, the formula should not be exactly the same for both families as the duplex grades have two phases, ferrite and austenite, with different chemistries. We should normally consider the chemistry of the lower-alloyed phase. The beauty of the duplex grades is that the ferrite phase contains more chromium and molybdenum than the austenitic phase but, conversely, most of the nitrogen has moved to the austenitic phase.

In the most nitrogen-alloyed duplex grades developed since the early 1990s, the chemistry has been optimized to have almost the same PREN number for both phases after solution annealing heat treatment. For example, the S32750 superduplex grade solution annealed at 1,075°C has the following chemistries for both phases:

– ferrite: 26.5% Cr, 5.8% Ni, 4.5% Mo and 0.06% N; PREN = 42.5

– austenite: 23.5% Cr, 8.2% Ni, 3.5% Mo and 0.48% N; PREN = 42.5

For the same alloy but with only 0.2% N, the optimal heat treatment temperature to obtain equivalent PREN numbers for both phases is 1,180°C. Such a temperature is not recommended for a solution annealing treatment of the alloy since higher ferrite content and higher nitrogen solubility in the ferritic grains will occur; this could result in lower corrosion resistance properties due to the precipitation of nitrides and/or gamma 2 [BER 93].

Some authors recommend the use of the PREN formula with 30 instead of 16 for the nitrogen. This is logical as practically the austenite is the lower alloyed phase and nitrogen goes mainly in it. As a result nitrogen increases in the austenitic phase, the weakest corrosion resistance phase of the duplex alloy, and is almost twice that of the bulk material. The argument could be counterbalanced by the fact that pitting often occurs at the grain boundaries.

Finally, it is surprising that the PREN number does not take into account the nickel content, which is known to play a role in the corrosion-resistance properties of the stainless steels. The lack of effect of nickel results, most probably, from the test conditions (oxidizing and acidic solution) where nickel content has almost no effect on the strength of the passive film. CPT tests performed in other test conditions, i.e. solutions where nickel additions are know to be very beneficial for the corrosion resistance of the alloy, present different CPT formulae. In those cases, nickel content is introduced in the formula.

The PREN formula issued from the G 48 test is the most common and, to some extent, is very useful to rank the different stainless steels as oxidizing conditions and chloride contamination are the most likely conditions in which pitting corrosion develops. A typical ranking map of stainless steel grades by using the PREN formula is presented in Figure 2.24.

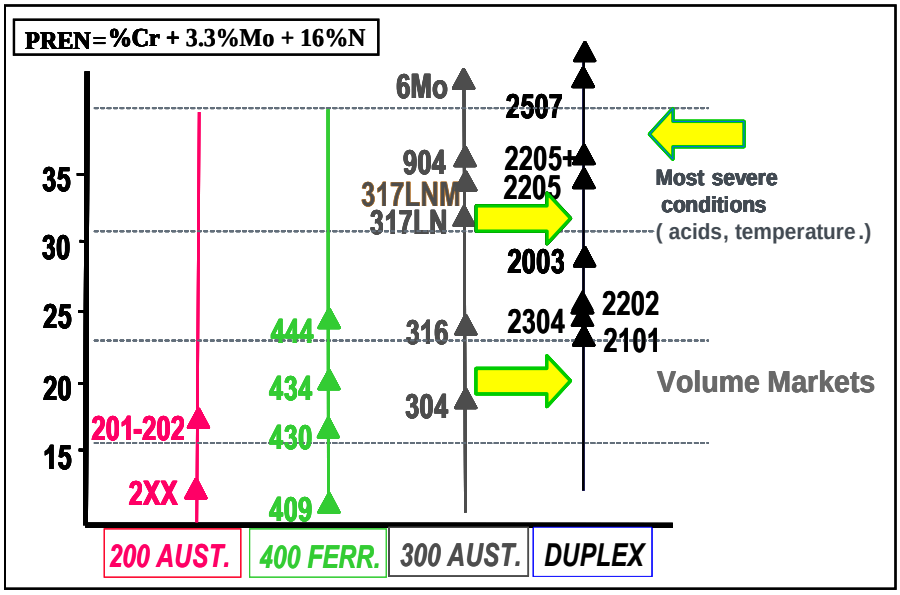

Figure 2.24. *Stainless steels families and PREN numbers*

Figure 2.24 clearly illustrates that the duplex stainless steels are designed with PREN values higher than 20; i.e. higher than the PREN value of the 304 grade. The 2205 type duplex is the most popular of the duplex family and has a PREN value in the 33-36 range, almost equal to the PREN value of the 904LN grade (35). The 2205 duplex grade is, in several in-service applications, competing with the 317LM(N) or 904L(N) grades. Superduplex grades have a PREN value higher than 40, generally in the 41-43 range, and compete with the superaustenitic grades (6Mo) having a PREN value close to 42. All these grades are designed for the most severe corrosion-resistance applications where stainless steels are specified. Duplex steels are, for the stainless steel market, considered as niche markets as their volume comprises less than 1% of the stainless steels applications.

More interestingly when considering "volume" applications (304 grades represent more than 50% of the total stainless steel production) is the newly developed family called "lean" duplex. As presented in Figure 2.24, most of them are designed to have a PREN value in the 22-24 range, equivalent to the PREN of 316L grade and they compete well with the 304 and 316 grades in most of the markets considered for their development. The lean duplexes are alternative, cost-economic choices to 304 and 316 grades in most of the corrosion-resistance applications where those popular grades are already specified [CHA 07a].

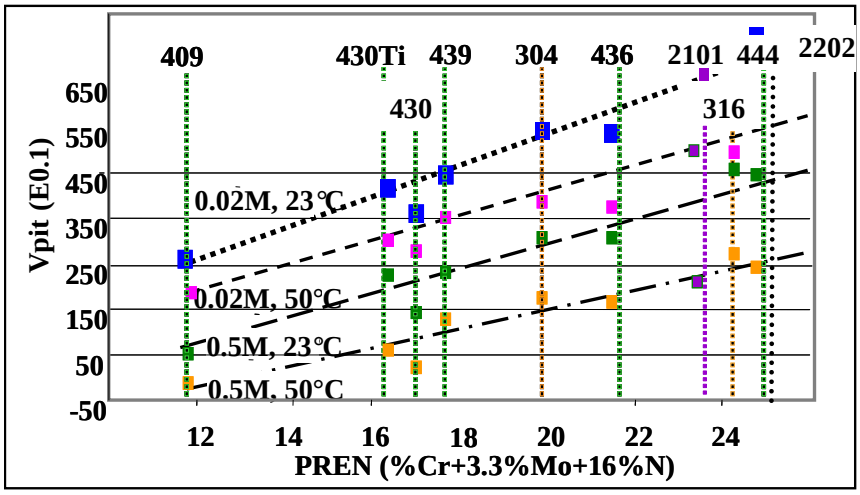

Figure 2.25. *Effects of temperature and chloride content on V_{pit} values*

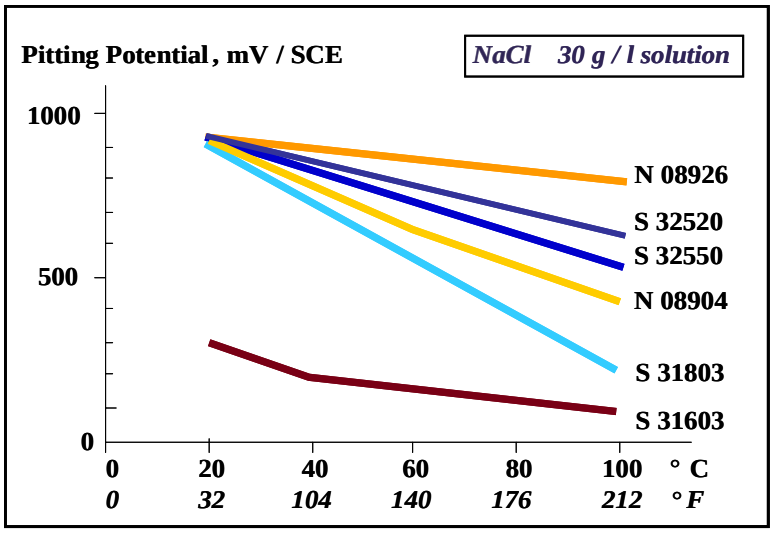

Figure 2.26. *Effect of temperature on the pitting potential (30g/l NaCl solution)*

The real conditions of uses of 304 and 316 grades are generally much less severe conditions than $FeCl_3$ solutions. Typical real solutions of aqueous media contain chlorides, sulfur species, diluted acids, etc., with a pH in the 4-9 range and at relatively low temperature (inferior to 50°C). Figure 2.26 presents the critical pitting potential (Vpit/Ep) of several stainless steels at different temperatures in several aqueous solutions containing moderate chloride additions. The PREN ranking is almost confirmed in those conditions. Lean duplex grades perform better than 304 and most of the ferritic grades. They are close to 316L.

For more severe conditions (Figure 2.26), 316 is again not to be used whereas duplex 2205 or superduplex grades are to be considered to replace costly highly-alloyed austenitic grades. This is clearly the case for marine environments, as well as medium and high temperature oxidizing and chloride-containing solutions. Those conditions are observed in industrial applications, such as pulp and paper, coal power station gases scrubbing, phosphoric acid and sulfuric acid industrial solutions.

2.4.3.4. *Pitting corrosion and duplex microstructure*

The new generation of duplex grades, defined at the Beaune 91 conference, presented higher nitrogen contents than the first duplex grade definition. The nitrogen effect on high temperature dual-phase stability has already been emphasized but its beneficial effect on pitting corrosion of duplex grades is outstanding due to combined effects on phase balance and local nitrogen content (Figure 2.27) [COM 91]. The main conclusions are as follows:

– the optimum pitting corrosion resistance is obtained close to the 50% ferrite/50% austenite volume ratio;

– higher nitrogen content significantly improves the pitting corrosion resistance of the alloy mainly for the lower ferrite contents and as a result, makes the steel less sensitive to phase balance when alloyed with nitrogen.

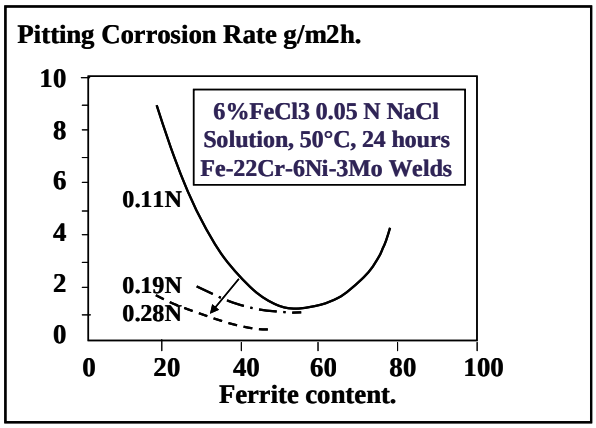

Figure 2.27. *Effects of nitrogen content in S32205 welds on ferritic phase balance and pitting corrosion rate*

The results are explained by the combination of several mechanisms:

– an increase of the nitrogen addition mainly affects the chemistry of the austenitic phase as nitrogen solubility in ferrite is very low;

– the increase in nitrogen in the austenite also induces a slight increase in the austenitic phase of molybdenum and chromium alloying elements;

– nitrogen additions increase the austenite ratio for a given nickel, chromium, and molybdenum content;

– nitrogen additions slow down the diffusion coefficient of chromium and molybdenum at high temperature and as a result, the steel is less sensitive to intermetallic phase precipitations.

Direct and indirect effects of nitrogen alloying on the chemistry of both phases make the PREN value of the austenite phase shifting to a lower value than the ferritic phase. Pit initiation area also moves from austenitic (γ) grains to α/γ or α/α grain boundaries. Conversely, an increase of the nickel alloying element may

have a negative effect on pitting corrosion as the austenite ratio is increased and a dilution effect of nitrogen occurs.

Those phenomena have thus significant effects on the welded structures; coarsening of ferritic grain in HAZ is often observed when optimum welding conditions are not selected, particularly for the lower nitrogen content grades. Some gamma 2 or nitrides may form. The welded metal is characterized by an as-cast microstructure with well-known segregation effects, which may induce intermetallic phase precipitations mainly for the superduplex grades due to their very high chromium and molybdenum contents. Over-alloying of filler metal and additions of nitrogen in the shielding gas will be recommended. Figures 2.28 presents CPT values of welded structures compared to that of the base metal determined with the G48 A test method.

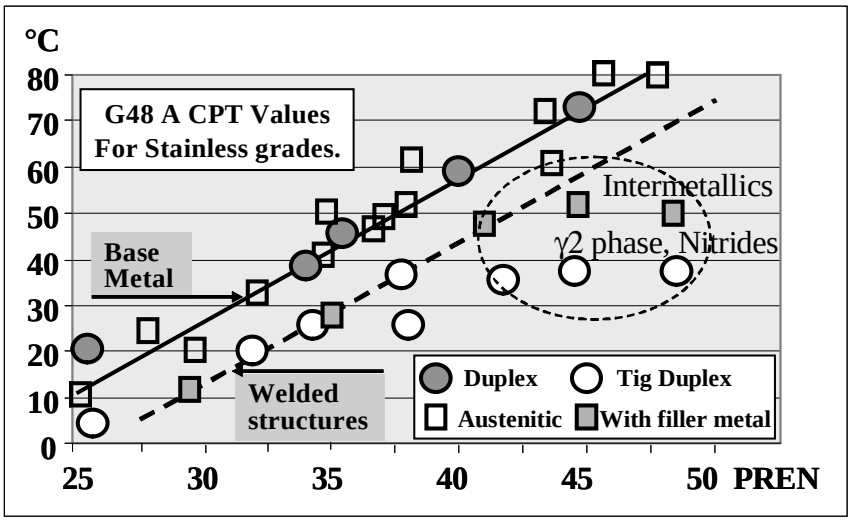

Figure 2.28. *CPT values of base metal and welded stainless steels*

Welded structures have a loss of about 15°C in CPT values, compared to solution-annealed wrought grades of equivalent PREN values. To obtain equivalent CPT values between a base metal and a welded structure a minimum over-alloying of 4-5 units of the PREN value is required. For most alloyed duplex grades, welded metal alloying has to be optimized with welding parameters as they are much more sensitive to phase precipitations, which have a strong negative effect on CPT values (Figure 2.29). Heat treatments of superduplex grade S32520 in the 700-1,000°C range is known to induce intermetallic phase precipitations (chi–sigma) as well as possible gamma 2 or nitrides at lower temperatures. Those phases are known to be enriched in chromium and as a result, local chromium depletion zones are created,

which explains the higher sensitivity of the alloy to locally resist pitting corrosion in acidified, chloride-containing solutions. Specific over-alloyed grades, of the austenitic Ni-based (625 family) filler metals, have been developed for the most critical corrosion-resistance properties [CHA 91].

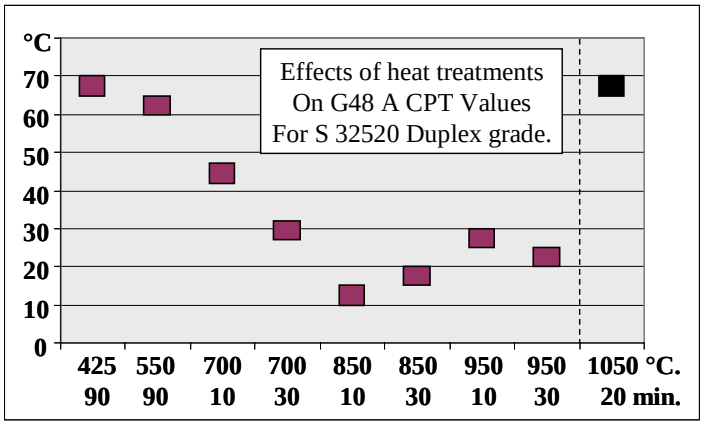

Figure 2.29. *CPT values alloy S32520, heat treated in several time-temperature conditions, determined with the G48 A test method*

2.4.3.5. *Crevice corrosion mechanisms*

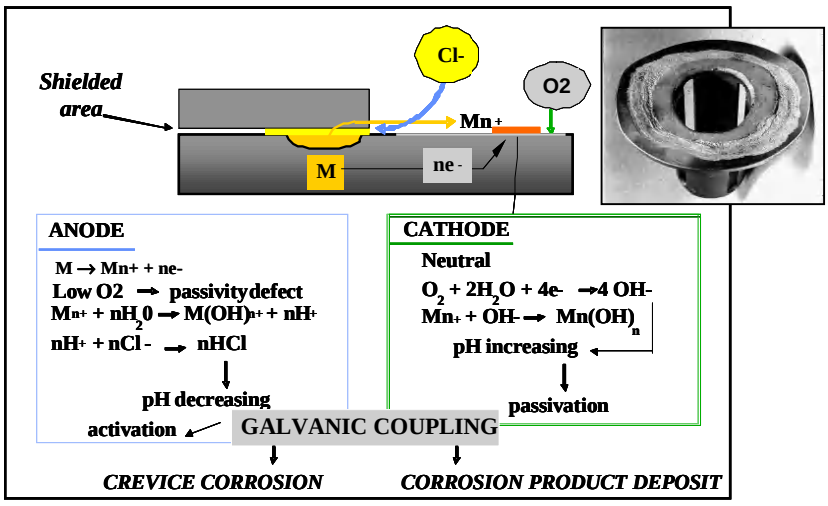

Figure 2.30. *Crevice corrosion mechanisms of stainless in chloride-containing solutions*

Crevice corrosion occurs in confined zones, such as a small gap between overlapping compounds, under a joint, under deposits, lack of penetration zones of welded structures, under remaining oxides scaling, etc. In the immediate vicinity of the crevice, there is almost no convective exchange with the bulk solution and the oxygen present in the occluded zone may rapidly be exhausted by the local cathodic reaction. As a result, only the anodic reaction exists in the crevice area and the cathodic reaction takes place near of the occluded zone, on the remainder metallic surface.

Due to this “differential aeration” phenomenon, a galvanic coupling starts to develop in non-passivated materials; this results in an immediate increase of corrosion mechanisms. In the case of stainless steels protected by a passive film, an incubation period is observed. The dissolution of metallic cations across the passive film is sufficient to enrich the crevice in these ions as a confined zone exists. These hydrolyzed cations produce a progressive significant increase in acidity. With time, the acidity drops to values as low as pH 1 (it may take several months). Chloride ions from the solution penetrate the confined zone and contribute both to ensure the electric neutrality – formation of HCl – and attack the passive film. In the confined area, the passive film starts progressively to dissolve (Figure 2.30). When a given pH is reached, the anodic dissolution mechanisms suddenly increase. This pH is called the pH of depassivation (pHd) and it is specific for given stainless steel. In short, when an occluded zone exists, the acidity, often of the HCl type due to the presence of chloride ions, starts locally to increase and, at a critical pH referred to “the depassivation pH”, crevice corrosion starts (Figure 2.31). Crevice corrosion initiation, therefore, occurs after an “incubation period”, which is the time necessary for the locally pH to drop lower than pHd. Thus, the crevice corrosion mechanisms proceed in two steps: initiation and propagation.

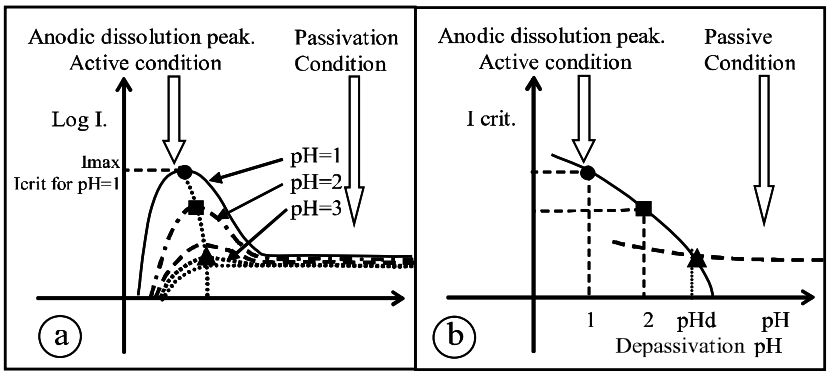

Figure 2.31. *a) Typical evolution of polarization curves (I/E) determined with several pH (additions of HCl) in a 2 M NaCl deaerated solution. b) Determination of the pH of depassivation (pHd) of an alloy*

The initiation step is related to the properties of the passive film, i.e. its ability to resist the aggression of the external conditions, and the propagation step is significantly dependant on the kinetics of the anodic dissolution steps, where nickel content plays a role. As an indirect effect, crevice propagation rates are dependant upon the structures.

2.4.3.6. *Typical crevice corrosion-resistance data*

Figure 2.32 presents typical depassivation data measured on Icrfit/pH curves determined for several stainless steels. It is observed that the chromium and molybdenum contents are the most significant elements determining the pHd value of stainless steels. When considering the propagation of the corrosion, nickel seems to be one of the most critical elements. The critical current curves have a significant reduced slope when moving to lower pH for the austenitic grades. Duplex S32205 grade performs much better than 316 austenitic grades, whereas duplex S32304 is better than 304 and almost equivalent to the 316 austenitic grades.

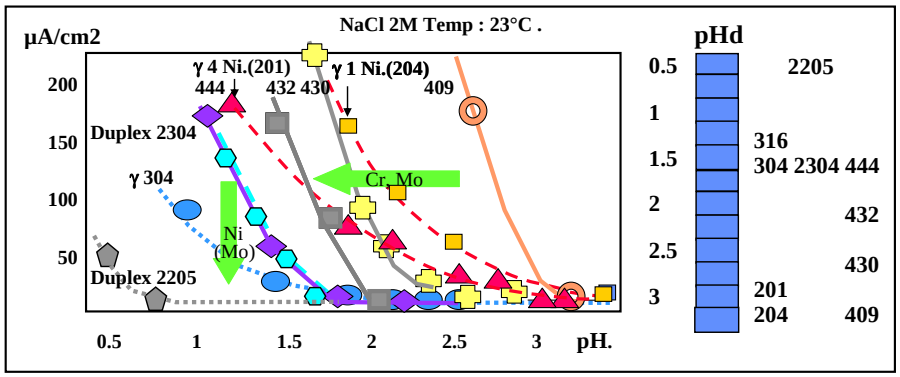

Figure 2.32. *Depassivation potentials of stainless steels determined in a NaCl 2M solution*

Figure 2.33 presents the critical crevice temperatures (CCT) of several stainless steels determined using the ASTM G78 method, as well as the critical pitting temperatures (CPT) determined using the ASTM G48A test method. The tests are performed in a FeCl3 solution, which is a strong acidic and oxidizing solution. The CCT values obtained are lower than CPT values for the same alloy. The PREN value is for both corrosion mechanisms and is a good method to rank the properties of stainless steels.

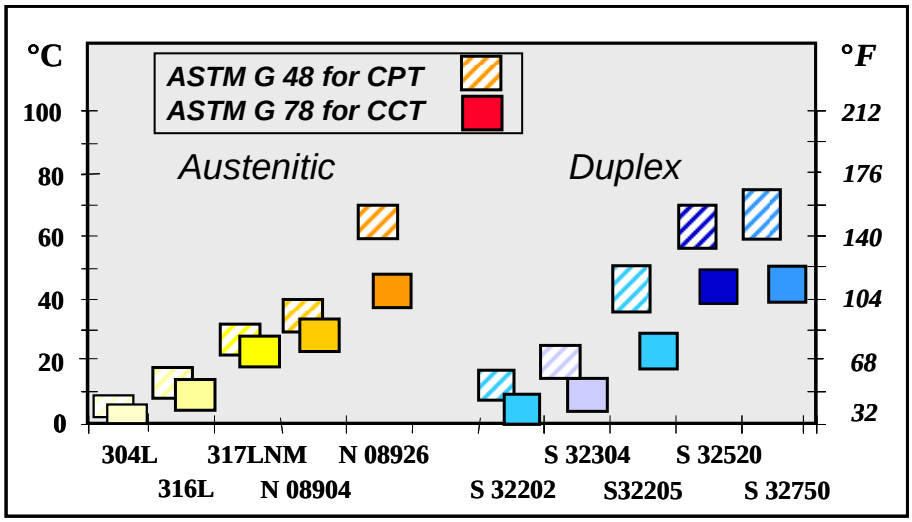

Figure 2.33. *CCT determined in $FeCl_3$ solution (ASTM G78 method) compared to CPT determined using the ASTM G48 method*

Phase precipitations resulting from inadequate heat treatments or remaining segregated zones also have significant negative effects on the crevice corrosion-resistance properties of stainless grades. This is particularly the case for more alloyed austenitic and duplex grades. Similar results have been observed for pitting corrosion-resistance properties. On a microscopic scale, competition between pitting corrosion and crevice corrosion may occur as the local increase of acidity may also weaken the passive film and a pit is formed before reaching the pHd value. One of the alternative mechanisms to initiate crevice corrosion is pitting corrosion. In many test results obtained in the laboratory, multi-pit areas have been observed near a creviced area (mainly lower alloyed stainless).

Crevice corrosion appears to be one of the most critical corrosion mechanisms to take into account when material specification is concern. Furthermore, in most of the in-service corrosion resistance applications, special care regarding design considerations, as well as assembly procedures, including welding, may considerably improve the life span of the equipment avoiding crevice configurations, which are often the areas where corrosion first starts. This is also relevant to the choice of an appropriate design, which will reduce the risk of developing under-deposit crevices.

2.4.4. *IGC*

2.4.4.1. *IGC mechanisms*

Grain boundaries are zones separating two grains of different structures or at least different crystallographic orientations. They are, in fact, “disordered zones” favorable for the initiation and nucleation of precipitates of metallic compounds, such as carbides and nitrides, or even intermetallic phases, such as sigma, gamma, chi, Laves phases, R phases. They also attract local enrichments of numerous solute elements, such as phosphorus, silicon, and boron. These intergranular zones may exhibit a strong sensitivity to localized attack in some corrosive media. This phenomenon is referred to IGC. The phenomenon is mainly encountered in the conditions where stainless steels should develop a passive state [BER 93].

IGC often results from chromium-depletion zones near grain boundaries resulting from chromium-rich precipitates (Figure 2.34). The local reduced chromium content considerably lowers the ability of the steel to resist corrosive media by forming a locally passive film. As a result, corrosion starts and propagates along the grain boundaries. Local galvanic couplings and confinement zones may even enhance the corrosion mechanisms. Those precipitations often ensue from improper manufacturing heat treatments to slow the cool down in the 850°C/200°C region after solution annealing treatment. Improper welding conditions may lead to the same phenomenon in the HAZ. This is also the case for service conditions when the material is exposed to high service temperatures. Welded structures including the HAZ are of primary concern. Stainless steels that have undergone satisfactory heat treatment are almost immune to intergranular attack as they do not exhibit chromium-depletion zones at grain boundaries.

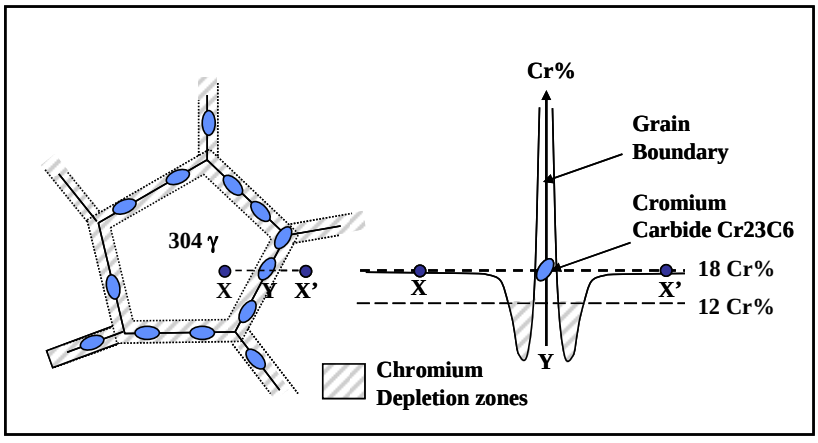

Figure 2.34. *Schematic diagram of chromium-depletion phenomenon occurring on grain boundaries in a 304 austenitic stainless steel suffering from carbide precipitations*

2.4.4.2. *Structure and IGC*

Austenitic structures are more sensitive than ferritic ones to IGC as the diffusion coefficient of chromium is lower in the austenitic phase than in the ferritic phase. Duplex grades are very resistant to IGC, although they have significant nitrogen additions (Figure 2.35). This is explained by some particular properties of duplex alloys:

– a small grain size microstructure, resulting from the dual phase, which increases the surface of the grain boundaries per volume unit surface;

– chromium carbides and nitrides precipitates preferentially, at the α/γ interface, which reduce the number of precipitations per unit surface;

– chromium carbide precipitates proceed from an eutectoid transformation of the ferrite (α → γ + Cr23C6), which makes precipitations discontinuous and a moving grain boundary;

– nitrides (hexagonal Cr_2N) may appear simultaneously to carbide precipitations as their enthalpies of formation at around 900°C are similar. This is particularly the case for the highest nitrogen-alloyed duplex;

– chromium comes mainly from the ferrite, enriched zone in chromium of the duplex structure, which reduce the chromium depletion of austenite;

– ferritic grains at the proximity of the precipitates provide “fresh” chromium due to his higher diffusion coefficient in the ferritic structure.

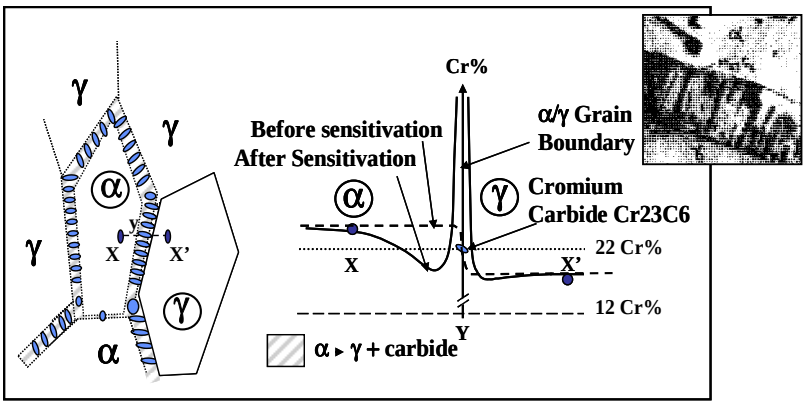

Figure 2.35. *Schematic diagram of carbide precipitations effects in a duplex grade*

Stainless steels – mainly austenitic grades – may also encounter IGC in the non-sensitized stage. This often occurs in highly oxidizing media containing high-valency metallic ions. Most of the investigations related to this type of corrosion have been performed in a boiling concentrated nitric acid. Such conditions often bring stainless steel to a transpassive state. Phosphorous and silicon have been observed as playing a significant role in intergranular attack [CHA 91a].

For the 65% HNO_3 solution, 100% austenitic, highly nickel-alloyed grades, are considered. The absence of ferrite reduces the risk of intergranular carbide precipitations on the few ferritic islands existing in the standard austenitic grades. Duplex grades once again have attractive properties under those conditions as they offer a high chromium content and an almost immune state when considering sensitization (section 2.4.2.3).

2.4.4.3. *Evaluation of IGC*

Several tests have been standardized for determining whether a given steel (chemistry+structure) is sensitive or not to IGC. These tests include three steps:

– an appropriate sensitization treatment consisting of a determined heat treatment to induce the intergranular precipitation of carbides/nitrides;

– exposing the alloy in the sensitivity stage in a carefully selected corrosive environment;

– an evaluation of the intergranular attack.

These tests consist of imposing a redox couple into the system, chosen most often from the Strauss test ($Cu^{2+}/Cu^{+}/Cu$ redox couple), the Streicher test (Fe3+/Fe2+ redox couple), and the Huey test (Cr^{6+}/Cr^{3+} redox couple). Those redox couples have been identified on the polarization curve shown schematically in Figure 2.36. It is equivalent to imposing the potential on the metal to be tested with a potentiostatic generator.

In the case of duplex steels, more alloyed grades than 304/316 austenitics, the use of appropriate solutions and comparison between polarization curves determined on both as-received material and the sample in the sensitivity state are recommended [BER 93].

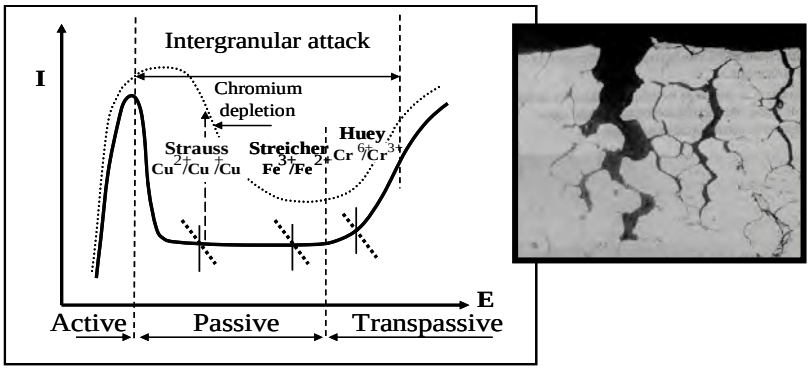

Figure 2.36. *Typical current-potential polarization curve and redox potential of standard intergranular reactants used*

2.4.5. *SCC*

2.4.5.1. *Stress corrosion mechanisms*

SCC is a phenomenon that occurs under the combined influence of an aggressive environment and static mechanical loading. The stress system must include at least one positive (tensile) component. The process takes place often in media, which apparently are minimally corrosive. Furthermore, in most cases it is very difficult to detect cracking before having reached catastrophic proportions. The process is thus extremely dangerous.

Stress corrosion phenomena are characterized by significant features including:

– the specificity of each material/medium combination, the extreme sensitivity to particular conditions, and often-mild nature of the corrosive environment;

– the low stress levels required for crack initiation (incubation period);

– the relatively slow crack propagation rates;

– the brittle nature and crystallographic morphology of the cracks.

Figure 2.37 presents schematically the polarization curves typical potential ranges where stress corrosion may develop. SCC of stainless steels occurs preferentially in certain ranges of potential, which are often narrow, leading to relatively unstable protective films. The role of the instability of the passive film seems to be a critical point for the stainless steels. Indeed, even if it is known that cases of SCC appears when metal does not have a protective film, it remains true that the SCC occurs in relatively low corrosive media, but when general corrosion is enhanced, SCC disappears [COM 93].

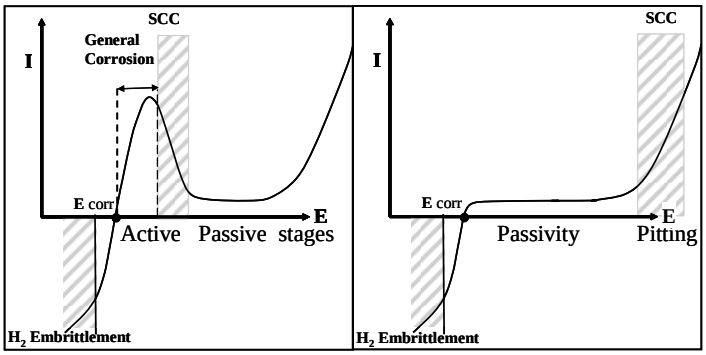

Figure 2.37. *Ranges of potentials where SCC behavior of stainless steels can be promoted in aqueous environments: a) acidic solutions with low tendency to passivate and b) neutral oxidizing conditions – stable passivity*

Cracks in SCC mechanisms appear after an incubation period or initiation time before crack formation and need to be created. One defines a threshold stress σ_f (smooth surface) and a critical stress concentration factor K_{ISSC} (in the presence of a pre-existing crack) below which an existing crack does not propagate. Threshold stresses are often in the magnitude of 0.5-0.7 of the yield stress, even lower in some cases, and a K_{ISSC} factor in the range of 8 to 25MPa.m$^{1/2}$ is often observed. The crack limit thus generally lies in the typical range of residual stresses.

For crack initiation there is no reliable criterion, at present, for predicting whether a given system will be prone to SCC. The most frequent conditions for stainless steels are neutral oxidizing conditions (close to pitting potential) where chloride ions, sulfur ions, and temperature are known to enhance the SCC susceptibility and the more acidic conditions at potentials in the neighbour of the dissolution peak (sensitivity increases with the drop of pH). Hot caustic solutions (when the passive film is unstable) are also known to generate SCC phenomena.

Typical propagation rates of cracks are in the 10-6 to 10-11 m/s range, which is relatively slow when compared to failures under static loading. The propagation rate generally reaches a plateau when mechanical loading is continuously increased. When the loading reaches the KIC value, catastrophic crack propagation occurs. Temperature increases often lead to an increase of SCC susceptibility or at least there always exists a minimum temperature under which SCC is unable to take place.

Several propagation mechanisms have been proposed. The conditions prevailing at the front tip (composition of the medium, stress, temperature, microstructure) are difficult to quantify but have a significant effect on the nature and kinetics of the

local reactions, which lead the cracking propagation. Clear evidence of discontinuous propagation have been discovered through metallographic (striations perpendicular to the crack propagation for transgranular cracking) and acoustic investigations. The principal processes that can be involved in the crack propagation stage are:

– Surface reactions:

- the anodic reaction (dissolution, modified media, redox effects, etc.),
- the cathodic reaction (reduction of water and other species),
- the adsorption of particular species (hydrogen, which may diffuse, chlorine or sulfide ions).

– Local modification of the metal at the crack tip:

- absortion of hydrogen, which increases dislocation mobility,
- vacancies generated by the dissolution mechanisms,
- formation of depleted zones by selective dissolution,
- plastic strains due to stress concentrations effects,
- phase transformations (martensite in the unstable austenite).

– Mechanical failure:

- at the surface: disbonding, cleavages, etc.,
- ahead of the surface: hydrogen traps, pile-up of dislocations, inclusions.

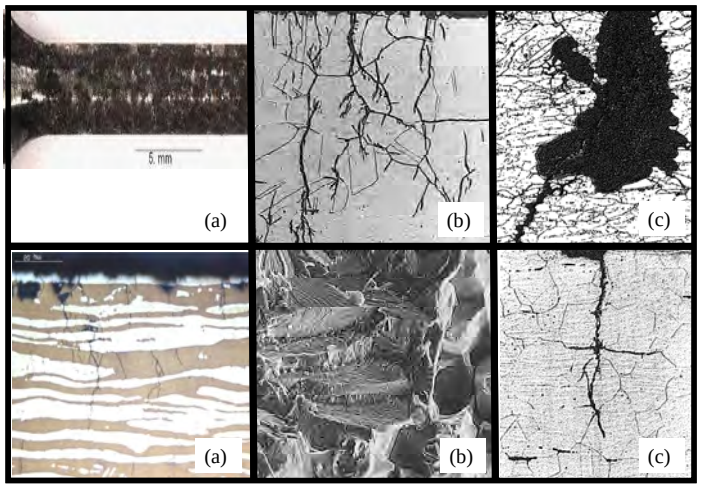

Figure 2.38. *SCC figures of stainless steels in several conditions: a) 32202 duplex grade in 165 g/l NaCl, pH= 4.5), T= 150°C, p(H_2S)=0.05 b. b) 316 grade in deaerated 50% NaOH at 200°C (mixed cracking). c) 316 grade in aerated 170 ppm NaCl solution at 200°C (cracks start at pits)*

Several mechanisms can explain the SCC propagation. Naturally, rather sensitized grain boundaries will promote intergranular behavior while low stacking fault energy grades may more easily encounter (pseudo-) cleavage behavior [COM 93].

A coherent model must be able to account for the brittle nature of the cracks, which propagate slowly under a low static stress in an otherwise ductile material. In many cases, the two faces of the crack show an almost perfect geometrical correspondence. Cracks propagate preferentially on specific high-density crystallographic planes. Those facts argue for complex mechanisms where the dissolution process is not the only contributor to crack propagation but that other mechanisms, such as adsorbed and absorbed hydrogen, combined with local stress concentrations may lead to local deformations with pile-up of dislocations or local cleavages. Crack propagation can be discontinuous due to cyclic behavior of the applied stresses.

Some illustrations of SCC fractures of stainless steels are presented in Figure 2.38. Figure 2.39 presents typical properties of austenitic and duplex grades in neutral chloride media at high temperature, and illustrates the well-known critical nickel content (8-10%) in stainless steel when considering SCC resistance properties [COM 93].

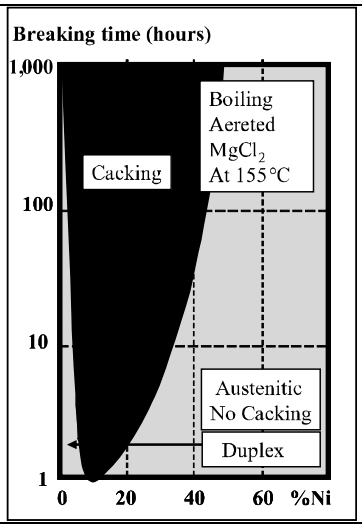

Figure 2.39. *Influence of nickel alloying on the SCC of stainless steels in $MgCl_2$ solutions*

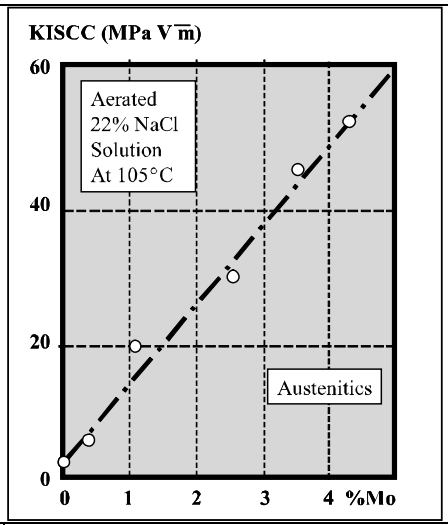

Figure 2.40. *Influence of molybdenum alloying on KISCC values of austenitic stainless steels*

Molybdenum additions in stainless steels are also known to improve the resistance of the stainless steels to SCC in most of the conditions investigated. Figure 2.40 illustrates the beneficial effects of molybdenum additions on the cracking threshold value in 22% NaCl solution at 105°C [COM 93].

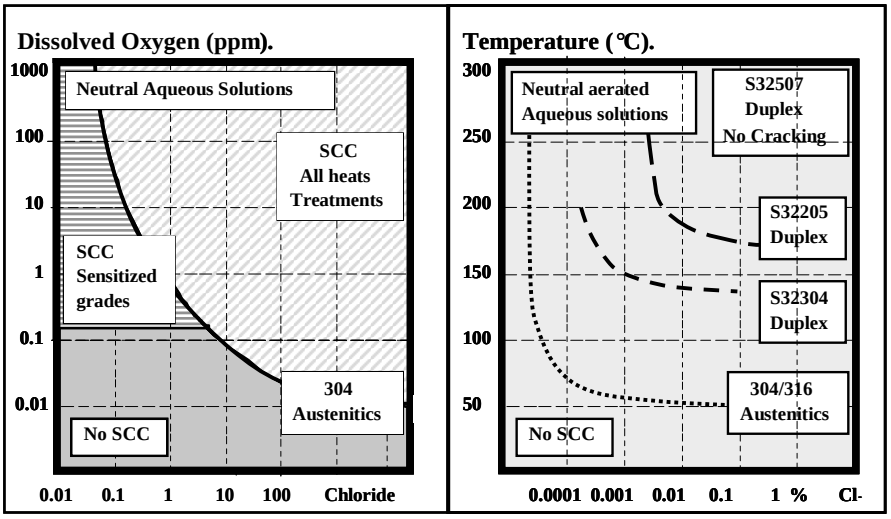

Figure 2.41. *Influence of alloying elements (nickel and molybdenum) on the SCC of stainless steels in chloride containing solutions*

2.4.5.2. *Duplex stainless steels and SCC behavior*

For concentrated oxidizing media, such as boiling 44% $MgCl_2$ solutions (154°C), duplex grades appear to offer no advantage over austenitic grades for plastically deformed specimens. They all fail after exposure for a minimum of few tens of hours. In contrast, the superiority of the two-phase structure is obvious when the specimens are loaded in bending in the elastic range.

Nitrogen additions in duplex stainless steels have been found to increase both the yield strength and ratio between threshold stress for cracking and yield strength. The absolute value of critical cracking stress is thus raised significantly. However, stresses higher than 50% of the yield strength has always induced cracking in these materials in boiling 44% $MgCl_2$ solution. Moreover, rapid failure can occur when the specimen is plastically strained even for 1-2% of yield strength. Equivalent results have been observed at 200°C in oxidizing solution containing only 100 ppm NaCl and 100 ppm oxygen. Crack propagation is increased by plastic strain.

A numbers of detailed investigations have shown that when plastic deformation occurs, a twinning mechanism in the ferrite starts, which leads to extensive local depassivation effects (particularly in the case of cyclic deformation). As a result, in the most severe conditions, anodic dissolution locally starts and the ferritic structure begins to embrittle due to hydrogen uptake (hydrogen from cathodic reaction and/or presence of local acidified solution). Conversely, in less aggressive conditions, before the damage is irreversible, healing mechanisms of the passive film take place. Extra chromium and molybdenum additions are beneficial for the healing kinetics of the passive film.

Finally, austenitic-ferritic grades show complex behavior in high temperature chloride-containing media. Although they are sensitive to stress cracking, in many cases they can offer a significant improvement compared with the behavior of the austenitic grades (Figure 2.40). These properties are related to:

– the high mechanical properties of the duplex grades, which increase the threshold value of plastic deformation;

– the smaller grain size of the two phases microstructure;

– the mechanical and electrochemical coupling effects between the two phases;

– the ability of the grades, due to their high PREN values, to (re)-passivate in neutral oxidizing, as well as in relatively highly acidified solutions.

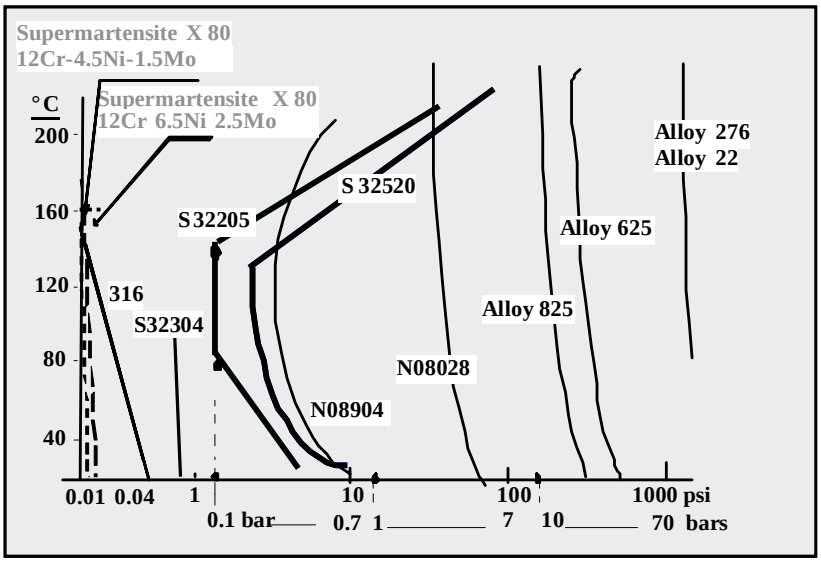

Figure 2.42. *Limit of uses of stainless and nickel alloys in H_2S environmental applications*

In media containing both chlorides and sulfides (H_2S), often encountered in the oil and gas industries, the risk of SCC for duplex grades, even at room temperature, exists. Fortunately, those extreme conditions are not often encountered in real life (pHs generally higher than 4 and simultaneous occurrence of low pH and high chloride or H_2S concentrations are rare).

Figure 2.42 illustrates the improved performances of duplex grades when compared with standard austenitic (304/316) or super-martensitic grades. They have been found the most cost-effective choice in many cases and have been used safely for more than 50 years. More details will be presented concerning oil and gas applications, as well as the success story of duplex grades in the pulp and paper industries dealing with diluted sodic solutions, as well as acidic media containing chlorides and thiosulfates at the end of this article [CHA 00].

2.4.6. *Fatigue and corrosion fatigue*

2.4.6.1. *Corrosion-fatigue mechanisms*

Corrosion-fatigue phenomena result from the combined effects of mechanical stress and chemical attack often in fairly non-aggressive media. Corrosion-fatigue is even more harmful than SCC due to the cyclic nature of the material loading. The damage resulting from corrosion-fatigue is mostly unpredictable and can occur in less specific conditions than SCC phenomena. Almost all material-medium systems may lead to corrosion-fatigue damage (not needing specific rest potential conditions, etc.). The main characteristic features are:

– corrosion facilitates the initiation stage of the fatigue crack and as a result, numerous cracks develop in a more branched morphology than under classical fatigue conditions;

– crack propagation is enhanced under corrosion-fatigue conditions as local conditions at the crack tip are more aggressive than in pure fatigue conditions.

The mechanical damage due to fatigue is mainly related to the stress cycles, and is relatively independent of time. This component is predominant in high stresses and frequencies, as well as in some low frequency conditions when damage of the passive film is negligible (including possible fast healing of passive film phenomena).

Conversely, the effect of the environment is very sensitive to time. This component starts to be dominant in most low frequency conditions. For very low frequencies, typically corresponding to slow strain rates (<10-7 s-1), the corrosion-fatigue processes and, more practically, the crack morphology is close to that in

SCC. This type of loading often corresponds to thermal fluctuations (including start up and shut-down cycles of industrial plants) or swell.

2.4.6.2. *Duplex stainless steels and fatigue-corrosion behavior*

Figure 2.43 presents fatigue-resistance properties (un-notched samples, rotational bending test) in air and seawater-type solutions compared with their mechanical properties (UTS) for several stainless steel families, including the duplex grades [CHA 91]. The main conclusions can be summarized as follows:

– in air, the fatigue limit of most of the stainless steels is close to 0.5 ratio of their UTS value. For cold-worked or precipitation-hardened conditions with UTS values higher than 1,000 MPa a ratio of 0.4 and even lower is often recorded;

– in seawater conditions, martensitic grades present a sharp drop in fatigue limit. The ratio with UTS values could be as low as 10%. Most of the austenitic grades of the 304 and 316 families are characterized by a value included in the range of 0.25/0.4 when determining the fatigue limit/UTS ratio. Duplex grades perform very well as their ratio remains almost equivalent to their ratio determined in air, i.e. close to 0.4 UTS;

– the relative drop in fatigue strength when comparing results in air and seawater environments of the different stainless steel grades is clearly linked to the intrinsic ability of the alloy to resist corrosion mechanisms, i.e. pitting corrosion. In those conditions (seawater testing), a direct link between resistance and chemical composition through the PREN formula is again observed. For duplex grades and superaustenitic grades having a PREN value higher than 40, no significant drop of fatigue limit is observed when tested in room temperature seawater conditions and compared with air conditions (extremely good behavior of those steels when considering room temperature pitting corrosion and re-healing properties of the passive film) [COM 93].

Figure 2.44 presents some fatigue-corrosion test results and fatigue crack growth properties of duplex grades in chloride-containing solutions. The negative effects of an increase of potential on fatigue properties of 25% Cr duplex grades are also presented.

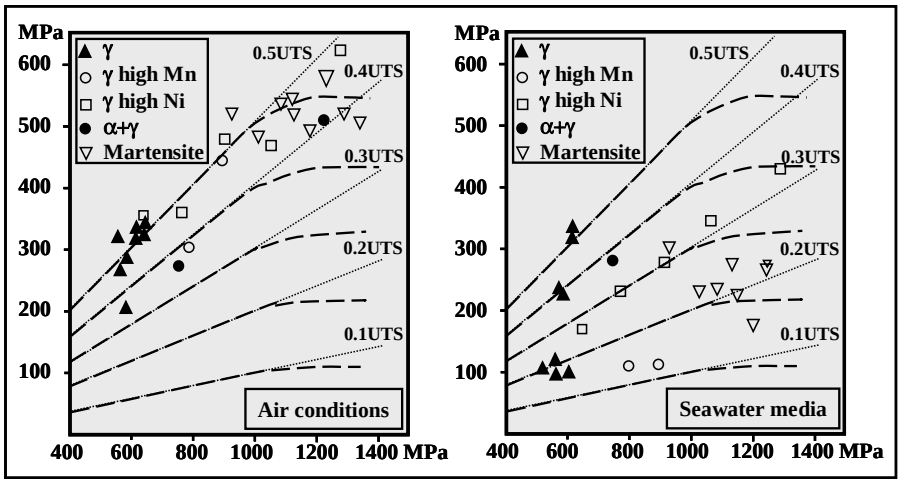

Figure 2.43. *Fatigue strength limit versus UTS in air and seawater for several stainless steels (un-notched bend fatigue sample)*

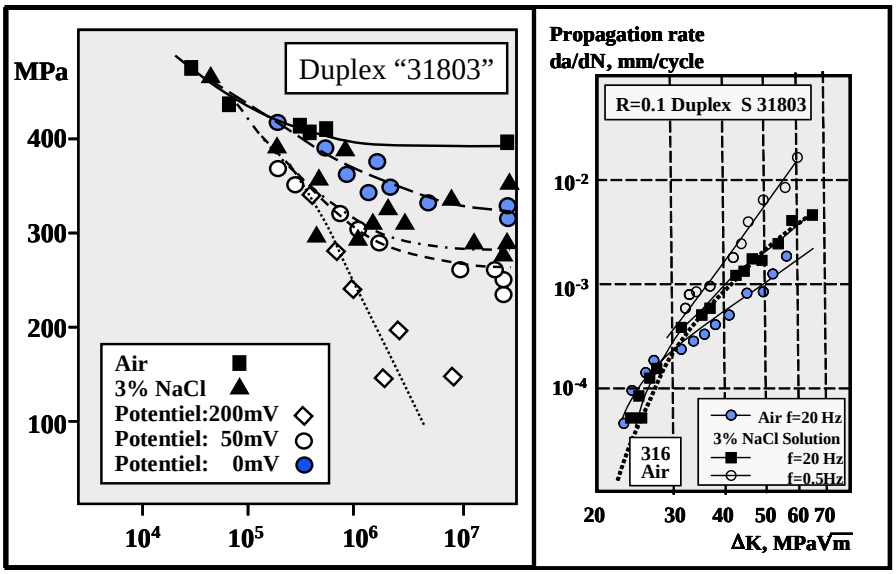

Figure 2.44. *Influence of imposed potential and chlorides on fatigue properties (stress intensity factor versus crack growth rate) of duplex grades*

These data demonstrate the difficulty of predicting real behavior of alloys without performing tests with selected operating conditions, which closely simulate industrial condition for both structural compounds (real heat treatment, welded structures, temperature, media, etc.). Indeed, the aggressive conditions of the environment become paramount under low loading conditions. Moreover, the conditions at the crack tip (media composition, redox potential, etc.) can be markedly different from those of the "free" surfaces. Re-healing mechanisms of the passive film can be strongly affected and accelerated crack propagation effects could be observed.

The nitrogen increase in the new generation of duplex grades has strongly improved the fatigue corrosion resistance of the former duplex grades by strengthening both the mechanical properties and corrosion resistance of the austenitic phase. In the highly nitrogen-alloyed duplex grades, the ferritic phase is often the weakest phase of the alloy and when plastically deformed the ferrite may undergo complex deformation mechanisms including twinning, which may promote crack propagations mechanisms, particularly in the low redox conditions, where hydrogen is a pertinent factor to enhance crack velocity.

In conclusion, fatigue and fatigue corrosion-resistance behavior of duplex stainless steels can be seen at least equivalent to that of the austenitic grades in majority of the industrial applications. Nevertheless, care must be taken to choose an alloy with sufficient corrosion resistance in the intended environment, particularly in cases where a high ferrite content area of the duplex (HAZ) could lead to an accelerated crack propagation (typically with hydrogen effect). Fortunately, such conditions are rare and in real life, duplex often has excellent behavior.

2.5. Some complex corrosion behaviors encountered in industrial applications

2.5.1. *Marine environments and seawater applications*

Seawater is a "living" media. A bio-film generally forms on the surface of the stainless steel when exposed to quiescent water. The cathodic reaction is markedly depolarized and free potential shift slowly to much higher potentials (Figure 2.47). The kinetics of this shift depends on salinity, water temperature, and local bio-diversity. With an increase in temperature up to 40°C, more bio-film starts to disappear (micro-organisms are killed). As a result, stainless steels have a much stronger tendency to pit and crevice at room temperature in natural seawater compared with synthetic media (Figure 2.46). The 304 and 316 grades are clearly not immune to seawater corrosion. Duplex grades have been extensively used with success and are substituting high nickel and molybdenum austenitic grades.

Experience has shown that when considering prolonged exposure to natural seawater, over-alloying is requested and that in the most severe conditions (stagnant seawater) a minimum PREN value of 40 is requested for both the duplex and austenitic families. A guide of material selection for seawater applications is presented in Figure 2.47. Effects of water velocity, geometrical configurations, free chlorine contents and temperature are the main parameters to identify [JAC 07a].

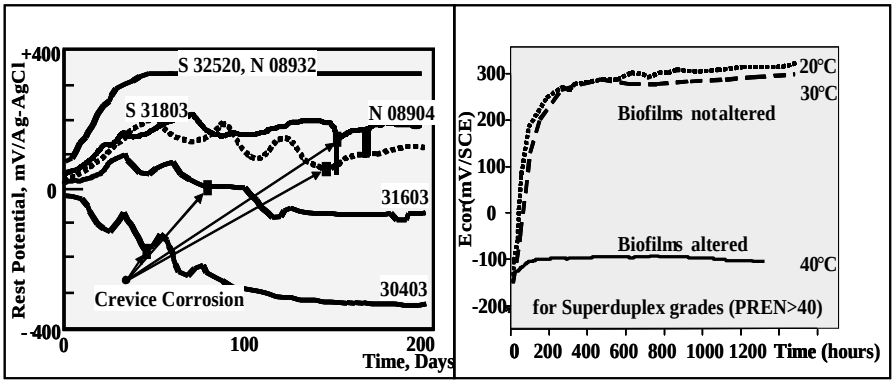

Figure 2.45. *Effects of chemical composition of stainless steels and temperature on the rest potential of samples immersed in natural seawater*

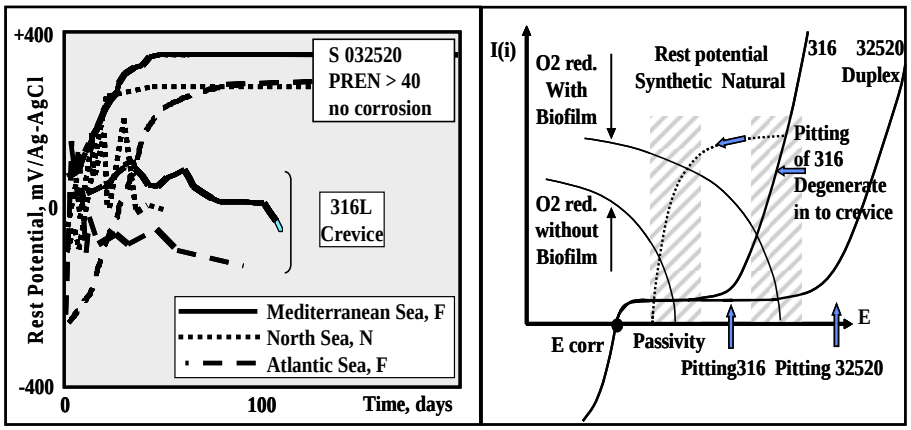

Figure 2.46. *The 316 and S32520 grades behavior in several natural seawater media*

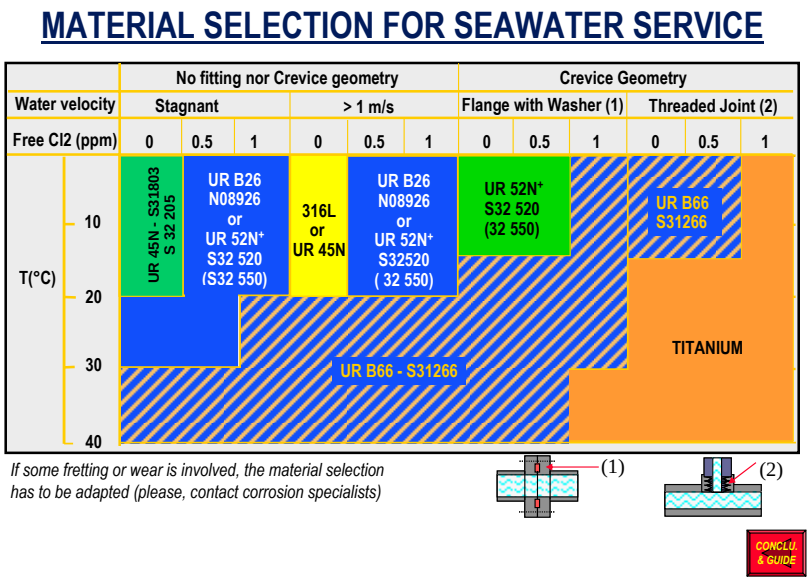

Figure 2.47. *Materiel selection guide map for seawater applications*

2.5.2. *Thermal desalination plants*

The multi-effect distillation (MED) installation consists of several consecutive cells operating at decreasing levels of pressure and temperature from the first cell (hot, 145.4°F/63°C) to the last (cold, about 104°F/40°C). As the boiling temperature of water depends on its pressure, the lower the pressure, the lower the boiling temperature (Figure 2.48). In the first cell, a horizontal tube bundle is installed in a thermally insulated chamber. The make-up seawater is sprayed over the horizontal tubes and the internal heating fluid causes it to boil. The concentrated salt solution (the brine) falls to the bottom of the compartment by gravity. The vapor produced from evaporated seawater in this first effect can be used as the heating fluid for the second effect. The boiling temperature and pressure of cell (n+1) will be lower than in cell n. This recovery of heat from effect to effect can be repeated several times. The heat supplied to the evaporator is then only that necessary to heat the make-up seawater in the first cell and to vaporize the product of this cell [JAC 07a]. The number of effects is a result of the following constraints:

– maximum brine temperature shall not exceed 145.4°F/63°C in order for the multi-effect system to fully benefit from a reduced scale deposit;

– the temperature of the last effect stays slightly higher than that of the cooling seawater;

– overall temperature range, the number of effects is deducted from the specific heat consumption required, which, in general, is the result of an optimization between investment costs and running costs in order to produce the lowest cost water.

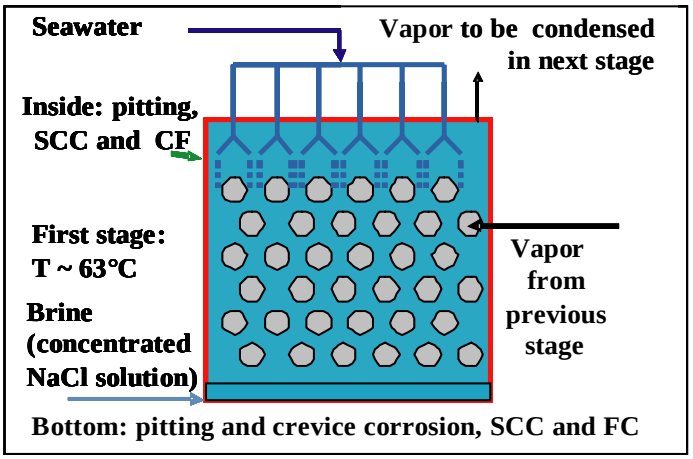

Figure 2.48. *The multi-effect distillation (MED) installation*

In the thermal desalination process, operating conditions in the evaporators may result in the development of several corrosion mechanisms. Stainless steels may suffer from pitting, crevice, stress or fatigue corrosion. In neutral or slightly basic environments, as is the case for seawater, pitting corrosion is possible if oxygen or another oxidizing species (able to be reduced) is present. If the process is well monitored, then localized pitting or crevice corrosion of stainless steels cannot occur because the solution is in a de-aerated condition.

Nevertheless, corrosion can be initiated during equipment shutdowns of the installation (venting is usually performed when internal temperature falls down to 104-122°F/40-50°C) or during disruptive conditions, which allow air into the system. In those cases, the oxygen concentration increases and supports the onset of localized corrosion. Crevice corrosion requires the additional condition of a confined zone in which the solution is not renewed (under a deposit, such as calcium sulfate, in the bottom of a cell during a shutdown). In summary, most of the major factors for initiating localized corrosion of stainless steels, such as a high concentration in chlorides, elevated temperature, and the presence of oxygen, are often combined with local stress concentrations (welds) and cyclic solicitations. In the past, alloyed austenitic grades were often selected for industrial applications.

During the Duplex 2007 International Conference, J. Peultier [JAC 07a] presented an overview of the uses of duplex grades in thermal desalination plants. It was concluded that recently some engineering companies have completely shifted from austenitic to duplex grades. The use of the 2205 has resulted in cost savings by weight reduction and low maintenance costs due to its excellent corrosion-resistance properties. Recently, the 2304 lean duplex material has been introduced for the less severe conditions (Figure 2.49).

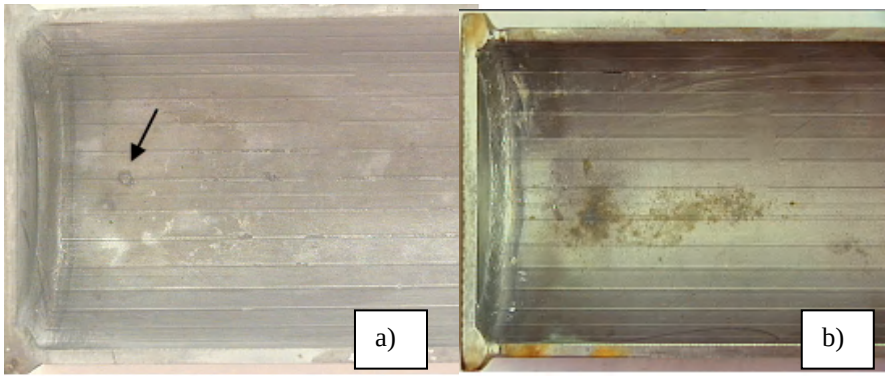

Figure 2.49. *Photograph of cleaned UNS S32304 after exposure in cell a) n°1 and b) n°12 of a multiple effect distillation equipment of a thermal desalination plant (pitting)*

2.5.3. *Industrial experiences with severe chloride-containing environments*

The most severe conditions concerns the uses of stainless steels in complex conditions where simultaneous increase of temperature, chloride/chlorine content in the media, and possible drop of pH occurs. Some limits of use of the duplex grades, including some newly developed alloys and austenitic grades, are presented in Figure 2.49 [KOB 07, YAM 07].

Linkages resulting from both pitting/crevice and stress corrosion phenomena have been reported in many industries dealing with hot, concentrated saline solutions. One typical case is the corrosion associated with brine solution/salt deposits resulting from seawater evaporation (sea water in contact with heated tubes, etc.). As a result, wetting/heating cycles and/or drop evaporation tests have been developed.

Extensive tests performed with a modified drop evaporation test have shown that when duplex 22Cr or 25Cr grades are subject to wetting by sea water (offshore platform) a threshold temperature of 70°C is found to be safe when local applied

stresses are of the magnitude of 90% of the yield stress. The critical temperature for coating duplex products on offshore applications could thus be revised.

Obviously, damage results from complex interactions between chemical analysis of the grade (higher PREN values are preferred even if nitrogen effects seem weaker at temperatures higher than 65°C), microstructure (avoid phase transformations), temperature (worst when increased), local potential (avoid overly oxidizing conditions), level of oxygen, level of stresses (SCC start in the microplastic deformation zones). In most of the cases, microplastic deformations are the initiation zones and as a result, design considerations and appropriate welding parameters are very importance. In closed loops with control of the free oxygen, higher temperatures can be considered with safe use.

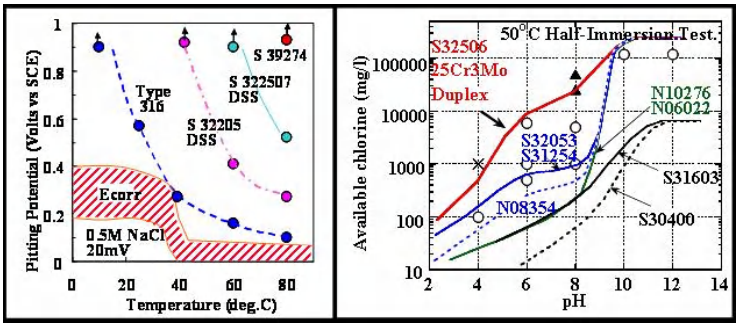

Figure 2.50. *Effects of temperature, chloride content, and pH on pitting corrosion resistance of duplex grades*

2.5.4. *Oil and gas industry*

Several extended papers issued from oil and gas companies [KOB 07, YAM 07] underline the very satisfactory behavior of 22 and 25Cr duplex grades, which have been used for more than 25 years in a large set of applications, i.e. top side, sub-sea piping, manifolds, umbilicals, wells, fire systems, safety panels, etc.

Some failures have been observed. Most of them are related to unintended service conditions including poor design, high local stresses, overloaded conditions, unexpected microstructure defects (sigma phase), local saturated brine solutions (evaporation/condensation phenomena associated with high temperature), and some hydrogen induced stress corrosion (HISC) cases (Figure 2.50). In order to avoid HISC phenomena, the DNV RP F112 document has been prepared, as well as possible implementations. Clearly, HISC results from a source of atomic hydrogen (generally cathodic protection by sacrificial electrodes), high local stresses (overload phenomenon associated with stress concentration factors such as surface

irregularities) and possible improper microstructures (sigma phase precipitations, high ferrite contents in HAZ or welds, etc.). Castings and forged products with large grain sizes seem to be more sensitive to HISC phenomena [HAN 07, JOH 07a, JOH 07b].

The Aker Kvaerner paper [DOB 07] underlines the possible benefits of the use of lean duplex in structural applications for platforms. Pipe racks, pipe supports, architectural walls, insulation claddings, and cable trays could be typical applications where carbon steel is replaced by lean duplexes. Typical cost savings of 20 to 40% are considered when including material costs and welding plus corrosion-resistant coatings. Aluminum stairs and ladders are also to be proposed in lean duplex. In most of those applications, the existing 316 grade should be replaced by a lean duplex. Nevertheless, special care should be taken in material selection, taking in to account the in-service conditions as a wide range of chemistries are proposed (PREN from 23 to 28) among the lean duplexes.

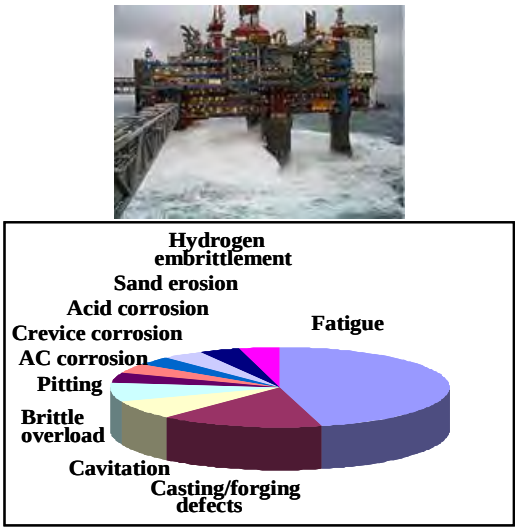

Figure 2.51. *Origins of cases of failure in the oil and gas industries*

2.5.5. *Flue gas desulferization (FGD) pollution-control equipment of coal thermal plants*

In March 2005, the Environmental Protection Agency (EPA) instituted the Clean Air Interstate Rule (CAIR), which will reduce the SO_2 and/or NO_x emissions across 28 eastern states of USA and the District of Columbia. At full implementation in 2015, CAIR will reduce power plant SO_2 emissions 73% below the 2003 emission

levels. Equivalent decisions have been taken all around the world, including west-European countries, Korea, Japan, and more recently China. As a consequence, pollution-control equipment has to be installed or retrofitted on a majority of the coal-fired power plants. The most commonly used technology, applied in more than 80% of the existing installations, consists of scrubbing the polluted gas with a slurry of lime $Ca(OH)_2$ or limestone $CaCO_3$ in water (Wet FGD Process). The aggressive constituents of the raw gas are SO_2, SO_3, HCl, and HF, with SO_2 being the most concentrated. SO_2 and SO_3 containing condensate forms of H_2SO_3 and H_2SO_4, which react with Ca^{2+} and H_2O to form sulfate compounds, which precipitate as $CaSO_4$. HCl and HF form $CaCl_2$ and NaF, which remain in the slurry. The chemical composition of the slurry is monitored in order to insure an efficient neutralizing effect [PEU 07, RIC 07].

In some parts of the process aggressive conditions may be generated, which can cause severe corrosion problems. Among them the mixing zone gas phase/liquid neutralizing solution at the entrance of the scrubber. In this area, the hot, polluted gas is sprayed with the neutralizing slurry. Complete mixing of both phases may not be accomplished. Due to the closure of the water circuit, areas near the top and bottom of the absorber may also be exposed to severe corrosion conditions with either condensates or saturated acid gas, with high chloride content or under deposit corrosion. The slurry reaction tank is not a very corrosive area as the pH is generally controlled to around 4.5-5.5. However, due to closure of water circuits and to the composition of some coal grades, the chloride content can be very high and sometimes fluoride anions are also present. In addition, erosion by solid sulfate salts produced by the chemical reaction between SO_2/H_2SO_3 and lime or limestone can destroy the passive layer on various parts of the tank, mainly the agitators.

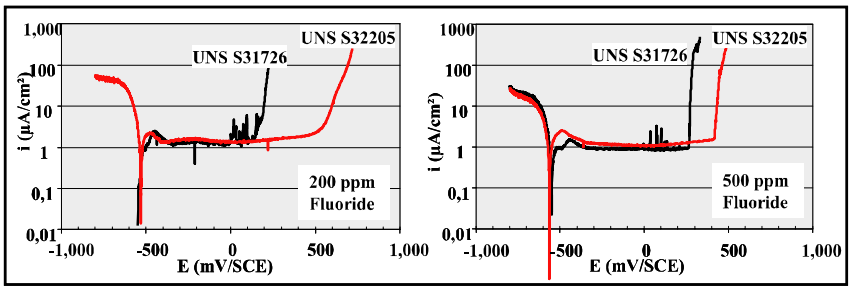

a) b)

Figure 2.52. *Polarization curves for UNS S31726 and UNS S32205 in a 3% chloride and a) 200 or b) 500 ppm fluoride-containing sulfuric acid solution at pH 5 and 140°F/60°C*

The very beneficial behavior of duplex grades in those neutral medium oxidizing conditions is evident in Figure 2.51. Typical diagrams illustrating the large passive domain of duplex grades are presented in Figure 2.52. A guide for material selection charts, including chloride and fluoride content, pH, temperature, etc., is presented in Figure 2.53. The S32205 duplex grade behaves better than the 317LMN grade and is to be selected in severe medium environments (up to 10,000 ppm chloride at 55°C and pH 5). Higher chlorides uses (40,000 ppm) require superduplex grades preferentially with copper additions or even 6Mo austenitic grades [PEU 07].

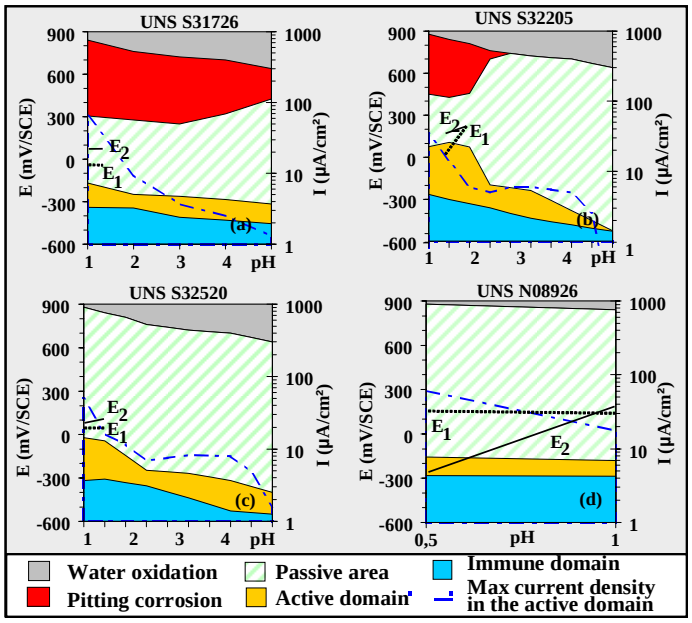

Figure 2.53. *Potential – pH diagram in 3% chloride containing sulfuric acid media at 140°F/60°C for UNS S31726, UNS S32205, UNS S32520, and UNS N08926 grades (E_1 and E_2: free corrosion potentials before and after depassivation, respectively)*

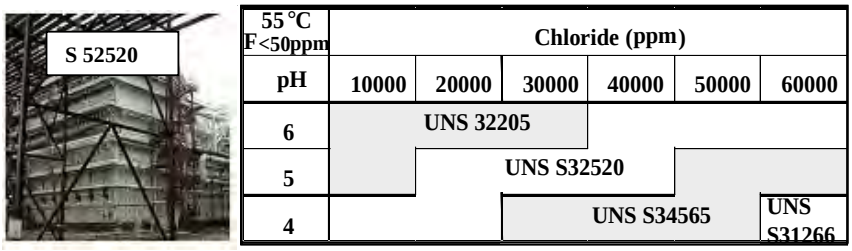

Figure 2.54. *Material selection chart for FGD scrubber systems (Terruel, Spain Unit)*

2.5.6. *Some other industrial applications*

Other interesting successful duplex application with, for some of them, 20/30 years of positive experience are well known. The pulp and paper industry is obviously one of them. Digester, pulp storage tanks, drums, bleaching equipment, paper machines are made out duplex (Figure 2.54). The uses of lean duplex are considered more and more frequently for the less corrosive conditions. This includes the uses of lean duplex in liquor tanks and suction roll [BER 07a, EYZ 07, CHA 07a].

Urea plants are also a very specific market for duplex grades. Specific grades have been developed for the urea-carbamate stripper and condenser. Austenitic 25Cr 22Ni 2Mo can be replaced by highly alloyed duplex grades [KOB 07, NYM 07]. We should also point out one of the most versatile and successful uses of duplex grades: the chemical tanker applications. The 2205 alloy is now the standard grade, able to be considered to carry most chemicals. For the less corrosive applications (barges) 2304 is now also considered [JAC 07b].

Figure 2.55. *a) Paper pulp storage tank in New Zealand made of the S32304 duplex grade. b) Pulp and paper digesters in USA made of the S32205 duplex grade. c) A chemical tanker made of the S32205 duplex grade (La Tour Pomerol). d) A chemical tanker under construction made of the S32205 duplex grade*

2.5.7. *Building and construction*

Finally, one of the newly developed applications for duplex grades, including lean alloys concerns building and construction. Due to their cost advantages when considering weight saving aspects (high mechanical properties) and maintenance cost savings (21/23%Cr providing more corrosion resistance than the 304 grades). Typically, the Eiffel tower should have been built from lean duplex (e.g. 2304). At least 30% weight saving, tons of painting, millions of hours for maintenance could have been saved. The same is true for the Golden Gate Bridge of San Francisco, but, in that case, the 2205 duplex should have been considered for marine environment purposes. Recently, the Millennium Bridge in York has been designed and built with the 2205 duplex. In front of Guggenheim Museum in Bilbao a 2304 duplex footbridge has been erected. Now, reinforced duplex bars are specified for corrosion-free bridges even in marine environments [FAN 07, ZIL 07]. Duplex grade 2205 has shown no pitting corrosion and a complete passive behavior over more than 900 mV polarization in $Ca(OH)_2$, pH 12.6, NaCl saturated solutions, whereas austenitic steel with 2.5 Mo suffered from pitting [COR 07]. The market for duplex reinforced bars is evaluated to millions of tons.

Recently, investigations confirm the advantages of stainless steel in fire safety conditions. Higher temperatures can be considered without damage, as well as greater safety margins. Having 30 minutes instead of 20 minutes to escape a building can make a difference. In this respect, once again duplex grades offer cost savings [BER 07b].

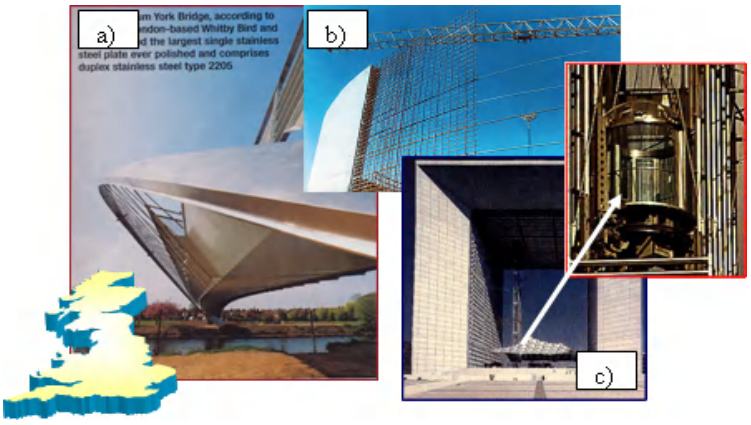

Figure 2.56. *a) York Millennium Bridge made out of 2205 duplex plates. b) Concrete-reinforced bars made out duplex grade melts. c) An elevator of the Grand Arche in Paris (duplex 2205 grade)*

2.6. Conclusions

Duplex stainless steel compositions, including some recent developments, have been presented. Undoubtedly, creativity is still there and new duplex grades and applications are still emerging. Among them the so-called lean duplexes (2101, 2202, etc) targeting the replacement of the austenitic grades, 304 and 316, are under extensive investigation, as are some highly alloyed duplex grades for specific applications.

In the second part of the chapter, extensive data concerning the behavior of the different stainless steels families, when considering the different corrosion mechanism, have been presented. Excellent results have been obtained for duplex grades in most of the conditions investigated. This is particularly the case in localized corrosion resistance in oxidizing, chloride or sulfur species, stress corrosion behavior, and IGC. This explains why the 22% chromium grades are an alternative answer for most applications where high Mo 316 grades, 317LM grades and even 904 grades are used. The 25% chromium duplex grades are to be considered for the most corrosive applications and can be considered to substitute the 6Mo grades in most of these applications. The duplex grades due to their high mechanical properties and their low alloying element costs often present the cost-saving solution. In many cases, due to their low maintenance costs, they can even be considered to replace carbon steels protected by painting and/or linings.

Finally, field experience, of several decades, in highly corrosive industrial environments, concerning mainly the lean duplex grades, the S32205 and S32507 (+Cu,W) grades, have been presented. After more than 20 years in in-service applications, including sea water applications, desalination plants, oil and gas, pulp and paper, chemical tankers, building and construction, etc, their extremely positive behavior has confirmed the research work and convictions of the duplex pioneers.

2.7. References

[AUD 93] AUDOUARD J.P., “Uniform Corrosion”, chapter 8 in LACOMBE P., BARROUX B. and BERANGER G., *Stainless Steels*, Les Editions de Physique, pp. 255-301, 1993.

[BAR 93] BAROUX B., BERANGER G., LEMAIRE C., “Passivity and Passivity Breakdown in Stainless Steels”, Chapter 5 in LACOMBE P., BARROUX B. and BERANGER G., *Stainless Steels*, Les Editions de Physique, pp.163-182, 1993.

[BER 91] BERNARDSSON S., “The corrosion resistance of duplex stainless steels”, *Duplex Stainless Steels ‘91 International Conference*, Beaune, Oct. 28-30, France, Les Editions de Physique, pp. 185-210, 1991.

[BER 93] BERANGER G., CHARBONIER J.C., "Intergranular Corrosion of Stainless Steels", Chapter 11 in LACOMBE P., BARROUX B. and BERANGER G., *Stainless Steels*, Les Editions de Physique, pp. 405-434, 1993.

[BER 07a] BERGSTROM D.S., DUNN J.J., HASEK D.R., "Benchmarking of duplex stainless steels vs. conventional stainless steel grades", *International Conference & Expo, Duplex Stainless Steels '07*, Grado, , Italy, June 17-20, 2007.

[BER 07b] BERTELLI R., CRISTEL R., "Stainless steelfire resistance: low nickel DSS preliminary results", *International Conference & Expo, Duplex Stainless Steels' 07*, Grado, Italy, June 17-20, 2007.

[CHA 91a] CHARLES J., BERNHARDSON S., "The duplex stainless steels: materials to meet your needs". *Duplex Stainless Steels '91 International Conference*, Beaune, Oct. 28-30, France, Les Editions de Physique, pp. 3-48, 1991.

[CHA 91b] CHARLES J., "Super duplex stainless steels: structures and properties", *Duplex Stainless Steels '91 International Conference*, Beaune, Oct. 28-30, France, Les Editions de Physique, pp. 151-168, 1991.

[CHA 97] CHARLES J., "Why and where duplex stainless steels", *Duplex Stainless Steel '97 International conference & Expo*, Oct. 21-23, Maastricht, The Netherlands, pp. 29-42, 1997.

[CHA 00] CHARLES J., "10 years later, obviously duplex grades in industrial applications look like a success story", *Duplex International Conference*, Vence, Italy, pp. 1-12, 2000.

[CHA 07a] CHARLES J., "Duplex Stainless Steels", a review after DSS'07 International conference held in Grado, *Stainless Steel World International Conference & Expo*, Maastricht, The Netherlands, May 6-8, 2007.

[CHA 07b] CHARLES J., "Past, present and future of duplex stainless steels", *International Conference & Expo, Duplex Stainless Steels' 07*, Grado, Italy, June 17-20, 2007.

[COM 91] COMBARDE P., AUDOUARD, J.P., "Duplex stainless steels and localized corrosion resistance", *Proceeding of the DSS Conference*, Beaune, France, October, p. 257, 1991.

[COM 93] COMBRADE P., "Stress Corrosion Cracking and Corrosion Fatigue", chapter 10 in LACOMBE P., BARROUX B. and BERANGER G., *Stainless Steels*, Les Editions de Physique, pp. 331-402, 1993.

[COR 07] CORREIRA M.J., SALTA M.M, FONSECA I.T.E., TELEGGDI J., "Corrosion resistance of duplex stainless steels in $Ca(OH)_2$ saturated solutions", *International Conference & Expo, Duplex Stainless Steels '07*, Grado, Italy, June 17-20, 2007.

[DES 93] DESESTRET A. and CHARLES J., "The Duplex Stainless Steels", Chapter 18 in LACOMBE P., BARROUX B. and BERANGER G., *Stainless Steels*, Les Editions de Physique, pp. 615-658, 1993.

[DOB 07] DOBLE O., HAVN T., "Lean Duplex Stainless", *Steel for Structural Applications, International Conference & Expo, Duplex Stainless Steels '07*, Grado, Italy, June 17-20, 2007.

[EYZ 07] EYZOP D., SJÖSTRÖM J., KÄLLGREN O., "304SRG: a growing market for paper mill suction rolls", *International Conference & Expo, Duplex Stainless Steels '07*, Grado, Italy, June 17-20, 2007.

[FAN 07] FANICA A., MAIORANA E., "UNS S 32205 for bridge construction: an experience of application", *International Conference & Expo, Duplex Stainless Steels '07*, Grado, Italy, June 17-20, 2007.

[GAG 07] GAGNEPAIN J.C., SOULIGNAC P., "Why duplex usages will continue to grow?" *International Conference & Expo, Duplex Stainless Steels '07*, Grado, Italy, June 17-20, 2007.

[HAN 07] HANNAH I., PATERSON S., "Reducing risk of hydrogen induced stress cracking (HISC) in duplex stainless steel for subsea applications", *International Conference & Expo, Duplex Stainless Steels '07*, Grado, Italy, June 17-20, 2007.

[JAC 07a] JACQUES S., PEULTIER J., SOULIGNAC P., "Desalination plants – why using duplex stainless steels", *International Conference & Expo, Duplex Stainless Steels '07*, Grado, Italy, June 17-20, 2007.

[JAC 07b] JACQUES S., HAGI G., "Tour Pomerol chemical tanker: eight years experience with duplex EN 1.4462", *International Conference & Expo, Duplex Stainless Steels '07*, Grado, Italy, June 17-20, 2007.

[JOH 07a] JOHANSSON K.A., STRANDMYR O., EIE G.E., HAGERUP O., "25 years with duplex", *From Tommeliten to Gjoea, International Conference & Expo, Duplex Stainless Steels '07*, Grado, Italy, June 17-20, 2007.

[JOH 07b] JOHNSEN R., NYHUS B., WASTBERG S., "New improved method for HISC testing of stainless steels under cathodic protection", *International Conference & Expo, Duplex Stainless Steels '07*, Grado, Italy, June 17-20, 2007.

[KOB 07] KOBA Y., YASHI I., KOIDE N., "Corrosion resistance of duplex stainless steels in hypochlorite solutions", *International Conference & Expo, Duplex Stainless Steels '07*, Grado, Italy, June 17-20, 2007.

[NYM 07] NYMAN M.L., KIVISAKK U., HOLMQUIST M., GORANSSON K., "Performances of SAF2707HD (UNS32707) in severe chloride containing environments", *International Conference & Expo, Duplex Stainless Steels '07*, Grado, Italy, June 17-20, 2007.

[PEU 07] PEULTIER J., GAGNEPAIN J.C., SOULIGNAC P., "Duplex and superduplex stainless steel grades for wet desulfurisation systems", *International Conference & Expo, Duplex Stainless Steels '07*, Grado, Italy, June 17-20, 2007.

[RIC 07] RICHARD R.L., "20+ of successful FGD experience with superduplex (UNS32550) at the Gibson generation station", *International Conference & Expo, Duplex Stainless Steels '07*, Grado, Italy, June 17-20, 2007.

[YAM 07] YAMASHHITA M., MATSUMOTO S., HIROHATA N., "Corrosion resistance and properties of duplex stainless steels", *International Conference & Expo, Duplex Stainless Steels '07*, Grado, Italy, June 17-20, 2007.

[ZIL 07] ZILI G., FATTRINI F., MAIORANA E., "Application of duplex stainless steel for welded bridge construction in aggressive environment", *International Conference & Expo, Duplex Stainless Steels '07*, Grado, Italy, June 17-20, 2007.

Chapter 3

Phase Transformation and Microstructure

3.1. Introduction

This chapter will cover most of the phase transformations occurring in duplex stainless steels, related microstructures, and their influence on mechanical and corrosion properties.

The continuing development of duplex stainless steels has resulted in complex steel compositions (see Table 3.1) containing substantial amounts of alloying elements. These alloying elements are, of course, introduced in the steel for one or more reasons, but the final aim is mainly to obtain better mechanical properties and/or higher corrosion resistance. As usual, the benefits of such additions invariably come attached to unavoidable disadvantages, the most important being the potential microstructural instability of the material. During processing or usage, duplex stainless steels are subject to various phase transformations starting from the liquid state down to subzero temperatures. In the majority of the cases the formation of such phases is undesirable so that careful processing is needed to avoid or, at least, to minimize them.

Ferritic-austenitic stainless steels with a duplex microstructure can be classified in two sub-groups (see Table 3.1): 1) alloys with low carbon content (0.01 wt% ≤C ≤0.08 wt%), frequently mechanically worked (wrought alloys); and 2) alloys with high carbon content (0.3 wt% ≤C ≤0.5 wt%), used in the as-cast condition. Wrought

---

Chapter written by Angelo Fernando PADILHA and Ronald Lesley PLAUT

Duplex Stainless Steels Edited by Iris Alvarez-Armas and Suzanne Degallaix-Moreuil

duplex stainless steels offer a very interesting combination of properties, such as corrosion resistance, mechanical strength, ductility, toughness, and weldability. Duplex steels of higher carbon content show lower toughness and ductility but have an excellent wear resistance.

Type	UNS design.	C	Mn	Si	Cr	Ni	Mo	N	Others	PRE-range
AISI 329	S32900	≤0.20	≤1.00	≤0.75	23.0-28.0	2.50-5.00	1.00-2.00			26.3-34.6
Avesta 3RE60	S31500	≤0.03	1.2-2.0	1.4.-2.0	18.0-19.0	4.25-5.25	2.5-3.0	0.05-0.10		27.1-30.5
W. Nr. 1.4460	S32900	≤0.07	≤2.0	≤1.0	25.0-28.0	4.5-6.0	1.3-2.0	0.05-0.20		30.1-37.8
W. Nr. 1.4462	S31803	≤0.03	≤2.00	≤1.00	21.0-23.0	4.50-6.50	2.50-3.50	0.08-0.20		30.5-37.8
44LN	S31200	≤0.03	≤2.0	≤1.0	24.0-26.0	5.5-6.5	1.2-2.0	0.14-0.20		30.2-35.8
Ferralium 255	S32550	≤0.04	≤1.50	≤1.00	24.0-27.0	4.50-6.50	2.00-4.00	0.10-0.25	Cu=1.50-2.50	35.2-43.0
7-Mo PLUS	S32950	≤0.03	≤2.0	≤0.60	26.0-29.0	3.50-5.20	1.00-2.50	0.15-0.35		31.7-42.8
SAF 2507	S32750	≤0.03	≤1.2	≤1.0	24.0-26.0	6.0-8.0	3.0-5.0	0.24-0.32	Cu=0.50	37.7-47.6
UR52N+	S32520	≤0.03	≤1.5	≤0.8	24.0-26.0	5.5-8.0	3.0-5.0	0.20-0.35	Cu=0.50-3,0	37.1-48.1
W. Nr. 1.4464		0.30-0.50	≤1.50	≤2.0	26.0-28.0	4.0-6.0	2.0-2.50			
W. Nr. 1.4822	J92605	0.30-0.50	≤1.50	1.0-2.0	23.0-25.0	3.50-5.50				

Table 3.1. *Chemical composition (in wt%) of some typical duplex stainless steels*

Duplex stainless steels are frequently used in aqueous solutions containing chlorides, where they have substituted (with the advantages of major reductions in weight and welding times) the austenitic stainless steels that are more susceptible to stress and pitting corrosion. Pitting corrosion resistance in stainless steels is mainly linked to the chromium (Cr), molybdenum (Mo), and nitrogen (N) contents. At the end of the sixties, some relationships [DES 93] were suggested relating pitting corrosion resistance (PRE = pitting resistance equivalent) to the content of these three elements:

$$\text{PRE} = \%\,\text{Cr} + 3.3\,\%\,\text{Mo} + (16 \text{ or } 30)\,\%\,\text{N} \qquad [3.1]$$

where compositions are in wt%.

The value of “30” for nitrogen in equation [3.1] is valid for austenitic steels, while “16” is used for duplex steels. Chromium and molybdenum are ferrite formers, they concentrate mainly in ferrite, whereas nitrogen and nickel (Ni) are

linked mainly to austenite. In the initial development steps, duplex steels had low nitrogen levels and were quite susceptible to pitting corrosion. Some modern duplex steels have higher nitrogen levels (0.2 to 0.32 wt%), which give a higher pitting corrosion resistance to austenite, comparable to ferrite. Here it should be mentioned that an exaggerated increase in the nitrogen level leads to an increase in the austenite level beyond the level adequate for mechanical resistance. Several duplex stainless steels contain about 3 wt% Mo. For long exposure times in chloride-rich environments, such as sea water, a level of PRE >40 is nowadays considered satisfactory. Alloys containing PRE >40 are known as “superduplex”.

3.2. Phase diagrams and typical phases

In 1927, Bain and Griffith [BAI 27] reported their results on the Fe-Cr-Ni-system and mentioned the existence of a two-phase field comprising austenite and ferrite. This was, probably, the first mention of the duplex type stainless steels. The ternary Fe-Cr-Ni diagram is the basic diagram for stainless steels (see Figure 3.1). It shows the presence of only three solid phases: austenite (γ), ferrite (α) and sigma phase (σ).

However useful equilibrium phase diagrams might be, they are rarely sufficient to predict the resulting microstructure after solidification. As a result “practical” methods were developed. Among these, the best-known one is the Schaeffler diagram. Schaeffler [SCH 47, SCH 48, SCH 49] divided the alloying elements in two groups: ferrite and austenite stabilizers. He also developed a formula by means of which the elements of each group could be expressed as a chromium equivalent and as a nickel equivalent.

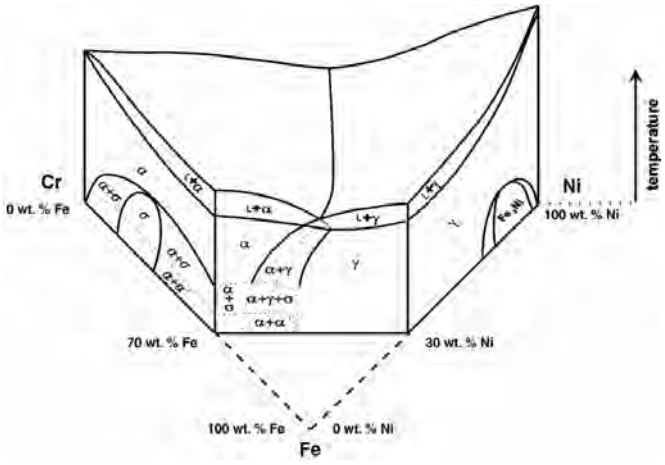

Figure 3.1. *3D view of the Fe-Cr-Ni equilibrium diagram [POH 07]*

An example of such a diagram is presented in Figure 3.2. The regions of the diagram represent the microstructures that can be observed for each class of stainless steels. Schaeffler‘s method, therefore, allows a rough evaluation of the microstructure as a function of the steel composition; however, it does not take into consideration the influence of the cooling rate and aging heat treatments. These diagrams have also been used to estimate the microstructure of the weld metal. The empirical formulas and the experiments present a considerable scatter with regard to the determination of the amount of delta ferrite in austenitic weld metal. DeLong [DEL 74] suggested a comparative method for delta ferrite determination that has been adopted as a standard procedure by the International Welding Institute (IWI).

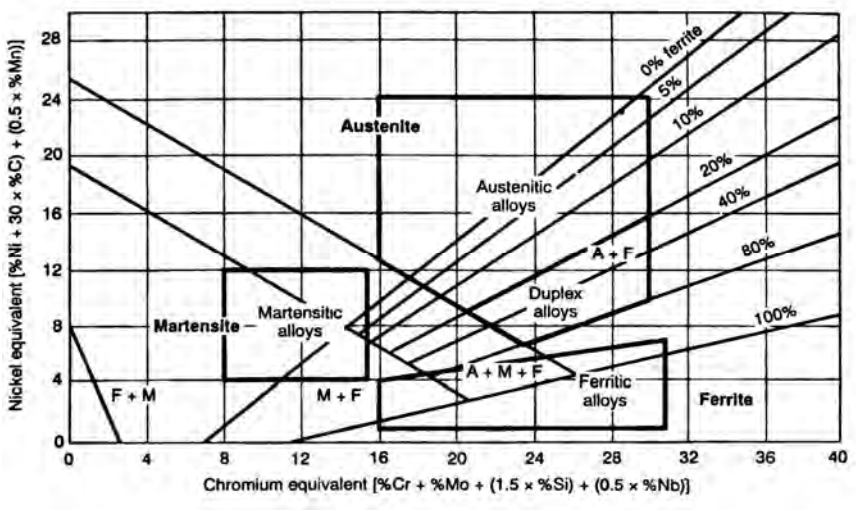

Figure 3.2. *Schaeffler’s constitution diagram for stainless steels. The typical compositional ranges of the ferritic, martensitic, austenitic, and duplex alloys have been superimposed on this diagram [DAV 94]*

Phase diagrams are important to predict the phases present in duplex stainless steels. Nevertheless, they have limitations due to complexity of multicomponent thermodynamic calculations; the number of relevant components is often more than five and published diagrams are rarely found to contain more than four components. For instance, non-metallic elements, such as carbon and nitrogen, are usually present in duplex stainless steels in relatively small quantities, but their effect can be extremely important. Table 3.2 presents the crystal structures and the compositions of the phases which may appear in duplex stainless steels. The occurrence of these phases will be discussed in the following sections.

Phase	UNIT CELL	Atoms per cell	Space group	Lattice parameters (nm)	Composition
Main phases					
Austenite (γ)	fcc	4	Fm3m	a = 0.358-0.362	(Fe,Cr,Ni,Mo,N)
Ferrite (δ or α)	bcc	2	Im3m	a = 0.285-0.289	(Fe,Cr,Ni,Mo)
Martensite (α′)	bcc	2	Im3m	a = 0.285-0.289	(Fe,Cr,Ni,Mo,N)
Martensite (ε)	hcp	2 (6)	$P6_3/mmc$	a = 0.250-0.255; c = 0.410-0.420	(Fe,Cr,Ni,Mo,N)
Intermetallic phases					
Sigma (σ)	bct	30	$P4_2/mnm$	a = 0.87-0.92; c = 0.4554-0.48	$(Fe,Ni)_x(Cr,Mo)_y$
Chi (χ)	bcc	58	I43m	a = 0.881-0.895	$Fe_{36}Cr_{12}Mo_{10}$; $(Fe,Ni)_{36}Cr_{18}Mo_4$
Laves (η)	hex.	12	$P6_3/mmc$	a = 0.473-0.483; c = 0.772-0.786	Fe_2Mo; Fe_2Nb; Fe_2Ta; Fe_2Ti; Fe_2W
G	fcc	116	Fd3m	a = 1.115-1.120	$Ni_{16}Nb_6Si_7$; $Ni_{16}Ti_6Si_7$; $(Ni,Fe,Cr)_{16}(Nb,Ti)_6Si_7$
R	hex.	53 (159)	R3	a = 1.08-1.10; c = 1.92-1.94	$Fe_{22}Mo_{18}Cr_{13}$; $(Fe,Ni)_{10}Cr_5Mo_3Si_2$
Carbides					
$M_{23}C_6$	fcc	116	Fm3m	a = 1.057-1.068	$(Cr, Fe, Mo)_{23}C_6$; $(Cr_{16}Fe_5Mo_2)C_6$
MC	ord fcc	8	Fm3m	a = 0.4131-0.4698	(Ti,Nb,V)C
M_6C	fcc	112	Fd3m	a = 1.085-1.128	$(Fe, Mo, Nb,Cr)_6C$
M_7C_3	pseudo hex.	40	Pnma	a = 1.395-1.400; c = 0.452-0.453	$(Cr,Fe)_7C_3$
Nitrides					
MN	ord fcc	8	Fm3m	a = 0.4097-0.4577	CrN, ZrN;TiN; NbN; VN
M_2N	hexagonal	9	P31m	a = 0.475-0.480; c = 0.443-0.447	$(Cr,Fe)_2N$
Z-phase	tetragonal	6	P4/nmm	a = 0.303-0.306; c = 0.738-0.740	CrNNb

Table 3.2. *Crystal structures and compositions of the most common phases that may occur in duplex stainless steels*

3.3. Solidification

Low carbon stainless steels can solidify (see Figure 3.3) by several mechanisms or modes [ALL 95]: ferritic or mode A ($L \rightarrow L + \delta \rightarrow \delta$); ferritic-austenitic or mode B ($L \rightarrow L + \delta \rightarrow L + \delta + \gamma \rightarrow \gamma + \delta$); austenitic-ferritic or mode C ($L \rightarrow L + \gamma \rightarrow L + \gamma + \delta \rightarrow \gamma + \delta$) and austenitic or mode D ($L \rightarrow L + \gamma \rightarrow \gamma$). Duplex steels of lower carbon content solidify in a ferritic structure (mode A) and the austenite forms in the solid state (see phase diagram of Figure 3.3). The *liquidus* temperature is about 1,445 to 1,450°C and *solidus* is about 1,385 to 1,390°C. In the case of high carbon duplex stainless steels (for example, steel type W. Nr. 1.4464 in Table 3.1), the first phase to solidify is also ferrite. The residual liquid enriched in austenite-stabilizing elements (carbon, nitrogen, nickel, and manganese) solidifies forming austenite (mode B) and the chromium-rich carbide of the type M23C6 (M=Cr, Fe, Mo).

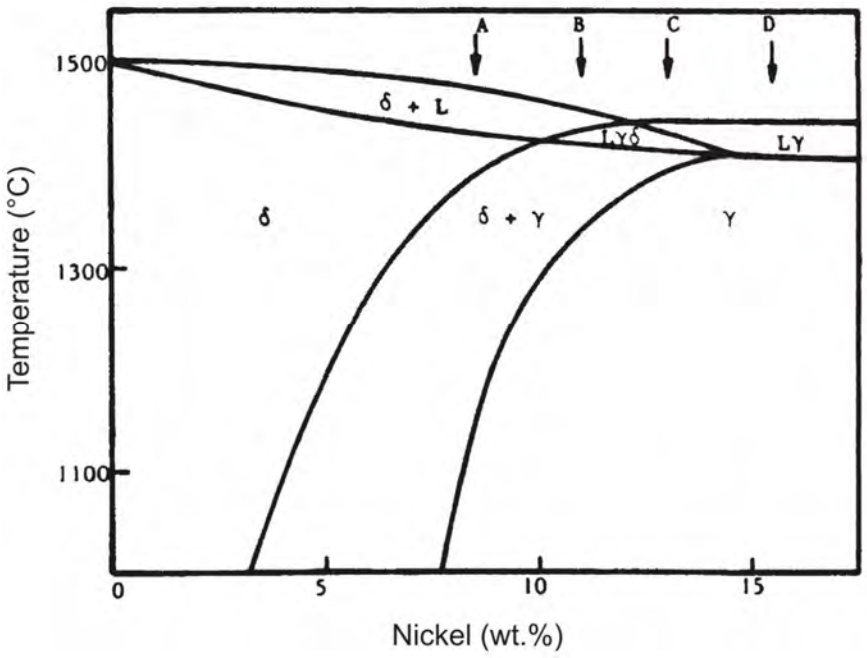

Figure 3.3. *Section through Fe-Ni-Cr phase diagram at 19% Cr showing four solidification modes [ALL 95]*

3.4. Austenite precipitation

The formation of austenite between 1,200 and 650°C occurs by the nucleation and growth and follows a C-curve kinetics as shown schematically in the TTT diagram of Figure 3.4.

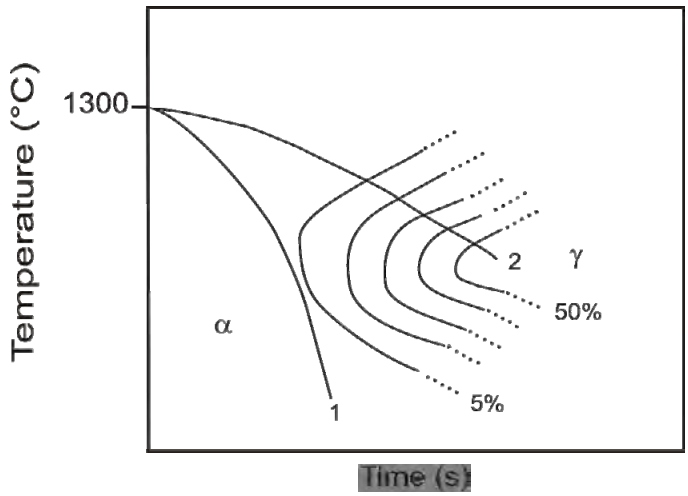

Figure 3.4. *Schematic TTT diagram showing the partial decomposition of ferrite (α) into austenite during cooling [REI 90]*

The ferrite → austenite transformation in duplex stainless steels is very similar to the austenite → proeutectoid ferrite transformation in hypoeutectoid low-alloy carbon steels. Initially, austenite precipitates at the ferrite/ferrite grain boundaries and grows with Widmanstätten morphology into the interior of the grains. Afterwards, austenite also precipitates as intragranular side-plate islands. The formation of Widmanstätten austenite laths accompanies a sharp surface relief similar in appearance to that of martensite and exhibits a well-defined $(110)\alpha$ // $(111)\gamma$ habit plane with the growth direction parallel to $[\bar{1}\,11]\alpha$ // $[\bar{1}\,10]\gamma$] [OHM 95]. Southwick and Honeycombe [SOU 80] examined the decomposition of ferrite to austenite in a 26% Cr-5% Ni duplex stainless steel. Figure 3.5 shows the isothermal transformation diagrams. Figure 3.5a was obtained following direct quenching and Figure 3.5b was obtained by isothermal aging following water quenching, both after solution annealing at 1,300°C. In both types of treatment, the reaction rate is very fast and the ferrite decomposition is nearly complete in a few minutes.

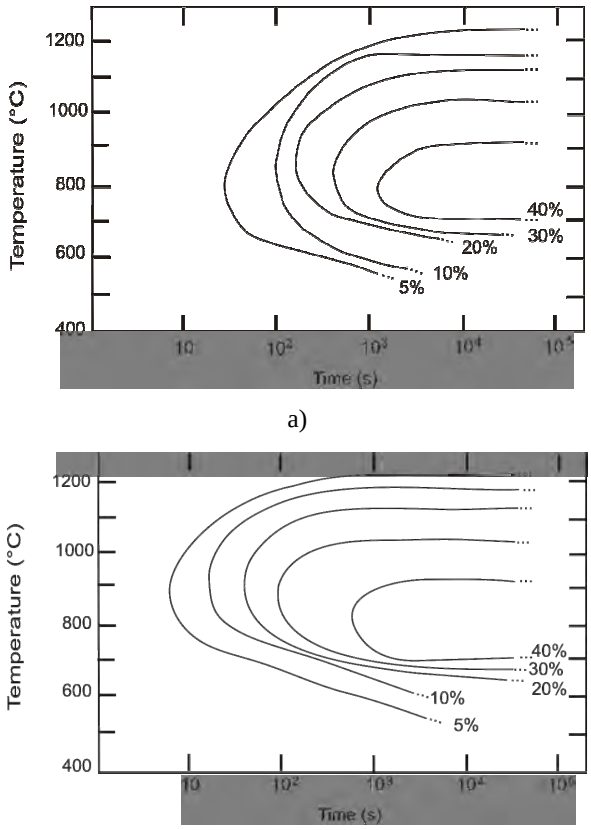

Figure 3.5. *Isothermal transformation diagram for decomposition of ferrite into austenite from solution treatment at 1,300 ºC, a) following direct quenching and b) following water quenching [SOU 80]*

During hot working (between 1,200 and 1,050°C) a microstructure forms with alternating ferrite and austenite lamellae (see Figure 3.6). The fact that the α/γ interface energy is lower than the α/α and γ/γ grain boundary energies induces the formation of that typical lamellar microstructure. After hot forming, solution annealing (between 1,000 and 1,100°C) followed by a rapid quench is necessary to restore the mechanical properties and the corrosion resistance. Below 1,000°C the proportion of ferrite to austenite can only be slightly modified.

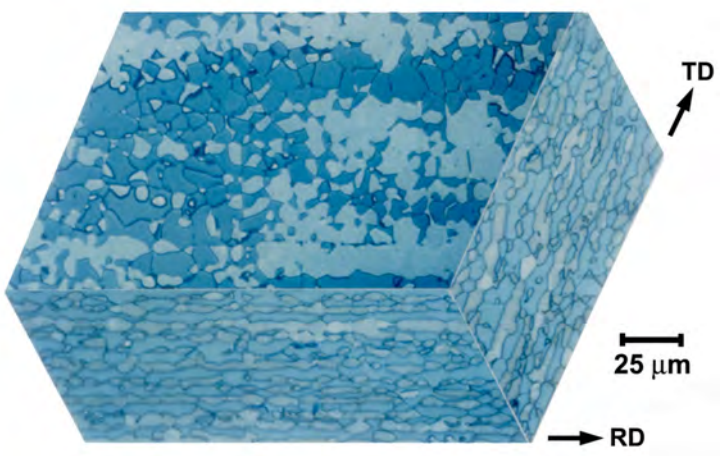

Figure 3.6. *3D composed micrograph of rolled duplex stainless steel. Optical microscopy [REI 93]. Ferrite is the darker phase. Etched with Behara II*

Ferrite strengthening occurs by solid solution hardening with preferential participation of chromium, molybdenum, and silicon, whereas austenite is strengthened mainly by nitrogen. The partition of the ferrite and austenite stabilizing elements after casting is strongly related to the cooling rate from the liquid [HER 08].

3.5. Phase changes occurring below 1,000°C

When exposed to temperatures lower than 1,000°C, duplex stainless steels are subject to various phase transformations. In the 970 to 650°C temperature range, intermetallic phase precipitation may occur, mainly the sigma (σ) and the chi (χ) phases, apart from carbides and nitrides. In the 300 to 500°C temperature range, alpha-prime (α') may be formed, which causes the well-known 475°C embrittlement in ferrite.

The schematic and semi-quantitative TTT diagram of Figure 3.7 shows the temperature ranges in which precipitation of different phases can occur in duplex stainless steels between 1,000 and 300°C. Below 300°C, austenite, if plastically deformed, transforms partially into martensite. Annealing of the worked material leads, in turn, to the martensite reversion into austenite and to recrystallization. In the following, we will briefly discuss each one of these phase transformations.

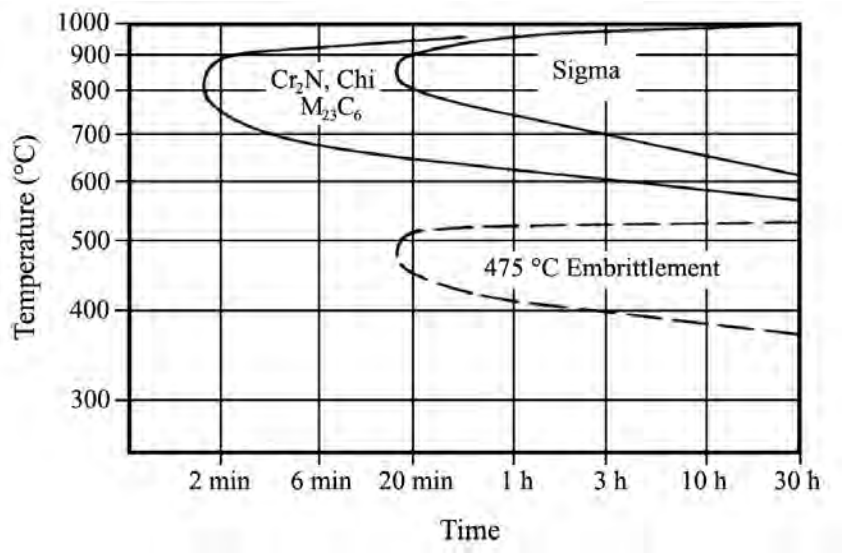

Figure 3.7. *Schematic and semi-quantitative TTT diagram showing the precipitation of different phases that can occur in duplex stainless steels [REI 90, PAD 07]*

3.5.1. *Chromium carbide ($M_{23}C_6$) precipitation*

Most of the duplex stainless steels present low levels of carbon content, less than 0.03 wt% and the maximum amount of precipitated carbide is only about 0.5 vol.%. However, because of the high mobility of carbon, carbide precipitates prior to the formation of other phases at the very early stages of aging [LEE 99, WIL 91, SOU 82]. The $M_{23}C_6$ precipitation occurs predominantly in the temperature range of 900-700°C, for short exposure times (≤0.5 h), but also in the temperature range of 700-550°C after longer exposures.

Carbon is preferentially partitioned in the austenite phase, but the precipitation of $M_{23}C_6$ carbide occurs mainly at austenite/ferrite interfaces following the eutectoid reaction $\delta \rightarrow M_{23}C_6 + \gamma_2$ and causing the migration of the interface boundary into the ferrite phase region (see Figure 3.8). As carbides grow into the ferrite phase, the chromium depleted zone on the ferrite side of the ferrite/austenite interface transforms into austenite which has a low chromium content [WIL 91]. The new austenite is called secondary austenite. As a consequence, the resistance to sensitization of the steel is decreased.

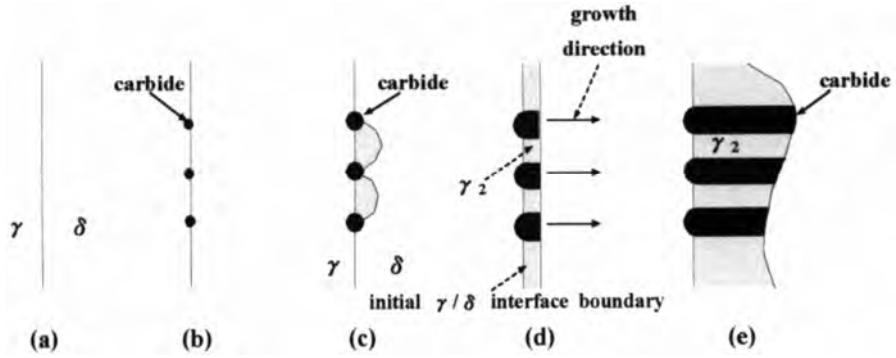

Figure 3.8. *Schematic diagram showing the microstructural evolution of lamellar $M_{23}C_6$ precipitation and the migration of the ferrite/austenite interface boundary, adapted from [LEE 99]*

3.5.2. *Chromium nitride (Cr_2N) precipitation*

Modern duplex stainless steels are intentionally alloyed with nitrogen and some alloys (see Table 3.1) contain up to 0.35 wt% N. Nitrogen is a very strong austenite stabilizer and causes a shift to high temperatures of the two phase field (δ+γ) in the pseudo-binary section of the Fe-Cr-Ni phase diagram (see Figure 3.3). Nitrogen in solid solution delays the intermetallic phase formation. The precipitation of small amounts of the hexagonal nitride Cr_2N can occur in austenite in the same temperature range and nearly simultaneously with $M_{23}C_6$. Nitride precipitation in duplex stainless steels is very important during welding.

During welding, as the ferritized microstructure cools rapidly, the ferrite becomes supersaturated in nitrogen, resulting in a competition between chromium nitride and austenite precipitation. As shown by Ramirez and colleagues [RAM 03], the microstructure formed during rapid cooling consists of large ferrite grains with a low volume fraction of allotriomorphic and Widmanstätten austenite in addition to abundant intragranular nitrides (Cr_2N rods or CrN plates). This microstructure results in degradation of the mechanical and corrosion properties of the welded joint.

Hexagonal nitride Cr_2N and cubic nitride CrN were also found by Liao [LIA 01] in the weld heat-affected zones (HAZs) of a duplex stainless steel. CrN nitrides precipitated in the adjacency to Cr_2N precipitates, displaying film-like or minute platelet-like shapes. Cr_2N precipitates appeared as rod-like or tetragonal shapes, and the size of Cr_2N precipitates tends to increase with decreasing cooling rate.

3.5.3. *Chi phase (χ) precipitation*

Chi (χ) phase may occur in austenitic, ferritic, and duplex stainless steels and its precipitation is associated with negative effects on corrosion and mechanical properties. While sigma phase is present in the binary Fe-Cr system, chi phase appears only in the Fe-Cr-Mo ternary and in the Fe-Cr-Ni-Mo and Fe-Cr-Ni-Ti quaternary systems [KAS 54, HUG 59, OKA 78]. Still in comparison with the sigma phase, chi (χ) phase is richer in molybdenum and poorer in chromium [NIL 93, DUP 01, CAL 05, CAL 06, CAL 09, MIC 06]. The occurrence of the chi (χ) phase in stainless steels is conditioned to a minimum in the molybdenum content (about 2 wt%).

Chi phase nucleates mainly at the ferrite/austenite interface but also at the ferrite/ferrite grain boundaries [DUP 00]. It is stable at lower temperatures and in a narrower temperature (between 900 and 600°C) range than sigma phase, but χ appears to transform into σ after long aging time [NIL 93]. A detailed investigation on the morphology, crystallography and defects of the intermetallic χ-phase precipitated in a UNS S31803 duplex stainless steel has been performed by Redjaïmia and co-authors [RED 04]. The chi phase has been less studied than the sigma phase, it occurs in lower amounts than sigma, nonetheless its presence is also considered to be detrimental to the steel properties. For instance, a drastic drop in toughness was detected [CAL 06, CAL 09] in the steel SAF 2205 for a very low intermetallic phase content, about 0.5–1%, even before sigma phase formation, when only a few small chi phase particles could be detected at a high magnification by metallographic techniques.

3.5.4. *Sigma phase (σ) precipitation*

Sigma phase is probably the most studied intermetallic compound. In 1907, even before the discovery of stainless steels, Treischke and Tamman [TRE 907] studied the Fe-Cr system and proposed the existence of an intermetallic compound containing chromium in the 30 to 50 wt% range. In 1927, Bain and Griffiths [BAI 27] studied the Fe-Cr-Ni system and observed a hard and fragile phase, which they called constituent B, from “brittle”. In 1936, Jett and Foote [JET 36] called it sigma (σ) phase and in 1951, Bergmann and Shoemaker [BER 51] determined, through crystallography, its structure in the Fe-Cr system. It has a tetragonal structure with 30 atoms per unit cell. Precipitation of sigma phase in stainless steels can occur in the austenitic, ferritic and austenitic-ferritic duplex structure types. The precipitation of this intermetallic phase causes crucial losses in toughness and in corrosion resistance.

Recent studies [PAD 01, VIL 06] showed that the kinetics of sigma σ phase precipitation is faster for the austenitic stainless steels, but slower for the duplex stainless steels. In the case of duplex stainless steels, precipitation can be complete in a few hours and consume all the ferrite of the microstructure [COR 97]. Precipitation in this case occurs between 975 and 650°C and can be represented by an eutectoid-type reaction: $\alpha \rightarrow \gamma^* + \sigma$, where γ^* is a chromium and molybdenum depleted austenite if compared to a non-transformed austenite (see Figures 3.9 and 3.10). Precipitation starts at the α/γ interface and moves into the ferrite grain until the ferrite is practically exhausted.

The sigma phase grows into ferrite instead of growing into the austenite because sigma is rich in ferritizing elements, such as chromium, molybdenum, and silicon, and is poor in austenitizing elements, such as nickel, carbon, and nitrogen. Furthermore, the diffusion in ferrite is faster than in austenite. Up to 800°C, the eutectoid morphology is nearly lamellar resulting from the sigma and austenite cooperative growth, whereas around 900°C the sigma phase precipitates in a massive morphology, leading to a microstructure called divorced eutectoid. Conversely, the nucleation of the sigma phase along ferrite/ferrite grain boundaries suggests that the direct reaction $\alpha \rightarrow \sigma$ can also occur. The new austenite (γ^*) is essentially a Fe-Ni alloy, which is practically molybdenum-free and whose chromium content is low. Therefore, the precipitation of the sigma phase in stainless steels makes it highly susceptible to localized corrosion at the sigma/austenite interface [KOB 99].

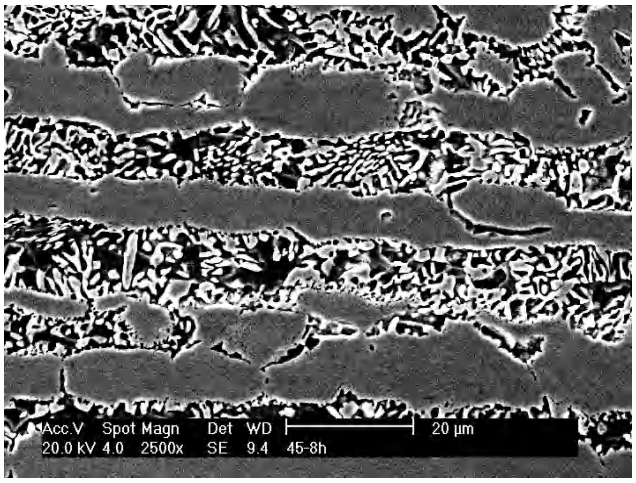

Figure 3.9. *Sigma phase precipitation in duplex stainless steel W. Nr. 1.4462 (UNS S31803), observed using scanning electron microscopy. (Courtesy of D. M. Escriba Villanueva, University of Sao Paulo, Brazil)*

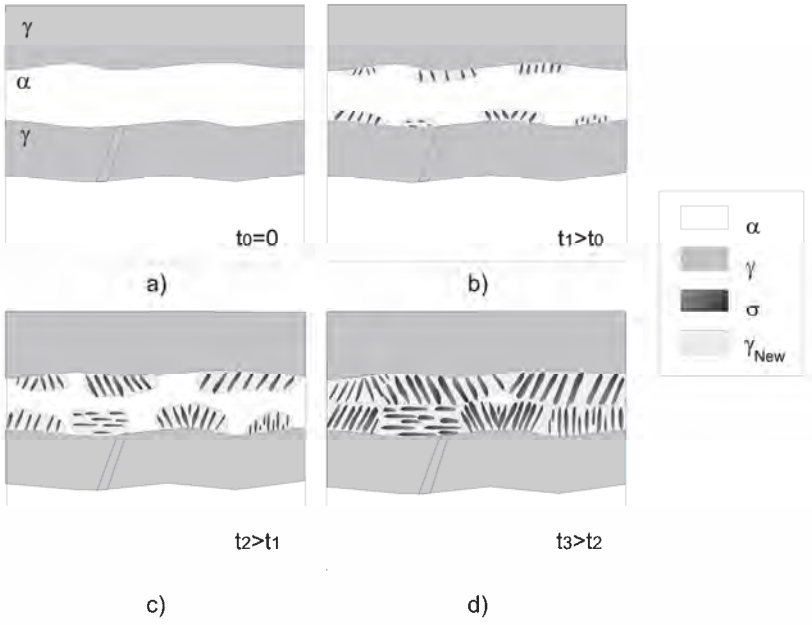

Figure 3.10. *Schematic diagram showing sigma phase formation in a duplex stainless steel via eutectoid decomposition of the ferritic phase [VIL 06]*

Usually, an increased austenite content in a duplex stainless steel promotes sigma phase formation due to an increased content in alloying elements (Cr, Mo and Si) in the ferrite phase [MAE 83, NOR 81].

Several authors [NIL 93, VIL 06] reported the sigma phase in duplex and superduplex steels containing 35-55 wt% Fe, 24-40 wt% Cr, and 11-25 wt% Mo. In comparison with the other phases (initial α, initial γ, precipitated χ and γ^*) and with the steel composition, the following sequences are observed: for Cr ($\sigma > \alpha \cong \chi >$ steel $> \gamma > \gamma^*$); for Ni ($\gamma^* > \gamma >$ steel $> \alpha \cong \chi \cong \sigma$) and for Mo ($\chi > \sigma > \alpha >$ steel $> \gamma > \gamma^*$).

The TTT diagram of Figure 3.11 compares the precipitation temperature ranges and the precipitation kinetics of sigma phase, chi phase, nitride, and secondary austenite γ_2 (in this case, formed simultaneously with the Cr_2N precipitation) for the SAF 2507 duplex stainless steel.

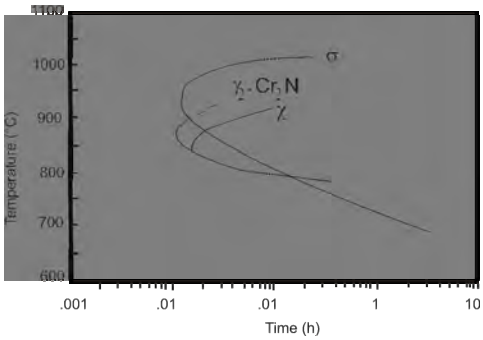

Figure 3.11. *TTT diagram of the SAF 2507 duplex stainless steel solution annealed at 1,000°C, adapted from [NIL 93]. The C-curves represent a first visible sign of each phase using scanning electron microscopy*

Machado and Padilha [MAC 00] studied the precipitation behavior of a duplex steel containing high manganese (17 wt%) and very high nitrogen (0.54 wt%) contents. They detected sigma phase precipitation both in ferrite and in austenite. The ferritic phase decomposed very fast into the sigma phase plus austenite ($\alpha \rightarrow \gamma^{*} + \sigma$). The first phase to precipitate in the austenite was the hexagonal chromium nitride (Cr_2N). The sigma phase was formed in austenite following the chromium nitride precipitation.

The impact toughness decreases rapidly with increasing amounts of sigma phase. Already about 1% of sigma phase implies an impact value drop of about 50% relative to the initial condition (solution annealed and quenched) [NIL 93, CAL 06, CAL 09, NOR 81]. The harmful effects of the sigma phase on the corrosion resistance of duplex stainless steels have been evaluated through different corrosion tests, such as general corrosion tests, pitting potential tests, crevice corrosion tests, intergranular corrosion tests, and stress corrosion tests [KOB 99]. It must be emphasized, however, that the dissolution of sigma phase takes place in a few minutes during solution annealing at 1,050°C [POH 04].

Finally, it should be mentioned that some authors [POH 04, POH 07] classify the austenite occurring in duplex stainless steels in accordance to the austenite formation mechanism (see Table 3.3).

Type	Formation
Primary (γ_1)	During solidification: $L \rightarrow \delta + \gamma_1$
Secondary (γ_2)	Precipitation from ferrite: $\delta \rightarrow \delta + \gamma_2$
Tertiary (γ_3)	Eutectoid reaction: $\delta \rightarrow \sigma + \gamma_3$

Table 3.3. *Types of austenite formed in duplex stainless steels [POH 04, POH 07]*

3.5.5. *Alpha prime (α′) formation*

Embrittlement of the ferrite phase in stainless steels, both ferritic and duplex, caused by their exposure to temperatures around 475°C (885°F) has been discussed in the literature for more than half a century [BAN 42, FIS 53]. The main responsible factor for this embrittlement is the presence of the alpha prime (α‘) phase formed by spinodal decomposition in the 300 to 550°C temperature range [SOL 78, TAV 00, WEN 04]. Computer simulation supposing spinodal decomposition yields, for the Fe-Cr alloys, microstructures that are very similar to the experimental structures observed by the atom probe technique [DAN 04]. However, spinodal decomposition is not the only microstructural change responsible for 475°C embrittlement and the precipitation of the G phase, a silicide rich in nickel, molybdenum and manganese (see Table 3.2), is also frequently mentioned in the literature [DAN 04, BON 90, MAT 97].

The alpha prime (α‘) phase contains essentially chromium and iron, has a BCC structure and is coherent with ferrite. The alpha prime (α‘) precipitates are small, in the range of 20 to 200 Å, and have a high coarsening resistance, even for long exposure times. The two atoms (Fe and Cr) show very similar atomic sizes and present also similar X-ray and electron-scattering amplitudes, which along with the small precipitate size, hinders their direct observation even using transmission electron microscopy. Structural analysis by electron or X-ray diffraction presents similar difficulties. For the same reasons, it is also difficult to analyze them through chemical microanalysis techniques. Some special techniques, such a low-angle neutron scattering [ANG 89, ISA 90] and Mössbauer spectroscopy [SOL 78, KUW 92, KUW 06] are frequently employed in their study. The presence of the α‘ phase has an important effect on the mechanical and corrosion properties. Significant changes in electric properties, in the specific weight, and in the coercive force were also observed. These changes in physical properties can be removed by annealing at about 600°C (1,100°F) for 1 hour [FIS 53].

Hardness, yield stress, and tensile strength are increased, while elongation and impact resistance are decreased by the presence of alpha prime (α‘). In general, time-wise, the loss in toughness (embrittlement) is slower than the rate of hardening [PRA 01]. Ferrite without alpha prime (α‘), presents wavy glide lines due to the numerous gliding systems in the BCC structure and its high stacking fault energy enhancing dislocation cross-slip. The presence of alpha prime (α‘) changes this situation, it hinders the dislocation movement, restricting slip to a few crystal planes. This causes some straight slip lines, typical of FCC and low stacking fault energy alloys, such as in austenitic stainless steels or brasses. Some authors consider that alpha prime (α‘) containing ferrite predominantly deforms by twinning [ANG 89, ISA 90] and that the straight deformation lines mentioned above are, in reality,

deformation twins. Ferrite embrittlement due to the presence of alpha prime (α‘), in general, presents a cleavage type brittle fracture at room temperature.

Corrosion resistance is also affected by the presence of alpha prime (α‘). Bandel and Tofaute [BAN 42] observed that the presence of alpha prime (α‘) significantly reduced the corrosion resistance in a solution of boiling nitric acid. Pitting corrosion resistance, determined by cyclic polarization tests, in a solution of 3.5 wt% NaCl, is also significantly reduced by the presence of alpha prime (α‘) [TER 08].

The magnitude of the effects of alpha prime (α‘) on the material properties depends chiefly on the chromium content of the alloy and it increases with an increase in chromium content. According to Bonnet *et al.* [BON 90] the difference in aging response between molybdenum bearing and molybdenum-free duplex stainless steels are related to the G phase (see Table 3.2) precipitation favored in molybdenum-containing steels.

This type of embrittlement leads to a cleavage fracture in the ferritic regions (see micrograph of Figure 3.12). Ductility is determined by the austenitic regions and is characterized by a dimple-like fracture. Austenite volume fraction also plays an important role. Increasing the chromium content in the alloy (and thereby the ferrite volume fraction) raises the sensitivity of the material to this type of embrittlement. The extent of embrittlement increases with ageing time in the 350-550°C (660-1,020°F) temperature range, while a maximum embrittlement occurs at about 475°C (885°F).

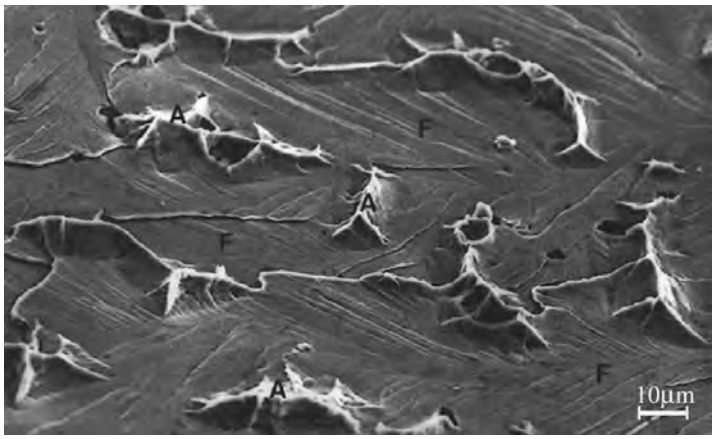

Figure 3.12. *Ferrite brittle cleavage fracture (475°C – embrittlement) caused by alpha prime (α‘) in a duplex stainless steel, using scanning electron microscopy with secondary electrons [REI 90]. A= austenite; F = ferrite*

3.6. Cold working and annealing

Duplex stainless steels are very interesting materials with respect to their plastic deformation and recrystallization, due to the different characteristics of the two more important phases within their microstructure. The bcc ferrite phase has numerous slip systems and a higher stacking fault energy (SFE), whereas the fcc austenite phase shows less slip systems than ferrite and very low stacking fault energy [REI 96]. Furthermore, during cold working there is a partial phase transformation of austenite into α‘ (bcc) martensite [REI 96, HE 99, FAR 04], as illustrated in the micrograph of Figure 3.13.

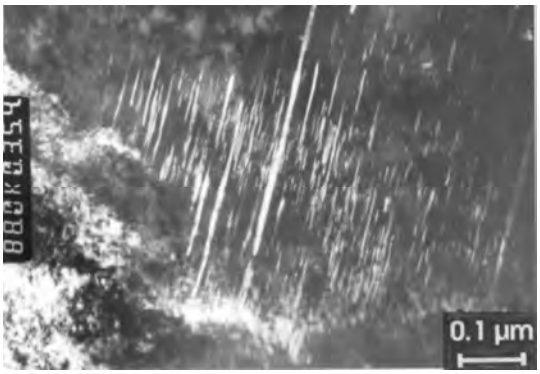

Figure 3.13. *Alpha prime (α‘) strain-induced martensite observed in the austenite phase of the duplex stainless steel W. Nr. 1.4462 (UNS S31803) after cold rolling 62% thickness reduction, observed by using transmission electron microscopy [REI 93]*

Figure 3.14 illustrates interesting aspects of plastic deformation of the duplex stainless steel UNS S31803. Figure 3.14a shows a comparison of nanohardness measurements performed on both phases as a function of sheet thickness reduction during rolling at room temperature. The strain-hardening rate of austenite is actually higher than that of ferrite. However, it is not as high as expected due to the very low SFE of austenite (about 10-20 mJ/m^2). A single-phase austenitic stainless steel with the same chemical composition as the austenite in a duplex stainless steel would certainly present a higher strain hardening. The reason for that behavior is the partition of plastic deformation occurring within both phases, during cold rolling. The strain hardening of austenite is very high at low deformations, but at about 15% thickness reduction it gets increasingly concentrated within the ferrite phase, which has a larger number of active slip systems and a considerably higher SFE [REI 96]. Figure 3.14b presents the evolution of the α‘ (bcc, ferromagnetic) martensite in austenite during cold rolling for the same steel. Strain-induced martensite occurs

mainly within the range of 20 to 50% thickness reduction, reaching saturation at higher reductions.

It should be pointed out that cathodic hydrogen charging can also lead to an α′ (bcc, ferromagnetic) martensite formation in the austenite of the duplex stainless steels [GLO 05].

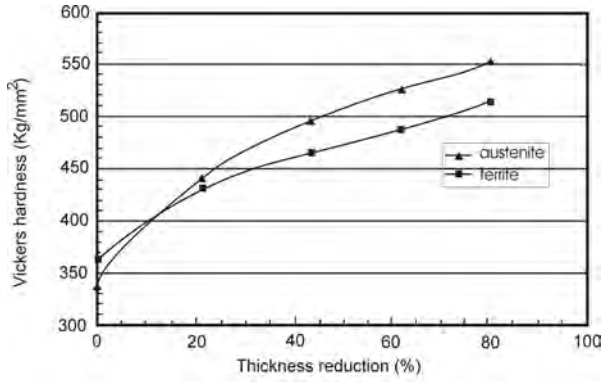

a)

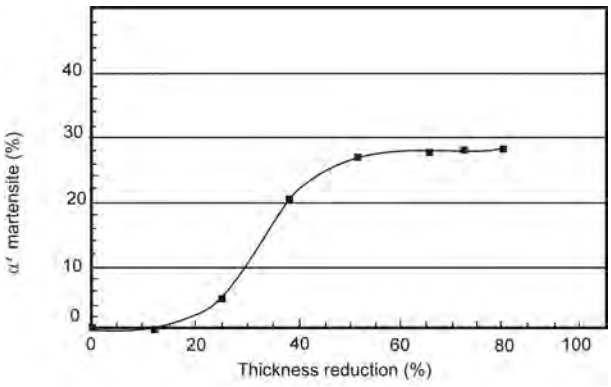

b)

Figure 3.14. *Cold rolling behavior of the duplex stainless steel UNS S31803 (W. Nr. 1.4462) as a function of thickness reduction: a) nanohardness (a load of 0.01 N was used) of ferrite and austenite during plastic deformation; b) strain-induced α‘ (bcc) martensite content in austenite during plastic deformation [REI 96]*

During annealing of cold-worked duplex stainless steels three main transformations can take place: martensite (strain-induced martensite) reversion to

austenite, recrystallization of ferrite and recrystallization of austenite [REI 98]. After a few minutes at 600°C, the martensite reversion to austenite is complete, that means, the martensite reversion takes place at least 150°C lower than the recrystallization of ferrite and, in any case, 250°C below the recrystallization of austenite. The strain hardening and the driving force for recrystallization of austenite are actually higher than those of ferrite. Moreover, considering that recrystallization is a thermally activated phenomenon, and that the diffusion is much faster in ferrite than in austenite, recrystallization kinetics in ferrite are faster than in austenite. Extensive recovery takes place in ferrite during annealing, while the deformation substructure of austenite remains nearly unrecovered until the beginning of recrystallization. Recrystallization in austenite occurs in a more discontinuous manner than in ferrite. The eutectoid transformation of ferrite to sigma phase plus austenite slows down recrystallization kinetics in both ferrite and austenite phases [REI 93, REI 98]. Figure 3.15 presents the kinetics of ferrite recrystallization, austenite recrystallization, and sigma phase formation in a TTT diagram for a duplex stainless steel.

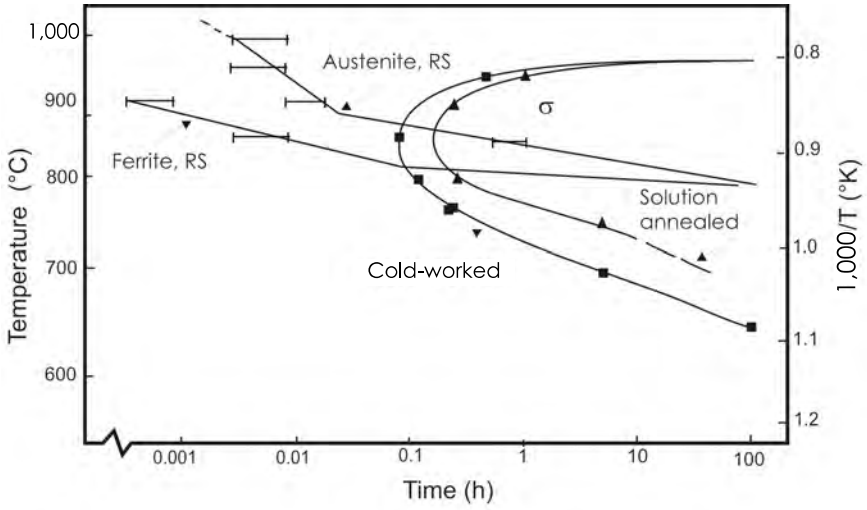

Figure 3.15. *Time-temperature-transformation diagram after solution annealing (curve A) and after 20% thickness reduction by cold rolling (all curves) for the duplex stainless steel UNS S31803 (W. Nr. 1.4462). RS = recrystallization start [REI 98]*

3.7. Final remarks

Duplex stainless steels present a very attractive combination of corrosion and mechanical properties; however, they are susceptible to several transformations between room temperature and the liquid state, limiting their use. As stated by Dr.

J.O. Nilson, quoted by Widmark [WID 93], some years ago "production and use of (duplex) stainless steels is similar to driving a car on a road in the Austrian Alps. It is safe if you are a good driver with experience." This chapter is intended to provide some background in order to avoid major problems during the heat treatment and usage of this very interesting class of steels.

3.8. References

[ALL 95] ALLAN G. K., "Solidification of austenitic stainless steels", *Ironmaking and Steelmaking*, vol. 22, no. 6, p. 465-477, 1995.

[ANG 89] ANGLADA M., RODRIGUEZ, J., ISALGUÉ A., "Influence of the plastic strain amplitude on the stability of the spinodal microstructure in the cyclic deformation of a Fe-28Cr-2Mo-4Ni-Nb alloy", *Scripta Metallurgica*, vol. 23, no. 9, p. 1633-1638, 1989.

[BAI 27] BAIN E. C., GRIFFITHS E., "Introduction to the iron-chromium-nickel alloys", *Trans. AIME*, vol. 75, p. 166-213, 1927.

[BAN 42] BANDEL G., TOFAUTE W., "Die Versprödung von hochlegierten Chromstählen im Temperaturgebiet um 500º", *Archiv für das Eisenhüttenwesen*, vol. 14, p. 307-319, 1942.

[BER 51] BERGMAN G., SHOEMAKER D. P., "The space group of the σ-FeCr crystal structure", *Journal of Chemical Physics*, vol. 19, no. 4, p. 515-515, 1951.

[BON 90] BONNET S., BOURGOIN J., CHAMPREDONDE J., GUTTMANN D., GUTTMANN M., "Relationship between evolution of mechanical properties of various cast duplex stainless steels and metallurgical and aging parameters: outline of current EDF programmes", *Materials Science and Technology*, vol. 6, no. 3, p. 221-229, 1990.

[CAL 05] CALLIARI I., MAGRINI M., RAMOUS E., "Measurements of secondary phases content in a 22Cr 5Ni duplex stainless steel", *Praktische Metallographie (Practical Metallography)*, vol. 42, no. 2, p. 75-88, 2005.

[CAL 06] CALLIARI I., ZANESCO M., RAMOUS E., "Measurements of secondary phases content in a 22Cr 5Ni duplex stainless steel", *Journal of Materials Science*, vol. 41, no. 22, p. 7647-7649, 2006.

[CAL 09] CALLIARI I., BRUNELLI K., DABALÀ M., RAMOUS E., "Measuring secondary phases in duplex stainless steels", *JOM*, vol. 11, no. 1, p. 80-83, 2009.

[COR 97] CORTIE M. B., JACKSON E. M., "Simulation of the precipitation of sigma phasein duplex stainless steels", *Metallurgical and Materials Transactions A*, vol. 28A, no. 12, p. 2477-2484, 1997.

[DAN 04] DANOIX F., AUGER P., BLAVETTE D., "Hardening of aged duplex stainless steels by spinodal decomposition", *Microscopy and Microanalysis (Microscopy Society of America)*, vol. 10, no. 3, p. 349-354, 2004.

[DAV 94] DAVIS J. R. (Editor), *ASM Speciality Handbook: Stainless Steels*, Ohio, ASM International, 1994.

[DEL 74] DeLONG W. T., "Ferrite in austenitic stainless steel weld metal", *Welding Journal*, vol. 53, no. 7, Research Supplement, 1974, p. 273s-286s.

[DES 93] DESESTRET A., CHARLES J., "The duplex stainless steels", in LACOMBE P., BAROUX B., BERANGER G., *Stainless steels*, Les Ulis, Les Editions de Physique, p. 612-658, 1993.

[DUP 00] DUPREZ L., De COOMAN, B. C., AKDUT N., "Microstructure evolution during isothermal annealing of a standard duplex stainless steel type 1.4462", *Steel Research*, vol. 71, no. 10, p. 417-422, 2000.

[DUP 01] DUPREZ L., De COOMAN B. C., AKDUT N., "Redistribution of the substitutional elements during σ and χ phase formation in a duplex stainless steel", *Steel Research*, vol. 72, no. 8, p. 311-316, 2001.

[FAR 04] FARGAS G., MANERO J. M., ANGLADA M., MATEO A., "Influencia de los tratamientos térmicos en la deformación en frío de los aceros inoxidables dúplex", *Revista de Metalurgia* (Madrid), vol. 40, no. 3, p. 219-223, 2004.

[FIS 53] FISCHER R. M., DULLIS E. J., CARROL K. G., "Identification of the precipitate accompanying 885°F embrittlement in chromium steels", *Transactions of The Metallurgical Society of AIME (Journal of Metals)*, vol. 197, no. 5, p. 690-695, 1953.

[GLO 05] GLOWACKA A., WOZNIAK M. J., SWIATNICKI W. A., "AFM study of austeno-ferritic stainless steel microstructure after cathodic hydrogen charging", *Journal of Alloys and Compounds*, vol. 404-406, no. 1, p. 595-598, 2005.

[HE 99] HE J., HAN G., FUKUYAMA S., YOKOGAWA K., "Tensile behaviour of duplex stainless steel at low temperatures", *Materials Science and Technology*, vol. 15, no. 8, p. 909-920, 1999.

[HER 08] HERRERA C., de LIMA N. B., KLIAUGA A. M., PADILHA A. F., "Microstructure and texture of duplex stainless steel after melt-spinning processing", *Materials Characterization*, vol. 59, no. 1, p. 79-83, 2008.

[HUG 59] HUGHES H., LLEWELYN D. T., "χ phase in the Fe-Cr-Ni-Ti system", *Journal of The Iron and Steel Institute*, vol. 192, p. 170, 1959.

[ISA 90] ISALGUÉ A., ANGLADA M., RODRIGUEZ-CARVAJAL, J., De GEYER A., "Study of the spinodal decomposition of an Fe-28Cr-2Mo-4Ni-Nb alloy by small-angle neutron scattering", *Journal of Materials Science*, vol. 25, no. 12, p. 4977-4980, 1990.

[JET 36] JETT E. R., FOOTE F., "The Fe-Cr alloy system", *Metals and Alloys*, vol. 7, no. 8, p. 207-210, 1936.

[KAS 54] KASPER J. S., "The ordering of atoms in the chi-phase of the iron-chromium-molybdenum system", *Acta Metallurgica*, vol. 2, no. 3, p. 456-461, 1954.

[KOB 99] KOBAYASHI D. Y., WOLYNEC S., "Evaluation of the low corrosion resistant phase formed during the sigma phase precipitation in duplex stainless steels", *Materials Research* (Brazil), vol. 2, no. 4, p. 239-247, 1999.

[KUW 92] KUWANO H., ISHIKAWA Y., YOSHIMURA T., HAMAGUCHI Y., "Characterization of the spinodal decomposition of Fe-Cr alloys by Mössbauer spectroscopy", *Hyperfine Interactions*, vol. 69, no. 1-4, p. 501-504, 1992.

[KUW 06] KUWANO H., IMAMASU H., "Determination of the chromium concentration of phase decomposition products in an aged duplex stainless steel", *Hyperfine Interactions*, vol. 168, no. 1-3, p. 1009-1015, 2006.

[LEE 99] LEE K. M., CHO H. S., CHOI D. C., "Effect of isothermal treatment of SAF 2205 duplex stainless steel on migration of δ/γ interface boundary and growth of austenite", *Journal of Alloys and Compounds*, vol. 285, no. 1-2, 156-161, 1999.

[LIA 01] LIAO J., "Nitride precipitation in weld HAZs of a duplex stainless steel", *ISIJ International* (Japan), vol. 41, no. 5, p. 460-467, 2001.

[MAC 00] MACHADO I. F., PADILHA A. F., "Aging behaviour of 25Cr-17Mn high nitrogen duplex stainless steel", *ISIJ International* (Japan), vol. 40, no. 7, p. 719-724, 2000.

[MAE 83] MAEHARA Y., OHMORI Y., MURAYAMA N., FUJINO N., KUNITAKE T. "Effects of alloying elements on σ phase precipitation in δ-γ duplex phase stainless steels", *Metal Science*, vol. 17, no. 11, p. 541-547, 1983.

[MAT 97] MATEO A., LLANES L., ANGLADA M., REDJAÏMIA A., METAUFER G., "Characterization of the intermetallic G-phase in an AISI 329 duplex stainless steel", *Journal of Materials Science*, vol. 32, no. 17, p. 4533-4540, 1997.

[MIC 06] MICHALSKA J., SOZANSKA M., "Qualitative and quantitative analysis of σ and χ phases in 2205 duplex stainless steel", *Materials Characterization*, vol. 56, no. 4-5, p. 355-362, 2006.

[NIL 93] NILSON J. O., WILSON A., "Influence of isothermal phase transformations on toughness and pitting corrosion of super duplex stainless steel SAF 2507", *Materials Science and Technology*, vol. 9, no. 7, p. 545-554, 1993.

[NOR 81] NORSTRÖM L.-Å., PETTERSSON S., NORDIN S., "σ-Phase embrittlement in some ferritic-austenitic stainless steels", *Materialwisseschaft und Werkstofftechnik*, vol. 12, no. 7, p. 229-234, 1981.

[OHM 95] OHMORI Y., NAKAI K., OHTSUBO H., ISSHIKI Y., "Mechanism of Widmanstätten austenite formation in a δ/γ duplex phase stainless steel", *ISIJ International* (Japan), vol. 35 no. 8, p. 969-975, 1995.

[OKA 78] OKAFOR I. C. I., CARLSON O. N., "Equilibrium studies on chi phase-strengthened ferritic alloy", *Metallurgical Transactions* A, vol. 9A, no. 11, p. 1651-1657, 1978.

[PAD 01] PADILHA A. F., PIMENTA Jr F. C., REICK W., "A comparative study on the precipitation of the sigma phase in a superferritic and in a duplex stainless steel", *Zeitschrift für Metallkunde*, vol. 92, no. 4, p. 351-354, 2001.

[PAD 07] PADILHA A. F., PLAUT R. L., RIOS P. R., "Stainless steel heat treatment", Chapter 12 in TOTTEN, G. E., *Steel Heat Treatment Handbook: Metallurgy and Technologies*, vol. 2, 2nd Edition, CRC Press, Boca Raton, p. 695-739, 2007.

[POH 04] POHL M., STORZ O., "Sigma-phase in duplex-stainless steels", *Zeitschrift für Metallkunde*, vol. 95, no. 7, p. 631-638, 2004.

[POH 07] POHL M., STORZ O., GLOGOWSKI T. "Effect of intermetallic precipitation on the properties of duplex stainless steel", *Materials Characterization*, vol. 58, no. 1, p. 65-71, 2007.

[PRA 01] *Practical Guidelines for the Fabrication of Duplex Stainless Steels*, International Molybdenum Association (IMOA), London, Revised Edition, 2001 (www.imoa.org.uk).

[RAM 03] RAMIREZ A. J., LIPPOLD J. C., BRANDI S. D., "The relationship between chromium nitride and secondary austenite precipitation in duplex stainless steels", *Metallurgical and Materials Transactions A*, vol. 34A, no. 8, p. 1575-1597, 2003.

[RED 04] REDJAÏMIA A., PROULT A., DONNADIEU P., MORNIROLI J. P., "Morphology, crystallography and defects of the intermetallic χ-phase precipitated in a duplex (δ+γ) stainless steel", *Journal of Materials Science*, vol. 39, no. 7, p. 2371-2386, 2004.

[REI 90] REICK W., POHL M., PADILHA A. F., 'Three types of embrittlement in ferritic-austenitic duplex stainless steels", *Metalurgia International* (Brazil), vol. 3, no. 8, p. 46-50, 1990.

[REI 93] REICK W.K., Kaltumformung und Rekristallisation eines rostbeständigen ferritisch-austenitischen Duplex-Stahles (in German), PhD Thesis, Ruhr-Universität Bochum, 1993.

[REI 96] REICK W., POHL M., PADILHA A. F., "Determination of stacking fault energy of austenite in a duplex stainless steel", *Steel Research*, vol. 67, no. 6, p. 253-256, 1996.

[REI 98] REICK W., POHL M., PADILHA A. F., "Recrystallization-Transformation combined reactions during annealing of a cold rolled ferritic-austenitic duplex stainless steel", *ISIJ International* (Japan), vol. 38, no. 6, p. 567-571, 1998.

[SCH 47] SCHAEFFLER A. L., "Selection of austenitic electrodes for welding dissimilar metals", *Welding Journal*, vol. 26, no. 10, Research Supplement, p. 603s-620s, 1947.

[SCH 48] SCHAEFFLER A. L., "Welding dissimilar metals with stainless electrodes", *Iron Age*, vol. 162, no. 7, p. 73-79, 1948.

[SCH 49] SCHAEFFLER A. L., "Constitution diagram for stainless steel", *Metal Progress*, vol. 56, no. 11, p. 680,680B, 1949.

[SOL 78] SOLOMON H. D., LEVINSON L. M. "Mössbauer effect study of 475ºC embrittlement of duplex and ferritic stainless steels", *Acta Metallurgica*, vol. 26, no. 3, p. 429-442, 1978.

[SOU 80] SOUTHWICK P. D., HONEYCOMBE R. W. K., "Decomposition of ferrite to austenite in 26%Cr-5%Ni stainless steel", *Metal Science Journal*, vol. 14, no. 7, p. 253-261, 1980.

[SOU 82] SOUTHWICK P. D., HONEYCOMBE, R. W. K., "Precipitation of M23C6 at austenite/ferrite interfaces in duplex stainless steel", *Metal Science Journal*, vol. 16, no. 10, p. 475-481, 1982.

[TAV 00] TAVARES S. S. M., da SILVA M. R., NETO J. M., "Magnetic property changes during embrittlement of a duplex stainless steel", *Journal of Alloys and Compounds*, vol. 313, no. 1-2, p. 168-173, 2000.

[TER 08] TERADA M., HUPALO M. F., COSTA I., PADILHA A. F., "Effect of alpha prime due to 475 ºC aging on fracture behavior and corrosion resistance of DIN 1.4575 and MA 956 high performance ferritic stainless steels", *Journal of Materials Science*, vol. 43, no. 2, p. 425-433, 2008.

[TRE 907] TREITSCHKE W., TAMMAN G., "Über die Legierungen des Eisens mit Chrom", *Zeitschrift für Anorganische Chemie*, vol. 55, p. 402-411, 1907.

[VIL 06] VILLANUEVA D. M. E., PIMENTA Jr F. C., PLAUT R. L., PADILHA, A. F. "Comparative study of sigma phase precipitation of three types of stainless steels: austenitic, superferritic and duplex", *Materials Science and Technology*, vol. 22, no. 7, p. 1098-1104, 2006.

[WEN 04] WENG K. L., CHEN H. R., YANG J. R., "The low-temperature aging embrittlement in a 2205 duplex stainless steel", *Materials Science Engineering A*, vol. 379, no. 1-2, p. 119-132, 2004.

[WID 93] WIDMARK H., "Thirty years of stainless steel development", *Scandinavian Journal of Metallurgy*, vol. 22, no. 3, p. 156-64, 1993.

[WIL 91] WILLIS C. F., GRONSKY R., DEVINE T. M., "Carbide precipitation in welds of two-phase austenitic-ferritic stainless steel", *Metallurgical Transactions*, vol. 22A, no. 12, p. 2889-2902, 1991.

Chapter 4

Welding Processes, Microstructural Evolution and Final Properties of Duplex and Superduplex Stainless Steels

4.1. Introduction

The study of weldability of duplex and superduplex stainless steels (DSS and SDSS, respectively) is a fundamental task for their proper industrial application. During welding, two main problems may arise, due to the evolution of microstructure during cooling: the achievement of a not well-balanced austenite-to-ferrite ratio and the precipitation, in the fusion zone (FZ) and heat-affected zone (HAZ), of secondary phases that generally decrease the corrosion resistance and the toughness of the alloy.

The FZ and HAZ microstructure could be very different from that of the base material as a function of both chemical composition and thermal history. In this chapter, the problems relating to the microstructural evolution of DSS and SDSS will be presented:

– by describing the kinetics of $\delta \rightarrow \gamma$ phase transformation;

Chapter written by Franco BONOLLO, Alberto TIZIANI and Paolo FERRO.

Duplex Stainless Steels Edited by Iris Alvarez-Armas and Suzanne Degallaix-Moreuil

– by analyzing the isothermal and anisothermal transformations leading to the formation of phases and precipitates, which are generally detrimental for the mechanical and corrosion properties;

– by examining, with some examples, the effect of the thermal history induced by the welding process on the austenite-to-ferrite ratio and on precipitation phenomena;

– by reviewing the welding solutions (in terms of materials choice, processes, and filler metals) that can lead to optimized microstructures in welding joints.

4.2. δ-ferrite → austenite transformation

The favorable combination of chemical and mechanical characteristics is directly related to the microstructure of DSS and SDSS, which, in turn, derives from their thermal history. Their excellent technological behavior is guaranteed, *in primis*, by an optimized microstructure, characterized by only two phases, austenite and ferrite, in a opportunely balanced ratio, as pointed out in the Introduction and Chapter 3.

By knowing the factors that can influence the ratio, the optimization of processes and parameters for the technological operations using DSS can be reached.

The microstructural evolution during cooling of such alloys can be explained by means of the Welding Research Council (WRC) diagram (Figure 4.1) where the effects of different alloying elements are summarized with the Cr_{eq}/Ni_{eq} parameter

$$Ni_{eq} = \%Ni + 35\cdot\%C + 20\cdot\%N + 0.5\cdot\%Mn + 0.25\cdot\%Cu \quad [4.1a]$$

$$Cr_{eq} = \%Cr + \%Mo + 1.5\cdot\%Si + 0.7\cdot\%Nb \quad [4.1b]$$

By using the diagram in Figure 4.1, where some of the most common DSS and SDSS are indicated, it can be observed how such steels, immediately after solidification, are characterized by a fully δ-ferrite microstructure.

During the subsequent cooling, below the δ-solvus temperature (which falls into the 1,300-1,200°C interval, varying with the chemical composition of the steel), the solid transformation δ-ferrite → austenite occurs, with the consequent achievement of the two-phase austenitic-ferritic microstructure (Figure 4.2).

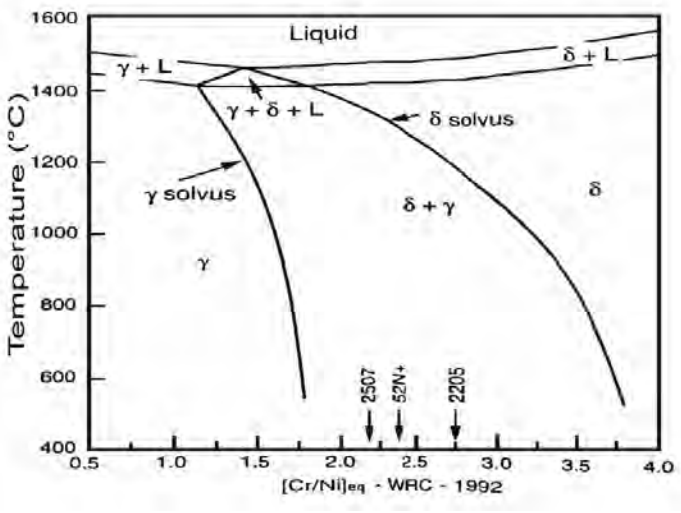

Figure 4.1. *WRC diagram relating to DSS and SDSS [NIL 92]*

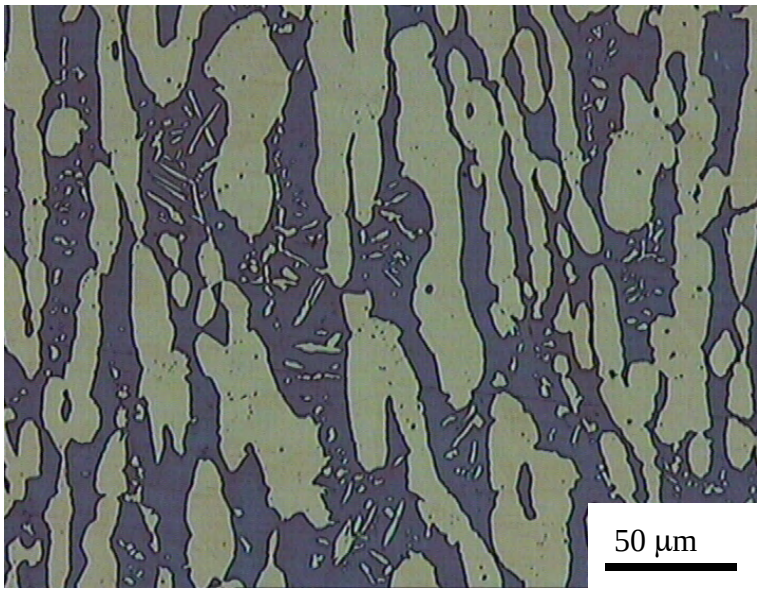

Figure 4.2. *Typical microstructure of a rolled UNS 32750 SDSS (clear phase: austenite; dark phase: ferrite)*

The kinetics of such a reaction has been widely studied in literature. By analyzing the isothermal transformations of a 26%Cr-5%Ni DSS, Southwick and Honeycombe [SOU 80] found that this reaction follows the Avrami equation [4.2]:

$$\frac{V_\gamma}{V_m(T)} = 1 - \exp[-b(T) \cdot t^{n(T)}], \qquad [4.2]$$

where

V_γ = austenite volume fraction at time t;

V_m = equilibrium austenite volume fraction;

T = temperature;

b,n = experimental parameters.

More recently, Atamert and King [ATA 92] have introduced the relation

$$V_\gamma = C1 + C2 \cdot (Cr_{eq} - Ni_{eq}) + C3 \cdot \Delta t_{1,250\text{-}800}, \qquad [4.3]$$

where, besides the symbols above defined,

$\Delta t_{1,250\text{-}800}$ = cooling time interval from 1,250 to 800°C,

C1, C2 and C3 = constants.

A substantially similar relation was proposed by Lindblom and Hannerz [LIN 91]:

$$V_\gamma = k_i (\Delta t_{12\text{-}8})^m, \qquad [4.4]$$

where, besides the symbols just defined, Δt12-8 is the time interval, during cooling, from 1,200 to 800°C and m and k_i are composition-dependent parameters.

In short, the amount of austenite that forms starting from δ-ferrite is inversely dependent on the cooling rate in the temperature interval between 1,200°C (solvus temperature) and 800°C (temperature below which the kinetics of transformation is very low so that the austenite-to-ferrite ratio does not change significantly – see Figure 4.1).

The ferrite and austenite phases have a different chemical composition at room temperature (RT). Austenite is more rich in γ-stabilizing elements (Ni, N, Mn, Cu, C), while ferrite is more rich in α-stabilizing elements (Cr, Mo, Si, Nb). For each element, the partition coefficient can be introduced, defined as the ratio between the amounts of that element in ferrite and austenite, respectively. For example, Table 4.1 collects the partition coefficients of Ni, Cr, and Mo measured on a SDSS SAF 2507 [BON 98].

It is important to point out that such partition coefficients are strictly cooling-rate dependent. The partition of the elements between ferrite and austenite is a diffusive phenomenon. Slow cooling allows an efficient partitioning of the elements between the two phases, on the basis of their thermodynamic characteristics. Rapid cooling, by inhibiting the diffusion, tends to make the austenite and ferrite composition homogenous, thus leading the partition coefficients to values very close to 1.

	Partition coefficient		
Material	Cr	Ni	Mo
SAF 2507	1.1	0.6	1.8

Table 4.1. *Partition coefficients in a SAF 2507 stainless steel [BON 98]*

4.3. Secondary and intermetallic phases precipitation during welding processes

In the temperature interval ranging from 1,000 to 300°C, different secondary and intermetallic phases may precipitate in DSS and SDSS, in an amount dependent both on thermodynamic and kinetic factors. References [KAR 99, NOW 06] offer a review of these precipitates, which are intermetallic compounds (σ, χ, R, π, τ), carbides, and nitrides (Cr_2N, M_7C_3, $M_{23}C_6$), and secondary austenite (γ_2). Furthermore, a spinodal decomposition of ferrite may take place in the 500-300°C interval.

Dedicated TTT and CCT diagrams are available for describing the time and temperature evolution of these precipitates, which may also occur when DSS and SDSS are cooled to RT after the welding process or are submitted to multipass welding operations. As an example, Figure 4.3 displays the CCT diagram for the SDSS, SAF 2507, showing the amount of sigma phase formed as a function of the cooling rate.

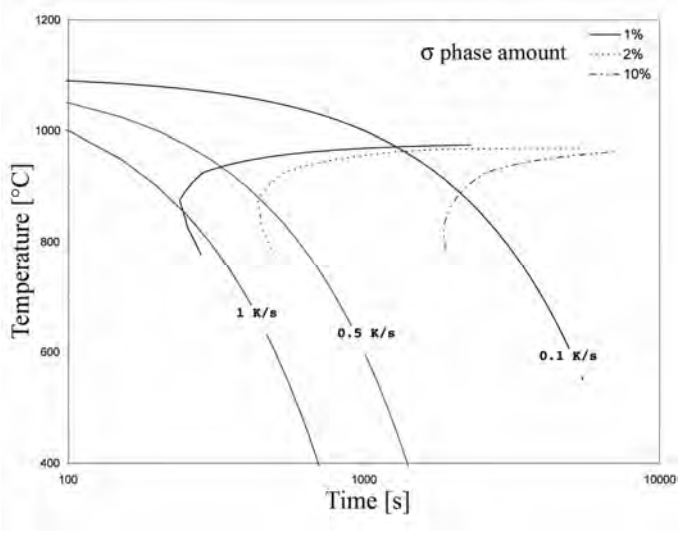

Figure 4.3. *CCT diagram relative to σ-phase precipitation for a SAF 2507 SDSS [BON 98]*

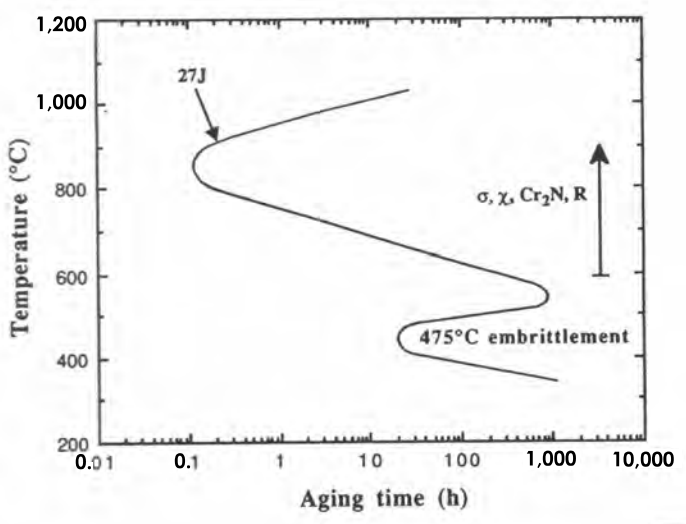

Figure 4.4. *Iso-toughness curve for SAF 2507 SDSS [NIL 92]*

As a general remark, the presence of these precipitates is detrimental for the toughness behavior of the steels, as shown in Figure 4.4. Furthermore, the elements

promoting the precipitation of intermetallic phases (Cr, W, Mo) usually improve pitting resistance: consequently, such a precipitation is usually associated with a decrease of the pitting resistance of the ferritic phase, which becomes more sensitive to corrosion phenomena.

Thus, a key issue, when welding DSS and SDSS, is that of avoiding (controlling the process parameters or by post-welding heat treatments) the presence of precipitates.

4.4. Welding processes for DSS and SDSS

The industrial use of DSS and SDSS is related to the realization of welding joints [LEF 99, AVE 02, BON 94a]. The main welding processes are generally applicable to such steels:

– gas tungsten arc welding, GTAW;

– gas metal arc welding, GMAW;

– shielded metal arc welding, SMAW;

– flux-cored arc welding, FCW;

– plasma arc welding, PAW;

– submerged arc welding, SAW;

– electron beam welding, EBW;

– laser welding, LW.

The microstructural evolution of the steel depends on the thermal fields induced during the process both in the FZ and in the HAZ. Such thermal fields depend, in turn, on the heating source used. It is thus appropriate to group the abovementioned welding processes into two main categories:

– conventional arc welding processes, characterized by a quite high, but distributed on a relatively large surface, thermal input (power used is about 1×10^2 W/cm^2),

– innovative high power density welding processes (PAW, LW, EBW), characterized by a very localized power (up to 1×10^6 W/cm^2 in the case of EBW and LW) and by the key-hole formation (Figure 4.5).

The first category of welding processes is characterized by cooling rates that are not particularly high and by poor directionality: multipass welding is needed if

plates with significant thickness have to be joined. Conversely, the high power density of the innovative processes enables the welding of high thicknesses (up to 10–12 mm) in a single run, but, very high cooling rates are induced in the workpiece [BON 94a, GRE 99]. The FZ and HAZ microstructural evolution is the result of such different boundary conditions, and is described separately for the two welding processes categories.

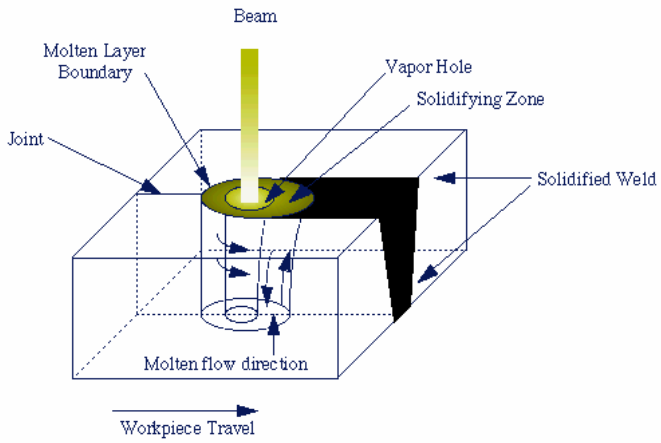

Figure 4.5. *Schematic representation of LW or EBW process with the key-hole formation*

4.4.1. *Conventional arc welding processes*

Conventional arc welding processes are widely used for industrial applications of DSS and SDSS. The main characteristics of the thermal fields induced by such technologies can be summarized as follows:

a) quite limited cooling rate, in the critical temperature range for the achievement of a balanced microstructure (1,200-800°C: typically, $\Delta t_{12\text{-}8}$ ranges from 1 to 30-40 seconds);

b) a relatively slow cooling rate (in FZ and HAZ) in the critical temperature intervals for the secondary phases precipitation;

b) a poor directionality (i.e. the energy distribution in the arc becomes wider and the distance from the electrode increases), which substantially reduces the welding thickness achievable by a single run.

Such characteristics (and their induced effects) depend on the steel typology considered (the chemical composition influences the thermal properties of the steel, as well as the kinetics of the ferrite $\delta \rightarrow$ austenite transformation) and on the thicknesses to be welded (according to which the process parameters are chosen). In general, the first aspect is positive as it allows the maintenance of a near optimum austenite-to-ferrite ratio on the bead and in the adjacent zone (thus minimizing the risk of localized corrosion). Moreover, the austenite-to-ferrite ratio in the bead can be further controlled by using suitable filler metals (Ni-enriched; Table 4.2) and/or nitrogen as a shielding gas when possible. The enrichment in nickel and nitrogen, promoted by the filler metal and shielding gas, respectively, favor austenite stabilization. The different partitions of the elements associated with the improvement of pitting corrosion resistance (Cr and Mo preferentially in ferrite, N in austenite) allows both phases to obtain particularly high and similar PREN values [AVE 02].

Steel to be welded	Product	AWS Designation	Typical chemical composition ($\%_{pond}$)				
			C	Cr	Ni	Mo	N
2304	Electrode	--	0.02	24.5	9.0	--	0.12
2304 and 2205	Electrode	E2209-17	0.02	23.0	9.5	3.0	0.15
		E2209-17	0.02	23.0	9.5	3.0	0.17
		E2209-15	0.02	23.0	9.5	3.0	0.16
	Wire	ER2209	0.02	23.0	8.5	3.1	0.17
	Flux cored wire	E2209T0-4	0.03	23.0	9.0	3.1	0.13
		E2209T0-4	0.03	23.5	9.5	3.4	0.14
		E2209T1-4	0.03	23.0	9.5	3.5	0.16
2507	Electrode	--	0.03	25.5	10.0	3.6	0.23
	Wire	--	0.02	25.0	9.5	4.0	0.25

Table 4.2. *Main types of filler metals used for the welding of DSS and SDSS [AVE 02]*

Conversely, the aspects mentioned in b) and c) can lead to some problems. In fact, the use of multipass welding and the relatively long permanence in the critical temperature range (950-700°C), can promote secondary phase precipitation, particularly in SDSS (because of their greater amount of alloy elements), which degrades corrosion resistance and/or mechanical properties [NIL 92, NIL 96]. For this reason, the following prescriptions/precautions should be adopted in arc welding of DSS and SDSS:

– avoiding any pre-heating treatment before welding;

– in the case of multipass welding, using an interpass temperature lower than 150°C.

When post-welding heat treatments have to be carried out (in general, they are not necessary if the filler metal is used), the cooling must to be suitably rapid in order to avoid intermetallic phase precipitation. Table 4.3 summarizes the recommended temperatures for post-weld heat treatments.

	Steel type		
	SAF 2304	SAF 2205	SAF 2507
Heat treatment temperature (°C)	950-1050	1020-1100	1040-1120

Table 4.3. *Post-welding heat treatment temperature relating to DSSs [AVE 02]*

4.4.2. *Innovative high power density processes*

In this kind of welding process, the first result of the high focusing degree of the heat input in a very small zone (typical diameters of the laser and electron beam used for welding are less than 1 mm) is the achievement of very deep weld beads, with depths (by single-pass welding) greater than 10 mm [BON 94a]. As an example, Figure 4.6 shows the results obtained in a melt run trial by means of electron beam and laser beam welding tests on the SDSS SAF 2507. The abovementioned focusing of the beam determines very high cooling rates (in the case of laser and electron beam welding, values in the range of some thousands of degree per second were estimated [BON 93a, ZAM 94]). The practical consequences of rapid cooling are various:

– the $\Delta t_{12\text{-}8}$ parameter is characterized by values much lower then 1 second: this means that the austenite formation is rather problematic. In DSS the amount of austenite in the final microstructure of the bead is about 15-20% [BON 93a]. The situation improves in SDSS due to the greater content of γ-stabilizing elements, whereby the amount of austenite achieved is 30-35% [BON 94a, BON 96];

– the high cooling rate tends to inhibit the diffusive phenomena: the partition of the elements between austenite and ferrite (according to their γ-stabilizing or α-stabilizing behavior, respectively) is less effective (Table 4.4) [GRE 96];

– a greater amount of ferrite, characterized by a more diluted chemical composition (in particular, with a Cr and Mo content less than the optimal value), is thus reached: such ferrite will result in being more sensitive to pitting and stress corrosion compared with austenite (Figure 4.7) [BON 95, BON 96].

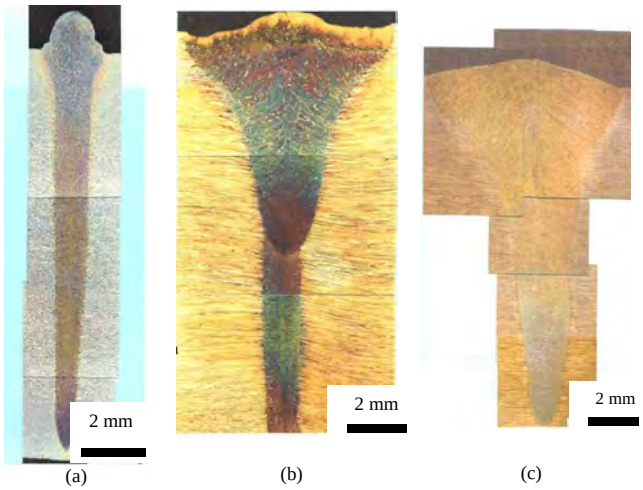

Figure 4.6. *Macrographs of the beads obtained by means of EBW a), EBW with "cosmetic" pass b), LBW c) on a 10 mm thick plate of SDSS [BON 94a]*

Material and process	Partition coefficient		
	Cr	Ni	Mo
SAF 2507 LW, 10 kW, 1.6 m/min	1.0	0.9	1.1

Table 4.4. *Partition coefficients in the weld bead of a laser-welded SAF 2507 steel [GRE 96]*

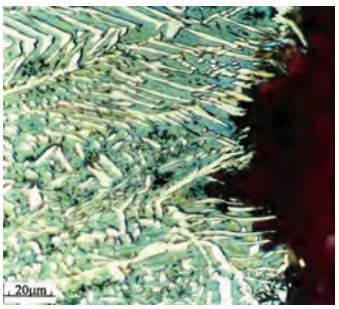

Figure 4.7. *Preferential corrosion of ferrite (green phase) relating to a SDSS SAF 2507 electron beam welded joint [BON 95]*

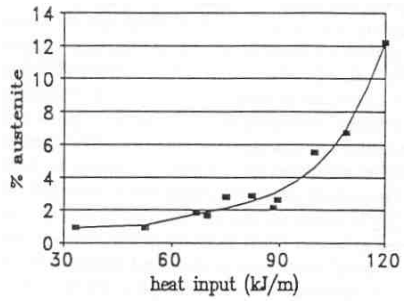

Figure 4.8. *Percentage of austenite versus heat input obtained in DSS UR45 laser welded joints [BON 93b]*

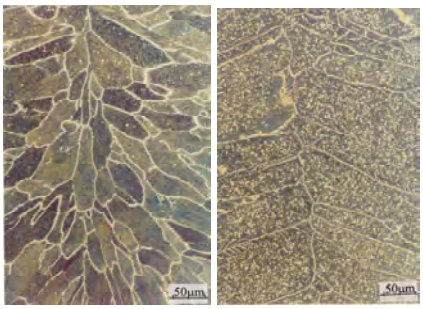

(a) (b)

Figure 4.9. *Typical microstructures of a laser-welded SDSS SAF 2507 steel as a function of the process parameters: a) 10 kW, 3 m/min; b) 8 kW, 1.4 m/min [BON 96]*

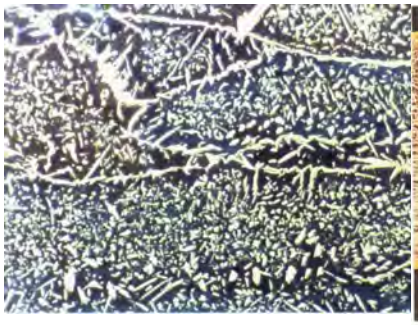

Figure 4.10. *Typical microstructure of the zone subjected to a cosmetic pass in electron beam-welded SDSS SAF 2507 [BON 94a]*

Figure 4.11. *Microstructure of a plasma-welded SDSS SAF 2507 (thickness: 3 mm) [BON 94a]*

In order to avoid such problems, microstructural evolution control can be achieved:

– by controlling and optimizing the process parameters with particular attention to the heat input (as described in Figure 4.8, which refers to the DSS UR 45 [BON 93a]); as an example, Figure 4.9 shows the microstructures obtained by laser welding a SAF 2507 SDSS and by varying the power and welding speed [BON 96],

– by using, where possible, cosmetic passes, which, in addition to optimizing the superficial geometry of the bead, can make the achievement of the austenite/ferrite balance (Figure 4.10) easier [BON 94a],

– by considering potentialities and limits of each welding technique: if thicknesses smaller than 5-6 mm have to be welded, a single-pass plasma welding can be used; the cooling, in the range between 1,200-800°C, is less rapid compared to that induced by laser or electron beam-welding, and thus a more balanced microstructure can be reached (Figures 4.11–4.12) [BON 94a],

– by using filler metals enriched with austenitizing-elements (see chemical composition reported in Table 4.2) and, when possible, nitrogen as a shielding gas [BON 93a, BON 94b],

– by carrying out (if the geometric characteristics of the joint are suitable) a solution post-weld heat treatment in order to restore the correct austenite-to-ferrite ratio in the bead [BON 93a].

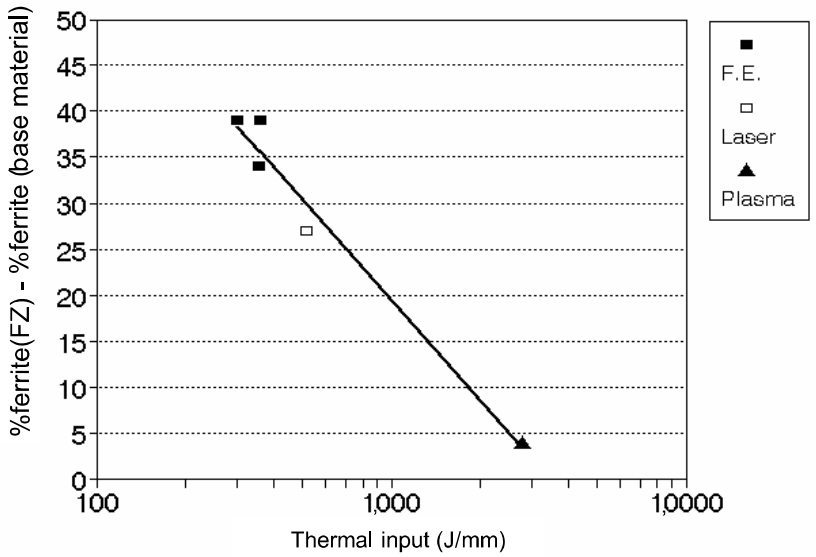

Figure 4.12. *Difference between the ferrite percentage in the bead and in the base material as a function of the adopted welding process [BON 94a]*

On the other side, the high cooling rate induced by high power density processes has further effects:

– a very narrow HAZ is produced (in the range of about 10 μm) as shown in Figures 4.6, 4.11 and 4.13 [BON 94b, GRE 00],

– the critical temperature interval for intermetallic phases precipitation (in particular σ and χ) is rapidly crossed during cooling, thus without detrimental consequences (Figure 4.14) [BON 98, GRE 96],

– in the presence of ferrite with an over-saturation of nitrogen (as a consequence of the rapid cooling), precipitation of chromium nitrides can occur, with detrimental effects on corrosion behavior; in Figure 4.15 such precipitation related to laser beam welding of a SAF 2507 is evident [BON 96].

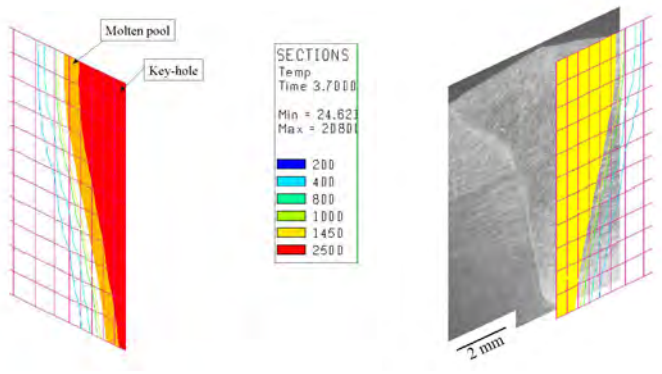

Figure 4.13. *Finite element model of a laser welding process. It can be noted how the 800°C isotherm curve is very close to the fusion one, as a confirmation of the small size of the HAZ [GRE 00]*

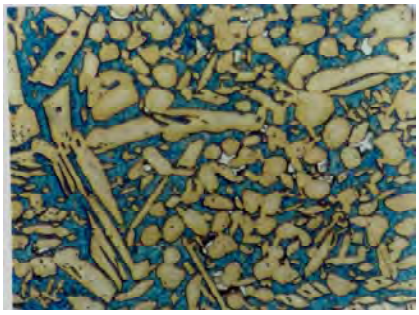

Figure 4.14. *Start of σ phase precipitation (white phase) in a SDSS SAF2507 laser-welded joint, maintained at 850 °C for 7 min [BON 98, GRE 96]*

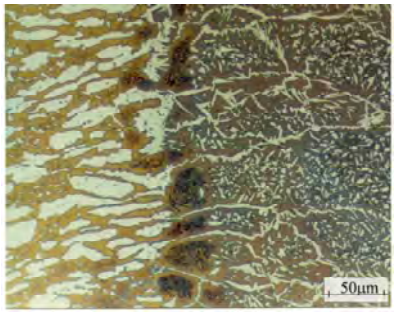

Figure 4.15. *Chromium nitrides precipitation in the HAZ of a SDSS SAF 2507 laser-welded joint [BON 96]*

4.5. Final remarks

Welding is a key process for the application of DSS and SDSS: to fully take advantage of the potential of these steels, significant attention must be paid to their welding-induced thermal history, which may lead to:

– the achievement of an unbalanced austenite-to-ferrite ratio;

– the precipitation of undesired phases (especially for multipass welding).

In the first case, the control of the heat input and the selection of filler wire (which should be enriched in austenite-stabilizer elements) is crucial, to obtain the correct amount of austenite and ferrite. In the second case, it is fundamental to achieve appropriately high cooling rates (to decrease the time interval in the critical temperature range).

Thus, the welding process should be optimized, so that the best possible compromise in terms of cooling rate is found: if the cooling rate is too high, an excess of ferrite is produced, whereas if it is too slow, embrittling phases can precipitate.

4.6. References

[AND 90] ANDERSSON J.-O., HÖGLUND L., JÖNSSON B., ÅGREN J., in G. R. PURDY, *Fundamentals and Applications of Ternary Diffusion*, Pergamon Press, New York, p. 153-163, 1990.

[ATA 92] ATAMERT S., KING J.E., “Super duplex stainless steels. Part 1. Heat affected zone microstructures”, *Mat. Sci. Tech.*, vol. 8, p. 896-911, 1992.

[AVE 02] Avesta Polarit Datasheet, “Duplex stainless steels”, AvestaPolarit AB, Avesta, Sweden, 2002.

[BON 93a] BONOLLO F., GIORDANO L., TIZIANI A., ZAMBON A., “Microstructural optimisation of laser beam welded duplex stainless steels”, *Proc. Conf. Innovation Stainless Steels*, Firenze, Associazione Italiana di Metallurgia, Milan, p. 3.251-3.258, 1993.

[BON 93b] BONOLLO F., TIZIANI A., ZAMBON A., CRISTOFOLINI I., PENASA M., “Effect of laser welding parameters on the microstructure of duplex stainless steels”, *Proc. 9th Int Duplex Stainless Steels ‘94 Symp. Gas Flow and Chemical Lasers*, Creta,; SPIE v.1810, Washington, p. 636-639, 1993.

[BON 94a] BONOLLO F., TIZIANI A., PENASA M., “An experimental approach to CO2 laser welding of duplex stainless steels (UNS S 31803)”, *Proc. Conf. Eurojoin 2*, Firenze, Istituto Italiano della Saldatura, Genoa, p. 667-676, 1994.

[BON 94b] BONOLLO F., TIZIANI A., ZAMBON A., PENASA M., "Laser beam welding of superduplex stainless steels", *Proc. Conf. Duplex Stainless Steels '94*, Glasgow (1994), paper n. 108; The Welding Institute, Abington, 1994.

[BON 95] BONOLLO F., BRUNORO G., TIZIANI A., ZUCCHI F., "Studio del comportamento a corrosione sotto tensione di acciai inossidabili superduplex saldati mediante laser", *Rivista Italiana della Saldatura*, Istituto Italiano della Saldatura, Genova, vol. 3, p. 273-276, 1995,

[BON 96] BONOLLO F., BRUNORO G., TIZIANI A., ZUCCHI F., "Comportamento a corrosione sotto tensione di acciai inossidabili superduplex saldati mediante plasma e fascio elettronico", *Rivista Italiana della Saldatura*, Istituto Italiano della Saldatura, Genova vol. 2, p. 125-132, 1996.

[BON 96] BONOLLO F., GREGORI A., TIZIANI A., "Saldatura di acciai superduplex mediante processi non convenzionali: confronto tra Laser, Fascio Elettronico e Plasma", *Proc. 1° Conferenza Nazionale sulla Saldatura e le Costruzioni Saldate*, Genoa, June 29 - July 3, Istituto Italiano della Saldatura, Genova, p. 49-64, 1996.

[BON 98] BONOLLO F., GREGORI A., TIZIANI A., NILSSON J.-O., "A study on microstructural evolution of superduplex steels (SAF 2507) induced by isothermal heat treatment", *Proc. 11th Congress of The International Federation for Heat Treatment and Surface Engineering*, Firenze, October 19-21, Associazione Italiana di Metallurgia, Milan, vol. 3, p. 291-300, 1998.

[BOW 72] BOWMAN A.L., ARNOLD G.P., STORMS E.K., NERESON N.G., "The crystal structure of Cr23C6", *Acta Crystall. B*, vol. 28, p. 3102-3103, 1972.

[CAH 68] CAHN J.W., "Spinodal decomposition", *Trans AIME*, vol. 242, p. 166-180, 1968.

[CHA 91] CHARLES J., "Super duplex stainless steels – structure and properties", *Proc. Conf. Duplex Stainless Steels '91*, Les Editions de Physique, Les Ulis Cedex, p. 3-48, 1991.

[COL 68] COLOMBIER L., HOCHMANN J., *Stainless and Heat Resisting Steels*, St. Martin's Press, New York, 1968.

[ERI 34] ERIKSSON S., "Röntgenundersökningar över systemet järn-krom-kväve", *Jernkontorets Ann.*, vol. 118, p. 530-542, 1934.

[EVA 57] EVANS D.A., JACK K.H., "Interstitial alloys with the structure of β-manganese", *Acta Crystall.*, vol. 10, p. 769-770, 1957.

[GRE 96] GREGORI A., Saldatura laser, E.B., plasma di acciai inossidabili superduplex: microstrutture e proprietà, Degree Thesis, University of Padua, 1996.

[GRE 99] GREGORI A., NILSSON J.-O., BONOLLO F., "Quantitative assessment of intermetallic phase precipitation in a super duplex stainless steel weld metal using automatic image analysis", *Materials Science Forum*, Trans. Tech. Publications, Svizzera vol. 318-320, p. 829-834, 1999.

[GRE 00] GREGORI A., BONOLLO F., GIORDANO L., TIZIANI A., "Optimisation of high energy welding processes for SDSS employing Finite Element simulation", *Proc. Conf. 6th World Duplex Stainless Steel Conference*, Venezia, October 19-21, Associazione Italiana di Metallurgia, Milan, p. 549-559, 2000

[HAL 66] HALL E.O., ALGIE S.H., "The sigma phase", *Metall. Rev*., vol. 11, p. 61-88, 1966.

[HER 86] HERTZMAN S., ROBERTS W., LINDENMO M., "Microstructure and properties of nitrogen alloyed duplex stainless steel after welding treatments", *Proc. Conf. Duplex Stainless Steels '86*, p. 257-267, 1986.

[HER 89] HERTZMAN S., *Influence of Spinodal Decomposition on Impact Strength of SS 2377 Duplex Stainless Steel Weldments*, Internal report, Swedish Institute for Metals Research, Stockholm, 1989.

[HIL 61] HILLERT M., "A solid solution model for inhomogeneous systems", *Acta Metall.*, vol. 9, p. 525-535, 1961.

[JOS 91] JOSEFSSON B., NILSSON J.-O., WILSON A., "Phase transformations in DSS and the relation between continuous cooling and isothermal heat treatment", *Proc. Conf. Duplex Stainless Steels '91*, Les Editions de Physique, Les Ulis, p. 67-78, 1991.

[KAR 99] KARLSSON L., "Intermetallic phase precipitation in duplex stainless steels and weld metals: metallurgy, influence on properties, welding and testing aspects", *Weld. Res. Conc. Bull.*, vol. 438, p. 1-23, 1999.

[KAS 54] KASPER J.S., "The ordering of atoms in the chi-phase of the iron-chromium-molybdenum system", *Acta Metall*., vol. 2, p. 456-461, 1954.

[LEF] LEFFLER B., "Stainless steels and their properties", AvestaPolarit AB, Avesta, Sweden.

[LIN 91] LINDBLOM B.E.S., HANNERZ N., "Austentite reformation in HAZ of ferritic austenitic stainless steels", *Proc. 3rd World Conf. Duplex Stainless Steels '91*, Beaune, Les Editions de Physique, Les Ulis, p. 951, 1991.

[MAE 83a] MAEHARA Y., FUJINO N., KUNITAKE T., "Effects of plastic deformation and thermal history on σ-phase precipitation in duplex phase stainless steels", *Trans. ISIJ*, vol. 23, p. 247-255, 1983.

[MAE 83b] MAEHARA Y., OHMORI Y., KUNITAKE T., "Effect of σ-phase precipitation on hot ductility in δ-ferrite-austenite duplex stainless steels", *Metals Technol*., vol. 10, p. 296-303, 1983.

[MAE 83c] MAEHARA Y., OHMORI Y., MURAYAMA J., FUJINO N., KUNITAKE T., "Effects of alloying elements on σ-phase precipitation in δ-γ duplex phase stainless steel", *Metal Sci*., vol. 17, p. 541-547**,** 1983.

[NIL 91] NILSSON J.-O., LIU P., "Aging at 400-600°C of submerged arc welds of 22Cr-3Mo-8Ni duplex stainless steel and its effect on toughness and microstructure", *Mater. Sci. Techn*., vol. 7, p. 853-862, 1991.

[NIL 92] NILSSON J.-O., "Overview – super duplex stainless steels", *Mater. Sci. Techn*., vol. 8, p. 685-700, 1992.

[NIL 95] NILSSON J.-O., KARLSSON L., ANDERSSON J.-O., "Secondary austenite formation and its relation to pitting corrosion in duplex stainless steel weld metal", *Mater. Sci. Eng*., vol. 11, p. 276-283, 1995.

[NIL 96a] NILSSON J.-O., "The physical metallurgy of duplex stainless steels", *Proc. Conf. Duplex Stainless Steels '96*, 1996.

[NIL 96b] NILSSON J.-O., HUHTALA T., JONSSON P., KARLSSON L., WILSON A., "Structural stability of super duplex stainless weld metals and its dependence on tungsten and copper", *Metall. Mater. Trans. A*, vol. 26A, p. 1-13, 1996.

[NOR 86] NORBERG P., "Applicability of duplex stainless steels above 300°C", *Proc. Conf. Duplex Stainless Steels '86*, p. 298-302, 1986.

[NOW 06] NOWACKI J., LUKOJC A., "Microstructural transformation of heat affected zone in duplex steel welded joint", *Materials Characterization*, vol. 56, p. 436-441, 2006.

[OKA 92] OKAMOTO H., "The effect of tungsten and molybdenum on the performance of super duplex stainless steels", *Proc. Conf. Application of Stainless Steels '92*, vol. 1, p. 360-369, 1992,.

[PUG 50] PUGH J.W., NISBETH J.D., "A study of the iron-chromium-nickel ternary system", *Trans. AIME*, vol. 188, p. 268-276, 1950.

[RED 91] REDJAÏMIA A., METAUER G., GANTOIS M., "Decomposition of delta ferrite in a Fe-22Cr-5Ni-3Mo-0.03C duplex stainless steel-a morphological study", *Proc. Conf. Duplex Stainless Steels '91*, Les Editions de Physique, Les Ulis, vol. 1, p. 119- 126, 1991.

[RID 51] RIDEOUT S., MANLEY W.D., KAMEN E.L., LEMENT B.S., BECK P.A., "Intermediate phases in ternary alloy systems of transition elements", *Trans AIME*, vol. 191, p. 872-876, 1951.

[ROU 70] ROUAULT A., HERPIN P., FRUCHART R., "Études cristallographique des carbures Cr7C3 et Mn7C3", *Ann. Chim*., vol. 5, p. 461-470, 1970.

[SOL 79a] SOLOMON H. D., DEVINE T. M., “Influence of microstructure on the mechanical properties and localized corrosion of duplex Uranus 50, ASTM STP”, in ABRAMS *et al.* (Eds.), *MiCon 78: Optimization of Processing, Properties and Service Performance Through Microstructure Control*, ASTM STP 672, p. 430-461, 1979.

[SOL 79b] SOLOMON H.D., KOCH E., “High temperature precipitation of α’ in a multicomponent duplex stainless steel”, *Scripta Metall*., vol. 13, p. 971, 1979

[SOL 84] SOLOMON H.D., DEVINE T.M., “Duplex stainless steels – a tale of two phases”, *Proc. Conf. Duplex Stainless Steels*, ASM, Materials Park, OH, p. 693-756, 1984.

[SOU 80] SOUTHWICK P.D., HONEYCOMBE R.W.K., “Decomposition of ferrite to austenite in 26%-5%Ni stainless steel”, *Met. Sci*., vol. 14, p. 253-261, 1980

[SUN 85] SUNDMAN B., JANSSON B., ANDERSSON J.-O., “The Thermo-Calc Databank System”, *Calphad*, vol. 9, p. 153-190, 1985.

[WIL 96] WILSON A., NILSSON J.-O., “Modeling the CCT-diagram of intermetallic phase formation in DSS from isothermal experiments”, *Scand. J. Metall*., vol. 25, p. 178-185, 1996.

[ZAM 94] ZAMBON A., BONOLLO F., “Rapid solidification in laser welding of stainless steels”, *Materials Science and Engineering*, vol. A178, p. 203-207, 1994.

Chapter 5

Thermal Embrittlement of Cast Duplex Stainless Steels: Observations and Modeling

5.1. Introduction

Stainless steels are iron-based alloys containing more than 12 wt% chromium. The stainless character of these alloys is due to the formation at their surface of a protective, enriched chromium layer. In aqueous environments these materials must contain higher chromium additions (30%). Moreover, the addition of other elements, such as nickel, molybdenum, silicon or nitrogen can improve the corrosion resistance of these steels [BER 91].

Austenitic, ferritic and martensitic steels have been known since the beginning of the 20th century [CAS 90]. Duplex stainless steels (DSS) containing both austenite and ferrite phases were discovered in the 1930s. These materials combine both excellent corrosion resistance and good mechanical properties.

The introduction in the mid 1970s of new steel-making processes, such as AOD (argon oxygen decarburizing) or VOD (vacuum oxygen decarburizing) and their continuing development have allowed a better control of residual elements, such as carbon (<0.03%), oxygen and sulfur (<0.01%), and a closer control of chemical composition, in particular, nitrogen. It is shown later that this control of chemistry allows the adjustment of the relative amounts of ferrite and austenite in DSS. There is now a wide variety of DSS used in the as-cast condition, which is the subject of this

Chapter written by André PINEAU and Jacques BESSON

Duplex Stainless Steels Edited by Iris Alvarez-Armas and Suzanne Degallaix-Moreuil

chapter. The most widely used compositions of cast stainless steels are reported in Table 5.1.

Material	Cr	Ni	Mo	Mn (max)	C (max)	Si (max)
CF3	17.0–21.0	8.0–12.0	—	1.50	0.03	2.00
CF8	18.0–21.0	8.0–11.0	—	1.50	0.08	2.00
CF20	18.0–21.0	8.0–11.0	—	1.50	0.20	2.00
CF30	26.0–30.0	8.0–11.0	—	1.50	0.30	2.00
CF3M	17.0–21.0	9.0–13.0	2.0-3.0	1.50	0.03	1.50
CF8M	18.0–21.0	9.0–12.0	2.0-3.0	1.50	0.08	2.00

Table 5.1. *ASME specifications for cast duplex stainless steels (compositions in weight percent)*

DSS can be strongly embrittled when they are aged over the temperature range between 300 and 500°C. This embrittlement effect is mainly associated with the α/α' demixtion of the solid solution of the ferrite phase (see Chapter 3). This effect is, therefore, directly dependent on the amount of ferrite, as illustrated in Figure 5.1 [CHU 92] and on the solidification microstructure, as shown in Figure 5.2 [MEY 88].

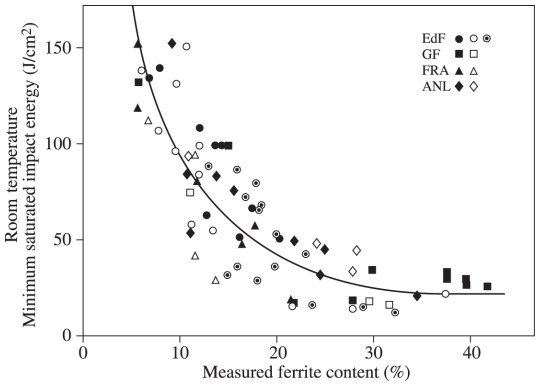

Figure 5.1. *Charpy U notch impact fracture toughness at 20°C as a function of ferrite content, in various cast duplex stainless steels, from Chung [CHU 92]*

In the literature many studies have been devoted to cast stainless steels and in particular DSS (see e.g. [DES 90, CHA 91, CHA 94]). The first aim of this chapter is to provide general information related to the development of these materials. The second aim is to review the mechanisms of embrittlement of these materials when

they are aged over the temperature range between 300 and 500°C. The third aim is to illustrate the variations in the mechanical properties of these steels after thermal aging. Various materials of CF8M type (see Table 5.1) containing different amounts of ferrite are presented for this purpose. The fourth aim of this chapter is to identify the mechanisms responsible for this embrittlement effect due to thermal aging. Finally, it is shown how the scatter in test results and the size effect observed in fracture toughness measurements can be modeled.

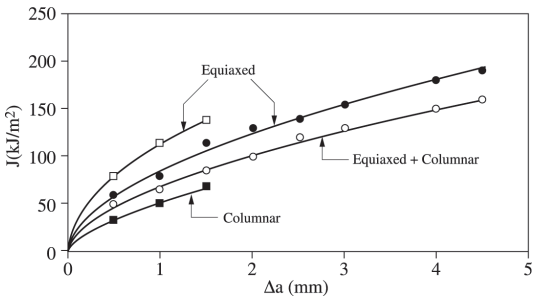

Figure 5.2. *Influence of solidification microstructure on $J/\Delta a$ curves for a CF8M steel (Heat Y3296) aged 1,000 hours at 400°C and tested at 320°C, from Meyzaud et al. [MEY 88]*

5.2. Composition, elaboration, microstructure, and mechanical properties

5.2.1. *Influence of chemical composition*

Cast DSS can be described as aggregates of ferritic grains with a BCC structure of a lattice parameter close to 0.286 nm and austenitic grains with a FCC structure with a lattice parameter between 0.358 nm and 0.362 nm, depending on the chemical composition. The relative percentage of ferrite (phase) depends on the chemical composition and the solution heat-treatment applied to the cast material. The Fe-Ni-Cr ternary phase diagrams shown in Figure 5.3 illustrate the importance of the addition of nickel and chromium on the microstructure of these materials [RIV 80, HAY 90]. The alloying elements are classified into two families (see e.g. [GUI 67, BAV 90]):

(i) the γ formers: Ni, C, N, Mn, Co, Cu,

(ii) the α formers: Cr, Mo, Si, Nb, Ti, Al, W, V, Ta.

Schaeffler [SCH 49] introduced the concept of Cr and Ni equivalents. This author has proposed a diagram that can be used to predict the formation of ferrite and austenite

as a function of material chemical composition. This diagram has been modified by Delong [DEL 60] and other authors. The diagram proposed by Zingg and Geiger [ZIN 57] is shown in Figure 5.4.

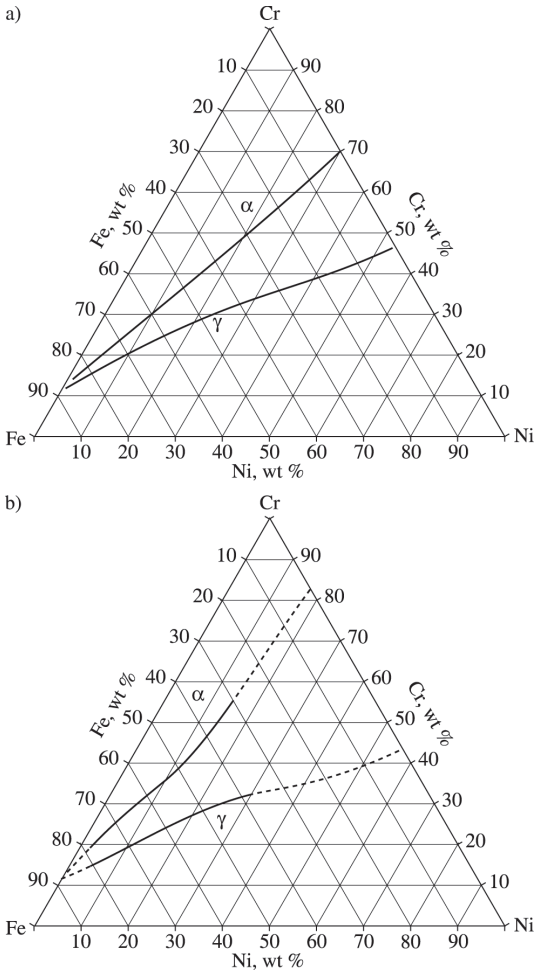

Figure 5.3. *Isothermal sections of the Fe-Ni-Cr ternary system at 1,200°C (a) and 1,100°C (b). Sections obtained from thermodynamical calculations showing the separation between the dual phase α/γ domain and the single-phase (α and γ) domains, from Hayes et al. [HAY 90]*

Many empirical expressions have been proposed, based on the concept of equivalent Cr and Ni. The expression introduced by Leger *et al.* [LEG 88] states:

$$Cr_{eq} = Cr + 1.21Mo + 0.48Si + 0.14Nb - 4.99$$

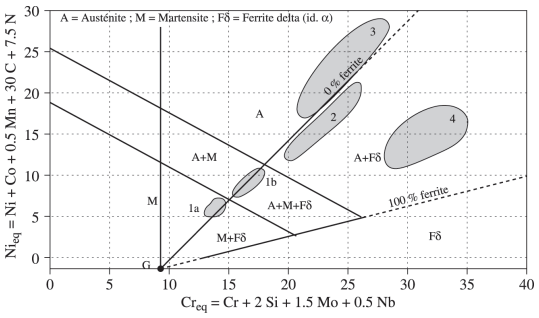

Figure 5.4. *Structural diagram for cast stainless steels (wt%), from Leger [LEG 93], after Zingg and Geiger [ZIN 57]*

$$\begin{aligned} Ni_{eq} &= Ni + 24.5C + 0.11Mn - 0.0086Mn^2 + 2.77 \\ \delta(\%) &= 95.49\left(Cr_{eq}/Ni_{eq}\right)^3 - 225.96\left(Cr_{eq}/Ni_{eq}\right)^2 \\ &\quad -191.35\left(Cr_{eq}/Ni_{eq}\right) - 58.27 \end{aligned} \qquad [5.1]$$

where $\delta(\%)$ is the ferrite/austenite ratio.

More recently, using thermodynamical calculations, Raghavan and Antia [RAG 94] have calculated the equivalence coefficients relative to chromium for several former elements. Their results show that the values that have to be adopted for the equivalence depend on the solution temperature and on the nickel content present in the material. The alloying elements tend to partition into the ferrite or the austenite phase, depending on their α (or γ) former character. The usual values found for this partition coefficient are shown in Figure 5.5, which applies to cast CF8M-type DSS [JOL 92a, SAN 96, MAR 96a].

5.2.2. *Solidification of DSS*

The morphology of the ferrite phase in DSS depends on the solidification path and of the ferrite→austenite phase transformation, which takes place in the solid state. Various solidification sequences have been reviewed by Suutala *et al.* [SUU 79] (see also Brooks and Thompson [BRO 91]).

One way of representing the complexities of solidification in a simplified way is through plots of Cr_{eq} versus Ni_{eq}, as illustrated in Figure 5.6 [SUU 79, SUU 83]). Suutala *et al.* collected numerous data in Figure 5.6 where the arrowed line separating predominantly austenitic to predominantly ferritic solidification has a slope of 0.67 ($Cr_{eq}/Ni_{eq}1.50$). That this distinction can be made on the basis of a constant Cr_{eq}/Ni_{eq}

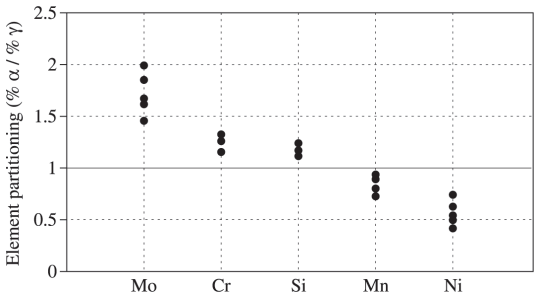

Figure 5.5. *Typical values for the partition coefficient of various elements between ferrite and austenite phases in DSSs of CF8M type (from results of Joly [JOL 92a], Sanchez [SAN 96] and Marquis and Cossard [MAR 96a])*

ratio is understandable from the ternary liquidus, which in the region of most data of Figure 5.6 has its axis very nearly along a line of constant Cr/Ni ratio, in fact very nearly at the ratio 3Cr/2Ni. (For a description of the ternary Fe-Ni-Cr diagrams, see Chapter 3.)

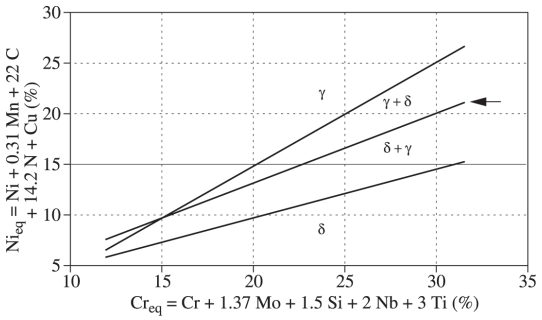

Figure 5.6. *Graph summarizing the solidification modes of stainless steels as a function of their composition (wt%), from Brooks and Thompson [BRO 91]*

It can be seen from Figure 5.6 that many stainless steels containing 60-70% Fe have compositions that lie close to the eutectic through (liquid→austenite+ferrite), and often have allowable composition ranges that span the eutectic reaction. Simple rules can be given for the solidification sequence of these stainless steels with the definition of Cr_{eq} and Ni_{eq} adopted by Suutala [SUU 83] (see Figure 5.6):

$$\begin{aligned} Cr_{eq} &= Cr + 1.37Mo + 1.5Si + 2Nb + 3Ti \\ Ni_{eq} &= = Ni + 22C + 0.31Mn + 14.2N + Cu. \end{aligned} \qquad [5.2]$$

(i) $\left(Cr_{eq}/Ni_{eq}\right) < 0.9$: Liquid $\rightarrow$ Liquid $+ \gamma \rightarrow \gamma$

(ii) $0.9 < \left(Cr_{eq}/Ni_{eq}\right) < 1.5$: Liquid $\rightarrow$ Liquid $+ \gamma \rightarrow$ Liquid $+ \gamma + \delta \rightarrow \gamma + \delta$

(iii) $1.5 < \left(Cr_{eq}/Ni_{eq}\right) < 1.95$: Liquid $\rightarrow$ Liquid + $\delta \rightarrow$ Liquid $+ \delta + \gamma \rightarrow \delta + \gamma$

(iv) $\left(Cr_{eq}/Ni_{eq}\right) > 1.95$: Liquid $\rightarrow$ Liquid $+ \delta \rightarrow \delta + \gamma$

It should be added that CF8M steels, which are the only materials examined in this chapter, have a composition corresponding to case (iv). The dual-phase microstructure of these materials results from the partial $\delta \rightarrow \gamma$ phase transformation occurring in solid phase, either during cooling or after annealing heat treatment.

5.2.3. *Microstructure of cast CF8M DSS*

DSS are used for the fabrication of large components (pipes, elbows) of the primary loop of the cooling system in pressurized water reactors (PWR). These components are produced by casting. The processing route together with the chemical composition of these materials leads to specific microstructures.

Solidification produces large ferrite grains (δ) about 10 mm in size. These grains have a basaltic shape when the solidification occurs along specific orientations, such as in centrifugally cast pipes where $\langle 100 \rangle_\delta$ is oriented parallel to the radial direction of the tubes. Otherwise in the absence of a preferential cooling direction or in the center of thick parts, the δ grains adopt random orientations. As cooling proceeds, austenitic grains (γ, size $\approx$1 mm) are formed in the ferrite according to the Kurdjumov-Sachs relations: $\{111\}_\gamma // \{110\}_\delta$ and $\langle 110 \rangle_\gamma // \langle 111 \rangle_\delta$ [BRO 91]. These grains are defined as areas where the austenite phase keeps the same crystallographic orientation. However some primary δ ferrite remains untransformed, as shown Figure 5.7 and as schematically described in Figure 5.7d. This results in an interconnected percolated network of both phases, which form laths whose spacing is typically 10 μm. These materials are consequently characterized by different length scales:

– 10 μm: the material consists of two percolated networks of austenite and ferrite. Both phases are single crystals. The material may also contain some shrinkage cavities,

– 1 mm: at this scale, the material consists of austenitic grains containing ferritic laths,

– 1 cm: at this scale, the material consists of an aggregate of composite austenitic grains.

The amount of ferrite controls the mechanical properties of these materials. Several techniques, including X-ray diffraction and magnetic measurements, are used

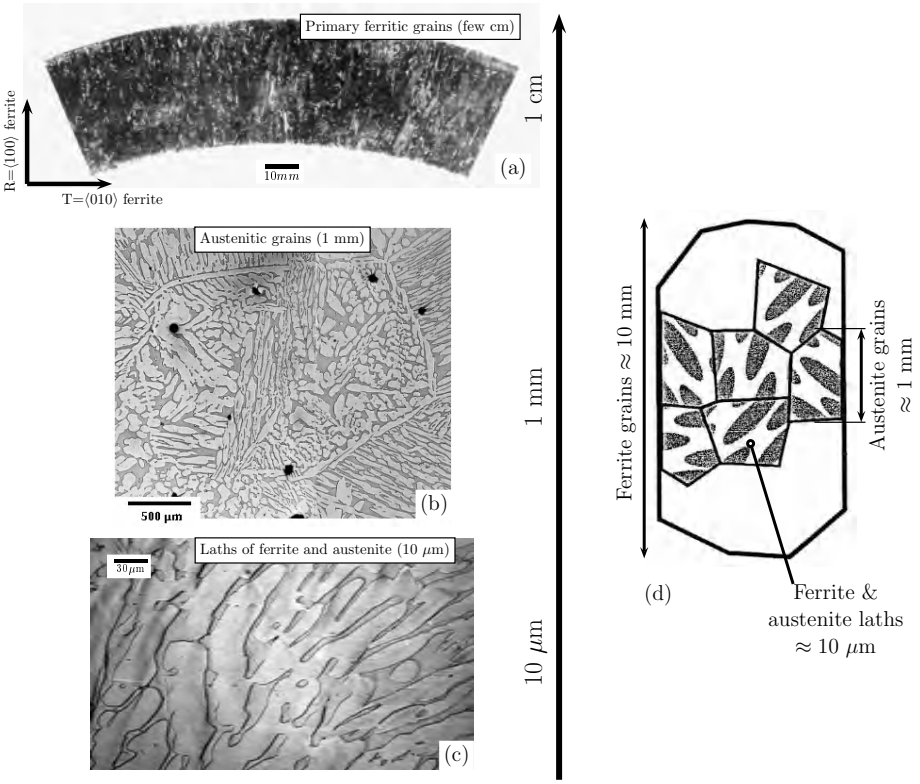

Figure 5.7. *Micrographs showing the three characteristic length scales of cast DSS. Example of heat Y4331 (a, b, c). (d) Diagram showing primary ferrite, and the duplex (austenite + ferrite) microstructure*

to determine this amount. Several empirical relations have been proposed to estimate the amount of ferrite knowing the composition and the heat treatment. Bonnet *et al.* [BON 90] have adjusted an empirical relation using the experimental results obtained on a large number of CF8 and CF8M heats. This relation applies to ferrite content covering the range between 4% and 33%:

$$\begin{aligned} \mathrm{Cr_{eq}} &= \mathrm{Cr} + \mathrm{Mo} + 0.65\mathrm{Si} - 17.6 \\ \mathrm{Ni_{eq}} &= \mathrm{Ni} + 20\mathrm{C} + 8.3\mathrm{N} + 0.08\mathrm{Mn} - 5.18 \\ \delta(\%) &= 21.8\left(\mathrm{Cr_{eq}}/\mathrm{Ni_{eq}}\right)^2 - 5.96\left(\mathrm{Cr_{eq}}/\mathrm{Ni_{eq}}\right) + 3.39 \times 400/(1500 - T) \end{aligned} \quad [5.3]$$

where T is the annealing temperature in °C. More recently, using thermodynamical calculations, Longbottom and Hayes [LON 94] have proposed an equation that gives

not only the amount of ferrite, but also the mean composition of both phases. However, the accuracy of those predictions remains limited as other factors, such as the thickness of cast parts, must also be considered [LEG 81].

5.2.4. *Mechanical properties of DSS*

As a rule in the absence of aging effect, i.e. in the as-cast or annealed conditions, these steels exhibit relatively high strength properties and maintain a good ductility [PIC 79]. These properties result from their dual-phase microstructure. These materials are more ductile than the ferritic stainless steels, due to the presence of the tough austenitic phase. The yield stress and the ultimate tensile strength increase, while the tensile elongation decreases, with the amount of ferrite, as shown in Figure 5.8 [ROU 90]. Large values for the Charpy U notch fracture toughness (150-200 J/cm^2) are observed in the initial condition, as shown in this figure. However, an increase in the ferrite content leads to an increase of the ductile-to-brittle transition temperature [KIE 84].

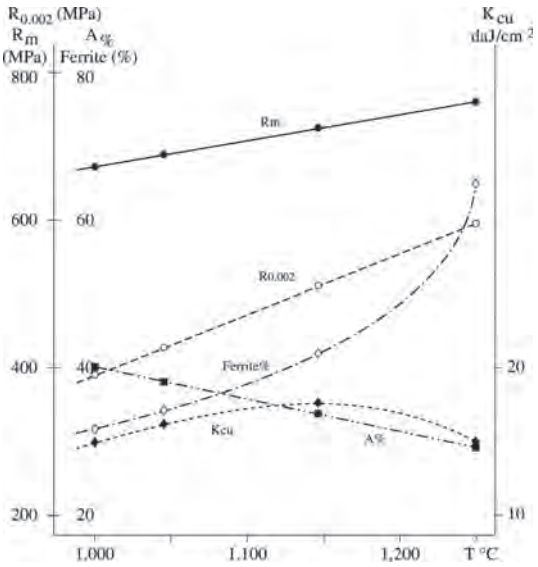

Figure 5.8. *Influence of ferrite content on the tensile properties ($R_{0.002}$, R_m, $A_{\%}$) and the Charpy U impact notch fracture toughness (K_{cu}) of cast DSS (taken from Rouby and Blanchard [ROU 90])*

5.3. Thermal embrittlement of the ferrite phase in DSS

5.3.1. *Binary Fe–Cr stainless steels*

The embrittlement phenomenon of ferritic stainless steels aged in the temperature range between 300 and 500°C was known when the first pressurized water reactors were constructed. At that time, the extrapolation of the aging kinetics established on ferritic steels at temperatures higher than 400°C did not predict that aging could actually take place in DSS aged at temperatures as low as 320°C. It is now well established that the kinetics of thermal aging in the ferritic phase of DSS are much larger than those expected and that a number of large components fabricated with these materials must be replaced before the initial expected life of 30-40 years.

The physical mechanisms explaining this thermal embrittlement effect have been largely investigated, in particular in binary Fe-Cr alloys. Fisher *et al.* [FIS 53] showed in the early 1950s the formation of nanometric particles, using transmission electron microscopy (TEM) observations. This new phase, named α', has a BCC structure with a lattice parameter between that of pure iron ($a = 0.2885$ nm) and that of pure chromium ($a = 0.2866$ nm). This α' phase is formed with a cube/cube orientation relation with the ferrite matrix. The formation of this phase is due to a spinodal decomposition of the solid solution, as shown by the phase diagram in Figure 5.9 [WIL 58]. Advanced techniques, including atom probe field ion microscopy (APFIM), have enabled visualization of the formation of small clusters of a few atoms and to identify their composition (see e.g. Auger *et al.* [AUG 90]). Moreover, several authors have applied the spinodal theory developed by Hillert [HIL 61] and Cahn [CAH 62, CAH 68] to the Fe–Cr system. Three comprehensive studies on this subject have been published by Miller and his coworkers [MIL 95]. Contrary to the phase transformations controlled by nucleation and growth, the spinodal decomposition leads to the concept of a macroscopically diffuse interface between the solute-rich and the solute-poor regions, with a corresponding "surface" energy that tends to zero in the limit, as schematically shown in Figure 5.10 [CAH 68].

The spinodal decomposition leads to significant strengthening effect and produces a large reduction in the ductility of the ferrite phase. The first metallurgical factor controlling this strengthening effect is the chromium content, as expected, and as illustrated in Figure 5.11, where the data reported by Bandel and Tofaute [BAN 42] and Riedrich and Loib [RIE 41] are shown.

Nickel is also an element that has to be considered as the content of this element in the ferrite phase of DSS is about 7 wt%. Results obtained on Fe-26 Cr base material containing additions of nickel up to 8 wt% are reproduced in Figure 5.12. These results clearly show that the addition of this element accelerates the formation of the phase rich in chromium [BRO 90a, BRO 90b, GUT 91]. These observations are in good agreement with the thermodynamical calculations made by Hayes *et al.* [HAY 90].

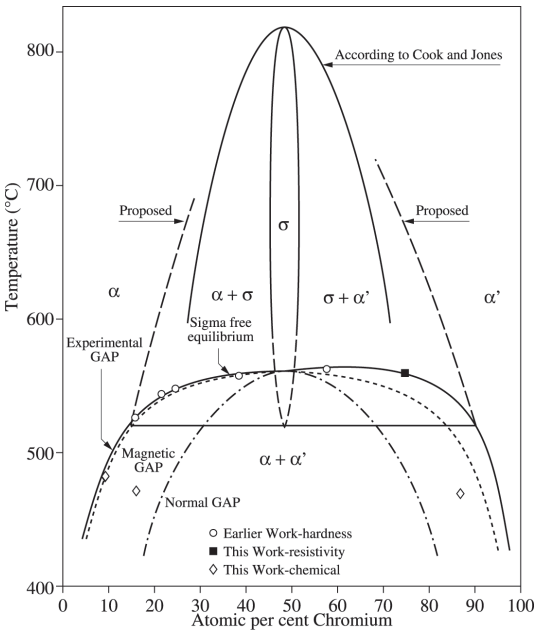

Figure 5.9. *Fe-Cr phase diagram (taken from Williams [WIL 58])*

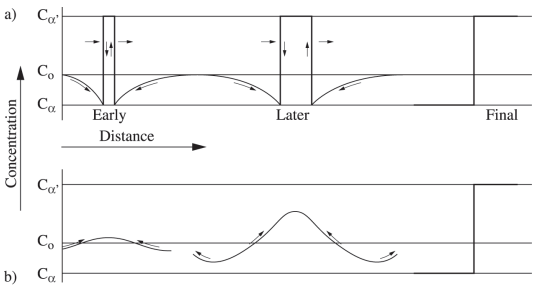

Figure 5.10. *Sketch showing compositional modifications due to nucleation and growth a) and to spinodal decomposition b)*

These authors have shown a shift towards lower chromium content of the spinodal tie line when the amount in nickel is increased.

Similarly interstitial atoms, like nitrogen and carbon, also seem to favor the acceleration of the embrittlement due to the formation of the α' phase (see

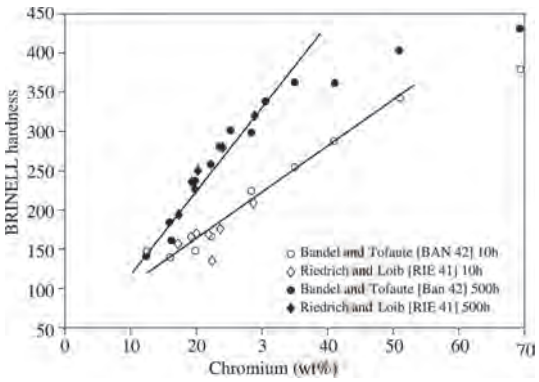

Figure 5.11. *Variations of Brinell hardness as a function of chromium content in ferritic stainless steels aged 10 and 500 hours at 500°C (taken from Riedrich and Loib [RIE 41] and Bundel and Tofaute [BAN 42])*

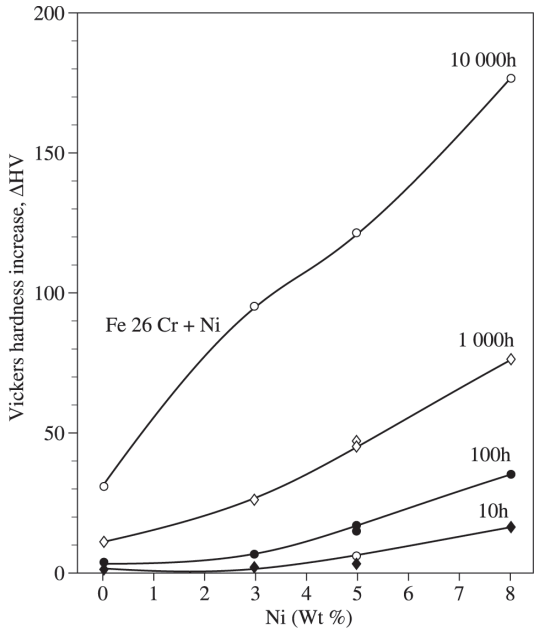

Figure 5.12. *Influence of nickel on aging of a ferritic stainless steel, Fe-26Cr-Ni at 400°C (taken from Guttmann [GUT 91], after Brown et al. [BRO 90b])*

e.g. Courtnall and Pickering [COU 76], Henry *et al.* [HEN 79], Golovin *et al.* [GOL 92]).

5.3.2. *DSS:* α/α' *demixtion, phase G and other precipitation reactions*

DSS thermally aged between 280 and 450°C are known to eventually be embrittled by the spinodal decomposition of the ferrite phase. However, the presence of other alloying elements, such as nickel or silicon, generates the formation of other phases, such as the G phase, which is often observed in steels of the CF8 and CF8M type.

5.3.2.1. *Spinodal decomposition in the ferrite phase*

The α/α' spinodal decomposition of the ferrite phase in DSS has been largely investigated using various techniques. In particular it has been shown, using the APFIM technique, that the local chemical fluctuation amplitudes in chromium content increase with aging time while the mean distance between these fluctuations increases also with aging time. These observations were reported by Auger *et al.* [AUG 90]. The results are shown in Figure 5.13.

It should be mentioned that Chung and Chopra [CHU 88, CHU 91] seem to be the only authors to have reported the precipitation of α' particles with a disk shape. However, as noted by Hayes *et al.* [HAY 90], the materials studied by Chung and Chopra belong to the CF3 and CF8 families. In these materials the ferrite has a composition very close to the spinodal tie line, and the $\alpha \rightarrow \alpha'$ phase transformation can consequently occur by classical nucleation and growth processes.

5.3.2.2. *Other precipitation reactions*

The precipitation of the G phase has often been observed in CF8 and CF8M steels, when they have been aged for a sufficiently long time. This phase has a FCC structure with a complex unit cell of 116 atoms and a lattice parameter between 1.09 and 1.11 nm. The composition of this phase is $Ni_{16}Si_7Ti_6$ with many elements, such as Cr, Fe, Mo, Mn, V, Nb, Ta, Hf, Zr, that can be substituted for Ni. These materials can also give rise to other precipitation reactions, such as:

– the precipitation of $M_{23}C_6$ chromium-rich carbides,

– the formation of secondary (or reversed) austenite, γ_2, which precipitates within the ferrite. The formation of this γ_2 phase is observed for aging temperatures

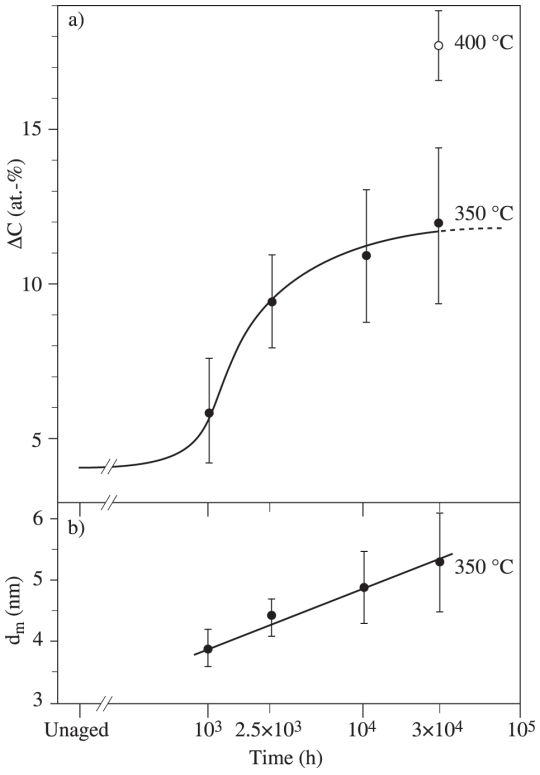

Figure 5.13. *Spinodal decomposition. Evolution of the chromium concentration amplitude a), the mean distance between compositional fluctuations b) as a function of aging time at 350°C (taken from Auger et al. [AUG 90])*

higher than 400°C and is likely associated with the formation of $M_{23}C_6$ particles.

5.3.2.3. *Kinetics of reaction*

It seems difficult to decouple the influence of the various precipitation phenomena observed in these steels. However, TTT diagrams similar to the diagram shown in Figure 5.14 proposed by Chung and Chopra [CHU 88] have been published.

In spite of the complexities of these materials the results shown in Figure 5.14 indicate that "accelerated" aging treatments applied at a temperature (for instance, 400°C) are not necessarily representative of in-service conditions. Therefore, it is not

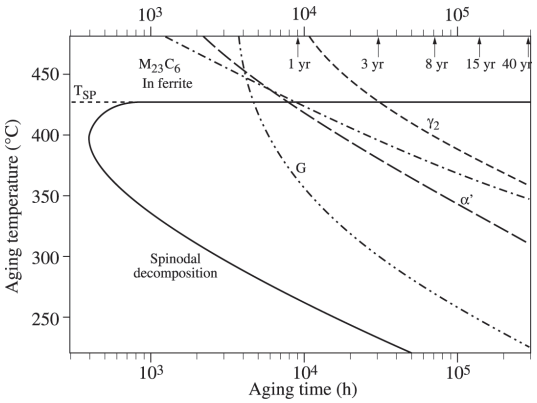

Figure 5.14. *TTT diagram for cast DSS aged between 250 and 450°C. Spinodal decomposition α/α'. Nucleation and growth of G, α' phases and $M_{23}C_6$ carbides. Precipitation of reversed austenite, γ_2 (taken from Chung and Chopra [CHU 88])*

surprising that a number of authors have shown that the apparent activation energy for the deterioration of the mechanical properties of the CF8M type steel is not constant, but changes with temperature. The results obtained by Bonnet *et al.* [BON 90] are reported in Figure 5.15.

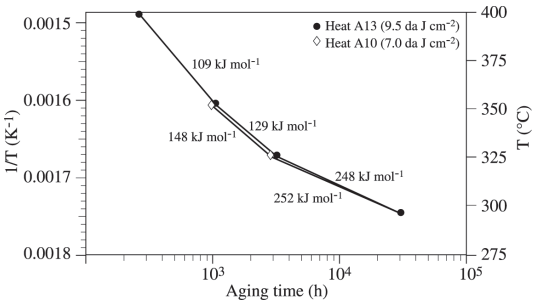

Figure 5.15. *Apparent activation energy as a function of aging temperature in two cast DSS (taken from Bonnet et al. [BON 90]). The time on the x axis corresponds to an impact fracture toughness of 95 and 70 J/cm^2 in heats A13 and A10, respectively*

5.3.3. *DSS: consequences of thermal aging on mechanical properties*

In DSS, thermal aging between 300 and 500°C gives rise to an increase of the hardness of the ferrite phase, and the local embrittlement of this phase is similar to the effect observed in single phase ferritic stainless steels. However, the consequences of the α/α' demixtion on the global behavior of the DSS depend on several factors related to the ferrite phase, including:

– the amount,

– the size of ferritic laths,

– the geometric distribution of both phases.

5.3.3.1. *Mechanisms of hardening of the ferrite phase*

Numerous studies devoted to "475°C" embrittlement of ferritic stainless steels or DSS have shown that this embrittlement is mainly related to the increase in the hardness of the ferrite phase due to the α/α' phase transformation. Typical results obtained on various types of DSS aged at 400°C are shown in Figure 5.16. As noted by Chopra [CHO 91], it is usually observed that after aging at this temperature, the hardness of the ferritic phase reaches a maximum value after about 5,000 or 10,000 hours. The value of this maximum largely depends on the material. The longest aging times seem to have been applied by Trautvein and Gysel [TRA 82]. These authors have aged CF8 and CF8M steels between 300 and 500°C for period of up to 70,000 hours. No over-aging effect that would have corresponded to a decrease of the hardness after a certain time has been observed.

The "475°C" embrittlement phenomenon is accompanied by large modifications in the deformation modes of the ferrite phase. After aging the deformation is strongly localized in thin slip bands and the ferrite phase tends to deform not only by slip but also by mechanical twinning. The continuity of the deformation at the interface between the FCC matrix and the BCC phase can easily take place due to the Kurdjumov-Sachs crystallographic relations between these phases.

Several authors have attempted to model the hardening mechanisms associated with the α/α' phase transformation (see e.g. Williams [WIL 57], Lagneborg [LAG 67a, LAG 67b, LAG 67c]). These studies have concluded that the α' zones are sheared by dislocations, and the strengthening effect is attributed to various contributions:

– two mechanisms are linked to the strong lattice friction force in the chromium-rich regions in addition to the creation of new interfaces between the sheared particles and the matrix [LAG 67a, LAG 67b, LAG 67c],

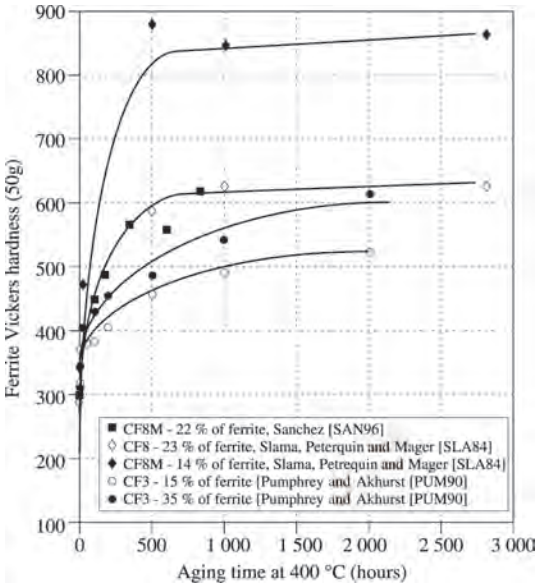

Figure 5.16. *Variation of the ferrite hardness as a function of aging time at 400°C in various heats of cast DSS*

– two other mechanisms are related to the lattice mismatch between the chromium-rich zones and the chromium-poor regions, and to the difference in elastic constants between these zones. These two mechanisms are usually those that are involved to explain the hardening effect associated with compositional modulations (see e.g. Kato [KAT 81], Park *et al.* [PAR 96]).

5.3.3.2. *Mechanical properties*

Thermal aging of DSS produces only slight increases in their yield stress. The ultimate tensile strength is increased. The tensile elongation and the reduction of area at fracture decrease significantly (see e.g. Slama *et al.* [SLA 84]).

The embrittlement effect has been largely investigated using Charpy V (or U) notch impact specimens. Examples showing the variation of the impact toughness in a CF8M steel aged at 350 or 400°C are shown in Figure 5.17 [SAN 96]. In this figure, it is observed that aging produces a decrease of the upper shelf energy and a shift to higher temperatures of the ductile-to-brittle transition. In a given material the variations of the Charpy transition curve stabilize when the hardness of the ferrite

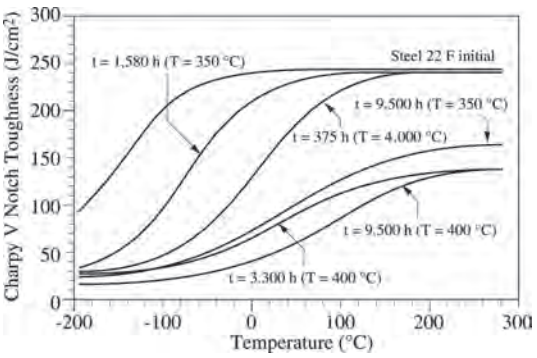

Figure 5.17. *Charpy V notch impact fracture toughness as a function of test temperature in a DSS of CF8M type containing 22% ferrite and aged at 350 and 400°C (taken from Sanchez [SAN 96])*

phase has reached its maximum value. The values of the impact fracture toughness depend strongly on the amount of ferrite, as expected (see Figure 5.18), but also on the presence of molybdenum, which seems to accelerate the embrittlement kinetics (see e.g. Bonnet *et al.* [BON 90], Massoud *et al.* [MAS 92]). In Figure 5.18 parameter P on the x axis gives equivalence between time and temperature. This parameter introduced by Trautwein and Gysel [TRA 82] is written as:

$$P = \log_{10} t + 0.434 \left[\frac{U}{R} \left(\frac{1}{673.2} - \frac{1}{T} \right) \right] \qquad [5.4]$$

where t is the aging time and T the aging temperature (in K), while U is the apparent activation energy and R is the Boltzman constant. Parameter P is equal to 1 for an aging time of 10 hours at 400°C and its definition implies that the value of the activation energy, U, does not change with temperature, which is not necessarily the case, as underlined previously.

It has also been shown that the fracture toughness of DSS measured by curves is strongly affected by thermal aging (see e.g. Chopra [CHO 91], Sanchez [SAN 96]). Detailed results on the variation of the fracture toughness are given in the following sections devoted to the modeling of damage mechanisms in these steels.

Many studies have been devoted to the description of the "475°C" embrittlement effect produced by thermal aging of DSS (see e.g. Bonnet *et al.* [BON 90], Joly [JOL 92a], Duval [DUV 92], Verhaeghe [VER 95], Sanchez [SAN 96], Devillers-Guerville [DEV 98], Bugat [BUG 00]). The studies performed in the authors' laboratory are presented in sections 5.4–5.7. Here, it is enough to say that after deformation the ferrite is damaged. Three damage modes for this phase can be

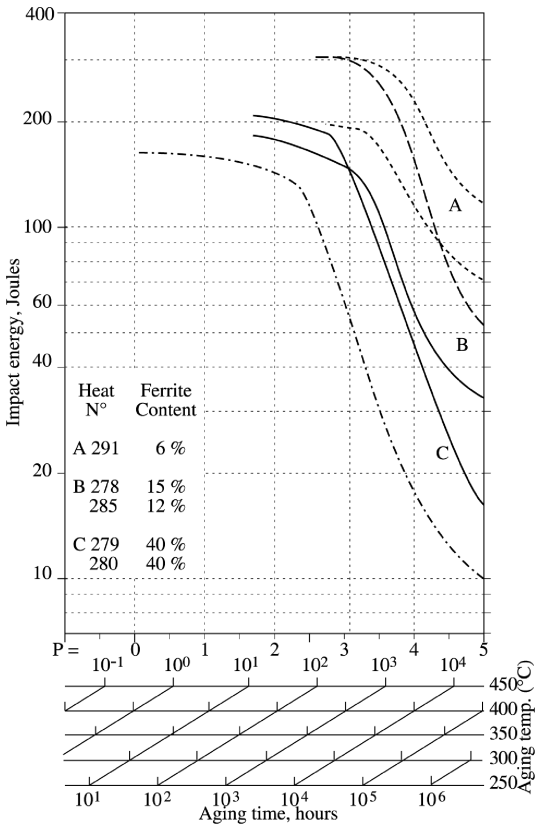

Figure 5.18. *Influence of ferrite content on "475°C" embrittlement of cast DSS (taken from Trautwein and Gysel [TRA 82])*

distinguished depending on the test temperature and the level of embrittlement. These damage modes are summarized in Figure 5.19.

The ferrite phase remains ductile when the material is not aged or only slightly embrittled. In these conditions the fracture surfaces are covered by ductile dimples, and it is difficult to identify both phases from the examination of the fracture surfaces.

The ferrite is damaged by the formation of cleavage cracks along {100} planes when the material is more embrittled and tested at relatively low temperature, i.e. 20°C. These microcracks are stopped at the interface between the ferrite and austenite phases. They initiate cavities by crack blunting in the austenite phase. These cavities grow and coalesce leading to final fracture. The nucleation of cleavage microcracks strongly depends on the aging conditions. Dislocation pile-ups can nucleate the

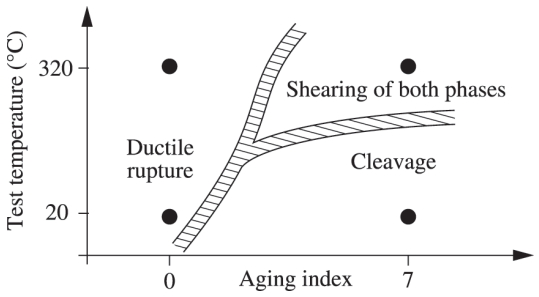

Figure 5.19. *Graph showing different damage modes in cast DSS as a function of an aging index (increasing from 1 to 7) and test temperature (taken from Duval [DUV 92])*

formation of these microcracks. However, a number of authors have also shown that these cleavage microcracks can be preferentially nucleated at the intersection of mechanical twins (see e.g. Bonnet *et al.* [BON 90], Joly [JOL 92a], Marrow and Harris [MAR 96b, MAR 96c], Marrow and Bury [MAR 97]). Quantitative information on the formation of these cleavage cracks are given in the following sections devoted to damage modeling of DSS.

There exists a third damage mode that has been identified on aged materials tested at higher temperature, typically 300°C. This mode corresponds to preferentially shearing along crystallographic planes of the ferrite phase. In Figure 5.19 the frontiers between the three modes of damage are shown schematically. Their contours are poorly known. In this chapter, we will only concentrate on the damage mechanism corresponding to the formation of cleavage cracks in the ferrite phase.

The influence of "475°C" embrittlement on the fatigue crack growth rate (FCGR) behavior of aged DSS has also been investigated. The results obtained on two heats containing about 30% ferrite can be found elsewhere [CAL 04]. Both materials were parts of two statically cast elbows. Material E1 was annealed 10 hours at 1,100°C, water quenched and then aged 2,400 hours at 400°C. This material was also tested in the re-annealed condition. Material taken from elbow EK was annealed 8 hours at 1,100°C and water quenched. It was tested in the as-received (un-aged) condition and after aging 10,000 hours at 400°C. Tests on Material EK re-annealed (un-aged) were also performed. Both materials were strongly embrittled after aging since their Charpy fracture toughness measured at RT was close to 15-20 J/cm^2. The effect of solidification macrostructure (equiaxed versus columnar) was also studied.

The results of FCGR measurements on those two materials tested in the equiaxed condition are reported in Figure 5.20. In this figure it is noted that the scatter in the results is relatively large. This has been attributed to the coarse solidification structure of these materials. FCGRs in aged material EK are five times higher than

in the re-annealed material and three times higher than in the as-received (un-aged) condition. In aged steel E1, which is less brittle than aged steel EK, the effect of aging on the FCGR behavior only appears at high ΔK. This increase in FCGRs has been attributed to ferrite cleavage and to the resulting irregular shape of the crack front. These results show that the "475°C" embrittlement produces an increase in FCGRs. However, the effect on fatigue behavior is less pronounced that the effect on fracture toughness.

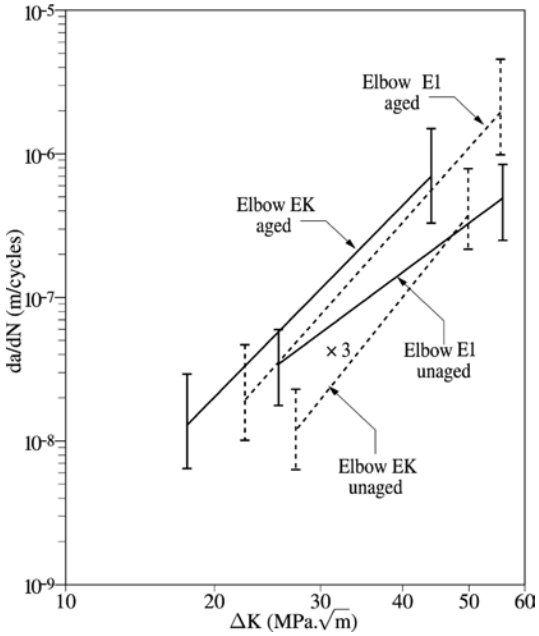

Figure 5.20. *Fatigue crack growth rates as a function of stress intensity factor amplitude, ΔK. Two materials tested: elbow EK, elbow E1 (see Table 5.2)*

5.4. Materials investigated and embrittlement heat treatments

5.4.1. *Materials – heat treatments*

In the authors' laboratory several materials of the CF8M family have been investigated. Two materials (Y4331 and Y3296) were centrifugally cast pipes (external diameter: 40 cm, internal diameter: 32 cm). Due to this processing route, the ⟨100⟩ axis of the ferrite corresponds to the radial (R), tangential (T), and

longitudinal (L) directions of the pipe. As indicated previously, these materials have a pronounced basaltic solidification microstructure. Three other heats (BL, BP, and BQ) are statically cast ingots ($215 \times 65 \times 45$ mm^3). Test specimens were taken from the center of the ingots, except where otherwise stated. Therefore their solidification microstructure is equiaxed and isotropic. Materials EK and E1 were taken from statically cast elbows (see Figure 5.21 where the orientations are given). All the details concerning the preparation of these materials can be found elsewhere [JOL 92a, DEV 98, BUG 00].

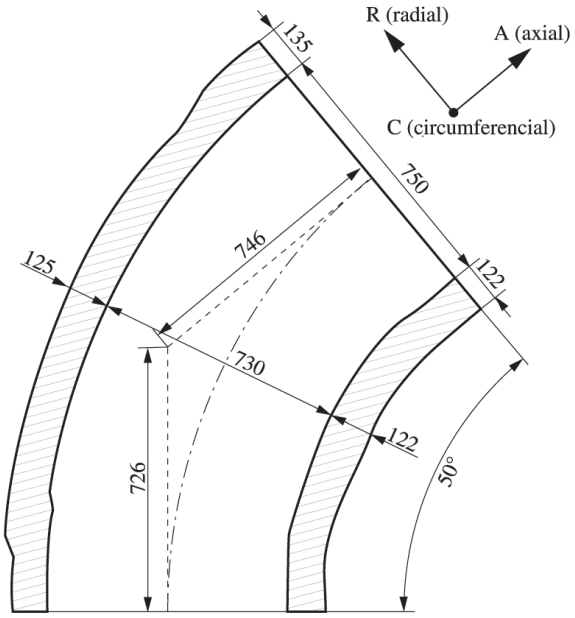

Figure 5.21. *Elbow E1. Diagram (all dimensions in mm) and orientations*

The composition of all materials is given in Table 5.2. In this table the values of Creq and Nieq were calculated using equation [5.2]. It is noted that in all cases the $\left(Cr_{eq}/Ni_{eq}\right)$ ratio is larger than 2, which means that all materials solidify as ferrite and then partially transform to austenite during cooling and annealing heat-treatments. The values of the amount in ferrite (δ) as determined from magnetic measurements are also included in Table 5.2. These results show that large differences in ferrite could thus be obtained.

Micrographs showing the microstructure of three typical materials (Y4331, BT and BL) are shown in Figure 5.22 [BES 00]. It can be seen that the ferrite laths in

Material	C	Cr	Ni	Mo	Mn	Si	S	P	N	δ (%)	Cr_{eq}	Ni_{eq}	(Cr_{eq}/Ni_{eq})
Y 4331	0.045	20.61	9.84	2.61	0.74	1.25	0.002	0.026	0.046	20.0	26.5	11.9	2.24
Y 3296	0.036	21.21	10.36	2.76	0.65	1.36	ND	0.026	0.039	30.5	27.0	12.0	2.25
BL	0.040	20.18	9.66	2.60	0.58	1.15	ND	ND	0.032	22.1	25.5	11.2	2.28
BP	0.032	19.62	9.97	2.50	0.63	1.27	ND	ND	0.027	17.2	25.0	11.3	2.22
BT	0.038	20.45	10.86	2.58	0.51	1.10	ND	ND	0.045	14.4	25.6	12.5	2.05
EK	0.033	21.14	9.67	2.51	0.88	1.07	0.004	0.018	0.052	28.0	26.4	11.6	2.28
E1	0.033	21.68	9.61	2.64	0.82	0.94	0.0005	0.023	0.057	33.0	26.8	11.4	2.35

Table 5.2. *Chemical compositions of investigated materials (wt%)*

	Y 4331	Y 3296	BL	BP	BT	EK T2-S2	EK T7-S7	E1
Temperature (°C)	400	400	400	400	400	350	400	400
Time (hours)	700	8,000	30,000	30,000	30,000	3,000	10,000	2,400
Ferrite HV_{50}	516±130	711±215	785±84	795±84	860±123	640±90	760±88	600
Austenite HV_{50}	196±16	246±33	265±34	265±30	265±24	203±15	199±15	ND

Table 5.3. *Heat treatments and hardness of the ferrite and austenite phases*

material Y4331 are much larger than those in materials BL and BT. This is due to large differences in cooling rates between these materials.

The materials were aged at 400 or 350°C, as indicated in Table 5.3. In this table we have included the values of the hardness of ferrite and austenite (50 g load) after aging. Material BT contains the harder ferrite while materials Y4331 contain the softer ferrite. This result can be explained by microprobe analysis of the chemical compositions of the ferrite, which are reported in Table 5.4. This table shows that the ferrite of material BT contains more nickel and more chromium than the ferrite of BL and BP materials, which were given the same heat-treatment (30,000 hours, 400°C). This result is thus in good agreement with the observations reported in the previous section on the effect of chemical composition on the spinodal decomposition.

5.4.2. *Mechanical properties*

The tensile properties of all these materials have been measured at 25°C. The results are reported in Table 5.5 [DEV 98]. In this table, we have also included the values of the Charpy U notch fracture toughness determined at RT. It is observed that, in a given material, the increase of the hardness of the ferrite phase due to thermal aging coincides with a decrease of the impact fracture toughness, as shown in Figure 5.23 where the results obtained on EK material ($\delta = 28\%$) are reported. In this figure, we have also reported the results obtained by Alegre and Gutierrez-Solana [ALE 04] and Sanchez [SAN 96, SAN 02] on two DSS containing 18 and

		Cr	Ni	Mo	Mn	Si
Ferrite	Y 4311	24.79	6.82	3.64	ND	1.26
	Y 3296	25.84	7.45	3.57	0.68	1.26
	BL	24.84	6.33	3.74	0.56	1.30
	BP	24.21	6.63	3.67	0.60	1.40
	BT	25.78	6.95	3.85	0.46	1.22
	EK	25.20	6.75	3.40	0.86	1.22
	E1	25.84	6.67	3.57	0.88	1.11
Austenite	Y4331	19.75	10.96	2.27	ND	1.13
	Y3296	20.47	11.50	2.18	0.75	1.12
	BL	19.20	10.10	2.21	0.61	1.13
	BP	19.46	10.62	2.29	0.67	1.27
	BT	20.27	11.44	2.35	0.52	1.10
	EK	20.30	10.80	2.10	0.96	1.10
	E1	20.68	10.61	2.25	0.96	0.98

Table 5.4. *Chemical compositions (wt%) of the ferrite and austenite phases in the investigated materials, taken from Joly [JOL 92a] and Devillers [DEV 98]*

	Y 4331	Y 3296	BL	BP	BT	EK T2-S2	EK T7-S7	E1
$\sigma_{Y0.2}$ (MPa)	327 (313)	370 (360)	365	352	354	367 (340)	356	357
UTS (MPa)	722 (622)	735 (650)	781	760	722	720 (620)	644	727
A (%)	20 (45)	3 (33)	25	41	26	18 (35-40)	5	11
KCU (20°C)	30 (172)	7 (187)	35	68	27	25 (195)	15 (195)	20 (240)
KCU (320°C)	ND	ND	ND	ND	ND	ND	(25)	ND

Table 5.5. *Tensile mechanical properties and Charpy U notch fracture toughness at 25°C. The numbers given in brackets correspond to measurements made at 300°C*

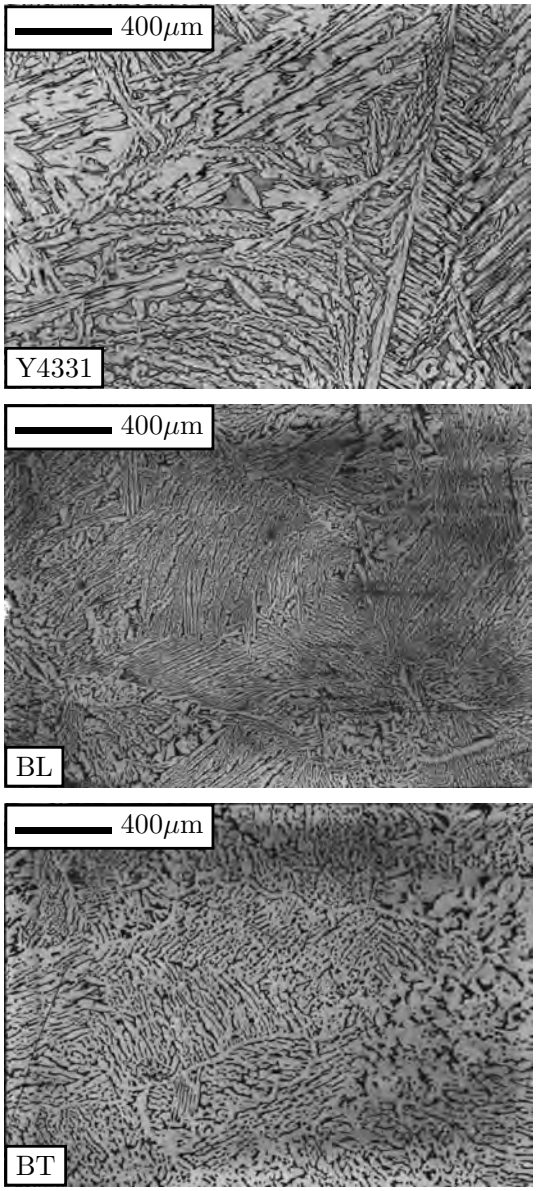

Figure 5.22. *Microstructure of the investigated materials*

22% of ferrite phase. These results clearly show that the level of embrittlement in these materials depends on the amount of ferrite and on the hardness of this phase.

Another important behavior, not shown here, but later in this chapter, is observed when measuring the fracture properties of these cast materials. It is the large scatter in test results and the size effect. This results from the coarse microstructure of these steels. The modeling of the scatter and the size effect is detailed in the following sections.

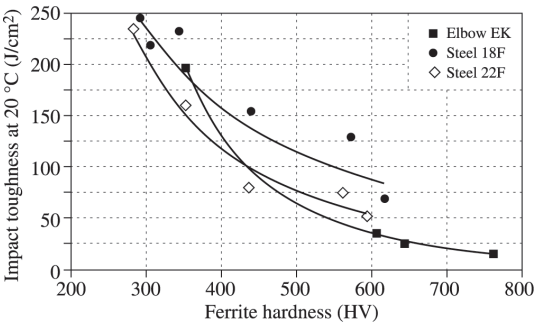

Figure 5.23. *Variation of the Charpy U notch impact fracture toughness as a function of the Vickers hardness of the ferrite phase in three DSS: elbow EK (δ% = 28) (taken from Devillers [DEV 98], steel 18F (δ% = 18) and steel 22F (δ% = 22) (taken from Sanchez [SAN 96])*

5.5. Damage and rupture

Figure 5.24a illustrates the damage process in heat Y4331: cleavage crack nucleation in the ferrite and subsequent growth in the austenite due to extensive plastic deformation. This deformation is clearly evidenced by slip lines shown on Figure 5.24a in the austenite. Cracks nucleated in the ferrite tend to transform into cavities, which eventually coalesce leading to final failure. Although rupture is initiated by cleavage, the overall fracture mechanism remains ductile, as stated previously.

Nucleation cracks are not evenly distributed in the material even in cases (e.g. tensile test) where macroscopic stresses and strains are uniform. Cracks tend to form clusters as shown on Figure 5.24b. These clusters corresponds to zones where the orientations of ferrite and austenite remain constant. The size of these clusters is about 1 mm. At this scale, the material consists of austenitic grains containing ferrite laths. This type of microstructure can be described as a “percolated bicrystal”.

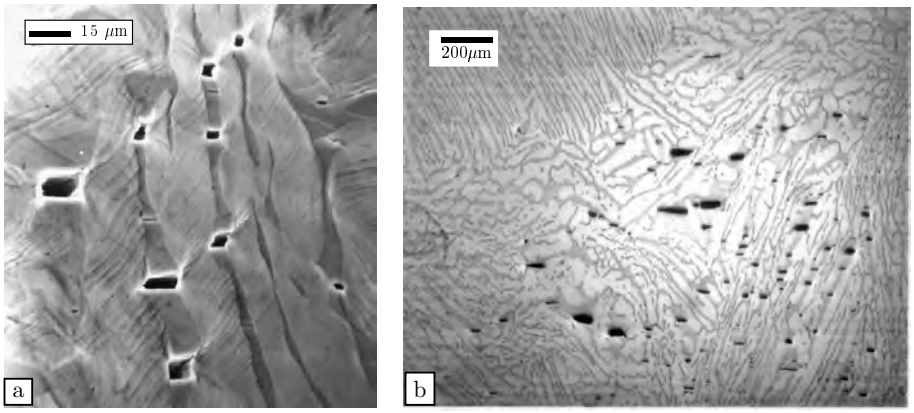

Figure 5.24. *a) Surface crack nucleation in the ferrite and subsequent void growth during a tensile test at RT. b) Heterogenous damage growth inside an austenite grain (size ≈1 mm). Heat Y4431*

In the bicrystal, both phases are related by the Kurdjumov-Sachs crystallographic relationship, as indicated previously.

Damage can be quantified on prestrained specimens. Tensile tests were performed on rectangular bars (cross section: 4×10 mm^2, length: 30 mm). The method, which has been extensively described in [JOL 92a, JOL 92b, JOL 95], is summarized in the following. Samples are polished and subsequently deformed in order to reach different levels of plastic deformation. For each level, the surface of the specimen is observed using scanning electron microscopy (SEM) allowing the determination of the position of cleavage cracks. Voronoï cells are then drawn around those cracks. Results obtained for material BT are shown in Figure 5.25 for macroscopic plastic strains equal to 2.5, 4.5 and 6.5%. These observations were used to determine the surface crack nucleation rate: dN_a/dp where N_a is the number of observed cracks and p the plastic strain. However, this quantification remains two-dimensional (2D) and it becomes necessary to determine the shape of the cracks in order to derive a three-dimensional (3D) damage evaluation. Small notched bars were predeformed and subsequently unembrittled by annealing at 600°C for 2 hours so that the ferrite becomes ductile. The bars were then fractured and the rupture surface was subsequently observed using SEM. Cleavage zones correspond to cracks nucleated in the embrittled material. Tests interrupted for different plastic strains have shown that individual cleavage cracks do not grow after being nucleated. In order to derive an effective porosity corresponding to the cleavage cracks, it is assumed that a crack has the same mechanical effect as a spherical void having the same projected area on the fracture surface. It is then

possible to define a nucleation porosity rate, f_n , which is equal to:

$$\dot{f}_n = A_n \dot{p} = G \frac{dN_a}{dp} \dot{p} \qquad [5.5]$$

where G is a non-dimensional geometrical factor [JOL 91, JOL 92a, JOL 95]. The nucleation rate parameter A_n can be defined as an average over an area much larger than the cluster size or defined locally in each cluster using the appropriate Voronoï tesselation. It was found that A_n can be considered as constant at the macroscopic scale (average value of A_n) or inside the clusters (local value) [JOL 92a, JOL 92b, JOL 95].

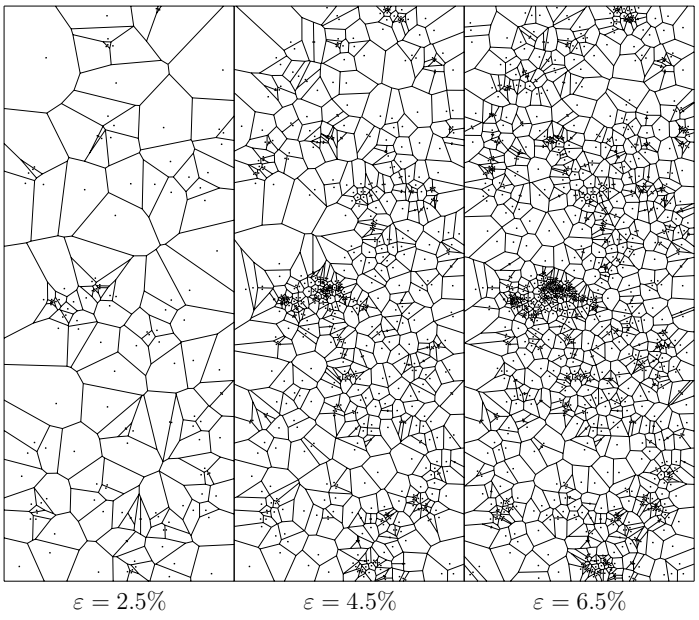

Figure 5.25. *Voronoï cells associated with cracks for different macroscopic plastic deformations (BT material). The observed areas correspond to a rectangle of a size equal to 10×25 mm^2 [DEV 98]*

Damage clustering cannot be explained by the texture of the ferrite as this phase has a pronounced texture due to the solidification conditions with most ferrite grains having their (100) poles aligned with the radial, axial and tangential directions of the pipe. Ferrite can almost be considered as a single crystal and, therefore, cannot be responsible for the small number of cracked grains. The austenite is much less textured as the Kurjumov-Sachs orientation relationship allows for 24 different orientations for the austenite. In addition, the crack cluster size (≈ 1 mm) corresponds to the austenite grain size determined using electron back scatter diffraction (EBSD) [BUG 01].

The effect of austenite crystallographic orientation on preferential cracking of ferrite was studied by orienting the macroscopic tensile axis with respect to the austenite orientation. This was achieved in different areas of prestrained specimens, which were representative of crack free zones or cracked zones [JOL 90]. Results are shown in Figure 5.26a. From this figure, it can be observed that ferrite cracking is prevented when the loading axis is close to the $(100)_\gamma$-$(111)_\gamma$ zone. Conversely, a loading axis close to the $(110)_\gamma$ direction promotes cracking. This study was complemented by analysing the austenite deformation mode to distinguish zones under single slip and zones under multiple slip. Results are reported in Figure 5.26b and indicate that single slip zones closely correspond to cracked areas. One possible explanation for this correlation could be the following. Strain incompatibility between austenite and ferrite, resulting from the difference in hardness and crystallographic structures, can easily be relaxed by multiple slip in the austenite if the tensile axis is close to the $(100)_\gamma$-$(111)_\gamma$ zone. When the tensile axis is close to $(110)_\gamma$, single slip prevails and stress relaxation can only occur by mechanical twinning and eventually cracking by cleavage.

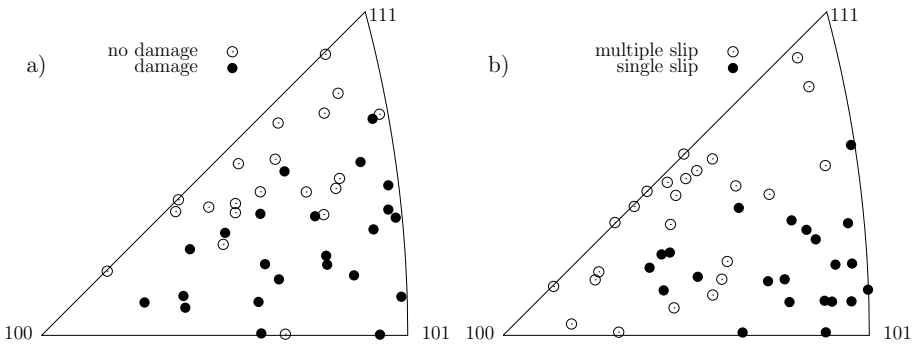

Figure 5.26. *Orientation of the tensile axis with respect to the austenite crystal showing a) damaged and undamaged grains, b) grains under single or multiple slip. The macroscopic strain level is 9.5% [JOL 90]*

5.6. Scale effect and scatter

As microstructutal heterogenities leading to the formation of crack clusters have a size of the same order of magnitude as those of the laboratory samples used to characterize both plastic and fracture behavior, scatter and size effects are expected to be observed when carrying out mechanical tests. This trend is exemplified in the case of axisymmetric tensile smooth (TB) and notched (NT_χ) bars (geometry is

shown on Figure 5.27). Ductility is measured using the mean diametral deformation $\bar{\varepsilon}$ defined as:

$$\bar{\varepsilon} = 2\ln\left(\frac{\phi_0}{\phi}\right) \qquad [5.6]$$

where ϕ is the minimum diameter of the specimen and ϕ_0 its initial value. Values of the mean diametral deformation at failure ($\bar{\varepsilon}_R$) are plotted in Figure 5.27 for the different sample geometries and for three materials (Y4331, BT and BL, see Table 5.2). Ductility is shown to decrease with increasing notch severity. A large scatter is observed on $\bar{\varepsilon}_R$. Due to the limited availability of the ingot materials (BT and BL), fewer and smaller ($\phi_0 = 6$ mm) samples were tested in this case. Scatter is high for all materials. In addition, it should be noted that smooth specimens exhibit strains to failure similar to NT_{10} samples, whereas theories based only on a critical cavity growth ratio [RIC 69, MCC 71, BER 81] would predict an important increase.

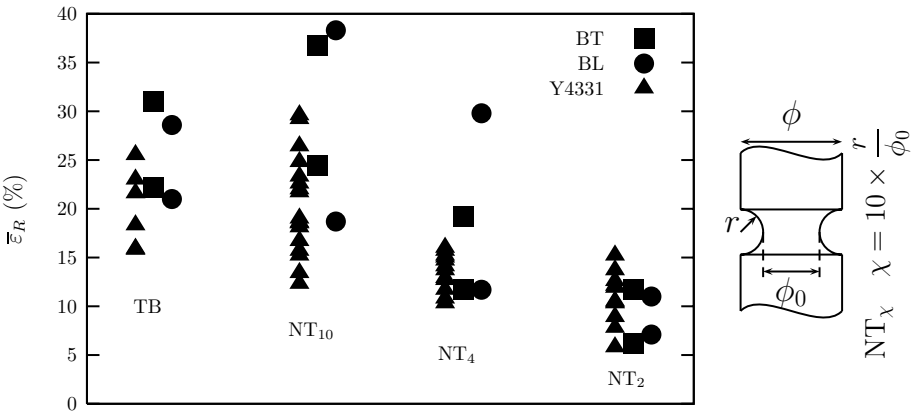

Figure 5.27. *Strain to failure for the three different materials (see Table 5.2) and various geometries. $\phi_0 = 10$ mm for the Y4331 material and $\phi_0 = 6$ mm for materials BT and BL*

Scatter is usually associated with size effects. In order to investigate this effect, samples homothetic to the NT_{10} geometry were used (Y4331 material). Their minimum diameter was either smaller (6 mm) or larger (15 mm) than the nominal one (10 mm). Results are reported in Figure 5.28. As expected, scatter and average values decrease with increasing specimen size.

Charpy specimens (U, V notched, and precracked) were also used under quasi–static loading conditions. Tests carried out using an instrumented Charpy impact test machine (speed 5 m/s) resulted in fracture energies similar to those obtained for quasi–static loading [DEV 98]. Geometries are shown on Figure 5.29a. Samples were

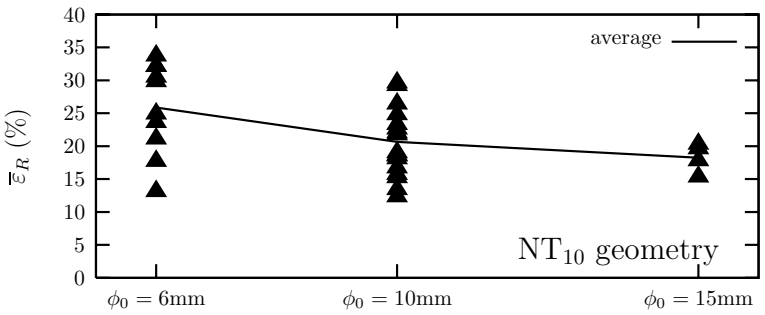

Figure 5.28. *Strain to failure for homothetic NT_{10} specimens (Y4331 material)*

prepared so that principal stresses were developed in the same direction as for tensile bars. For the pipe material (Y4331), the crack propagated in the radial direction. For the ingots, the crack direction corresponded to the second longest dimension of the ingot. On these specimens, ductility is given as a fracture energy that can be divided in two parts: 1) initiation energy, which corresponds to the energy dissipated before the initiation of a macrocrack, 2) propagation energy, which corresponds to the energy needed to propagate the macro-crack. Examinations of samples have shown that crack initiation corresponds to the maximum load. An example of load-displacement curve is given in Figure 5.29b. This figure also shows the initiation and propagation energies.

Results obtained for all materials are gathered in Figure 5.30. Energies for U–notched specimens are indicated in Figure 5.30a showing large dispersions on both initiation and propagation energies. Results for different geometries (U, V–notched, and precracked) are indicated in Figure 5.30b. It is shown that initiation energy decreases with increasing notch severity whereas the propagation energy remains constant but dispersed. Figure 5.30c shows the effect of varying the specimens thickness, *e*: scatter on initiation energy is reduced together with average values when the specimen thickness is increased. Conversely, the propagation energy appears to be independent of the thickness. It can be concluded that size effects mainly affect initiation.

Crack propagation in material Y4331 was also studied using compact tension (C(T)) specimens according to the ASTM E 813-89 standard. Based on this procedure, the J-integral values versus crack extension (Δa) were plotted for several repeated tests. Results are shown in Figure 5.31 showing a large scatter on both crack initiation characterized by $J_{0.2}$ and crack propagation resistance characterized by the tearing modulus dJ/da. In agreement with results obtained on Charpy specimens, dispersion is more important on initiation than on crack propagation.

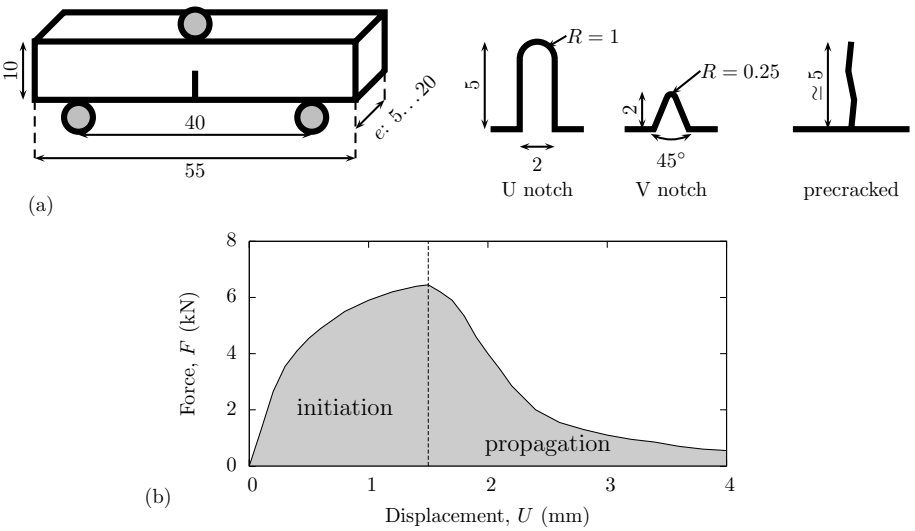

Figure 5.29. *a) Geometry of Charpy (U, V, and precracked) specimens (dimensions in mm). b) Load-displacement curve showing the calculation of initiation and propagation energies (Y4331 material)*

5.7. Modeling of rupture

5.7.1. *Constitutive equations*

Materials are modeled using continuum damage mechanics. Models are based on the plastic criterion depending on the porosity introduced by Gurson [GUR 77] and modified by Tvergaard and Needleman [TVE 84, BEC 88, TVE 90]. This criterion is given by:

$$\Phi = \frac{\sigma_{eq}^2}{\sigma_*^2} + 2q_1 f_t \cosh\left(3q_2 \frac{\sigma_m}{2\sigma_*}\right) - 1 - q_1^2 f_t^2 \qquad [5.7]$$

where σ_{eq} is the von Mises equivalent stress, and σ_m the mean stress. σ_* is the yield stress of the undamaged matrix corresponding to isotropic hardening, which is assumed to be deterministic (although a slight dispersion was experimentally observed). f_t is the total porosity expressed as the sum of the growth porosity f_g corresponding to void growth and the effective porosity due to nucleation, f_n:

$$f_t = f_g + f_n \qquad [5.8]$$

q_1, q_2 are material constants. In the present study, the following values were used: $q_1 = 1.5$ and $q_2 = 1.0$. These values are often used in the literature. It is worth

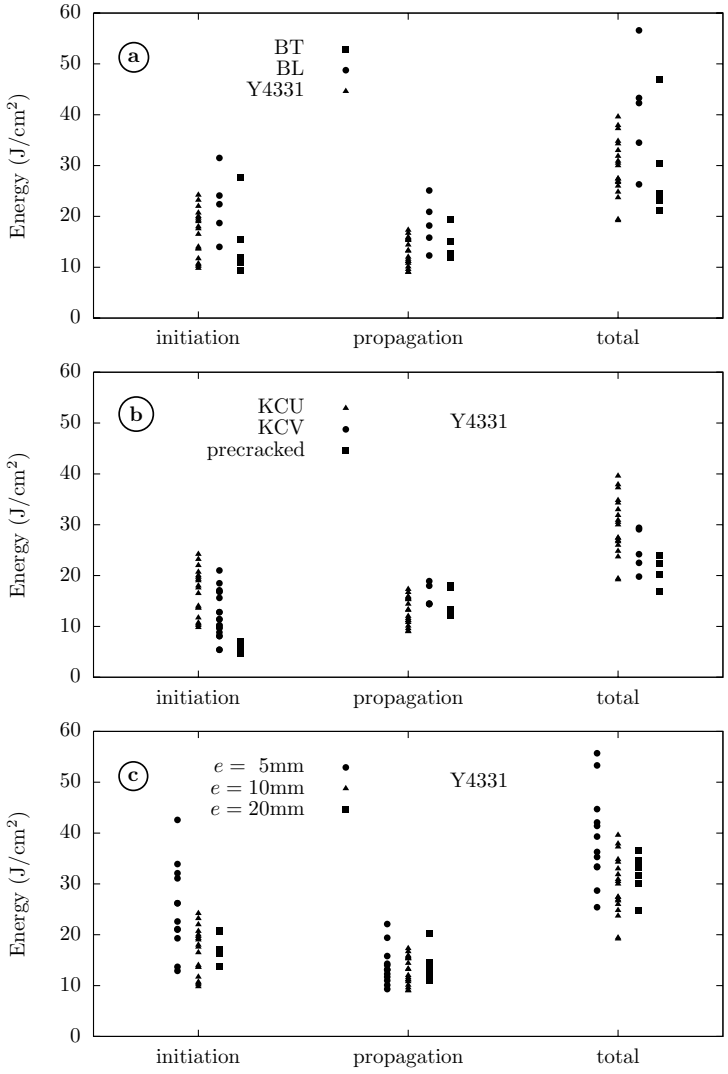

Figure 5.30. *Initiation, propagation and total energies for Charpy specimens: a) U–notched specimens, b) U, V, and precracked specimens for Y4331 material, c) influence of specimen thickness for U-notched specimens (Y4331 material)*

noting that the accelerating function $f_\star$ introduced by Tvergaard and Needleman to account for coalescence of adjacent voids, is not used in the present model. Assuming normality of plastic flow with respect to the yield surface, the plastic strain rate tensor

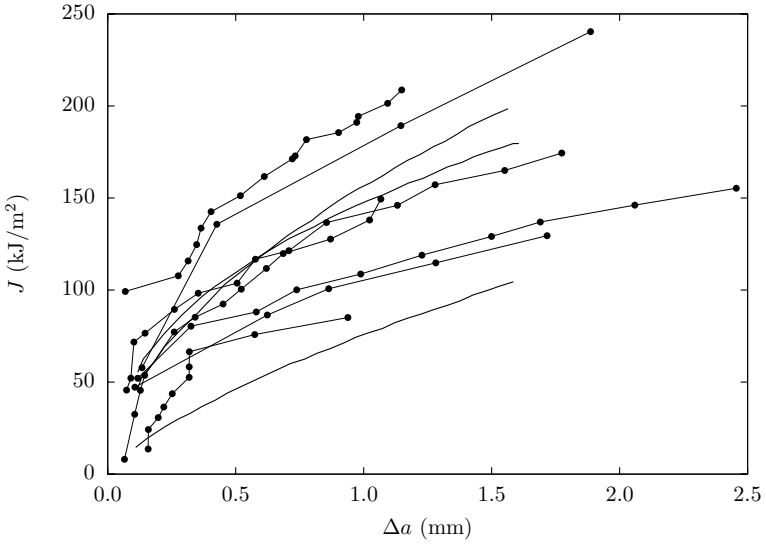

Figure 5.31. *Steel Y4331 tested at 20°C. Experimental $J/\Delta a$ curves (full lines, taken from Devillers [DEV 98]; symbols, taken from Joly [JOL 92a])*

$\underline{\dot{\varepsilon}}_p$ is given by:

$$\underline{\dot{\varepsilon}}_p = (1 - f_g)\,\dot{\lambda}\frac{\partial \Phi}{\partial \underline{\sigma}} \qquad [5.9]$$

where $\underline{\sigma}$ is the stress tensor. The plastic multiplier, $\dot{\lambda}$, is given by the consistency condition $\dot{\Phi} = 0$. The evolution of the matrix plastic strain, p, is obtained writing the equivalence of the microscopic and the macroscopic plastic dissipation [SHI 76]:

$$(1 - f_g)\,\sigma_* \dot{p} = \underline{\sigma} : \underline{\dot{\varepsilon}}_p \qquad [5.10]$$

The evolution of the porosity, f, is obtained writing mass conservation:

$$\dot{f} = (1 - f_g)\,\mathrm{tr}\underline{\dot{\varepsilon}}_p \qquad [5.11]$$

According to the microstructural observations, the evolution of the effective nucleation porosity is given by equation [5.5]. As previously mentioned, it is assumed that a crack has the same mechanical effects as a spherical pore having the same projected surface. This assumption is supported by extensions of the Gurson model to voided materials containing elliptical cavities [GOL 94, GOL 97]. Failure occurs when f_t is equal to $1/q_1 = 66\%$.

The previous equations were implemented in an object oriented finite element (FE) simulation software [FOE 97, BES 98] using a fully implicit integration scheme.

Finite strains are accounted for using a corotational configuration [SID 01] such that the tensor rates should be interpreted as Jauman rates. In the following, updated Lagrangian eight-node quadratic elements with reduced integration (4 Gauss points) are used with either axisymmetric elements (smooth and notched bars) or plane strain elements (Charpy and CT specimens). It is well known that in the case of damaging materials, FE calculations strongly depend on the mesh size [SAA 86, LIU 94, DOG 95]. This can be solved either by using non-local continuum damage mechanics [BAZ 88] or by fixing a mesh size, which is then considered as a material parameter [XIA 95, GUL 00]. Note that in both cases, it is necessary to determine a material characteristic length. In the following, all calculations were performed with initially square elements whose size h is equal to 250 μm.

5.7.2. *Modeling of material heterogenities*

To account for random crack nucleation and clusters, the material is represented as a 2D square grid. A value for A_n is assigned to each square according to a statistical distribution. A FE mesh is then superposed to this grid as depicted in Figure 5.32. Each Gauss point corresponds to a grid cell and a given value. The grid size λ is equal to 1 mm (mean austenite grain size). As a 2D random grid is used, the different zones are then modeled as rings (axisymmetric case) or bars (plane strain case). Heterogenities are, therefore, modeled using a characteristic length (grid size) and a statistical distribution. The following values were used for A_n:

	$\langle A_n \rangle$	range
Y4331	0.6	0.1...1.0
BL	0.3	0.1...0.6
BT	0.3	0.1...0.6

The relative dispersion on A_n was calculated based on the local damage rate measured in the clusters. The experimental distribution laws were given in [DEV 97, DEV 98]. A limited number of compression tests were carried out to finely tune the average value $\langle A_n \rangle$ as damage was not observed during those tests. It should be outlined that due to the high crack density, stresses in compression are significantly higher than in tension [DEV 98].

5.7.3. *Role of heterogenities*

Simulations of notched tensile bars (NT_{10}) were carried out to investigate the effect of damage nucleation rate heterogenities on ductile failure. Using data relative to material Y4331, computations assuming a uniform crack nucleation rate were compared with computations done with the experimentally observed distribution.

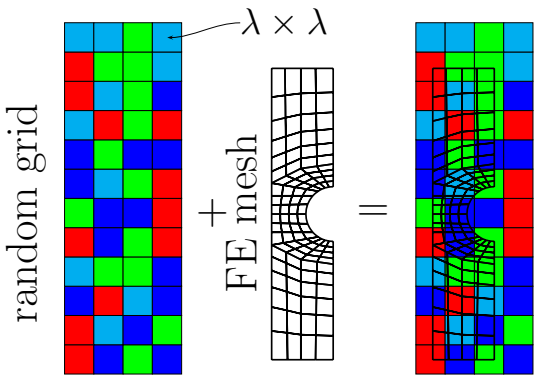

Figure 5.32. *Schematic representation showing how a random value is attributed to each Gauss point of a mesh. The position of each Gauss point in the grid is used to determine the value of the random parameter*

Figure 5.33 shows load-displacement curves computed for homogenous nucleation rates: $A_n = 0.6$ (average value) and $A_n = 1.0$ (maximum value). Simulation with the minimum value ($A_n = 0.1$) largely overestimates ductility. Using $A_n = 0.6$ still overestimates ductility but enables the behavior of the structure to be correctly described; on the other hand, using $A_n = 1.0$ leads to an underestimation of the load and to a good evaluation of the average ductility. Figure 5.33 also shows results obtained for different random drawings which enables representation of the experiments: overall behavior, ductility and dispersion (see also Figure 5.27). Illustrations of damage distribution in the notched zone before rupture are also shown. Uniform distribution produces a flat fracture surface whereas taking into account heterogenities enables the production of a "wavy" fracture surface, which is qualitatively in agreement with experimental observations.

The comparison of results obtained with the average value of A_n and random distributions (having the same mean value) shows that heterogenities only slightly affect the material's behavior but greatly reduce its ductility. One consequence of this observation is that homogenization techniques can be used to predict the behavior of heterogenous materials but should be questioned when trying to predict failure.

5.7.4. *Modeling size effect*

As previously mentioned, the mesh size has to be considered as a material parameter. When modeling size effects, samples of different sizes must be meshed

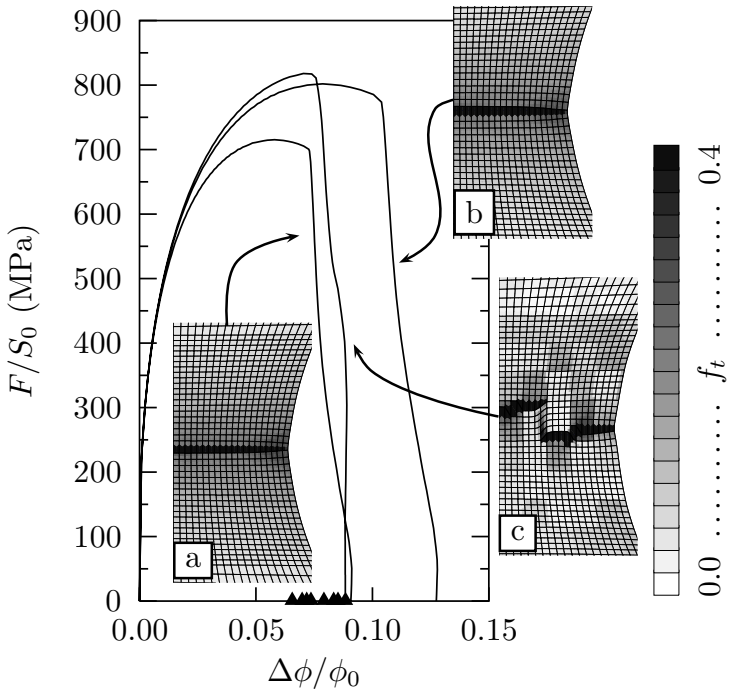

Figure 5.33. *Notched bar (NT_{10}): a) Homogenous with $A_n = 1.0$, b) Homogenous with $A_n = 0.6$, c) Heterogenous. Gray level contours show the values of f_t at Gauss points. Solid symbols on the x–axis indicate simulated strains to failure for other specimens computed with random values for A_n. (ϕ_0: Minimum initial specimen diameter, $\Delta\phi$: diameter variation, F: force, S_0: initial minimum cross-section)*

using a constant element size so that fewer elements are used in the case of smaller samples [DEV 97, DEC 97]. The characteristic length of the microstructure λ (Figure 5.32) is also kept constant. An example of the procedure is given in Figure 5.34. Square microstructures ($n \times n$ grains) have been computed to evidence the size effect. Each grain is meshed using four plane strain elements. Results for $n = 1 \ldots 10$ show that both the mean value and scatter decrease with increasing specimen size.

5.7.5. *Comparison with experimental results*

Figure 5.35a compares the simulated and experimental strains to failure, $\bar{\varepsilon}_R$, for smooth and notched bars having different notch radii. In all cases, the initial minimum

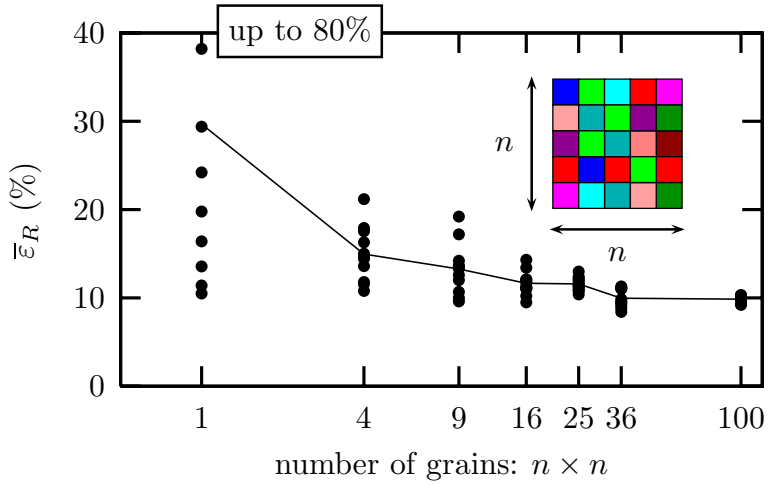

Figure 5.34. *Simulation of size effects*

diameter, ϕ_0, was 10 mm. It is observed that the proposed model is able to predict the average ductilies and to give a good estimation of the experimental dispersion. As the damage mechanism is essentially strain controlled, the ductilities depend less strongly on stress triaxiality than in the case of void growth controlled rupture. In particular, average ductilities for smooth tensile bars are equal to those observed on NT_{10} notched bars. However, dispersion is reduced. This is related to a size effect as the deformed volume in a smooth bar is larger than in a notched bar having the same initial diameter. The model is able to account for this effect.

Figure 5.35b compares the simulated and experimental strains to failure in the case of homothetic NT_{10} notched bars. Size effects, consisting of both the decrease of scatter and the decrease of average values as the specimen size increases, are well represented. Predictions appear to be better for large specimens. In all cases, simulations tend to underestimate the actual scatter. This is probably due to the fact that 3D calculations are needed to fully represent the actual nature of the heterogenities.

Results for Charpy specimens are reported in Figure 5.36a and b. Experimental and simulated crack initiation energies (as defined on Figure 5.29) are compared for U and V-notched samples. 2D simulations cannot model the effect of varying the specimen thickness, but appear to give a good approximation of both mean value and scatter for specimens having a 10 mm thickness. Crack propagation energy is plotted as a function of crack area in Figure 5.36b. In order to obtain the experimental data points, several U-notched samples with a thickness of 10 mm, were used. The tests

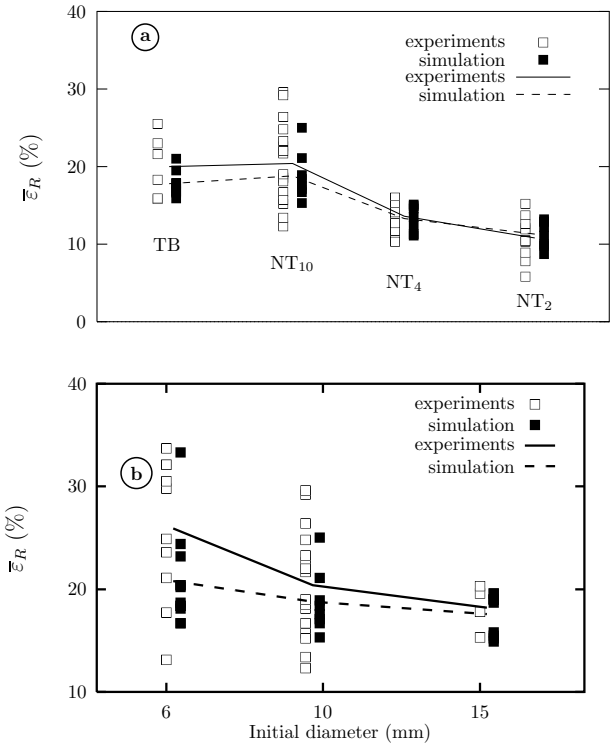

Figure 5.35. *Comparison of experiment and simulated ductilities (material Y4331). Average values are represented by lines. a) Geometry effect, b) Size effect*

were stopped after initiation. The crack surface was then oxidized (400°C, 3 hours) to mark the crack front. The specimens were then fully fractured in order to measure the crack surface. Simulations were performed assuming a constant value for $A_n = 0.6$ as it was shown (Figure 5.30) that the propagation energy was independent on the specimen type (U or V) and specimen thickness. Comparison of experiments and simulation (Figure 5.36b) validates this hypothesis.

C(T) specimens were computed using a random distribution of nucleation rates. The crack extension Δa and the load-displacement curves were computed and subsequently used to compute the J-integral according to the ASTM E 813–89 standard. In particular, experimental and simulated J-Δa curves were adjusted using the following expression:

$$J = C\,(\Delta a)^n \qquad [5.12]$$

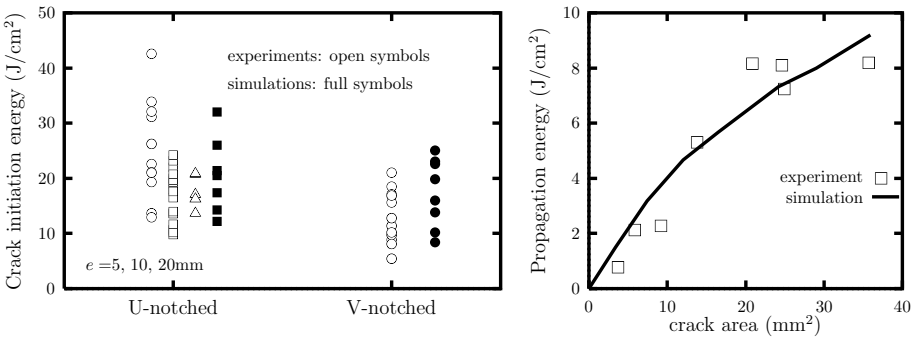

Figure 5.36. *a) Crack initiation energy for U ($e = 5$,10,20 mm) and V ($e = 10$ mm) samples, b) crack propagation energy as a function of the crack area*

These adjustments are reported in Figure 5.37 for five different simulations and compared with the experimental range (shaded area). It can be noticed that both values of J at initiation (i.e. $J_{0.2}$) and the tearing modulus dJ/da are correctly represented. In particular, the present model accounts for the fact that initiation leads to more dispersion on initiation ($J_{0.2\text{mm}}$) than on propagation (dJ/da). The experimental relative dispersion (defined as the ratio of the standard deviation over the average value) on $J_{0.2\text{mm}}$ is equal to 40% whereas it decreases to 30% for dJ/da. Simulated values are 25 and 19%, respectively. Once again, the simulation underestimates dispersion.

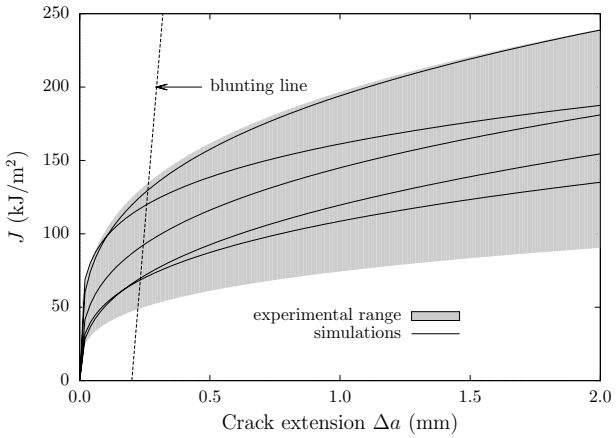

Figure 5.37. *Simulation of C(T) specimens. Material Y4331*

5.8. Conclusion

In this chapter, the so-called 475°C thermal embrittlement of cast DSS was presented. The main cause for the decrease of mechanical properties (i.e. impact resistance and toughness) is the embrittlement of ferrite when the material is aged in a temperature range between 300 and 500°C. Ferrite becomes brittle because of the formation of nanometric α' "particles" due to a spinodal decomposition of the Fe/Cr solid solution. This decomposition leads to a significant strengthening of the ferrite so that critical cleavage stresses can be reached locally. However ferrite embrittlement is deleterious if the ferrite content is high enough (i.e. larger than 20%) so that embrittlement of the duplex steel can be prevented if the ferrite content is controlled. Damage by ferrite cleavage is highly heterogenous in the material as the damage rate depends on the relative orientation of austenite domains with respect to the macroscopic loading. As the microstructure is relatively coarse, this leads to a large scatter of mechanical properties measured on laboratory size specimens. A scale effect is also observed. Models including plastic hardening and damage growth can be proposed to represent the fracture behavior of these materials after aging taking into account scatter and scale effects.

5.9. References

[ALE 04] J.M. ALEGRE AND F. GUTIÉRREZ-SOLANA, "A Gurson-Tvergaard based model to simulate the fracture of aged duplex stainless steels," *Fatigue and Fract. Engng Mater. Struct.*, vol. 27, 1171–1182, 2004.

[AUG 90] P. AUGER, F. DANOIX, A. MENAND, S. BONNET, J. BOURGOIN AND M. GUTTMANN, "Atom probe and transmission electron microscopy study of aging of cast duplex stainless steel," *Materials Sci. Technol.*, vol. 6, n. 3, 301–313, 1990.

[BAN 42] G. BANDEL AND W. TOFAUTE, "Die Versprödung von hochlegierten Chromstählen im temperaturgebiet um 500°C," *Archiv für das Eisenhütttenwesen*, vol. 15, n. 7, 307–320, 1942.

[BAV 90] J.C. BAVAY, "Aciers inoxydables austénitiques," Chapter 16 in B. BAROUX, G. BÉRANGER P. LACOMBE, ed, *Les Aciers Inoxydables*, Les Editions de Physique, p. 565–610, 1990.

[BAZ 88] Z.P. BAZANT AND G. PIJAUDIER-CABOT, "Non local continuum damage. localization, instability and convergence," *J. Appl. Mech.*, vol. 55, 287–294, 1988.

[BEC 88] R. BECKER, A. NEEDLEMAN, O. RICHMOND AND V. TVERGAARD, "Void growth and failure in notched bars," *J. Mech. Phys. Solids*, vol. 36, 317–351, 1988.

[BER 81] F.M. BEREMIN, "Cavity formation from inclusions in ductile fracture of A508 steel," *Met. Trans.*, vol. 12A, 723–731, 1981.

[BER 91] S. BERNHARDSSON, "The corrosion resistance of duplex stainless steels," In J. CHARLES AND S. BERNHARDSSON, eds, *Proceedings of Duplex Stainless Steels 91, Beaune*, vol. 1, Les Editions de Physique, p. 185–210, 1991.

[BES 98] J. BESSON, R. LE RICHE, R. FOERCH AND G. CAILLETAUD, "Application of object-oriented programming techniques to the finite element method. Part II – application to material behaviors," *Revue Européenne des éléments finis*, vol. 7, 567–588, 1998.

[BES 00] J. BESSON, L DEVILLERS-GUERVILLE AND A. PINEAU, "Modeling of scatter and size effect in ductile fracture: application to thermal embrittlement of duplex stainless steels," *Engng Fract. Mech.*, vol. 67, n. 2, 169–190, 2000.

[BON 90] S. BONNET, J. BOURGOIN, J. CHAMPREDONDE, D. GUTTMANN AND M. GUTTMANN, "Relationship between evolution of mechanical properties of various cast duplex stainless steels and metallurgical and aging parameters: outline of current EDF programmes," *Mater. Sci. Technol.*, vol. 6, n. 3, 221–229, 1990.

[BRO 90a] J.E. BROWN, A. CEREZO, T.J. GODFREY, M.G. HETHERINGTON AND G.D. SMITH, "Quantitative atom probe analysis of spinodal reaction in ferrite phase of duplex stainless steel," *Mater. Sci. Technol.*, vol. 6, n. 3, 293–300, 1990.

[BRO 90b] J.E. BROWN, M.G. HETHERINGTON, G.D. SMITH AND P.H. PUMPHREY, "The thermal ageing of alloys modelling the ferrite phase in stainless steel castings," in *Fatigue, Degradation and Fracture – 1990, The 1990 Pressure Vessels and Piping Conference*, Nashville, Tennessee, p. 175–185, 1990.

[BRO 91] J.A. BROOKS AND A.W. THOMPSON, "Microstructural development and solidification cracking susceptibility of austenitic stainless steels welds," *Int. Mater. Rev.*, vol. 36, n. 1, 16–44, 1991.

[BUG 00] S. BUGAT, Comportement et endommagement des aciers austéno–ferritiques vieillis: une approche micromécanique, PhD thesis, Ecole des Mines de Paris, 2000.

[BUG 01] S. BUGAT, J. BESSON, A.-F. GOURGUES, F. N'GUYEN AND A. PINEAU, "Microstructure and damage initiation in duplex stainless steels," *Mater. Sci. Engng A*, vol. A317, 32–36, 2001.

[CAH 62] J.W. CAHN, "On spinodal decomposition in cubic crystals," *Acta Metall.*, vol. 10, 179–183, 1962.

[CAH 68] J.W. CAHN, "Spinodal decomposition," *Trans. Metall. Soc. AIME*, vol. 242, 166–180, 1968.

[CAL 04] V. CALONNE, A.F. GOURGUES AND A. PINEAU, "Fatigue crack propagation in cast duplex steels: thermal ageing and microstructural effects," *Fatigue and Fract. Engng Mater. Struct.*, vol. 27, 31–43, 2004.

[CAS 90] R. CASTRO, "Historique des aciers inoxydables," Chapter 1 in B. BAROUX AND G. BÉRANGER P. LACOMBE, ed, *Les Aciers Inoxydables*, Les Editions de Physique, p. 1–9, 1990.

[CHA 91] J. CHARLES, "The duplex stainless steels: materials to meet your needs." In J. CHARLES AND S. BERNHARDSSON, eds, *Proceedings of Duplex Stainless Steels 91, Beaune*, vol. 1, Les Editions de Physique, p. 3–48. 1991.

[CHA 94] J. CHARLES, "Structure and mechanical properties of duplex stainless steels." In *Proceedings of Duplex Stainless Steels 94, Glasgow*, vol. 1, Materials and Properties, Abington Publishing, 1994.

[CHO 91] O.K. CHOPRA, *Estimation of Fracture Toughness of Cast Stainless Steels During Thermal Aging in LWR Systems*. Technical report, Gov. Res. Announc. Index, NUREG/CR-4513/XAB, 1991.

[CHU 88] H.M. CHUNG AND O.K. CHOPRA, "Kinetics and mechanism of thermal aging embrittlement of duplex stainless steels." In J.R. WEEKS AND G.J. THEUS, eds, *Environmental Degradation of Materials in Nuclear Power Systems – Water Reactors*, The Metallurgical Society, p. 359–370, 1988.

[CHU 91] H.M. CHUNG AND O.K. CHOPRA, "Characterization of duplex stainless steels by TEM, SANS and APFIM techniques." In W. ALTERGOTT AND E. HENNEKE, eds, *Characterization of Advanced Materials, Monterey*, Plenum Press, New York, p. 123–147, 1991.

[CHU 92] H.M. CHUNG, "Aging and life prediction of cast duplex stainless steel components," *Int. J. Pressure Vessels Piping*, vol. 50, 179–213, 1992.

[COU 76] M. COURTNALL AND F.B. PICKERING, "The effect of alloying on the 485°C embrittlement," *Met. Sci.*, vol. 10, 273–276, 1976.

[DEC 97] K. DECAMP, L. BAUVINEAU, J. BESSON AND A. PINEAU, "Size and geometry effects on ductile rupture of notched bars in a C-Mn steel: experiments and modelling," *Int. J. Frac.*, vol. 88, n. 1, 1–18, 1997.

[DEL 60] W.T. DELONG, "A modified phase diagram for stainless steel weld metals," *Met. Prog.*, p. 98–100, 1960.

[DES 90] A. DESESTRET AND J. CHARLES, "Les aciers inoxydables austéno-ferritiques." Chapter 18 in B. BAROUX AND G. BÉRANGER P. LACOMBE, ed, *Les Aciers Inoxydables*, Les Editions de Physique, p. 631–678, 1990.

[DEV 97] L. DEVILLERS-GUERVILLE, J. BESSON AND A. PINEAU, "Notch fracture toughness of a cast duplex stainless steel: modelling of experimental scatter and size effect," *Nucl. Eng. Design*, vol. 168, 211–225, 1997.

[DEV 98] L. DEVILLERS-GUERVILLE, Rupture d'aciers inoxydables austéno–ferritiques moulés, fragilisés par vieillissement à 350–400°C: Aspects microstructuraux — Simulation numérique de la dispersion et des effets d'échelle, PhD thesis, Ecole des Mines de Paris, 1998.

[DOG 95] I. DOGHRI, "Numerical implementation and analysis of a class of metal plasticity models coupled with ductile damage," *Int. J. Numer. Meth. Engng*, vol. 38, n. 20, 3403–3431, 1995.

[DUV 92] C. DUVAL, Contribution à l'étude de l'endommagement des aciers austéno-ferritiques vieillis, PhD thesis, Ecole Centrale de Paris, 1992.

[FIS 53] R.M. FISHER, E.J. DULIS AND K.G. CARROLL, "Identification of the precipitate accompanying 885°F embrittlement in chromium steels," *J. Met.*, 690–695, 1953.

[FOE 97] R. FOERCH, J. BESSON, G. CAILLETAUD AND P. PILVIN, "Polymorphic constitutive equations in finite element codes," *Comp. Meth. Appl. Mech. Engng*, vol. 141, 355–372, 1997.

[GOL 92] I.S. GOLOVIN, V.I. SARRAK AND S.O. SUVOROVA, "Influence of carbon and nitrogen on solid solution decay and 475°C embrittlement of high chromium ferritic steels," *Met. Trans. A*, vol. 23A, 2567–2579, 1992.

[GOL 94] M. GOLOGANU, J.B. LEBLOND AND J. DEVAUX, "Approximate models for ductile metals containing non-spherical voids – case of axisymmetric oblate ellipsoidal cavities," *J. Engng Mater. Technol.*, vol. 116, 290–297, 1994.

[GOL 97] M. GOLOGANU, Étude de quelques problèmes de rupture ductile des métaux, PhD thesis, University of Paris 6, 1997.

[GUI 67] P. GUIRALDENQ, "Action alphagène et gammagène des principaux éléments d'addition dans les aciers inoxydables nickel-chrome dérivés du type 18-10," *Mém. Sci. Rev. Métall.*, vol. LXIV, n. 11, 907–939, 1967.

[GUL 00] A.S. GULLERUD, X. GAO, R.H. DODDS JR AND R. HAJ-ALI, "Simulation of ductile crack growth using computational cells: numerical aspects," *Engng Fract. Mech.*, vol. 66, 65–92, 2000.

[GUR 77] A.L. GURSON, "Continuum theory of ductile rupture by void nucleation and growth: Part I – yield criteria and flow rules for porous ductile media," *J. Engng Mater. Technol.*, vol. 99, 2–15, 1977.

[GUT 91] M. GUTTMANN, "Intermediate temperature aging of duplex stainless steels." A review. In J. CHARLES AND S. BERNHARDSSON, eds, *Proceedings of Duplex Stainless Steels 91, Beaune*, vol. 1, Les Editions de Physique, p. 79–92, 1991.

[HAY 90] F.H. HAYES, M.G. HETHERINGTON AND R.D. LONGBOTTOM, "Thermodynamics of duplex stainless steels," *Mater. Sci. Technol.*, vol. 6, 263–272, 1990.

[HEN 79] A. HENDRY, S.F. MAZUR AND K.H. JACK, "Influence of nitrogen on 475°C embrittlement of high-chromium ferritic steels," *Met. Sci.*, vol. 13, 482–488, 1979.

[HIL 61] M. HILLERT, "A solid-solution model for inhomogeneous systems," *Acta Metall.*, vol. 9, 525–534, 1961.

[JOL 90] P. JOLY, R. COZAR AND A. PINEAU, "Effect of crystallographic orientat ion of austenite on the formation of cleavage cracks in ferrite in an aged duplex strainless steel," *Scripta Metall. Mater.*, vol. 24, 2235–2240, 1990.

[JOL 91] P. JOLY AND A. PINEAU, "Local versus global approaches to elastic-plastic fracture mechanics. Application to ferritic steels and a cast duplex stainless steel." In *Defect Assessment in Components – Fundamentals and Applications*, Mechanical Engineering Publications, London, p. 381–414, 1991.

[JOL 92a] P. JOLY, Etude de la rupture d'aciers inoxydables austéno–ferritiques moulés, fragilisés par vieillissement à 400°C, PhD thesis, Ecole des Mines de Paris, 1992.

[JOL 92b] P. JOLY, Y. MEYZAUD AND A. PINEAU, "Micromechanisms of fracture of an aged duplex stainless steel containing a brittle and a ductile phase: development of a local criterion of fracture." In J. GIOVANOLA, ed, *Advances in Fracture/Damage Models for the Analysis of Engineering Problems*, ASME, p. 151–180, 1992.

[JOL 95] P. JOLY AND A. PINEAU, "Modelling of the effect of thermal aging of duplex stainless steels on their fracture toughness," *Scand. J. Metall.*, vol. 24, n. 5-6, 226–236, 1995.

[KAT 81] M. KATO, "Hardening by spinodally modulated structure in b.c.c. alloys," *Acta Metall.*, vol. 29, 79–87, 1981.

[KIE 84] R. KIESSLING, "31st Hatfield Memorial Lecture: Stainless steels – materials in competition," *Met. Technol.*, vol. 11, 169–180, 1984.

[LAG 67a] R. LAGNEBORG, "Deformation in an iron-30% chromium alloy aged at 475°C," *Acta Metall.*, vol. 15, 1737–1745, 1967.

[LAG 67b] R. LAGNEBORG, "Metallography of the 475°C embrittlement in an iron-30% chromium alloy," *Trans. ASM*, vol. 60, 67–78, 1967.

[LAG 67c] R. LAGNEBORG, "Yielding and fracture of fe-30%cr alloys subjected to 475°C embrittlement," *Acta Polytec. Scand.*, vol. 62, 1–40, 1967.

[LEG 81] M.T. LEGER, "Prévision et contrôle du taux de ferrite dans les moulages en acier inoxydable," *Fonderie – Fondeur d'aujourd'hui*, vol. 10, 15–23, 1981.

[LEG 88] M.T. LEGER, P. DEGAS, J.C PLUMEREZ, P. OULD AND Y. MEYZAUD, "Caractéristiques physiques d'aciers inoxydables austénitiques moulés pour réacteurs à eau pressurisée," *Fonderie – Fondeur d'aujourd'hui*, vol. 78, 31–49, 1988.

[LEG 93] M.T. LEGER AND R. FIGUET, "Performances d'aciers moulés inoxydables austénoferritiques élaborés au four à induction," *Fonderie – Fondeur d'aujourd'hui*, vol. 128, 25–38, 1993.

[LIU 94] Y. LIU, S. MURAKAMI AND Y. KANAGAWA, "Mesh-dependence and stress singularity in finite element analysis of creep crack growth by continuum damage mechanics approach," *Eur. J. Mech.*, vol. 13A, n. 3, 395–417, 1994.

[LON 94] R.D. LONGBOTTOM AND F.J. HAYES, "Effects of variations in alloying element content and temperature on the austenite-ferrite phase balance in duplex stainless steels." In *Proceedings of Duplex Stainless Steels 94*, Glasgow, vol. 1, Materials and Properties, Abington Publishing, 1994.

[MAR 96a] E. MARQUIS AND G. COSSARD, *Fragilisation d'un Acier Austéno-Ferritique*. Technical report, Rapport de stage d'option de 2éme année ENSMP, 1996.

[MAR 96b] T.J. MARROW, "The fracture mechanism in 475°C embrittled ferritic stainless steels," *Fatigue and Fract. Engng Mater. Struct.*, vol. 19, n. 7, 919–933, 1996.

[MAR 96c] T.J. MARROW AND C. HARRIS, "The fracture mechanism of 475°C embrittlement in a duplex stainless steel," *Fatigue and Fract. Engng Mater. Struct.*, vol. 19, n. 7, 935–947, 1996.

[MAR 97] T.J. MARROW AND N. BURY, "The brittle fracture of 475°C embrittled cast duplex stainless steel," *Fatigue and Fract. Engng Mater. Struct.*, vol. 20, n. 4, 565–571, 1997.

[MAS 92] J.P. MASSOUD, J.C. VAN DUYSEN AND G. ZACHARIE, Vieillissement Thermique Entre 300 et 400°C d'Aciers Inoxydables Austéno-ferritiques Moulés. Technical report, Collection de notes internes de la Direction des Etudes et Recherches EDF, N° 93, NB00024, 1992.

[MCC 71] F. A. MCCLINTOCK, *Plasticity Aspects of Fracture*, Academic Press, p. 47–218, 1971.

[MEY 88] Y. MEYZAUD, P. OULD, P. BALLADON, M. BETHMONT AND P. SOULAT, "Earing resistance of aged cast austenitic stainless steels." In *Proceedings of the International ENS/ANS Conference on Thermal Reactor Safety, NUCSAFE 88*, Avignon, vol. 1, p. 397–406, 1988.

[MIL 95] M.K. MILLER, J.M. HYDE, M.G. HETHERINGTON, A. CEREZO, G.D. SMITH AND C.M. ELLIOTT, "Spinodal decomposition in Fe-Cr alloys: experimental study at the atomic level and comparison with computer models (I, II and III)," *Acta Metall. Mater.*, vol. 43, n. 9, 3385–3426, 1995.

[PAR 96] K.H. PARK, J.C. LASALLE, L.H. SCHWARTZ AND M. KATO, "Mechanical properties of spinodally decomposed Fe-30wt%Cr alloys: yield strength and aging embrittlement," *Acta Metall.*, vol. 34, n. 9, 1853–1865, 1996.

[PIC 79] C. PICHARD AND G. NECTOUX, "Aspects métallurgiques dans la fabrication des pièces moulées pour l'énergie nucléaire," *Hommes et Fonderie*, 1979.

[RAG 94] V. RAGHAVAN AND D.P. ANTIA, "The chromium equivalents of selected elements in austenitic stainless steels," *Met. Trans. A*, vol. 25A, 2675–2681, 1994.

[RIC 69] J.R. RICE AND D.M. TRACEY, "On the ductile enlargement of voids in triaxial stress fields," *J. Mech. Phys. Solids*, vol. 17, 201–217, 1969.

[RIE 41] G. RIEDRICH AND F. LOIB, "Versprödung chromreicher Stähle im Temperaturgebiet von 300 bis 600°C," *Archiv für das Eisenhüttenwesen*, vol. 15, n. 4, 175–182, 1941.

[RIV 80] V.G. RIVLIN AND G.V. RAYNOR, "Phase equilibria in iron ternary alloys I: Critical evaluation of constitution of chromium-iron-nickel system," *Int. Metall. Rev.*, vol. 25, 21–38, 1980.

[ROU 90] M. ROUBY AND P. BLANCHARD, "Propriétés physiques et mécaniques des aciers et alliages inoxydables." Chapter 4 in B. BAROUX AND G. BÉRANGER P. LACOMBE, ed, *Les Aciers Inoxydables*, Les Editions de Physique, p. 565–610, 1990.

[SAA 86] K. SAANOUNI, J.-L. CHABOCHE AND C. BATHIAS, "On the creep crack growth prediction by a local approach," *Engng Fract. Mech.*, vol. 25, n. 5/6, 677–691, 1986.

[SAN 96] L. SANCHEZ ARAMBARU, Fragilizacion por envejecimiento a baja temperatura en aceros inoxidables austenoferriticos, PhD thesis, University of Cantabria, Santander, 1996.

[SAN 02] L. SANCHEZ AND F. GUTIERREZ-SOLANA, "Correlation between impact resistance and fracture toughness in aged duplex stainless steels." In D. FRANÇOIS AND A. PINEAU, eds, *From Charpy to Present Impact Testing*, ESIS Publication 30, p. 87–94, 2002.

[SCH 49] A.L. SCHAEFFLER, "Constitution diagram for stainless steel welds, quoted by Desestret and Charles, 1990," *Met. Progrs*, vol. 56, n. 11, 680–680B, 1949.

[SHI 76] S. SHIMA AND M. OYANE, "Plasticity theory for porous metals," *Int. J. Mech. Sci.*, vol. 18, 285–291, 1976.

[SID 01] F. SIDOROFF AND A. DOGUI, "Some issues about anisotropic elastic-plastic models at finite strain," *Int. J. Solids Struct.*, vol. 38, 9569–9578, 2001.

[SLA 84] G. SLAMA, P. PETREQUIN AND T. MAGER, "Effect of ageing on mechanical properties of austenitic stainless steel castings and welds." In L.E. STEELE K.E. STAHLKOPF, ed, *Light Water Reactor Structural Integrity*, p. 211–240, 1984.

[SUU 79] N. SUUTALA, T. TAKALO AND T. MOISIO, "The relationship between solidification and microstructure in austenitic and austenitic-ferritic stainless steel welds," *Met. Trans. A*, 10A:512–514, 1979.

[SUU 83] N. SUUTALA, "Effect of solidification conditions on the solidification mode in austenitic stainless steels," *Met. Trans. A*, vol. 14A, 191–197, 1983.

[TRA 82] A. TRAUTWEIN AND W. GYSEL, "Influence of long-time aging of CF8 and CF8M cast steel at temperatures between 300 and 500°C on impact toughness and structural properties." In A.S. MELILLI V.G. BEHAL, ed, *Stainless Steel Castings*, ASTM–STP 756, American Society for Testing and Materials, p. 165–189, 1982.

[TVE 84] V. TVERGAARD AND A. NEEDLEMAN, "Analysis of the cup–cone fracture in a round tensile bar," *Acta Metall.*, vol. 32, 157–169, 1984.

[TVE 90] V. TVERGAARD, "Material failure by void growth to coalescence," *Adv. Appl. Mech.*, vol. 27, 83–151, 1990.

[VER 95] B. VERHAEGHE, Etude microstructurale des modes de déformation et de rupture d'un acier austénoferritique vieilli thermiquement, PhD thesis, Institut National Polytechnique de Grenoble, 1995.

[WIL 57] R.O. WILLIAMS, "Theory of precipitation hardening: isotropically-strained system," *Acta Metall.*, vol. 5, 385–392, 1957.

[WIL 58] R.O. WILLIAMS, "Further studies of the iron-chromium system," *Trans. Met. Soc. AIME*, vol. 212, 497–502, 1958.

[XIA 95] L. XIA, C.F. SHIH AND J.W. HUTCHINSON, "A computational approach to ductile crack growth under large scale yielding conditions," *J. Mech. Phys. Solids*, vol. 43, n. 3, 389–413, 1995.

[ZIN 57] E. ZINGG AND T. GEIGER, "Metallurgische und metallkundliche Problem bei 12 bis 15% Chromstahlguss (quoted by [LEG 1993])," *Schweizer Archiv für angewandte Wissenschaft und Technik*, vol. 23, 71–78, 1957.

Chapter 6

Low-Cycle Fatigue at Room Temperature

6.1. Introduction

Owing to their excellent mechanical and technological properties, i.e. high toughness, as well as very good corrosion resistance, duplex stainless steels (DSSs) are widely used for many structural applications, e.g. in thermal and nuclear power plants and in chemical plants. In such applications, structural materials are often subjected to variable mechanical and/or thermal loading, corresponding to highly variable stress fields, which lead to fatigue damage. In metallic materials, the term "fatigue" includes all microstructural changes occurring under cyclic loading and leading to an integrity lost of the component.

Most of the fatigue failures observed in service are the result of reversed cyclic loading, eventually superimposed to static loading, under atmospheric conditions or under thermal and/or corrosive environment. Fatigue damage proceeds by cyclic plastic deformations, nucleation and coalescence of microcracks and formation and propagation of the final macrocrack independent of the loading mode (stress- or strain-control) and of the environmental conditions. The fatigue strength (FS) of a material is macroscopically characterized by the fatigue life, or number of cycles to failure, as a function of the cyclic loading level.

In high-cycle fatigue (HCF), the cyclic plastic deformation is concentrated in only some grains in the material. Conversely, in low-cycle fatigue (LCF), a cyclic plastic deformation appears in each grain of the material. At the microscopic scale, the development of specific dislocation structures is associated with cyclic plastic

---

Chapter written by Iris ALVAREZ-ARMAS.

Duplex Stainless Steels Edited by Iris Alvarez-Armas and Suzanne Degallaix-Moreuil

deformation in LCF. At the macroscopic scale, a cyclic hardening and/or softening phase appears at the beginning of cycling, often followed by a stabilization phase, and always followed by a softening phase associated with the propagation of a macrocrack. It is interesting to note that nucleation (the initiation) of microcracks occurs early in the fatigue life, even during the hardening/softening phase. Thus the limit between initiation and propagation phases is not precisely defined.

Usually in HCF the mechanical tests are stress-controlled; conversely, in LCF, they are strain-controlled.

This chapter and the following one are essentially devoted to LCF behavior under uniaxial and multiaxial loading at room temperature of DSSs. Chapters 8 and 9 describe the analysis of strain partitioning between ferrite and austenite phases during LCF and the macro and micromodeling of monotonic and cyclic mechanical behavior at room temperature (RT), respectively. Finally, Chapter 10 will be devoted to LCF behavior of DSS at intermediate temperature.

6.2. Cyclic hardening/softening process

In this section, we give some of the most accepted forms of describing cyclic plastic deformation behavior of metals to apply then to a bi-phased steel.

6.2.1. *Basic characteristics of cyclic deformation*

The damage produced by cyclic loading can be traced back to its early stages by observation of the microstructure, by measurement of the mechanical properties and by following the evolving surface relief and later by observing the crack initiation and growth. The early stages of this process comprise the formation and stabilization of a characteristic internal dislocation structure accompanied by initial cyclic hardening or softening. This is followed by the localization of the cyclic plastic strain into bands called persistent slip bands (PSB; Figure 6.1a), running parallel to low index crystallographic planes, which were found to be responsible for the occurrence of extrusions and intrusions on the surface of the fatigued material. It is generally agreed that fatigue cracks are nucleated within PSB (Figures 6.1b and c).

During LCF the surface densities of microcracks are high and often more than 80-90% of the resulting fatigue life consists of the evolution of these microstructurally short cracks, i.e. cracks with sizes of the order of the grain size of the material. Conversely, the last stage, the propagation of a macroscopic crack in a smooth specimen under constant amplitude loading, consumes only a small fraction

of the fatigue life. Thus, in most cases, the period of short crack growth determines the LCF life of a specimen and also of a structural component.

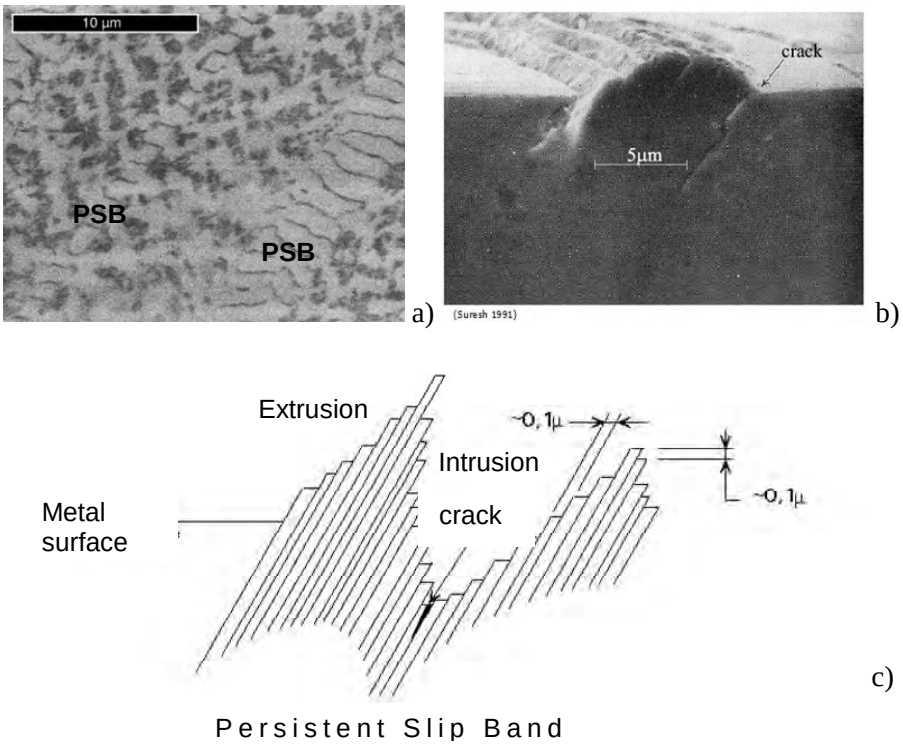

Figure 6.1. *a) Dislocation arrangement characteristic of a PSB structure; b) slip bands with intrusions and extrusions formed on the surface of a grain subjected to cyclic loading [SUR 91]; c) schematic representation of a PSB*

6.2.2. *Analysis and presentation of results*

The study of uniaxial LCF behavior of a metallic material is performed on cylindrical smooth (unnotched) specimens under different cyclic deformation levels. A total or plastic strain controlled test under a cyclic triangular reversed wave leads to a time-dependent response of the material in terms of the stress amplitude. Stress response is monitored during cyclic loading, and the number of cycles to failure is recorded for these tests. A schematic representation of a completely reversed strain controlled test is shown in Figure 6.2.

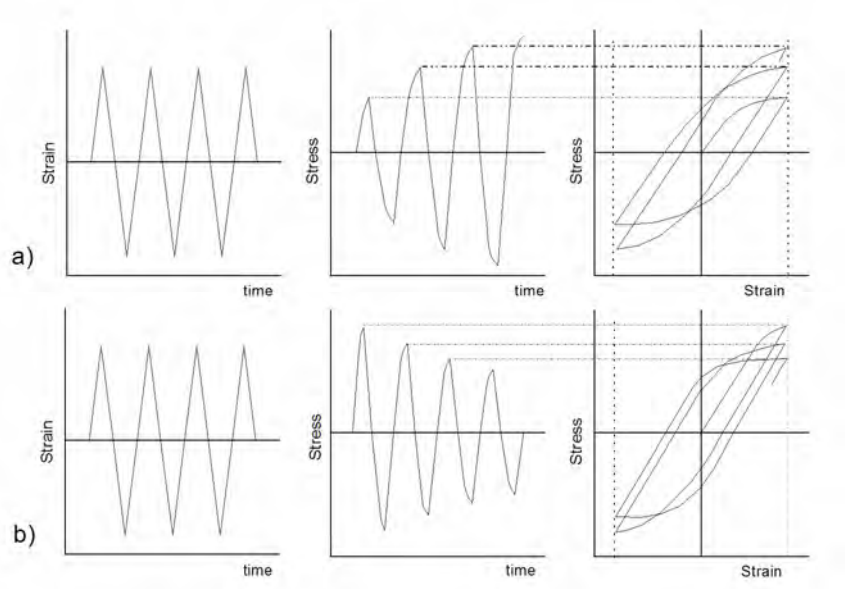

Figure 6.2. *Completely reversed strain controlled tests and two possible stress responses, namely cycle hardening and softening*

LCF corresponds to a sufficiently high strain level for yielding before the maximum strain is reached on each cycle of loading. Stress amplitude usually varies; if it increases, the material is said to cyclically harden, if it decreases, the material is said to cyclically soften. However, this behavior tends to stabilize such that the variation in the stress amplitude is small after an initial period of transient cyclic hardening and/or softening. Once the behavior is stabilized, a closed stress-strain hysteresis loop occurs during each strain cycle. This stabilization of the loop indicates that the stress necessary to attain the given strain amplitude has assumed a constant value that will be reproduced in all subsequent cycles until noticeable specimen cracking develops. At this point the stress range required to achieve a given strain range decreases to reflect the onset of specimen failure.

A stable hysteresis loop is shown schematically in Figure 6.3a to illustrate the important feature of such a graph. The vertical tip-to-tip distance defines the stress range and the horizontal tip-to-tip distance represents the total strain range $\Delta\varepsilon_t$ that consists of elastic and plastic components. The plastic strain range, which is related to dislocation movement, is given by the width of the hysteresis loop measured along the zero-stress abscissa in this case. Another feature of the hysteresis loop is that the E slope of the straight segment (lead reversal regime) is equal to the modulus of elasticity of the material.

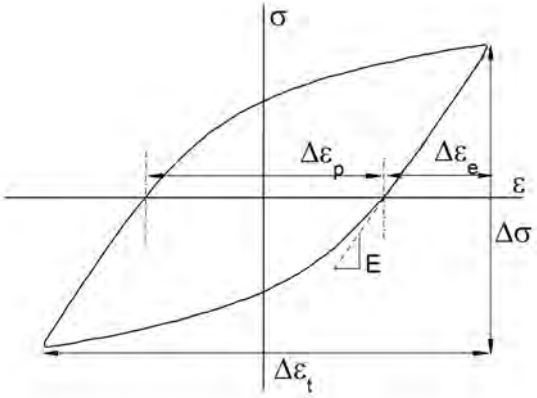

a)

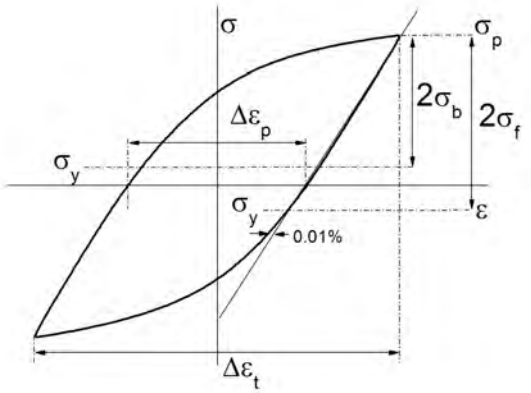

b)

Figure 6.3. *Stabilized hysteresis loop during LCF: a) definition of the parameters; b) flow stress components: the friction stress and the back stress*

Generally, the motion of a dislocation is opposed to short-range barriers, which can be overcome by thermal activation, and to long-range forces from other dislocations. The flow stress consists of two contributions: one is the thermal component, σ^*, and the other is the athermal component σ_G, which is almost independent of temperature apart from the small variations of the shear modulus G with temperature. Thus, according to Seeger [SEG 57]:

$$\sigma = \sigma^* + \sigma_G \quad [6.1]$$

In LCF tests, the applied stress varies between fixed limits. To calculate the components of the flow stress corresponding to the hysteresis loop, the method proposed by Kuhlmann-Wilsdorf and Laird [KUH 79] and Handfield and Dickson [DIC 89] was used. Other methods were proposed in the literature, which are more or less complex [POL 91]. Upon this method, the flow stress obtained from the hysteresis loops is the result of two kinds of resistance to plastic deformation: the friction stress, σ_f, and the back stress, σ_b. The friction stress corresponds to the resistance the dislocations have to overcome to keep moving in the crystalline lattice. The back stress is associated with pile-ups of dislocations that were built after overcoming the friction stress.

This well-known method is illustrated in Figure 6.3b. At the peak stress, the applied stress, σ_p, is the sum of the friction stress and the back stress. On lowering the applied stress, the friction stress will oppose the backward motion of dislocations. Reversed plasticity will be obtained when the applied stress, yield stress, σ_y, aided by the back stress, can overcome the friction stress. The friction stress and the back stress can be simply determined as follows:

$$\sigma_p = \sigma_f + \sigma_b \quad [6.2a]$$

$$\sigma_y = \sigma_f - \sigma_b \quad [6.2b]$$

Information on the kind of obstacles to dislocation movement can be obtained from the measurement of these stresses. Figure 6.3b shows a hysteresis loop on which a straight line is drawn (determined from a least squares fit) coincident with the most linear part of one side of the loop. The value of the yield stress, just as in monotonic tensile tests, is somewhat arbitrarily determined. In the present analysis, σ_y for each hysteresis loop was defined as the stress corresponding to an offset of 0.01 pct plastic strain (indicated in the figure) with the drawn line representing the elastic part of the loop. This analysis was performed on each digitally recorded loop (more than 200 points per loop) by a computer program [ARM 00].

If a series of LCF strain-controlled tests are performed for one material at different constant strain amplitudes, different saturated hysteresis loops will be obtained. The so-called “cyclic stress-strain curve” (CSS curve) is defined by the locus of the tips of the steady-state hysteresis loops as is shown in Figure 6.4. When the material cyclically hardens the CSS curve lies above the corresponding monotonic curve or first quarter of cycle of the LCF test, or below it when the material cyclically softens. The relative position of both curves is characteristic of the accommodation behavior (cyclic hardening/softening) of the material.

The bi-logarithmic diagram of the stress amplitude versus the plastic strain amplitude using data obtained at the tip of the stable hysteresis loop have been found to yield the linear relation:

$$\sigma_a = K'.(\varepsilon_p)^{n'} \qquad [6.3]$$

where *K'* and *n'* are cyclic coefficients, typical values or *n'* are between 0.1 and 0.2. This method of plotting will be recognized as identical to that used in the identification of the strain-hardening coefficients in a monotonic stress-strain curve or on the first quarter of cycle of a LCF test.

The response of a material to cyclic loading is characterized by the above CSS relation and its LCF strength is characterized by the fatigue life in terms of the number of cycles to failure. The test can be performed up to the detection of a crack of a specific dimension, or up to fracture. As the number of cycles necessary to propagate a macrocrack through the whole cross-section and thus to achieve complete fatigue fracture of the small laboratory specimen is low, in most situations, the fatigue life curve does not differ significantly from the macrocrack initiation curve. The propagation of the principal crack corresponds to a loss of strength of the specimen and then, we can define the criterion of fracture as a conventional decrease of the elastic modulus of the tensile part in comparison with that of the compression part. This criterion has been used in the work on uni-axial LCF of DSS.

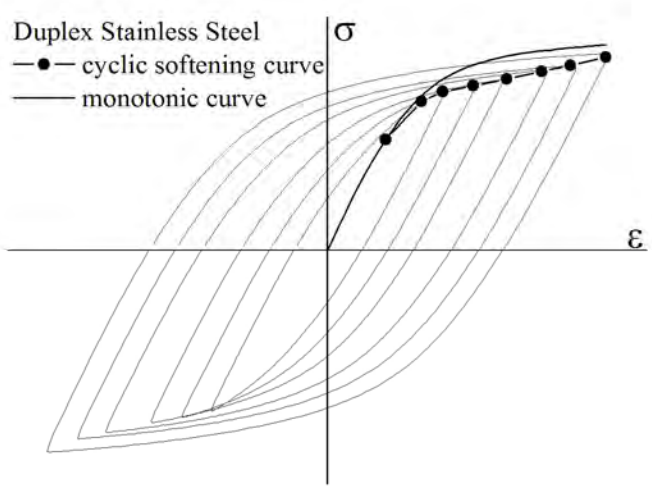

Figure 6.4. *CSS curve of a series of cyclic deformation tests in which the material cyclically softens*

As the shape of the hysteresis loop changes during cycling, the cyclic hardening/softening behavior of the material is often characterized by changes in the stress amplitude and eventually in the plastic strain amplitude if the test is controlled by the total strain range. Figure 6.5 shows the cyclic stress response curve of an austenitic stainless in five different total strain-controlled fatigue tests. According to the applied total strain level, the figure illustrates the path by which the material arrives at the final cyclic flow stress level.

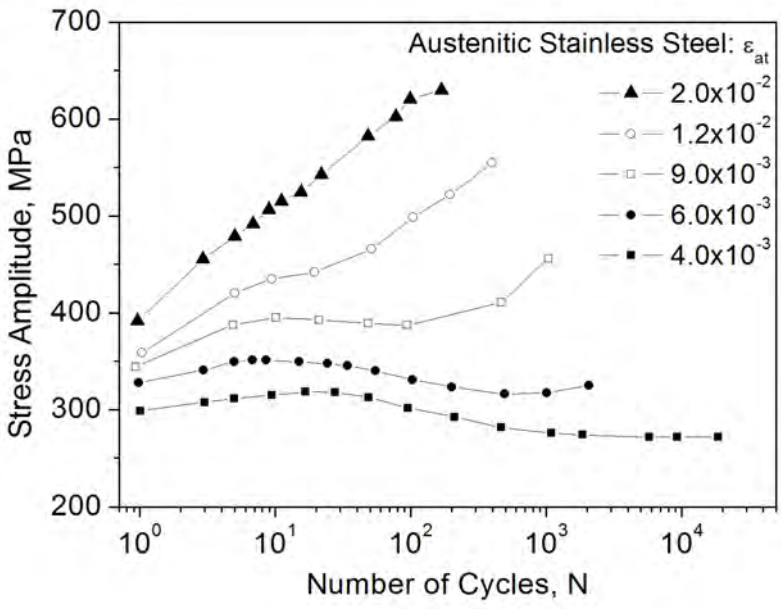

Figure 6.5. *Cyclic stress response curves of the SUS304-HP steel at five different total strain amplitudes at RT [YE 06]*

The studies on body-centered cubic (BCC) materials have revealed different cyclic hardening/softening behavior depending on chemical composition. Low-alloyed ferritic steel is characterized by hardening followed by saturation at high-strain amplitudes, while in the low amplitude, domain cyclic softening was observed [ROV 91] (Figure 6.6a). High-alloyed ferritic steel is characterized by a long-term cyclic softening in a wide domain of amplitudes and a tendency to saturation for the highest strain amplitude [KRU 01] (Figure 6.6b).

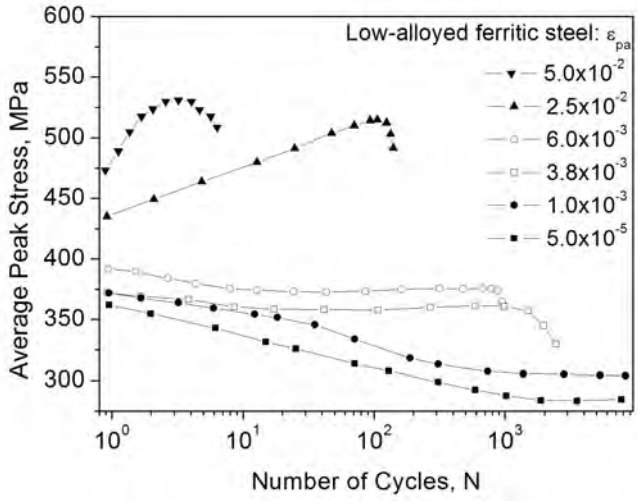

a)

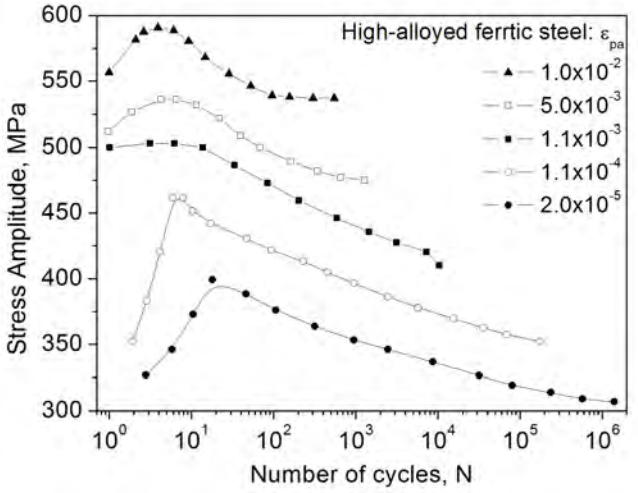

b)

Figure 6.6. *a) Cyclic stress response at different plastic strain amplitude of: a) a low-alloyed ferritic steel [ROV 91]; b) high-alloyed ferritic stainless steel (X10CrAl24) [KRU 01]*

The ferritic/martensitic steels with relatively low chromium contents (9-12% Cr) are adequate for the nuclear industry due to their irradiation resistance. This kind of steel, with its complex initial structure, exhibits a continuing cyclic softening during LCF (Figure 6.7).

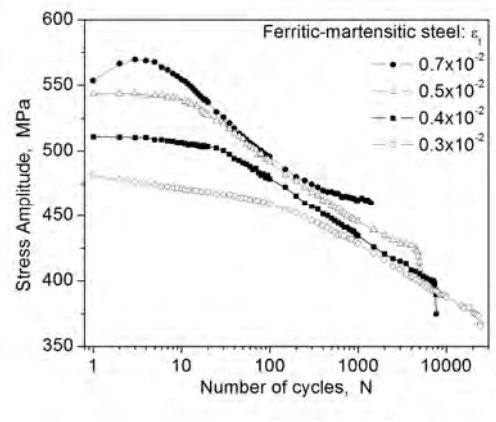

Figure 6.7. *Cyclic stress response curves of the ferritic/martensitic steel (EUROFER 97) at different total strain amplitudes at RT*

Stress-cycling results provide a definition of fatigue life in terms of the applied stress. The typical S-N curves (still called Wöhler curves), stress amplitude vs. the number of cycles to failure, indicate an increase in fatigue life as the stress amplitude decreases and an eventual trend towards a stress asymptote. This asymptote of the S-N curve defines the "fatigue limit" or "endurance limit" as the stress amplitude below which fatigue failure will not occur. Materials that fail exhibit a definite horizontal segment in the S-N curve, and the fatigue limit is chosen as the stress amplitude corresponding to 10^7 or 10^8 cycles. When the stress amplitude stems from different ratios, R, in tension and compression, where R is defined as:

$$R = \sigma_{\min} / \sigma_{\max} \neq -1 \qquad [6.4]$$

an increase of the fatigue limit is observed. Figure 6.8 shows a family of S-N curves for various R ratios, which indicates the effect of the mean stress on the fatigue life. The dashed vertical line identifies maximum stress values for a constant fatigue life of 10^7 cycles.

In most strain-controlled tests, after the accommodation phase (cyclic hardening/softening phase) the stress amplitude, σ_a, attains a saturation stage where both the elastic, ε_e, and the plastic strain component, ε_p, of the applied strain amplitude remain constant or saturate. From these results, it is, therefore, possible to plot these components versus the corresponding number of cycles to failure. Coffin [COF 54] and Manson [MAN 53] found that the fatigue life, N_f, depends foremost on plastic strain range, $\Delta\varepsilon_p$, and, they formulated the well-known LCF life law:

$$\frac{1}{2}\Delta\varepsilon_{pl} = \varepsilon_f^{'}.(2N_f)^c \qquad [6.5]$$

where $\varepsilon_f^{'}$ is the fatigue ductility coefficient (close to the tensile ductility) and c (typically in the range of –0.5 to –0.7) the fatigue ductility exponent. Both parameters can be calculated from the experimental data using the least square fit procedure. The fatigue ductility coefficient is the extrapolated plastic-strain amplitude to one-half cycle. Therefore, it is correlated with the fracture strain, ε_f, which can be found from the tensile test.

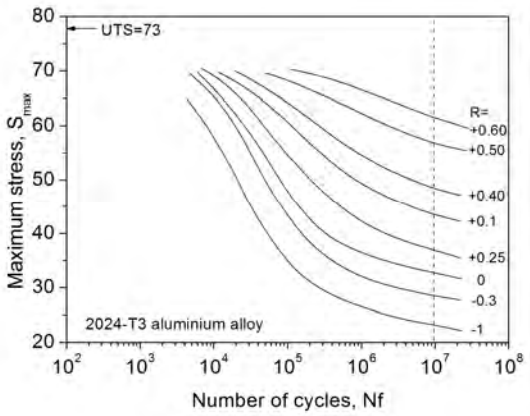

Figure 6.8. *A family of S-N curves showing the effect of the R ratio on fatigue life for axial loading of 2024-T3 aluminum [CON 75]*

6.3. Uniaxial cyclic plasticity in DSSs

The physical mechanisms of cyclic plasticity are closely related to lattice defects, which, at the same time, are strongly dependent on the lattice structure. The lattice structure influences the slip character of the dislocations and the type of final dislocation structure.

BCC metals represent a very important group of materials widely used in engineering practice among which belong the ferritic steels. Their cyclic plastic behavior is strongly dependent on temperature, strain rate, and amount of interstitial or substitutional atoms [MUG 81]. This is caused by specific properties of screw dislocations in the BCC lattice, which possess three-fold symmetry and a high Peierls stress. Due to these properties, the long-range motion of screw dislocations is thermally assisted via the formation of kink pairs. Owing to the strong temperature dependence of screw dislocation mobility, a “low-temperature regime” and a “high-

temperature regime" are defined in BCC metals. The transition temperature depends on the strain rate for iron-based alloys and at usual strain rates it is close to or slightly above RT. Therefore, RT cyclic straining corresponds to the intermediate or low temperature regime. The high-temperature regime is characterized by small friction stress (a thermally activated component) and the dislocation arrangement is similar to that of face-centered cubic (FCC) metals. The main characteristic of the low-temperature regime is large effective stress, large stress asymmetry, and easy activation of secondary slip systems.

In general, FCC metals exhibit higher work-hardening rates than BCC metals because of the more stable dislocation interactions possible in the FCC structure. However, within the austenitic stainless steels, there are two factors that influence the extent of work hardening: 1) the stacking fault energy (SFE) of the matrix, according to composition, and 2) the stability of the matrix. In the chromium-nickel austenitic steels, as nickel is one of the elements that raises the SFE, it is expected that the highest nickel alloys would show the lowest work hardening. The elements chromium, manganese, carbon, and nitrogen, among others, tend to lower the stacking fault energy of the austenite. Plastic deformation of such solid solutions not only produces stable dislocation interactions but also, after heavy deformations, fine deformation twins, both factors contributing to the high flow stresses observed in deformed alloys. Nevertheless, the largest effect on work-hardening rates is the instability of the austenite matrix by martensite transformation. By this means, yield stress can substantially increase, causing a decrease in the ductility of the steel. A detailed review on this matter is given by [HON 90].

In DSS both lattice structures are present, the austenite and the ferrite. The former is very susceptible to changes in nitrogen content due to the higher partition coefficient [CHA 91] in relation to ferrite. In this respect, the main evolution in the chemical composition of this family of steels has been the progressive increase in the nitrogen content. Therefore, it is expected that as an interstitial element nitrogen alloying modifies the strengthening mechanisms at least in the austenite for different generations of DSSs.

6.3.1. *First generation: low-nitrogen DSS*

One of the pioneering works in fatigue of DSS was carried out by Magnin *et al.* [MAG 88a, b] who studied the cyclic deformation behavior of a DSS (near UNS designation S32404) with 0.07 wt% of nitrogen and 50α:50γ phase proportion. The cyclic behavior conducted within a plastic strain amplitude (ε_{pa}) range of 10^{-4}-10^{-2} showed cyclic hardening during the early stage of fatigue life followed by cyclic softening until fracture, within the whole strain range. In order to compare the cyclic behavior of this steel with those of single-phase austenitic and ferritic steels, they

also carried out tests on single-phase steels with chemical compositions similar to that of the individual constituent phases. From the CSS curves and the Coffin-Manson curves of the three materials, the authors have proposed that the fatigue behavior of the duplex alloy was related at high ε_{pa} to the basic fatigue mechanisms in the ferritic phase; whereas at low $\varepsilon_{pa,}$ it is controlled by the fatigue mechanisms in the austenitic phase, fig. 6.9 a). In order to complete this work, Mateo *et al.* [MAT 96] had to repeat these results for AISI 329, extending the plastic strain amplitude from about 3×10^{-5} to 6×10^{-3} and analyzed the CSS curve and the associated dislocation structures developed in each phase in the whole plastic strain amplitude domains. Figure 6.9b shows the CSS curve for AISI 329 (S32900) and that of Magnin *et al.* They found two changes of slope in the CSS curve, one at ε_{pa} lower than 10^{-4} corresponding to a low cyclic strain-hardening rate and the second at $\varepsilon_{pa} = 6\times10^{-4}$ that indicates the limit towards a third regime. Table 6.1 summarizes the dislocation structures developed in each phase in the entire range of plastic deformation amplitudes.

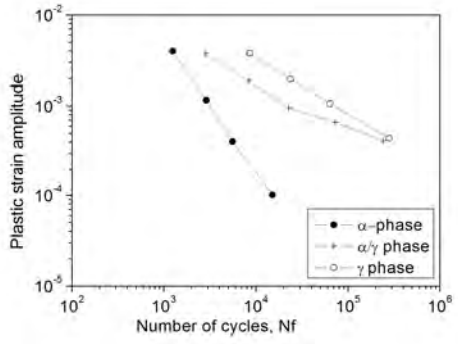

a)

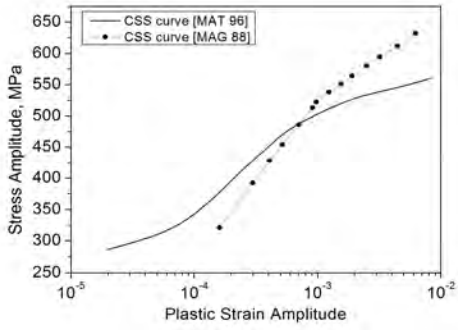

b)

Figure 6.9. *a) Coffin-Manson curves of a DSS containing 0.07 wt% of N compared with curves for the corresponding single phase austenitic and ferritic steels. b) CSS curves of AISI-329 DSS (S32900) [MAT 96] and Uranus 50 (S32404) [MAG 88a, b])*

Phase	$\varepsilon_{pa} < 10^{-4}$	$10^{-4} < \varepsilon_{pa} < 6 \cdot 10^{-4}$	$6 \cdot 10^{-4} < \varepsilon_{pa} < 10^{-3}$	$\varepsilon_{pa} > 10^{-3}$
Austenite	Planar arrays and pile-ups. 1 slip system	Planar arrays and more slip systems	Planar arrays † Ill-formed cell structure	Planar arrays Cellular structure †Well-formed cell structure
Surface			*Extrusions/cracks	*Extrusions/cracks
Ferrite	No changes	Loop patches of dislocations and ill-defined channels	Vein structure to well-defined wall-channel structure	Wall and cell structure
Surface			†Extrusions-cracks	*Extrusions/cracks †Crack nucleation at phase boundaries
*[MAG 88a,b]; †[ALV 07]				

Table 6.1. *Dislocation structures developed in AISI 329 DSS in each phase for different regions of plastic strain amplitudes*

Alvarez-Armas *et al.* [ALV 07, ALV 99] investigating the S32900 DSS with an unbalanced proportion of phases (α 30:γ 70) found a strong activity in the ferritic phase in the range of strain amplitudes between 6×10^{-4} and 10^{-3}. They observed a mixture of vein and well-defined wall-channel structures in all of this range. The dislocation structures were associated with extrusions-intrusions and microcracks at the surface of the ferritic phase. For $\varepsilon_{pa} > 10^{-3}$, well-formed wall structure in the ferrite and cell structure in the austenite have given rise to the nucleation of microcracks in phase boundaries (Figure 6.10).

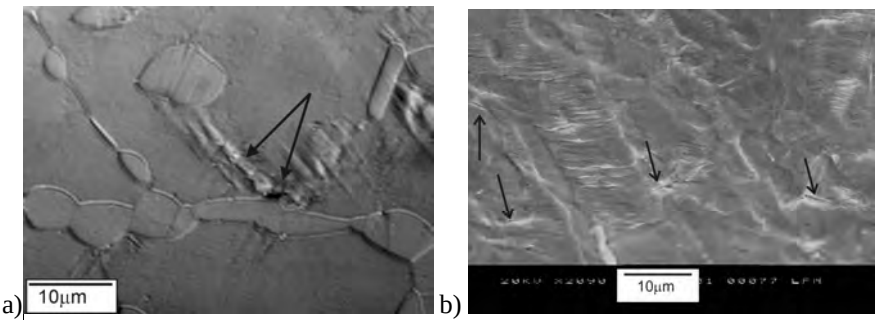

Figure 6.10. *Crack initiation in S32900 DSS cycled at a total strain range of: a) $\Delta\varepsilon_t = 0.8\times10^{-2}$ and b) 1.2×10^{-2}, which are associated with plastic strain amplitude at midlife of $\Delta\varepsilon_p = 2.5\times10^{-3}$ and 6.5×10^{-3}, respectively*

6.3.2. *Second generation: standard and high-alloyed DSS*

In the early 1970s, a "second generation" of duplex steels was introduced with improved welding properties and tensile strength (TS) mainly through nitrogen alloying. The most common duplex grade today is EN 1.4462 or 2205 (UNS S31803/S32205), which has a nominal composition of 22% Cr, 5% Ni, 3% Mo, and 0.16% N. This steel is used in a great number of applications in a wide variety of product forms. The increased strength creates opportunities for reduction in tube wall thickness and resists manipulation damage. More highly alloyed grades have existed for some time with 25% Cr, designated S32550 under the international nomenclature, which contains up to 2% Cu. These alloys were originally developed as-cast steels and have been used extensively in the offshore industry and for sulfuric acid service.

The fatigue properties of these grades have been studied by various authors [DEG 95, KRU 97, VOG 99]. Vogt *et al.* [VOG 99] explored the cyclic properties of a high-alloyed S32550 with 0.15 wt% of nitrogen over a wide interval of total strain ranges. They found that low strain leads to a rapid saturation after a short period of weak softening, while larger strain values result in accommodation behavior. Plotting the CSS curve, they found a change in the mechanical behavior near $\varepsilon_{pa} = 5\times10^{-4}$ similar to that reported by other authors [MAG 88a,b; MAT 96]. Unfortunately, Vogt *et al.* did not explore strains lower than 10^{-4} in order to confirm the three different cyclic strain hardening rates reported in the older duplex AISI 329.

	$\varepsilon_{pa} < 10^{-3}$	$10^{-3} < \varepsilon_{pa} < 10^{-2}$	$10^{-2} < \varepsilon_{pa}$
Austenite	Planar arrangements	Planar arrangements	Pronounced band structure and micro-twins
Surface specimen	Extrusions	Extrusions	Extrusions
Ferrite	Homogenous distribution of single dislocation segments and loose arrangements	Matrix and vein structure to wall-channel structure	Wall, labyrinth and sometimes cell structure
Surface specimen	No relief	Early formation of extrusions	Extrusions

Table 6.2. *Dislocation structures developed in the constituent phases of a S32550 DSS 0.16 wt% of nitrogen for different plastic strain amplitudes [VOG 99]*

The dislocation structures found in high-alloyed duplex grade S32550 in the range $10^{-4} < \varepsilon_{pa} < 10^{-2}$ are summarized in Table 6.2. Although the austenitic phase develops a relief of extrusions from low strain amplitudes, the localization in the ferrite occurs after a major rearrangement of dislocation structure.

The transformation of matrix and veins in the ferrite to wall-channel structure near and above 10^{-2} is evidence of the strain localization associated with extrusions at the specimen surface. Consequently, at high strain amplitudes, the crack initiation occurs in the ferrite.

Degallaix *et al.* [DEG 95] studied a S31803 DSS with two different contents of nitrogen 0.11 wt% (A-F11) and 0.18 wt% (A-F18). The beneficial effect of nitrogen content has been revealed by noticeable improvements in the CSS response, as well as in fatigue life, as a consequence of plastic strain reversibility in the austenitic phase (Figure 6.11). From the microstructure viewpoint, the austenitic phase exhibits planar behavior only at low strain levels, $\varepsilon_{pa} < 10^{-3}$. At higher strains, εpa > 4.5 · 10-3, the austenite develops cell and wall structure.

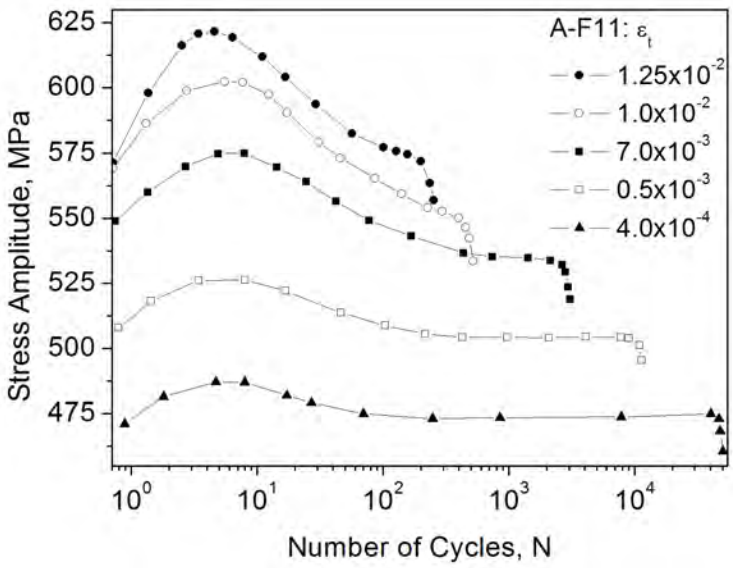

Figure 6.11a. *Cyclic hardening/softening curves of S31803 DSS with 0.11 wt% N*

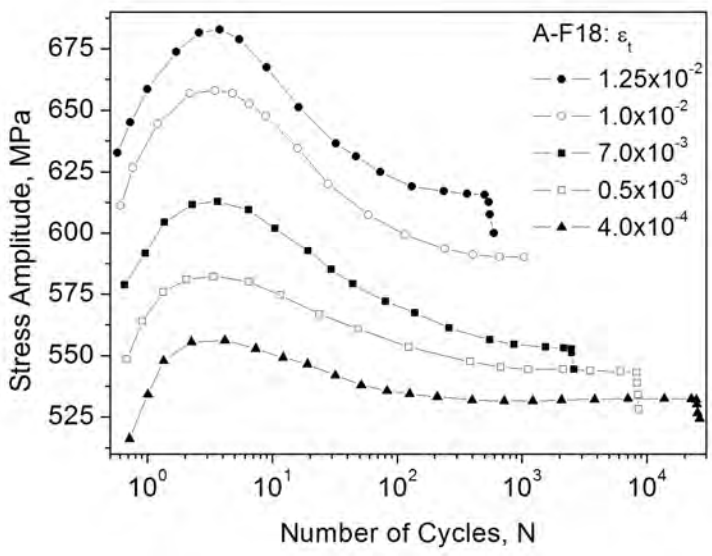

Figure 6.11b. *Cyclic hardening/softening curves of S31803 DSS with 0.18 wt% N [DEG 95]*

6.3.3. *Third generation: superduplex*

The high-alloyed DSS with higher nitrogen content between 0.20-0.35 wt% are known as superduplex stainless steels (SDSS). They were originally developed to resist corrosion in sea water and used for extreme environments. The most common types are the UNS S32750/S32760, which have now been in service since 1990. The major characteristic of these DSSs is their extremely high-yield stress, twice that of austenitic grades and higher in comparison with other DSS. The TS is also high, while the elongation is greater than 25% [CHA 91].

Table 6.3 summarizes the evolution in the mechanical properties of the most popular grades in the form of hot-rolled plates or bars, including the first-generation DSS with no nitrogen alloying and lean DSS with lower nickel contents. In Table 6.3, the fatigue limit is given for certain steels associated with two different fatigue test types, rotating bending fatigue with R = –1 and pulsating tensile fatigue with R=0.1. The corresponding fatigue limits show the influence of the mean stress and the stress gradient on the critical stress for fatigue.

The FS is defined as the fatigue limit (maximum stress or stress amplitude with R = –1) in the Wöhler curves between 10^6-10^7 stress cycles. For metallic materials, the ratio FS/TS, where FS is defined with R= – 1, is usually almost independent of TS and takes values between 0.65 and 0.70 for the high nitrogen steels and around 0.45 for low-nitrogen duplex steels. These values clearly indicate an improvement of the fatigue limit of the high-nitrogen duplex steels in comparison with those of the older generation.

Grade	Cr	Ni	Mo	N	0.2%YS MPa	TS MPa	El %	FS† MPa
First-generation DSSs								
S31500	18.0-19.0	4.25-5.25	2.5-3.01	---	450	720		±290[2]
S32404	20.5-22.5	5.5-8.8	2.0-3.0	---				±250[2]
S32900	23.0-28.0	2.5-5.0	1.0-2.0	---	400	690	18	±270[2]
Lean DSSs								
S32304	21.0-24.0	3.0-5.5	---	0.05-0.2	450	690	35	±445[1] 450[4]
S32101	21.0-22.0	1.25-1.70	0.1-0.8	0.20-0.25	480	700	35	500[4]
Second-generation or standard DSSs								
S32550	24.0-27.0	4.5-6.5	2.9-3.9	0.10-0.25	550	760	35	±500[2]
S32205	19.5-21.5	4.5-6.5	3.0-3.5	0.14-0.2	500	767	35	±450[1] 510[4]
Third-generation DSSs or superduplex								
S32750 S32760	24.0-26.0 24.0-26.0	6.0-8.0 60-8.0	3.0-5.0 3.0-4.0	0.24-0.32 0.20-0.30	600	800	35	±500[3] 550[4]
†In air at room temperature: rotating bending fatigue tests [1][JOH 91]; [2] [HAY 92] in [CHA 91]; [3][FER 03]; [4] [OUT 05] pulsating tensile fatigue tests (R=0.1)								

Table 6.3. *Chemical compositions and mechanical properties of different grades and generations of DSSs. Typical mechanical properties of hot-rolled plates or bar products*

The cyclic hardening/softening curves of S32750 DSS clearly exhibit two behaviors. Indeed, low applied strain leads to a rapid saturation after a tiny softening. Second, the increment of the strain amplitude enhances hardening and softening during the accommodation phase that can lead to a saturation stage or a continuous softening until rupture [ALV 06]. Figure 6.12 exhibits the cyclic response of the SDSS type S32750 and Table 6.4 summarizes the main fatigue results.

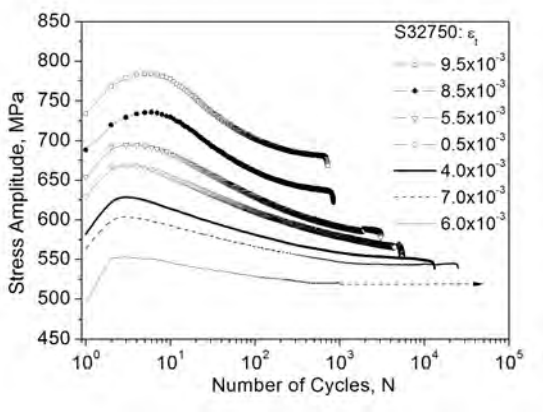

Figure 6.12. *Cyclic response of S32750 SDSS to LCF at RT*

$\Delta\varepsilon_t$ %	$\Delta\varepsilon_p$*	σ_{Max} MPa	σ_a* MPa	$\varepsilon_{1/4}$ %	$\sigma_{1/4}$ MPa	δ_{soft}	δ_{hard}	N_f
1.9	1.2×10^{-2}	784	675	0.95	704	12.7	6.3	340
1.7	1.0×10^{-2}	735	633	0.84	661	13.0	6.3	800
1.1	6.0×10^{-3}	695	590	0.55	652	15.0	6.0	3100
1.0	0.4×10^{-3}	670	565	0.50	597	15.0	6.1	5500
0.8	2.5×10^{-3}	630	555	0.40	555	13.1	7.6	14000
0.7	1.5×10^{-3}	603	545	0.34	544	11.9	6.6	26000
0.6	7.5×10^{-4}	552	510	0.29	497	5.0	9.9	
* At midlife								

Table 6.4. *Fatigue results obtained after LCF of a S32750 SDSS*

The plastic strain range, $\Delta\varepsilon_p$, corresponds to the value obtained at saturation or, if it is not attained, at midlife, $N_f/2$. σ_a defines the stress amplitude at midlife, which corresponds to a "conventional" stabilized cycle. Lastly, $\sigma_{1/4}$ and $\varepsilon_{1/4}$ correspond to the stress and the strain, respectively, measured after the first quarter of cycle and δ_h and δ_s represent the hardening and the softening rates defined, respectively, by $\delta_h = (\sigma_{max} - \sigma_{1/4}) / \sigma_{max}$ and $\delta_s = (\sigma_{max} - \sigma_{sat}) / \sigma_{max}$.

The dislocation structure developed at rupture is summarized in Table 6.5. Although the austenitic phase exhibits planar arrangements of dislocations

practically for all the applied strain amplitudes, at εpa ≈ 10-3, the ferritic phase presents a pronounced evolution of the microstructure suggesting that the plastic deformation evolves from micro-yielding observed at $\varepsilon_{pa} < 10^{-3}$ to a massive process of deformation at higher strain.

	$\varepsilon_{pa} < 10^{-3}$	$10^{-3} < \varepsilon_{pa} < 8.10^{-3}$	$10^{-2} < \varepsilon_{pa}$
Austenite	Planar arrangements	Planar arrangements	Less planar, more cellular structure
Surface	Extrusions	Extrusions	Extrusions
Ferrite	Homogeneous distribution of single dislocation segments and loose arrangements	Matrix and vein structure to wall-channel structure	Uni- and bidirectional wall and cell structure
Surface	No relief	From slip marks to extrusions	Pronounced extrusions

Table 6.5. *Dislocation structures developed in a S32750 SDSS at fatigue rupture*

Nitrogen-alloyed DSSs exhibit similar behavior (Table 6.2), but not the first-generation S32900 DSS (Table 6.1). In first-generation DSSs, the evolution from vein structure to well-defined wall-channel structure between $6\times10^{-4} < \varepsilon_{pa} < 10^{-3}$, which is intimately related to strain localization, develops at lower strain amplitudes than for the high-nitrogen-alloyed DSS.

Figure 6.13 illustrates the lifetime results according to equation [6.5] obtained for the three DSSs, S32750, S32205 and S32900, with different nitrogen contents, 0.27, 0.17, and 0.06 wt% (third, second, and first-generation DSS, respectively). Applying a linear regression analysis to the experimental data of S32750 DSS at strain ranges, $\Delta\varepsilon_{pa} > 10^{-3}$, the parameters of the Coffin-Manson law were estimated as c = –0.55 and $\varepsilon_f^{'}$ = 0.39. The extrapolation of this law to the first quarter of cycle approximates the strain value corresponding to the TS measured in a tensile test, which agrees with that given by the producer. It is interesting to note that there is only one slope for the three alloys and its value is the same as that for the most ductile metals with high mechanical strength over the slope range between –0.4 and –0.7 [CHA 91]. However, the intersecting values for S32205 is slightly lower, and more markedly so in the case of S32900, $\varepsilon_f^{'}$ = 0.2. The fatigue lifetime shows a strong dependence on nitrogen content due to the enhancement of the strain reversibility in the high-nitrogen steels at least for similar wrought material (hot-rolled and solution-annealed bars) and comparable morphological texture. On the contrary, the low-nitrogen S32900 DSS with very low nitrogen content (70% α: 30% γ) exhibits the shortest fatigue lives.

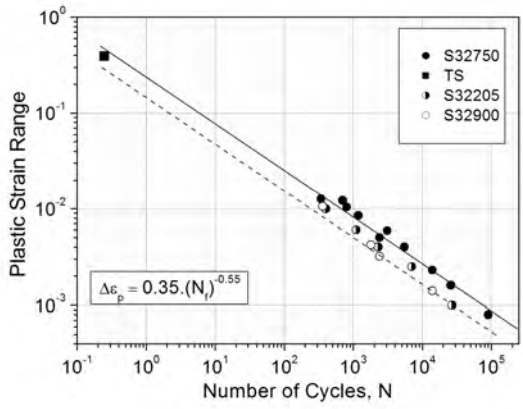

Figure 6.13. *Coffin-Manson curves of the three generations of DSS*

6.3.4. *Role of nitrogen alloying in DSS*

Nitrogen is an interesting alloying element that increases the resistance to corrosion, enhances thermal stability of the two phases, and improves the strength of the material [DUP 91]. Regarding the beneficial effects of nitrogen addition on mechanical properties, many contributions have appeared in the literature, initially in austenitic [DEG 86, BYR 87, GRU 89, VOG 93, FOC 93] and then in DSS [FOC 91, NIL 92, VOG 94, DEG 95, RAW 96, MAT 01, BLI 05].

One of the most important considerations in analyzing plastic deformation behavior of DSS alloys with different nitrogen contents is related to the dislocation behavior in each constituent phase and the mechanical response. It is well-known that the addition of nitrogen in austenitic steels raises the values of the yield stress and the tensile strength [BYR 87]. Hence, similar behavior is expected for the austenitic phase of a DSS. In this respect, Dakhlaoui *et al*. [DAK 07] have determined the parameters characterizing the individual elasto-plastic mechanical behavior in the constituent phases of three DSSs with different nitrogen contents, 0.09, 0.17, and 0.25 wt%, respectively, by X-ray diffraction during in-situ uniaxial tensile tests. They have developed an elasto-plastic model of DSS behavior. In these calculations, two families of planes were considered for the ferrite (i.e. {110} <111> and {112} <111>) and only one for the austenite (i.e. <110> {110} to evaluate the yield stress and the tensile strength in each phase. Table 6.6 summarizes the steel characteristics, including the nitrogen content, the yield stress, $\sigma_{0.2}$, the tensile strength, TS, the elongation, EL.

The increasing yield stress levels observed with higher nitrogen content can be in part attributed to the increasing nitrogen content. It is well established that the interstitially dissolved nitrogen in austenitic stainless steels is responsible for a number of strengthening phenomenon. For example: 1) nitrogen produces an exceptional solid solution strengthening effect [BYR 87], 2) gives rise to a large negative temperature dependence of yield stress at low temperature [GRU 89] and 3) it also promotes planar slip [DEG 86, SAS 89, BYR 87].

DSS	N wt%	$\sigma_{0.2}$ (MPa)	TS (MPa)	El %	$\sigma_{0.2}$ (MPa)	
					α-ph	γ-ph
X2 Cr Ni 23.4	0.09	400	600	25	455	235
X2 Cr Ni Mo 22.5.3	0.17	480	680	25	620	370
X2 Cr Ni Mo 25.6.3	0.25	550	770	25	750	460

Table 6.6. *Mechanical properties for tensile test with strain rate 10^{-4} s^{-1} and the yield stress in the ferritic and austenitic phases*

Dislocation movement through a lattice containing randomly distributed interstitial nitrogen has an inversely proportional square root dependency on nitrogen concentration [GRU 89]. Depending on temperature, the mobility of the nitrogen atoms can be small in comparison with the mobility of dislocations. In such cases, nitrogen distribution in stainless steel is not totally random. Nitrogen has greater affinity for chromium atoms than for iron atoms and is repelled by nickel atoms [BYR 87]. Thus, due to local elemental statistical concentration variation within the lattice, there will be regions within the matrix where chromium atoms are clustered. These will serve as preferential interstitial sites to which nitrogen atoms will be attracted. This type of matrix strengthening is often referred to as being due to short-range ordering (SRO) [GRU 89]. As a dislocation moves through a nitrogen-strengthened stainless steel lattice, it encounters such local obstacles. The dislocation will be stopped until either it can overcome the interstitial-chromium cluster or the nitrogen atoms diffuse away from its preferred site. In either case, the energy required to move on the dislocation through the lattice – and thus the yield stress – is a function of temperature, applied stress, nitrogen concentration, and alloy composition.

Figure 6.14 illustrates the variations of the stress amplitudes at midlife/saturation and the corresponding values of their components, the friction and back stresses calculated according to equation [6.2], against the plastic-strain ranges for the three families of DSS. Applying equation [6.3] to the set of stress amplitude curves of the three generations of DSSs, it is observed that the cyclic strain-hardening coefficient *n'* increases with nitrogen content; i.e. *n'* = 0.05, 0.08 and 0.11 for the S32900, S32205, and S32750 DSS, respectively. These values support the

improved FS observed in Table 6.3 with nitrogen content. Regarding the stress components, it is interesting to note that although the friction stress holds a constant value of nearly 250 MPa regardless the nitrogen content [ALV 06], the back stress raises its values with the nitrogen content. Only the S32900 grade, with very low-nitrogen content, deforms cyclically with equal values for the two components σ_f and σ_b. Abel *et al*. [ABE 98] have observed, in a comparative study of LCF behavior of three types of stainless steels – austenitic, ferritic, and duplex – that larger friction stress components correspond to a more ductile behavior in the deformation process and to a reduced fatigue resistance. In summary, the response of the back stress is intimately related to the nitrogen content and is responsible for the enhancement of the cyclic strain-hardening coefficient associated with the three grades.

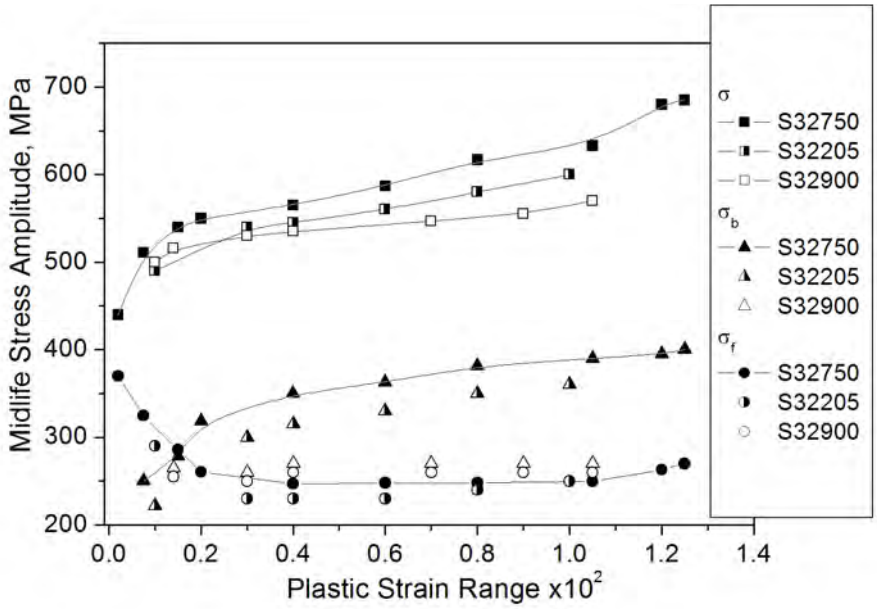

Figure 6.14. *CSS curves of the applied, back, and friction stresses attained at midlife for the three grades of DSS, S32900, S32205, and S32750 with 0.06, 0.17, and 0.26 wt% of nitrogen*

Therefore, higher nitrogen content results in two effects, i.e. higher proportion of austenitic phase and higher back stress. As a consequence, the high strength of the austenitic phase because of the high nitrogen content assists the ferritic phase during plastic deformation delaying the development of strain localization produced by the formation of well-formed wall and channel structure. Thus, the development of intrusions and extrusions in the specimen surface takes place later in the fatigue life.

Finally, it is interesting to analyze the variation of the back stress with the plastic strain range in Figure 6.14. Indeed, near $\Delta\varepsilon_p \approx 1.5\times10^{-3}$, the back stresses of the three grades have shown similar values meanwhile the gap between them increases towards higher plastic strain ranges. Near $\Delta\varepsilon_p \approx 1.5\times10^{-3}$, the dislocation structure in the ferrite is composed of loop patches of dislocations and the austenite presents planar arrays in all the steel grades. That means that while the austenite is plastically active, the ferritic phase contributes slightly to the deformation (micro-yielding). However, beyond this strain value, the high-nitrogen steel, S32750, presents a strong difference in microstructures in comparison with the older generation S32900. Strong strain localization observed in the form of refined walls characterizes the ferritic phase in the S32900, while vein structure is present in the S32750 (Figure 6.15a and c, respectively).

Conversely, the austenitic phase in the S32900 presents an ill-formed cellular structure with an early formation of PSB, while in the S32750 the planar arrangement of dislocations is present (Figure 6.15b and d, respectively). At higher strain ranges $\Delta\varepsilon_p > 6.0\times10^{-3}$, the ferritic phase of S32750 also starts to form zones of localized deformation through the rearrangements of veins into refined wall structure (Figure 6.15e). The austenitic phase starts showing also some changes in the microstructure as that exhibited in Figure 6.15f.

The formation of a cellular structure in some grains as a result of the formation of Lomer-Cottrell barriers, indicated by arrows, indicates the formation of a stronger microstructure. It is important to mention that the cellular structure observed in the austenitic phase of the S32750 is not formed due to cross-slip of the dislocations as in the case of the older-generation DSS. However, other authors [MAT 01] have not found changes in the dislocation structure of the austenitic phase even at higher strains. Finally, the low-nitrogen steel S32900 for the same plastic deformation presents clear evidence of the formation of PSB in the austenite and a well localization of the deformation in the ferritic phase (Figure 6.15g).

Therefore, regarding the back stress values, the additional increment observed at high strain ranges for the high nitrogen steel, S32750, can be related to the presence of Lomer-Cottrell barriers. In fact, Kubota *et al*. [KUB 98], suggest that dislocation-walls, formed through the production of Lomer-Cottrell locks, can behave like grain boundaries in the sense that they become obstacles to the movement of dislocations increasing the strain hardening rate in the austenitic phase. This fact agrees with the occurrence of an apparent saturation stage during cycling at plastic strain ranges above 8×10^{-3} (Figure 6.12).

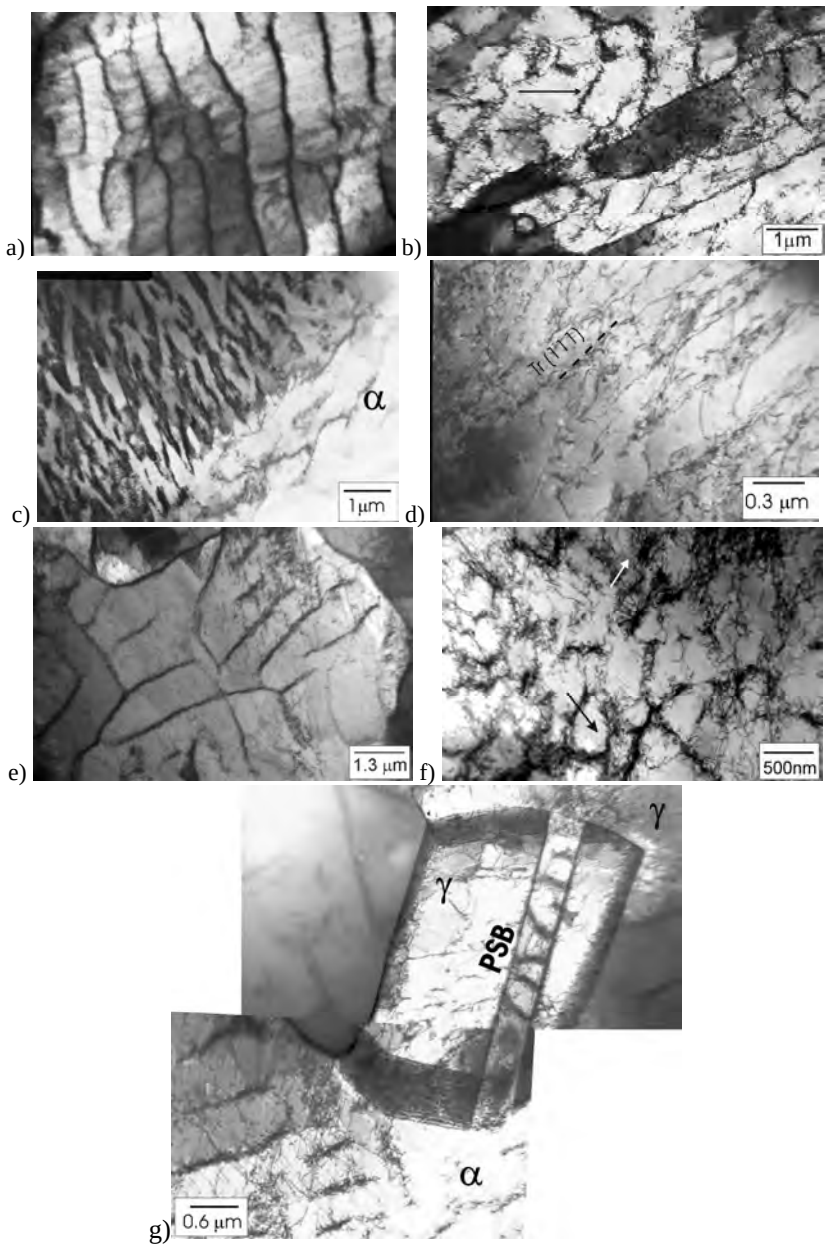

Figure 6.15. *Dislocation structures developed at fracture on: S32900 deformed at $\Delta\varepsilon_p = 2.3\times10^{-3}$ a) ferrite and b) austenite; S32750 deformed at $\Delta\varepsilon_p = 2.3\times10^{-3}$ c) ferrite and d) austenite; S32750 deformed at $\Delta\varepsilon_p = 6.0\times10^{-3}$ e) ferrite and f) austenite; g) S32900 deformed at $\Delta\varepsilon_p = 6.0\times10^{-3}$. All the tests were carried out at $\dot{\varepsilon} = 2\times10^{-3}$*

6.3.5. *Behavior of the friction stress during cycling and its influence on the cyclic softening*

The friction stress, σ_f, in DSS results from two contributions; the first is the lattice friction in the ferritic phase, σ_{LF}, and the second is due to short-range interactions of nitrogen atoms with dislocations, especially in the austenitic phase, σ_N [VOG 94].

Therefore, considering additivity of these contributions, the following relation can be used:

$$\sigma_f = \sigma_{LF} + \sigma_N \qquad [6.6]$$

According to Figure 6.14, it is reasonable to consider that the contribution of the lattice friction to the overall friction stress is about 250 MPa. Therefore, for estimating the contribution of nitrogen atoms to the friction stress, the following considerations must been done. Firstly, nitrogen atoms are mainly distributed in the austenite because of a better solubility in a FCC matrix [KOL 87]. Then, due to the greater affinity of nitrogen atoms with chromium atoms [RAW 96], there will be regions within the matrix where chromium atoms will be clustered, at least at low temperature [GRU 89]. In fact, the limit between high and low temperatures for nitrogen in an austenitic matrix is about 130°C, which is the temperature where the yield strength increases significantly [UGG 89]. These chromium-cluster regions will offer preferential interstitial sites to which nitrogen atoms will be attracted.

The stress required to bend the dislocation to the critical angle, φ, is calculated in an analogous way to that used to determine the stress required to operate a Frank-Reed source (Figure 6.16). An appropriate line tension balance at the critical angle shows that the necessary shear stress for dislocation motion is given by:

$$\tau \cong \frac{Gb}{L^*}\cos(\varphi/2) \qquad [7]$$

where L* is the effective distance between obstacles, G the shear modulus and b the Burgers vector. For strong obstacles φ is small and L* = L, where L is the distance between obstacles. Friedel has considered the case for weak obstacles and has shown that as $\varphi \rightarrow \pi$, $L^* \approx L / [\cos(\varphi/2)]^{1/2}$, thus, the stress required to bend a dislocation is given by:

$$\tau \cong \frac{Gb}{L}[\cos(\varphi/2)]^{3/2} \qquad [6.8]$$

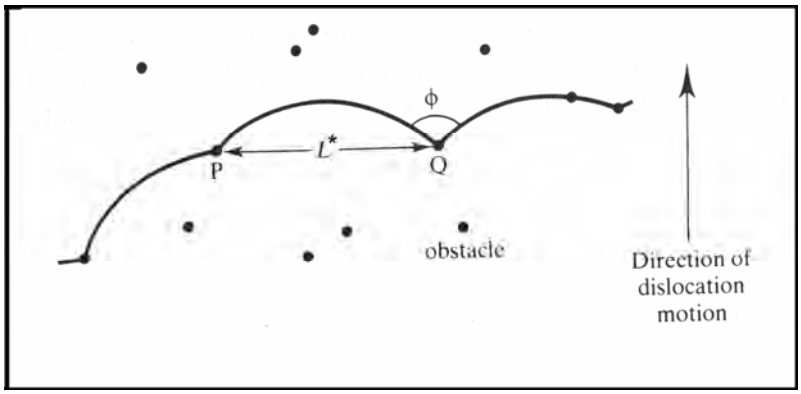

Figure 6.16. *A dislocation held up by a random array of obstacles. The stress required to bypass the obstacles depends on the effective spacing L* and the angle φ to which the dislocation line is bent before it breaks through the obstacle*

Consequently, to estimate the contribution of nitrogen atoms to the friction shear stress, τ_N, it is necessary to assess not only the spacing between obstacles, but also the nature of these obstacles as well. If they are weak, the dislocation line is nearly straight, and the spacing between obstacles, L*, is larger than the mean center-to-center distance between atoms, L. One practical way to assess this parameter can be made evaluating activation parameters in a commercial AISI 316 austenitic steel and in a S32750 DSS [ALV 06]. The results have revealed an increment of the activation volume from $150b^3$ to $250b^3$ in the single-phase austenitic steel and an increase from $170b^3$ to $230b^3$ during the first 10 cycles in DSS**.** Byrnes *et al*. [BYR 87] working on austenitic steels with different nitrogen contents have measured an activation volume of $250b^3$ at RT using (static) stress relaxation and strain-rate change experiments. Using the definition of the activation volume $V^* = b^2L^*$, where b and L* have the aforementioned meaning, the initial effective distance can be taken as $L^* \approx 170b$. Thus, according to Friedel´s model, a critical angle close to π would produce an initial stress due to nitrogen atoms of $\sigma_N = M_\gamma \tau_N \approx 50$MPa (where M_γ is the Taylor factor and has a value close to 3 according to [MAT 01], and τ_N is the friction shear stress associated with nitrogen). The value of $\sigma_N \approx 50$ MPa together with the estimated lattice friction $\sigma_{LF} \approx 250$ MPa gives a good approximation of the friction stress observed at the beginning of fatigue life ($\sigma_f \approx 300$MPa) as could be estimated from Figure 6.17. This plot contains one of the cyclic curves exhibited in Figure 6.12 dissociated in its components, the back and the friction stresses, σ_b and σ_f, respectively. As cycling proceeds, the friction stress decreases due to the unpinning of dislocations from nitrogen atoms and L* grows to a stabilized value of 250b (or something higher seeing the growth rate in the activation volume for the DSS during the first 10 cycles).

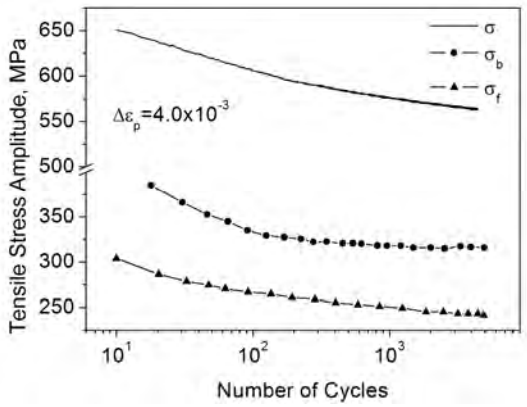

Figure 6.17. *Evolution of the stress amplitude components, the back stress, σ_b, and the friction stress, σ_f, with the number of cycles at $\Delta\varepsilon_p = 4.0\times10^{-3}$*

Finally, and referring again to Figure 6.14, the decreasing values of the friction stress found below $\Delta\varepsilon_p < 2.0\times10^{-4}$ could be rationalized as a direct consequence of a model of weak obstacles, i.e. higher applied stresses produce larger L* and thus decreasing stress values acting on the dislocation segments.

6.4. Final remarks

The aim of the present contribution was to collect and present in a concise way information from the literature and from my own research results, the evolution of the mechanical properties, especially during cycling of DSS with increasing amounts of nitrogen. The main conclusion is that this alloying element substantially enhances the FS of these steels. Due to the poor solubility of nitrogen in the ferritic phase, almost all the nitrogen atoms are dissolved in the austenitic phase. In this way, nitrogen in solid solution in the austenite modifies the behavior of dislocations by changing the slip mode from wavy to planar confining them to their slip planes and increasing the work-hardening rate and thus the TS. With a high work-hardening rate, the uniform straining prior to plastic instability increases and the total ductility at fracture also increases. An analogous improvement on the cyclic response is also observed through the cyclic work-hardening coefficient, *n'*, which is responsible for higher values of FS of high-alloyed DSS. The fatigue life also presents a pronounced enhancement due to higher values of the fatigue ductility coefficient $\varepsilon_f^{'}$. The effect of nitrogen-alloying atoms on these properties is manifested in the higher values of the back stress while the friction stress remains unalterable regardless of the steel grade.

6.5. Acknowledgments

This work was supported by the Agencia Nacional para la Promoción de la Ciencia y Técnica (ANPCYT), the Consejo Nacional de Investigaciones Cientícas y Técnicas (CONICET) of Argentine and by the cooperation program ECOS-Sud/MINCyT between France and Argentina (Code A06E01). I thank Dr M.C. Marinelli for the contribution to transmission electron micrographs.

6.6. References

[ABE 98] ABEL A., FLETCHES D., GRAHAM M. D., "Low cycle fatigue of stainless steels; a comparative study", in RIE K.-T., PORTELLA P. D., *Low Cycle Fatigue and Elasto–Plastic Behavior of Materials*, Elsevier, p. 69-74, 1998.

[ALV 99] ALVAREZ-ARMAS I., ARMAS A. F., "Dislocation structure of a duplex stainless steel during low cycle fatigue at room temperature", in BILDE-SORENSEN J. B., CARTENSEN J. V., HANSEN N., JUUL JENSEN D., LEFFERS T., PANTLEON W., PEDERSEN O.B., WINTHER G., *Deformation-Induce Microstructure: Analysis and relation to Properties. Proceeding of the 20th RISO International Symposium on Material Science*, September 6-10, Rosakilde, Denmark, p. 233-238, 1999.

[ALV 06] ALVAREZ-ARMAS I., MARINELLI M.C., HEREÑÚ S., DEGALLAIX S.. ARMAS A.F., "On the cyclic softening behavior of SAF 2507 duplex stainless steel", *Acta Materialia*, vol. 54, n. 19, p. 5041-5049, 2006.

[ALV 07] ALVAREZ-ARMAS I., MARINELLI M. C., MALARRIA J. A., DEGALLAIX S., ARMAS A. F., "Microstructure associated with crack initiation during low-cycle fatigue in a low nitrogen duplex stainless steel", *Int. J. Fatigue*, vol. 29, n. 4, p. 758-764, 2007.

[ARM 00] ALVAREZ-ARMAS I., ARMAS A., HEREÑÚ S., DEGALLAIX S., DEGALLAIX G., "Cyclic behavior of DIN 1.4460. Duplex stainless steel between room temperature and 773K", *Fatigue & Fracture of Engineering Materials & Structures*, vol. 26, p. 27-35, 2003.

[BLI 05] BLIZNUK T., MOLA M., POLSHIN E., POHL M., GAVRILJUK V., "Effect of nitrogen on short-range atomic order in the feritic δ phase of a duplex steel", *Mater. Sci. Engn. A*, vol. 405, n. 1-2, p. 11-17, 2005.

[BYR 87] BYRNES M. L. G., GRUJICIC M., OWEN W. S., "Nitrogen strengthening of a stable austenitic stainless steel", *Acta Metall*., vol. 35, n. 7, p. 1853-62, 1987.

[CHA 91] CHARLES J., "Superduplex stainless steel: structure and properties", in: CHARLES J., BERNHARDSSON S., *Duplex Stainless Steels '91*, October 28-30, Beaune, Les Editions de Physique, p. 3-48, 1991.

[COF 54] COFFIN L.F. “A study of the effects of cyclic thermal stresses on a ductile material”, *Trans. ASME*, vol. 76, p. 931-950, 1954.

[CON 75] CONWAY J.B., STENTZ R.H., BERLING J.T., *Fatigue, Tensile and Relaxation Behavior of Stainless Steels*, TID 26135. Technical Information Center, Office of Information Services. United states Atomic Energy Commission, 1975.

[DAK 06] DAKHLAOUI R., BACZMANSKI A., BRAHAM C., WRONSKI S., WIERZBANOWSKI K., OLIVER E. C., “Effect of residual stresses on individual phase mechanical properties of austeno-ferritic duplex stainless steel”, *Acta Mater.*, vol. 54, p. 5027–5039, 2006.

[DAK 07] DAKHLAOUI R., BRAHAMA C., BACZMANSKI A., “Mechanical properties of phases in austeno-ferritic duplex stainless steel – surface stresses studied by X-ray diffraction”, *Mat. Scie. Eng. A*, vol. 444, p. 6-17, 2007.

[DEG 86] DEGALLAIX-MOREUIL S., Rôle de l’azote interstitiel et combiné sur le comportement en plasticité cyclique et monotone d’aciers inoxydables austénitiques Z2 CND 17-12 (AISI 316L-316LN), PhD Thesis, University of Science and Technology of Lille-Flandres-Artois, 1986.

[DEG 95] DEGALLAIX S., SEDDOUK A., DEGALLAIX G., KRUML T., POLAK J., “Fatigue damage in austenitic-ferritic duplex stainless steel”, *Fatigue Fract. Engng. Struct.*, vol. 18, p. 65-77, 1995.

[DIC 89] DICSON J.I., BOUTIN J., HANDFIELD L., “A comparison of two simple methods for measuring cyclic internal and effective stresses”, *Mater. Scie. Eng.*, vol. 63, L7-L11, 1989.

[DUP 91] CHARLES J., BERNHARDSSON S. (Eds), *Duplex Stainless Steels’91*, Les Editions de Physique, 28-30 October, Beaune, 1991.

[FER 03] www.nationalmetaldistributors.com-download-Ferralium Leaflet.pdf.

[FOC 91] FOGT J., MAGNIN T., VOGT J.-B., “Nitrogen alloying in duplex stainless steels”, in CHARLES J., BERNHARDSSON, S., *Duplex Stainless Steels ‘91*, October 28-30, Beaune, Les Editions de Physique, p. 49, 1991.

[FOC 93] FOCT J., AKDUT N., “Cleavage-like fracture of austenite in duplex stainless steel”. *Scripta Metall. et Mater.*, vol. 29, p. 153-158, 1993.

[GRU 89] GRUJICIC M., NILSSON J.O., OWEN W.S., THORVALDSSON T., “Basic deformation mechanisms in nitrogen strengthened stable austenitic stainless steel”, in FOCT J., HENDRY A., *High Nitrogen Steels – HNS-88. Proc. of the International Conference on High Nitrogen Steel*, May 18-20, 1988, Lille, The Institute of Metals, London, p.151-165, 1989.

[HAY 92] HAYNES A.G., “Duplex and high alloy corrosion resisting steels”, *Lloyd’s Register Technical Association*, London, paper no. 6, Session 1990-91, p. 1-38, 1992.

[HON 90] HONEYCOMBE R.W.K., *Steels. Microstructure and Properties*, Metallurgy and Materials Science Series. Edward Arnold, 1990.

[JOH 91] JOHANSSON R.E., GROTH H. L., "Corrosion fatigue and fatigue data for duplex stainless steels", in Charles J., Bernhardsson S., *Duplex Stainless Steels '91*, October 28-30, Beaune, Les Editions de Physique 1991, p. 283-293.

[KOL 87] KOLTS J. SRIDHAR N., "Effects of nitrogen on the selective dissolution of a duplex stainless steel", *Corrosion*, vol. 43, no. 11, p. 646-665, 1987.

[KRU 97] KRUML T., POLAK J., OBRTLIK K., DEGALLAIX S., "Dislocation structures in the bands of localised cyclic plastic strain in austenitic 316L and austenitic-ferritic duplex stainless Steels", *Acta Mater.*, vol. 45, n. 12, p. 5145-5151, 1997.

[KRU 01] KRUML T., POLAK J., "Fatigue softening of X10CrAl24 ferritic steel", *Mat. Sci. Eng. A*, vol. 319–321, p. 564–568, 2001.

[KUB 98] KUBOTA S., XIA Y., TOMOTA Y., "Work-hardening behavior and evolution of dislocation-microstructures in high-nitrogen bearing austenitic steels", *ISIJ International*, vol. 38, n. 5, p. 474-481, 1998.

[KUH 79] KUHLMANN-WILSDORF D., LAIRD C., "Dislocation behavior in fatigure. II Friction stress and back stress as inferred from an analysis of hysterisis loops", *Mater. Sci. Engng*., vol. 37, 111-120, 1979.

[MAG 88a] MAGNIN T., LARDON J. M., COUDREUSE L., " A new approach to low cycle fatigue behavior of a duplex stainless steel based on the deformation mechanisms of the individual phases", in SOLOMON H.D., HALFORD G.R., KAISAND L.R., LEIS B.N., *Low Cycle Fatigue*, ASTM – STP 942, Philadelphia, p. 812-823, 1988.

[MAG 88b] MAGNIN T., LARDON L. M., "Cyclic deformation mechanisms of a two-phase stainless steel in various environmental conditions", *Mat. Sci. Engng. A*, vol. 104, p.21-28, 1998.

[MAN 53] MANSON S.S., "Behavior of materials under conditions of thermal stress", *National Advisory Committee for Aeronautics*, technical note 2933, 1953.

[MAT 96] MATEO A., LLANES L., ITURGOYENS L., ANGLADA M., "Cyclic stress-strain response and dislocation substructure evolution of a ferrite-austenite stainless steel", *Acta Mater*., vol. 44, n. 3, p. 1143-1153, 1996.

[MAT 01] MATEO A., GIRONÉS A., KEICHEL J., LLANES L., AKDUT N., ANGLADA M., "Cyclic deformation behavior of superduplex stainless steels", *Mat. Sci. Engng. A*, vol. 314, p. 176–185, 2001.

[MUG 81] MUGHRABI H., HERZ K., STARK X., "Cyclic deformation and fatigue behavior of α-iron and mono- and polysrystals", *Int .J. Fract.*, vol. 17, p. 193-220, 1981.

[NIL 92] NILSSON J.-O.,"Super duplex stainless steels", *Mat. Sci. Tech*., vol. 8, p. 685-700, 1992.

[OUT 05] *Duplex Stainless Steel*, 1008EN-GB: 4, Centrum Tryck AB, Avesta, Sweden, www.outokumpu.com, November, 2005

[POL 91] POLAK J., *Cyclic Plasticity and Low Cycle Fatigue Life of Metals*, Academia Prague, 1991.

[RAW 96] RAWERS J., GRUJICIC M., "Effects of metal composition and temperature on the yield strength of nitrogen strengthened stainless steels", *Mater. Sci. Engng. A*, vol. 207, p. 188-194, 1996.

[ROV 91] ROVEN H.J., NES E., "Cyclic deformation of ferritic steel – I. Stress-strain response and structure evolution", *Acta Metall. et Mater*., vol. 38, n. 8, p. 1719-33, 1991.

[SAS 89] SASSEN J., GARRAT-REED A. J., OWEN W. S., "Electron microscopy of austenitic Fe Ni Cr alloys containing nitrogen", in FOCT J., HENDRY A., *High Nitrogen Steels-HNS-88. Proc. of the International Conference on High Nitrogen Steels*, May 18-20, Lille, The Institute of Metals, London, p. 159-162, 1989.

[SEG 57] SEEGER, A., "The mechanism of glide and work hardening in face-centered cubic and hexagonal close-packed metals", in FISHER J.C., JOHNSTON W.G., THOMSON R. and VREELAND Jr T., *Dislocations and Mechanical Properties of Crystals*, John Wiley & Sons, p. 243-329, 1957.

[SOU 91] SOUSSAN A., DEGALLAIX S., MAGNIN T., "Work-hardening behavior of nitrogen-alloyed austenitic stainless steels", *Mat. Scie. Engng. A*, vol. 142, n. 2, p. 169-176, 1991.

[STR 96] STUBBINS J.F., GELLES D.S., "Fatigue performance and cyclic softening of F82H, a ferritic-martensitic steel", *J. Nucl. Mat.*, vol. 233-237, p. 331-335, 1996.

[SUR 91] SURESH S., *Fatigue of Materials*, 2nd Edition, Cambridge University, 1991.

[UGG 89] UGGOWITZER P. J., HARZENMOSER M., "Strengthening of austenitic stainless steels by nitrogen", in FOCT J., HENDRY A., *High Nitrogen Steels-HNS-88. Proc. of the International Conference on High Nitrogen Steels*, May 18-20, Lille, by The Institute of Metals, London, p. 174-179, 1989.

[VOG 93] VOGT J.-B., MAGNIN T., FOCT J., "Effective stresses and microstructure in cyclically deformed 316l austenitic stainless steel: effect of temperature and nitrogen content", *Fatigue Fract. Engng. Mater. Struct.*, vol. 16, n. 5, p. 555-64, 1993.

[VOG 94] VOGT J.-B., MESSAI A., FOCT J., "Cleavage fracture of austenite induced by nitrogen supersaturation", *Scripta Metall. et Mater.*, vol. 31, n. 5, p. 549-554, 1994.

[VOG 99] VOGT J.-B., SAADI B. A., FOCT J., "Analysis of the fatigue dislocation structure in a duplex stainless steel alloyed with nitrogen", *Z. Metallkd.*, vol. 90, p. 323-328, 1999.

[YE 06] YE D., MATSUOKA S., NAGASHIMA N., SUZUKI N., "The low-cycle fatigue, deformation and final fracture behavior of an austenitic stainless steel", *Mat. Sci. Eng. A*, vol. 415, p. 104–117, 2006.

Chapter 7

Multiaxial Low-Cycle Fatigue Behavior at Room Temperature

7.1. Introduction

Structural components are usually loaded under multiaxial stresses. Usual multiaxial loading modes are the pure shearing state, equi-biaxial stress state, plane strain state, and internal pressure combined with other loadings. Even when the macroscopic loading is uniaxial, a multiaxial stress state exists where a notch or other geometric discontinuity exists. Biaxial and multiaxial fatigue were the specific topics of the international conferences, ICMF1 to ICMF4, followed by the international conferences, ICMFF5 to ICMFF7, held in different countries around the world every 3 or 4 years since 1982.

In multiaxial high-cycle fatigue (HCF), it is only necessary to introduce the notion of equivalent stress, using, for example, the von Mises or Tresca criterion. In low-cycle fatigue (LCF), it is necessary to precisely study the behavior of the material under multiaxial fatigue loading, which can be different of that under uniaxial fatigue, especially if the variable stress components are not in-phase. If all stress components are proportional at each time, we speak of "proportional loading"; in the opposite case, we speak of "non-proportional loading". In other words, the loading is proportional if the principal stress directions remain fixed in time with respect to geometric axes of the structural component, and the loading is non-

Chapter written by Suzanne DEGALLAIX-MOREUIL.

Duplex Stainless Steels Edited by Iris Alvarez-Armas and Suzanne Degallaix-Moreuil

proportional if the principal stress directions rotate in time with respect to these geometric axes. In many materials, a non-proportional cyclic loading leads to higher strain hardening than a proportional one. This phenomenon is called “non-proportional cyclic hardening” or “over-hardening”.

During a non-proportional cyclic loading, several dislocation slip systems are activated, more than under uniaxial or proportional loading. As a consequence, the material hardens more under non-proportional loading than under uniaxial or proportional loading. Nevertheless, the over-hardening under non-proportional loading seems to be linked more with the interactions between slip systems than with the number of activated slip systems. Thus the stacking fault energy of a material plays an important role. The lower it is, the stronger is the cyclic over-hardening. Moreover, because under multiaxial LCF the cyclic plastic strain mechanisms are different from those under uniaxial LCF, the fatigue lives are also different. That explains why the study of the behavior of materials under multiaxial fatigue is important. The first part of the chapter (section 7.2) provides basic mechanical elements necessary to understand the multiaxial LCF results on DSS related then in section 7.3.

7.2. Multiaxial LCF – introduction

7.2.1. *Multiaxial LCF: specimens and tests*

Various geometries of mechanical test specimens are used for studying LCF behavior under multiaxial fatigue. The most usual geometry has a thin cylindrical tubular useful part-loaded in tension/compression-torsion, or in tension/compression -internal and/or external pressure, with or without torsion. The benefit of this geometry is the quasi-homogenity of stress and strain fields in the thickness of the tube thin wall. So, the behavior of the material elementary volume can be characterized. Other specimen geometries are used, but they need complex specific grips and testing machines, such as bi-axes or three-axes machines, and above all, the stress and strain states in the specimens are difficult to analyze.

Only tension/compression-torsion LCF tests, which are biaxial fatigue tests (only two principal stresses are non-null) were performed on duplex stainless steels (DSS). Thus we will focus only on those tests. Such tests are carried out on a tension/compression-torsion servo-hydraulic testing machine. A load cell is mounted in series with the specimen; it measures the axial load and the torque. A biaxial extensometer is attached to the useful part of the specimen; it measures the axial strain and the shear strain.

7.2.2. *Definitions*

The comparison of the multiaxial LCF behavior of a material with the uniaxial LCF behavior requires the definition of equivalent stresses and equivalent strains under multiaxial loading. Von Mises equivalence criterion is usually used. Direction 1 is parallel to the tube axis, and direction 2 is the tube tangential direction. Because of the low thickness of the tube, the normal stress, σ_{11}, and the shear stress, τ_{12}, are calculated as:

$$\sigma_{11} = \frac{F}{S} \qquad [7.1]$$

with

$$S = \pi \frac{\Phi_{ext}^2 - \Phi_{int}^2}{4}$$

$$\tau_{12} = \frac{C}{B} \qquad [7.2]$$

with

$$B = \frac{\pi}{12} \cdot \left(\Phi_{ext}^3 - \Phi_{int}^3 \right)$$

$$\varepsilon_{11} = \frac{\Delta l}{l} \text{ and } \gamma_{12} = \frac{\Phi_{int} + \Phi_{ext}}{4} \cdot \frac{\Delta \alpha}{l} \qquad [7.3]$$

where F is the axial load, C is the torque, Φ_{ext} and Φ_{int} are the external and internal tube diameters, l is the gauge length, and α is the rotation angle between the extreme sections of the gauge length. Because of the low strains involved in LCF, true stress and strain are assumed to be equal to conventional stress and strain.

Von Mises equivalent stress is thus defined as:

$$\sigma_{Mises}^{eq} = \sqrt{\sigma_{11}^2 + 3\tau_{12}^2} \qquad [7.4]$$

and if ε_{11} and γ_{12} are the total normal and shear strains, respectively, von Mises equivalent total strain is defined as:

$$\varepsilon_{Mises}^{eq} = \sqrt{\varepsilon_{11}^2 + \frac{\gamma_{12}^2}{3}} \qquad [7.5]$$

From the total normal and shear strains, we define the plastic normal and shear strains as:

$$\varepsilon_{11}^p = \varepsilon_{11} - \frac{\sigma_{11}}{E_{11}} \text{ and } \gamma_{12}^p = \gamma_{12} - \frac{\tau_{12}}{G_{12}} \qquad [7.6]$$

with E_{11} the Young modulus in 1-direction and G_{12} the shear modulus in 12-plane.

Von Mises equivalent plastic strain is thus defined by analogy as:

$$\varepsilon_{Mises}^{p,eq} = \sqrt{\varepsilon_{11}^{p2} + \frac{\gamma_{12}^{p2}}{3}} \qquad [7.7]$$

Under proportional loading, the equivalent stress and plastic strain enable the definition of the equivalent stress and plastic strain amplitudes, $\sigma_{Mises,a}^{eq}$ and $\varepsilon_{Mises,a}^{p,eq}$, and twice these values, called the equivalent stress and plastic strain ranges, $\Delta\sigma_{Mises}^{eq}$ and $\Delta\varepsilon_{Mises}^{p,eq}$. They can be thus compared with uniaxial stress and plastic strain amplitudes and ranges. The method is usually extrapolated to any case of tension/compression-torsion loading, proportional or non-proportional. During cycling, σ_{Mises}^{eq} and $\varepsilon_{Mises}^{p,eq}$ can thus be calculated at each time during cycling.

For simplification in the following text, σ_{11}, τ_{12}, ε_{11}, γ_{12}, ε_{11}^p and γ_{12}^p will be written $\sigma, \tau, \varepsilon, \gamma, \varepsilon^p$ and γ^p, respectively, and for equivalent quantities, the subscript Mises will be omitted.

LCF tests are usually total strain-controlled, under cyclic loading. A LCF test under cyclic total strain control will thus be characterized by three parameters, which are the loading path, its amplitude and its mean value. The loading path is defined in plane $\left(\varepsilon, \gamma/\sqrt{3}\right)$ (Figure 7.1a). The loading amplitude ε_a is the radius of the smallest circle circumscribed to the loading path, and the coordinates of the center of this circle define the mean strain vector, ε_m. The stress response of the material is defined cycle per cycle in plane $\left(\sigma, \sqrt{3}\tau\right)$ (Figure 7.1b). The amplitude of the stress response, σ_a^{eq}, is the radius of the smallest circle circumscribed to the stress response, and the coordinates of the center of this circle define the mean stress

vector, σ_m^{eq}. The normal and shear plastic strains are then calculated, and the response of the material can thus be also defined in plane $\left(\varepsilon^p, \gamma^p/\sqrt{3}\right)$.

7.2.3. *Study procedure*

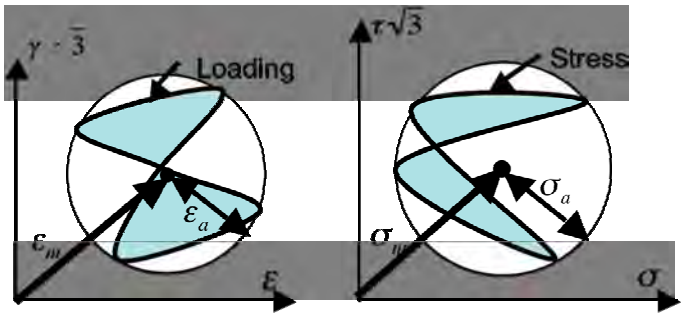

Figure 7.1. *a) Definition of the loading path for a biaxial LCF test under total strain control. b) Definition of the stress response*

By analogy with uniaxial LCF behavior study, the results of multiaxial LCF tests are analyzed in terms of cyclic hardening/softening curves (equivalent stress amplitude, σ_a^{eq}, as a function of the number of cycles), stress-strain hysteresis loop evolutions in planes (σ,ε) and (τ,γ), and cyclic stress-strain curves (stabilized equivalent stress amplitude as a function of stabilized equivalent plastic or total strain amplitude).

Figure 7.6 (in section 7.3.3) shows some examples of proportional and non-proportional loading paths used in total strain-controlled LCF tests, i.e. those used in the multiaxial LCF study of a DSS.

7.2.4. *Multiaxial LCF lives*

As in uniaxial LCF, multiaxial LCF lives are usually defined according to a failure criterion. LCF lives are sometimes defined as the number of cycles up to complete fracture of specimen or structure, but this number of cycles is the sum of the numbers of cycles for crack initiation and crack propagation. Nevertheless, the failure of a structure is usually associated with its loss of functionality, often a long time before its complete fracture. Thus the LCF life is commonly associated, not

with the complete fracture, but with a conventional stiffness loss. For a specimen tested in multiaxial LCF, a usual LCF life criterion is a conventional decrease of the equivalent stress amplitude, relative to a reference equivalent stress amplitude, for example, the stabilized equivalent stress amplitude.

7.2.5. *Presentation of the results*

By analogy with the presentation of uniaxial LCF results, in multiaxial LCF, the results are given in terms of: 1) cyclic hardening/softening curves or equivalent stress amplitude as a function of the number of cycles, 2) cyclic stress-strain curves, or stabilized equivalent stress amplitudes as a function of the equivalent total strain amplitude, 3) LCF strength curves (Manson-Coffin curves), or equivalent total, plastic and elastic strains as functions of the number of cycles to failure. Moreover, the response of the material can be given cycle by cycle in planes (σ, ε), (γ, τ), $(\sigma, \sqrt{3}\tau)$ and $(\varepsilon^p, \gamma^p/\sqrt{3})$.

7.2.6. *History effect*

Very often in structural components, the cyclic loading levels are not constant. They can be variable in amplitudes and/or in loading directions, per repeated blocks, even completely randomly. They also can be variable. The order of cyclic loading levels applied has an influence on the response of the material, depending on its initial microstructural state. A memory effect can also occur when the loading path changes during multiaxial cyclic loading. All these phenomena are called “loading history effect” or “loading memory effect”.

7.2.7. *Ratcheting behavior*

Usually, under uniaxial loading, LCF tests are carried out under total or plastic strain control, with a zero mean strain and a triangular form of strain signal with a constant strain rate. If the mean strain is different of zero, the mean stress decreases rapidly during cycling, by a relaxation phenomenon.

Conversely, if the uniaxial LCF tests are carried out under stress-control, with a mean stress different of zero, three types of behavior can be observed (Figure 7.2). If the stress-strain behavior stabilizes as elastic behavior, i.e. the width of the stress-strain hysteresis loop is zero, we speak of “shakedown”; if the stress-strain behavior stabilizes as elastic-plastic behavior, i.e. the width of the stress-strain hysteresis loop is not negligible but stabilizes, we speak of “accommodation”; if the stress-strain behavior does not stabilize, the width of the stress-strain hysteresis loop is not

negligible and the mean strain increases from cycle to cycle, the phenomenon is thus similar to creep behavior, we thus speak of “cyclic creep” or “ratcheting effect”. This phenomenon can be defined as a plastic strain accumulation.

The term “ratcheting” refers more precisely the mean strain increment per cycle. If the mean stress is much lower than the stress amplitude, the ratcheting effect can be observed in both tension and compression. Conversely, if the mean stress is of the same order of magnitude as the stress amplitude (for instance, under repeated tension stresses), the ratcheting effect is observed only in tension. Moreover, if the mean stress is low enough, the mean strain stops rapidly increasing. Conversely, if the mean stress is high enough, the mean strain increases with cycling. The mean strain rate increases rapidly at first, and then it can remain constant during an important part of the life, before a new acceleration occurs up to fracture.

Under tension/compression-torsion loading, the LCF tests are usually carried out under equivalent total strain control with a given shape of the loading path (simple relation between axial strain and shear strain) and a null equivalent mean strain. If the equivalent mean strain is different from zero, as under uniaxial loading, the mean stress decreases rapidly during cycling, by a relaxation phenomenon. The multiaxial LCF tests are also sometimes carried out under equivalent stress control, with a null or non-null equivalent mean stress. For instance, in some actual structures, an alternate shear stress is superimposed to a constant axial stress, or an alternate normal stress is superimposed to a constant shear stress. If the equivalent mean stress is different of zero, a ratcheting effect can occur.

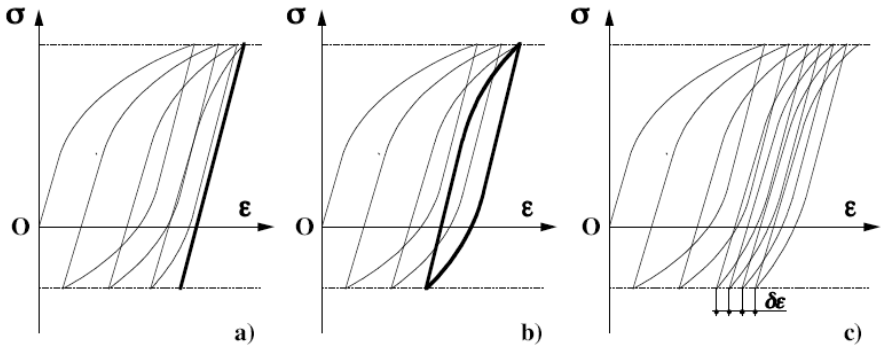

Figure 7.2. *Responses to a uniaxial cyclic loading under stress-control: a) shakedown; b) accommodation; c) ratcheting*

7.3. Biaxial LCF of a DSS type 25-07

7.3.1. *Introduction*

In the literature, very few studies deal with the multiaxial LCF behavior of the DSSs. Only [AUB 01, AUB 03a-b, AUB 04a-c, AUB 05 and AUB 08] studied a DSS in uniaxial (tension/compression) and biaxial (tension/compression-torsion) LCF at room temperature. The objective was mainly to study the cyclic elastic-plastic behavior of the material and to define the cyclic elastic-plastic constitutive law useful for structure conception (see Chapter 8).

The LCF tests in tension/compression were carried out up to fracture. Conversely, the LCF tests under tension/compression-torsion were stopped before fracture most of the time, and then very few fatigue lives were measured. The tests were carried out under various constant total strain amplitudes; others were carried out under variable total strain amplitudes by steps of increasing, decreasing or alternate levels. For the tension/compression-torsion tests, various proportional and non-proportional loading paths were studied. These tests and the results are reported below.

7.3.2. *Material, specimens, and testing equipment*

The material studied is a second-generation DSS Z2 Cr Ni Mo 25-07 alloyed with 0.17 wt% nitrogen (UNS S32550). The chemical composition is given in Table 7.1. It was supplied in the shape of a forged bar of 76 mm diameter. It was solution treated for 1 hour at 1,060°C and then water-quenched, in order to distribute all interstitial and substitution atoms in solid solution. The resulted microstructure contains 40%vol. of austenite and 60%vol. of ferrite. The microstructure is shown in Figure 7.3 in longitudinal and transversal sections of the bar.

The microstructure is typical for a forged DSS. It consists of austenitic islands elongated in the bar axis direction, drowned in a ferritic matrix. The austenitic grains are quite equiaxial with a mean size of 10 μm. The ferritic grains are much larger, with a shape factor of about 3 and a mean size of 30 μm. The microstructural morphology looks isotropic in the transverse section. Nevertheless tensile tests in longitudinal and transversal directions of the bar show that the initial macroscopic tensile behavior is quasi-isotropic.

C	Cr	Ni	Mo	Mn	Si	N	Cu	P	S	Fe
0.024	24.68	6.54	2.84	0.79	0.62	0.17	0.07	0.021	<0.003	balanced

Table 7.1. *Chemical composition of the forged DSS Z2 Cr Ni Mo 25-07 (0.17 wt% N) tested in multiaxial LCF (in wt%)*

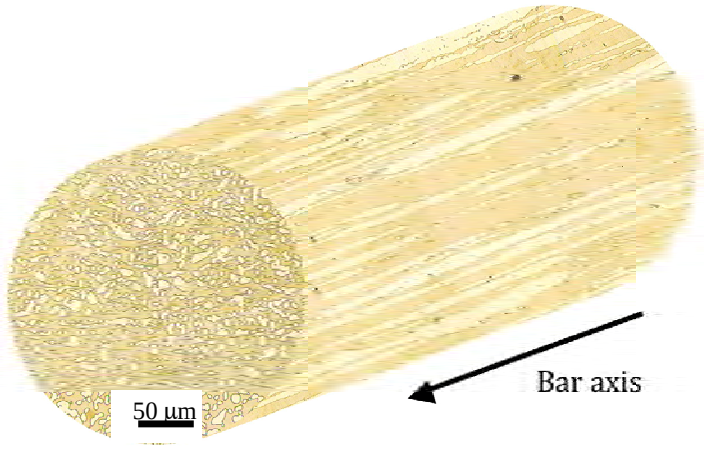

Figure 7.3. *Microstructure of the forged DSS Z2 Cr Ni Mo 25-07 (0.17 wt% N) tested in multiaxial LCF (austenite in light, ferrite in dark)*

Monotonic tests were performed under pure tension and pure torsion loading, respectively, and cyclic tension/compression, and cyclic tension/compression-torsion tests were also performed. Two specimen shapes were used. For the monotonic tension and cyclic tension/compression tests, the specimens were cylindrical and button-headed. The cylindrical part was 15 mm in length with a 10 mm gauge length and a 10 mm diameter. For the torsion and tension/compression-torsion tests, the specimens were tubular and button-headed. The cylindrical part had a 25 mm external diameter, a 22 mm internal diameter, and a 35 mm length with a 25 mm gauge length. Figure 7.4 precisely defines the geometries of these specimens.

Two servo-hydraulic testing machines were used for the mechanical tests. The monotonic tension and the cyclic tension/compression tests were performed on a uniaxial testing machine with a load capacity of 100 kN. The monotonic and cyclic torsion and tension/compression-torsion tests were performed on a biaxial testing

machine with a tension load capacity of 100 kN and a torque capacity of 1,000 Nm, the loads and torques were measured using a strain gauge biaxial loading cell. The total strain in the tension and tension/compression tests was measured using a strain gauge uniaxial extensometer, and the total longitudinal and shear strains in the torsion and tension/compression-torsion tests were measured using a biaxial strain gauge extensometer (Figure 7.5). The LCF tests and the data acquisition were performed using NI LabVIEW software. All the tests were performed under equivalent total strain control, at the equivalent total strain rate 6.6×10^{-4} s^{-1}. This total strain rate was chosen in order to compare the multiaxial LCF results with those found in the literature on austenitic stainless steels.

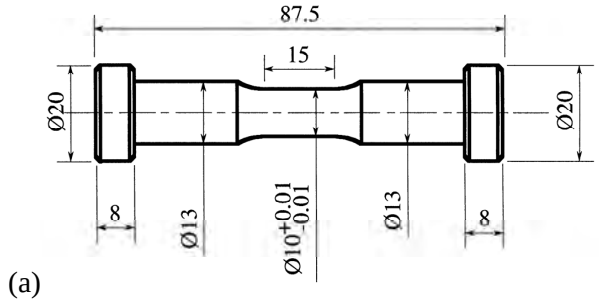

(a)

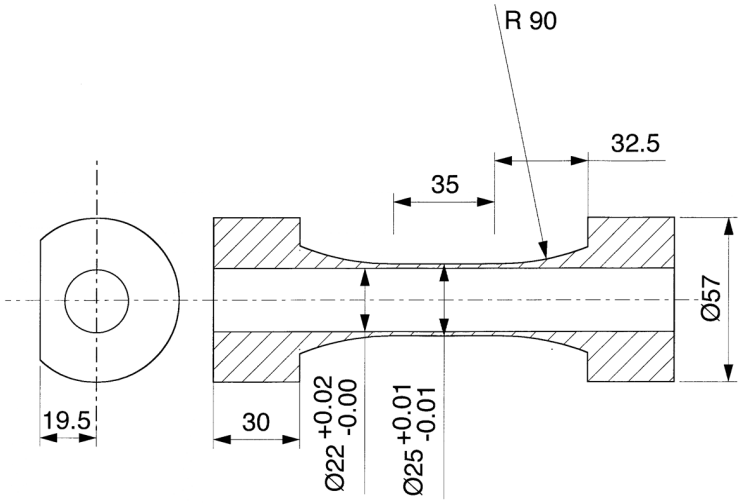

(b)

Figure 7.4. *Geometries of the test specimens: a) tension/compression test specimens; b) tension/compression-torsion test specimens*

The objectives of the monotonic tests were to obtain the usual mechanical properties of the material. The longitudinal elasticity modulus (Young modulus, Y) and the shear elasticity modulus (Coulomb modulus, G), the tension and shear yield stresses at 0.02% of plastic deformation (YS_{ten} and YS_{tor}), the tensile strength (TS), and the elongation (EL%, for a gauge length equal to the diameter) were measured and are given in Table 7.2.

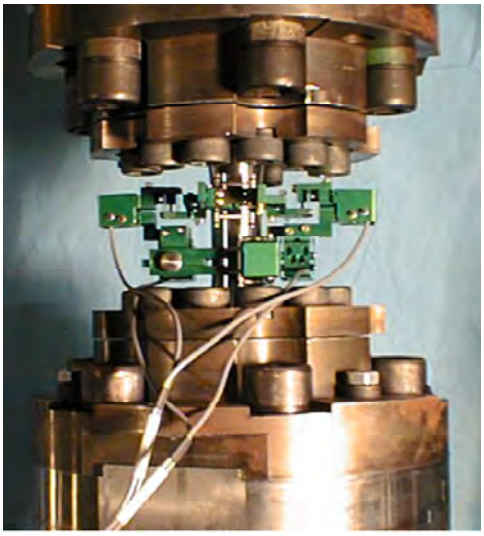

Figure 7.5. *Biaxial strain gauge extensometer used for tension/compression-torsion tests*

Young modulus (GPa)	Coulomb modulus (GPa)	YS_{ten} (MPa)	YS_{tor} (MPa)	TS (MPa)	EL (%)
198	63	435	312	1024	45

Table 7.2. *Usual mechanical properties of the forged DSS Z2 Cr Ni Mo 25-07 (0.17 wt% N)*

7.3.3. *LCF test conditions*

Fully reversed LCF tests were performed under tension/compression and under tension/compression-torsion loading with various total strain amplitudes. Because the in-service strain amplitudes are usually moderate, the studied total strain amplitudes were limited to 1% in tension/compression, and 0.8% in tension/compression-torsion. The total strain amplitude of 0.5% was extensively studied, because many of the LCF test results on austenitic and ferritic stainless

steels in the literature can be found at this total strain amplitude. Therefore a comparison of the LCF behaviors of austenitic, ferritic and DSSs can be made.

The tests with proportional loading path were performed in fully reversed tension/compression, in purely alternate torsion and in purely alternate tension/compression-torsion at 45° in plane $\left(\varepsilon, \gamma/\sqrt{3}\right)$. These loading paths are defined in the first line in Figure 7.6. Most of the LCF tests in fully reversed tension/compression were performed up to fracture on longitudinally polished specimens. At least two, even three tests were performed at the same total strain amplitude. These results were used for the comparison between multiaxial and uniaxial cyclic behaviors. The other proportional tests were performed either by steps with increasing total strain amplitudes, or with the equivalent total strain amplitude of 0.5%. The tests were performed in steps at each amplitude level up to stress stabilization before applying the next strain level.

The tests with non-proportional loading path were performed with a square, a clover, an hourglass, or a circle loading path. All these loading paths are defined in the second line in Figure 7.6. One test with a circle loading path was performed with the equivalent total strain amplitude of 0.5% up to fracture, and another in steps of increasing equivalent total strain amplitudes. For the other loading paths, the tests were performed with the equivalent total strain amplitude of 0.5% up to equivalent stress stabilization.

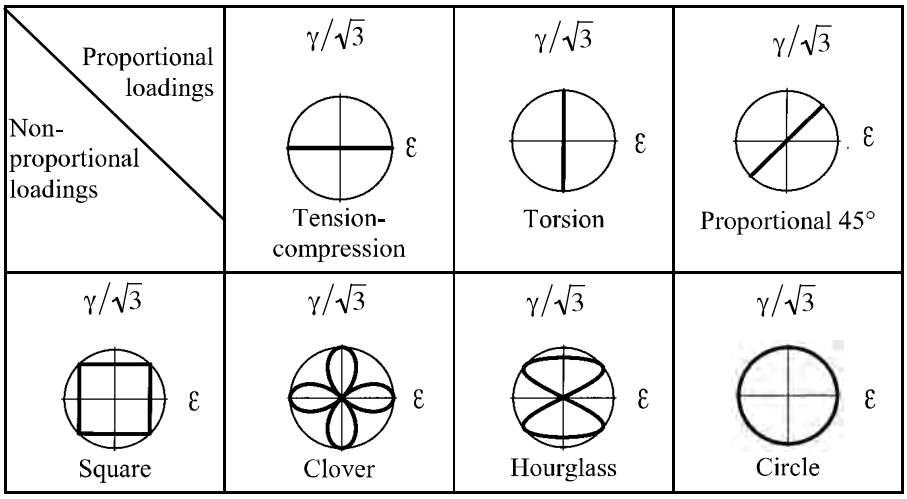

Figure 7.6. *Proportional and non-proportional tension/compression-torsion loading paths tested in multiaxial LCF on the forged DSS Z2 Cr Ni Mo 25-07 (0.17 wt% N) [AUB 01]*

At first, the isotropy of the material's mechanical behavior was verified by measuring the linearity (or proportionality) limits between stresses and strains under uniaxial and multiaxial loadings. Yield stresses were defined conventionally with an offset of plastic strain equal to 0.02%. Figure 7.7 shows that the initial isotropy hypothesis can be considered as satisfied. We thus confirm that von Mises equivalents can be used for both stresses and strains under multiaxial loading.

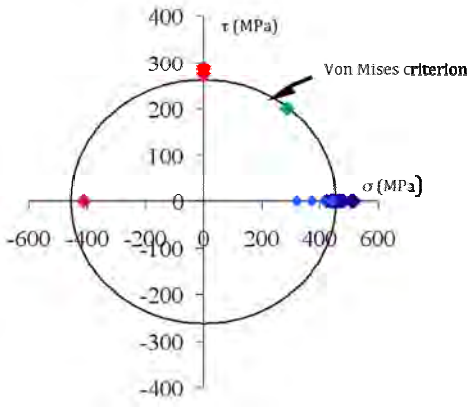

Figure 7.7. *Validation of the initial mechanical isotropy hypothesis for the forged DSS Z2 Cr Ni Mo 25-07 (0.17% N) [AUB 01]*

7.3.4. *Multiaxial cyclic behavior*

In order to compare the behavior under uniaxial and biaxial LCF, the tension-compression test results are presented first. Then they will be taken as reference.

7.3.4.1. *Tension/compression LCF test results*

The cyclic hardening/softening curves at room temperature under fully reversed tension/compression loading are given in Figure 7.8a in semi-logarithmic diagram and in Figure 7.8b in linear diagram. The second presentation allows the evaluation of the respective parts of accommodation, stabilization, and macrocrack propagation in the fatigue life.

Under tension/compression, the forged DSS Z2 Cr Ni Mo 25-07 (0.17 wt% N) exhibits an accommodation phase characterized by a hardening followed by a softening, before stabilization of the stress amplitude. The higher the strain amplitude is, the more pronounced both hardening and softening are, and the longer they last. The softening is always more pronounced than the hardening; as a

consequence, the cyclic stress-strain curve is below the monotonic stress-strain curve (symbols + in Figure 7.11).

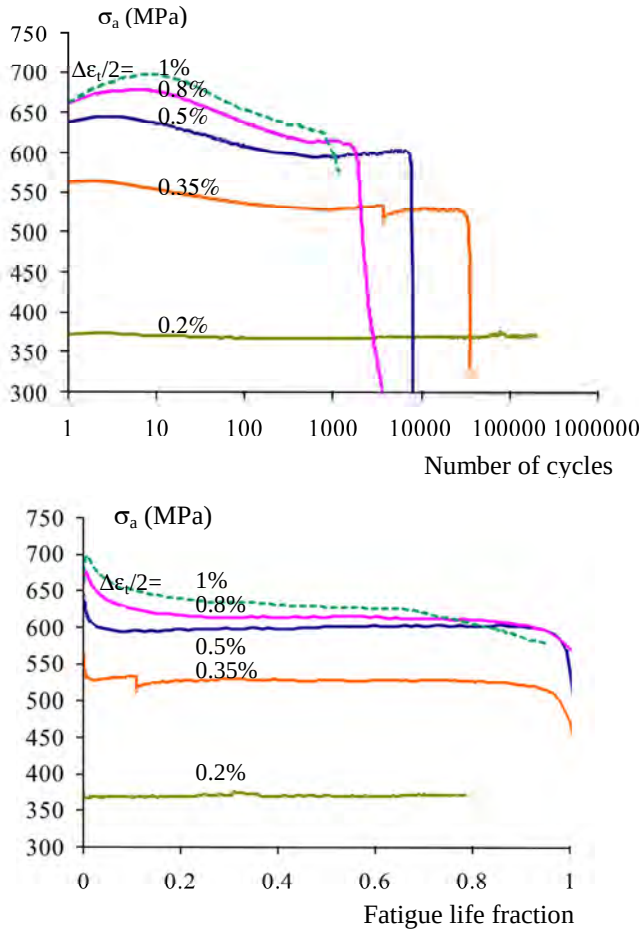

Figure 7.8. *Cyclic hardening/softening curves of the forged DSS Z2 Cr Ni Mo 25-07 (0.17 wt% N) tested in fully reversed tension/compression LCF: a) in semi-logarithmic diagram; b) in linear diagram [AUB 01]*

The Manson-Coffin curve of the forged DSS Z2 Cr Ni Mo 25-07 (0.17% N) at room temperature relative to uniaxial LCF is given in Figure 7.9 in a bi-logarithmic diagram. The elastic and plastic strain amplitudes and ranges were measured on the hysteresis loops, with a yield stress criterion at 0.02% of residual plastic strain. The

fatigue life, N_f, was defined as the stress amplitude at the cycle corresponding to a drop of about 10% of the tension stress amplitude relative to the midlife stress amplitude. The Manson-Coffin and Basquin relations obtained by linear regression from this diagram are the following:

$$\varepsilon_a^p = 5.05 N_R^{-0.86}$$

$$\varepsilon_a^e = 0.007 N_R^{-0.10}$$

Thus:

$$\varepsilon_a = \varepsilon_a^p + \varepsilon_a^e = 5.05 N_R^{-0.86} + 0.007 N_R^{-0.10} \qquad [7.8]$$

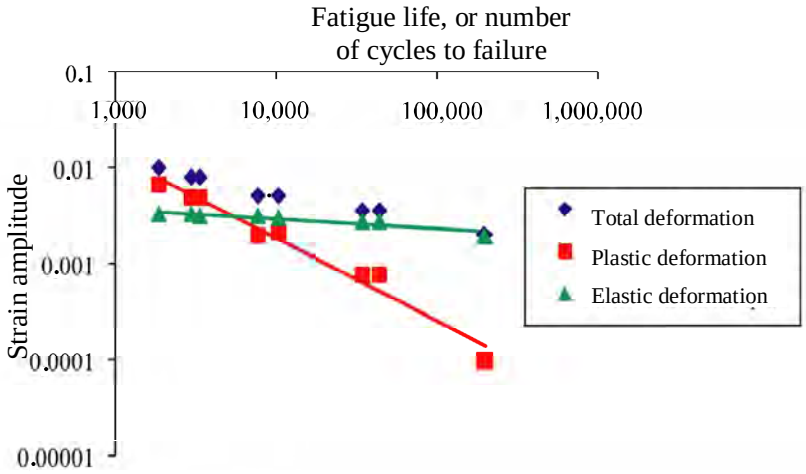

Figure 7.9. *Manson-Coffin curves of the forged DSS Z2 Cr Ni Mo 25-07 (0.17% N) tested in uniaxial tension/compression LCF [AUB 01]*

7.3.4.2. *Proportional LCF test results*

The cyclic hardening/softening curves of the forged DSS Z2 Cr Ni Mo 25-07 (0.17% N) at room temperature under fully reversed torsion loading and fully reversed proportional (45°) tension/compression-torsion loading at the equivalent total strain amplitude of 0.5% are given in Figure 7.10. The cyclic tension/compression LCF test results are added for comparison.

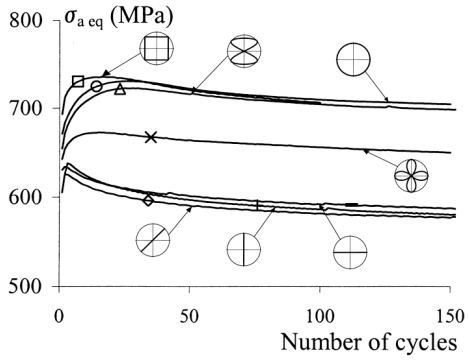

Figure 7.10. *Cyclic hardening/softening curves of the forged DSS Z2 Cr Ni Mo 25-07 (0.17% N) tested in LCF under non-proportional cyclic loading, compared with that under proportional cyclic loading ($\Delta\varepsilon_t/2$=0.5%) [AUB 01]*

The same stress amplitude levels and the same evolutions are observed, whatever the proportional loading path. Indeed, under proportional loading, the orientation of the stress principal directions does not change during cycling. The slip systems activated in the grains of the polycrystal are not very numerous and do not change very much during cycling. Also as the material is isotropic, the same behavior is observed whatever the orientation of the stress principal directions. As a consequence, the cyclic stress-strain curves are approximately the same for all proportional loading paths, and lie just below the monotonic stress-strain curve (Figure 7.11).

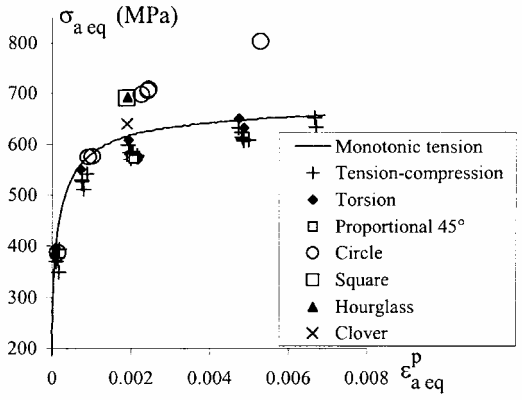

Figure 7.11. *Cyclic stress-strain curves of the forged DSS Z2 Cr Ni Mo 25-07 (0.17% N) tested in LCF under non-proportional cyclic loading, compared with those under proportional cyclic and monotonic loadings [AUB 01]*

7.3.4.3. *Non-proportional LCF test results*

The cyclic hardening/softening curves at room temperature of the forged DSS Z2 Cr Ni Mo 25-07 (0.17% N) under non-proportional cyclic loading at the equivalent total strain amplitude of 0.5% are given in Figure 7.10. The results of tests under proportional cyclic loading, including tension/compression loading, are added for comparison. The hardening/softening characterizing the accommodation phase is longer under non-proportional cyclic loading than under proportional cyclic loading. The stress amplitude levels under non-proportional cyclic loading are higher than that under proportional cyclic loading. This is characteristic of a cyclic over-hardening.

The highest stress amplitude level is observed for hourglass, circle, and square loading paths (+120 MPa at the stabilized cycle). The stress amplitude level for clover loading path is intermediate between the two previous (+75 MPa at the stabilized cycle). The over-hardening observed under non-proportional cyclic loading, compared with stress level under proportional cyclic loading, was also observed in AISI 316L austenitic stainless steels. Its level is much higher in 316L SS (+225 MPa at the stabilized cycle) than in the DSS studied here, at the same total strain amplitude $\Delta\varepsilon_t/2=0.5\%$ [CAL 97, BEN 87]. It follows the cyclic stress-strain curves under non-proportional cyclic loading given in Figure 7.11.

The order of over-hardening levels as a function of the cyclic loading path is close to that observed in [CAL 97] at $\Delta\varepsilon_p/2\approx0.3\%$ on an AISI 316L austenitic stainless steel, except that the stress level for the hourglass loading path is slightly higher than the stress level for the circle, square and clover loading paths for the 316L SS.

7.3.4.4. *Loading history effect*

The loading history effect (or loading memory effect) on the stress response of the forged DSS Z2 Cr Ni Mo 25-07 (0.17% N) in LCF at room temperature was studied in [AUB 04a] and [AUB 05]. This effect was studied thanks to strain-controlled tension/compression-torsion tests by constant loading steps of different successive levels. The influences of strain amplitude, mean strain, and loading path on the stress responses were studied.

Each test was carried out with three successive steps, the first and the third steps were identical, while the second one differed by only one loading parameter, the strain amplitude, the mean strain, or the loading path. Taking into account the scattering encountered in LCF test results, it was considered that a history effect exists if the stress amplitude in the considered step varies of at least 10 MPa from

that on a virgin specimen tested under the same loading conditions. Typical results are presented in Figures 7.12 and 7.13.

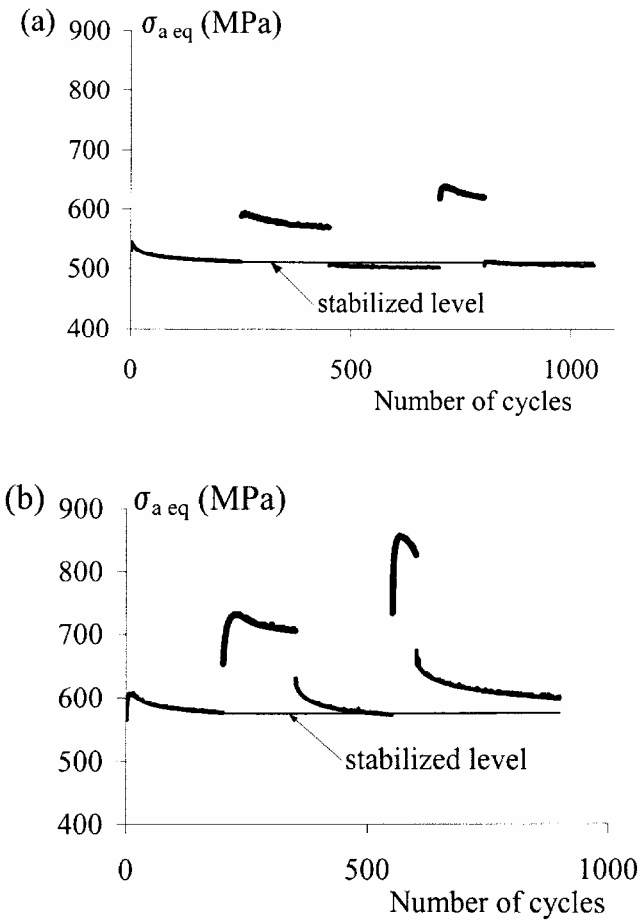

Figure 7.12. *Cyclic hardening/softening curves of the forged DSS Z2 Cr Ni Mo 25-07 (0.17% N) tested in LCF: a) under tension/compression, b) under tension/compression-torsion, both at the successive equivalent total strain amplitudes: 0.35, 0.5, 0.35, 0.8 and 0.35% [AUB 01, AUB 04a, AUB 05]*

First, a mean strain has no incidence on the stress response level, provided that it is enough high to plasticize the material, allowing the corresponding mean stress relaxes. Second, a loading history effect exists only in the plastic deformation

domain. Third, as observed in [TAN 85, LEM 88, FRA 01], no history effect exists if the straining steps successively applied correspond to increasing loading levels (Figure 7.12), or if the loading paths successively applied induce increasing strain-hardening levels (Figure 7.13). Conversely, if the straining steps successively applied correspond to decreasing loading levels, a history effect appears only if the difference between the successive equivalent stress levels is large enough.

These results are similar to that observed by other authors on other materials [TAN 85, BEN 89, MUR 89, CAI 91, DOO 91, DEL 93, CLA 96]. The history effect is clearly lower in the DSS than in austenitic stainless steels [AUB 01, AUB 04a, AUB 05].

The sensitivity of austenitic and ferritic stainless steels to the loading history was previously studied under uniaxial [MOU 97] and multiaxial [TAN 85, MUR 89, DOQ 91] cyclic loadings. It was shown that a severe loading history effect exists in austenitic stainless steels, while it is negligible in ferritic stainless steels. That was attributed by [CHR 92] and [POL 91] to the different crystallographic structures of austenite and ferrite (face-centered cubic and body-centered cubic, respectively), and their specific dislocation slip modes. Indeed, in the austenite, the dislocation slip is rather planar, while in the ferrite the dislocation cross-slip is relatively easy.

The works previously cited and other studies in the literature have shown that in materials with difficult cross-slip, the effect of loading history is more pronounced than in materials with easy cross-slip [POL 91]. The Masing effect [MAS 23] is another phenomenon characteristic of materials that do not exhibit a history effect. A material exhibits the Masing effect when the stress-strain hysteresis loop loading and un-loading parts follow unique curves in relative coordinates, whatever the strain amplitude level. The Masing effect is observed preferentially in materials with easy cross-slip [CHR 92, POL 91], such as ferritic steels compared with austenitic steels.

Moussavi [MOU 97] studied the Masing effect in a DSS and in an austenitic and a ferritic stainless steel, with compositions close, respectively, to those of individual phases of the DSS. He observed a strong Masing effect in the ferritic steel, a slight Masing effect in DSS type 2205, and almost no Masing effect in the austenitic steel. The austenitic phase of the DSS studied by [AUB 01] exhibits planar dislocation slip (see section 7.3.7), due to a relatively low stacking fault energy lowered even more by allowing nitrogen, while the ferritic phase exhibits complex dislocation slip. The sensitivity of a DSS to the loading history can thus be attributed to its austenitic phase, as previously proposed by [MOU 97].

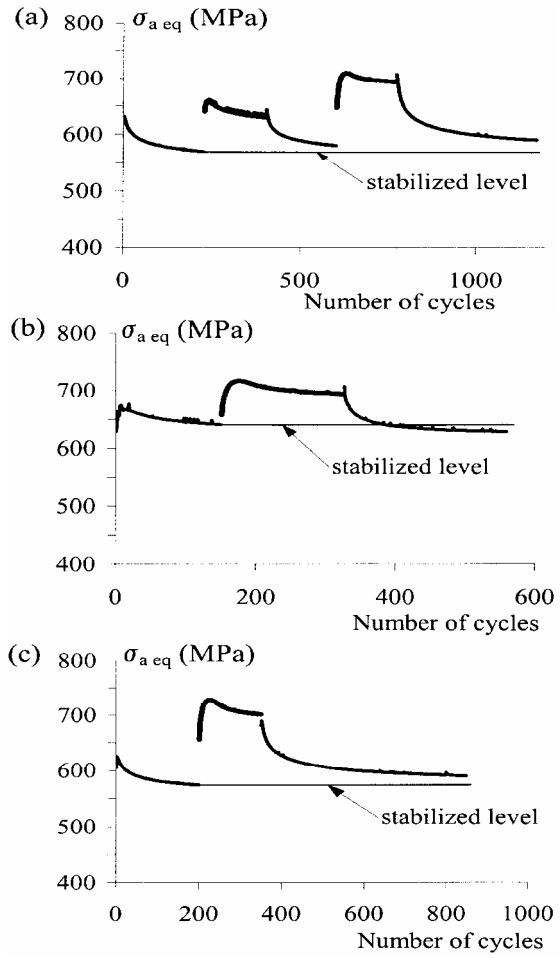

Figure 7.13. *Cyclic hardening/softening curves of the forged DSS Z2 Cr Ni Mo 25-07 (0.17% N) tested in tension/compression-torsion LCF at the equivalent strain amplitude of 0.5%, following successive loading paths: a) torsion, clover, torsion, circle, torsion, b) clover, circle, clover loading paths, c) proportional 45°, circle, proportional 45°, [AUB 01, AUB 04a, AUB 05]*

7.3.5. *Multiaxial LCF lives*

Unfortunately, very few results on multiaxial LCF lives exist in DSS. Indeed, the studies of multiaxial LCF on a DSS by Aubin *et al.* [AUB 01, AUB 03a, AUB 03b, AUB 08] were devoted to the cyclic stress-strain behavior and did not deal with the fatigue strength in terms of fatigue lives. Thus, only one fatigue life result under a

circle loading path at the equivalent strain amplitude 5×10^{-3} was compared to the fatigue life under uniaxial LCF, on test specimens with the same surface state. The results in terms of fatigue life and stress and strain amplitudes at stabilized cycles are given in Table 7.3. At the same total applied strain amplitude of 5×10^{-3}, there is a ratio of about 5 between the lives under uniaxial and multiaxial loadings, respectively, for a ratio of 0.8 between the stabilized stress amplitudes and a ratio of 0.86 between the stabilized plastic strain amplitudes. If there were no multiaxial loading effect but only plastic strain effect, the ratio between fatigue lives would be only 1.2 according to the Manson-Coffin law given in section 7.3.4.1.

Although few results of multiaxial LCF lives of DSS exist, literature search results show two main results: 1) in many different materials, such as aluminium alloys, austenitic stainless steels, mild steels, the fatigue lives under pure torsion loading are longer that those under uniaxial tension/compression loading, essentially due to a longer crack propagation phase [MNI 08, DOQ 91]; 2) under non-proportional multiaxial LCF, the fatigue lives are shorter than under proportional multiaxial fatigue [SOC 87, DOQ 91, CAI 91, WEI 93].

Test conditions in plane (ε, $\gamma/\sqrt{3}$)			Characteristics at stabilized cycle			Number of cycles to failure
Loading path	Mean strain	Equivalent strain amplitude	$\varepsilon_a^p, \varepsilon_a^{p,eq}$ ($x10^{-3}$)	σ_a, σ_a^{eq} (MPa)	σ_m (MPa)	N_f
Tension/compression	0; 0	5×10^{-3}	2.15	578	-5; 0	4900
Circle	0; 0	5×10^{-3}	2.49	691	0; 6	980

Table 7.3. *Comparison of results for two LCF tests performed under uniaxial and biaxial loadings at the same total equivalent strain level*

7.3.6. *Ratcheting behavior*

The ratcheting behavior at room temperature of the forged DSS Z2 Cr Ni Mo 25-07 (0.17% N) was studied by [BUL 02, AUB 04b, AUB 04c] under uniaxial tension/compression cyclic loading and biaxial tension/compression-torsion cyclic loading. The tests were stress controlled at the constant loading rate of 25 MPa/s. Each test was characterized by its mean stress, its stress amplitude, and its loading path, tension/compression, pure torsion (both proportional loading paths), square and cross (both non-proportional loading paths; Figure 7.14).

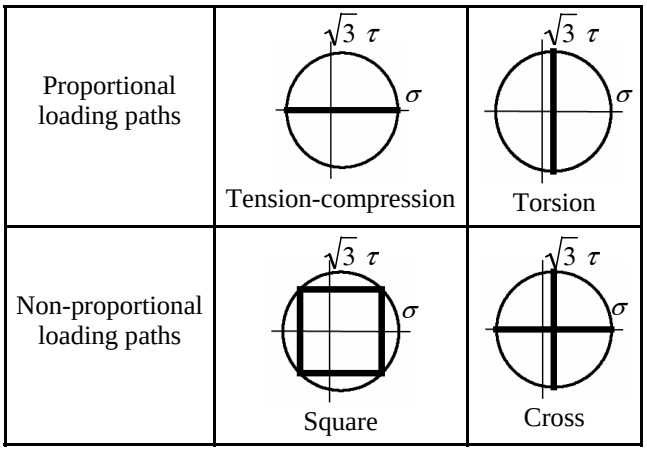

Figure 7.14. *Proportional and non-proportional tension/compression-torsion loading paths tested in multiaxial ratcheting in the forged DSS Z2 Cr Ni Mo 25-07 (0.17% N) [BUL 02]*

At first, the ratcheting existence domain has been briefly explored in uniaxial tension/compression. The total strain rate was measured at cycle 100. The ratcheting effect was assumed to occur when the strain rate was higher than 10^{-4} per cycle at cycle 100. The results are given in plane (σ_m, σ_a) in Figure 7.15.

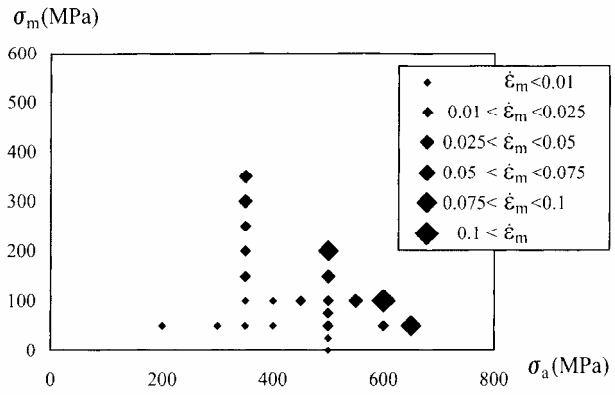

Figure 7.15. *Existence domain of the ratcheting effect under uniaxial tension/compression loading (total strain rate in %/s) [BUL 02]*

In order to remain in a domain of moderate ratcheting for an industrial use, the biaxial ratcheting domain studied was limited to the ranges 450-500 MPa for the

stress amplitudes and 100-150 MPa for the mean stresses. Figure 7.16 gives the results of three uniaxial tension/compression ratcheting tests under different mean stresses and stress amplitudes, in terms of mean strain as a function of the number of cycles. Figure 7.17 compares the results of four biaxial tension/compression-torsion ratcheting tests in terms of equivalent mean strain as a function of the number of cycles, for two proportional loading paths (tension/compression and pure torsion) and two non-proportional loading paths (square and cross loading paths), under the same mean stress (100 MPa in tension) and the same equivalent stress amplitude (500 MPa).

Under tension/compression, the same moderate ratcheting effect is observed for the tests under σ_m=100 MPa, σ_a=500 MPa, and σ_m=150 MPa, σ_a=450 MPa, while the ratcheting effect is much higher under σ_m=150 MPa, σ_a=500 MPa (Figure 7.16). The ratcheting effect depends strongly on the loading path, as previously observed by [HAS 92b, BOC 97, POR 00] on austenitic stainless steels. Under the same equivalent mean stress and the same stress amplitude, σ_a^{eq} = 500 MPa, σ_m=100 MPa (in pure tension), the DSS exhibits a ratcheting effect negligible under alternate torsion, low under a cross-loading path, and relatively significant under square and tension/compression loading paths (Figure 7.17). Note that results under the cross-loading path (composed alternatively of tension/compression and pure torsion cyclic loadings) are intermediate between the results under cyclic loading paths in tension/compression and in alternate torsion, but nevertheless much closer to the results under alternate torsion. Further ratcheting results of Hassan *et al.* [HAS 08] on an AISI 304L austenitic stainless steel under the same loading path conditions, show comparable results, except that results under the cross-loading path are much closer to the tension/compression results than to the alternate torsion results.

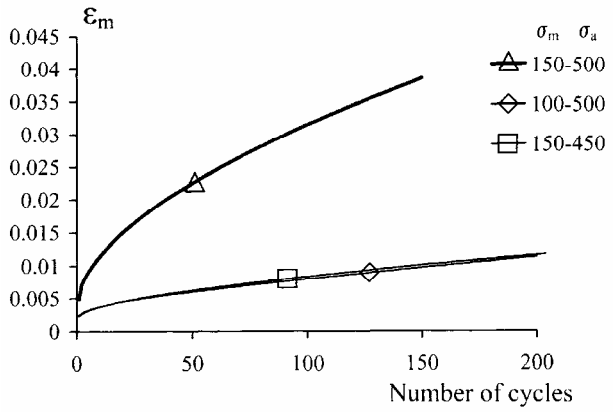

Figure 7.16. *Uniaxial tension/compression ratcheting test results under the following conditions: σ_a=450 and 500 MPa, σ_m=100 and 150 MPa [AUB 04b]*

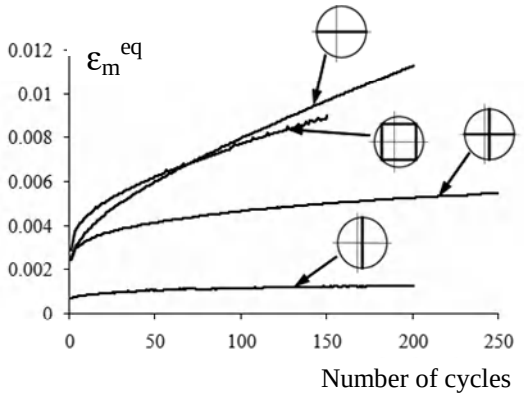

Figure 7.17. *Tension/compression-torsion biaxial ratcheting test results under the following conditions:* σ_a^{eq} *= 500 MPa,* σ_m*=100 MPa [AUB 04b]*

Results from the literature seem to show that in austenitic stainless steels too, the ratcheting effect depends strongly on the loading path. It is lower under biaxial loading than under uniaxial loading [HAS 92a-b, HAS 08, BOC 97, POR 00]. Therefore, the life prediction from uniaxial ratcheting tests would be conservative in relation to the ratcheting effect under biaxial loading [CHA 94].

7.3.7. *Microstructural evolutions in multiaxial LCF*

The response of materials to LCF loading under strain control, in terms of stress evolution and number of cycles to failure, is closely related to the dislocation structures, which develop during cyclic loading. The dislocation structures in uniaxial and biaxial non-proportional LCF at room temperature were studied on the forged DSS Z2 Cr Ni Mo 25-07 (0.17% N) by transmission electron microscopy (TEM) and compared, after fracture by Petrenec *et al.* [PET 05], and during cycling by Evrard *et al.* [EVR 08a and b]. All the analyzed specimens were tested in LCF under total strain control with the same equivalent total strain amplitude of 5×10^{-3} and the same equivalent total strain rate 6.6×10^{-4} s^{-1}.

Petrenec *et al.* [PET 05] studied and compared the dislocation structures after fracture in two specimens fatigued under symmetrical tension/compression cyclic loading and tension/compression-torsion cyclic loading following a circle path centered on zero total strain, respectively. The common equivalent total strain amplitude of 5×10^{-3} corresponded to saturated equivalent stress amplitudes of 578 and 691 MPa, to equivalent plastic strain amplitudes of 2.15×10^{-3} and 2.49×10^{-3} and to fatigue lives N_f = 4,900 and N_f = 980 cycles, in uniaxial and in biaxial loadings,

respectively. The dislocation structures were studied using a transmission electron microscope, STEM Philips CM-12. The thin foils were taken parallel to the specimen axis and prepared using the double-jet technique. The diffraction diagram and the Kikuchi lines were used to define the foil orientation.

Characteristic dislocation structures observed after tension/compression LCF are shown in Figure 7.18. In the austenitic grains, dislocation bands parallel to the trace of one, often two active {111} planes are present (Figure 7.18a-b). In the ferritic grains, one, sometimes two systems of dislocation-rich veins alternate with dislocation-poor channels are observed (Figure 7.18a-c).

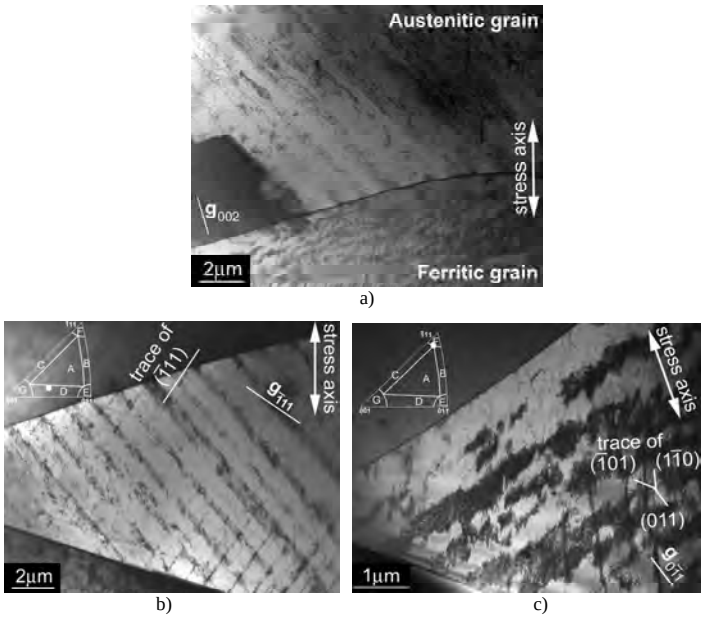

Figure 7.18. *a) Dislocation structures observed in the forged DSS Z2 Cr Ni Mo 25-07 (0.17% N) tested in fully reversed uniaxial tension-compression LCF under the total strain amplitude* $\varepsilon_a=5\times10^{-3}$*; b) dislocation structure in another austenitic grain,* $\boldsymbol{S}_a = [\bar{1}49]$, $\boldsymbol{n}_f = [\bar{1}\,\bar{5}2]$, $\boldsymbol{B} = [\bar{2}\,\bar{3}1]$*; c) detail of Figure a: dislocation structure in ferritic grain.* $\boldsymbol{S}_a$ *is near to* $[\bar{1}11]$, $\boldsymbol{n}_f = [\bar{5}\,\bar{9}3]$, $\boldsymbol{B} = [\bar{2}\,\bar{2}1]$, *[PET 05]*

Characteristic dislocation structures observed after tension/compression-torsion fatigue are shown in Figure 7.19. In Figure 7.19a and c, a cell structure is observed in the austenitic grain, and a wall structure in neighboring ferritic grain. However, cell structure in the austenitic grain shows an appreciable variability, with cells

extended in one direction in a part of the grain, and wall or labyrinth structures in other parts, detail of cell and wall mixed structure is given in Figure 7.19b. Also in the ferritic grains, the cell structure presents some variability, with cell walls more or less condensed, and sometimes intersected by straight thin bands corresponding to intense plastic strain localization along {110} crystallographic planes (Figure 7.19c).

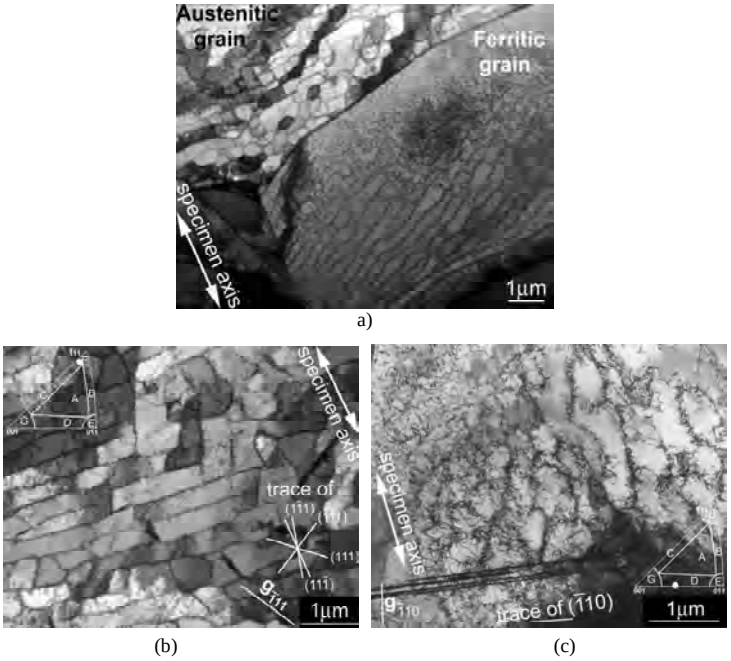

Figure 7.19. *a) Dislocation structures observed in forged DSS Z2 Cr Ni Mo 25-07 (0.17% N) tested in biaxial tension-compression/torsion LCF with circle loading path, zero mean strain and the equivalent total strain amplitude* $\varepsilon_a^{eq}=5\times10^{-3}$ *up to failure; b) detail of Figure a: dislocation structure in austenitic grain,* $\boldsymbol{S}_a = [\bar{4}45]$, $\boldsymbol{n}_f = [2\,\bar{3}4]$, $\boldsymbol{t}_z = [761]$, $\boldsymbol{B} = [\bar{1}67]$; *c) detail of Figure a: dislocation structure in ferritic grain.* $\boldsymbol{S}_a = [037]$, $\boldsymbol{n}_f = [\bar{3}\,\bar{3}1]$, $\boldsymbol{t}_z = [8\bar{7}3]$, $\boldsymbol{B} = [\bar{2}\,\bar{2}1]$, *[PET 05]*

The comparison of dislocation structures at failure produced by uniaxial and biaxial non-proportional cyclic loading with moderate strain amplitudes thus shows considerable differences. The dislocation structures are more condensed under non-proportional biaxial cyclic loading. Under uniaxial loading, one preferential slip system is essentially activated, while under biaxial non-proportional loading, at least two slip systems are activated. These features correspond to the different cyclic stress-strain responses in these two types of cyclic loading. Moreover, specific

intense straight dislocation bands in some ferritic grains give evidence of severe plastic strain localization.

Evrard *et al.* [EVR 08a, EVR 08b] studied and compared the dislocation structures before fatigue testing and at different times during cycling under symmetrical uniaxial tension/compression loading and under tension/compression-torsion loading following a square path centered on zero strain. For all these tests, the equivalent total strain amplitude was 5×10^{-3}. Moreover, two tests at the same total strain amplitude were carried out up to fracture. Under uniaxial loading and biaxial loading, respectively, the saturated equivalent stress amplitudes were 580 and 647 MPa, the equivalent plastic strain amplitudes were 2.10×10^{-3} and 2.03×10^{-3} and the fatigue lives were 6,000 and 1,500 cycles.

Two interrupted LCF test series were performed. These tests were interrupted at different numbers of cycles, to analyze the evolution of dislocation structures. The dislocation structures were studied using a Philips EM300 transmission electron microscope operating at 100 kV. Thin foils were prepared from slices taken perpendicular to the stress axis in the cylindrical plain specimens fatigued under uniaxial cyclic loading up to cycles 2, 20 and 550, i.e. during cyclic hardening, during softening, and at stabilization, respectively. In the case of biaxial fatigue tests, thin foils were taken parallel to the specimen axis in thin wall tubular specimens fatigued up to cycles 21 and 300, i.e. during cyclic hardening and cyclic softening, respectively.

Figure 7.20 shows the cyclic hardening/softening curves obtained for both types of tests and defines the times when TEM observations of the dislocation structures were performed.

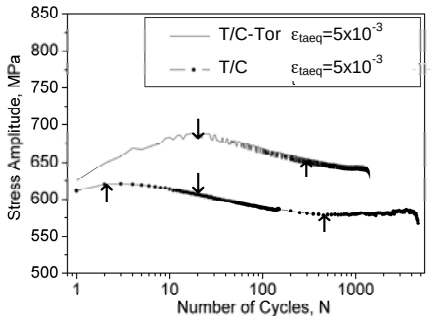

Figure 7.20. *Cyclic hardening/softening curves of the forged DSS Z2 Cr Ni Mo 25-07 (0.17% N) tested in tension/compression and in tension/compression-torsion (square loading path) LCF at the equivalent strain amplitude of 0.5%. Definition of the TEM observation times performed on LCF test specimens*

TEM observations revealed an evolution of the dislocation structures with the number of cycles for both types of loading (Figures 7.21 and 7.22). Under uniaxial loading, the dislocation structure in the austenite is planar, with one or two activated slip systems, whatever the number of cycles. Only the dislocation density increases during cycling. Conversely, in the ferrite, the dislocation structure changes strongly during cycling. At cycle 2, very few sparse dense homogenous dislocation arrangements are observed, while at cycle 20, the dislocation density is already high and bundles are observed. At cycle 550, a structure of walls and channels is observed, with high and low dislocation densities, respectively. Under biaxial loading, the dislocation structures are qualitatively similar to the previous ones but much earlier marked. Up to three planar slip systems can be observed in the austenite during all the fatigue life. The ferritic phase exhibits a homogenous arrangement of dislocations at cycle 20 and well-developed walls and channels, even labyrinth structures, at cycle 300.

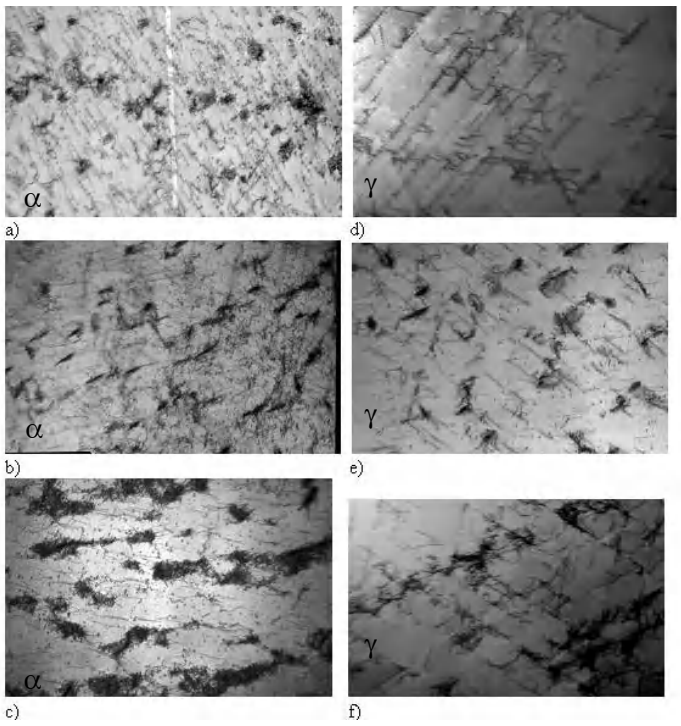

Figure 7.21. *TEM observations in the forged DSS Z2 Cr Ni Mo 25-07 (0.17% N) tested in fully reversed tension/compression LCF at the total strain amplitude of 5×10^{-3}. Dislocation structure developed in ferritic phase: a) cycle 2, b) cycle 20, c) cycle 550. Planar arrangement of dislocations developed in austenitic phase: d) cycle 2, e) cycle 20, f) cycle 550, [ALV 08, EVR 08a]*

It is well known that, in LCF, the rearrangement of dislocations in substructures, such as persistent slip bands, wall and channel structures, labyrinths or cells, i.e. in high and low dislocation density zones, corresponding to a plastic strain localization, leads to a cyclic softening. Therefore, the TEM observations suggest that the cyclic softening in DSS is at least partially due to the ferrite, where the rearrangement of dislocations into low and high dislocation density zones is clearly observed. In other respects, previous works [DEG 86, MAT 01, LEE 05] showed that austenitic and DSSs alloyed with nitrogen exhibit in LCF an accommodation phase characterized by a hardening rapidly followed by a softening, before stress stabilization. Hardening and softening are all the more intense when the nitrogen content is high. Thus in DSSs, probably both austenitic and ferritic phases participate in the cyclic softening.

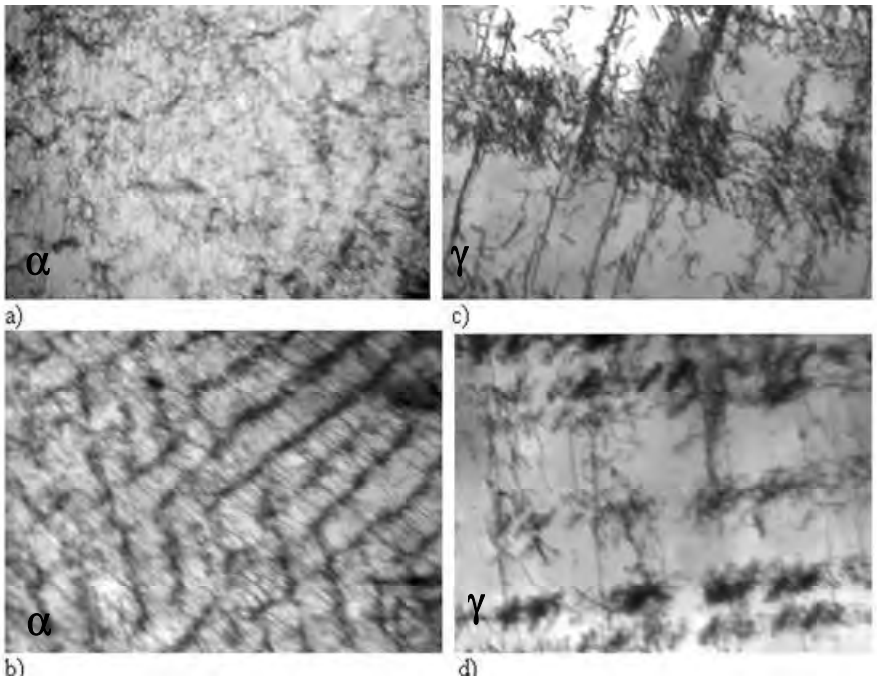

Figure 7.22. *TEM observations in the forged DSS Z2 Cr Ni Mo 25-07 (0.17% N) tested in tension/compression-torsion (square loading path) LCF at zero mean strain and at the equivalent strain amplitude of 5×10^{-3}. Dislocation structures developed in the ferritic phase: a) cycle 20, homogenous distribution of dislocations; b) cycle 300, channel/ wall and labyrinth structure. Planar arrangements of dislocations developed in austenitic phase c) at cycle 20, d) at cycle 300 [ALV 08]*

7.4. Conclusions

In this chapter, the multiaxial LCF behavior at room temperature of a second-generation DSS was presented and compared with the behavior under uniaxial cyclic loading. The following main conclusions can be drawn. The behavior in multiaxial LCF is quite different from that observed under uniaxial cyclic loading, especially if loading paths are non-proportional. An over-hardening is the main feature observed. The higher the non-proportionality is, the higher this over-hardening is. Then, a loading history effect is observed under multiaxial loading. The effects are intermediate between those observed in ferritic and austenitic steels, because of the bi-phased structure of the DSS. Finally, the microstructural observations allow us to understand the respective roles of austenite and ferrite under proportional and non-proportional cyclic plastic loading. The modeling of the uni- and multiaxial LCF results of the forged DSS Z2 Cr Ni Mo 25-07 (0.17% N) studied here is proposed in Chapter 9 of this book.

7.5. Acknowledgments

This work was supported by cooperation program ECOS-Sud/MINCyT between Ecole Centrale de Lille in France and Institute of Physics of Rosario in Argentina (project code A06E01). I would like to thank Prof. J. Polak, Prof. M. Petrenec, and Dr S. Hereñú for the TEM micrographs.

7.6. References

[ALV 08] I. ALVAREZ-ARMAS, P. EVRARD, V. AUBIN and S. DEGALLAIX, “On the cyclic softening behaviour of a duplex stainless steel”, in P. D. PORTELLA, T. BECK, M. OKAZAKI, Eds, *Proceedings of 6th Int. Conf. on Low-Cycle Fatigue (LCF6)*, Berlin, Sept. 8-12, DVM, p. 65-70, 2008.

[AUB 01] V. AUBIN, Plasticité cyclique d’un acier inoxydable austéno-ferritique sous chargement biaxial non-proportionnel, PhD thesis, University of Lille 1, 2001.

[AUB 03a] V. AUBIN, P. QUAEGEBEUR and S. DEGALLAIX, “Cyclic plasticity of a duplex stainless steel under nonproportional loading”, *Mater. Sci. Eng. A*, vol. 346, no. 1-2, p. 208-215, 2003.

[AUB 03b] V. AUBIN, P. QUAEGEBEUR and S. DEGALLAIX, “Cyclic behaviour of a duplex stainless steel under multiaxial loading: experiments and modeling”, in A. CARPINTERI, M. DE FREITAS and A. SPAGNOLI Eds., *ESIS STP Biaxial/Multiaxial Fatigue and Fracture*, Elsevier, p. 401-422, 2003.

[AUB 04a] V. AUBIN, P. QUAEGEBEUR and S. DEGALLAIX, “Loading history in fatigue: effect of strain amplitude and loading path”, *Journal of ASTM International*, vol. 1, no. 10, Nov/Dec, p. 505-518, 2004.

[AUB 04b] V. AUBIN and S. DEGALLAIX, "Ratcheting modeling of a duplex stainless steel: model based on yield surface distortion", in *Proceedings of 7th Int. Conf. on Biaxial and Multiaxial Fatigue and Fracture*, Berlin, June 28-July 1, DVM, p. 273-278, 2004.

[AUB 04c] V. AUBIN and S. DEGALLAIX, "Ratcheting modeling based on yield surface distortion", in *Proceedings of Advanced Methods in Validation and Identification of Nonlinear Constitutive Equations in Solid Mechanics, Euromech 458*, Moscow, September 21-23, Moscow University Press, p. 17-18, 2004.

[AUB 05] V. AUBIN, P. QUAEGEBEUR and S. DEGALLAIX, "Load history effect in fatigue: effect of strain amplitude and loading path", in P. C. MCKEIGHAN and N. RANGANATHAN, Eds., *Fatigue Testing and Analysis Under Variable Amplitude Loading Conditions, ASTM STP 1439*, American Society for Testing and Materials, West Conshocken, PA, p. 505-518, 2005.

[AUB 08] V. AUBIN, "Dialogue modèle-expérience en fatigue oligocyclique des aciers inoxydables", Doctoral research, University of Lille 1, 2008.

[BEN 87] A. BENALLAL D. MARQUIS, "An experimental investigation of cyclic hardening of 316 stainless steel under complex multiaxial loadings", in *Proceedings of the 9th SMIRT Conference*, Paper L10/3, 1987.

[BEN 89] A. BENALLAL, Thermoviscoplasticité et endommagement des structures, PhD Thesis, University Paris 6, 1989.

[BOC 97] L. BOCHER and P. DELOBELLE, "Etude expérimentale du comportement cyclique d'un acier du type 316L sous chargement multiaxial complexe en traction-torsion pressions interne et externe", *Journal de Physique III*, vol. 7, p. 1755-1777, 1997.

[BOC 98] L. BOCHER, D. JEUNE, P. ROBINET and P. DELOBELLE, "On the utility of complex multiaxial cyclic loadings in tension-torsion-internal and external pressures, to improve the formulation of the constitutive equations", in K-T RIE and P.D. PORTELLA, Eds., *Low-Cycle Fatigue and Elasto-Plastic Behaviour of Materials*, Elsevier, 1998, p. 223-228.

[BUL 02] A.-L. BULTHE, Etude expérimentale et modélisation du comportement en déformation progressive d'un acier duplex, DEA, University of Lille 1, 2002.

[CAI 91] G. CAILLETAUD, V. DOQUET and A. PINEAU, "Cyclic multiaxial behaviour of an austenitic stainless steel: microstructural observations and micromechanical modelling", in K. KUSSMAUL, D. MCDIARMID and D. SOCIE *Fatigue Under Biaxial And Multiaxial Loading, ESIS10*, Mechanical Engineering Publications, London, p. 131-149, 1991.

[CAL 97] S. CALLOCH, Essais triaxiaux non-proportionnels et ingénierie des modèles de plasticité cyclique, PhD Thesis, Ecole Normale Supérieure de Cachan, 1997.

[CAL 99] S. CALLOCH and D. MARQUIS, "Triaxial tension-compression tests for multiaxial cyclic plasticity", *International Journal of Plasticity*, vol. 15, p. 521-547, 1999.

[CHA 94] J.L. CHABOCHE, "Modeling of ratcheting: evaluation of various approaches", *European Journal of Mechanics A/Solids*, vol. 13, p. 501-518, 1994.

[CHR 92] H.J. CHRIST and H. MUGHRABI, “Microstructure and fatigue”, in K. T. RIE, Ed., *Low-Cycle Fatigue and Elasto-Plastic Behaviour of Materials*, vol. 3, Elsevier, London, 1992, p. 56-69.

[CHR 96] H.J. CHRIST and H. MUGHRABI, “Cyclic stress strain response and microstructure under variable amplitude loading”, *Fatigue and Fracture of Engineering Materials and Structures*, vol. 19, no. 2/3, p. 335-348, 1996.

[CLA 96] M. CLAVEL and X. FEAUGAS, “Micromechanisms of plasticity under multiaxial cyclic loading”, in A. PINEAU, G. CAILLETAUD and T. C. LINDLEY Eds., *Multiaxial Fatigue and Design, ESIS 21*, Mechanical Engineering Publications, London, p. 21-41, 1996.

[DEG 86] S. DEGALLAIX, Rôle de l’azote interstitial et combiné sur le comportement en plasticité cyclique et monotone d’aciers inoxydables austénitiques Z2 CND 17-12 (AISI 316L-316LN), PhD Thesis, University of Lille 1, 1986.

[DEG 95] S. DEGALLAIX, A. SEDDOUKI, G. DEGALLAIX, T. KRUML and J. POLÀK, “Fatigue damage in austenitic-ferritic duplex stainless steels”, *Fatigue and Fracture of Engineering Materials and Structures*, vol. 18, p. 65-77, 1994.

[DEL 93] P. DELOBELLE, “Synthesis of the elastoviscoplastic behavior and modelization of an austenitic stainless steel over a large temperature range, under uniaxial and biaxial loadings, part I: behavior”, *International Journal of Plasticity*, vol. 9, p. 65-85, 1993.

[DOO 91] S.H. DOONG and D.F. SOCIE, “Deformation mechanisms of metals under complex non-proportional cyclic loading”, in K. KUSSMAUL, D. MCDIARMID and D. SOCIE Eds, *Fatigue Under Biaxial and Multiaxial Loading, ESIS10*, Mechanical Engineering Publications, London, p. 305-320, 1991.

[DOQ 90] V. DOQUET, and A. PINEAU, “Extra hardening due to cyclic non-proportionnel loading of an austenitic stainless steel”, *Scripta Metallurgica et Materialia*, vol. 24, p. 433-438, 1990.

[DOQ 91] V. DOQUET and A. PINEAU, “Multiaxial Low-Cycle Fatigue Behaviour of a Mild Steel”, in K. Kussmaul, D. McDiarmid and D. Socie Eds, *Fatigue Under Biaxial and Multiaxial Loading, ESIS10*, Mechanical Engineering Publications, London, p. 81-101, 1991.

[DOQ 96] V. DOQUET and M. CLAVEL, “Stacking-fault energy and cyclic hardening of FCC solid solutions under multiaxial non-proportional loadings”, in A. PINEAU, G. CAILLETAUD and T. C. LINDLEY Eds., *Multiaxial Fatigue and Design, ESIS 21*, Mechanical Engineering Publications, London, p. 43-60, 1996.

[ELB 07] A. EL BARTALI, Apport des mesures de champs cinématiques à l’étude des micromécanismes d’endommagement en fatigue plastique d’un acier inoxydable duplex, PhD Thesis, Ecole Centrale de Lille, 2007.

[ELB 08] A. EL BARTALI, “Surface observation and measurement techniques to study the fatigue damage micromechanisms in a duplex stainless steel”, *International Journal of Fatigue*, in press (doi:10.1016/j.ijfatigue. 2008.11.003).

[EVR 08a] P. EVRARD, Modélisation polycristalline du comportement élasto-plastique d’un acier inoxydable austéno-ferritique, PhD Thesis, Ecole Centrale de Lille, and University of Rosario, 2008.

[EVR 08b] P. EVRARD, V. AUBIN, S. DEGALLAIX, D. KONDO and I. ALVAREZ-ARMAS, "A bi-phased polycrystalline model for the cyclic softening of a duplex stainless steel in uniaxial and biaxial cyclic loading", in P. D. PORTELLA, T. BECK, M. OKAZAKI, Eds., *Proceedings of 6th Internl Conf. on Low-cycle fatigue (LCF6)*, Berlin, September 8-12, DVM, p. 59-64, 2008.

[EVR 08c] P. EVRARD, S. HERENU, V. AUBIN, I. ALVAREZ-ARMAS and S. DEGALLAIX, "Dislocation structure evolution of DSS in uniaxial and biaxial cyclic loadings", in *VIIth International Conference "Fatigue damage"*, Hyannis, 2008.

[FRA 01] M. FRANÇOIS, "A plasticity model with yield surface distorsion for non-proportional loading", *International Journal of Plasticity*, vol. 17, p. 703-717, 2001.

[HAS 92a] T. HASSAN and S. KYRIAKIDES, "Ratcheting in cyclic plasticity – Part I: uniaxial behavior", *International Journal of Plasticity*, vol. 8, pp. 91-116, 1992.

[HAS 92b] T. HASSAN, E. CORNA and S. KYRIAKIDES, "Ratcheting in cyclic plasticity – Part II: multiaxial behavior", *International Journal of Plasticity*, vol. 8, p. 117-146, 1992.

[HAS 08] T. HASSAN, L. TALEB and S. KRISHNA, "Influence of non-proportional loading on ratcheting responses and simulations by two recent cyclic plasticity models", *International Journal of Plasticity*, vol. 24, p. 1863-1889, 2008.

[ICMFF1 to 4] *International Conferences on Biaxial/Multiaxial Fatigue*, held in USA in 1982, in UK in 1985, in Germany in 1989, in France in 1994.

[ICMF5 to 8] *International Conferences on Biaxial/Multiaxial Fatigue and Fracture*, held in Poland in 1997, in Portugal in 2001, in Germany in 2004, in UK in 2007.

[KRU 97] T. KRUML, J. POLÀK, K. OBRTLÌK and S. DEGALLAIX, "Dislocation structures in the bands of localised cyclic plastic strain in austenitic 316L and austenitic-ferritic duplex stainless steels", *Acta Metallurgica*, vol. 45, p. 5145-5151, 1997.

[LEE 05] H. J. LEE, C. S. LEE and Y. W. CHANG, "Role of nitrogen in the cyclic deformation behavior of duplex stainless steels", *Metal. and Mater. Trans. A*, vol. 36A, p. 967-976, 2005.

[LEM 88] J. LEMAITRE and J.L. CHABOCHE, *Mécanique des Matériaux Solides*, Dunod, Bordas, 1988.

[MAS 23] G. MASING, "On Heyn's hardening theory of metals due to inner elastic stresses", *Wiss. Veröff. Siemens-Konzern*, vol. 3, p. 231-239, 1923.

[MAT 01] A. MATEO, A. GIRONÈS, L. LLANES, N. AKDUT and M. ANGLADA, "Cyclic deformation behaviour of superduplex stainless steels", *Mater. Sci. Eng. A*, vol. 314, , p. 176-185 2001.

[MNI 08] R. MNIF, Caractérisation en fatigue d'un alliage cuivreux, PhD Thesis, University of Sfax, 2008.

[MOU 97] E. MOUSSAVI, Ecrouissage cyclique d'aciers inoxydables austénitique, Ferritique et austéno-ferritique: Influence de l'histoire du chargement, PhD Thesis, University of Lille 1, 1997.

[MUR 89] S. MURAKAMI, M. KAWAI and Y.J. OHMI, “Effects of amplitude-history and temperature-history on multiaxial cyclic behavior of type 316 stainless steel”, *Journal of Engineering Materials and Technology*, vol. 111, p. 278-285, 1989.

[PET 05] M. PETRENEC, V. AUBIN, S. DEGALLAIX and J. POLAK, “Dislocation structures of a duplex stainless steel in uniaxial and biaxial cyclic loading”, *Materials Science Forum*, vol. 482, p. 179-182, 2005.

[POL 91] J. POLAK, *Cyclic Plasticity and Low-Cycle Fatigue Life of Metals*, 2nd edition, Elsevier, 1991.

[POR 00] L. PORTIER, S. CALLOCH, D. MARQUIS and P. GEYER, “Ratcheting under tension-torsion loadings: experiments and modelling”, *International Journal of Plasticity*, vol. 16, p. 303-335, 2000.

[SOC 87] D. SOCIE, “Multiaxial fatigue damage models”, *Journal of Engineering Materials and Technology*, vol. 109, p. 293-298, 1987.

[TAN 85] E. TANAKA, S. MURAKAMI and M. OOKA, “Effects of plastic strain amplitudes on non-proportional cyclic plasticity”, *Acta Mechanica*, vol. 57, p. 167-182, 1985.

[WEI 93] J. WEISS and A. PINEAU, “Continuous and sequential multiaxial low-cycle fatigue damage in 316 stainless steel”, in D. L. MCDOWELL and R. ELLIS, Eds., *Advances In Multiaxial Fatigue*, *ASTM STP 1191*, American Society for Testing and Materials, Philadelphia, p. 183-203, 1993.

Chapter 8

Partition of Cyclic Plasticity in the 25Cr-7Ni-0.25N Duplex Stainless Steel Investigated by Atomic Force Microscopy

8.1. Introduction

The coexistence of two phases in approximately equivalent proportions, as for duplex stainless steels (DSS), requires the consideration of their individual properties of plastic deformation to predict the most reliable description of the macroscopic behavior of the alloy. The parameters that tend to complicate the prediction are the mechanical properties, especially when they strongly differ (such as hardness or yield stress, work-hardening exponent and toughness), and the loading conditions. Under fatigue, these parameters also strongly influence the prediction, but we have to consider the specific characteristics of the stress response to strain when the solicitation is cyclic instead of monotonic. Indeed, while a metallic alloy can only harden under monotonic loading, it can exhibit either a cyclic hardening or a cyclic softening under cyclic loading. In this way, in a tensile test, both phases undergo hardening and contribute to the strength increase, but in fatigue tests, while one of the two phases cyclically hardens, the other can cyclically soften, which results in a moderate strength increase.

Based on earlier transmission electron microscopy (TEM) studies [MAT 96, VOG 99], the cyclic stress-strain behavior of DSS is described by three well-known cyclic deformation regimes in low-cycle fatigue (LCF): “austenite-like” behavior,

---

Chapter written by Jean-Bernard VOGT, Daniel SALAZAR and Ingrid PRORIOL SERRE.

Duplex Stainless Steels Edited by Iris Alvarez-Armas and Suzanne Degallaix-Moreuil

mixed response, and “ferrite-like” behavior at lower, intermediate, and upper deformation levels, respectively. Figure 6.9 of this book is an example taken from [MAT 96] showing the different regimes for a 0.07%N DSS. For other DSS, the plastic strain amplitude transition values change from one regime to another.

This description raises the question of the strain mapping at the micro-meso scale of this material. For DSS, the microstructure must be investigated at different scales, which requires making use of many sophisticated techniques. The strain accommodation to stress applied in these alloys generally occurs by gliding of dislocations or mechanical twinning. These bulk events extend to the external surface of the material and produce a roughness that can sometimes give rise to corrosion-deformation damage.

TEM, certainly the most popular technique for the study of plastic deformation from analysis of dislocations, has the limitation that the information provided is too qualitative, too local, and originates from a very small portion of the material. Moreover, it needs special preparation of thin foils and cutting the specimen. However, using the channeling contrast of backscattered electrons in scanning electron microscopy (SEM) [e.g. SCH 96, LEB 07] enables image dislocation arrangements at the same time on larger areas containing several grains. Promising techniques are those that can combine high resolution analysis of plastic deformation marks and large areas of analysis, including a high number of grains at different locations of the specimen. Vignal *et al.* [VIG 05] obtained original results using nanoindentation and point grids deposited by electron beam lithography as tools for the measurements of matter displacement, but the number of grains investigated were too few. The slip bands formed by shearing of the crystallographic planes contain individual steps that can be imaged at a high resolution using field electron gun SEM (FEG-SEM) and atomic force microscopy (AFM). AFM has the advantage that it does not involve any electron matter interactions, as is the case for SEM. Secondary electron images of tips or sharp edges are sometimes difficult to obtain due to their high emissivity and the resulting over-brightness. The second advantage of AFM is that the *z*-coordinate can be very accurately measured (with a resolution of the order of nm) during the scanning of the surface in the x and y directions. In single-phased materials, the benefit of the high-resolution images acquired by AFM has been used successfully as a complementary method for plasticity investigation. At present, progress in the understanding of the plasticity mechanisms based on AFM investigations have been mainly addressed single-phased materials, such as copper, brass, 316L austenitic stainless steel, X10CrAl24 ferritic stainless steel, nickel-bases superalloys, TiAl [MAN 03, RIS 03, WEJ 04, HER 05]. In dual-phased materials, AFM has been very scarcely employed. Recently, however, the partition of plasticity after monotonic tensile loading of a DSS has been discussed as a function of the plastic strain, elucidating the interaction between austenite and ferrite [SER 08].

The objective of the study is to discuss the cyclic accommodation of a DSS subjected to cyclic deformation using AFM investigation of the surface topography created in the two phases; specifically to highlight the role played by each phase – austenite and ferrite – on the macroscopic behavior and to understand how they interact.

8.2. Material

The material used in this study was a high-nitrogen DSS provided as industrially manufactured 45 mm × 10 mm rods. The material has the chemical composition listed in Table 8.1 and was heat-treated at 1,070°C for 20 minutes, then water-quenched.

Element	Cr	Ni	Mo	Mn	N	Si	Fe
wt%	25.3	7.16	3.54	0.48	0.25	0.22	Bal

Table 8.1. *Chemical composition of the studied duplex stainless steel*

An electrochemical etching (80 ml HNO_3, 120 mL H_2O) has been used to reveal the microstructure. As shown in Figure 8.1, it consists of a ferrite matrix containing aligned austenite islands resulting from the rolling process.

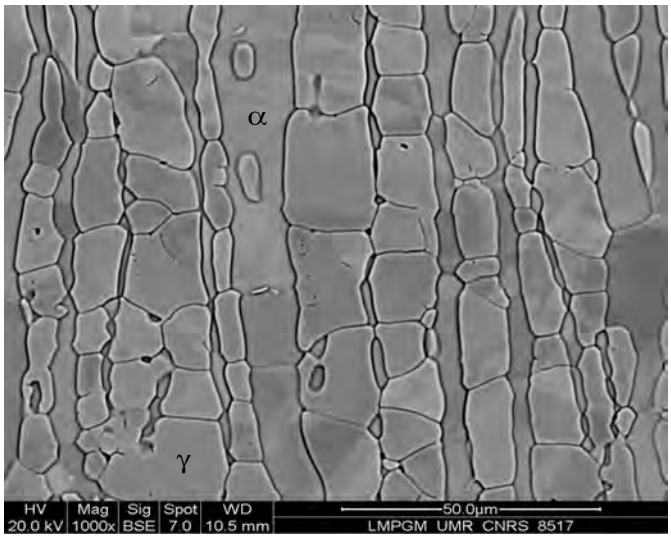

Figure 8.1. *SEM-BSE micrograph showing the typical microstructure of the DSS alloy (rolling direction: vertical axis)*

From EBSD measurements, it was found that the alloy contains 49% α and 51% γ. The mean grain diameter was 6.5 (±2.7) μm for γ and 10 (±6.2) μm for α. It is important to note that the two phases had a random distribution.

Though the austenite is strongly enriched with nitrogen, it does not exhibit a very high hardness value. In the standard heat treatment, both phases have nearly the same hardness $H_v{}^{\alpha}{}_{10} = 320$ for ferrite and $H_v{}^{\gamma}{}_{10} = 312$ for austenite.

8.3. Experimental procedure

8.3.1. *Fatigue testing*

Fatigue tests were performed at room temperature and in laboratory atmosphere using an electro-mechanical machine and an adapted setup for flat specimens. These were 3 mm thick, 6 mm wide, and 12 mm in gage length. The specimen surfaces were first mechanically polished and then electro-polished with a 25% perchloric acid, 70% acetic acid, and 5% water solution under a potential of 14 V. This is a critical stage in the experimental procedure because a topographic relief between the two phases of the alloy is required for the posterior analyses by AFM, but at the same time the relief cannot be too large because the vertical displacement of the AFM tip is limited.

Symmetric tension-compression fatigue tests were carried out at a total strain $\Delta\varepsilon_t = 0.5\%$ and 1.6%, using a triangular waveform mode at a constant strain rate of 4×10^{-3} s^{-1}. The deformation was measured by means of an extensometer directly stuck on the gauge length. These values of strain range were chosen according to a preliminary study of the mechanical response of the alloy under LCF [MAS 02].

Figure 8.2 shows the evolution of the stress amplitude versus the number of cycles for the tests concerned with this study. A log-scale has been used because it emphasis the initial accommodation period. The diagram also includes the behavior of the same alloy that has been aged at 475°C for 200 h. In the annealed condition, the stress is quite stable for the test carried out at $\Delta\varepsilon_t = 0.5\%$, while a short hardening precedes a strong softening before stabilization of the stress for the test at $\Delta\varepsilon_t=1.6\%$. Aging leads to a hardening period and an increase of the stress as compared with the test for the annealed alloy as found elsewhere [LLA 99, VOG 02].

Tests were carried out up to failure. In addition, for the strain range $\Delta\varepsilon_t = 1.6\%$, interrupted fatigue tests were carried out on a same specimen at 0.15% (5 cycles), 3.5% (100 cycles), 25% (730 cycles), and 60% (1,680 cycles) of the fatigue life, N_f, for observations at AFM.

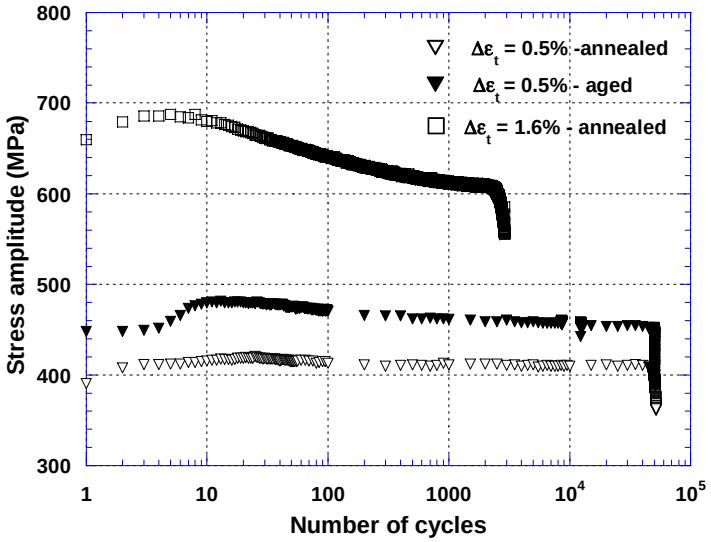

Figure 8.2. *Stress response to strain cycling for the DSS in the annealed and aged conditions*

8.3.2. *AFM*

Two different AFM were employed according to whether the fatigue tests needed to be interrupted or not. For tests carried up to failure, the fatigue specimens were cut to extract the gage length and, therefore, a Veeco Nanoscope III* AFM was employed in contact mode. A silicon nitride pyramidal tip (angle equal to 35°, radius of curvature inferior to 15 nm) has been used. For statistical analysis, the analyzed area had a size of 145 μm × 145 μm and was composed of four scanned zones. Each had a size of 75 μm × 75 μm (512 pixels per line) and they were spaced out at 70 μm.

The interrupted fatigue tests required an AFM allowing large size specimens. AFM observations were performed using a Digital III AFM in tapping mode with a Veeco anisotropic pyramidal tip MPP-11100 (front angle 15°, back angle 25°, side angle 17.5°, and radius of curvature inferior to 10 nm). In order to ensure a representative study, four different areas of 60 μm × 60 μm (taking into account different local distributions of ferrite-austenite) were analyzed. Four 30 μm × 30 μm AFM images were composed of each area. Additionally, in order to increase the lateral resolution of the three-dimensional (3D) data and to study the evolution of particular surface slip markings in detail, a few images were taken at 10 μm × 10 μm.

All AFM investigations were carried out at room temperature and in air atmosphere. Both the error signal mode and topographic mode images were used to generate high-resolution 3D quantitative data.

8.3.3. *SEM*

To connect the evolution of the deformation induced topography with the microstructure, a FEI Quanta 400 scanning electron microscope equipped with a HKL Electron Bask Scattered Diffraction (EBSD) system was employed for a crystallographic description in each phase of the grains involved in the AFM analysis.

8.4. Cyclic behavior at a low strain range

As pointed out in the introduction, at low strain amplitudes, the DSS is usually qualified as exhibiting “austenitic-like” behavior. Indeed, fatigue dislocation structures are easily identified in the austenite in the bulk of the material. Extrusion emergence and crack initiation in austenite tend to suggest that the accommodation of cyclic plasticity is only related to the behavior of austenite. Consequently, ferrite is supposed to be passive during most of the fatigue life and its main contribution occurs during fatigue crack propagation.

The objective of this investigation was to study the extent to which ferrite plays any role in the accommodation of the plasticity at low strain ranges; specifically, the presumed passivity of ferrite in this range of deformation will be discussed.

8.4.1. *Methodology*

In order to study the possible contribution of ferrite in the accommodation of cyclic plasticity, a heat treatment affecting only ferrite and not austenite was applied. It consists of aging at 475°C for 200 h after the annealing heat treatment performed on the DSS. Spinodal decomposition is known to operate for this condition in ferrite and leads to a strong hardening, while the austenite remains unchanged. Nevertheless, both annealed and aged materials have the same grain size and volume fraction of phases. A schematic representation of the microstructure with the individual hardness values is given in Figure 8.3.

Changing the annealing treatment for the aging one enables comparison of the plasticity activity of austenite grains embedded in a more or less deformable matrix. The assumption of an exclusively austenitic behavior at low strain is expected to be discussed.

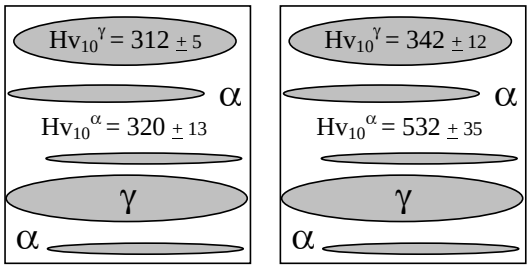

Figure 8.3. *Schematic representation of the microstructure and hardness after a) annealing treatment and b) aging treatment*

8.4.2. *Qualitative analysis of the surface relief after fatigue*

The activity of plastic deformation is studied in each phase of the materials. A grain will be considered as "active" if any change is detected after cyclic loading as compared with the initial state. Before cycling, the electro-polished surface exhibits a roughness value of Ra <4 nm and an offset between phases of about 200 nm.

The AFM images acquired at the surface specimen of both annealed and aged DSS after fatigue at $\Delta\varepsilon_t = 0.5\%$ shows the most noticeable changes concerning the austenitic phase (Figure 8.4). It is outstanding that the surface of all the ferrite grains of the aged DSS remains totally unaltered against 60% of the ferrite grains in the annealed material. In the modified ferrite grains, slip bands with features of those observed in monotonic loading [SER 08] are identified and do not display fatigue slip markings. The first observations suggest a weak contribution of ferrite to the cyclic accommodation of the plastic deformation. Therefore, the investigation focuses on the slip markings at the surface of the active austenite grains.

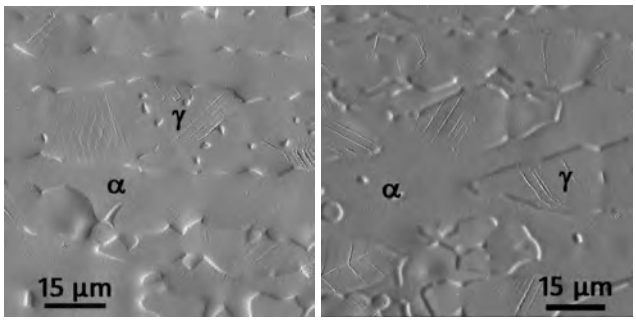

Figure 8.4. *Error mode AFM images of the specimen surface of annealed (left) and aged (right) DSS after failure fatigue at $\Delta\varepsilon_t$=0.5% ($\Delta\varepsilon_p^a$≈0.044%); load axis = horizontal*

The slip markings at the surface of the austenite grains could be classified in three categories. The first concerns very thin slip lines (Figure 8.5, left) typical of those formed under monotonic straining [SER 08] and does not reflect an accumulation of plastic deformation. The second are well-formed extrusions, as often reported for single-phase austenitic stainless steel, the so-called "ribbon-like" extrusions. These appear as rectilinear, parallel extrusions (Figure 8.5, left) and frequently cross the entire grain. These extrusions are homogenously spread out, and, in a given grain, are often separated from each other by parts by undeformed matter. Finally, slip markings combining (monotonic) slip bands and extrusions, later called "mixed morphology", could also be distinguished (Figure 8.5, left).

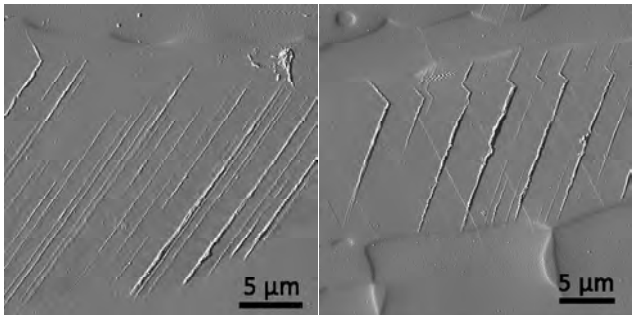

Figure 8.5. *AFM images showing (right) dense network of slip lines, mixed extrusions, and extrusions relief, and (left) well-developed extrusions and secondary slip traces at the surface of the austenite grains of the annealed DSS after fatigue failure at* $\Delta\varepsilon_t$*=0.5%*

This morphology suggests the emergence of extrusions from existing (monotonic) slip bands. For this strain range $\Delta\varepsilon_t$= 0.5%, single slip is predominant and less than 20% of the austenite active grains exhibited secondary slip traces. This secondary slip system was adorned with (monotonic) thin slip lines that entirely cross the grain (Figure 8.5, right).The three categories of slip markings were found as well in the annealed DSS as in the aged one.

The ribbon-like extrusions had roughly a triangular morphology in transverse section (Figure 8.6). For this loading condition, the height of the ribbon-like extrusions varied mainly between 10 nm and 60 nm, but in some cases could be 120 nm high. Along a given extrusion, the height and the profile were rather constant, but could vary from one extrusion to another inside the same grain (Figure 8.6). For a given extrusion, some variations in height were noticed at the vicinity of grain boundaries. However, the height was not affected by twin boundaries where the extrusion simply continued in a different direction.

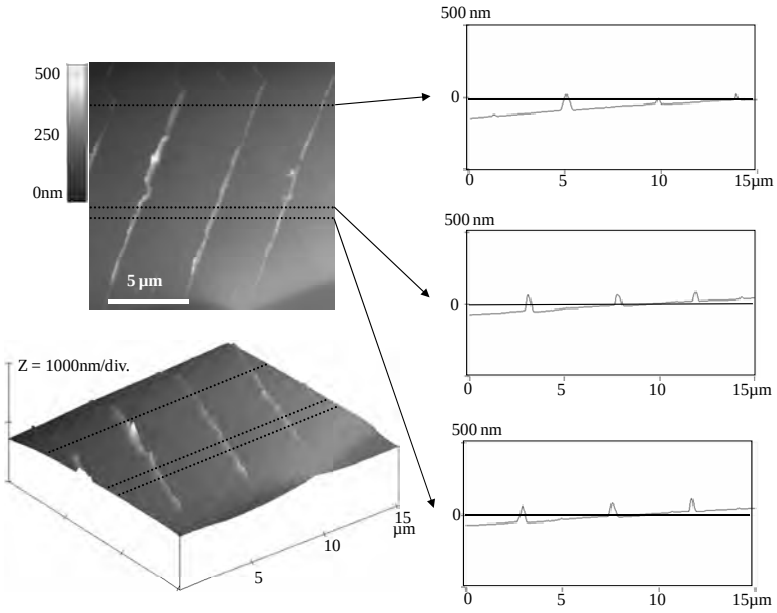

Figure 8.6. *AFM image and height of ribbon-like extrusions at the surface of austenite grains after fatigue at $\Delta\varepsilon_t$ = 0.5% ($\Delta\varepsilon_p^a \approx 0.44\%$). a) Height mode AFM image, b) 3D reconstruction, and c) profiles*

8.4.3. *Influence of heat treatment on the population of austenite grains involved in the plastic activity*

With a surface area of 435 µm × 145 µm scanned by the AFM tip for each material, 355 austenite grains in the annealed DSS and 474 grains in the aged DSS were investigated. Although the heat treatment is supposed to affect neither the volume fraction nor the grain size, it was found that the grain size of the austenite was slightly smaller in the analyzed zone than in the aged material. This, in addition to some differences in phase arrangement, affected the number of analyzed grains.

The fraction of active grains was very similar in both DSS (Figure 8.7). Therefore, the difference in plastic properties of the ferrite does not influence the number of austenite grains in the accommodation of cyclic plasticity. Triggering plasticity activity of austenite grains depends on the crystallographic orientation [VIL 02] and on the applied strain amplitude, [VOG 99, MAT 01]. From EBSD experiments, it has been found that active grains were associated with a slip system with a Schmid factor (µ) higher than 0.4. Some grains with µ < 0.35 appeared to be active, but they only contained thin slip lines or mixed extrusions.

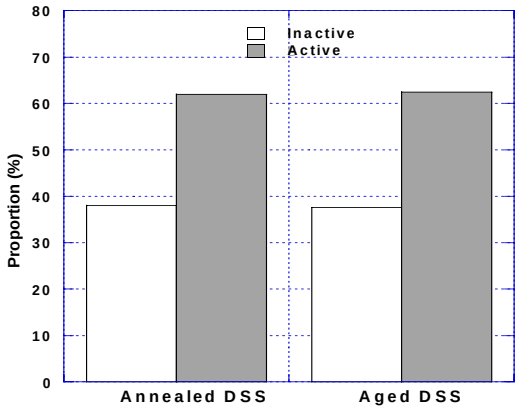

Figure 8.7. *Proportion of active and inactive austenite grains involved in cyclic plasticity at $\Delta\varepsilon_t$=0.5% ($\Delta\varepsilon_p^a$≈0.044%) in the annealed and aged DSS*

In these active grains, the percentage of grains containing thin slip lines, mixed extrusions and ribbon-like extrusions is reported Figure 8.8.

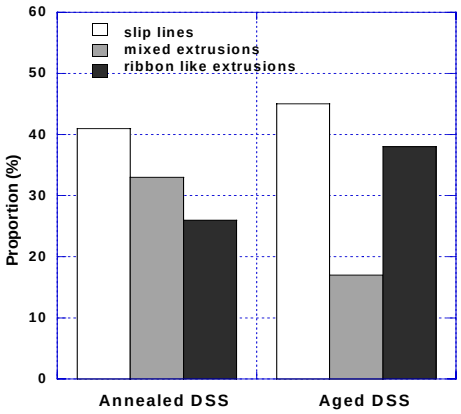

Figure 8.8. *Proportion of slip lines, mixed extrusions, and ribbon-like extrusions in active austenite grains involved in the annealed and aged DSS fatigued at $\Delta\varepsilon_t$=0.5% ($\Delta\varepsilon_p^a$≈0.044%)*

The fraction of grains containing thin slip lines is nearly the same for both alloys and would suggest no effect of the ferrite on the austenite response. However, the fraction of ribbon-like extrusions is much higher in the aged DSS than in the annealed, and therefore, the inverse for the mixed extrusions. Taking into account

Nakai's work [NAK 00], only mixed extrusions and ribbon-like extrusions reflected the irreversible cyclic activity. If it is thought that mixed extrusions, a mixture of extrusion and slip lines, is a transient stage in the formation of ribbon-like extrusions, the relief at the surface of austenitic grains is more developed in the aged DSS than in the annealed, and therefore, the plastic activity is more intense. This is an intermediate conclusion that does not take into account the dimensions of the extruded bands.

8.4.4. *Estimation of the irreversible plastic deformation from AFM measurements*

The primary parameter that will be used to evaluate the irreversible plastic deformation is the height of extrusion, δ, in the same way as is used for a monocrystal subjected to a tensile loading above its yield stress and followed by unloading. If the crystal is now deformed under compression, as it occurs during the first cycle of fatigue, an amount of matter can slip to compensate that moved during tension. The crystal recovers its original form plus an extrusion (Figure 8.9).

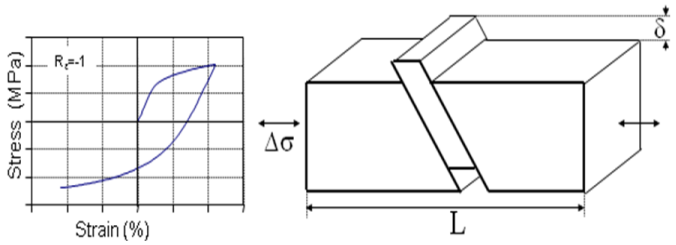

Figure 8.9. *Schematic representation of irreversible deformation in a tensile-compression cycle*

If the crystal has a length, L, then the irreversible plastic deformation related to this step is defined by equation [8.1]:

$$\gamma = \frac{2|\delta|}{L} \qquad [8.1]$$

and the total irreversible plastic deformation by the sum of all elementary deformations:

$$\gamma^{irrev} = \frac{\sum_{i=1}^{m} 2|\delta_i|}{L} \qquad [8.2]$$

where m is the number of extrusions.

For a polycrystalline material, the extrusions resulting from cyclic loading do not emerge from the complete surface of the specimen. The cyclic plastic activity and the relief at the surface of the grains are connected to grains specificities. First, the length of extrusions is limited by the size and morphology of the grain and the location in the grain size (see a_1 et a_2 in Figure 8.10). Secondly, some extrusions do not cross completely the grain (see a_3 in Figure 8.10). Therefore, the correct estimation of irreversible plastic deformation at grains surface does not depend only of the height but also of their width a.

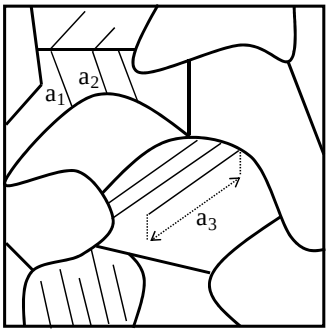

Figure 8.10. *Schematic representation of the different dimensions of extrusions according to the grain specificities in a polycrystalline material*

This imposes to normalize the extrusion width against the grain size d_{grain}. The width a now becomes a^{norm}:

$$a^{norm} = \frac{a}{d_{grain}} \qquad [8.3]$$

With the normalized value of extrusion width a^{norm}, and the corresponding extrusion height δ, we can estimate the amount of extruded matter for each grain decorated by a relief witness to the cyclic plastic deformation, and then the irreversible plastic deformation:

$$\gamma_{grain}^{norm} = \frac{\sum_{i=1}^{n} 2|\delta_i| a_i^{norm}}{d_{grain}} \qquad [8.4]$$

where n is the number of extrusions in the grain.

Finally, the total irreversible plastic deformation measured at the specimen surface appears to be the sum of elementary irreversible plastic deformations of all considered active grains.

This can be written as:

$$\gamma^{irrev} = \frac{\sum_{i=1}^{p} 2|\delta_i| a_i^{norm}}{\sum_{k=1}^{g} d_{grain_k}} \qquad [8.5]$$

where p is the number of extrusions in the whole zone and g the number of grains in the investigated zone.

Because each active grain does not deform equivalently, a statistical analysis was performed to evaluate the irreversible plastic deformation grain by grain for each material. The result is reported in Figure 8.11.

The distributions fit a log normal law (Figure 8.12). From these distributions, we can see that the maximum value is higher and shifted to the left for the aged alloy. It can, therefore, be concluded that, for the same plastic deformation imposed to the material, the active austenite grains in the aged DSS exhibit a higher and more intense irreversible plastic deformation mark at the specimen's surface than the annealed DSS.

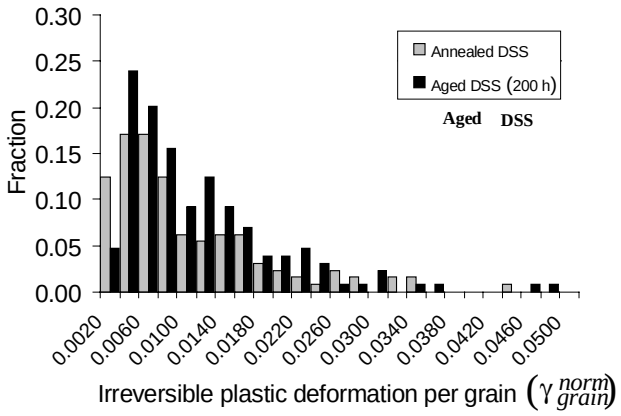

Figure 8.11. *Distribution of irreversible plastic deformation per active austenite grain at the surface the annealed and aged DSS ($\Delta\varepsilon_t$=0.5% -$\Delta\varepsilon_p^a$≈0.044%)*

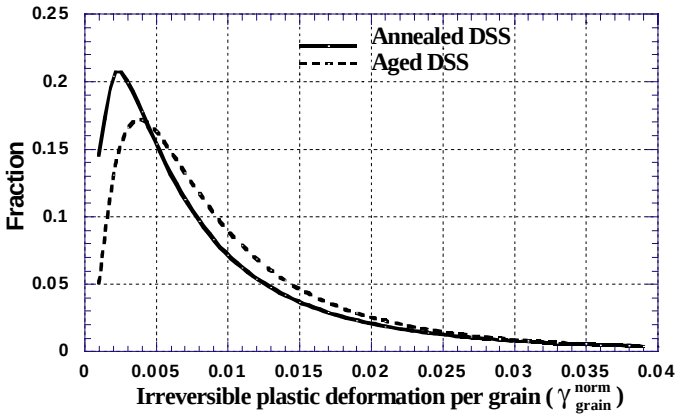

Figure 8.12. *Statistical lognormal distribution of irreversible plastic deformation per active austenite grain at the surface the annealed and aged DSS ($\Delta\varepsilon_t$=0.5% -$\Delta\varepsilon_p^a$≈0044%)*

For the calculation of the total irreversible plastic deformation of the specimen, we have to take into consideration the grains that have dimensions excessively different from the average grain size. These do not express the representative behavior of the majority of the studied grains and can influence the results. This is especially true for the very large size grains, which have the potentiality to activate a higher number of parallel slip planes. Additional statistical analyses, using the BoxPlot method, have suggested involving grains with a size that is <25 μm for the calculation. The results are reported in Table 8.2.

Using the same range of grain size, the irreversible plastic deformation measured at the specimen is 0.0022 for the annealed DSS and 0.0028 for the aged DDS, which is an increase of the plasticity activity 25% higher in the austenite grains of the aged DSS than in the annealed.

DSS	Cumulated plastic deformation	Amount of extruded matter ($\Sigma\ \delta_{grain}^{norm}$)	Effective gage length ($\Sigma\ d_{grain}$)	Irreversible plastic deformation at surface (γ_{irrev})
Annealed	2288 %	10490 nm	4752 μm	0.00220750
Aged	2381 %	14402 nm	5177 μm	0.00278224

Table 8.2. *Estimation of irreversible plastic deformation in the annealed and aged DSS after fatigue at $\Delta\varepsilon_t$=0.5% - $\Delta\varepsilon_p^a$≈0.044%*

8.4.5. *Concluding remark*

In a DSS cyclically deformed at a low strain range, the fact that marks of deformation are mainly concentrated in austenite does not imply that ferrite has no participation in the accommodation of cyclic plasticity. In an annealed DSS, the common idea that ferrite is passive means that ferrite does not contribute to the cyclic plasticity accommodation in the same way as austenite does.

8.5. Cyclic behavior at a high strain range

The stress response to strain cycling at $\Delta\varepsilon_t = 1.6\%$ indicates a complex response consisting of a cyclic hardening-softening period. Both phases exhibit typical fatigue dislocation structures, which prove their participation in the accommodation of the deformation [SAL 08]. Also, much attention has been paid to crack initiation sites according to the phase. However, few studies have been devoted to understanding how the two phases interact during cycling to accommodate the deformation.

The objective of this section is to discuss the contribution of each phase to the accommodation and their coupling effect, and to highlight the key parameters that promote strain concentration and strain distribution. The role of phase boundaries will be specifically analyzed because they are known to influence short crack behavior [e.g. VOG 94, STO 01].

8.5.1. *Identification of slip markings*

The high-resolution AFM images enabled us to distinguish the different slip markings according to their morphology. The different morphologies and their classification appear on the AFM micrographs taken after 60% of the fatigue life (Figure 8.13).

In the austenite phase of the DSS, slip markings can be classified into three different types according to their morphologies and their average height. The slip markings consist of rectilinear slip lines (height less than 20 nm), ribbon-like extrusions (height between 20-75 nm and up to 100 nm), or a mixed morphology (extrusion beginning along the slip lines).

However, in the ferrite phase, the classification is more complex because the formation of slip markings originates not only from the bulk properties of the ferrite but is also assisted by the neighboring austenite. The former are curvilinear slip

traces (less than 10 nm in height), as observed in previous work on the monotonic behavior of DSS [SER 08], located in the interior of the ferrite grains, while the latter appear as straight slip lines near the α/γ boundaries (continuation of the PSM in γ). Other persistent slip markings more typical of cyclic deformation were observed and can be separated into three groups: rectilinear band-like extrusions (Figure 8.14a), curvilinear cord-like extrusions (Figure 8.14b; height between 15-50 nm), and "highly rugged" (HR) areas frequently located at the phase boundaries.

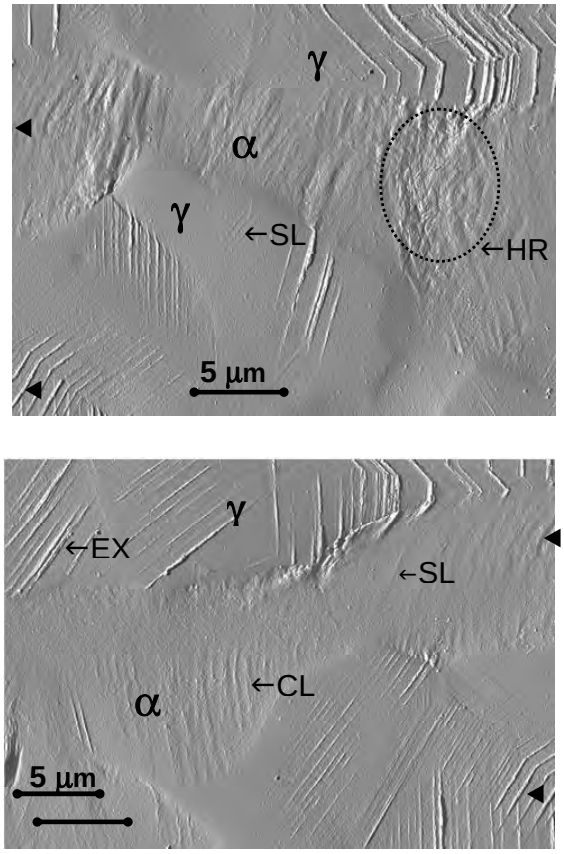

Figure 8.13. *AFM (signal error) micrographs with almost all kinds of slip markings. SL= slip line, CL=cord-like extrusion, EX=ribbon-like extrusion, HR=highly rugged area (◀: images overlap at this symbol)*

(a) band-like extrusions

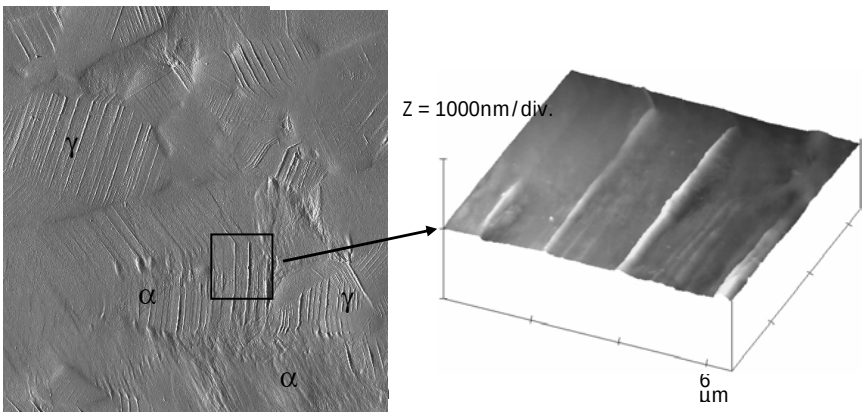

(b) cord-like extrusions

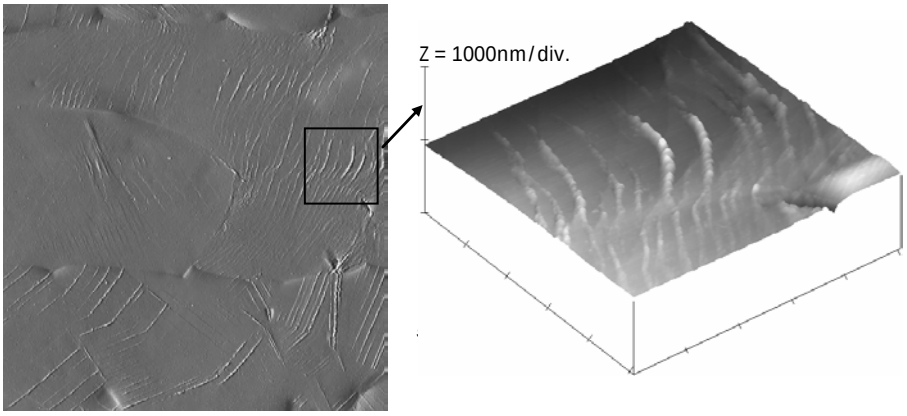

Figure 8.14. *Error-mode AFM images and 3D view of a) band-like extrusions and b) cord-like extrusions at the surface of ferritic grains after fatigue at* $\Delta\varepsilon_t$*=1.6% (*$\Delta\varepsilon_p^a$*= 0.883%)*

The HR zones are found only in ferrite and not in austenite in DSS. A HR zone consists of a system of alternating hills and valleys with a small periodicity that seems to follow the same direction (Figure 8.15). Height differences between peak and valleys reach more than 100 nm and the highest values are measured near austenitic active grains, as shown in Figure 8.15.

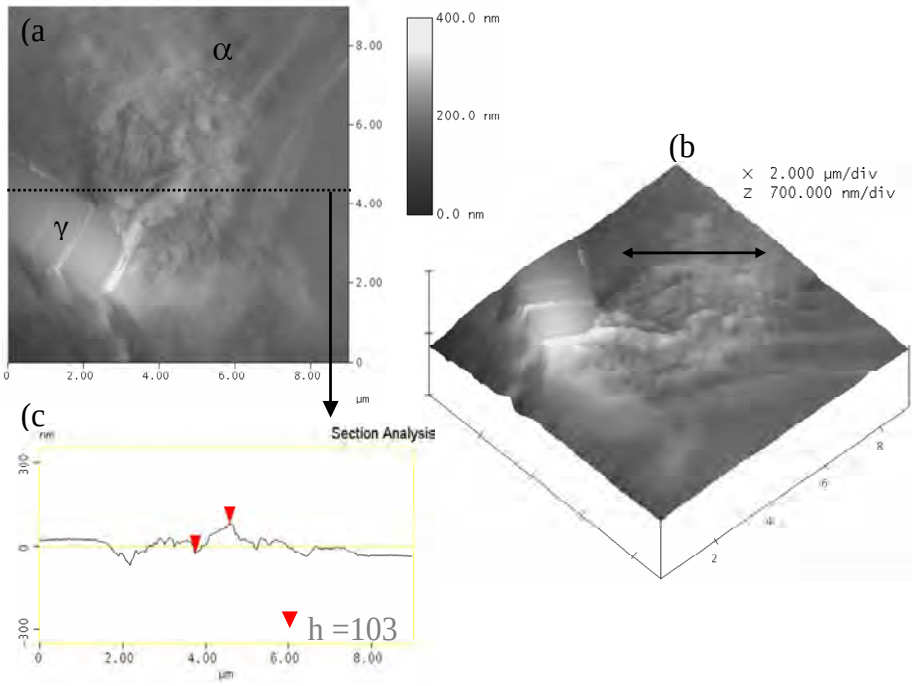

Figure 8.15. *AFM topographic a) 2D and b) 3D images showing a HR area in α; c) section detail of the dashed line in a) showing the height difference at the HR zone. Double arrow line in b) shows the direction of the small peaks and valleys*

8.5.2. *Relief evolution with cycling*

The results will be presented considering each phase separately. As in the previous section, one grain was considered as "active" when changes occurred at the surface and as "inactive" one when no obvious topographic modification was detected.

8.5.2.1. *Relief evolution during cyclic deformation in austenite*

For the four selected areas, the surface features and their evolution in the γ phase are similar, and the results presented here are the average of these four areas. Surface modifications start to develop early in fatigue life (near 40% of active grains after five cycles). The grain activity almost increases during the very first 3.5% of N_f and then evolves at a moderate rate for the rest of the fatigue life (Figure 8.16). This weak increase is generally related to twin boundaries at a neighbor active grain.

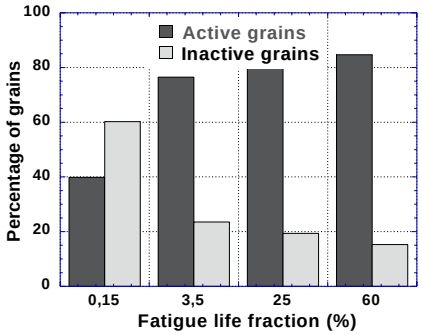

Figure 8.16. *Evolution of the plasticity partition versus fatigue life fraction in γ grains of the DSS in terms of active and inactive grains*

The straight slip lines with a mean height step between 10 and 20 nm, probably formed during the first quarter of cycle, is the main feature of the slip markings after five cycles (Figure 8.17, 0.15% N_f).

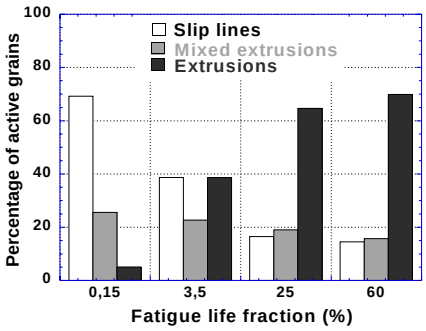

Figure 8.17. *Evolution of the plasticity partition versus fatigue life fraction in γ grains of the DSS in terms of slip marking morphology*

Slip localization in these lines transforms them progressively into extrusions. The formation of the so-called extrusions occurs by local displacement of matter in the slip line giving rise to mixed morphology. Increasing the number of cycles results in well-formed extrusions. After 100 cycles (3.5% N_f), the slip markings have a double height distribution, 25-45 nm and 15-20 nm, which corresponds, respectively, to the well-formed extrusions and to the slip mixed bands. Further cycling results in the growth of extrusions up to 75 nm at 25% of the fatigue life, more than 100 nm at 60% of the fatigue life. Slip traces corresponding to a secondary slip system are observed at 60% of fatigue life in a few grains in areas

close to the grain boundary (19% of the active grains). At this level of the fatigue life, little and irregular intrusions are detected running parallel to one side of the extrusions, but AFM [POL 03] is not the most suitable tool for direct evaluation of their depth from the metallic surface.

An example of the evolution of the PSMs at a same austenite grain surface is shown Figure 8.18 after 0.15, 3.5, 25, and 60% of the fatigue life.

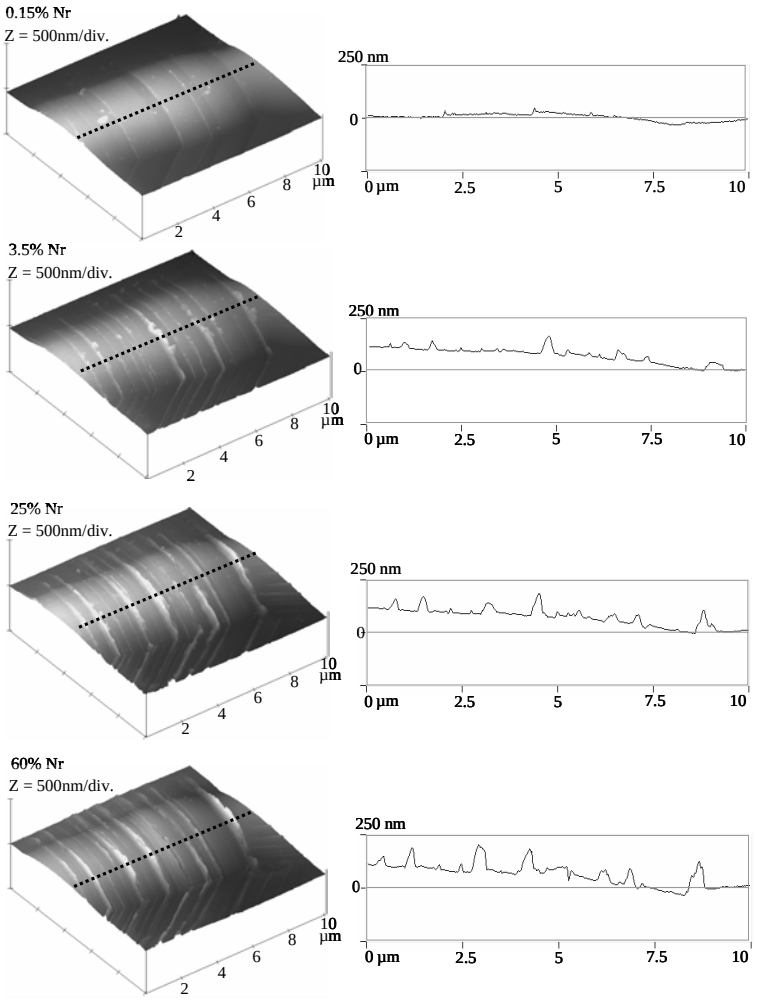

Figure 8.18. *Topographic 3D image showing the extrusions and section detail of the PSMs in austenite at a) 0.15%, b) 3.5%, c) 25%, and d) 60% of the fatigue life*

8.5.2.2. *Relief evolution during cyclic deformation in ferrite*

As opposed to observations in austenite, the surface activity in ferrite during the first percentages of the fatigue life is weak. The surface feature, mainly consisting of slip lines, is similar after five cycles (0.15% of the fatigue life) and 100 cycles (3.5% of the fatigue life) where less than 25% of ferrite grains are active (Figure 8.19).

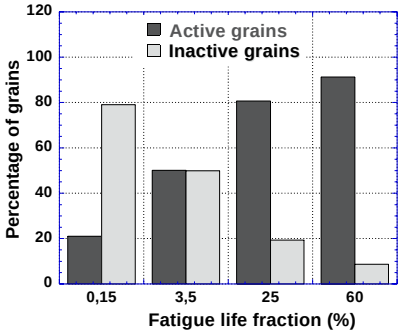

Figure 8.19. *Evolution of the plasticity of the DSS in terms of active and inactive α grains with fatigue life fraction*

Occasionally, extrusion emergences with irregular heights (between 17 and 26 nm) were observed. Real activity in ferrite seems to occur after 25% of the fatigue life where the band-like extrusions, the cord-like extrusions, and the HR areas can be easily identified. Eighty percent of ferrite grains are active after 60% of the fatigue life, but it was observed that inside a given grain HR areas could be sided with undeformed zones. It is interesting to note that in both phases slip bands are growing during cycling (Figure 8.20), even in austenite, although ferrite contributes later in the fatigue than austenite.

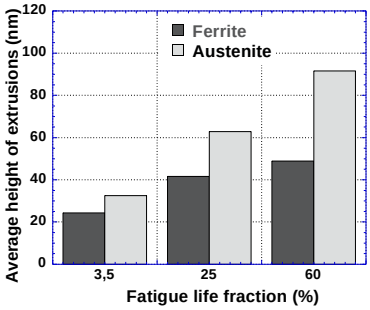

Figure 8.20. *Comparison between average height of extrusions in α and γ grains of the DSS with fatigue life*

8.5.3. *Role of crystallographic parameters*

8.5.3.1. *Role of crystallographic orientation*

For the two phases, the Euler angles of each grain (obtained via EBSD) and the angle of the persistent slip markings (PSMs) with the load axis were used to identify the activated slip system and calculate the Schmid factor (μ) for 12 and 48 main possible glide systems considered in face-centered cubic (FCC) and body-centered cubic (BCC) materials, respectively, according to the procedure explained in [VIL 02].

In agreement with the results of Villechaise *et al.* [VIL 02], the system of the trace observed for the most active austenite grains corresponds to one that has the highest Schmid factor, here $\mu > 0.4$. Only a few grains with $\mu < 0.37$ were found to be considered as active. In ferritic grains, the identification of the slip systems is complex, two or more slip systems are related to the same traces and the μ values do not appear to be a guarantee of the grain activity. Several grains with $\mu < 0.3$ were plastically active. Therefore, the Schmid factor is not the determining parameter to induce the surface activation in α grains in agreement with Girones's results [GIR 04].

8.5.3.2. *Role of crystallographic misorientation between α and γ phases*

HR zones have been described as likely sites of localized deformation. Man *et al.* [MAN 03] attributed this morphology to the activation of a second slip system. HR zones are frequently located near the α/γ boundaries and they are rarely observed in a whole grain. Height differences between peak and valleys reach more than 100 nm and the highest values are measured near austenitic active grains.

In order to find factors promoting the formation of these HR zones, the Kurdjumov-Sachs (K-S) relation, previously proposed by different authors to explain the damage process in DSS [ALV 07, BUG 01], was verified for all the situations in the α–γ analyzed areas.

The K-S crystallographic relation is used to identify the presence of complex semi-coherent interfaces; this relation is obtained between FCC and BCC crystals when the closest-packed planes are parallel to each other: $\{110\}_{bcc}//\{111\}_{fcc}$ with $<1\text{-}11>_{bcc}//<0\text{-}11>_{fcc}$. Euler angles of each grain were used to calculate the angle between the two glide systems. The relation was considered satisfied when the angle between the systems was maximum 10°. For the analyzed α–γ couples, the HR zones in ferrite were always associated with an austenitic strained grain where the relation was not satisfied (Figure 8.21).

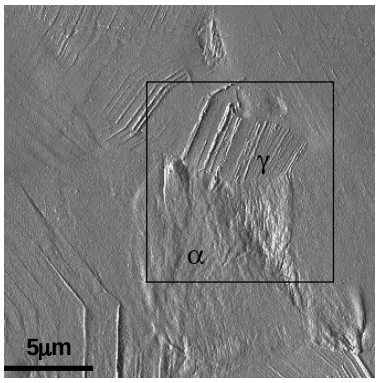

Figure 8.21. *Error-mode AFM image of the relief at a α:γ boundary where the K-S is not fulfilled*

When the relation was fulfilled for a pair, no surface changes or a slight continuation of the γ-extrusion were observed in ferrite (Figure 8.22).

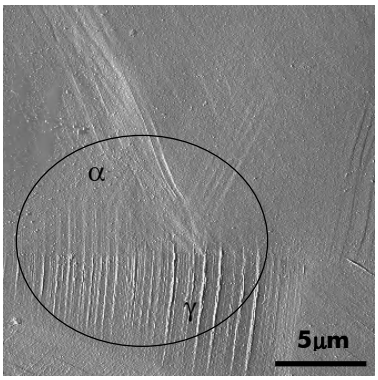

Figure 8.22. *Error-mode AFM image of the relief at a α:γ boundary with a fulfilled K-S relation*

Therefore, high plastic activity developed in the γ grain and the crystallographic mismatch between the concerned α–γ grains (based on the K-S relation) are two necessary conditions for the nucleation of HR zones near the interfaces, and therefore, to a preferential site for crack nucleation at the phase boundaries in fatigued DSS.

8.5.4. *Role of phase distribution on plasticity activity of the ferrite*

As suggested by Stolarz *et al.* [STO 01], the layout of phases affects the cyclic properties of DSS. Therefore, the variation in morphology of the phases and in their layout on the activity of plasticity has been investigated. Four zones have been identified (Figure 8.23). The first, Zone 1, is characterized by large islands with a large distance between them and with austenite grain size slightly higher than in the other areas. Zone 2 is characterized by austenitic islands with a slightly smaller size and closer each other than in the Zone 1. The third zone consists of an area with a rather round and very large islands of austenite and some isolated grains embedded in the ferrite matrix. Finally, Zone 4 is composed of many isolated austenitic grains inside the ferrite matrix. A clear dependence of the slip markings morphologies during cycling with the phase layout was found as can be seen Figure 8.23.

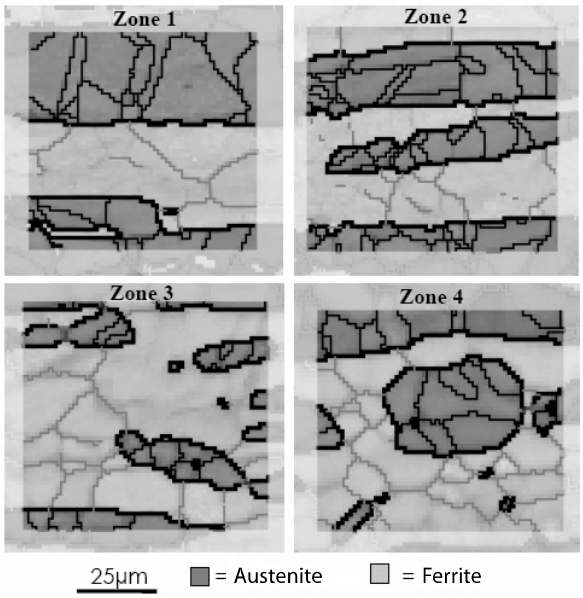

Figure 8.23. *Aspect of the 4 zones depicting variation in phase morphology and layout (EBSD reconstructed image)*

The comparison between the results obtained in Zone 1 and Zone 2 shows that the distance between austenite islands, as well as their size, is a key factor in the evolution of the different morphologies. Regarding Zone 2, the different morphologies observed at the surface change more rapidly as compared with Zone 1; for instance, HR zones in 50 and 75% of grains after 25 and 60% of the fatigue life, respectively. In Zone 1, no morphology typical of the irreversible cyclic

plasticity is observed before 25% of the fatigue life and no HR zone is observed even after 60% of the fatigue life. In Zone 3, where the morphology layout seems to be more random, the evolution of one given morphology to another is more progressive. Finally, the morphologies in the grains of Zone 4 show a rapid evolution during the first percentage of the life and then stabilize whereby all active grains exhibit morphologies typical of irreversible plastic deformation marks.

These results clearly show that the factors influencing the mechanisms of plasticity in the ferrite phase, and therefore, the crack initiation sites must be considered at a mesoscopic scale. Moreover, it is important not to reduce the analysis at the ferrite grain population scale but to take into account the neighboring austenitic phase.

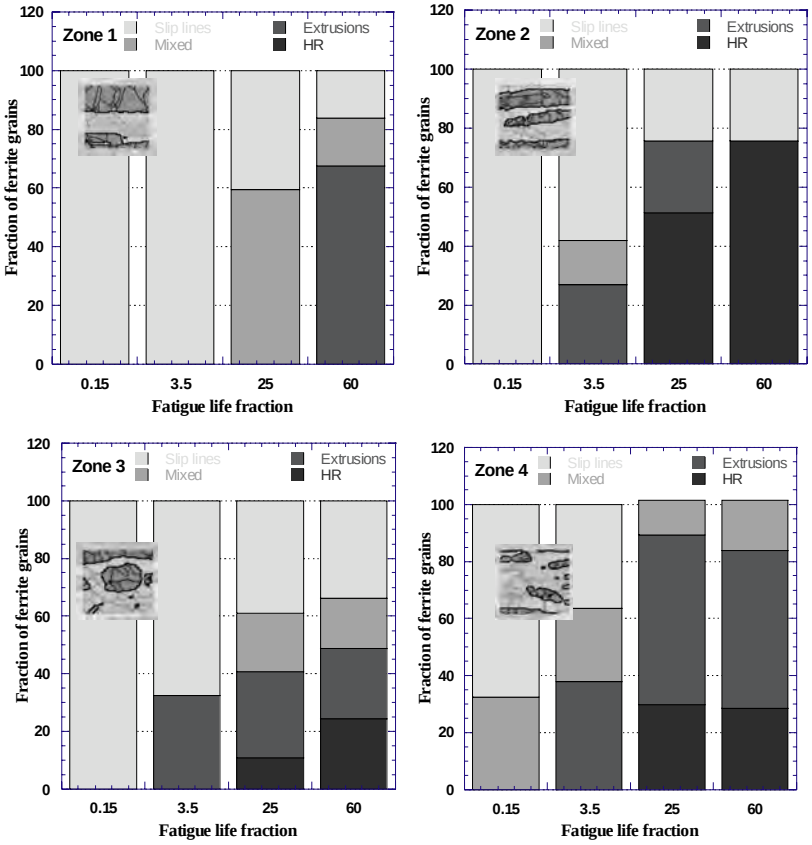

Figure 8.24. *Evolution of the types of slip marking morphologies during cycling according the phase layout*

8.5.5. *Concluding remarks*

At high strain amplitudes, it is obvious that both phases contribute to the accommodation of cyclic plasticity. Nevertheless, this type of analysis enables the role of each phase and their interactions to be highlighted. It also shows the importance of the microstructural scales to which attention must be paid. Finally, the evolution of the relief enables the explanation of the macroscopic response of the DSS. Initially, the stress response to strain cycling is given essentially by the austenite phase. After the first quarter cycle, slip lines emerge and transform into extrusions at the maximum of the stress amplitude (end of cyclic hardening). These extrusions grow in size and in quantity during cyclic softening. Once the stress stabilizes, ferrite becomes appreciably active in terms of surface irreversible deformation. At this stage, the macroscopic response is connected to the two phases, whereas previously it was only governed by the response of the austenite. Nevertheless, austenite remains active even during the stabilization period as indicated by the growing of extrusions. In ferrite, extrusion growth saturates, but HR zones form in which the strain localizes and promotes crack initiation.

8.6. Conclusions

DSSs are promising materials for future applications. Due to their unique microstructure, they provide interesting properties, especially under fatigue loading. However, their microstructure is complex, and extensive research into physical fatigue damage mechanisms is required to improve their usage properties. Investigations carried out at the mesoscopic scale and microscopic scale are of prime importance to understand their macroscopic behavior. The present study has shown that AFM appears to be a useful tool for answering these fundamental questions. DSS cannot be reduced to a simple composite material. Austenite and ferrite deform according to their own metallurgical characteristics, but one very distinctive property is their mutual interaction to accommodate cyclic plastic deformation.

8.7. References

[ALV 07] ALVAREZ-ARMAS I., MARINELLI M.C., MALARRIA J.A., DEGALLAIX S., ARMAS A.F., “Microstructure associated with crack initiation during low-cycle fatigue in a low nitrogen duplex stainless steel”, *Int. J. Fatigue*, vol. 29, p. 758-764, 2007.

[BUG 01] BUGAT S., BESSON J., GOURGUES A. -F., N’GUYEN F., PINEAU A., “Microstructure and damage initiation in duplex stainless steels”, *Mater. Sci. Eng. A*, vol. 317, p. 32-36, 2001.

[GIR 04] GIRONÈS A., VILLECHAISE P., MATEO A., ANGLADA M., MÉNDEZ J., “EBSD studies on the influence of texture on the surface damage mechanisms developed

in cyclically loaded aged duplex stainless steels", *Mater. Sci. Eng. A*, vol. 387-389, p. 516-521, 2004.

[HER 05] HÉRIPRÉ E., CREPIN J., ROOS A., SERRE I., CHABOCHE J-L., "Experimental and numerical study of plastic behaviour and crack propagation in gamma-based TiAl microstructures", in *Proc. EUROMECH-MECAMAT EMMC8*, September 13-15, Paris, 2005.

[LEB 07] LEBER H. J., NIFFENEGGER M., TIRBONOD B., "Microstructural aspects of low cycle fatigued austenitic stainless tube and pipe steels", *Materials Characterization*, vol. 58, p. 1006–1015, 2007.

[LLA 99] LLANES L., MATEO A., VILLECHAISE P., MÉNDEZ J., ANGLADA M., "Effect of testing atmosphere (air/in vacuo) on low cycle fatigue characteristics of a duplex stainless steel", *Int. J. Fatigue*, vol. 21, p. 119-125, 1999.

[MAN 03] MAN J., OBRTLIK K., POLAK J., "Study of surface relief evolution in fatigued 316L austenitic stainless steel by AFM", *Mater. Sci. Eng.* A, vol. 351, p. 123-132, 2003.

[MAS 02] MASSOL K, VOGT J.-B., FOCT J., "Fatigue behavior of new duplex stainless steels upgraded by nitrogen alloying", *ISIJ International*, vol. 42, p. 310-315, 2002.

[MAT 96] MATEO A., LLANES L. ITURGOYEN L., ANGLADA M., "Cyclic stress strain response and dislocation substructure evolution of a ferrite-austenite stainless steel", *Acta Mat.*, vol. 44, p. 1143-1153, 1996.

[NAK 00] NAKAI Y., OHNISHI K., KUSUKAWA T., "Observations of fatigue slip bands and stage I crack initiation process in alpha brass using scanning atomic microscopy", ASTM Special technical publication, p.122-135, 2000.

[POL 03] POLAK J., MAN J., OBRTLIK K., KRUML T., "The shape of extrusions and intrusions produced by cyclic straining", *Z. Metallkd.*, vol. 12, p. 1327-1330, 2003.

[RIS 03] RISBET M., FEAUGAS X., GUILLEMER-NEEL C., CLAVEL M., "Use of AFM to quantify slip irreversibility in a nickel-base superalloy", *Scripta Mat.*, vol. 49, p. 533-538, 2003.

[SAL 08] SALAZAR D., Etude du partage de la plasticité cyclique d'un acier duplex par AFM, PhD Thesis, University of Lille, 2008

[SCH 96] SCHWAB J., BRETSCHNEIDER J., BUQUE C., BLOCHWITZ C. and HOLSTE C., "Application of electron channelling contrast to the investigation of strain localization effects in cyclically deformed fcc crystals", *Phil. Mag. Letters*, vol. 74, p. 449- 454, 1996.

[SER 08] SERRE I., SALAZAR D., VOGT J.-B., "Atomic force microscopy investigation of surface relief in individual phases of deformed duplex stainless steel", *Mater. Sci. Eng.*, vol. 492, p. 428-433, 2008

[STO 01] STOLARZ J., FOCT J., "Specific features of two phase alloys response to cyclic deformation", *Mater. Sci. Eng. A*, vol. 319-321, p. 501-505, 2001.

[VIG 05] VIGNAL V., FINOT E., OLTRA R., LACROUTE Y., BOURILLOT E., DEREUX A., "Mapping the 3D-surface strain field of patterned tensile stainless steels using atomic force microscopy", *Ultramicroscopy*, vol. 103, p. 183–189, 2005

[VIL 02] VILLECHAISE P., SABATIER L., GIRARD J.C. “On slip band features and crack initiation in fatigued 316L austenitic stainless steel: Part 1: Analysis by electron back-scattered diffraction and atomic force microscopy”, *Mater. Sci. Eng. A*, vol. 323, p.377-385, 2002.

[VOG 94] VOGT J.-B., MESSAI A., FOCT J., “Factor influencing the LCF behaviour of a DSS : “effect of strain amplitude and nitrogen content”, in *Conf. Conference Duplex Stainless Steels DSS ‘94*, Glasgow, TWI Publishing, paper 11, 1994.

[VOG 99] VOGT J.-B., AIT SAADI B., FOCT J., “Analysis of the fatigue dislocation structures in a duplex stainless steel alloyed with nitrogen”, *Z. Metallkd.*, vol. 9, p. 323-328, 1999.

[VOG 02] VOGT J.-B., MASSOL K., FOCT J., “Role of the microstructure on fatigue properties of 475°C aged duplex stainless steels”, *Int. J. Fatigue*, vol. 24, p. 627-633, 2002.

[WEJ 04] WEJDEMANN C., PEDERSEN O. B., “AFM study of the intense slip localization causing fatigue crack initiation in polycristalline brass”, *Mater. Sci. Eng. A*, vol. 387-389, p. 556-559, 2004.

Chapter 9

Macro- and Micromodeling of the Monotonic and Cyclic Mechanical Behavior of a Forged DSS

9.1. Introduction

The mechanical behavior of duplex stainless steels under monotonic and cyclic loadings has already been presented in Chapters 6 and 7. This chapter highlights constitutive modeling needed for dimensioning structure components in finite element calculation. Three approaches can be used to simulate the experimental behavior of a metallic alloy. The first uses a macroscopic approach based on the evolution of observable macroscopic variables (load, stress, strain, temperature, etc.) and internal variables in order to account for the phenomena observed [ARM 66, MRO 67, CHA 83, BEN 87, CHA 91, TAN 94, CAL 99]. The validity of this type of model is often limited to the experimental data used for its identification.

The second approach, called micromechanical, accounts for macroscopic and microscopic phenomena through the evolution of variables on the grain scale [CAI 92, LEB 93, ABD 04]. A third approach consists of the use of the finite element method for simulating a polycrystalline aggregate, large enough to be an representative volume element of the material [BAR 01a and b]. The main drawback of this last approach is that it requires long calculation times, currently incompatible with the simulation of fatigue tests.

Chapter written by Véronique AUBIN and Pierre EVRARD.

Duplex Stainless Steels Edited by Iris Alvarez-Armas and Suzanne Degallaix-Moreuil

The two first approaches have been used to account for the mechanical behavior under monotonic and cyclic loading of a forged duplex stainless steel type Z2 CrNiMo 25-07 alloyed with 0.17% N. The experimental results have already been presented in Chapter 7, some of them will then be shown again only for the purpose of validating the numerical results.

9.2. Macroscopic modeling of the mechanical behavior

9.2.1. *Thermodynamic frame*

Two categories of constitutive models have been developed in the past, based on various thermodynamic assumptions:

– the current state of the material depends only on current values and on the history of observable variables (total strain, load, temperature, etc.). Hereditary models, such as the endochronic theory, are based on this assumption [KRE 75, BOR 96];

– the current state of the material depends only on the current values of the observable and internal variables. Various evolution laws for the internal variables have been proposed, such as the multisurface approach [MRO 67], the two-surface theory [DAF 75], and models based on differential equations [ARM 66]. It has been shown that these approaches are equivalent, at least under certain conditions [MAR 79].

Only this last approach will be presented here. The current state of a material at a point in time is defined by variables, observable and internal, depending only on this point. The evolution of these internal variables is based on the thermodynamics of irreversible processes [LEM 88].

A thermodynamic potential is assumed, generally the free energy density, ψ, which depends on observable variables (ε, T, etc.) and on internal variables, V_k. Thermodynamic forces (σ, s, A_k) are defined by derivation of ψ with respect to the associated variables. In the case of irreversible phenomena, the thermodynamic potential is not sufficient to describe the evolution of the system, it is necessary to know the evolution of internal variables. To be thermodynamically admissible, the evolution laws of internal variables must guarantee that the dissipation remains positive, in agreement with the second principle of thermodynamics.

9.2.2. *General formulation of constitutive laws for the description of elasto-plastic mechanical behavior*

In the macroscopic analysis of stresses and strains, one assumption generally made is that a domain of linear elastic behavior exists, in which the stress rate and strain rate are proportional. The prediction of the macroscopic mechanical behavior is then based on hardening variables describing the changes of the position, the size, and the shape of this domain. The experimental measurement of this domain allows direct access to the hardening variables without needing to assume a constitutive law and identify it.

The first way to access this information is the analysis of the hysteresis loops [COT 53]. In uniaxial fatigue, this method is relatively simple to carry out and was then widely used to characterize the cyclic mechanical behavior of metallic materials (Chapters 6 and 10). However, this method gives access to only two points of the yield surface, i.e. the boundary of the elastic domain. In order to obtain more information, specific tests have to be performed.

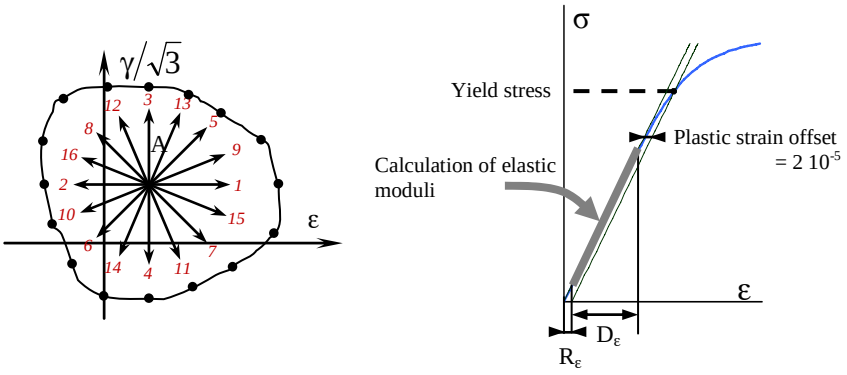

Figure 9.1. *Method of measurement of a yield surface: a) position of the measurement points of one yield surface, b) measurement of one yield stress*

The dynamic measurement of a yield surface consists of a set of small incursions in the plastic domain from the elastic one, on a same specimen. From a point, A, belonging to the elastic domain, a radial loading path is applied in the plane (ε, $\gamma/\sqrt{3}$) (Figure 9.1a). Elastic moduli, E and G, are measured during strain range, D_ε (Figure 9.1b). The yield stress is reached when the equivalent plastic strain reaches a given offset value. The loading is then reversed back to point A and a new yield stress is sought (Figure 9.1a). Several yield stresses are measured in this way. As each measurement of one yield stress moves and distorts the yield surface,

the chosen offset has to be as small as possible. As the aim of this measurement consists of measuring very small non-linearities, it is necessary to verify that it is not disturbed by sensor noise. The offset chosen was six times greater than the noise, i.e. 2×10^{-5}. Otherwise, the choice of a norm to calculate equivalent plastic strain is not completely objective towards the yield surface, as this norm is defined with a criterion which is not necessarily the criterion verified by the material. Nevertheless, as long as the offset remains small, the choice of the norm has a small influence.

Figure 9.2 shows yield surfaces measured during the first cycle of a cyclic tension-compression test carried out in the forged duplex stainless steel presented in Chapter 7. Yield surfaces were measured on the virgin material, after ¼ cycle (Figure 9.2a) and after ¾ cycle (Figure 9.2b). The initial yield surface is elliptic in plane (σ, $\sqrt{3}\,\tau$). This observation has been confirmed by conventional yield stresses measured with the same offset. At low plastic strain offset, the forged duplex stainless steel studied is then anisotropic. After plastic loading, the yield surface is no longer elliptic but shows a rounded nose in the direction of loading and a flattening on the opposite side. When the loading is reversed, this half-moon shape is observed again but its direction is reversed at each half cycle. This half-moon shape was observed in the literature in aluminum alloys [BUI 69, PHI 79, ROU 85, HEL 86, LOS 04], austenitic stainless steels [ELL 83, WU 91], and in a ferritic steel [HEL 86]. No significant alteration of yield surface size is observed in duplex stainless steel during the cycles. Therefore, no isotropic hardening exists. However, the yield surface moves during each half cycle, which means that a significant kinematic hardening develops during cycling.

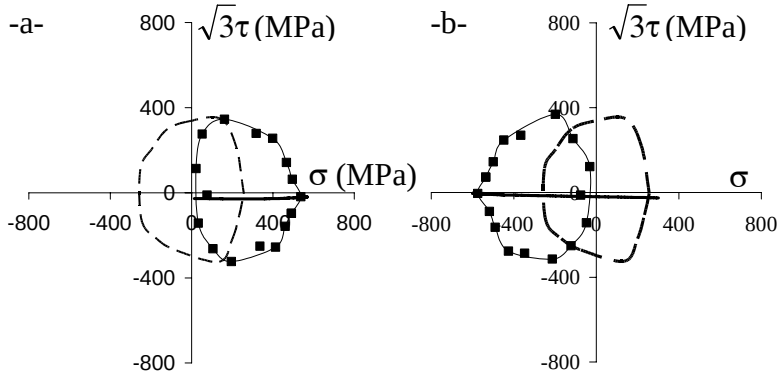

Figure 9.2. *Yield surfaces measured on virgin material (in dashed lines), after loading with a tension-compression test with a strain amplitude of 0.5% in the forged duplex stainless steel presented in Chapter 7 after a) ¼ cycle and b) ¾ cycle*

9.2.3. *Basis model*

Experimental measurements of yield surface in various metallic materials validate the assumption of the existence of an elasticity domain [MIC 76, PHI 79, WU 91, AUB 02, LOS 04]. It is nevertheless obvious that, after plastic loading, an isotropic plasticity criterion, such as von Mises or Tresca criteria, no longer describes the real yield surface of the material, as it distorts in a complex way under loading. However, in order to simplify the modeling and as long as the numerical simulation is acceptable, an isotropic relationship, like the von Mises relationship, can be used to describe the boundary of this domain. Moreover, this domain moves and gets larger or smaller under the loading. This is taken into account by two hardening variables: the isotropic and kinematic hardening variables, called R (back stress) and X (friction stress) respectively (Figure 9.3 and Chapter 6). These variables define the size and the position, respectively, of the elastic domain. They can be linked to the movement of dislocations (see Chapter 6 and section 9.2 concerning the micromechanical modeling).

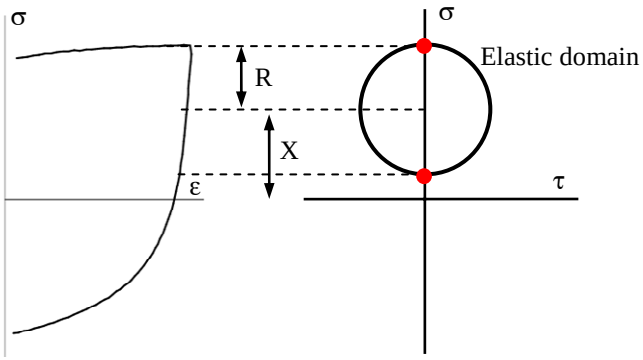

Figure 9.3. *Definition of the isotropic R and kinematic X hardening variables, position and size of the elastic domain*

9.2.3.1. *Yield function*

The yield function of an isotropic material, according to von Mises criterion, is given by:

$$f(\underline{\underline{\sigma}}, R, \underline{\underline{X}}) = J_2(\underline{\underline{\sigma}} - \underline{\underline{X}}) - R - k \qquad [9.1]$$

where k is the initial radius of the elastic domain and $J_2(\underline{\underline{\sigma}} - \underline{\underline{X}})$ is defined as:

$$J_2(\underline{\underline{\sigma}} - \underline{\underline{X}}) = \sqrt{\frac{3}{2}(\underline{\underline{s}} - \underline{\underline{X}}) : (\underline{\underline{s}} - \underline{\underline{X}})} \qquad [9.2]$$

$\underline{\underline{s}}$ is the deviatonic part of the Cauchy stress tensor $\underline{\underline{\sigma}}$:

$$\underline{\underline{s}} = \underline{\underline{\sigma}} - \frac{1}{3} tr\, \underline{\underline{\sigma}}\ \underline{\underline{I}} \qquad [9.3]$$

Inside the domain defined by this surface, the material has a pure elastic behavior. The relationship between stress and elastic strain can be written using the Hooke tensor $\underline{\underline{A}}$:

$$\underline{\underline{\varepsilon}}^e = \underline{\underline{A}} : \underline{\underline{\sigma}} \qquad [9.4]$$

The plastic strain rate is considered normal to the yield surface (normality assumption), which corresponds to experimental observations. The plastic strain rate can be written as follows:

$$\dot{\underline{\underline{\varepsilon}}}^p = \dot{\lambda} \frac{\partial f}{\partial \underline{\underline{\sigma}}} = \dot{\lambda}\, \underline{\underline{n}} \qquad [9.5]$$

The normal $\underline{\underline{n}}$ to the yield surface is then:

$$\underline{\underline{n}} = \frac{\partial f}{\partial \underline{\underline{\sigma}}} = \frac{3}{2} \frac{\underline{\underline{s}} - \underline{\underline{X}}}{J_2(\underline{\underline{\sigma}} - \underline{\underline{X}})} \qquad [9.6]$$

Let $\dot{p}$ the cumulated plastic strain rate:

$$\dot{p} = \dot{\lambda} = \sqrt{\frac{2}{3} \dot{\underline{\underline{\varepsilon}}}^p : \dot{\underline{\underline{\varepsilon}}}^p} \qquad [9.7]$$

The value of $\dot{\lambda}$ is obtained with the consistency relationship:

$$\dot{f} = 0 \qquad [9.8]$$

9.2.3.2. *Kinematic hardening*

The kinematic hardening variable X represents the position of the center of the elastic domain in the stress space. The first constitutive laws taking into account the kinematic hardening have been proposed by Prager [PRA 58] and by Ziegler

[ZIE 59]. These laws propose a linear evolution of the kinematic hardening, which is not sufficient to accurately describe the cyclic hardening. Kinematic hardening is relatively well taken into account by the laws proposed by Armstrong and Frederick [ARM 66], Marquis [MAR 79], and Chaboche and Roussalier [CHA 83]. These laws are equivalent to the Mroz rule [MRO 67] and to two surface models [KRI 75, DAF 75].

The evolution of the kinematic hardening takes the non-linear form:

$$\dot{\underline{\underline{X}}} = \frac{2}{3} C \, \dot{\underline{\underline{\varepsilon}}}^{p} - \gamma \varphi(p) \, \underline{\underline{X}} \, \dot{p} \qquad [9.9]$$

with

$$\varphi(p) = \varphi_{\infty} + (1 - \varphi_{\infty}) e^{-\omega p} \qquad [9.10]$$

This formulation allows the hardening change from the initial cycle to the stabilized one. Two non-linear kinematic hardening variables are recommended in order to describe both hysteresis loops and amplitude effect. The use of a second quasi-linear hardening variable accounts for a hardening at a given amplitude after stabilization at a lower amplitude.

9.2.3.3. *Isotropic hardening*

The isotropic hardening variable R describes the increase of the size of the elastic domain under loading. As for kinematic hardening, a non-linear form is necessary to accurately describe the hysteresis loops and the cyclic hardening. The evolution of the isotropic hardening variable is described by:

$$\dot{R} = b \, (Q - R) \, \dot{p} \qquad [9.11]$$

The model presented above is the basis model on which all the macroscopic modeling of the forged duplex stainless steel studied will be built. It will be called model NLK (for non-linear kinematic) in later sections.

9.2.3.4. *Identification of model parameters for forged DSS Z2 Cr Ni Mo 25-07 presented in Chapter 7*

The identification of the parameters of model NLK needs the use of several uniaxial tests. As the model requires 12 parameters (Table 9.1), the identification

cannot be carried out by hand but needs software to optimize parameter values. Various approaches based on the gradient-based method or on evolutionary algorithms exist [AND 07].

In order to give a physical meaning to these parameters, we analyzed the changes of isotropic and kinematic hardening components. The common procedure initially proposed by Cottrell [COT 53] and illustrated in Figure 9.4 is used here. Other methods have been proposed in the literature [POL 91]. The width of the elastic domain is defined with a conventional plastic strain of 2×10^{-4}. k is the initial yield stress. Kinematic X and isotropic R hardening components are also called friction stress and back stress respectively (see Chapter 6). Their evolutions are illustrated in Figure 9.5 for two tension-compression tests with strain amplitudes of 0.5 and 0.8%.

As shown in Chapter 7, the DSS exhibits a hardening phase followed by a softening phase before stabilization, moreover, *R* and *X* are monotonously increasing or decreasing, respectively. The combination of both hardenings, which do not have the same stabilization rate, gives the cyclic hardening/softening curve. The stabilized values obtained for *R* are quasi-identical for the two strain amplitudes tested whereas the higher the strain amplitude applied, the higher the stabilized level for *X*. The identification was performed with the aim of keeping the same direction of variation of the hardening variables and keeping them at the same stabilized level as experimentally observed. This identification was carried out using cyclic tension-compression tests with strain amplitudes in the range {0.35; 0.5; 0.8; 1.0 %}. Parameter values obtained for model NLK are listed in Table 9.1.

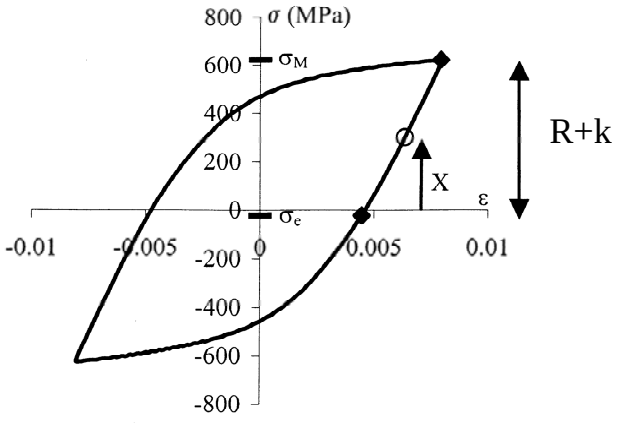

Figure 9.4. *Analysis of a hysteresis loops for the determination of X (kinematic hardening component) and R (isotropic hardening component), where k is the initial yield stress [COT 53]*

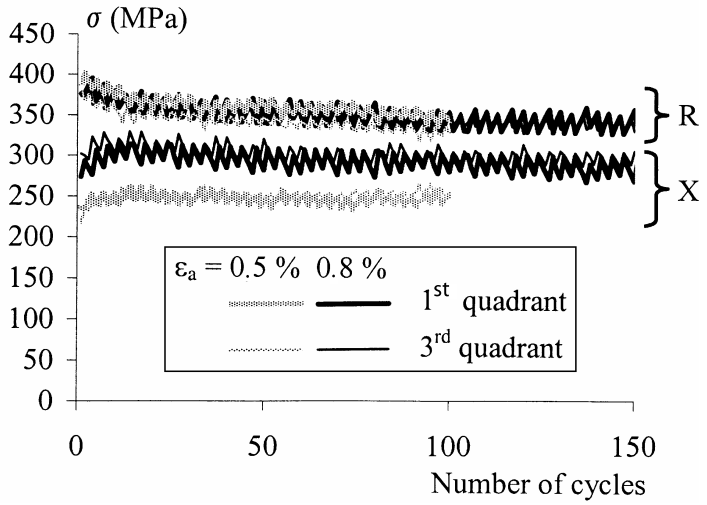

Figure 9.5. *Evolution of the hardening variables during two tension-compression cyclic tests in the forged DSS studied*

E	G	ν	k	C_1/γ_1	γ_1
190 GPa	65 GPa	0.3	390 MPa	180 MPa	1900
C_2/γ_2	γ_2	ω	φ_∞	b	Q
21,209 MPa	0.786	12.79	0.728	3.2	-84.5 MPa

Table 9.1. *Parameters of model NLK identified for the forged DSS studied*

Figure 9.6 shows the comparison between experiments and simulation, in terms of cyclic hardening/softening behavior and in terms of stabilized hysteresis loops. It can be seen that model NLK accounts for the hysteresis loops at the various strain amplitudes. The model predicts a hardening/softening evolution, although the stress levels do not always correspond to the experimental measurements. In particular, the number of cycles necessary to reach the maximum stress amplitude does not correspond to the experimental one and the stabilized state appears much sooner during the simulation. It can be noted that, experimentally, the higher the applied strain amplitude is, the slower the stabilization; however, numerically, it is to the contrary. This is due to the fact that hardening variables are assumed to vary according to the cumulated plastic strain.

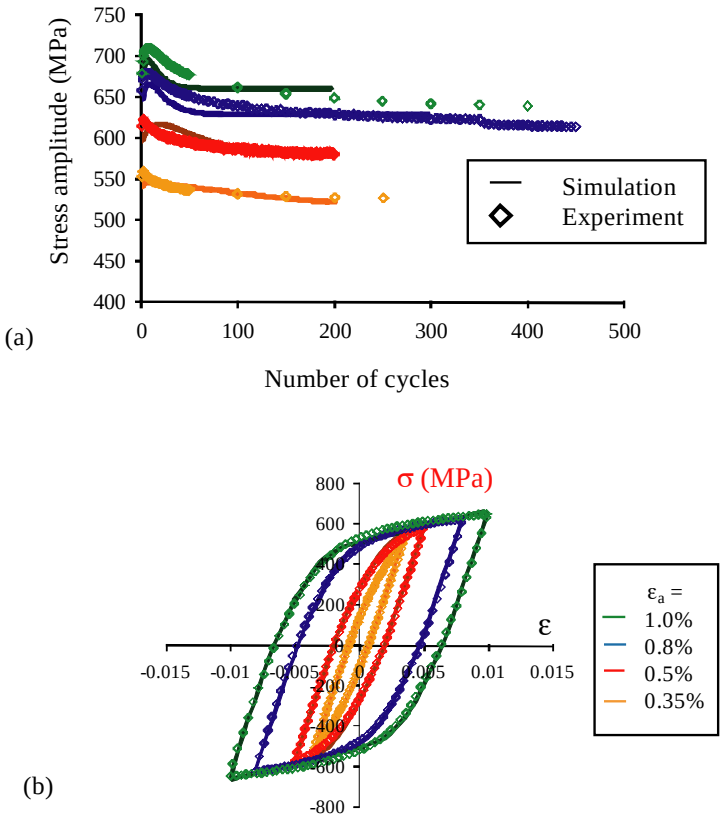

Figure 9.6. *Comparison between experimental results in the forged DSS studied and simulation for model NLK. a) Cyclic hardening/softening curves in tension-compression tests (ε_a = 0.35; 0.5; 0.8; 1.0 %); b) cyclic stress-strain hysteresis loops in tension-compression tests (ε_a = 0.35; 0.5; 0.8; 1.0%)*

It has been shown in Chapter 7 that duplex stainless steel exhibits an over-hardening under non-proportional loading paths. Tests presented in Chapter 7 have been simulated with this basis model. The experimental and numerical cyclic hardening/softening curves of a cyclic test carried out with a circle path and an equivalent strain amplitude of 0.5% on the forged duplex stainless steel studied are plotted in Figure 9.7. It appears clearly that model NLK is not able to represent the cyclic over-hardening observed under non-proportional loading and, therefore, underestimates the stabilized stress response of the circle test, confirming previous results [FAN 91, TAN 92, TAN 94, ABD 94, CAL 99, POR 00].

Add-ons to this basis model (NLK) are necessary to accurately predict the over-hardening induced by non-proportional loadings. Several modifications have been proposed in the literature to account for over-hardening, three of them will be studied in the following section.

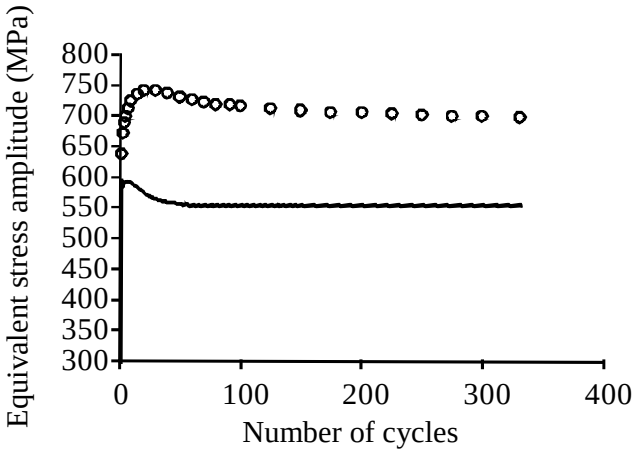

Figure 9.7. *Comparison between experiments in the forged DSS studied and simulation by model NLK, cyclic hardening/softening curve for a tension/compression-torsion test with circle path (ε_a = 0.5%)*

9.2.4. *Modeling of the over-hardening*

Three models are presented here, based on model NLK described above. They modify the hardening variables introducing a dependency on the non-proportionality of the loading. The more non-proportional the loading, the higher the hardening. In the two first models, the dependency on the non-proportionality concerns the isotropic hardening variable, whereas in the third model it concerns the kinematic hardening variable.

9.2.4.1. *Model proposed by Benallal, Marquis and Calloch (BMC)*

The first model was initially developed by Benallal and Marquis [BEN 87], and was then modified by Calloch and Marquis [CAL 99]. A non-proportionality parameter, A, is defined from the angle between tensors $\underline{\underline{X}}$ and $\dot{\underline{\underline{X}}}$ [BEN 87].

$$A = 1 - \cos^2 \frac{\left(\underline{\underline{X}} : \dot{\underline{\underline{X}}}\right)^2}{\left(\underline{\underline{X}} : \underline{\underline{X}}\right)\left(\dot{\underline{\underline{X}}} : \dot{\underline{\underline{X}}}\right)} \qquad [9.12]$$

The asymptotic value of the isotropic hardening (equation [9.11]) changes depending on the non-proportionality parameter, A:

$$\dot{Q} = D(A)(Q_{AS}(A) - Q)\dot{p} \qquad [9.13]$$

D(A) adjusts the rate of Q and Q_{AS} is the asymptotic value of Q, according to A following:

$$Q_{AS}(A) = \frac{gAQ_{\infty} + (1-A)Q_0}{gA + 1 - A} + Q_i\left(A^n(1-A) + A^n\right) \qquad [9.14]$$

This model considered the circle cyclic loading as the most hardening. This assumption was abandoned because it was too restrictive, and Q_{AS} modified [CAL 99].

9.2.4.2. *Model proposed by Tanaka*

The second model was developed by Tanaka [TAN 94]. As with the previous model, it is based on NLK equations and modifies the isotropic hardening equation to take into account loading non-proportionality. Another non-proportionality parameter is proposed, the circle cyclic loading is not considered as the most hardening. The model is written in the deviator space, the plastic strain, $\underline{E}^p$, and its norm, $\underline{u}$, are defined as follows:

$$\underline{E}^p \begin{cases} E_1 = \varepsilon_{11}^p \\ E_2 = \frac{2}{\sqrt{3}}\left(\frac{\varepsilon_{11}^p}{2} + \varepsilon_{22}^p\right) \\ E_3 = \frac{2}{\sqrt{3}}\varepsilon_{12}^p \\ E_4 = \frac{2}{\sqrt{3}}\varepsilon_{23}^p \\ E_5 = \frac{2}{\sqrt{3}}\varepsilon_{31}^p \end{cases} \quad \text{and} \quad \underline{u} = \frac{\dot{\underline{E}}^p}{\left\|\dot{\underline{E}}^p\right\|} \qquad [9.15]$$

ε_{11}^p, ε_{12}^p, ε_{22}^p, ε_{23}^p, ε_{31}^p are the five independent components of plastic strain $\underline{E}^p$.

Tanaka introduces a second-order tensor $\underline{\underline{C}}$ in the five dimension deviator space, called structural tensor:

$$\dot{\underline{\underline{C}}} = c_c \left[\left(\underline{u} \otimes \underline{u} \right) - \underline{\underline{C}} \right] \dot{p} \qquad [9.16]$$

A new non-proportionality parameter A is proposed, built from tensor $\underline{\underline{C}}$. In the case of proportional loading, A is 0. No assumption is made on the loading that leads to the highest non-proportionality in the sense of A:

$$A = \sqrt{\frac{Tr\left(\underline{\underline{C}}^t \underline{\underline{C}}\right) - \underline{u}\underline{\underline{C}}^t \underline{\underline{C}}\underline{u}}{Tr\left(\underline{\underline{C}}^t \underline{\underline{C}}\right)}} \qquad [9.17]$$

As in the previous model, the asymptotic value of the isotropic hardening changes according to the non-proportionality parameter A:

$$Q = A\left(q_N(q) - q_P(q)\right) + q_P(q) \qquad [9.18]$$

Where a new variable, q, is introduced; it allows amplitude effect to be accounted for. It is defined from an intermediate variable, $\underline{Y}$, which characterizes the position of a limit surface in the plastic strain space. $\underline{Y}$ and q are defined as follows:

$$\dot{\underline{Y}} = r_y \left(\underline{E}^p - \underline{Y} \right) \dot{p} \qquad [9.19]$$

$$q = \left\| \underline{E}^p - \underline{Y} \right\| \qquad [9.20]$$

Models proposed by Benallal, Marquis and Calloch (BMC), and by Tanaka are based on a link between isotropic hardening and non-proportionality of the loading. Experimentally, it has been shown for waspaloy [ABD 94] and for duplex stainless steel [AUB 03a] that the kinematic hardening also depends on the non-proportionality of the loading. Abdul-Latif *et al.* [ABD 94] proposed a modification of model proposed by Benallal, Marquis, and Calloch incorporating these observations.

9.2.4.3. *Model proposed by Abdul-Latif et al.*

In this third model, later called model ALCFS, the non-proportionality of the loading influences not only the isotropic hardening, but also the kinematic

hardening. The non-proportionality parameter is that initially proposed by Benallal [BEN 89] (equation [9.12]).

Abdul-Latif *et al.* took the basis evolution of the kinematic hardening (equation [9.9]), and changed the asymptotic value C according to:

$$\dot{C} = I(A)\,(C_{AS} - C)\,\dot{p} \qquad [9.21]$$

with

$$I(A) = (\Phi_x - \omega_x)\,A + \omega_x \qquad [9.22]$$

As the formulation of C_{AS} proposed in [ABD 94] supposed that the circle cyclic loading is the most hardening, its expression was modified by the present authors as follows [AUB 03a]:

$$C_{AS} = \frac{\eta_k\,A\,C_\infty + (1-A)\,C_0}{\eta_k\,A + 1 - A} + C_x\,(A^n\,(1-A) + A\,(1-A)^n) \qquad [9.23]$$

In the forged duplex stainless steel studied, no influence of non-proportional loading is observed on the isotropic part of the hardening, the expression of the isotropic hardening is then kept identical to that in model NLK.

9.2.4.4. *Comparison with experiments*

The parameters of model NLK given in Table 9.1 have been used here; only the new parameters of models BMC, Tanaka, and ALCFS have been identified on non-proportional cyclic loadings of forged duplex stainless steels with an equivalent strain amplitude of 0.5%.

Figure 9.8 compares the stabilized equivalent stress amplitudes in various loading conditions obtained with the four models presented to experimental results. Some tests were used during the identification stage (tension-compression tests, non-proportional cyclic tests with ε_a = 0.5%), the other tests have only been simulated with the models after identification. It can be seen again that model NLK is unable to reproduce the over-hardening observed under non-proportional loading. The three other models simulate stabilized equivalent stress amplitudes similar to those obtained experimentally during the tests used for the identification. Stress-strain relationships in cyclic tension-compression and cyclic torsion are also well reproduced. It can be underlined that only models Tanaka and ALFCS agree with all experimental results, contrary to model BMC, which fails to accurately predict the dependency to strain amplitude [AUB 03b].

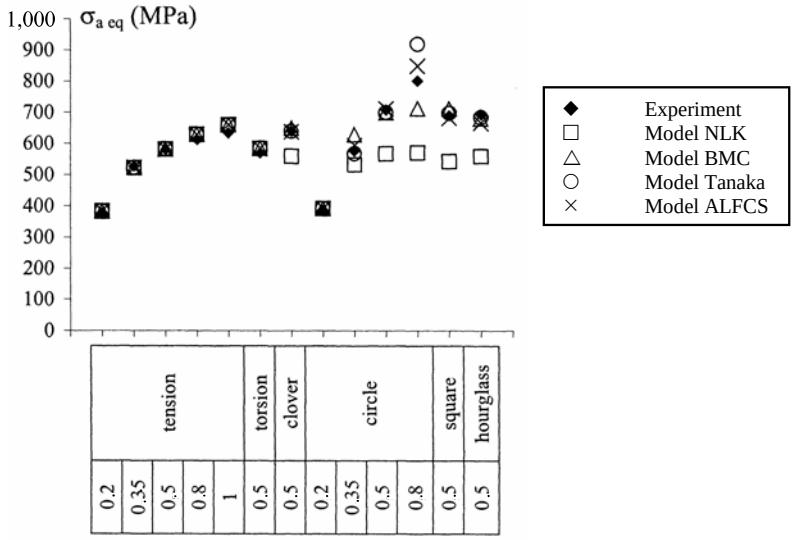

Figure 9.8. *Comparison between model predictions and experimental results on forged DSS in terms of equivalent stress amplitude at the stabilized cycles under various cyclic strain amplitudes (%) and loading paths*

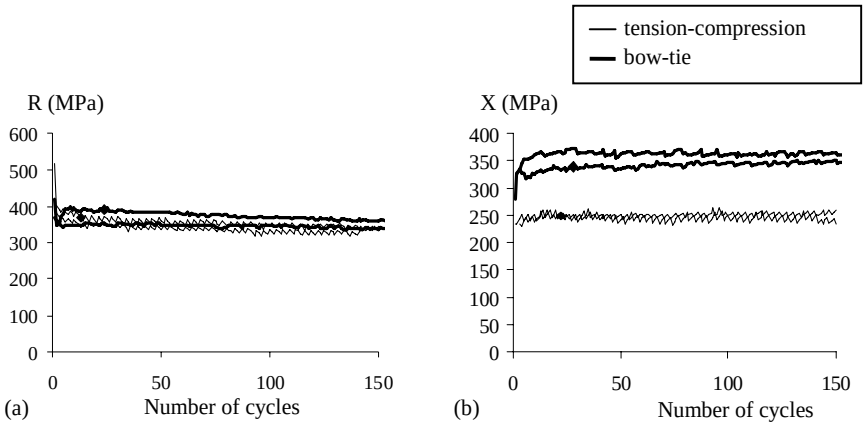

Figure 9.9. *Evolution of the hardening variables during two cyclic tests with a strain amplitude of 0.5% and a tension-compression loading and a bow-tie (non-proportional) loading. a) Isotropic component, b) kinematic component*

In conclusion, models Tanaka and ALFCS are able to simulate the experimental results observed under proportional and non-proportional cyclic loadings with various strain amplitudes. The comprehensive validation of these models, based on two conflicting assumptions concerning the link between non-proportional loadings and hardening variables (isotropic or kinematic components), needs thorough analysis, in order to identify hardening variables and mechanisms caused by over-hardening. Regarding the forged duplex stainless steel studied here, the evolution of hardening variables were measured during proportional and non-proportional cyclic loadings (Figure 9.9), showing that the isotropic variable, R, has the same value under proportional and non-proportional loading, whereas the kinematic variable, X, increases with non-proportionality of the loading.

9.2.5. *Conclusion*

Several macroscopic models have been presented, which enable monotonic and cyclic mechanical behaviors to be observed in a forged duplex stainless steel. More or less complex models can be used depending on the type of loading the material is subjected to. Nevertheless, this set of models poses two problems: the first concerns the identification of the material parameters. These models need a large experimental database for the identification, including notably non-proportional tests, which require experimental equipment that is not readily available. The second is more general and concerns the difficulty of linking these models to the physical mechanisms that cause the observed behavior. For these reasons, a multiscale model has been developed to take into account the bi-phased and polycrystalline nature of the material, and the physical mechanisms of plastic strain on the grain scale.

9.3. Micromechanical modeling

9.3.1. *Introduction*

Multiscale modeling consists of determining the macroscopic behavior of a heterogenous material from the mechanical behavior of its various constituents at the microscopic scale. The heterogenous material is replaced by an equivalent homogenous medium (EHM). The heterogenities can have various origins. In composite materials, fibers and matrix have very different mechanical behaviors. In polycrystalline materials, the heterogenity comes from the presence of grains of various orientations, these various orientations implying various mechanical behaviors, relative to the loading direction.

Multiscale modeling requires four steps:

– *the representation step* consists of the description of the microstructure of the material. It needs to describe the "phases" that constitute the material geometrically and mechanically. Here, one "phase" is an entity whose properties can be considered homogenous. A representative volume element (RVE) is then defined. The quality of the modeling is directly linked to the care exercised in this first step. The RVE defined must respect the condition of scale separation and define the microstructure and the physical mechanisms responsible for the mechanical behavior studied;

– *the localization step* links the stress and strain fields in each "phase" to macroscopic fields using a transition rule;

– *the phase behavior law* is based, at least partly, on the physical mechanisms causing the observed behavior. For a metallic material, the grain behavior law takes into account plasticity or viscoplasticity mechanisms. Slip systems have to be described;

– *the homogenization step* in which macroscopic strain fields are computed from local strain fields.

In the next sections, each step is detailed in the case of a forged duplex stainless steel [EVR 08a, EVR 08b]. Results obtained are analyzed and compared to the experimental results presented in Chapter 7.

9.3.2. *Representation of the material*

The microstructure and the grain morphology of the forged duplex stainless steel studied was analyzed using EBSD (electron back-scattered diffraction) as shown in Figure 9.10. Austenitic grains can be considered as spherical, whereas ferritic grains are stretched in the forged direction. Mean grain sizes in both phases are close: about 10 μm for austenitic grains and 30 μm for ferritic grains. There is no scale separation between phases and grains as the characteristic scale of the phases is about 20 μm, which is the size of two grains. Consequently, a single grain scale can be considered for forged duplex stainless steels. However, in the case of cast duplex stainless steels, small austenitic grains nucleate in large ferritic grains and two heterogenity scales have to be considered [BUG 99]. Forged DSSs present strong morphological anisotropy in the forging direction. Nevertheless, a crystallographic texture analysis of the forged DSS studied showed that the austenitic phase is not textured and the ferritic phase is only slightly textured.

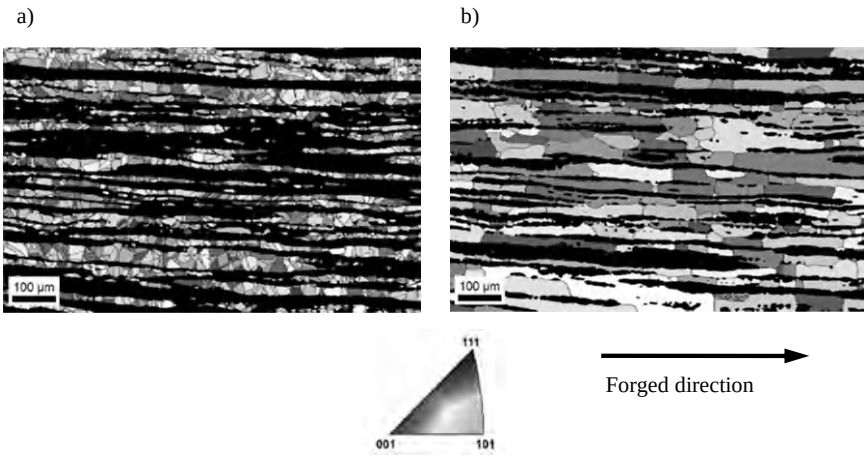

Figure 9.10. *EBSD map in the longitudinal direction of the forged duplex stainless steel: a) austenitic grains gray, ferrite in black, b) ferritic grains gray, austenite in black*

To study the influence of this morphology on mechanical behavior, monotonous tension tests and tension-compression tests were performed in the forging direction and perpendicular to the forging direction [EVR 08a, EVR 08b]. The stress-strain curves obtained are similar for both directions. Consequently, the global mechanical behavior can be considered as isotropic. It is then assumed that the austenite and ferritic grains are spherical, and the austenitic and ferritic phases are not textured. Hence, the same isotropic distribution of 40 crystallographic orientations was chosen for both austenitic and ferritic phases. Several authors have shown that isotropic distributions limited to 40 or 48 crystallographic orientations can satisfactorily account for macroscopic behavior of isotropic polycrystalline materials [PIL 90, CAI 92], the computation time is then reasonable. The increase of the number of crystallographic orientations can nevertheless improve the macroscopic response of the model and the distribution of grain responses.

In polycrystals, such as forged duplex stainless steels, no grain plays a particular role. Each grain can be considered as an inclusion in the sense of Eshelby and interacts with all other grains, austenitic or ferritic. The best way to take into account these interactions is to use a self-consistent model. In such a model, each grain, i.e. in duplex stainless steels each grain of austenite or ferrite, is surrounded by a matrix corresponding to the homogenous equivalent medium (HEM) wanted (Figure 9.11). N Eshelby problems have to be solved, the homogenized behavior of the material results from the combination of their own mechanical behavior and of the interactions of all the grains with the HEM.

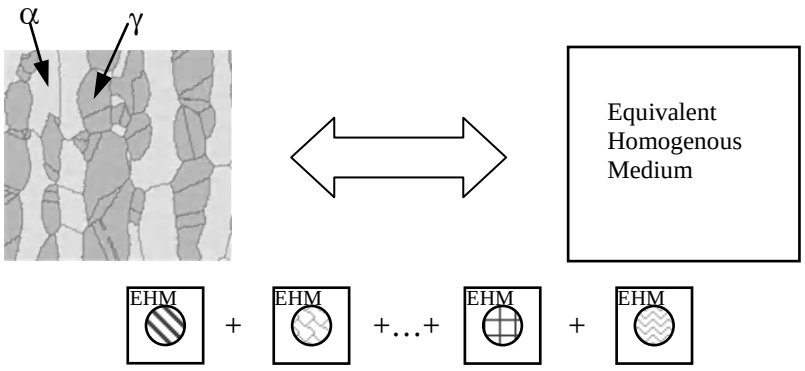

Figure 9.11. *Principle of the self-consistent scheme applied to forged DSS*

9.3.3. *Localization step*

The localization law defines the relationship between macroscopic and microscopic variables. To take into account the intergranular heterogenities in a polycrystal, a self-consistent model, as described above, is necessary. Based on the Eshelby solution [ESH 57], several proposals have extended this approach to elasto-platic strains [KRO 61, BUD 62, HIL 65, BER 79]. Moreover, two models have been proposed to simulate the response to proportional or non-proportional cyclic loadings: the localization law of Cailletaud [CAI 92] and Pilvin [PIL 90], and that of Molinari *et al.* [MOL 87, KOU 94, MOL 97]. In this chapter, only the localization law of Cailletaud and Pilvin [PIL 90, CAI 92] is presented, in a version adapted to the forged duplex stainless steel. The localization law proposed by Molinari *et al.* was also tested and gave similar results, but the calculation is more time-costly.

As it has been shown above, the one-site self-consistent scheme is used to account for the polycrystalline microstructure of the forged duplex stainless steel studied. Because austenitic and ferritic grains can be considered as spherical and the material isotropic, the classical Cailletaud and Pilvin localization law is used to calculate granular stresses [CAI 92]:

$$\underline{\underline{\sigma}}_{i}^{g} = \underline{\underline{\Sigma}} + \mu\left(\underline{\underline{B}} - \underline{\underline{\beta}}_{i}^{g}\right) \qquad [9.24]$$

Index, i, refers to austenitic (i = a) or ferritic (i = f) grains. $\underline{\underline{\sigma}}_i^g$ and $\underline{\underline{\Sigma}}$ are the grain stress and the macroscopic stress, respectively, and μ is the shear modulus. $\underline{\underline{\beta}}_i^g$ is the intergranular accommodation tensor, which acts for kinematic hardening and can be expressed by:

$$\dot{\underline{\underline{\beta}}}_i^g = \dot{\underline{\underline{\varepsilon}}}_i^{pg} - D_i\left(\underline{\underline{\beta}}_i^g - \delta_i \underline{\underline{\varepsilon}}_i^{pg}\right)\left\|\dot{\underline{\underline{\varepsilon}}}_i^{pg}\right\| \qquad [9.25]$$

where $\dot{\underline{\underline{\varepsilon}}}_i^{pg}$ is the grain plastic strain rate, D_i and δ_i are material parameters. These two material parameters (D_i and δ_i) are assumed to be identical for both phases, as grains of each phases interact with all other grains. Variable $\underline{\underline{B}}$ has been modified to take into account the bi-phased character of the material:

$$\dot{\underline{\underline{B}}} = f_a \sum_1^{40} f_g \dot{\underline{\underline{\varepsilon}}}_a^{pg} + f_f \sum_1^{40} f_g \dot{\underline{\underline{\varepsilon}}}_f^{pg} \qquad [9.26]$$

where f_a, f_f, and f_g are the volume fraction of austenitic phase (0.4), of ferritic phase (0.6), and of individual grains in the phase ($f_f = \frac{1}{40}$), respectively.

9.3.4. *Grain constitutive law*

At the grain scale, the plastic behavior is due to dislocation slip on various slip systems. For austenitic grains, 12 slip systems type {111} <110> are considered and for ferritic grains, 24 slip systems type {110} {112} <111> are considered. Hence, for each grain, the resolved shear stress, $\tau_i^{(s)}$, on slip system (s) in grain (g) is calculated from grain stress $\underline{\underline{\sigma}}_i^g$ by:

$$\tau_i^{(s)} = \underline{\underline{\sigma}}_i^g : \frac{1}{2}\left(\underline{n}_i^{(s)} \otimes \underline{b}_i^{(s)} + \underline{b}_i^{(s)} \otimes \underline{n}_i^{(s)}\right) \qquad [9.27]$$

where $\underline{n}_i^{(s)}$ and $\underline{b}_i^{(s)}$ define the slip direction and the direction normal to slip plane (s), respectively.

At room temperature, stress-strain curves for monotonous tension tests performed on FCC and BCC single crystals have similar evolutions. Hence, in a first approximation, the same grain constitutive law can be used to describe the mechanical behavior of austenitic and ferritic grains. The difference lies only in the values of parameters and in the nature of slip systems.

For both phases, the shear strain rate on slip system (s) can be calculated by a Norton-type law:

$$\dot{\gamma}_i^{(s)} = \left(\frac{\left|\tau_i^{(s)}\right| - \tau_{\mu i}^{(s)}}{K_i} \right)^{n_i} sign(\tau_i^{(s)}) \text{ if } \tau_i^{(s)} \geq \tau_{\mu i}^{(s)}, \quad \dot{\gamma}_i^{(s)} = 0 \text{ otherwise} \quad [9.28]$$

where K_i and n_i are viscosity parameters. The critical shear stress, $\tau_{\mu i}^{(s)}$, is obtained by the forest hardening model:

$$\tau_{\mu i}^{(s)} = \tau_i^0 + b_i \mu \sqrt{\sum_t h_i^{t(s)} \rho_i^t} \quad [9.29]$$

where τ_i^0, b_i, μ and $h_i^{t(s)}$ are, respectively, the initial critical shear stress, the Burgers vector, the shear modulus, and the interaction matrix, which characterizes the interactions between slip systems. A simple form of this matrix is chosen: diagonal terms are equal to one and non-diagonal terms are equal to a constant parameter, h_i. The evolution of dislocation density is given by:

$$\dot{\rho}_i^{(s)} = \frac{1}{b_i} \left(\frac{\sqrt{\sum_{t \neq s} \rho_i^t}}{L_i} - 2 y_{ci} \rho_i^{(s)} \right) \left| \dot{\gamma}_i^{(s)} \right| \text{ with } \rho_i^{(s)} (\gamma_i^{(s)} = 0) = \rho_i^0 \quad [9.30]$$

where L_i is a material parameter controlling the dislocation production and y_{ci} is a material parameter proportional to the characteristic length associated with the annihilation process of dislocation dipoles.

9.3.5. *Homogenization step*

The macroscopic behavior is obtained by a homogenization procedure using a mixture law. The macroscopic plastic strain rate is calculated as:

$$\underline{\underline{\dot{E}}}^{p} = f_a \underline{\underline{\dot{E}}}_a^{p} + f_f \underline{\underline{\dot{E}}}_f^{p} \quad \text{with} \quad \underline{\underline{\dot{E}}}_a^{p} = \sum_{g=1}^{N_g=40} f_g \, \underline{\underline{\dot{\varepsilon}}}_a^{pg} \quad \text{and} \quad \underline{\underline{\dot{E}}}_f^{p} = \sum_{g=1}^{N_g=40} f_g \, \underline{\underline{\dot{\varepsilon}}}_f^{pg} \qquad [9.31]$$

$\underline{\underline{\dot{\varepsilon}}}_i^{pg}$ is calculated by:

$$\underline{\underline{\dot{\varepsilon}}}_i^{pg} = \sum_s \frac{1}{2}\left(\underline{n}_i^{(s)} \otimes \underline{b}_i^{(s)} + \underline{b}_i^{(s)} \otimes \underline{n}_i^{(s)}\right)\dot{\gamma}_i^{(s)} \qquad [9.32]$$

Finally, the macroscopic total strain rate can be written as:

$$\underline{\underline{\dot{E}}} = \underline{\underline{\dot{E}}}^{p} + \underline{\underline{\dot{E}}}^{e} \quad \text{with} \quad \underline{\underline{\dot{E}}}^{e} = \frac{1}{2\mu}\left(I - \frac{\nu}{1+\nu}\underline{\underline{1}} \otimes \underline{\underline{1}}\right)\underline{\underline{\dot{\Sigma}}} \qquad [9.33]$$

where μ and ν are the shear modulus and the Poisson coefficient, respectively.

9.3.6. *Identification of model parameters*

The material parameters identification was performed in two steps. First some parameters (K_i, n_i, b_i, ρ_i^0) were identified from the literature. Parameters L_i have been obtained for each phase by the following expression [RAU 93]:

$$L_i = d_i \sqrt{(n-1)\,\rho_i^0} \qquad [9.34]$$

where d_i is the mean grain size and n the number of potential slip systems (i.e. 12 for austenitic grains and 24 for ferritic grains). Parameters obtained after this first step are given in Table 9.2.

Parameters	K_i (MPa.s^{-n}) [BUG 99]	n_i [BUG 99]	b_i (m) [FRA 93]	ρ_i^0 (m^{-2}) [FRA 93]	L_i [RAU 93].
Austenite	20	10	$2.53.10^{-10}$	10^{12}	33
Ferrite	20	10	$2.48.10^{-10}$	10^{12}	143

Table 9.2. *Grain constitutive law parameters identified from the literature*

The other parameters (τ_i, y_{ci}, h_i, D, δ) were identified by a procedure using the automatic optimization software SiDoLo, which is based on a Levenberg-Marquart minimization algorithm. This identification method consists of a quantitative comparison between experimental data and simulation results. Only a monotonous tension test and the first tension-compression hysteresis loop at 0.5% of total strain amplitude are used for the identification.

Furthermore, in order to keep physical values to the parameters, bounds are imposed during the automatic identification process. According to Baczmanski and co-workers [BAC 04], the following bounds are defined for both phases: 70 MPa $< \tau_a <$120 MPa and 180 MPa $< \tau_f <$250 MPa. Concerning the parameter proportional to the characteristic length associated with the dislocation annihilation process, the following bound is used: $y_{ci} <$20 nm [TAB 97]. Finally, according to discrete dislocation dynamic calculations, the following inequalities are defined for the matrix interaction parameters: $h_a <1$ and $h_f <1$ [MAD 01]. Furthermore, because the hardening rate is more important in austenitic than in ferritic polycrystals, the following inequality is considered during the optimization process: $h_a < h_f <1$. Table 9.3 gives the single crystal law parameters obtained after the automatic identification process. Results (Figures 9.12 and 9.13) show a good agreement between simulation and experimental data. It should be noted that the model is able to describe both the hardening and the Bauschinger effects.

Parameters	τ_i (MPa)	y_{ci} (nm)	h_i	D	δ
Austenite	100	2.5	0.8	200	0.3
Ferrite	214	2	0.5		

Table 9.3. *Grain constitutive law parameters obtained after automatic identification process for the forged duplex stainless steel studied*

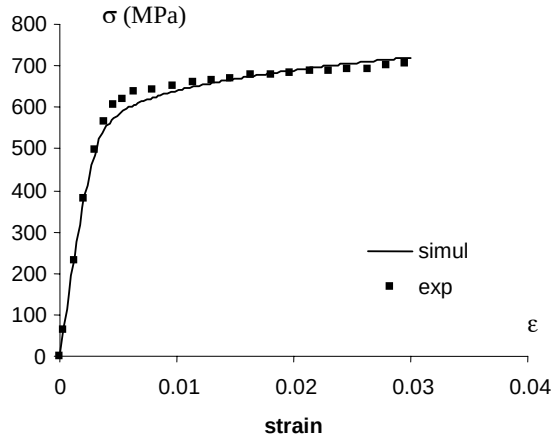

Figure 9.12. *Stress-strain curve of monotonous tension test: comparison between simulation and experimental results obtained on the forged DSS studied*

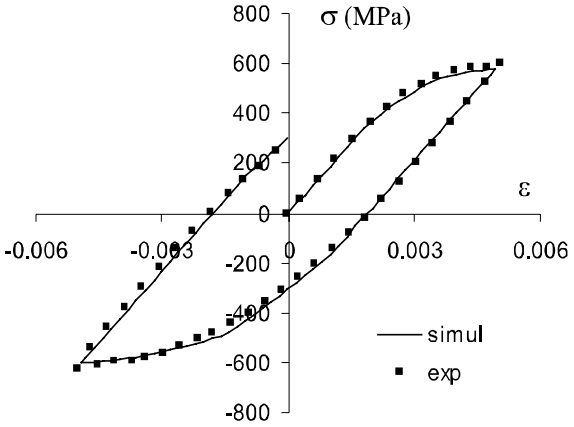

Figure 9.13. *First hysteresis loop in tension-compression with a strain amplitude of 0.5%: comparison between simulation and experimental results obtained on the forged DSS studied*

9.3.7. *Bi-phased polycrystalline model validation*

In the previous section, only two tests, a monotonous tension test and the first hysteresis loop in tension-compression at 0.5% of total strain amplitude, were used to identify the model parameters. To appreciate the robustness of the model, other tests were simulated and compared with experimental data.

Firstly, first hysteresis loops in tension-compression for various total strain amplitudes (0.35, 0.8, and 1%) were simulated. The results (Figure 9.14) show that the model is able to describe hysteresis loops and the Bauschinger effect for all strain levels. However, when the strain level increases, the Bauschinger effect is less well described.

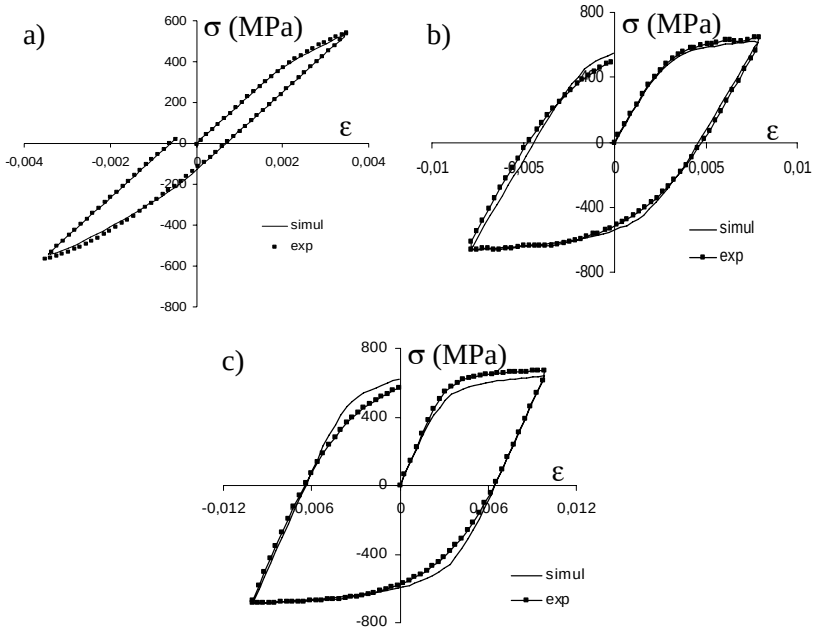

Figure 9.14. *First hysteresis loops in tension-compression: comparison between simulation and experimental results obtained on the forged DSS studied with strain amplitudes of a) 0.35%, b) 0.8%, c) 1%*

Secondly, first hysteresis loops in tension/compression-torsion for various loading paths, circle, square, hourglass, and clover, with equivalent total strain amplitude of 0.5% have been simulated. Results are presented in plane (axial stress, σ, shear stress, τ) (see Figure 9.15). The over-hardening observed under non-proportional cyclic loading is correctly described. This is all the more outstanding because the identification database did not contain any non-proportional tests. Localization laws proposed by Cailletaud and Pilvin and by Molinari combined with a crystalline granular law were previously used in the past to simulate non-proportional tests and the over-hardening in various materials [PIL 90, ABD 94, CAL99, DIN 00]. However, non-proportional tests were systematically included in the identification database. It seems that this type of model is more powerful than

first thought, as it is able to simulate the over-hardening induced by non-proportional loadings without introducing them during the identification step. Nevertheless, this assumption still needs to be confirmed on other materials and/or tests.

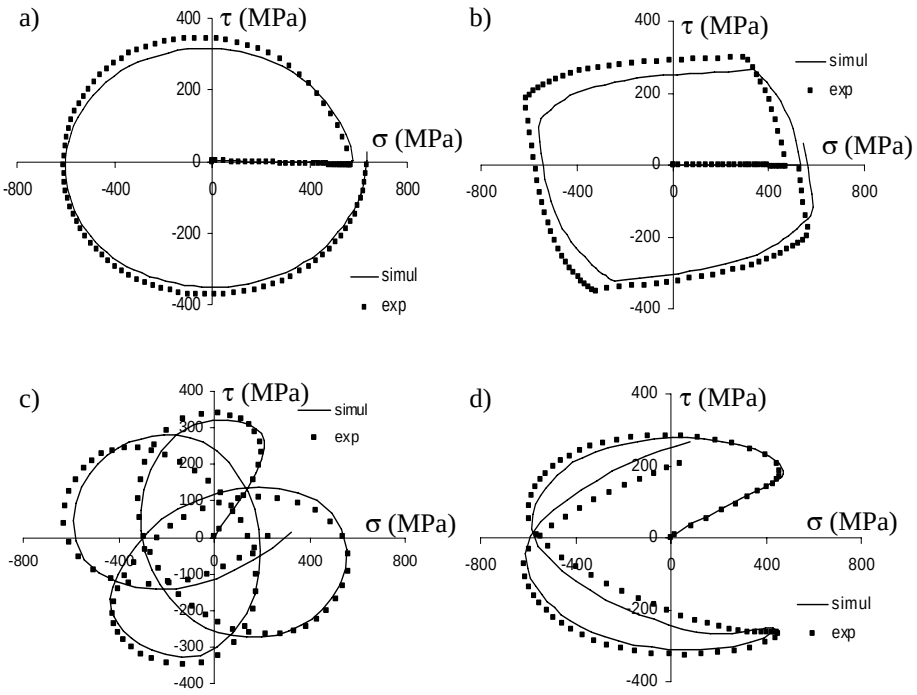

Figure 9.15. *First hysteresis loops in tension/compression-torsion with an equivalent total strain amplitude of 0.5%: comparison between simulation and experimental results obtained on the forged duplex stainless steel studied: a) circle loading path, b) square loading path, c) hourglass loading path, d) clover loading path*

With polycrystalline models, no assumption is made concerning the shape and the position of the yield surface. It is then necessary to measure it in a similar way as that used experimentally. After a given loading and from a point belonging to the elastic domain, n radial loadings are carried out numerically. When a given plastic strain is reached, the corresponding point is recorded.

Yield surfaces calculated on virgin duplex stainless steel and after a loading in tension up to a total strain amplitude of 0.5% are compared to experimental results

(Figure 9.16). It can be seen that the model accounts well for the general shape of experimental yield surfaces, as after proportional loading the yield surface shows a rounded nose in the direction of loading and a flattening in the opposite direction. However, although the nose is correctly described by the model, the position of the flattening is not and the size of the yield surface is then overestimated. This result could obviously be improved by using yield surface measurements during the identification, but the main interest of this model is its simulation capacity of effects not included in the identification database.

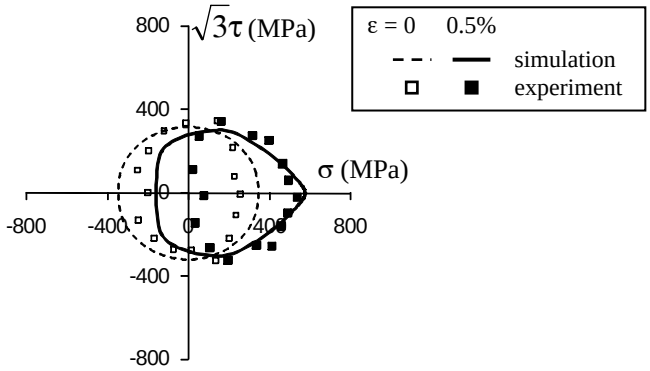

Figure 9.16. *Yield surfaces measured and simulated on virgin duplex stainless steel (in dashed lines) and after loading in tension up to a total strain of 0.5%*

9.3.8. *Modeling of the cyclic softening*

Experimental results show that, during the accommodation phase, the forged duplex stainless steel shows a cyclic hardening followed by a cyclic softening (Figure 9.6). The model described above is only able to simulate a monotonous evolution of the stress amplitude, a cyclic hardening, during the cyclic loading. The simulation of the stabilized loop overestimates greatly the stress amplitude observed experimentally (Figure 9.17) [EVR 08c]. These observations have justified the modification of the model presented above to account for the cyclic softening observed experimentally.

[EVR 08b] and [EVR 08c] studied and compared the dislocation structures at different stages of fatigue tests in the forged duplex stainless steel studied (see also Chapter 7). In austenite and ferrite, the dislocation distribution is initially globally homogenous. During cycling, the dislocation density increases. The distribution stays homogenous in austenite, also under non-proportional loading, whereas it becomes widely heterogenous in ferrite. Structures of walls and channels are

observed, with high and low dislocation densities, respectively. The rearrangements of dislocations in substructures, corresponding to plastic strain localization, lead to cyclic softening. Therefore, it has been assumed that at least part of the cyclic softening is due to the rearrangement of dislocations into low and rich dislocation density zones in the ferritic phase.

The grain constitutive law presented above has been modified to take into account the rearrangement of dislocations in ferritic grains. The critical shear stress in ferritic grains is decomposed in soft and hard zones (channels and walls) as [EST 08]:

$$\tau_{\mu f}^{(s)} = f_w^{(s)} \tau_{\mu w}^{(s)} + f_c^{(s)} \tau_{\mu c}^{(s)} \qquad [9.35]$$

where $\tau_{\mu w}^{(s)}$ and $\tau_{\mu c}^{(s)}$ are the critical shear stresses in walls and channels, respectively, and $f_w^{(s)}$ and $f_c^{(s)}$ the volume fractions of walls and channels, respectively.

The shear strain rate on slip system (s) in ferritic grains is now:

$$\dot{\gamma}_f^{(s)} = \left(\frac{\left| \tau_f^{(s)} \right| - \left(f_w^{(s)} \tau_{\mu w}^{(s)} + f_c^{(s)} \tau_{\mu c}^{(s)} \right)}{\mathrm{K_f}} \right)^{\mathrm{n_i}} sign(\tau_f^{(s)})$$

$$\text{if } \tau_{\mu f}^{(s)} \geq f_w^{(s)} \tau_{\mu w}^{(s)} + f_c^{(s)} \tau_{\mu c}^{(s)}, \quad \dot{\gamma}_f^{(s)} = 0 \text{ otherwise} \qquad [9.36]$$

The equations defining the critical shear stress and the evolution of dislocation density in walls are identical to their expressions in the initial model. However, in channels, dislocations are less numerous, their interactions can be neglected. The critical shear stress is then:

$$\tau_{\mu c}^{(s)} = \tau_{\mathrm{f}}^{0} + \mathrm{b_f} \mu \sqrt{\rho_c^{(s)}} \qquad [9.37]$$

The evolution of dislocation density becomes:

$$\dot{\rho}_c^{(s)} = \frac{1}{\mathrm{b_f}} \left(\frac{\sqrt{\rho_c^{(s)}}}{\mathrm{L_c}} - 2\mathrm{y_s} \rho_c^{(s)} \right) \left| \dot{\gamma}_f^{(s)} \right| \qquad [9.38]$$

where L_c controls the dislocation production and y_s is the annihilation distance of screw dislocations in channels. As walls and channels form from the same homogenous state, the initial critical shear stress, τ_f^0, and the initial dislocation density, ρ_f^0, are assumed to be the same. The evolution of $f_c^{(s)}$, with $f_w^{(s)} + f_c^{(s)} = 1$, is described by:

$$\dot{f}_c^{(s)} = H\left(1 - \frac{1}{f_\infty} f_c^{(s)}\right)\left|\dot{\gamma}^{(s)}\right| \quad \text{with} \quad f_c^{(s)}\left(\gamma^{(s)} = 0\right) = 0 \qquad [9.39]$$

where f_∞ is the asymptotic value of the channel volume fraction and H a parameter controlling the softening rate.

Two parameters (f_∞ and L_c) have been determined from measurements on TEM observations, the others were obtained by the inverse method from the hardening/softening curve with a strain amplitude of 0.5% in tension-compression.

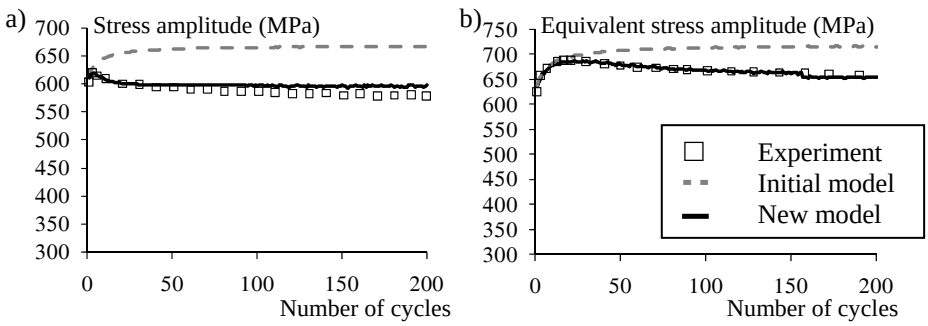

Figure 9.17. *Comparison between experiments in the forged DSS studied and simulations with initial and new models. a) Cyclic hardening/softening curves in tension-compression (ε_a = 0.35), b) cyclic hardening/softening curves with a square loading path (ε_a = 0.35)*

It can be seen in Figure 9.17 that the new model accounts for the hardening/softening observed in forged duplex stainless steel under uniaxial and multiaxial loadings. The accommodation phase is well described and the stabilized stress amplitude also. The model proposed has been validated on stabilized hysteresis loops and stabilized stress amplitudes with various loading paths [EVR 08c].

9.3.9. *Conclusion*

In this part a bi-phased polycrystalline model was proposed which adequately described the microstructure of a forged DSS. The local behavior of austenitic and ferritic grains is described by grain behavior laws, based on the crystallographic slip and the dislocation density evolution. The same mathematical formalism is used to describe the austenitic and ferritic grain behavior, the only differences lie in the number of slip systems and the values of parameters. A Cailletaud-Pilvin self-consistent model is used to link macroscopic and microscopic scales. It is important to note that a high number of parameters have been extracted from the literature and that only two tests have been used for the identification of the other parameters. Very simple and inexpensive tests are necessary for the identification. The model was then validated with a large experimental database (monotonous and cyclic tests with various strain amplitudes, multiaxial tests, yield surface evolution), which proves its robustness.

A modification of the model has been proposed to take into account the cyclic softening observed in forged duplex stainless steel. This modification is based on dislocation rearrangements observed during the cycling in the ferritic phase. With this modification, the micromechanical model is able to describe the accommodation phase and the stabilized state under uniaxial and multiaxial cyclic loadings.

9.4. General conclusion

Two approaches have been presented and used for the modeling of the mechanical behavior of a forged duplex stainless steel under monotonous and cyclic, uniaxial and multiaxial loadings. The first approach is based on the macroscopic analysis of the evolution of strains and stresses. The choice of the constitutive laws and the identification of their parameters have been made easier through the experimental analysis of the evolution of strengthening components during cycling loading. The basis model (model NLK) is able to account for the monotonous and cyclic behaviors observed in duplex stainless steel under uniaxial loading, and, in particular, for its cyclic hardening-softening behavior. Under multiaxial cyclic loadings, as the duplex stainless steel exhibits an over-hardening under non-proportional cyclic loadings, the basis model is no longer relevant. Several constitutive laws to take into account the over-hardening have been tested and compared. Models proposed by Tanaka [TAN 94] and Abdul-Latif *et al.* [ABD 94] accurately predict the stress-strain relationship obtained under cyclic non-proportional loading. Nevertheless, this family of models requires a large experimental database to identify the model parameters; therefore, a second method has then been explored.

The second approach takes into account the strongly heterogenous nature of the material. From the microstructure of the forged duplex stainless steel, only one scale of heterogenity has been revealed: the grains of austenite and ferrite. A single grain scale is then considered. Stresses in grains are calculated through a localization law from the macroscopic stress. The local behavior of austenitic and ferritic grains is described by grain constitutive laws, based on the crystallographic slip and dislocation density evolution. A very limited and simple experimental database is necessary to identify the material parameters, as most of them are taken from the literature.

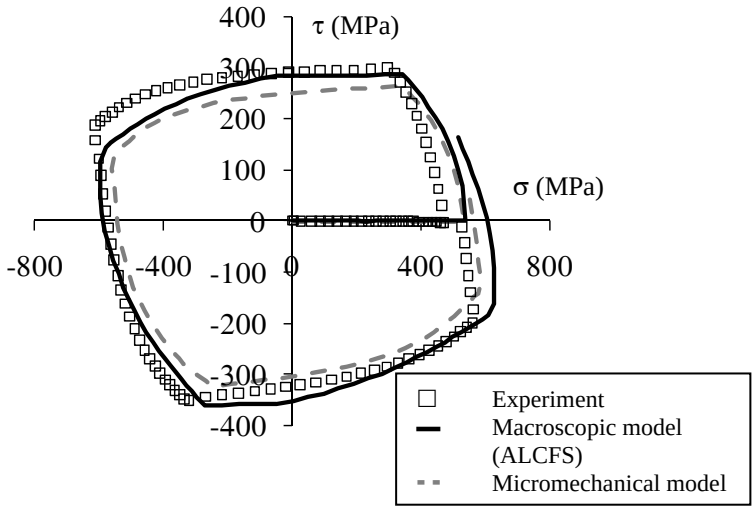

Figure 9.18. *First hysteresis loop in tension/compression-torsion with an equivalent total strain amplitude of 0.5% and a square loading path: comparison between experimental results and simulations obtained with model ALCFS and with the micromechanical model (forged duplex stainless steel)*

Although the models tested are based on very different approaches, both are able to account for the mechanical behavior observed in duplex stainless steel under monotonous and cyclic proportional and non-proportional loadings with very similar results (Figure 9.18). The two approaches proposed in this chapter are then pertinent to simulate the mechanical behavior of forged duplex stainless steels. For another duplex stainless steel, material parameters have to be identified on experimental monotonous and cyclic tests representative of in-service loadings. The choice of one of the two approaches presented in this chapter to simulate a given mechanical behavior will depend on the experimental database available and on the

knowledge of the material and of the physical mechanisms creating the observed behavior.

9.5. References

[ABD 94] ABDUL-LATIF A., CLAVEL M., FERNEY V. and SAANOUNI K., "On the modeling of nonproportional cyclic plasticity of waspaloy", *J. Eng. Mat. Tech.*, vol. 116, pp. 35-44, 1994.

[AND 07] ANDRADE-CAMPOS A., THUILLIER S., PILVIN P. and TEIXEIRA-DIAS F., "On the determination of material parameters for internal variable thermoelastic-viscoplastic constitutive models", *Int. J. Plast.*, vol. 23, pp. 1349-1379, 2007.

[ARM 66] ARMSTRONG P.J. AND FREDERICK C.O., *A Mathematical Representation of the Multiaxial Bauschinger Effect*, CEGB Report RD/B/N731, Berkeley Nuclear Laboratories, 1966.

[AUB 02] AUBIN V., QUAEGEBEUR P. and DEGALLAIX S., "Evolution of the plasticity surface during biaxial loading in duplex stainless steel", *J. Phys. IV*, vol. 12, pp. 195-202, 2002.

[AUB 03a] AUBIN V., QUAEGEBEUR P. and DEGALLAIX S., "Cyclic plasticity of a duplex stainless steel under non-proportional loading", *Mat. Sci. Eng. A*, vol. 346, no. 1-2, pp. 208-215, 2003.

[AUB 03b] AUBIN V., QUAEGEBEUR P. and DEGALLAIX S., "Cyclic behaviour of a duplex stainless steel under multiaxial loading: experiments and modeling", in A. CARPINTERI, M. DE FREITAS and A. SPAGNOLI Eds., *ESIS STP Biaxial/Multiaxial Fatigue and Fracture*, Elsevier, pp. 401-422, 2003.

[BAC 04] BACZMANSKI A. and BRAHAM C., "Elastoplastic properties of duplex steel determined using neutron diffraction and self-consistent model", *Acta Materiala*, vol. 52, pp. 1133-1142, 2004.

[BAR 01a] BARBE F., DECKER L., JEULIN D. and CAILLETAUD G., "Intergranular and intragranular behavior of polycrystalline aggregates. Part 1: F.E. model", *Int. J. Plast.*, vol. 17, pp. 513-536, 2001.

[BAR 01b] BARBE F., DECKER L., JEULIN D. and CAILLETAUD G., "Intergranular and intragranular behavior of polycrystalline aggregates. Part 2: results", *Int. J. Plast.*, vol. 17, pp. 537-563, 2001.

[BEN 87] BENALLAL A. and MARQUIS D., "Constitutive equations for nonproportional cyclic elasto-viscoplasticity", *J. Eng. Mat. Tech.*, vol. 109, pp. 326-336, 1987.

[BEN 89] BENALLAL A., Thermoviscoplasticité et endommagement des structures, PhD Thesis, University of Paris VI, 1989.

[BER 79] BERVEILLER M. and ZAOUI A., "An extension of the self-consistent schem to plastically-flowing polycristals", *J. Mech. Phys. Solids*, vol. 26, pp. 325-344, 1979.

[BOR 96] BORODII M.V., KUCHER N.K. and STRIZHALO V.A, "Development of a constitutive model for biaxial low-cycle fatigue," *Fatigue and Fracture of Engineering Materials and Structures*, vol. 19, pp. 1169-1179, 1996.

[BUD 62] BUDIANSKI B. and WU T.T., "Theroritical prediction of plastic strains of polycrystals", in *Proc. 4th US Nat Cong. Apll. Mech.*, p. 1175, 1962.

[BUG 99] BUGAT S., BESSON J. and PINEAU A., "Micromechanical modelling of the behaviour of duplex stainless steels", *Comput. Mat. Sci.*, vol. 16, pp. 158-166, 1999.

[BUI 69] BUI H.D., Etude de l'évolution de la frontière du domaine élastique avec l'écrouissage et relations de comportement élastoplastiques des métaux cubiques, PhD Thesis, University of Paris, 1969.

[CAI 92] CAILLETAUD G., "A micromechanical approach to inelastic behaviour of metals", *Int. J. Plast.*, vol. 8, pp. 55-73, 1992.

[CAI 95] CAILLETAUD G. and SAI K., "Stufy of plastic/viscoplastic models with various inelastic mechanisms", *Int. J. Plast.*, vol. 11, pp. 991-1005, 1995.

[CAI 94] CAILLETAUD G. and PILVIN P., "Utilisation des modèles polycristallins pour le calcul par éléments finis", *Revue Européenne des Eléments Finis*, vol. 3, no. 4, pp. 515–541, 1994.

[CAL 99] CALLOCH S. and MARQUIS D., "Triaxial tension-compression tests for multiaxial cyclic plasticity", *Int. J. Plast.*, Vol 15, pp. 521-549, 1999.

[CHA 83] CHABOCHE J.L. and ROUSSELIER G., "On the plastic and viscoplastic constitutive equations - Part I: Rules developped with internal variables concept", *J. Press. Vessel Techn.*, vol. 105, pp. 153-164, 1983.

[CHA 91] CHABOCHE J.L., NOUAILHAS D., PACOU D. and PAULMIER P., "Modeling of the cyclic response and ratchetting effects on inconel-718 alloy", *Eur. J. Mech. A/Solids*, vol. 10, pp. 101-121, 1991.

[COT 53] COTTRELL A.H., *Dislocations and Plastic Flow in Crystals*, Oxford university Press, London, 1953.

[DAF 75] DAFALIAS Y. F. and POPOV E. P., "A model of nonlinearly hardening materials for complex loading", *Acta Mech.*, vol. 21, pp. 173-192, 1975.

[DIN 00] DINGLI J.P., ABDUL-LATIF A. and SAANOUNI K., "Predictions of the complex cyclic behavior of polycrystals using a self-consistent modeling", *Int. J. Plast.*, vol. 15, pp. 521-547, 2000.

[ELL 83] ELLIS J. R., ROBINSON D. N. and PUGH C. E., "Time dependence in biaxial yield of type 316 stainless steel at room temperature", *J. Eng. Mat. Tech.*, vol. 105, pp. 250-256, 1983.

[ESH 57] ESHELBY, "The determination of the elastic field of an ellipsoidal inclusion, and related problems", *Proc. R. Soc. London*, vol. 241, pp. 376-396, 1957.

[EST 08] ESTRIN Y., TOTH L.S., MOLINARI A. and BRÉCHET Y., "A dislocation-based model for all hardening stages in large strain deformation", *Acta Mater*., vol. 46, pp. 5509-5522, 1998.

[EVR 08a] EVRARD P., AUBIN V., PILVIN P., DEGALLAIX S. and KONDO D., "Implementation and validation of a polycrystalline model for a bi-phased steel under non-proportional loading paths", *Mechanics Research Communications*, vol. 35, pp. 336-343, 2008.

[EVR 08b] EVRARD P., Modélisation polycristalline du comportement plastique cyclique d'un acier inoxydable duplex et validation expérimentale, PhD Thesis, Ecole Centrale de Lille, 2008.

[EVR 08c] EVRARD P., AUBIN V., DEGALLAIX S. and KONDO D., "Formulation of a new single crystal law to model the cyclic softening", *Mechanics Research Communications*, vol. 35, pp. 589-594, 2008.

[FAN 91] FAN J. and PENG X., "A physically based constitutive description for nonproportional cyclic plasticity", *J. Eng. Mat. Tech.*, vol. 113, pp. 245-262, 1991.

[FRA 91] FRANCOIS D., PINEAU A. and ZAOUI A., *Elasticité et plasticité*, Hermes, 1991.

[HEL 86] HELLING D. E., MILLER A. K. and STOUT M. G., "An experimental investigation of the yield loci of 1100-0 aluminum, 70:30 brass, and an overaged 2024 aluminum alloy after various prestrains", *J. Eng. Mat. Tech.*, vol. 108, pp. 313-320, 1986.

[HIL 65] HILL R., "Continuum micro-mechanics af elastoplastic polycristals", *J. Mech. Phys. Solids*, vol. 13, pp. 89-101, 1965.

[KOU 94] KOUDDANE R., ZOUHAL N. and MOLINARI A., "Complex loading of viscoplastic materials: micro-macro modelling", *Mat. Sci. Eng. A*, vol. 175, p. 31-36, 1994.

[KRE 75] KREMPL E., "On the interaction of rate and history dependance in structural metals", *Acta Metall*, vol. 22, p. 53-90, 1975.

[KRI 75] KRIEG R. D., "A practical two surface plasticity theory", *J. App. Mech.*, vol. 42, pp. 641-646, 1975.

[KRO 65] KRÖNER E., "Zur plastischen Verformung des Vielkristalls", *Acta Metall*., vol. 9, p. 155, 1965.

[LEB 93] LEBENSOHN R.A. and TOMÉ C.N., "A self-consistent anisotropic approach for the simulation of plastic deformation and texture development of polycrystals: application to zirconium alloys", *Acta Metall. Mater*., vol. 41, pp. 2611-2624, 1993.

[LEM 88] LEMAÎTRE J. and CHABOCHE J.L., *Mécanique des Matériaux Solides*, Dunod, Bordas, 1988.

[LOS 04] LOSILLA G. and TOURABI A., "Hardening of a rolled sheet submitted to radial and complex biaxial tensile loadings", *Int. J. Plast*., vol. 20, pp. 1789-1816, 2004.

[MAD 01] MADEC R., Des intersections entre dislocations à la plasticité du monocristal CFC: Etude par dynamique des dislocations, PhD Thesis, University of Paris XI Orsay, 2001.

[MAR 79] MARQUIS D., *Modélisation et identification de l'écrouissage anisotrope des métaux*, PhD Thesis, University of Paris VI, 1979.

[MIC 76] MICHNO M. J. and WILLIAM N. F., "An historical perspective of yield surface investigations for metals", *Int. J. Non-linear Mechanics*, vol. 11, pp. 59-82, 1976.

[MOL 87] MOLINARI A, CANOVA G.R. and AHZI S., "A self-consistent approach of the large deformation viscoplasticity", *Acta Metall.*, vol. 35, p. 2983-2987, 1987.

[MOL 97] MOLINARI A., AHZI S. and KOUDDANE R., "On the self-consistent modeling of elasto-plastic behavior of polycrystals", *Mech. Mat.*, vol. 26, pp. 43-62, 1997.

[MRO 67] MROZ Z., "On the description of anisotropic work hardening", *J. Mech. Phys. Sol.*, vol. 15, pp. 163-175, 1967.

[PHI 79] PHILLIPS A. and LEE C.-W., "Yield surfaces and loading surfaces. Experiments and recommendations", *Int. J. Sol. Struct.*, vol. 15, pp. 715-729, 1979.

[PIL 90] PILVIN P., Approches multiéchelles pour la prévision du comportement anélastique des métaux, PhD Thesis, University of Paris 6, 1990.

[POL 91] POLÀK J., *Cyclic Plasticity and Low-Cycle Fatigue Life of Metals*, Academia Prague, 1991.

[POR 00] PORTIER L., CALLOCH S., MARQUIS D. and GEYER P., "Ratchetting under tension-torsion loadings: experiments and modelling", *Int. J. Plast.*, vol. 16, pp. 303-335, 2000.

[PRA 58] PRAGER W., "A new method of analyzing stresses and strains in work hardening plastic solids", *J. App. Mech.*, vol. 23, pp. 493-496, 1958.

[RAU 93] RAUCH E.F. and THUILLIER S., "Plasticity and unstable flow mild steel", *Arch Metall*, vol. 38, pp. 167-177, 1993.

[ROU 85] ROUSSET M., Surface seuil de plasticité, détermination automatique et modélisation, PhD Thesis, University of Paris 6, 1985.

[TAB 97] TABOUROT L., FIVEL M. and RAUCH E., "Generalised constitutive laws for FCC single crystals", *Mat. Sci. Eng. A*, vol. 234-236, pp. 639-642, 1997.

[TAN 92] TANAKA E., "A nonproportionality parameter and a viscoplastic constitutive model describing both cyclic hardening and cyclic softening", in *International Seminar on Multiaxial Plasticity*, MECAMAT, pp.198-223, 1992.

[TAN 94] TANAKA E., "A nonproportionality parameter and a viscoplastic constitutive model taking into account amplitude dependences and memory effects of isotropic hardening", *Eur. J. Mech. A/Solids*, vol. 13, p. 155-173, 1994.

[WU 91] WU H. C. and YEH W. C., “On the experimental determination of yield surfaces and some results of annealed 304 stainless steel”, *Int. J. Plast*., vol. 7, pp. 803-826, 1991.

[ZIE 59] ZIEGLER H., “A modification of Prager’s hardening rule”, *Quart. Appl. Math*, vol. 17, pp. 55-65, 1959.

Chapter 10

Low-Cycle Fatigue at Intermediate Temperatures

10.1. Introduction

This chapter describes the cyclic behavior of two duplex stainless steels (DSSs) with different nitrogen contents unaged (as-received) and aged under thermal conditions (in a wide range of temperatures) related to their developed dislocation structures. The mechanical cyclic properties of these steels are discussed in terms of the influence of dynamic strain aging (DSA) and spinodal decomposition (SD).

Due to strong economical and environmental reasons, there has been a continuous increase in improving the efficiency of industrial and power plants. After the Carnot efficiency concept, the wider the gap between the higher and lower temperatures of an operating plant, the more efficient the process. From the beginning of the 19th century, this concept has driven the development of the industrial technology. Thus, components of industrial and power plants are often subjected to repeated thermal stresses as a result of temperature gradients that occur on heating and cooling during start-ups and shut-downs or during variations in operating conditions. Low-cycle fatigue (LCF) is an important consideration in the design and operation of high-temperature systems that are subjected to such repeated thermal stresses. Therefore, the LCF and creep-fatigue interaction play an important

Chapter written by Alberto F. ARMAS.

Duplex Stainless Steels Edited by Iris Alvarez-Armas and Suzanne Degallaix-Moreuil

role regarding the safe life design approach of steam generator components of nuclear fission reactors and heat-recovery steam generators.

Stainless steels are extremely useful as engineering materials because of their wide range of properties and resistance to environmental conditions. They have high ductility and toughness over a wide range of temperatures and exhibit excellent corrosion and high-temperature oxidation resistance. The most important property of stainless steels is undoubtedly their corrosion resistance, without which they would be little used because their mechanical properties and formability can be equaled or exceeded by much cheaper, but non-stainless, steels [PIC 84].

DSSs are regarded as an alternative to austenitic stainless steels due to their corrosion resistance, formability, and high strength. The two-phase mixture leads to a marked refinement of the grain size in both the austenite and ferrite. This, together with the presence of ferrite, makes the material approximately twice as strong as common austenitic steels. DSSs contain only about half the nickel content of typical austenitic stainless steels; therefore, they are less expensive and less sensitive to the price of nickel. With their high chromium content, they have excellent pitting and crevice corrosion resistance and chloride-stress corrosion resistance (see Chapter 2 of this book). During the last 20 years, DSSs have undergone considerable development, stimulated partly by the nickel shortages, increasing their applications in the offshore, power, oil, gas, petrochemical, paper and sugar industries [CRA 83]. Their unique combination of mechanical strength, thermal expansion coefficient [ELM 82], low temperature toughness, and corrosion resistance, makes them suitable for a wide range of engineering applications. The high strength allows the design of lighter components and hence a reduction of costs in piping, making them prominent in the oil industry. Their relatively low thermal expansion coefficient compared with austenitic stainless steels makes them useful for shell and tube heat exchangers. In addition, the improved stress corrosion cracking resistance in chloride environments at temperatures above 50°C qualifies DSSs as alternatives to the classical austenitic stainless steels (Fe-18Cr-8Ni wt%), which is dogged by stress corrosion problems [STR 86].

Since the discovery of metals as useful tool materials, man has been trying to strengthen them. A very effective strengthening mechanism can be obtained by the SD occurring in binary systems, which contains a miscibility gap. The Fe-Cr system, which is the basis for all stainless steels, contains a miscibility gap and exhibits SD. It is well known that the phenomenon of SD is also the cause of the “475°C embrittlement” that has limited the use of conventional ferritic stainless steels. In fact, some authors [NIC 80, MAR 96] have shown that this embrittlement causes an increase in hardness, but also a significant decrease in ductility and fracture toughness. The hardening phenomenon accompanying SD in ferritic stainless steels is now reasonably well understood [KAT 81]. The homogenous ferrite phase

decomposes into α (iron-rich) and α' (chromium-rich) phases, which develop an internal stress field responsible for the strengthening mechanism. The initial fluctuations of composition in the metastable parent phase, during SD, can be modeled to a first-order approximation at least by a sinusoidal equation [CHA 71]. However, this relationship breaks down when the volume fraction of the α' phase exceeds approximately 15%; at this point the α' may become interconnected to form an extremely fine duplex microstructure [MIL 87]. The α' regions exert a restraining effect on dislocation motion, owing to their different lattice parameter, chemical composition, and perhaps, magnetic properties, and are consequently responsible for hardening and embrittling the microstructure [GRO 73, PAR 86].

Because of their high chromium content, DSSs are prone to the 475°C embrittlement in the ferrite phase; so their applications are frequently confined to temperatures below about 300°C (see Chapters 3 and 5). However, the operating temperatures of cast DSS components for the cooling system of pressurized water reactors is about 320°C. Several studies were found in the literature regarding the aging effects on the evolution of mechanical properties of DSSs [SOL 83, PUM 90] (see Chapter 5). Nevertheless, aging effects on the fatigue properties of DSSs have been studied much less extensively, and the few available reports are mainly concentrated on the evolution of the fatigue properties of aged DSSs at room temperature [LLA 96].

Cyclic plastic loading gives rise to modifications of the internal structure of the material and simultaneous modifications of the stress-strain response. The interaction between solute atoms, such as carbon and nitrogen, in interstitial positions and dislocations gives rise to strong pinning and leads to the important phenomenon of strain aging. In particular, dynamic strain aging (DSA) occurs when the rate of straining is such that the interstitial atoms can diffuse and pin the mobile dislocations. Although the effects of strain aging on the cyclic mechanical behavior of steels are already well-known [COF 65], they have not been extensively studied in stainless steels. Several authors [RAO 86, ARM 88, ZAU 93] have reported the strong influence of DSA on the cyclic behavior of austenitic stainless steels. A marked cyclic hardening and an inverse dependence of the maximum tensile stress amplitude on both temperature and strain rate in the DSA domain was found in all cases. Conversely, Armas *et al.* [ARM 97] analyzed the cyclic behavior of the AISI 430 F ferritic stainless steel in the normalized condition and observed a pronounced cyclic hardening stage of extended duration when cycled between 350 and 450°C attributed to DSA phenomena. As DSSs consist of a substructure of ferritic and austenitic grains, it is expected that these steels could also present such manifestations under mechanical cycling at intermediate temperatures in addition to the SD in the ferrite. To our knowledge, only a few studies can be found in the literature regarding the DSA phenomenon in DSS.

The purpose of this chapter is to study the influence of temperatures up to 500°C on the cyclic behavior of a superduplex type DSS, UNS S32750, and a first-generation DSS, UNS S32900. The main difference between these steels lies in the deliberate addition of nitrogen as an alloying element. The study will be made for the steels under both thermal conditions, unaged (as-received) and aged. The main aim is to clarify the influence of the temperature on the cyclic life of the steel. In unaged samples, the objective is to analyze the influence of DSA on the fatigue life of the steel evaluating the possibility of the occurrence of SD and its influence on the mechanical response. For aged material, the influence of the SD on the lifetime is analyzed and the possible apparition of DSA manifestations and their effects are examined. These results will be discussed correlating them with observations performed by transmission electron microscopy (TEM) on both phases of DSSs.

10.2. Materials studied

The materials selected for this investigation were the commercial DSS type UNS S32750 (SAF 2507, EN 1.4410), called superduplex stainless steel (SDSS), produced by Sandvik AB, Sweden, and a first-generation type DSS, UNS S32900 (AISI 329, DIN W. Nr. 1.4460), produced by Villares Metals, Brazil. The chemical compositions (in weight percent) of the steels are given in Table 10.1.

UNS	C	N	Cr	Ni	Mo	Mn	Si	Cu	P	S	α/γ
S32900	0.027	0.04	24.10	4.80	1.49	1.29	0.43	0.15	0.034	0.007	72/28
S32750	0.015	0.26	24.85	7.00	3.79	0.40	0.30	0.31	0.015	0.0005	50/50

Table 10.1. *Chemical compositions of duplex steels in weight percent and ferrite/austenite volume fractions*

The steels were supplied in the form of cylindrical bars and were solid solution treated and then water-quenched. Figure 10.1 shows an optical micrograph of the longitudinal mean-section of the bars of both steels. Light areas are austenite and dark areas are ferrite. The resulting microstructure for type UNS S32750 consists of 50% vol. (28% vol. for type UNS S32900) austenite embedded in a ferritic matrix.

In both steels, the grain shape was highly elongated in the rolling direction. This direction is parallel to the loading axis of all tested specimens. Cylindrical specimens, with a gage length of 18.4 mm and a diameter of 5 mm, were machined from bars. The specimens were studied in LCF under two conditions: unaged (as-received) and aged. This last condition consisted of thermal treatment for 100 h at 475°C applied to the as-received samples. From previous studies, [VOG 02, WEN

04], it is known that, under these conditions, the kinetics of SD of the ferritic phase are the fastest, and the hardness attained after the first 100 h does not change appreciably even for much longer aging times. To observe the dislocation substructures, specimens were cut perpendicular and parallel (longitudinal) to the bar axis. The longitudinal discs were prepared to determine the orientation of the dislocation structure with reference to the loading axis. Foils were thinned with a double-jet electro-polishing technique using a solution of 10% perchloric acid and 90% ethanol. The foils were examined using two transmission electron microscopes: a conventional microscope (Philips EM300) operating at 100 kV, and a high-resolution microscope (Philips CM200 UT) operating at 200 kV.

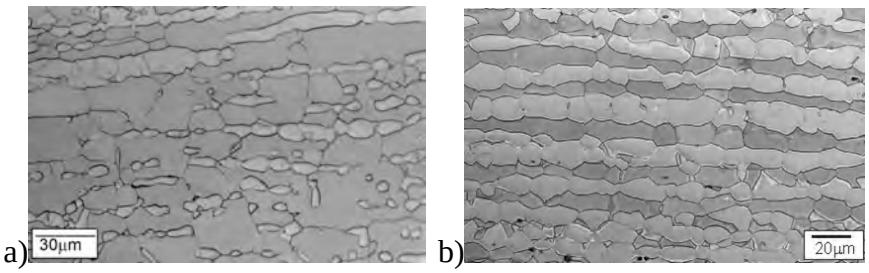

Figure 10.1. *Optical micrograph of unaged a) S32900 and b) S32750 viewed from in longitudinal section*

Figure 10.2a is a conventional TEM image of the ferrite phase in a non-deformed, unaged DSS sample. The typical “orange peel” appearance, characteristic of the SD observed in the ferrite phase of a specimen aged at 475°C for 100 h, can be seen in the dark-field micrographs obtained by TEM (Figure 10.2b). The observed contrast results from a different oxidation degree of the two phases during the preparation of the TEM thin foils [WEN 04]. Figure 10.2c is a higher magnification TEM image of the ferrite in an aged specimen showing the mottled contrast due to SD. This mottled image can be seen more clearly when the electron beam is aligned along the <001> zone axis. Spinodal alloys have anisotropic elastic properties and in the case of body-centered cubic (BCC) structure, <001> is the direction minimizing the elastic energy and favoring decomposition kinetics.

Figure 10.3 shows the strong influence of the aging treatment on the mechanical behavior of the alloy. The figure, corresponding to the stress response for the first half cycle of a cyclic test, exhibits the yield stress at 0.2% plastic strain for unaged and aged samples of type UNS S32900 DSS.

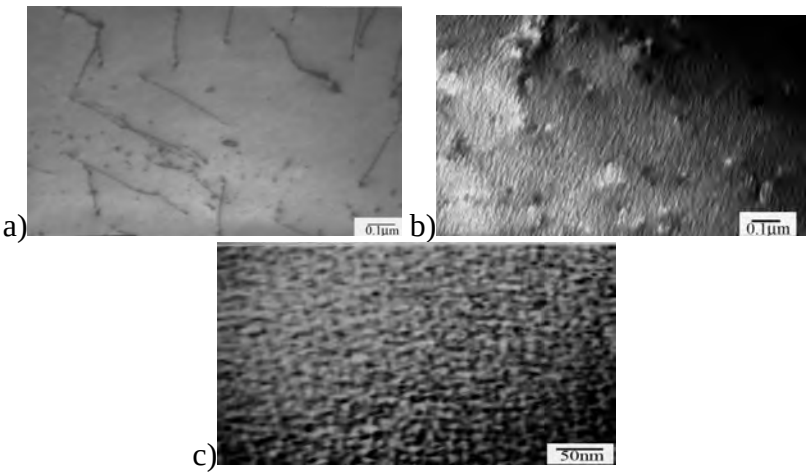

Figure 10.2. *Micrographs of the ferrite of a) unaged and b) aged samples of DSS obtained by conventional TEM. c) Image of the ferrite of an aged sample obtained with a higher magnification*

LCF tests were carried out under total or plastic strain control using a fully reversed triangular-form signal. Before testing, the specimens were mechanically polished to avoid any premature crack initiation. The specimens were tested in air in the temperature range 20-500°C. The average total strain rate in all the tests was 2×10^{-3} s^{-1}. (For a description of the LCF tests and the result presentation see Chapter 6.)

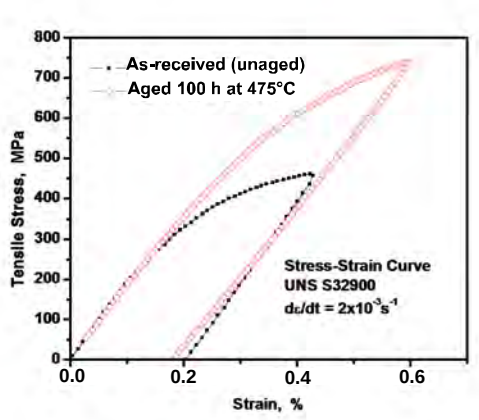

Figure 10.3. *Stress-strains curves for unaged and aged samples of UNS S32900 DSS (first half cycle of fatigue tests)*

10.3. UNS S32900 DSS

10.3.1. *Unaged (as-received) steel*

10.3.1.1. *Cyclic behavior*

In recent years, it has been reported [HER 01, ALV 03, GIR 06, ARM 08] that, similar to single-phase austenitic [ARM 88] and ferritic [ARM 97] stainless steels, DSSs also show manifestations of DSA in the form of pronounced cyclic hardening, inverse strain rate dependence, and anomalous dependence of the yield stress on temperature.

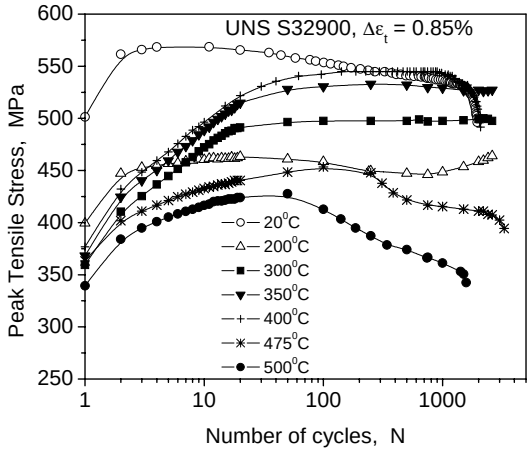

Figure 10.4. *Cyclic hardening/softening curves of unaged duplex stainless steel UNS S32900*

Figure 10.4 shows the stress response of DSS type UNS S32900 under cyclic total strain control in the temperature range between room temperature and 500°C for a total strain range of $\Delta\varepsilon_t$ = 0.85%. This figure exhibits the strong influence of temperature on the mechanical behavior of the steel. Cycle 1 (strictly speaking the first tensile loading) corresponds to a unidirectional tensile test. At this stage the figure already shows the typical static strain aging manifestation consisting of an anomalous flow stress increase between 300 and 500°C. Cycle 2 is the first true cycle. It can be observed that the most relevant feature of the curves occurs in a short period of the fatigue life, which is defined as an accommodation period that ranges from cycle 2 to cycle 20. This short period defines the cyclic hardening/softening behavior of the samples at each temperature. At room temperature and 200°C, an almost constant peak tensile stress is observed during this period. Between 300 and 500°C, coincident with the temperature range where

the anomalous behavior of the tensile flow stress for the first quarter of cycle is observed, a pronounced cyclic hardening takes place with steeper slopes corresponding to 350 and 400°C. At these same temperatures, cyclic hardening is followed by a saturation period that continues up to the failure of the specimen. At 475 and 500°C, the first stage of cyclic hardening is followed by a pronounced softening that continues up to a saturation period at 475°C and up to the failure of the specimen at 500°C.

Figure 10.5 shows the effect of temperature on the peak tensile stress at various cycles at the total strain range of 0.85%. The peak tensile stress for cycle 1 corresponds to the flow stress at the total strain amplitude in a monotonic tensile test; therefore, the curve corresponding to cycle 1 represents the temperature dependence of this flow stress. This curve shows, between 300 and 500°C, one of the typical aspects of dynamic strain aging in tensile tests, i.e. anomalous dependence of the flow stress on temperature. In addition, it is also evident that in the same temperature range, the accommodation period – cycles 2 to 20 – shows the most pronounced cyclic hardening.

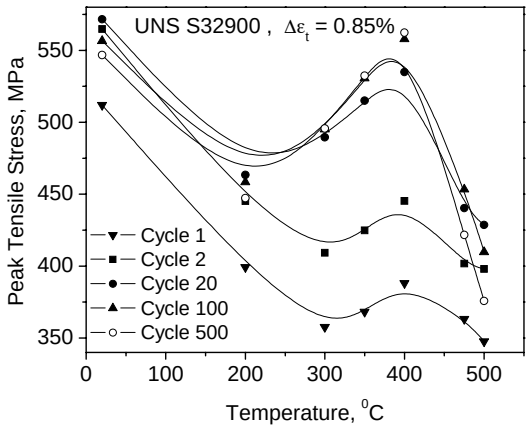

Figure 10.5. *Cyclic hardening of unaged DSS type UNS S32900 as a function of the temperature*

When DSA is the predominant process operating at certain temperatures, we would expect an inverse dependence of the stress amplitude with the strain rate [ARM 88]. To determine such anomalous phenomenon in the DSS, the strain rate influence on the peak tensile stress has been examined in the temperature domain between 20 and 500°C at a total strain range $\Delta\varepsilon_t$ =1.14%. The experimental procedure was the following: at each temperature, starting at room temperature, the

sample was cyclically loaded to reach, approximately 300 cycles, with a strain rate of 2.3×10^{-3} s^{-1}. This number of cycles corresponds to an almost stabilized peak tensile stress (σ_1) in most of the tests performed at different temperatures. Then, without any interruption of the test, the strain rate was decreased to 2.3×10^{-4} s^{-1} and after reaching stabilization, the peak tensile stress was measured (σ_2). The strain rate was finally decreased to 2.3×10^{-5} s^{-1} to obtain a new peak tensile stress value (σ_3). Stress increments $\Delta\sigma_2=\sigma_2-\sigma_1$ and $\Delta\sigma_3=\sigma_3-\sigma_1$ were defined. This procedure was repeated with increasing temperatures. Figure 10.6 shows both peak tensile stress differences as a function of temperature. At low temperatures, from room temperature to approximately 120°C, the stabilized stress shows a "normal" behavior, as it exhibits a lower peak tensile stress for the slower strain rates. Between approximately 120 and 480°C, higher peak tensile stresses correspond to slower strain rates.

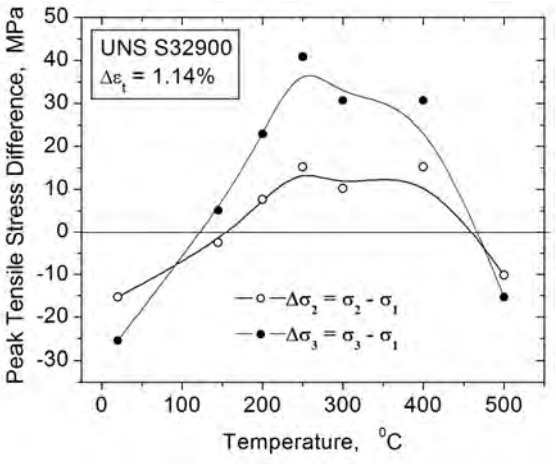

Figure 10.6. *Peak tensile stress differences as a function of the temperature for unaged type UNS S32900 DSS*

According to [MUG 97], the temperature range for the occurrence of DSA in single-phase ferritic steels tested with similar mechanical conditions lies between 130 and 430°C. Based on activation energy considerations, diffusing carbon atoms were proposed to be responsible for dynamic strain aging in these steels. However, the temperature range for DSA phenomena in single-phase austenitic steels was reported to be between 400 and 600°C [SRI 97]. Indeed, this range lies higher than that reported for ferritic steels. To rationalize this fact, it was proposed [TSU 83] that the DSA process in austenitic steels is associated with the interaction of dislocations with chromium atoms. The present results indicate that DSA in DSS UNS S32900 occurs in almost the same temperature range as that in ferritic steels.

In addition, it is also important to note the similar cyclic behavior observed at all temperatures in UNS S32900 steel to that reported in AISI 430F after an annealing treatment of 2 h at 1,050°C, followed by quenching in air [ARM 97]. Actually, both materials not only show a similar pronounced cyclic hardening at the beginning of the LCF tests within the DSA temperature range, but also a similar softening stage at 500°C. Conversely, no pronounced cyclic softening stage is observed in austenitic stainless steels at 500°C [SRI 97]. From these results, it seems that DSA in the present DSS is associated with the interaction of carbon atoms with dislocations in the ferritic phase.

10.3.1.2. *Mechanical behavior – microstructure correlation*

To analyze the correlation between the observed cyclic stress response of the material and the dislocation microstructure developed in each phase, thin foils of samples cycled up to failure were examined using TEM.

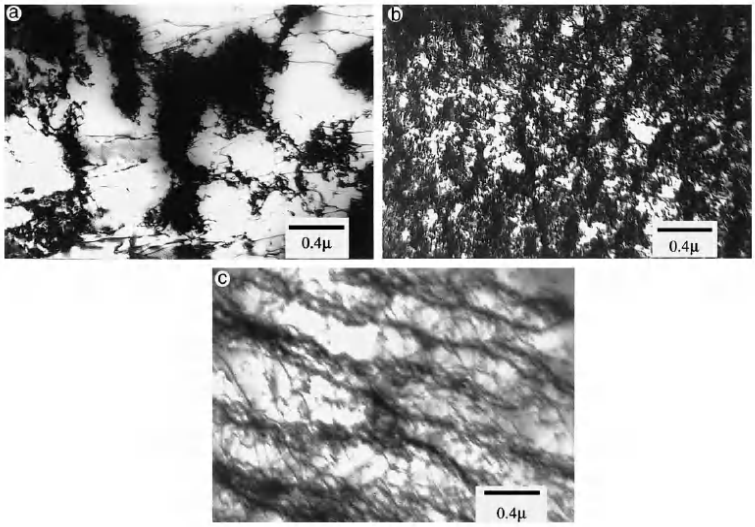

Figure 10.7. *Dislocation structure in ferritic grains [HER 01] at a) 200°C, b) 400°C and c) 500°C*

Figures 10.7a, b and c shows the dislocation structures found in the ferritic phase of specimens fatigued to rupture at 200, 400, and 500°C, respectively. At 200°C, dense dislocation bundles separated by wide and poorly defined channels can be observed. According to the anomalous cyclic behavior depicted in Figure 10.4, the temperature range where DSA effects are most pronounced lies roughly between 300 and 400°C. Figure 10.7b shows a striking dislocation structure developed in this

temperature range, specifically a high dislocation density arranged in uncondensed and poorly defined walls is seen. The results observed in the ferritic phase are similar to those obtained by other authors [PET 98] in tensile and cyclic tests of interstitial solid solution BCC alloys. It appears that the mutual interaction of the interstitial atoms with the gliding dislocations produces a high rate of dislocation multiplication in the ferritic phase. At temperatures above the range of DSA (Figure 10.7c), thermal activation gains importance, giving rise to a low dislocation density structure with thin and orderly walls at the end of the specimen life. Conversely, no remarkable structural changes have been found in the austenitic phase with temperature. The dislocation structure in the austenitic phase of DSS depends on the local deformation inside the austenitic grain. The structure varies from the arrangement of entangled dislocations near the center of the grain to an ill-formed cell structure near the grain boundary or in small grains. Figure 10.8 shows a small austenitic grain with an ill-formed cell structure.

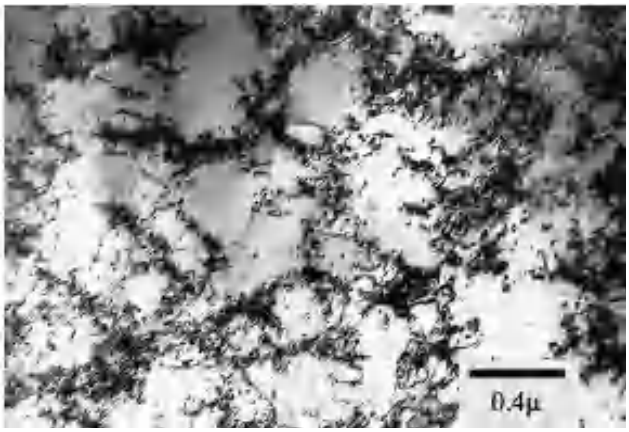

Figure 10.8. *Ill-formed cellular dislocation structure in an austenitic grain of a specimen of unaged DSS, UNS S32900, tested at 400°C*

10.3.2. *Aged steel*

10.3.2.1. *Cyclic behavior*

LCF tests performed in unaged and aged samples at room temperature, with a plastic strain range at half-life of 0.35%, showed the strong influence of the aging treatment on the mechanical behavior of the alloy [ARM 07]. A pronounced difference in fatigue life and loss of toughness when compared with the analogous unaged material was evident (Figure 10.9). The stress responses to strain cycling for the material in both conditions are exhibited in this figure where the peak tensile stress evolution of the stress-strain hysteresis loops is plotted versus the number of

cycles (or cyclic hardening/softening curves). For both conditions, the curves show that the steel cyclically softens after a very short hardening period reaching, for the unaged steel, a stabilization that continues up to failure. Conversely, in the aged steel, in addition to the strong increase of the stress level as a consequence of aging, the initial hardening is much more pronounced and the softening period is interrupted by the sudden break of the sample without achieving the stabilization of the stress. In some of the tests carried out on aged samples at room temperature, the first few cycles are characterized by load sudden drops and audible noises that could be caused by twinning [LLA 96]. The fracture surface of the aged samples has a brittle aspect and is essentially covered with transgranular brittle grain fracture (cleavage fracture).

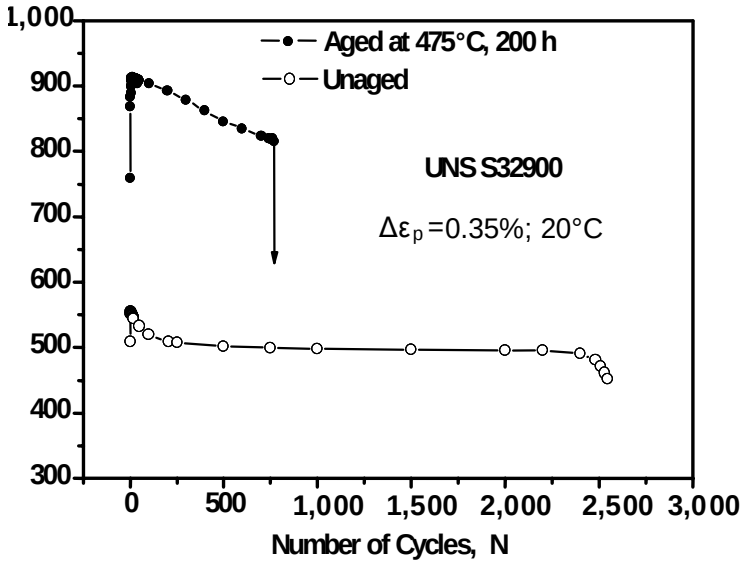

Figure 10.9. *Cyclic hardening/softening behavior comparison between unaged and aged samples cycled at room temperature with the same plastic strain range at half-life.*

The most surprising and interesting fact is the mechanical behavior observed in aged samples fatigued at 500°C [ARM 07]. Figure 10.10 compares cyclic hardening/softening curves of the unaged and aged samples tested at 500°C with a plastic strain range at half-life of 0.3%. For both heat treatment conditions, the steel shows, after a very short cyclic hardening period, cyclic softening that continues up to failure without achieving the stabilization of the stress. From the figure, it is worth noting that the pronounced softening displayed by the aged steel in comparison with the unaged one. This noticeable softening observed in the aged

sample leads to attain tensile peak stresses similar to that in the unaged sample after a few cycles. It should be also noted from Figure 10.10 that the cycling of the aged sample at 500°C is also beneficial in improving the fatigue life in comparison with the unaged sample.

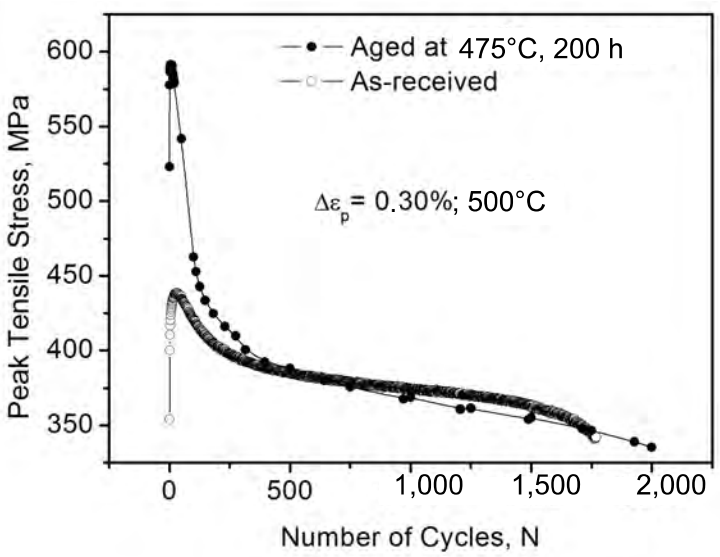

Figure 10.10. *Cyclic hardening/softening behavior comparison between unaged and aged samples cycled at 500°C with the same plastic strain range at half-life*

10.3.2.2. *Microstructural comparison between fatigued aged and unaged specimens*

Concerning the dislocation microstructure in the austenite phase of the aged DSS UNS S32900 tested in fatigue up to fracture at room temperature no remarkable difference was observed in comparison with that in the unaged steel. Incipient cell structure was observed depending on the region observed or the size of the grain. The microstructure observed in the ferrite phase of the aged steel tested at room temperature presents a huge difference with that of the unaged steel. A planar structure of dislocation bands crossing the entire ferritic grains is the more remarkable feature observed on this phase (Figure 10.11a). Park *et al.*, [PAR 86] working on an aged single-phase ferritic Fe-26Cr-1Mo alloy, found a localized dislocation structure in the form of bands similar to those observed here and they proposed that dislocation motion reduces the amplitude of the SD within the bands. Hence, these regions become energetically favorable for subsequent dislocation motion producing regions of localized deformation. Despite the similarity in the dislocation structure found in the single-phase ferritic steel and in the ferritic phase

of the present DSS both in aged states, no evidence of demodulation inside the bands could be confirmed by TEM observations.

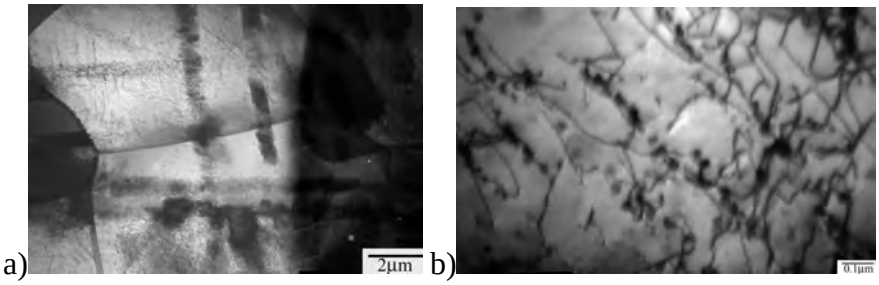

Figure 10.11. *Dislocation structures in ferritic grains of aged UNS S32900 cycled to rupture at (a) room temperature and (b) 500°C*

Ferritic grains of the strain-free regions (the threaded head of the sample) of aged samples cycled at 500°C show that the modulated structure of the SD remains and looks like that depicted in Figure 10.2b. However, from the microstructure observed in the ferritic grains of thin foils taken from the gage length of aged samples cycled at this temperature (Figure 10.11b), it is evident that the mottled appearance of the SD has disappeared and is replaced by a structure containing a low dislocation density and incoherent precipitates decorating the dislocations. On comparing Figures 10.2b and 10.11b, it is evident that the synergy of cycling and temperature has a huge influence on the aged samples.

10.4. UNS S32750 SDSS

10.4.1. *Unaged steel*

10.4.1.1. *Cyclic behavior*

Similar to the results found for type UNS S32900 DSS, [GIR 06] and [ARM 08] also found a pronounced cyclic hardening in unaged samples of SDSS UNS S32750 cycled at intermediate temperatures. The cyclic hardening-softening curves of this steel in the temperature range 20-500°C are shown in Figure 10.12. The flow stress corresponding to the maximal strain of the first tensile loading (cycle 1) strongly decreases from room temperature to 300°C. At 300°C, similar to the results observed in UNS S32900, begins a yield stress stabilization that is nearly the same in the temperature range 300-500°C.

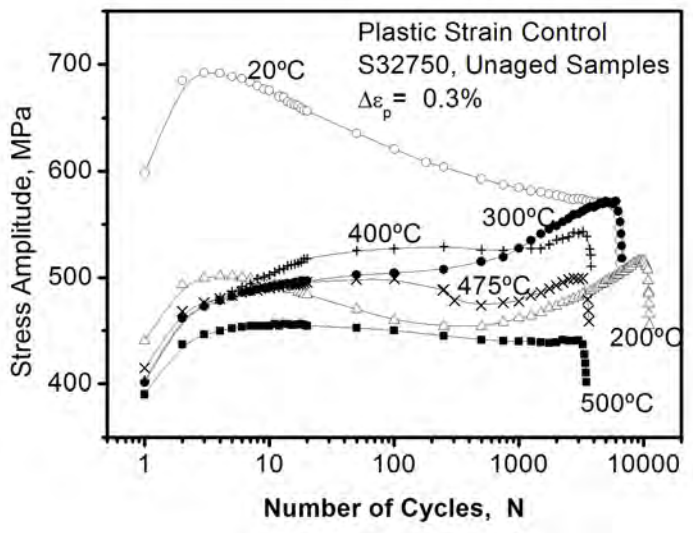

Figure 10.12. *Cyclic softening-hardening curves of as-received UNS S32750 fatigued under plastic strain control*

Considering the curves starting from cycle 2, which is the first cycle after a strain reversion, it is clear from the figure that the cyclic response of the SDSS shows a strong temperature dependence during most of its fatigue life. Similar manifestations of DSA were found in this steel, i.e. a pronounced cyclic hardening and an anomalous dependence of the stress amplitude on the strain rate. Moreover, the maximum effect of the phenomenon occurs in the same temperature range as for DSS type UNS S32900, i.e. 300-400°C. However, comparing Figures 10.4 and 10.12, it is evident that the cyclic hardening rate, a consequence of DSA, is much more pronounced in the steel UNS S32900.

At 300°C, the initial cyclic hardening is more marked and longer than at 200°C and is followed by a short stabilization period. After the stabilization, a linear secondary cyclic hardening takes place that continues up to an almost stable stage with a stress level comparable to that of the room temperature test. The cyclic behavior found at 400°C is similar to that at 300°C, but with a more pronounced initial hardening, a longer stabilization period and a less pronounced linear secondary hardening. At 475 and 500°C, after the initial hardening and stabilization period comparable to that at 300 and 400°C, cyclic softening occurs as observed in UNS S32900 DSS. However, for type UNS S32750 SDSS the softening is again

followed by a cyclic hardening (475°C) or by a saturation period (500°C) that culminates at the rupture of the sample.

10.4.1.2. *Mechanical behavior – microstructural correlation*

The microstructures developed inside the ferritic phase of the unaged SDSS at intermediate temperatures are similar to those observed in the unaged UNS S32900 DSS. At 300°C a high and homogenously distributed dislocation density was observed (Figure 10.13a). This structure is associated with the pronounced cyclic hardening taking place at temperatures between 300 and 400°C. This effect is a typical manifestation of DSA in the ferrite phase. Carbon atoms, originally dissolved in the ferrite matrix because of the factory thermal treatment, would be responsible for DSA phenomena.

An interesting feature is evident in Figure 10.12 at 475°C where the cyclic behavior shows hardening-softening followed by a secondary hardening. Gironés *et al.* [GIR 06] attributed the secondary hardening to the combined effects of DSA and "475°C embrittlement". Unfortunately, they did not explain the softening observed before the secondary hardening.

At 475°C the ferritic microstructure is characterized by lower dislocation density and smaller precipitates dispersed over the matrix (Figure 10.13b), compared with that at 400°C. A recovered dislocation structure with numerous precipitates was found at 500°C (Figure 10.13c). According to these results, at temperatures 475 and 500°C, and because of the combined effects of cycling and temperature, carbon atoms can precipitate at an enhanced rate as carbides. This effect produces an "over-aged" state in the ferrite, which causes a reduction of the stress carried by the material and a consequent softening process. The secondary hardening found at 475°C could be attributed to the DSA phenomenon that occurs in the austenite phase at high temperatures [ARM 88].

Moreover, at these two temperatures clear evidence of SD was observed in both unstrained (threaded head of the sample) and strained (gage length) parts of the specimens. Regarding the austenitic phase, the microstructure observed in the unaged SDSS steel cycled at all temperatures, consistent with the observations of other authors [GIR 86], has a planar slip character with mainly two active slip systems (Figure 10.13d). The ill-developed cell structure frequently observed in the austenite of type UNS S32900 DSS was not observed in the SDSS. This difference in microstructure is attributed to the higher amount in nitrogen content in type UNS S32750 SDSS. Planar slip character is mainly characteristic of high nitrogen austenitic steels [DEG 88, TAI 88].

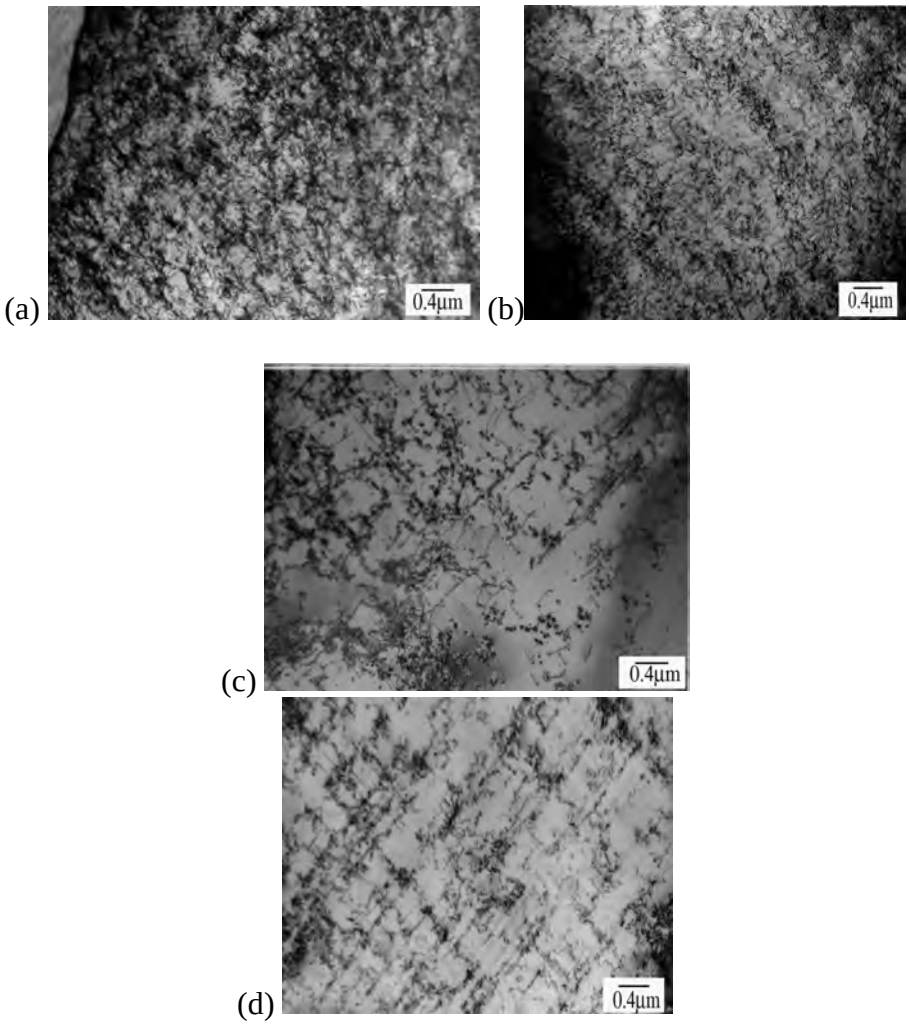

Figures 10.13. *Ferritic grains in unaged samples cycled up to failure at a) 300ºC, b) 475ºC, and c) 500ºC. d) Austenitic grain cycled up to failure at 300ºC*

10.4.2. *Aged SDSS*

The detrimental effect of the "475°C embrittlement" on LCF type UNS S32900 DSS was described in Section 10.3.2 of this chapter. A pronounced difference in fatigue life was exhibited at room temperature when compared with the unaged material. SDSS type UNS S32750 contains a higher volume fraction of austenite

phase, because of a higher concentration of nickel and, principally, the deliberate addition of nitrogen. This section reports the differences observed in this aged steel when compared with the aged first-generation DSS.

10.4.2.1. *Cyclic behavior*

The cyclic response of aged UNS S32750 shown in Figure 10.14 is quite different from that of unaged specimens of this steel (Figure 10.12).

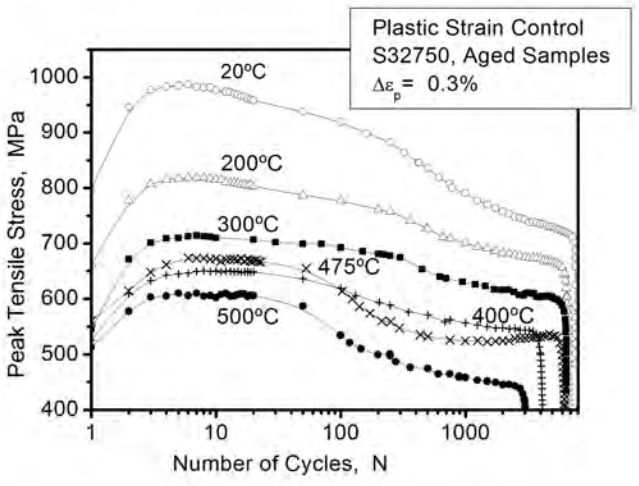

Figure 10.14. *Cyclic hardening-softening curves of aged UNS S32750 SDSS*

The cyclic hardening-softening curves obtained at 20, 200, 300, 400, 475 and 500°C with a constant plastic strain range of 0.3% and a total strain rate of approximately 2×10^{-3} s^{-1}, all exhibit an almost similar cyclic behavior independent of temperature. Compared with unaged steel, not only are higher stress amplitudes observed, but, also, very strong hardening rates (at room temperature, the stress amplitude increases in 200 MPa in the first five cycles). This initial short cyclic hardening was followed by a softening stage until failure that was independent of temperature. Only at 475°C does the cyclic softening stage turn into a slight hardening stage. This secondary stage, similar to that observed in unaged samples at this temperature, could not be attributed to an increase of modulated phases due to SD promoted by cycling. In fact, according to several authors, cycling of spinodal decomposed alloys contributes to a demodulation of the decomposed phases and not vice versa [PAR 86, LLA 96]. At this temperature, it could be expected that DSA phenomena occurring in the austenite phase will contribute to the observed cyclic hardening.

10.4.2.2. *Mechanical behavior – microstructural correlation*

In aged samples of SDSS tested in fatigue up to rupture, the characteristic dislocation structures in the austenite remains similar to that observed in unaged samples, i.e. planar arrangements of dislocations can be observed within the studied temperature range (compare Figures 10.13d and 10.15). This result means that the plastic activity within the austenite phase is almost independent of the extra hardness exhibited by the ferrite phase due to the SD. The steel behaves like a fiber composite material with the fibers aligned with the loading axis (see Figure 10.1b). It could be assumed that the different phases carry, at least in the interior of the grains, an equal amount of deformation. Thus, to a first approximation, the plastic activity in one phase is independent of the other. Microstructural observations of the austenite phase confirm this assumption. In all the cases, the austenite dislocation structure supports the conclusion that this phase plays only a secondary role in controlling the mechanical behavior of the steel.

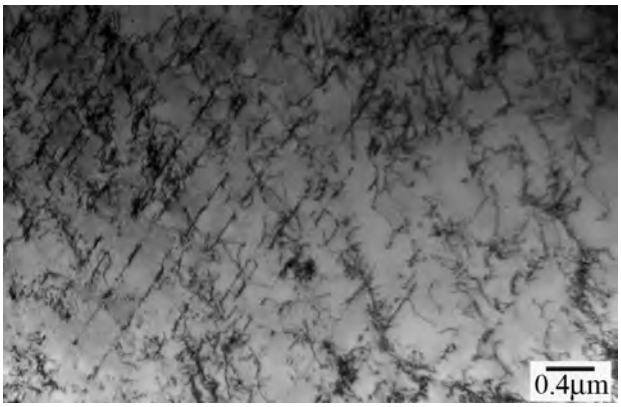

Figure 10.15. *Austenite grain of an UNS S32750 aged sample cycled at room temperature*

In order to analyze the influence of cycling on spinodal decomposed ferrite grains, thin foils were taken from the threaded head of the specimen (region without deformation) and compared using TEM with those taken from the gage length (deformed region). UNS S32900 DSS micrographs obtained from deformed regions of aged samples fatigued at temperatures up to 500°C show that the “orange peel” appearance of the SD remains in the ferritic grains. No evidence of partial or complete demodulation as a consequence of cycling (such as was proposed by [PAR 86, LLA 96]) could be confirmed by TEM observations on this steel. As a result of the low plastic activity, as a consequence of the SD, a very low dislocation density characterizes the dislocation structure in the ferrite phase of aged samples. The characteristic dislocation structure observed in this phase at each temperature,

similar to that observed in aged UNS S32900 DSS fatigued at room temperature (Figure 10.11a), is a band structure localized mainly on the {110} planes with the most favorable Schmid factors. The orientation of the bands structure with respect to the tensile axis was determined by trace analysis. In order to analyze the evolution of this bands structure during cycling, an interrupted test has been carried out at room temperature at the maximum hardening stage (10 cycles) to compare with the microstructure at rupture. Figure 10.16a shows the progressive building of random arrangements of linear dislocations and the incipient band formation. This almost homogenous distribution of dislocations could be the cause of the initial hardening in the ferrite phase. Figure 10.16b shows the dislocation structure observed in an aged ferrite grain fatigued at room temperature up to rupture. More developed and densely clustered dislocation bands were found to be the characteristic feature. The channels between the bands, with lower dislocation density when compared with Fig. 10.16a, present the modulated contrast of the SD. The substructural scenario within aged ferrite grains cycled at 300°C is very close to that described for room temperature (Figure 10.16c). On comparing Figures 10.13a and 10.16c, it is interesting to note the difference between the wavy slip mechanism in Figure 10.13a and the planar slip in the spinodal decomposed ferrite of Figure 10.16c. From these figures, it can be concluded that the SD reduces the possible slip systems in the BCC structure.

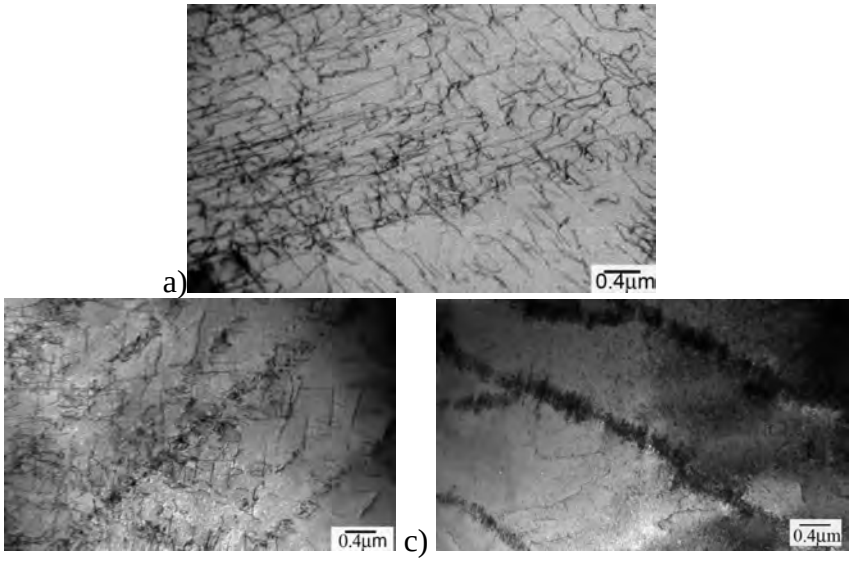

Figure 10.16. *Ferritic phase of aged samples of UNS S32750 cycled at room temperature after a) 10 cycles b) to failure. c) Ferritic grain cycled to rupture at 300°C*

The evolution from a structure of homogenous distribution of planar dislocations arrangements to localized dislocation bands with a lower dislocation density between bands in the hardened ferritic phase appears to be responsible for the softening observed at all temperatures. Park *et al.* [PAR 86] suggested that the stress increment due to SD is essentially temperature independent. Considering that a similar softening trend is observed in aged S32750 SDSS (Figure 10.14) over the entire temperature range, this work suggests that the softening mechanism produced by irreversible dislocation motion also seems to be athermal. It is interesting to note that no evidence of cyclic hardening due to DSA in the ferrite phase was found in the aged SDSS samples. The secondary hardening observed in aged samples cycled at 475°C can be related to the operation of DSA in the austenite phase according to [ARM 88]. At 500°C the presence of numerous precipitates inside and between the bands, provides evidence of an "over-aged" structure, which makes the movement of dislocations easier (Figure 10.17).

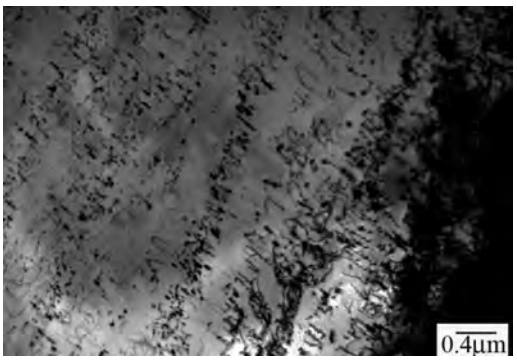

Figure 10.17. *Dislocation structure in a ferritic grain of aged sample of SDSS tested in fatigue up to rupture at 500°C*

10.4.2.3. *Analysis of the cyclic stress components*

A useful way to identify the physical mechanisms responsible for hardening or softening during cycling consists of studying the flow stress components derived from the hysteresis loops using the method originally proposed by Cottrell [COT 53] (see Chapter 6). It is assumed that the flow stress to produce plastic deformation during cyclic tests is composed of two contributions. One is a thermal component called "friction stress", σ_f, caused by short-range obstacles to dislocation slip and the other is called "back stress", σ_b, which is almost independent of the temperature and originated from long-range barriers, such as dislocation configurations, precipitates, and grain boundaries, too strong to be overcome with the thermal activation contribution. The applied stress is thus the sum of the friction stress and the back

stress. Information on the types of obstacles to dislocation movement can be obtained from the measurement of these stresses.

In this section, we analyze friction and back stresses for cyclic tests performed on unaged and aged samples of SDSS at 300°C. At this temperature, a pronounced cyclic hardening is observed in unaged samples (Figure 10.12), which is the typical manifestation of DSA. However, aged samples cycled at this temperature soften up to failure after a pronounced hardening of only few cycles of duration (Figure 10.14).

Figure 10.18 shows that, at 300°C, no remarkable changes in σ_f were observed during cycling. At this temperature, short-range obstacles such as solute atoms, like nitrogen or carbon atoms, have enough mobility not to be an obsticle for moving dislocatons. On the contrary, the cyclic behavior of the back stress is completely different for unaged and aged conditions. It is clear that it plays a more important role on the evolution of cyclic stress during cycling. Unaged samples show an increase of the back stress, which is correlated with the image of dense dislocation structures observed in Figure 10.13a inside the ferrite grains. Evidently, at this temperature and this strain rate, interstitial solute atoms, such as carbon or nitrogen, can interact with moving dislocations, slowing them down. This effect will produce an increase in the dislocation density.

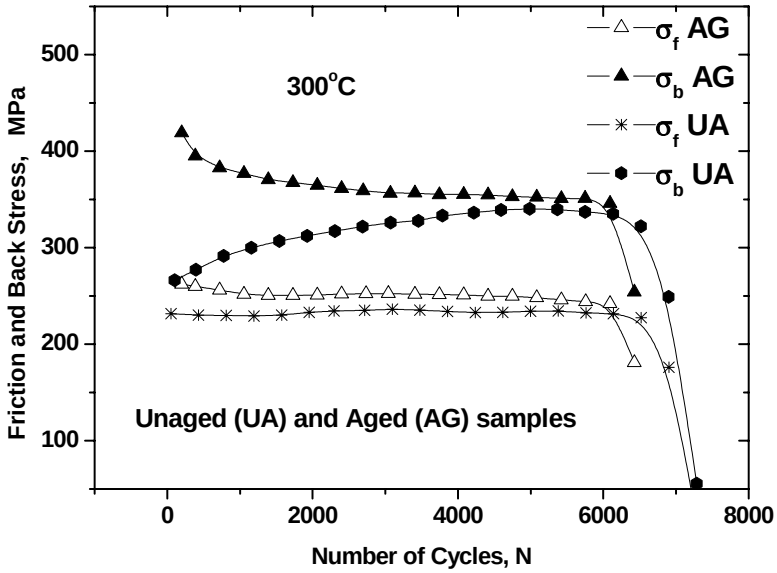

Figure 10.18. *Friction and back stresses of unaged and aged samples of DSS UNS S32750 cyclic tested at 300°C*

Aged samples exhibit a hardened ferritic phase. The evolution from an initial homogenous dislocation distribution, product of the initial pronounced hardening, to a microstructure of localized dislocation bands and almost dislocation-free channels between bands, as observed in Fig 10.16c, appears to be responsible for the decrease of σ_b.

10.5. Temperature influence on the fatigue life

Recently, Armas *et al.* [ARM 07] showed that aged samples of S32900 DSS fatigued at room temperature exhibit a pronounced difference in fatigue life and loss of toughness compared with the analogous unaged material. An initial cyclic hardening period that is more pronounced for the aged steel was accompanied by load drops and audible noises during each cycle. This initial hardening period was followed by a softening stage that ended in a catastrophic failure, which occurred much earlier than for the unaged material. However, the most surprising and interesting fact is the absence of any deleterious effect of "475°C embrittlement" on aged samples of the UNS S32750 SDSS cycled at room temperature (Figure 10.19).

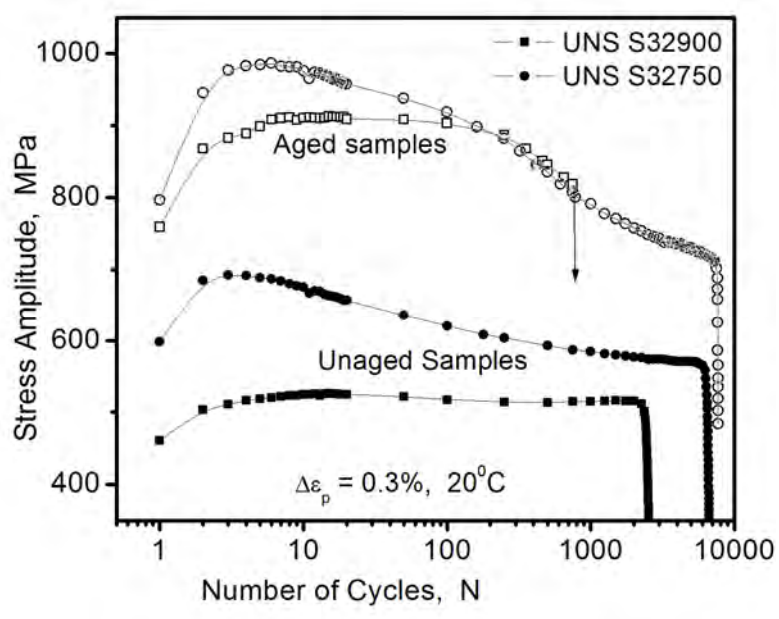

Figure 10.19. *Cyclic hardening/softening behaviour comparison between aged and unaged samples for DSS and SDSS fatigued at room temperature*

One of the objectives of this chapter is to clarify the influence of the temperature on the fatigue life of type UNS S32750 SDSS under both thermal conditions, unaged and 475°C-aged. The effects of testing temperature on the LCF life of this steel under both conditions are visualized in Figures 10.20 and 10.21. For comparison, the Coffin-Manson curve obtained for unaged S32750 SDSS at room temperature is plotted in both figures. At certain temperatures, some tests were carried out with different plastic strain ranges and are also included in the figures. DSA effects do not appear to appreciably affect the fatigue life of unaged samples. Between 400 and 500°C, a shortening of the fatigue life can be appreciated but that could be attributed to high temperature effects [POL 91].

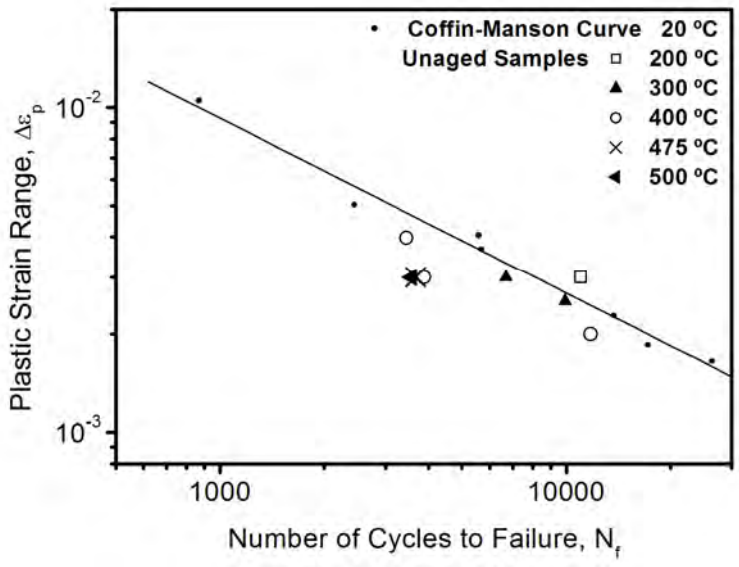

Figure 10.20. *Coffin-Manson curve of unaged UNS S32750 SDSS*

Conversely, aged samples cycled at temperatures up to 500°C did not show any remarkable shortening in their life that could not be also attributed to high temperature effects. It is worth noting in Figure 10.21 that tests performed on aged samples at room temperature with two different plastic strain ranges fit well with the Coffin-Manson curve for unaged samples. As previously mentioned, this behavior is completely different to that observed in a S32900 DSS (Figure 10.19) where a pronounced shortening of the number of cycles to failure occurred when comparing aged with unaged samples.

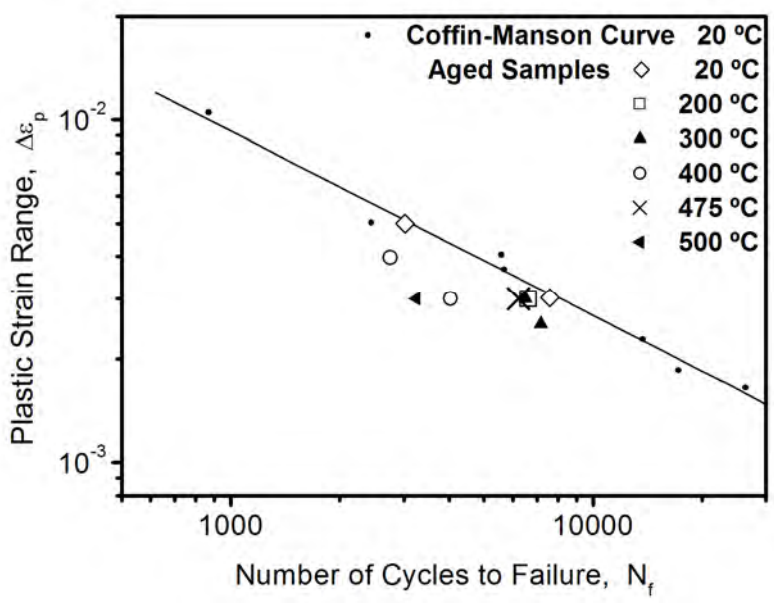

Figure 10.21. *Coffin-Manson curve of aged UNS S32750 SDSS*

10.6. Final remarks

DSS are materials that are not extensively used at intermediate temperatures, due the existence of the ferrite phase. In this chapter, it was shown that the "475°C embrittlement" of the ferrite phase produces the strengthening of the steel but also an important reduction in the fatigue life of the UNS S32900 DSS compared with the unaged material. However, the third-generation UNS S32750 SDSS does not show any important deleterious effect on its cyclic behavior at temperatures up to 500°C. Due to their chemical composition, principally nitrogen, the main differences between both steels is the volume fraction of phases (50%α/50%γ for UNS S32750 and 72%α/28%γ for UNS S32900). This difference in volume fraction promotes remarkable contrast between the cyclic mechanical behaviors of these steels. In the considered temperature range, the ferrite phase presents the most notable changes in dislocations structure, when it is cyclically loaded. In the temperature range 400-500°C, the austenite exhibits DSA manifestations near 500°C. Conversely, the ferrite presents DSA manifestations between 300 and 400°C with a pronounced cyclic hardening rate. Comparing the cyclic hardening rates of both unaged steels (Figures 10.4 and 10.12) the influence of the ferrite volume fraction is evident, giving a much more pronounced cyclic hardening rate for type UNS S32900 steel.

This difference in volume fractions of both phases also seems to be partially responsible for the difference in terms of the influence of the SD on the fatigue life of aged samples. The higher amount of austenite phase plays an important role on fatigue resistance. Although Figure 10.14 gives evidence of a pronounced cyclic softening at all temperatures in aged samples, it could not be confirmed experimentally that this softening is a consequence of a partial demodulation of the SD in the ferrite – by TEM or microhardness measurements. Only the evolution from a homogenous dislocation distribution to a structure of localized dislocation bands seems to promote the cyclic softening observed.

10.7. Acknowledgments

This work was supported by the Agencia Nacional para la Promoción de la Ciencia y la Técnica (ANPCYT), the Consejo Nacional de Investigaciones Científicas y Técnicas (CONICET) of Argentina and the Cooperation Program ECOS-Sud/MINCyT between France and Argentina (Code A06E01). I would like to thank Dr Silvina Hereñú for the TEM analysis and Mr Fernando Ugo for performing the mechanical tests.

10.8. References

[ALV 03] ALVAREZ-ARMAS I., ARMAS A.F., HEREÑÚ S., DEGALLAIX S. and DEGALLAIX G., "Correlation between cyclic deformation behaviour and microstructure in a Duplex Steel between 300 and 773K". *Fatigue Fract. Engng. Mater. Struct.*, vol. 26, p. 27-35, 2003.

[ARM 88] ARMAS A.F., BETTIN O.R., ALVAREZ-ARMAS I., RUBIOLO G.H., "Strain aging effects on the cyclic behaviour of austenitic stainless steels", *J. Nucl. Mater.*, vols. 155-157, p. 644-649, 1988.

[ARM 97] ARMAS A.F., ALVAREZ-ARMAS I, AVALOS M., PETERSEN C. and SCHMITT R., "High temperature cyclic stress-strain response of structural stainless steels for thermonuclear fusion reactors" in C. VARANDAS and F. SERRA (eds.), *Fusion Technology 1996*, Elsevier Science B.V., p. 1359, 1997.

[ARM 07] ARMAS A.F., DEGALLAIX S., DEGALLAIX G., HEREÑÚ S., MARINELLI M.C. and ALVAREZ-ARMAS I., "Beneficial effects induced by high temperature cycling in aged duplex stainless steel", *Key Eng. Mat.*, vols. 345-46, p. 339-342, 2007.

[ARM 08] ARMAS A.F., HEREÑÚ S., ALVAREZ-ARMAS I., DEGALLAIX S., CONDÓ A. and LOVEY F., "The influence of temperature on the cyclic behavior of aged and unaged super duplex stainless steels", *Mater. Sci. and Eng. A*, vol. 491, p. 434-439, 2008.

[CHA 71] CHANDRA D., SCHWARTZ L.H.; "Mössbauer effect study of the 475 °C decomposition of Fe-Cr", *Metall. Trans.*, vol. 2, p. 511-519, 1971.

[COF 65] COFFIN, L.F. Jr., "The effect of quench aging and cyclic-strain aging on low carbon steel", *Trans. ASME, J. Basic Eng.*, vol. 87D, p. 351-362, 1965.

[COT 53] COTTRELL A.H., *Dislocations and Plastic Flow in Crystals*, Oxford University Press, London, p. 111, 1953.

[CRA 83] CRAIG, B. D., "Evaluation and application of highly alloyed materials for corrosive oil", *Proceedings of the 1st International Conference on Duplex Stainless Steels*, p. 293, ASM, St Louis, 1982.

[DEG 88] DEGALLAIX S., DICKSON J.L., FOCT D.J., "Effects of nitrogen on fatigue and creep-fatigue behavior of austenitic stainless steels", in J. FOCT and A. HENDRY (eds.), *Proceedings of the High Nitrogen Steel Conference (HNS-88), – HNS88*, The Institute of Metals and the Société Française de Métallurgie, Lille, France, p. 380, 1988.

[ELM 82] ELMER J. W., OLSON D. L., MATLOCK D. K., "The thermal expansion characteristics of stainless steel weld metal", *Welding Research*, Suppl., p. 293s, 1982.

[GIR 06] GIRONÉS A., LLANES L., ANGLADA M., MATEO A., "Cyclic deformation of superduplex stainless steels at intermediate temperature", *Metall. Mater. Trans.*, vol. 37A, p. 3519-3530, 2006.

[GRO 73] GROBNER P.J., "The 885 °F (475 °C) embrittlement of ferritic stainless steels", *Metall. Trans.*, vol. 4, p. 251-20, 1973.

[HER 01] HEREÑÚ S., ALVAREZ-ARMAS I., ARMAS A.F., "The influence of dynamic strain aging on the low cycle fatigue of duplex stainless steels", *Scripta Mater.*, vol. 45, p. 739-745, 2001.

[KAT 81] KATO M., "Hardening by spinodally modulated structure in b.c.c. alloys", *Acta Metall.*, vol. 29, p.79-87, 1981.

[LES 81] LESLIE, W. C., *The Physical Metallurgy of Steel*, McGraw-Hill Hemisphere Publ. Corp., Washington, 1981.

[LLA 96] LLANES L., MATEO A., ITURGOYEN L., ANGLADA M., "Aging effects on the cyclic deformation mechanisms of a Duplex Stainless Steel", *Acta Mater.*, vol. 44, p. 3967-978, 1996.

[MAR 96] MARROW, T. J., "The fracture mechanism in 475°C embrittled ferritic stainless steels", *Fatigue Fract. Engng. Mater. Struct.*, vol. 19, p. 919-933, 1996 .

[MIL 87] MILLER M.K., "Morphology of low temperature phase transformations in the iron chromium system", in G.W. LORIMER (ed.), *Phase Transformations*, Institute of Metals, London, p. 39-43, 1987.

[MUG 97] MUGHRABI H., CHRIST H-J, "Cyclic deformation and fatigue of selected ferritic and austenitic steels: specific aspects", *ISIJ International*, vol. 37, p. 1154-1169, 1997.

[NIC 80] NICHOL T. J, DATTA A and AAGEN, G, "Embrittlement of ferritic stainless steels", *Metallurgical and Materials Transactions A*, vol. 11, p. 574-585, 1980.

[PAR 86] PARK K. –H., LA SALLE J.C., SCHWARTZ L.H., "Mechanical properties of spinodally decomposed Fe 30 wt% Cr alloys: yield strength and aging embrittlement", *Acta Metall.*, vol. 34, p. 1853-1865, 1986.

[PET 98] PETERSMEIER T.H., U. MARTIN U., D. EIFFER and OETTEL D.H., "Cyclic fatigue loading and characterization of dislocation evolution in the ferritic steel X22CrMoV121", *Int. J. Fatigue*, vol. 20, p. 51-255, 1998.

[PIC 84] PICKERING, F.B., "Physical metallurgical development of stainless steels", *Proc. of Conf. on Stainless Steel '84*, paper 2, p. 2, 1984.

[POL 91] POLAK J., *Cyclic Plasticity and Low Cycle Fatigue Life of Metals*, Academia, Prague and Elsevier, Amsterdam, 1991.

[PUM 90] PUMPHREY P.H. and AKHURST K.N.; "Aging kinetics of CF3 cast stainless steel in temperature range 300 - 400°C", *Mater. Sci. Technol*., vol. 6, p. 211–219, 1990.

[RAO 86] RAO K.B.S., VALSAN M., SANDHYA R., MANNAN S.L., RODRIGUEZ P., "Dynamic strain ageing effects in low cycle fatigue", *High Temperature Materials and Processes*, vol. 7, p. 171, 1986.

[SOL 83] SOLOMON H.D., DEVINE Jr T.D., "Duplex stainless steels – a tale of two phases", in R.A. LULA (ed.), *Proc. Conf. on Duplex Stainless Steels*, ASM, Metals Park, OH, p. 693-756, 1983.

[SRI 97] SRINIVASAN V. S., SANDHYA R., VALSAN M., BHANU SANKARA RAO K., MANNAN S. and SASTRY D. H., "The influence of dynamic strain ageing on stress response and strain-life relationship in low cycle fatigue of 316L(N) stainless steel", *Scripta Mater*., vol. 37, p. 1593-1598, 1997.

[STR 86] STREET, J. "Welding duplex stainless steel for arduous service", *Metal Construction, The Welding Institute Journal*, Cambridge, vol. 18, p. 565-569, 1986.

[TAI 88] TAILLARD R., FOCT J., "Mechanisms of the action of nitrogen interstitials upon low cycle behavior fatigue of 316 stainless steels", in J. FOCT and A. HENDRY (eds.), *Proceedings of the International Conference "High Nitrogen Steels – HNS88"*, The Institute of Metals and the Société Française de Métallurgie, Lille, France, p. 387-391, 1988.

[TSU 83] TSUZAKI K., HORI T., MAKI T., TAMURA I., "Dynamic strain ageing during fatigue deformation in Type 304 Austenitic Stainless Steel", *Mater. Sci. Eng. A*, vol. 61, p. 247-260, 1983.

[VOG 02] VOGT J.-B., MASSOL K., FOCT J., "Role of the microstructure on fatigue properties of 475°C aged duplex stainless steels", *Int. J. Fatigue*, vol. 24, p. 627-633, 2002.

[WEN 04] WENG K.L., CHEN H.R., YANG J.R., "The low-temperature aging embrittlement in a 2205 duplex stainless steel", *Mater. Sci. Eng.* A, vol. 379, p. 119-132, 2004.

[ZAU 93] ZAUTER R., PETRY F., CHRIST H-J., MUGHRABI H., "Thermomechanical fatigue behavior of materials", *ASTM STP*, vol. 1186, p. 70-90, 1993.

Chapter 11

Industrial Processing and Fatigue Response of DSSs

11.1. Introduction

Within the stainless steel world, duplex stainless steels (DSSs) have a low production volume percentage due to their high price and competition with higher-alloyed austenitic stainless steels in terms of mechanical properties and corrosion resistance. However, due to the outstanding combination of mechanical properties and chemical resistance, DSSs have conquered very important niches of today's industrial world. As a result, DSSs are used in the offshore and pulp and paper industries, in desalination plants, flue-gas cleaning, cargo tanks and pipe systems in chemical tankers, sea water systems, firewalls and blast walls on offshore platforms, bridges, components for structural design, storage tanks, pressure vessels, heat exchangers, water heaters, rotors, impellers, and shafts.

In order to fulfill all the requirements of all application fields, there are several industrial processing routes for DSSs. Industrially DSSs are mostly centrifugally cast into slabs, billets, or straight into complex parts, such as connecting joints for pipes, which are used, for example, in the off-shore industry. Slabs are rolled into flat-sheet products and billets, which are cast long products, both are usually further processed in the rolling mill (per-fell rolling) or by forging resulting in round bars, flat bars, angle plates, spring steels, wire rods, and D-bars.

Chapter written by Nuri AKDUT.

Duplex Stainless Steels Edited by Iris Alvarez-Armas and Suzanne Degallaix-Moreuil

Each processing route (casting, rolling, annealing, and forging) leaves its distinctive marks on the morphological and crystallographic texture, i.e. the microstructural and mechanical characteristics of the manufactured product. The morphology, i.e. the grain size, phase size, and phase volume fraction distribution, can elucidate the metallurgical aspects, such as strength, toughness, and corrosion and fatigue resistance. The crystallographic texture (orientation distribution function of all grains of each phase) is an exceptionally good tool to trace solid-state alterations of materials, even if they are not visible using the microscope. This multitude of parameters unavoidably complicates the comparison of data reported by different researchers in the past [MAG 88, DEG 93, VOG 95, MAT 96].

When talking about DSSs we have to recognize that there are two decisive influencing parameters on the (fatigue) properties of DSSs: the processing history and the chemical composition. The pseudo-binary Fe-Cr-Ni diagram (Figure 11.1) shows that austenite phase formation for the chemical composition of DSS 1.4462 starts at approximately 1,250°C. At 1,050°C, the austenite volume fraction reaches 50%. At this temperature DSS 1.4462 is usually quenched and solution annealing treated.

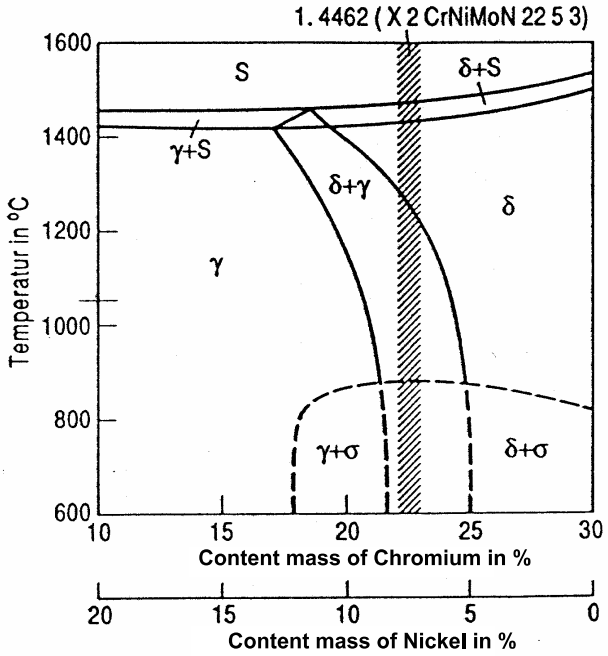

Figure 11.1. *Pseudo-binary cut through the ternary Fe-Cr-Ni system at 70% Fe [FOR 92]*

Magnin *et al.* [MAG 88] first detected the change of slope of the cyclic stress strain curves (CSSC) and Coffin-Manson curves of DSSs. They stated that "at high plastic strain amplitudes ($\Delta\varepsilon_p / 2 > 10^{-3}$) the behavior of the duplex alloy seems to approach that of the ferritic alloy and at low plastic strain amplitudes ($\Delta\varepsilon_p /2 < 10^{-3}$) that of the austenite alloys" (see Chapter 6, Figure 6.9a).

However, from this figure, the ferritic-like behavior of the α/γ duplex alloy at higher plastic strain amplitudes is not evident as the Coffin-Manson curves of both single-phase alloys approach each other. In this context, the unusually steep slope (≈ -1.5) of the ferritic alloy is striking considering that most ductile metals have slopes in the range of –0.4 to –0.7.

Unfortunately, Magnin *et al.* did not explain this behavior. However, from the tensile tests on DSSs, it can clearly be deduced that DSSs behave more like a ferritic stainless steel than an austenitic one meaning that a high yield strength and a relatively small elongation to fracture are typical. This chapter will address some of the standard DSS grades available on the European market, which produces most of the worldwide produced DSSs.

While considerable progress has been made (see Chapter 6) in the understanding of the fatigue behavior of low (0.07%) nitrogen-alloyed DSSs, there is still uncertainty as to the fatigue performance of DSSs with medium (0.11 to 0.18%) nitrogen contents and even a lack of knowledge of high nitrogen content (up to above 1%) on the fatigue performance of DSSs. This is by no means only of academic interest, as nowadays, the alloying element nitrogen is inseparably connected to (modern) DSSs (as well as austenitic stainless steels). Similarly, data on low- or no-Ni containing DSSs are not published so far.

Therefore, the aim of this chapter is to summarize the basics of the industrial production of DSSs and its effect on the morphological texture properties and the obtained fatigue resistances. In the following, it will be shown that the morphological texture resulting from the various possible processing routes compared with the chemical composition in terms of, for example, the nitrogen-content is mostly underestimated. However, as nitrogen is a very important interstitially alloying element in DSSs, as well as in (the newer Ni-free) austenitic and duplex stainless steels, an important subsection of this chapter (section 11.4) will deal with the effects of the interstitial alloying element nitrogen.

11.2. Morphological aspects

In single-phase materials, the only two morphological variables in the microstructure are the grain size and the grain shape. Thus, in a more complex

microstructure containing more than one phase, there are other variables to consider, especially the phase volume fractions and phase boundaries.

Worldwide, the so-called flat carbon steel (FCS) producers reacted with a variety of steel grades to the need and demand of the (automotive) market, e.g. dual-phase (DP), TRIP (transformation-induced plasticity), TWIP (twinning-induced plasticity) and complex-phase (CP) steels. A possible variety of stainless steels could be the so-called "TRIPLEX" steels, such as Fe-26Mn-11Al-1C [FRO 08]. To conquer a part of the huge FCS market, the worldwide stainless steel sector reacted and is actively working on developing a stainless steel grade that is cost challenging to the FCS sector. Irrespective of whether there will be a FCS or stainless steel version of an extremely low-cost austenitic steel, we have to consider the challenges the new product will have to face, e.g. automotive or the so-called white goods market.

In DSSs, we have to consider additional microstructural parameters, such as the volume fractions of the constituent phases, i.e. which phase is the matrix phase and which is the second phase. In addition, the following questions arise:

– are the phases aligned in a certain direction in relation to the initial (industrial) rolling direction or are they random, i.e. statistically distributed?

– does the microstructure look the same in the macroscopic rolling (RD), normal (ND) and transverse direction (TD)?

– is it possible that a DSS behaves isotropic macroscopically and is anisotropic microscopically?

– what effects could a morphologically larger (or finer) grain structure have on the fatigue resistance?

The answers to the above questions will be given hereafter.

Figure 11.2 shows the DSS grade, EN 1.4462, after different classical industrial processing steps, namely, in:

– the centrifugally cast state (Figure 11.2a),

– the forged state (Figure 11.2b),

– the cold-rolled sheet state (Figure 11.2c and d).

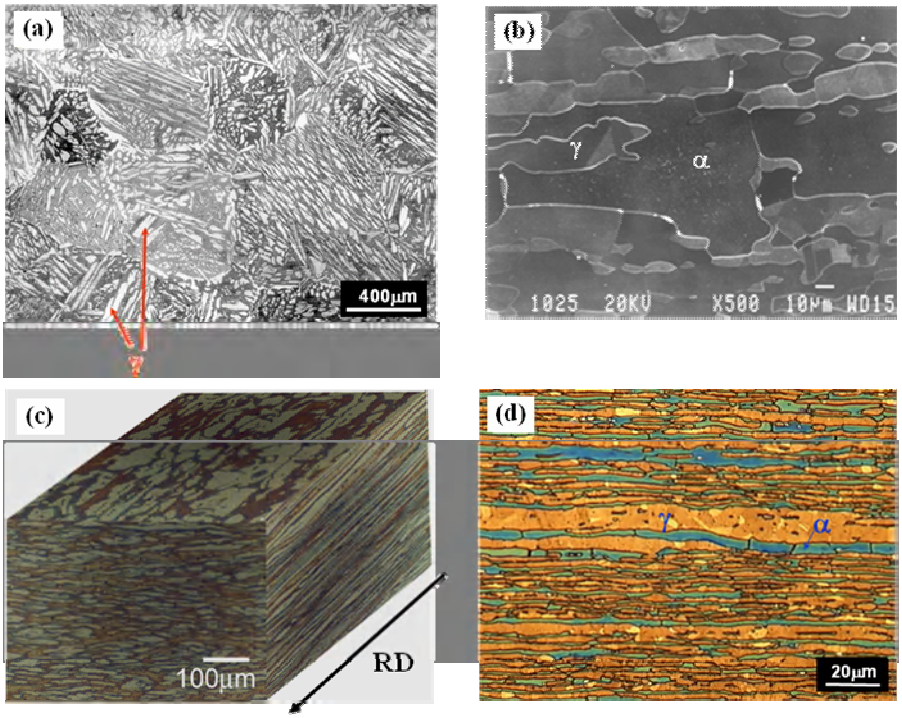

Figure 11.2. *DSS 1.4462 (2205): centrifugally cast structure a), longitudinal section (→RD) of an industrially forged round bar (longitudinal section of the bar; → forging direction FD) b), three-dimensional industrial cold-rolled structure c), longitudinal section (→RD) of an industrially cold-rolled and annealed DSS sheet d)*

When comparing the aforementioned three industrial production states, we have to realize and consider that the 2205 DSS is delivered in those three different microscopically and morphologically states according to the customers' wishes. However, note that the delivery state, i.e. their morphological texture also determines, among other properties, their fatigue response.

In former scientific publications [MAG 88, DEG 93, VOG 94, MAT 96], the fatigue resistance of DSS was often compared without mentioning the actual industrial or laboratory history of the DSS in question. This "history" is a key factor to understanding the behavior of DSSs.

The fundamental morphological issue is presented in Figure 11.2. The cast DSS structure (Figure 11.2a), which is often used, for example, in pipe nodes in the offshore industry, exhibits an overall macroscopically isotropic microstructure.

However, we can clearly see that each huge ferritic grain contains strongly "aligned" secondary austenitic grains, which are strongly anisotropic. Due to the chemical composition and thermomechanical treatment of DSS 1.4462, austenite is the second phase to precipitate and grow within the ferritic matrix grains. Compared with the cold-rolled and forged structures, the cast structure exhibits a clearly larger scale (see Figure 11.2).

After hot forging (or even cold forging, which also generates a not insignificant amount of heat) the microstructure looks again different. Here, the ferritic matrix phase is prone to dynamic recovery due to its high stacking fault energy (SFE), whereas the second austenitic phase tends to recrystallize dynamically. Both microscopical aspects are visible in Figure 11.2b.

In standard DSSs, ferrite constitutes the matrix phase (Figure 11.1) in which both phases, ferritic and austenitic, interpenetrate and are elongated in the rolling direction and, of course, the ferritic and austenitic "phase height" in the normal direction (ND) has been clearly reduced after (industrial) cold rolling (Figures 11.2c–d).

11.3. The role of morphological texture on the fatigue response

11.3.1. *The role of the fatigue axis direction*

It is obvious that the morphological texture of DSSs is a very important parameter regarding their fatigue lives. Perdriset *et al.* [PER 95] showed that in low-cycle fatigue, longitudinally oriented industrial cold-rolled samples have a 50% longer fatigue life than transversely oriented samples. The results in Figure 11.3 underline these findings.

This might be understood in terms of phase size perpendicular to the fatigue axis, in the following referred to as "morphological scale". Due to the different crystal structures of both phases, phase boundaries are obstacles for crack propagation. Thus, the smaller the morphological scale, the higher the phase boundary density and the longer the fatigue lives, i.e. delaying the structural failure.

Considering that ductile alloys are better for high cyclic strain applications than strong alloys, these are superior in low-strain applications. We might ask if it is possible to understand this behavior in terms of the higher ductility in the longitudinal direction rather than in the transverse direction. Unfortunately, there is no data available about the tensile and the Coffin-Manson curve of the DSS studied by Perdriset *et al.* [PER 95].

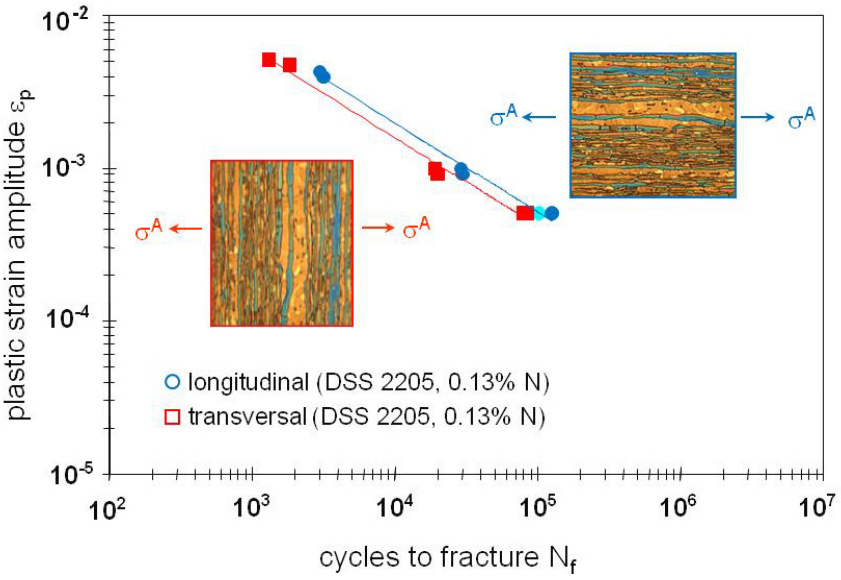

Figure 11.3. *For a given industrially cold-rolled and annealed DSS, the fatigue life is morphologically fatigue axis-direction dependant. Graphs reproduced after [PER 95]*

11.3.2. *The role of the morphological texture and scale*

To demonstrate the role of the morphological texture and scale on the fatigue lives of DSSs, the centrifugally cast structure (see Figure 11.2a) and industrial cold-rolled and annealed structures will be compared. The chemical compositions of both DSSs are listed in Table 11.1.

Element	Cast DSS (type 2205)	Bö A905
Cr	22.0	25.3
Ni	5.5	3.7
Mo	3.0	2.06
Mn	2.0	5.8
N	**0.15**	**0.35**
Cu	-	-
Si	1.0	0.2
Co	-	-
S	-	0.004
P	-	0.023
C	0.03	0.023

Table 11.1. *Chemical compositions in mass percent of the DSSs investigated [AKD 99]*

For a clear understanding on how the phase size, i.e. the morphological scale, affects the fatigue response of DSSs, it is important to have exactly the same chemical composition. The DSS Bö A905 was delivered as a standard, fine-grained (FG), cold-rolled and annealed material (Bö A905FG) comparable to Figure 11.2c and 11.2d and, after an additional heat treatment, a five-times coarser-grained (CG) version has been obtained (Bö A905CG). It is essential to note that no precipitates formed during the annealing treatment and that the chemical composition was truly identical. This latter point is of paramount importance to enable accurate conclusions to be drawn after testing.

According to Figure 11.4, the fatigue life increases with increasing morphological anisotropy and decreasing morphological scale. Although for all plastic strain amplitudes the morphologically isotropic coarse-grained cast DSS exhibits the shortest fatigue life, the morphologically anisotropic fine-grained DSS, A905FG, has the longest fatigue life. In the coarse-grained cast steel, low amplitude crack propagation along the austenitic rods is likely to be blocked by phase boundaries, whereas intergranular cracks may encounter less phase boundaries leading to a rapid reduction of fatigue life (see also section 11.5). This speculation is confirmed by the much longer fatigue lives given in Figure 11.4 of the rolled DSSs. In addition, the fact that, despite having an identical chemical composition and the same morphology, DSS A905FG has a longer fatigue life than the coarser-grained DSS, A905CG, clearly underlines the scale effect. Furthermore, Figure 11.4 clearly indicates that with increasing morphological anisotropy and decreasing morphological scale the fatigue limit shifts to higher plastic strain amplitudes. Although the morphologically isotropic coarse-grained cast DSS shows a fatigue limit for plastic strain amplitudes as low as 2.7×10^{-5} (the test was stopped after 2 million cycles), the morphologically anisotropic fine-grained DSS, A905FG, reaches its fatigue limit at plastic strain amplitudes as high as 1.1×10^{-4} (the test was stopped after 2.14 million cycles).

By comparing fatigue life curves of medium nitrogen-alloyed cast DSS with high nitrogen-alloyed coarse-grained DSS, A905CG (Figure 11.4) it might be concluded that besides the improvement of the plastic reversibility due to the morphology, the higher nitrogen contents increase the fatigue life of a DSS. The justification of this conclusion will be investigated and discussed in section 11.4. However, the following can already be concluded from Figure 11.4; the effect of the nitrogen-content is less pronounced than the effect of morphological texture and scale. A difference can only be seen at high-cycle fatigue (HCF) where the curves of Bö 905 FG and CG split and change their slopes after being almost parallel in the plastic strain amplitude mode until/after 2×10^{5} cycles. The fatigue limits of both steels are an estimation, whereby the fatigue limit of the A905FG might be lower than that plotted in Figure 11.4. In addition, it can be expected to be higher than that of A905CG.

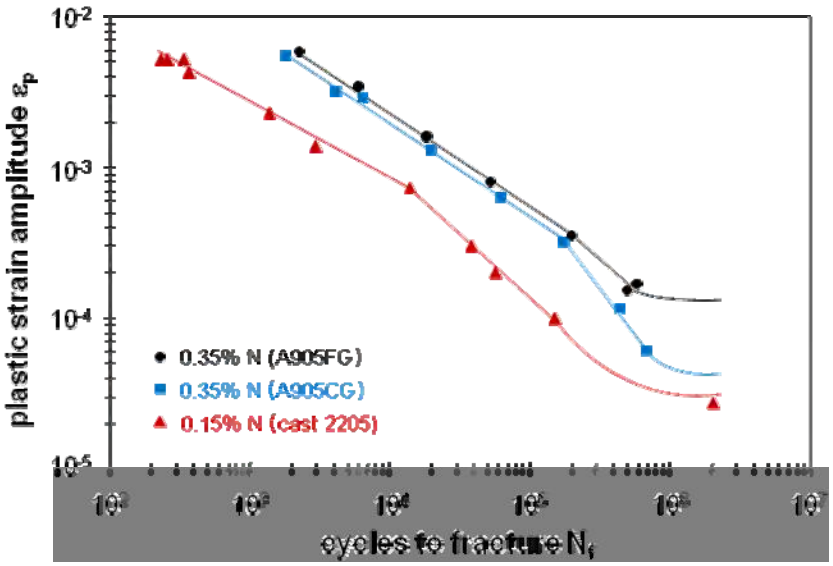

Figure 11.4. *Fatigue life curves of the cast DSS 1.4462 (2205) and a higher nitrogen-alloyed DSS from Böhler, Austria, in a standard, fine-grained (A905FG) and in a coarse-grained (A905CG) structure*

11.4. The role of nitrogen-content on the fatigue response of DSSs

The importance for nitrogen-alloying in stainless steels reflects itself in the *High Nitrogen Steels* conference series, founded in 1988, which has been running for more than 18 years [HNS 88, HNS 90, HNS 93, HNS 95, HNS 98, HNS 01, HNS 03, HNS 04, HNS 06] and whose successor is the modernized *International Conference on Interstitially Alloyed Steels* [IAS 08].

The alloying element, nitrogen, is known to have beneficial and detrimental effects on the properties of DSSs [HNS 88, HNS 90, HNS 93, HNS 95]. Nitrogen is the strongest interstitial solution-strengthening element [IRV 61], which is mainly dissolved in the austenitic phase. Consequently, in DSSs, nitrogen preferentially hardens the austenitic phase [FOC 93], but simultaneously decreases its ductility and even causes cleavage fracture at very high contents [AKD 96a]. Furthermore, the addition of nitrogen changes the slip character [WAH 89, GRU 89, SAS 89, LI 94, LI 94a, AKD 97] in the austenite from wavy to planar [AKD 97, TER 09] and the slip distribution from homogenous multiple slip to coarse localized single slip [AKD 97].

Like other non-metallic elements (hydrogen, helium, boron (in austenite), carbon, and oxygen), nitrogen is also an interstitial alloying element, which builds interstitial mixed crystals with iron and other transition elements of the fourth period of elements. Thereby, the interactions between nitrogen and the transition elements of the fourth period decreases from left to right, i.e. the precipitations of nitrogen with titanium, vanadium, chromium are stable, whereas those with cobalt, nickel and copper are unstable.

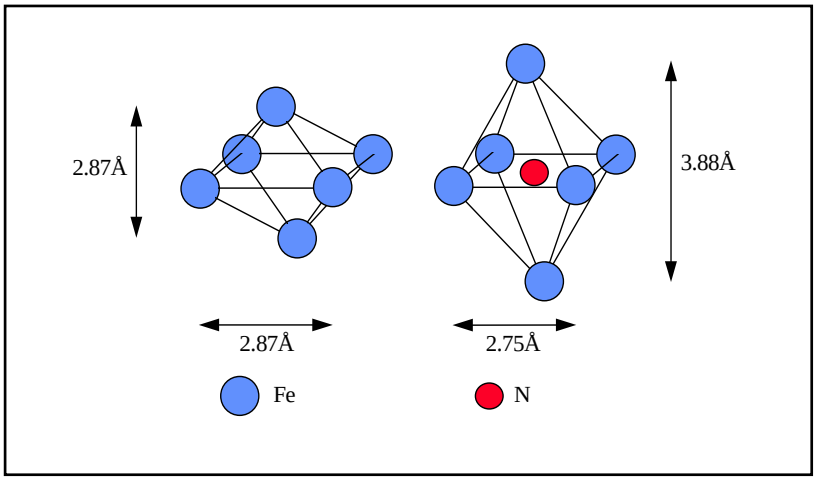

Figure 11.5. *Nitrogen in the octahedral holes leads to asymmetrical distortion of the α-Fe lattice [HEN 79]*

The diameter of nitrogen in iron is 1.44 Å. As Hendry *et al.* [HEN 79] showed, nitrogen leads to an asymmetric distortion of the α-Fe lattice (see Figure 11.5). The octahedral gaps/holes in α-Fe have a diameter of 0.19 Å, whereas in γ-Fe they have a diameter of 0.51 Å. Consequently, the isotropic strain in austenite is smaller than in ferrite. This might be the reason why, during rolling deformation in the ferritic phase of DSS, the 12 {110}<111> slip systems are mainly active, leading to a peak-type rolling texture (see Figure 11.6) [AKD 96b].

In addition, nitrogen is neither homogenously nor statistically distributed in the austenitic lattice but builds clusters with chromium and molybdenum [WAH 89] leading to the appearance of short- and long-range ordering. Consequently, the resulting interactions between nitrogen atoms, N-clusters, N-Me clusters, N-Me Guinier-Preston zones with dislocations, are large in both the face-centered cubic (FCC) and body-centered cubic (BCC) lattices [GAV 90]. The very strong solid solution strengthening effect, the planar character of dislocation glide, and the discontinuous yielding of austenite appear to be connected with these complexes.

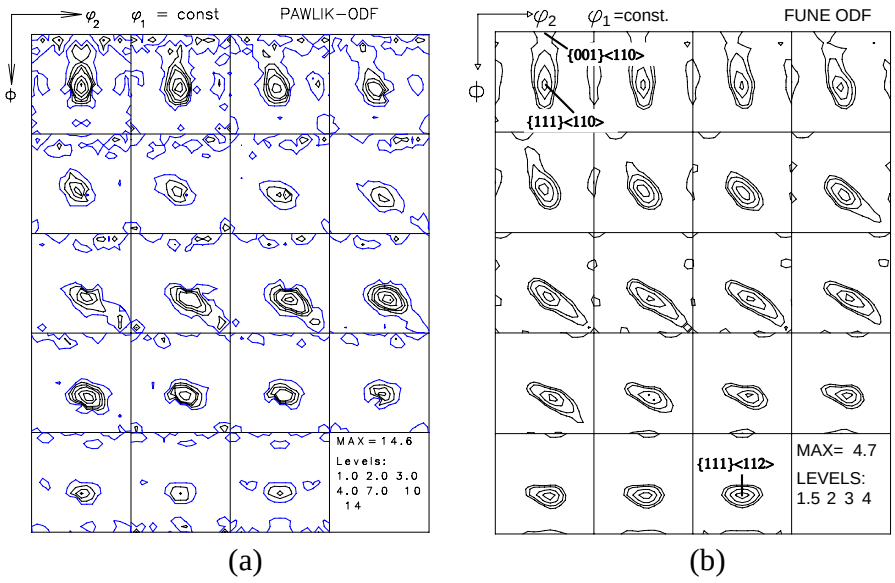

Figure 11.6. *Peak type rolling texture of a) the ferritic phase of DSS 1.4462 and b) the BCC β-phase of α/β brass (Cu40%Zn) after 80% thickness reduction by cold rolling at room temperature (center layer of the sheet) [AKD 96b]*

The alloying elements within all steels, including FCSs and stainless steels, including also (new generation of) DSSs, are grouped into ferrite ($Cr_{Eq.}$) and austenite ($Ni_{Eq.}$) stabilizing elements. According to their stabilizing strength, the various austenite and ferrite stabilizing elements are weighted with an empirical factor [SCH 49].

$$Cr_{Eq.} = \%Cr + \%Mo + 1.5\%Si + 0.5\%Nb + 2.0\%Ti \qquad [11.1]$$

$$Ni_{Eq.} = \%Ni + 30\%(C + N) + 0.5\%Mn \qquad [11.2]$$

In the nickel-equivalent, the factor 30 decreases down to 16 with increasing carbon and nitrogen contents. The Schaeffler diagram (Figure 11.7) predicts dependency of the chemical composition (nickel- and chromium-equivalents) upon which phases form within a steel grade after rapid cooling from high temperatures as it happens, e.g. during welding.

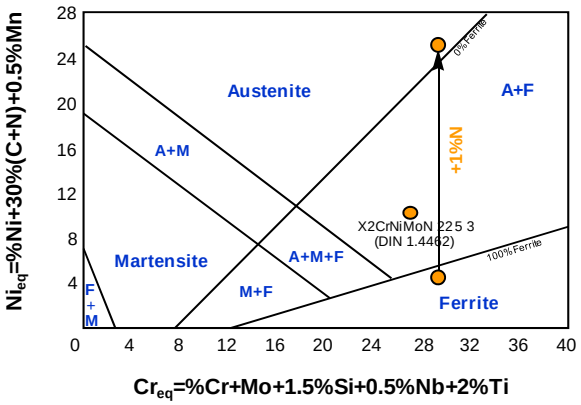

Figure 11.7. *Schaeffler diagram [SCH 49]*

In DSSs, ferrite usually constitutes the matrix phase, but as nitrogen is a very strong austenite stabilizer, which expresses itself in the so-called nickel-equivalent (see equation [11.2]) [SCH 49], the matrix phase can also become austenitic (see Figure 11.8) [AKD 96a].

Due to the different plastic properties of the austenite (FCC) and ferrite (BCC) phase, which phase constitutes the matrix is of great importance. For example, in the α/γ duplex steel, EN 1.4462, ferrite usually constitutes the matrix phase (Figure 11.2). With increasing nitrogen content and thus increasing nickel-equivalents, the matrix can become austenitic (Figure 11.8). The phase constituting the matrix phase is not only interesting from a welding standpoint, but also from a fatigue-resistance standpoint as the matrix phase plays an important role in this characteristic. However, this section will only deal with DSSs with a ferritic matrix.

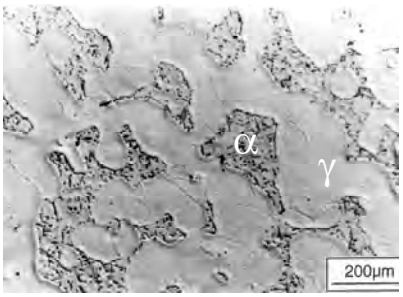

Figure 11.8. *At lower nitrogen contents ferrite constitutes the matrix (see Figure 11.2), whereas higher nitrogen contents, such as 0.62%, lead to an austenitic matrix with ferritic islands containing chromium nitride (Cr_2N) precipitates*

Higher nitrogen concentrations delay the formation of most precipitations. On the other hand, high nitrogen concentrations lead to the formation of Cr_2N precipitates within the α phase (Figure 11.8), which again leads to a lower corrosion, aging and brittleness resistance. Furthermore, during industrial production, nitrogen reduces the influence of the quenching speed.

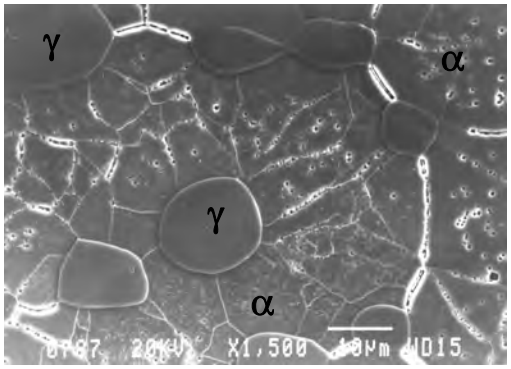

Figure 11.9. *DSS 1.4462 after a heat treatment (1 h at 1,100°C and quenched in water) [AKD96]*

The partition coefficient $[\%N]_\gamma/[\%N]_\alpha$ is large, meaning that nitrogen is mainly dissolved within the austenitic phase. Thus, DSS 1.4462 has the advantage that brittleness-promoting precipitations do not occur in the ferritic phase in regions near the austenitic phase, but are located at the ferritic grain and subgrain boundaries (Figure 11.9). The partitioning coefficient makes it necessary to deal with N in the austenitic phase and its effect on the SFE, which again determines many properties of the austenitic phase.

11.4.1. *Nitrogen and its effect on the SFE in the austenite*

Another very important effect of nitrogen alloying is that nitrogen changes the plasticity mechanisms of steels as nitrogen has a higher affinity to dislocations than carbon [GAV 90]. Thus, nitrogen alloying introduces the planar mode of dislocation glide in the austenitic phase as nitrogen atoms hinder cross-slip dislocation mode. This fact is related to the actual SFE.

There are many contradictory publications concerning the effect of nitrogen on the SFE. Older investigations, e.g [WAH 89], stated that the planar character of the deformation increases with increasing nitrogen content.

The latest publications the author is aware of [IAS 08] clearly confirm that, for a given chemical composition, nitrogen alloying can increase or decrease the SFE. In other words, nitrogen affects the SFE of Cr-Ni-based steel in a different way to a Cr-Mn-based steel. Manganese addition seems to significantly change the dislocation activity and behavior. In the Fe-21Cr-0.9N-23Mn alloy, dislocation cross-slip was observed frequently. This leads to the relaxation of the stress concentration at grain boundary and suppression of intergranular fracture. High manganese-alloyed austenitic stainless steels in combination with high nitrogen alloying leads to a higher SFE. With increasing SFE, the austenite behaves more and more like the ferrite, i.e. the cross-slip of screw dislocations becomes more and more suitable and possible.

The high manganese-alloyed variants of austenitic stainless steels and DSSs were not considered in earlier publications that investigated the effect of nitrogen alloying on stainless steels. For some time, the increasing or decreasing effect of nitrogen on the SFE was, and still is, in dispute [HNS 88, HNS 90, HNS 93, HNS 95, HNS 98, HNS 01, HNS 03, HNS 04, HNS 06, IAS 08].

Based on the above statements, by reducing the SFE, nitrogen obviously also affects the velocity of dislocations in such a way that with increasing nitrogen content the velocity of edge dislocations becomes reduced [VOG 93].

As mentioned earlier, planar slip (Figure 11.10) in nitrogen-alloyed austenitic stainless steels is attributed to short-range ordering effects between molybdenum, chromium, and nitrogen atoms [WAH 89, GRU 93]. Thereby, due to the high affinity of nitrogen with dislocations [GAV 87], cross-slip is impeded. Correspondingly, continuous planar-slip traces are visible in nitrogen-alloyed austenitic steels (Figure 11.11b). Following this idea, interrupted slip traces in nitrogen-free austenitic steels (Figure 11.11a) would be correlated with easier cross-slip, i.e. increasing SFE. Therefore, materials with a high SFE exhibit fairly well-developed sub-grain structures in which cross-slip can be observed.

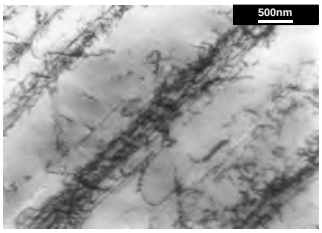

Figure 11.10. *Typical microstructure observed by transmission electron microscopy in the austenitic phase of the cast DSS showing bands of planar dislocation arrays embedded in a nearly dislocation-free matrix ($\varepsilon_{pa}=5.2\times10^{-3}$)*

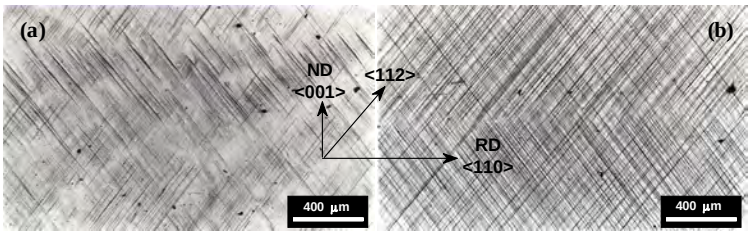

Figure 11.11. *Longitudinal sections of two initially 45° normal direction-rotated cube-oriented austenitic single crystals (AISI 316) after 5% thickness reduction by cold rolling, showing a) interrupted slip traces in the nitrogen-free crystal and b) continuous slip traces in the N-alloyed crystal [AKD 97]*

11.4.2. *The effect of nitrogen on the fatigue lives of DSSs*

As mentioned previously, comparison between the fatigue behaviors of different industrial DSS is complicated considering the whole complex of material parameters mentioned earlier in section 11.2. Therefore, it is not surprising that the Coffin-Manson curves (Figure 11.12) for these materials are scattered and difficult to compare, as, among other different parameters, the strain-control modes (plastic strain or total strain) were not the same. However, some trends appear to be evident.

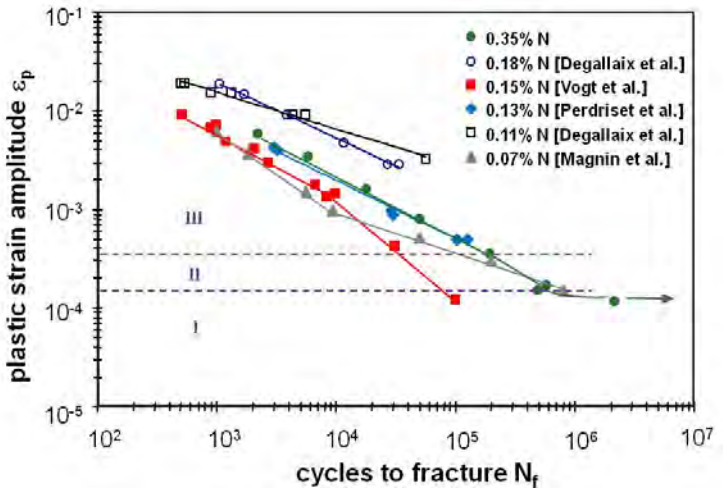

Figure 11.12. *Comparison of fatigue life curves of DSSs with comparable morphological textures but different nitrogen contents [MAG 88, DEG 93, VOG 95,PER 95]. The boundaries of the ranges I, II, and III for the high nitrogen-alloyed (0.35%) DSS, A905FG, are also shown*

According to Figure 11.12, a general fatigue life increasing effect of nitrogen cannot be detected. The fatigue life curves of DSSs with comparable morphological anisotropies and morphological scales, but with different nitrogen contents, reveal no consistent pattern. This might be attributed to the crystallographic texture development in both α and γ phases as a function of the production mode and deformation history. As is well known from the literature [LLA 93, MOR 94, PER 95a, CAR 97], the crystallographic texture has a pronounced effect on the cyclic stress-strain (CSS) response of metallic materials (texture influences the saturation stress up to 50%) and it must also considerably affect the fatigue response.

Similar to the low nitrogen-alloyed DSSs (see Figure 6.9b), the medium and high nitrogen-alloyed DSSs currently studied cover fatigue ranges I, II and III. The comparison of Figures 11.4 and 11.12 shows a pattern that is in agreement with the embrittling effect of high nitrogen contents [AKD 96a]; the extent of each stage, I, II, and III, as well as the cyclic hardening rates, correlated to them [VOG 95] are apparently a function of the nitrogen content. Increasing nitrogen contents seem to reduce the extent of the austenitic-ferritic regime II, i.e. nitrogen shifts the transition point between range II and III to lower plastic strain amplitudes and expands range III. The higher nitrogen content appears to promote an earlier onset of cyclic plastic strain concentration in the ferritic phase.

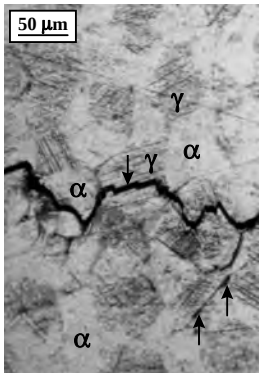

Figure 11.13. *At low plastic strain amplitudes in DSSs, only the austenitic phase (darker) is active. Range I fatigue cracks initiate in the austenitic grains and propagate from austenitic grain to austenitic grain and along phase boundaries, reproduced from [PED 98]*

Nitrogen changes the slopes of the fatigue life curves. This behavior was also observed for the single-phase austenitic grades, 316 and 316LN [NIL 88]. Contrary to 316LN and the 0.07% N DSS [MAG 88], the range II slopes of the DSSs

containing 0.15% N and 0.35% N are increasing instead of decreasing (Figures 11.4 and 11.12). The 0.35% nitrogen-alloyed DSSs reveal even higher slopes in range II than the medium nitrogen-alloyed DSSs, suggesting that the nitrogen-enhanced slip planarity (Figure 11.10 and 11.11 right) assists the transmission of cracks from the austenitic phase in which they initiate (Figure 11.13). Furthermore, the fatigue life curves of the 0.35% N-containing DSSs (Figures 11.4 and 11.12) reveal that the slopes of range II depend on the morphological scale: refinement of scale reduces the slope in ranges I and II, whereas the range III does not reveal such dependence.

The fact that for low plastic strain amplitudes, the fatigue life curve approaches that of single-phase ferritic steels does not necessarily suggest a reversal of the roles of the phases with respect to crack initiation. Surface damage inspection of fatigued steels confirmed that in the high nitrogen-alloyed DSSs, damage initiation starts at low amplitudes in the austenitic phase (see Figure 11.13). The discrepancy must somehow be related to the local γ grain orientations in combination with the nitrogen-enhanced slip planarity [AKD 97], as well as to the morphological scale and anisotropy.

After showing that the morphological texture and the chemical composition influence the fatigue response of DSSs, the next subsection will show that the strain control mode (plastic strain or total strain) and the cyclic softening of DSSs also play an important influencing role on the fatigue response of DSSs. Therefore, the following section will deal with lower nitrogen-alloyed DSSs, and especially, with the centrifugally cast DSS.

11.5. Cyclic plasticity and fatigue of nitrogen-alloyed DSSs – effects of cyclic softening

It is well established that in fatigue, DSSs with low nitrogen-contents (<0.1%) behave like composites with a hard ferritic (α) matrix and soft austenitic (γ) inclusions with shapes, orientations, and sizes depending on the chemical composition and thermomechanical processing history (see, e.g. [MAG 88, POL 93, MAT 96]). In this way, the fatigue of DSSs represents a theoretically interesting parallel with the fatigue of polycrystalline single-phase materials [PED 82, MUG 82, PED 90, LLA 93, LLA 94, LUO 96], which are turned into natural composites of hard multiple-slip oriented grains and soft single-slip oriented grains by cyclic hardening. In fact, Magnin *et al.* [MAG 88] showed that the “composite approach” provides a rationalization of their experimental observations of corrosion fatigue in a DSS subjected to cyclic deformation at constant plastic strain amplitudes in tension-compression, i.e. plastic strain-controlled cyclic deformation. Their observations are remarkably comprehensive, including the cyclic hardening and softening behavior, the preferred crack initiation sites, as well as the corrosion resistance as a function of

the imposed plastic strain amplitude. Magnin *et al.* [MAG 88] were the first to discover that there is a transition from low amplitude ("range I") behavior, below a critical plastic strain amplitude εI-II of about 10-3, to higher amplitude ("range II") behavior above the transitory plastic strain amplitude εI-II. According to Magnin *et al.* [MAG 88], the fatigue process is in range I dominated by local plasticity and damage of the γ phase. The range II process is dominated instead by damage of the α phase. This general picture appears to be further supported by transmission electron microscopy observations [POL 93, MAT 96] of the dislocation substructure in the α and γ grains as functions of the plastic strain amplitude in cyclic deformation at constant total strain amplitudes in tension-compression, i.e. total strain-controlled cyclic deformation. Nevertheless, the composite approach to DSSs still suffers from intriguing inconsistencies in its observational basis; compare for example [MAG 88] and [MAT 96].

However, recent publications [CHA 06] state and show that in an annealed DSS with nominally 0.3% N the austenitic phase yields first. This might be linked to the crystallographic local orientation of the austenitic grain and the number of its simultaneously available slip systems of the type {111}<110>. With very small plastic deformation, both phases yield under relatively large, but similar macroscopically applied stresses. The reason for this is twofold: 1) ferrites, in general, stainless or not, have lower yield strength than austenites; 2) austenites have, due to their 12 equivalent slip systems, a higher microplasticity. Consequently, an elastic or plastic loading can change the residual microstresses in the involved phases. Hence, damage and crack initiation in a two-phase alloy depend not only on the initial strength of each single phase, i.e. which phase is harder (mostly this is the austenitic phase due to its nitrogen content), but also their cyclic deformation-hardening behavior based on their SFE. However, after cyclic loading the weaker phase becomes damaged and hence will exhibit crack initiation first [CHA 06].

Again, apart from the morphology (phase and grain size and phase orientation concerning the macroscopic deformation direction or mode) the interaction between the two phases α and γ, i.e. the load transfer, their hardness (influenced by nitrogen), and the actual crystallographic texture, may also explain some discrepancies of the findings presented below. Therefore, one purpose of this subsection is to provide clarification by making a pattern visible concerning the influence of control mode on the cyclic softening, which is a dominant feature of DSS fatigue that is not met in the basic fatigue studies of pure FCC metals, such as, for example, copper and α-brass (Cu-30Zn).

During the last two decades, the industrial trend in stainless steel making has been to increase the nitrogen content in austenitic grades, as well as in DSSs. The direct technological motivation and industrial value of this chapter is the understanding of the effect of the increase of the nitrogen content in DSS (see e.g.

the HNS-series), which nowadays typically contain more than about 0.1% and up to 1.2% [STE 88, FOC 93, BAL 98, VOG 04, LAN 04, TER 09, ERI 08]. The beneficial effect of nitrogen is related to its preferential strengthening of the γ phase and improvement of corrosion resistance. Thus, the microhardness of the γ grains increases drastically as the total nitrogen content is increased, whereas the corresponding microhardness of the α phase is only very slightly increased [FOC 93, VOG 95, AKD 96]. This has important implications for the forming properties [AKD 96, AKD 96a], but as the relatively soft γ phase is the key feature in the composite approach to the low nitrogen-alloyed DSSs, it clearly becomes necessary to examine whether the approach needs modification for the DSSs of current industrial interest. Therefore, a neutron diffraction study [JEN 94] of the initial phase coupling in plastic strain-controlled fatigue of the centrifugally cast α/γ DSS with 0.15% N was carried out systematically. Hereafter, the cyclic plasticity and fatigue of this medium nitrogen-alloyed steel will be presented and discussed.

Optical microscopy (Figure 11.2a) showed a phase morphology characterized by coarse α grains (about 300-500 μm in diameter) within which the γ phase formed randomly oriented single crystals in the shape of 10-20 μm diameter rods of irregular cross-section and of lengths comparable with the grain diameter of the α phase. The volume fractions of the α and γ phases were about equal. Neutron diffraction revealed virtually no crystallographic texture, neither in the α phase nor in the γ phase. Rolling and forging produced [AKD 96, AKD 96b] a strong crystallographic texture in the α phase, a weak crystallographic texture in the γ phase, and a general alignment of the γ rods in the rolling direction. This morphological anisotropy is in the present as-cast steel confined to domains within individual α grains, whereas the steel as a whole is morphologically isotropic.

11.5.1. *Plastic strain-controlled cyclic deformation*

In plastic strain-controlled fatigue, the cyclic hardening, softening, and saturation behavior [FEL 67, FEL 67a] of the present medium nitrogen-alloyed steel was found to be qualitatively the same as the behavior of the low nitrogen steel studied by Magnin *et al.* [MAG 88]. Quantitatively, however, the softening:

$$\delta = \frac{\sigma_{max} - \sigma_{min}}{\sigma_{max}} \qquad [11.3]$$

where σ_{max} and σ_{min} are defined as in Figure 11.14, was found to increase markedly with the increase in nitrogen content, as well as with the decrease of the plastic strain amplitude. The strong cyclic softening is a major difference between the fatigue behavior of the nitrogen-alloyed DSS and the pure metals commonly investigated in basic fatigue studies [BAS 92, PED 96]. To emphasize this feature,

the cyclic stress behavior shall be presented not only by the conventional CSS curve (σ_{min} versus ε_p), but also by the σ_{max} versus ε_{pa} curve.

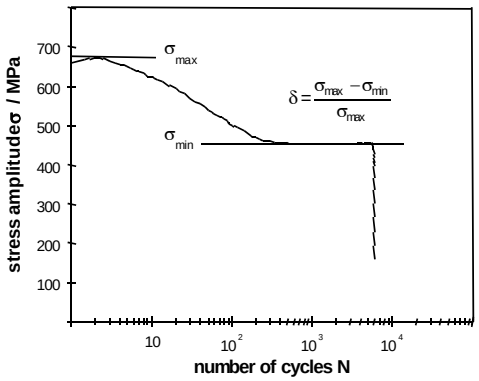

Figure 11.14. *Cyclic hardening-softening curve for a DSS ($\varepsilon_p = 3.4\times10^{-3}$ and N=0.35 wt%) with definitions of the maximum stress, σ_{max}, the minimum (or saturation) stress, σ_{min}, and the cyclic softening, δ, reproduced from [PED 98]*

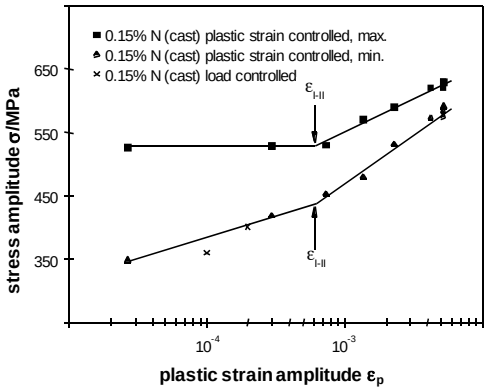

Figure 11.15. *With reduction of ε_p (from right to left of the graphs), the plastic strain-controlled saturation stress curve (bottom) differs increasingly from the maximum stress curve (top). The difference reflects the cyclic softening, δ. Both curves display a change of slope at the same amplitude, $\varepsilon_{I\text{-}II}$, which subdivides the curve into a low amplitude range I and a high amplitude range II*

Figure 11.15 illustrates the increasing difference between the σ_{max} and σ_{min} curves with decreasing plastic strain amplitude. Both curves display an almost discontinuous change of slope at $\varepsilon_{I\text{-}II}$, which is identified [Akdut and Pedersen, unpublished results, 1996] as the critical plastic strain amplitude for a transition from range I to range II, as in the composite approach [MAG 88].

Total strain controlled and incremental-step tests were avoided in the present study, as the object was mainly to examine the effect of nitrogen within the composite approach based on plastic strain-controlled cyclic deformation. As it turned out (section 11.5.2), the softening behavior is critically affected by the mode of deformation control and by including this effect the approach needs to be extended to total strain-controlled cyclic deformation. A few load-controlled fatigue life measurements were carried out in the initial phase of this work (see Figure 11.15 and the summary of experiments in Table 11.2).

Control mode	ε_p / 10^{-3}	σ / MPa	N_f	σ_{max} / MPa	σ_{min} / MPa	δ
Plastic	5.23		343	630	585	0.071
Plastic	5.25		232	630	593	0.059
Plastic	5.22		256	620	576	0.071
Plastic	4.26		365	620	575	0.072
Plastic	2.30		1,380	590	533	0.097
Plastic	1.37		2,937	570	481	0.156
Plastic	0.73		13,875	530	455	0.141
Plastic	0.30		38,417	529	420	0.206
Plastic	0.027		>2,000,000	526	350	0.335
Load	0.10	360	153,268			
Load	0.20	400	56,371			
Load	0.10	360	148,196			

Table 11.2. *Summary of cyclic deformation experiments on the as-cast DIN 1.4462 steel in plastic strain control and load control*

11.5.2. *The effect of the cyclic deformation mode and nitrogen-content on cyclic softening*

According to the observations of Magnin *et al.* [MAG 88], the cyclic softening δ during plastic strain-controlled cyclic deformation of low nitrogen-alloyed DSS is a decreasing function of the plastic strain amplitude ε_{pa}. As austenitic steels display large δ values with decreasing ε_{pa} and purely ferritic steels display virtually no softening effect at all ε_{pa} values, Magnin *et al.* [MAG 88] attributed the observed softening solely to cyclic softening of the austenitic phase in the DSS. They found that with decreasing ε_{pa} the austenitic phase increases its contribution to the softening, δ, while the contribution from the ferritic phase decreases. This behavior

was carefully documented by surface observations, which showed that cracks initiate in the austenitic phase at low ε_{pa} and in the ferritic phase at high ε_{pa}.

Once more, it becomes obvious that the manufacturing history, the resulting macroscopic morphology, the chemical composition, and the nitrogen content of a DSS play an important role in the fatigue response of DSSs. Thus, the results presented hereafter will make it obvious that both the chemical composition and morphological aspects of DSSs play a distinguished role and that we must investigate further to understand the interaction of both phases austenite and ferrite.

In Figure 11.16 the present measurements of δ for low (0.07%), medium (0.15%), and high (0.35%) nitrogen-alloyed DSSs are compared. DSSs with a morphologically anisotropic (low nitrogen-alloying) and isotropic (medium nitrogen-alloying) microstructure reveal an increasing softening with decreasing plastic strain amplitudes, while at 0.35% N, the softening increases with increasing plastic strain amplitude irrespective the microscopical scale (see section 11.3.2). Therefore, it appears that in all DSSs, from low to high nitrogen-alloyed, the austenitic phase is active at all plastic strain amplitudes, its relative contribution to the softening δ can be a decreasing or increasing function of ε_p (Figure 11.16).

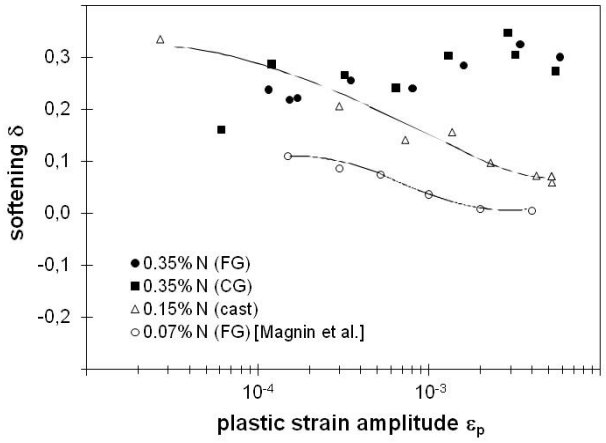

Figure 11.16. *Comparison between measurements of cyclic softening, δ, for the low nitrogen-alloyed DSS investigated by Magnin et al. [MAG 88], the cast DSS 1.4462 and the FG and CG high nitrogen-alloyed DSS presently studied in plastic strain control reveals an interesting pattern related to the morphological texture (isotropic cast, anisotropic FG and CG structures) and the nitrogen content (see Table 11.3) of the DSSs: softening increases with increasing nitrogen content and is additionally influenced by the morphological texture*

A comparison of the δ values measured in plastic strain control reveals an interesting pattern. The anisotropic FG morphologically identical DSSs with low and high nitrogen content show a very different softening behavior. While the softening of the low nitrogen-alloyed DSS increases with decreasing plastic strain amplitudes, δ of the high nitrogen-alloyed DSS shows an opposite behavior; it increases with increasing plastic strain amplitudes. This clearly proves that nitrogen has a strong influence on the softening of DSSs. It is interesting to mention that the morphological scale seems not to have an influence on the softening of DSSs. This can clearly be seen by comparing the chemically identical high nitrogen-alloyed DSSs, which differ solely in their microscopical scale, i.e. grain size.

The scattering of the measured δ values allows no conclusion concerning the effect of the microscopical scale. It is most likely that another morphological parameter than the microscopic scale is responsible for the scattering of the δ values. However, it seems evident that for both FG and CG high nitrogen-alloyed DSSs the softening increases with increasing plastic strain amplitude. The explanation of the softening behavior of the morphologically isotropic CG cast DSS with 0.15% N, however, is not evident.

Qualitatively, the δ-curve of the cast DSS is similar to the one of the low nitrogen-alloyed DSS, but the δ values of the cast DSS are on a higher level. The latter fact might be attributed to the higher nitrogen-content and/or the macroscopic isotropy. Further research is needed to understand the softening behavior of DSSs as a function of morphological texture, microscopical scale and chemical composition.

Element	DIN 1.4462 (cast DSS)	Bö A905	Magnin et al. [MAG 88]	Mateo et al. [MAT 96])	Vogt et al. in [HNS 95])	Perdriset et al. [PED 95])
Cr	22.0	25.3	21.7	24.6	24.16	21.8
Ni	5.5	3.7	7.0	5.4	5.48	5.68
Mo	3.0	2.06	2.5	1.4	3.27	2.77
Mn	2.0	5.8	1.7	1.73	1.2	1.68
N	**0.15**	**0.35**	**0.07**	**0.072**	**0.153**	**0.132**
Cu	-	-	0.08	0.21	-	0.075
Si	1.0	0.2	0.39	0.34	0.54	0.442
Co	-	-	0.06	-	-	-
S	-	0.004	-	-	0.001	-
P	-	0.023	-	-	0.021	-
C	0.03	0.023	0.02	0.036	0.022	0.022

Table 11.3. *Chemical compositions (in mass %) of the duplex stainless steels investigated in the present study and by [MAG 88, MAT 96, HNS 95, PED 95]*

11.5.3. *Cyclic stress-strain response of DSSs*

It is obvious that there is also an effect of the deformation control mode on cyclic softening. To demonstrate this, it has to be first noted that the nearly discontinuous change of slope in the plastic strain-controlled CSS curves is a prominent feature of total strain-controlled curves. Figure 11.17 shows, for example, a reproduction of the curves measured in total strain control for low and medium nitrogen-contents [DEG 95, VOG 95, PER 95, MAT 96]. The $\varepsilon_{I\text{-}II}$ value is well defined. With increase of nitrogen content the value of $\varepsilon_{I\text{-}II}$ is seen to decrease markedly, while the saturation stresses are seen to increase uniformly in range II and range I. It should be noted that the increase of σ_{min} is somewhat more pronounced in range II than it is in range I, and that this is matched by the decrease of softening observed (Figure 11.15) in total strain-controlled experiments, when ε_{pa} is decreased or when the nitrogen content is increased.

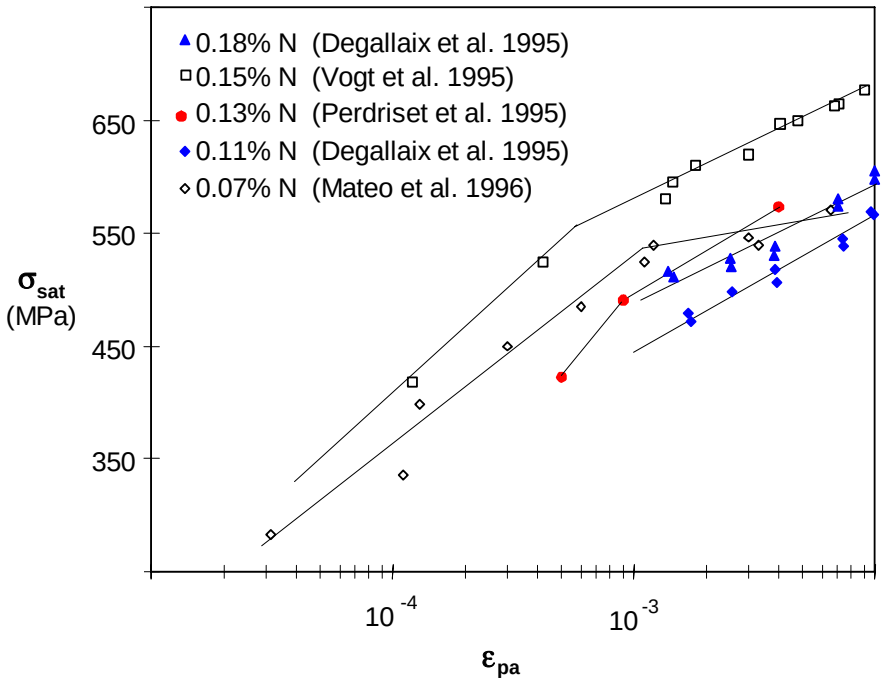

Figure 11.17. *Comparison of results from the literature on total strain-controlled cyclic deformation shows that increase of nitrogen content decreases $\varepsilon_{I\text{-}II}$ and increases the saturation stress in both ranges I and II, reproduced from [PED 98]*

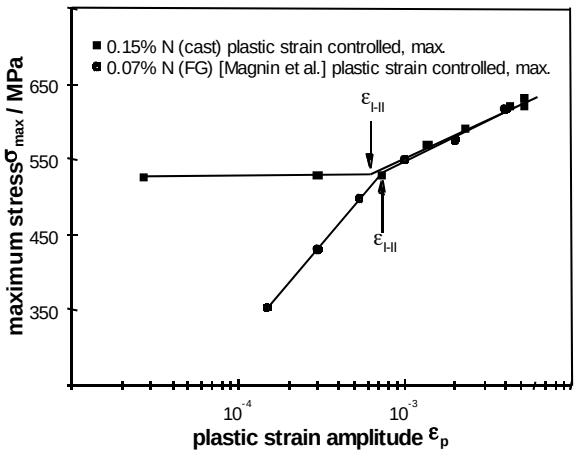

Figure 11.18. *In plastic strain-controlled cyclic deformation increase of nitrogen content decreases $\varepsilon_{I\text{-}II}$ and increases the maximum stress in both ranges I and II*

Within the range of compositions represented in Figure 11.17 the differences in nitrogen content change the stress amplitude by less than 20%. This can be seen by comparing the curves measured for 0.07 and 0.15% N or the curves measured for 0.11 and 0.18% N. These curves obviously cannot be understood purely in terms of their chemical composition. This is best seen by comparing the curve for 0.18 with that for 0.15% N. Considering their chemical composition, these curves should nearly coincide, and yet their saturation stress levels differ by about 10%. Thus, in addition to the nitrogen content, as stated in section 11.2, we have to consider the differences in morphological texture stemming from different production routes.

The nitrogen hardening effect in plastic strain-controlled cyclic plasticity is illustrated in Figure 11.19, which compares the present σ_{max} curve with the curve calculated from the σ_{min} and δ measurements by Magnin *et al.* [MAG 88] using equation [11.3]. The decrease of $\varepsilon_{I\text{-}II}$ with increase of nitrogen is just noticeable, but it is a striking feature that the only other apparent effect of the increased nitrogen content is to reduce the slope and raise the σ_{max} values in range I. Conversely, the σ_{max} values in range II are only very slightly increased. Of course, the present medium and low nitrogen steels differ in morphological anisotropy and scale, but while this difference affects fatigue lives markedly (section 9.5.4), its effect is only a rather small reduction in the σ_{max} and σ_{min} values.

The softening effect in plastic strain-controlled cyclic deformation is higher in the present medium nitrogen-alloyed steel than in the low nitrogen-alloyed steel

(Figure 11.16), and correspondingly the σ_{min} values in range II are lower (Figure 11.19) for the medium nitrogen steel, in complete contrast with the results obtained in the total strain-controlled experiments (Figure 11.17). The σ_{min} values remain higher for the high nitrogen steel throughout the major part of range I. Although the lowering of $\varepsilon_{I\text{-}II}$ with increase of nitrogen is marked, it is not sufficient to remove a relatively small upper part of range I, within which even the range I saturation stress is actually decreased by nitrogen addition.

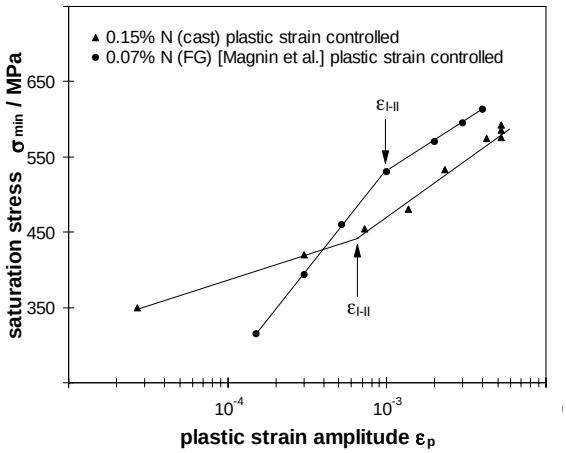

Figure 11.19. *In plastic strain-controlled cyclic deformation increase of nitrogen content decreases $\varepsilon_{I\text{-}II}$. The saturation stress is seen to increase in range I but decrease in range II*

11.5.4. *Fatigue lives of DSSs as a function of phase morphology and nitrogen content*

The present fatigue life curves (Figure 11.20) display a change of slope nearly coincident with the plastic strain amplitude $\varepsilon_{I\text{-}II}$, at which the cyclic stress strain curves change their slope. This behavior is similar to that observed by Magnin *et al.* [MAG 88] for the low nitrogen-alloyed DSS, for which the value of $\varepsilon_{I\text{-}II}$, however, is slightly higher. The essential difference is that the present steel displays significantly shorter fatigue lives in range I as well as in range II. Interestingly, the presented experimental results also reveal a fatigue limit at a plastic strain amplitude of $\varepsilon_{pa} \approx 3 \times 10^{-5}$. While the deformation control mode affects the CSS curves directly, it is less likely to influence the fatigue life curves. For a medium nitrogen-alloyed DSS with essentially the same morphology as the low nitrogen-alloyed DSS, Perdriset *et al.* [PED 95] found significantly increased fatigue lives in total strain control. Thus, it appears that for a given phase morphology, the addition of nitrogen increases fatigue life.

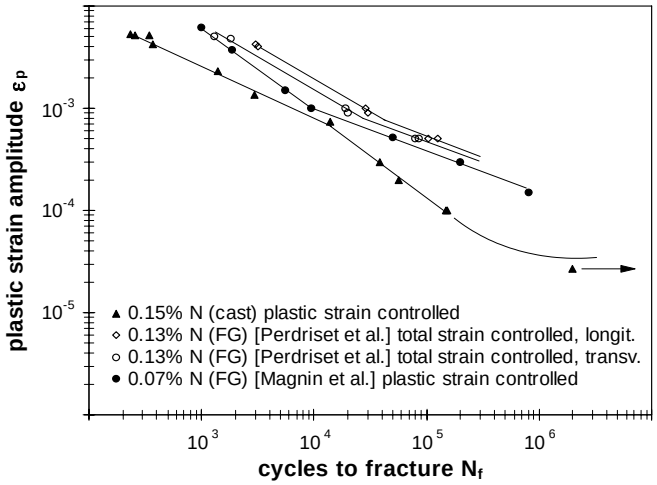

Figure 11.20. *Fatigue life curves of duplex stainless steels display considerable scatter but they all tend to display slope changes at $\varepsilon_{I\text{-}II}$ irrespective of deformation control mode. The scatter may be related to the N-content and phase morphology of the steels reproduced from [PED98]*

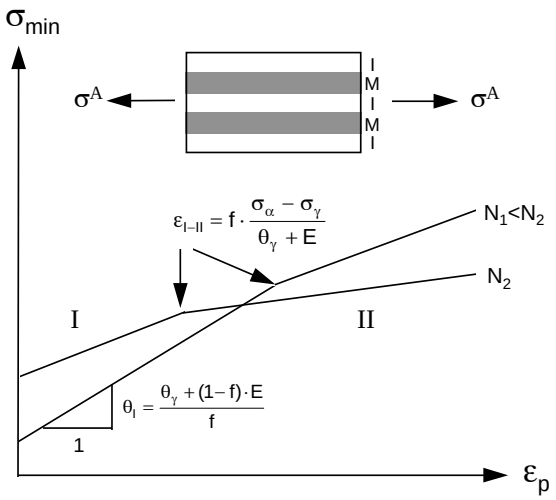

Figure 11.21. *The typical plastic strain controlled cyclic stress-strain response for nitrogen-containing DSSs with predictions of $\varepsilon_{I\text{-}II}$ and the stage I slope based on a simple analytical model with parallel coupled phases*

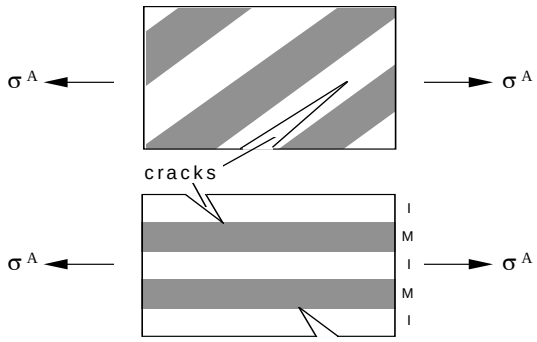

Figure 11.22. *Morphologically anisotropic duplex steels should display anisotropic crack growth resistances*

It appears that in plastic strain-controlled fatigue the effect of nitrogen on the CSS response is as illustrated in Figure 11.21. The CSS curve for the fully saturated (softened) steels is approximately bi-linear with a discontinuity of slope at the plastic strain amplitude $\varepsilon_{I\text{-}II}$ separating ranges I and II. The typical effect of increasing the nitrogen content is to reduce the value of $\varepsilon_{I\text{-}II}$, the slopes in ranges I and II as well as the saturation stress in range II. However, it increases the saturation stress in range I. Phase morphology may influence the CSS behavior in range I, but it appears to have its main influence on fatigue life (Figure 11.4). This general observational picture is consistent with the preferential nitrogen hardening of the austenitic phase, as seen from the present measurements of σ_{max} versus ε_p curves and, more directly, from microhardness tests [FOC 93] and neutron diffraction measurements [JEN 94] of lattice strains in the α and γ phases in the first quarter-cycle of a fatigue test.

The fatigue life curves presented in Figure 11.21 are consistent with a subdivision into ranges I and II with $\varepsilon_{I\text{-}II}$ decreasing for increasing nitrogen content, irrespective of the deformation control mode. However, a composite model involving only phase volume fractions cannot fully account for the observations. It is necessary to include more detailed morphological parameters, such as scale and anisotropy. This is best illustrated by the experiments of Perdriset *et al.* [PER 95] (see Figures 11.3 and 11.21), in which specimens were cut in different direction in a rolled medium nitrogen steel: longitudinal specimens, cut parallel to the rolling direction, are seen to display higher fatigue lives than transverse specimens, cut perpendicular to the rolling direction. As mentioned in section 11.5.3, a comparison with the fatigue life curve measured by Magnin *et al.* for low nitrogen steel also shows that nitrogen alloying by itself improves fatigue life.

The short fatigue lives measured for the present cast medium nitrogen-alloyed DSS appears to be due mainly to its lack of macroscopical morphological anisotropy. The orientation of the γ rods changes from one α grain to the next. Fatigue cracking presumably occurs much more easily in an α grain with its γ rods oriented at 45° to the direction of applied stress (Figure 11.22, top) than in the case of both phases being parallel oriented to the direction of applied stress (Figure 11.23, bottom). It is thus suggested that the presence of large α grains oriented for easy cracking explains the short fatigue lives measured and presented in this section. This interpretation immediately implies that rolling and increase of nitrogen content will improve the fatigue performance of the steel, although a damage model supporting the upper findings has not been provided yet. However, recently some remarkable work has been published regarding softening models as outlined in Chapters 6 and 9, e.g. one atomistic model [ALV 06] based on the contribution of the friction stress and a mechanical model related to back stress [EVR 08].

11.6. Summary and conclusions

This chapter about morphological texture has presented and discussed the effects of various influencing parameters on the fatigue response of DSSs, such as the effects of:

– industrial processing on the morphological texture,

– nitrogen content on the fatigue life,

– morphological texture and microscopical scale on the fatigue life,

– nitrogen alloying on the SFE,

– strain-control mode (plastic strain or total strain) on the cyclic softening,

– nitrogen alloying on the cyclic softening.

As this topic is very complex, it was intended that this chapter provide a thought-provoking introduction to the subject to stimulate further research. The following is a summary and conclusions on the salient points of the chapter.

Each industrial production step strongly influences the DSSs‘ morphological texture parameters, such as scale and anisotropy. It was shown that for a given phase morphology an addition of nitrogen increases fatigue life. The short fatigue lives measured for the presented CG cast medium nitrogen-alloyed DSS appears to be mainly due to its lack of macroscopical morphological anisotropy.

The typical effect of increasing the nitrogen content is to reduce the value of $\varepsilon_{I\text{-}II}$, reduce the slopes in ranges I and II, reduce the saturation stress in range II, but to

increase the saturation stress in range I. The phase morphology appears to have its main influence on fatigue life.

Latest publications confirm that the content of nitrogen for a given chemical composition of a stainless steel – in terms of substitutional elements – is the key factor for increasing or decreasing the SFE. With increasing SFE austenite behaves more and more like ferrite, i.e. cross-slip of screw dislocations becomes more and more suitable and possible.

The strain control mode (plastic strain or total strain) and the cyclic softening of DSSs also play an important influencing role on the fatigue response of DSSs. While the deformation control mode affects the CSS curves directly, it is less likely to influence the fatigue life curves.

The cyclic softening in DSSs is dependent on deformation control mode. CSS curves measured in total strain control differ increasingly from those measured in plastic strain control when the nitrogen content is increased.

A major limitation of the so-called composite approach, as it stands, is cyclic plasticity described purely in terms of phase volume fractions. An extension to fatigue will require a damage model and more detailed structural characterization, including characterization of morphological scale and morphological anisotropy. Encouragingly the present observations include a fatigue threshold, the level of which may be raised by increase of nitrogen content and refinement of the phase morphology, but it is clear that the composite approach must be further supplemented with a damage model to provide quantitative predictions of fatigue life.

To understand the softening behavior of DSSs as a function of morphological texture, microscopical scale and chemical composition, further research is needed.

11.7. References

[AKD 96] AKDUT N., in *Kaltverformung von Duplexwerkstoffen*, Shaker Verlag, Aachen, 1996.

[AKD 96a] AKDUT N., FOCT J., "Microstructure and Deformation Behaviour of High Nitrogen Duplex Stainless Steels", in *Int. Conf. on High Nitrogen Steels '95* [HNS95], *ISIJ International*, vol. 36, no. 7, p. 883-892, 1996.

[AKD 96b] AKDUT N., FOCT J., GOTTSTEIN G., "Cold rolling texture development of α/γ duplex stainless steels", *Steel Research*, vol. 67, no. 10, p. 450-455, 1996.

[AKD 97] AKDUT N., KEICHEL J., FOCT J., "The influence of nitrogen and orientation on the rolling deformation mechanisms of austenitic single crystals", *Steel Research*, vol. 68, no. 11, p. 495, 1997.

[AKD 99] AKDUT N., "Phase morphology and fatigue lives of nitrogen alloyed duplex stainless steels", *International Journal of Fatigue*, vol. 21, pp. S97-103, 1999.

[ALV 06] ALVAREZ-ARMAS I., MARINELLI M. C., DEGALLAIX S., ARMAS A. F. "On the cyclic softening behavior of SAF 2507 duplex stainless steel", *Acta Materialia*, vol. 54, pp. 5041–5049, 2006.

[BAL 98] BALITSKII A. I., DIENER M., MAGDOWSKI R., POKHMURSKLI V. I., SPEIDEL M. O., "Anisotropie of fracture toughness of austenitic high nitrogen chromium-manganese steel", in *Int. Conf. on High Nitrogen Steels '98*, Trans Tech Publications Ltd., Switzerland, 1998.

[BAS 92] BASINSKI Z. S., BASINSKI S., "Fundamental aspects of low amplitude cyclic deformation in face-centred cubic crystals", *J., Prog. Mater. Sci.*, vol. 36, pp. 89-148, 1992.

[BÜR 05] BÜRGEL R., *Festigkeitslehre und Werkstoffmechanik*, Vieweg+Teubner Verlag, 2005.

[CAR 97] CARSTENSEN J. V., PEDERSEN O. B., "Texture and grain-size effects on cyclic plasticity in copper and copper-zinc", *Mater. Sci. Engng.*,Vol. A243-236, pp. 497-500, 1997.

[CHA 06] CHAI G., LILLEBACKA R., LIN P. R., "Micro-deformation behavior and damage mechanisms in super duplex stainless steels", pp. 139-148, in *Int. Conf. on High Nitrogen Steels '06*, 29-31 August, Jiuzhaigou, 2006.

[CHA 08] CHAI G., "Influence of nitrogen contents on the static and dynamic strain ageing in super duplex stainless steels", in *Steel Research International*, no. 7, pp. 482-487, 2009.

[DEC 07] DE COOMAN B. C. *et al.*, *Materials Design, The Key to Modern Steel Products*, GRIPS media, 2007.

[DEG 93] DEGALLAIX S., SEDDOUKI A., NILSSON J. O., POLAK J., "Influence of nitrogen on monotonic and cyclic mechanical properties of duplex stainless steels", in *Int. Conf. on High Nitrogen Steels '93* , pp. 420-425, 14-16 September, Kiev, 1993.

[DEG 95] DEGALLAIX S., SEDDOUKI A., DEGALLAIX G., KRUML T., POLAK J., *Fatigue Fract. Engng. Struct.*, vol. 18, p. 65-77, 1995.

[DUL 64] DULIEU D., NUTTING J., "Effect of alloying elements on stacking fault energy in austenitic iron-nickel-chromium alloys", in *Metallurgical Developments in High-Alloy Steels. Special Report No. 86*, The Iron and Steel Institute, pp. 140-145, 1964.

[ERI 08] ERISIR E., PRAHL U., BLECK W., "Investigations on hot deformation and precipitation behaviour of high nitrogen steels", in *Int. Conf. on Interstitially Alloyed Steels 2008 (IAS 2008)* , pp. 37-44, 28 September –2 October, Pohang, 2008.

[EVR 08] EVRARD P., AUBIN V., PILVIN P., DEGALLAIX S., KONDO D., "Implementation and validation of a polycristalline model for a bi-phased steel under non-proportional loading paths", *Mech. Res. Commun.*, vol. 35, no. 5, pp. 336-343, 2008.

[FAW 68] FAWLEY R., QUADER M. A., DODD R. A., "Compositional effects on the deformation modes, annealin twin frequencies, and stacking fault energies of austenitic stainless steels", *TMS AIME*, vol. 242, pp. 771-778, 1968.

[FEL 67] FELTNER C. E., LAIRD C., "Cyclic stress-response of F.C.C. metals and alloys – I. Phenomenological experiments", *Acta Metallurgica*, vol. 15, pp. 1621-1632, 1967.

[FEL 67a] FELTNER C. E., LAIRD C., "Cyclic stress-response of F.C.C. metals and alloys – II. Dislocation structures and mechanisms", *Acta Metallurgica*, vol. 15, pp. 1633-1653, 1967.

[FOC 93] FOCT J., AKDUT N., "Cleavage-like fracture of austenite in duplex stainless steel", *Scripta Met. Mat.*, vol. 29, p. 153-158, 1993.

[FOR 92] FORCH K., GILLESSEN C., VON HAGEN I., WEIßLING W., "Nichtrostende ferritisch-austenitische Stähle - Eine Werkstoffgruppe mit großem Entwicklungspotential", *Stahl Eisen*, vol. 112, pp. 53-62, 1992.

[FRO 08] FROMMEYER G., RABLBAUER R., "Entwicklung hochfester und supraduktiler Leichtbaustähle für die Verkehrstechnik", in *Jahrbuch 2008*, Max-Planck-Institut für Eisenforschung, Düsselforf, Germany, 2008.

[FUJ 75] FUJIKURA M., TAKADA K., ISHIDA K., "Effect of manganese and nitrogen on the mechanical properties of Fe-18%Cr-10%Ni stainless steels", *Trans Iron Steel Inst. Jap*, vol. 15, no. 9, pp. 464-469, 1975.

[GAV 87] GAVRILJUK V. G., DUZ' V. A., YEFIMENKO S. P., KVASNEVSKI O. G., "Carbon distribution in steel", (in Russian) *Phys. Met. Metallogr.*, vol. 64, pp. 1132-1135, 1987.

[GAV 90] GAVRILJUK V. G., JEPHIMENKO S. P., "Distribution of nitrogen atoms, their interaction with dislocations and properties of high-nitrogen austenite", in *Int. Conf. on High Nitrogen Steels '90*, October 10-12, Aachen, Verlag Stahleisen, Düsseldorf, pp. 11-21, 1990.

[GAV 99] GAVRILJUK V. G., BERNS H., *High Nitrogen Steels*, Springer-Verlag, Berlin, pp. 51-65, 1999.

[GRU 89] GRUJICIC M., NILSSON J. O., OWEN W. S., THORWALDSSON T., "Basic deformation mechanisms in nitrogen strengthened stable austenitic stainless steels", in J. FOCT and A. HENDRY, Eds., *Int. Conf. on High Nitrogen Steels '88*, 18-20 May, Lille, The Institute of Metals, p. 151-158, 1989.

[GRU 93] GRUJICIC M., OWEN W. S., "Nitrogen Induced Ordering In Face-Centered Cubic Fe-Ni-Cr-N Solid-Solution Alloys", in *Int. Conf. on High Nitrogen Steels '93*, 14-16 September, Kiev, p. 686, 1993.

[HEN 79] HENDRY A., MAZUR Z. F., JACK K. H., "Influence of nitrogen on 475° embrittiement of high chromium ferritic steels", *Metal Science*, vol. 13, p. 482-486, 1979.

[HNS 88] *Int. Conf. on High Nitrogen Steels '88*, May 18-20, Lille, Eds. J. FOCT and A. HENDRY, The Institute of Metals, 1988.

[HNS 90] *Int. Conf. on High Nitrogen Steels '90*, October 10-12, Aachen, Eds. G. STEIN, H. WITULSKI, Verlag Stahleisen, Düsseldorf, 1990

[HNS 93] *Int. Conf. on High Nitrogen Steels '93*, September 14-16, Kiev, Eds. V. G. GAVRILJUK, V. M. NADUTOV, Institute for Metal Physics, Kiev, 1993.

[HNS 95] *Int. Conf. on High Nitrogen Steels '95*, Kyoto, Eds. M. KIKUCHI, Y. MISHIMA, 1995, *ISIJ International*, Special issue on High Nitrogen Steels, vol. 36, no. 7, 1996.

[HNS 98] *Int. Conf. on High Nitrogen Steels '98*, Espoo, Eds. H. HÄNNINEN, S. HERTZMAN, J. Romu, Trans Tech Publications Ltd, 1999.

[HNS 01] *Int. Conf. on High Nitrogen Steels '01*, Chennai, Eds. B. RAJ and K. MUDALI, 2001.

[HNS 03] *Int. Conf. on High Nitrogen Steels '03*, February, Zürich, Eds. M. O. SPEIDEL, C. KOWANDA, M. DIENER, vdf Hochschulverlag AG, 2003.

[HNS 04] *Int. Conf. on High Nitrogen Steels '04*, September 19-22, Ostende, Eds. N. AKDUT, B. C. DE COOMAN, J. FOCT, GRIPS media GmbH, 2004.

[HNS 06] *Int. Conf. on High Nitrogen Steels '06*, August 29-31, Jiuzhaigou, Eds. H. DONG, S. JIE, M. O. SPEIDEL, Beijing Metallurgical Industry Press, 2006.

[IAS 08] *Int. Conf. on Interstitially Alloyed Steels 2008 (IAS 2008)*, September 28-October 2, Pohang, Eds. N. AKDUT, B. C. DE COOMAN, H. S. Kim, 2008.

[IRV 61] IRVINE K. J., LLEWELLYN D. T. and PICKERING F. B., "High-strength austenitic stainless steels", *J. Iron Steel Inst.*, vol. 199, pp. 153-175, 1961.

[JEN 94] JENSEN M. T., BRØNDSTED P., JOHANSEN B. S., LORENTZEN T. PEDERSEN O. B., "Phase coupling and low cycle fatigue in a duplex stainless steel", *Proc. Int. Conf. on the Strength of Materials*, Sendai, Eds, H. OIKAVA, K. MARUYAMA, S. TAKEUCHI and M. YAMAGUCHI, The Japan Institute of Metals, pp. 489-492, 1994.

[LAN 04] LANG Y. P., RONG F., CHEN H. T., SHEN J. C., SPEIDEL M. O., DONG H., "Sudy of high nitrogen steel rebars for infrastructural applications", in *Int. Conf. on High Nitrogen Steels '04*, September 19-22, Ostende, Eds. N. AKDUT, B. C. DE COOMAN, J. FOCT, GRIPS media GmbH, 2004.

[LI 94] LI Y., LAIRD C., "Cyclic response and dislocation structures of AISI 316L stainless steel. Part 1: single crystals fatigued at intermediate strain amplitude", *Mater. Sci. Engng.*, vol. A186, p. 65-86, 1994.

[LI 94a] LI Y., LAIRD C., "Cyclic response and dislocation structures of AISI 316L stainless steel. Part 2: polycrystals fatigued at intermediate strain amplitude", *Mater. Sci. Engng.*, vol. A186, pp. 87-103, 1994.

[LLA 93] LLANES L., ROLLET A. D., LAIRD C., BASSANI J. L., "Effect of grain size and annealing texture on the cyclic response and the substructure of polycrystalline copper", *Acta Metall. Mater.*, vol. 41, 1993, pp. 2667-2679.

[LLA 94] LLANES L., BASANI J. L., LAIRD C., "Cyclic response of polycrystalline copper-composite-grain model", *Acta Metall.*, vol. 42, pp. 1279-1288, 1994.

[LUO 96] LUOH T., CHANG C. P., "Dislocation-free zones in fatigued copper polycrystals", *Acta Mater.*, vol. 44, pp. 2683-2695, 1996.

[MAG 88] MAGNIN T., LARDON J. M., COUDREUSE L., "A new approach to low cycle fatigue behavior of a duplex stainless steel based on the deformation mechanisms of the individual phases", in H. D. SOLOMON, G. R. HALFORD, L. R. KAISAND and B. N. LEIS, Eds, *Low Cycle Fatigue*, ASTM STP 942, American Society for Testing and Materials, Philadelphia, pp. 812-823, 1988.

[MAT 96] MATEO A., LLANES L., ITURGOYEN L., ANGLADA M., "Cyclic stress-strain response and dislocation substructure evolution of a ferrite-austenite stainless steel", *Acta Mater.*, vol. 44, no. 3, p. 1143, 1996.

[MOR 94] MORRISON D. J., "Influence of grain size and texture on the cyclic stress-strain response of nickel", *Mater. Sci. Engng.*, vol. A187, pp. 11-21, 1994.

[MUG 82] MUGHRABI H., WANG R., "Deformation of Polycrystals: Mechanisms and Microstructure", *Proceedings of the Second Risø International Symposium on Metallurgy and Materials Science*, pp. 87-98, Roskilde, Denmark, September 1982.

[NIL 88] NILSSON J.-O., "Effect of nitrogen on creep-fatigue interaction in austenitic stainless steels at 600ºC", in H. D. Solomon, G. R. HALFORD, L. R. KAISAND and B. N. LEIS, Eds, *Low Cycle Fatigue*, ASTM STP 942, American Society for Testing and Materials, Philadelphia, pp. 543-557, 1988.

[NOS 65] NOSKOVA N. I., PAVLOV V. A., NEMNONOV S. A., "A correlation between the stacking fault energy and structure of metals (in Russian)", *Physics Metals Metallogr.*, vol. 20, no. 6, p. 920-924, 1965.

[PED 82] PEDERSEN O. B., RASMUSSEN K. V., WINTER A. T., "The cyclic stress-strain curve of polycrystals", *Acta metall.*, vol. 30, pp. 57-62, 1982.

[PED 90] PEDERSEN O. B., "Overview no. 89 – Mechanism maps for cyclic plasticity and fatigue of single phase materials", *Acta metall.*, Overview No. 89, vol. 38, no. 7, pp. 1221-1239, 1990.

[PED 96] PEDERSEN O. B., "A static-dynamic model for the process of cyclic saturation in fatigue of metals", *Phil. Mag. A*, vol. 73, pp. 829-851, 1996.

[PED 98] PEDERSON O. B., "Micromechanisms of fatigue in high nitrogen duplex steels", in H. HÄNNINEN, S. HERTZMAN, J. ROMU, Eds., *Int. Conf. on High Nitrogen Steels '98*, Espoo, Trans Tech Publications Ltd, pp. 733-742, 1999.

[PER 95] PERDRISET F., MAGNIN T., CASSANGE T., HOCH P., DUPOIRON F., "Environmental effects on low cycle fatigue behaviour of Z3 CND 2205 duplex stainless steel", in T. G. GOOCH, Ed., *Proc. 4th Int. Conf. on Duplex Stainless Steels*, November 13-16, Glasgow, TWI, Woodhead Publishing, Abington, paper 13, 1995.

[PER 95a] PERALTA P., LLANES L., CZAPKA A., LAIRD C., "Effect of texture and grain size as independent factors in the cyclic behavior of polycrystalline copper", *Scripta Met. Mat.*, vol. 32, pp. 1877-1881, 1995.

[PET 78] PETROV Yu N., *Defects and Diffusionless Transformation In Steel* (in Russian), Naukova dumka, Kiev, 1978.

[POL 93] POLAK J., KRUML T., DEGALLAIX S., "Dislocation substructure in fatigued duplex stainless steel", *Scripta Metall.*, vol. 29, pp. 1553-1558, 1993.

[SAS 89] SASSEN J., GARRAT-REED A. J. and OWENS W. S., "Electron microscopy of austenitic Fe-Ni-Cr alloys containing nitrogen", in J. FOCT and A. HENDRY, Eds, *Int. Conf. on High Nitrogen Steels '88*, 18-20 May, Lille, The Institute of Metals, p. 159, 1989.

[SCH 49] SCHAEFLER A. L., "Constitution diagram for stainless steel", *Metall. Prog.*, vol. 56, pp. 680-680B, 1949.

[TAI 89] TAILLARD R., FOCT J., "Mechanisms of the action of nitrogen interstitials upon low cycle fatigue behaviour of 316 stainless steels", in J. FOCT and A. HENDRY, Eds, *Int. Conf. on High Nitrogen Steels '88*, pp. 387-391, 18-20 May , Lille, The Institute of Metals, 1988.

[STE 88] STEIN G., MENZEL J., DÔRR H., "Industrial manufacture of massively nitrogen-alloyed steels", in in J. FOCT and A. HENDRY, Eds, *Int. Conf. on High Nitrogen Steels '88*, pp. 32-38, 18-20 May, Lille, The Institute of Metals, 1988.

[STO 80] STOLTZ R. E., VANDER SANDE J. B., "The effect of nitrogen on stacking fault energy of Fe-Ni-Cr-Mn steels", *Metall. Trans.*, vol. 11A, no. 6, pp. 1033-1037, 1980.

[SUR 98] SURESH S., *Fatigue of Materials*, 2nd Edition, Cambridge University Press, 1998.

[TER 09] TERAZAWA Y., ANDO T., TSUCHIYAMA T., TAKAKI S., "Relationship between work hardening behavior and deformation structure in Ni-free high nitrogen austenitic stainless steels", *Steel Res. Int.*, vol. 80, no. 7, pp. 473-476, 2009.

[TIM 08] TIMOKHINA I. B., HODGSON P. D., RINGER S. P., ZHENG R. K., PERELOMA E. V., "Effect of bake-hardening on the structure-property relationship of multiphase steels for the automotive industry", *Steel Res. Int.*, vol. 80, no. 7, pp. 507-514, 2009.

[VOL 89] VOLLERTSEN F., VOGLER S., "*Werkstoffeigenschaften und Mikrostruktur*", C. HANSER, Ed., Verlag München Wien, 1989.

[VOG 91] VOGT J. B., FOCT J., REGNARD C., ROBERT G., DHERS J., "Low-temperature fatigue of 316L and 316LN austenitic stainless steels", *Metall. Trans. A*, vol. 22A, pp. 2385-2392, 1991.

[VOG 93] VOGT J. B., MAGNIN T., FOCT J., "Effective stresses and microstructure in cyclically deformed 316L austenitic stainless steel: effect of temperature and nitrogen content", *Fatigue Fract. Engng. Mater. Struct.*, vol. 16, pp. 555-564, 1993.

[VOG 95] VOGT J. B., MESSAI A., FOCT J., "Factors influencing the low cycle fatigue behaviour of a duplex stainless steel: effect of strain amplitude and nitrogen content", in T. G. GOOCH, Ed., *Proc. 4th Int. Conf. on Duplex Stainless Steels*, 13-16 November, Glasgow, TWI, Woodhead Publishing, Abington, paper 33, 1995.

[VOG 04] VOGT J.-B., POULON-QUINTIN A., FOCT J., "Effects of ageing on the fatigue behavior of new duplex stainless steels upgraded by nitrogen alloying", in N. AKDUT, B. C. DE COOMAN, J. FOCT, Eds, *Int. Conf. on High Nitrogen Steels '04*, 19-22 September, Ostende, GRIPS media GmbH, 2004.

[WAH 89] WAHLBERG G., ROLANDER U., ANDRÉN H. O., “Interaction between nitrogen and substitutional elements in the austenitic phase of duplex austenitic-ferritic stainless steels”, in J. FOCT and A. HENDRY, Eds, *Int. Conf. on High Nitrogen Steels ‘88*, 18-20 May, Lille, The Institute of Metals, pp. 163-168, 1988.

Chapter 12

Applications

12.1. Introduction

Duplex stainless steels (DSSs), or ferritic-austenitic stainless steel, have a long history, almost as long as that of stainless steels. They have existed commercially for almost 80 years and have thus constituted interesting technical alternatives to martensitic, ferritic, and austenitic stainless steels. Due to a favorable combination of properties, they attract interest in a very wide range of applications. Over the years, several duplex alloys have been developed and optimized to meet requirements on processing, fabrication, and application, and today different groups of DSS exist for a wide range of end-user applications. Most DSSs exhibit superior corrosion performance compared with standard austenitic grades due to the relatively high chromium contents. As a result of the steep increase of nickel price in recent years, the interest of using this type of low-nickel stainless steels has increased, particularly regarding leaner duplex alloys with corrosion resistance on level with commodity austenitic grades. The intention of this chapter is to describe the historical development of this family of steels, illustrate their merits, and through examples describe their main application areas. In this context it is pertinent to review the primarily technical reasons for selecting a DSS. These have been described in detail in many technical publications and a list of main reasons is given below:

– raw material cost (steel price);

Chapter written by Mats LILJAS and Fredrik SJÖHOLM.

Duplex Stainless Steels Edited by Iris Alvarez-Armas and Suzanne Degallaix-Moreuil

– weight saving (also in combinations with those below);

– uniform or pitting corrosion resistance;

– stress corrosion cracking resistance;

– resistance to intergranular corrosion;

– combination corrosion resistance and high mechanical strength;

– fatigue endurance (corrosion fatigue resistance);

– hardness/wear resistance;

– physical properties, such as thermal expansion;

– super plastic behavior.

In many cases more than one of these factors have been the reason for selecting a DSS.

12.2. Historical review

As with all evolution, ferritic-austenitic or DSSs have been developed to solve problems or to meet certain needs. Shortcomings of austenitic grades in the early days were a limited strength and susceptibility to intergranular corrosion due to difficulties in making low carbon steels. DSSs proved to be a clear improvement and both castings and forged products emerged quite early.

Avesta Steelworks in Sweden produced the two first commercial duplex alloys starting around 1930. One of the alloys, Avesta 453S, contained 26% Cr, 5% Ni and 1.5% Mo, and was used as an acid-proof material for roughly the same purposes as type 316, but to a lesser extent in plate form, as the steel was harder to work because of its greater hardness and higher strength [AVE 50]. The higher strength was, however, an advantage for certain components that were subjected to wear, such as spindles, pumps, shafts, etc. Avesta 453S had good casting properties and was used extensively to replace 316 type castings. The steel was chiefly used in the pulp and paper industry in sulfite and bleaching plants, but was also used to a large extent in dairies and other food industries for valves, pumps, etc. Early examples of applications are displayed in Figures 12.1-12.2.

The autoclave in Figure 12.2 was produced for Caulille in Belgium in 1933. The selection of material was obviously a success, as a second unit was supplied in 1936. The vessels were most probably used for the production of nitrocellulose, i.e. the material was exposed to a mixture of nitric acid, oleum and cellulose.

The other alloy, Avesta 453E, contained essentially 26% Cr and 4% Ni, and was employed as a heat-resistant grade. Due to its high chromium content it had a high scaling temperature, which was utilized in high temperature applications, e.g. for molten lead equipment and for pyrite kiln inserts.

Figure 12.1. *Brobeck cooler, fabricated in 453S for a sulfite mill, delivered in 1932*

Figure 12.2. *Autoclave in 453S for the production of gunpowder, delivered in 1933*

In 1936 J. Holtzer Steelworks was granted a French patent on DSSs with good resistance to intercrystalline corrosion [FRE 36]. One commercial steel established according to the patent contained 20% Cr, 8% Ni, 2.5% Mo and 1.5% Cu and was named Uranus 50. This steel was used in similar products and applications to 453S. Reported examples are cast propellers, dying machines, as well as vessels for petrochemical, chemical, food and the pulp and paper industries [HOC 65]. J. Holtzer Steelworks also offered heat-resistant duplex grades.

The concept of DSSs became very popular, particularly for use in the pulp and paper industry. In Sweden, most stainless steel producers manufactured the 26Cr-5Ni-1.5Mo grade. This steel was included in the Swedish standard (SIS 2324) in 1947 and later in the American standards as AISI 329.

Although the first DSSs were sometimes used successfully under conditions where austenitic steels could suffer from chloride-stress corrosion cracking (SCC) it was not until the 1950s that researchers showed the positive effect of the duplex microstructure in ensuring a high resistance to SCC. One duplex alloy, Sandvik 3RE60, was especially developed to combat this form of corrosion [SWE 65]. This steel grade found numerous applications in tube heat exchangers used in, for example, refineries and petrochemical industry during the 1960s and 1970s [BER 83]. Another example of selecting this grade due to its SCC resistance is from 1972 and is illustrated in Figure 12.3.

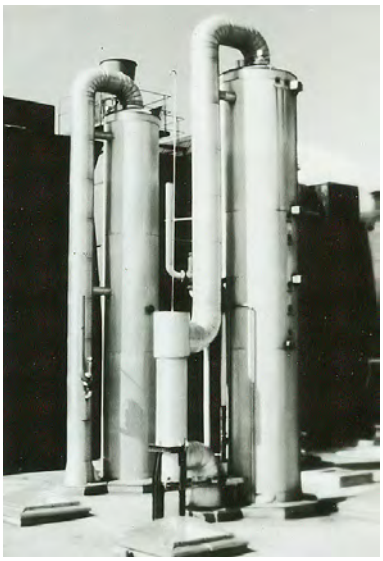

Figure 12.3. *Distillation columns made of 3RE60 for pharmaceutical industry*

A Swedish pharmaceutical industry installed two distillation columns made of 3RE60. The environment contained 5,000 ppm of chlorides at 100°C [OLS 94].

Several duplex grades, many of them further developments of the first steels, evolved during the years. A more modern, low-carbon version of 453S, named 25-5-1L, was selected in the mid-1970s for the production of polyvinyl chloride (PVC) where the vinyl chloride monomer (VCM) is recovered by simple flashing and stripping. The conditions in the stripping vessel may cause SCC in austenitic stainless steels. Therefore 25-5-1L was supplied for the vessels, as shown in Figure 12.4.

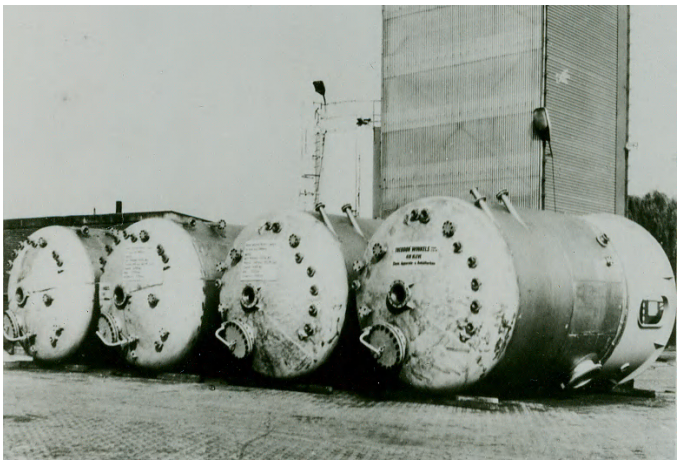

Figure 12.4. *Stripping vessels for vinyl chloride monomer production made in 25-5-1L*

For this particular process the operating temperature was about 85°C, the pH value 3-3.5, and the water phase had an average chloride content of 60 ppm, occasionally up to 150 ppm [OLS 94].

The dominating application areas for DSSs up to the 1970s were the pulp and paper, chemical, and petrochemical industries and pollution control equipment. Due to extensive research regarding this type of steel, the applicability in CO_2 and H_2S-containing environments, for example, in the oil and gas industry, increased. Improved metallurgical techniques, such as the argon-oxygen decarburization (AOD) process and better understanding of the duplex microstructure resulted in the introduction of the second generation of DSSs with much improved control of steel properties. In the same period there was an important commercial breakthrough for a 22Cr duplex grade for natural gas pipelines in the oil and gas industry [JOH 00].

Since then, DSSs have been used extensively for pipelines, as well as for many other applications in the oil and gas and offshore industries.

Inclusion of the modern duplex grades in pressure vessel standards, also in late 1970s, made it possible to use DSS in pressurized systems, such as pulp digesters, where the high strength could be utilized. The excellent corrosion resistance in acids of DSS made them ideal for chemical tankers and large tonnages of DSS material started to be used for this application in the 1980s.

In the expanding offshore oil and gas industry, there was a need for high-performance materials and 6Mo austenitic steels were selected due to their high resistance to the process environment and to seawater. However, superduplex grades, such as Zeron 100 and 2507, were developed to compete with the superaustenitic grades with good success. Today, large quantities of superduplex tubing are used in process systems and in umbilicals for the control of sub-sea systems. Also in the offshore industry, lean DSS has been used for blast walls on oil platforms based on the high strength combined with sufficient corrosion resistance.

Other areas where DSSs have partly replaced austenitic alloys are flue gas cleaning systems and seawater desalination plants. In the latter case a combination of duplex grades is used to meet different aggressive environments.

In more recent years lean duplex grades have emerged as an alternative to type 304 and 316 austenitic grades. This development has been very successful. The aim with these grades is also to replace construction steels, based on advantages of high strength and low maintenance costs. Increased use of such steels is now seen in bridges, storage tanks and other construction work. Lean DSSs are also used for construction of transport vehicles.

Most recently a new group of DSSs has been introduced; hyper duplex DSSs. They are very highly alloyed containing high levels of chromium, molybdenum, and nitrogen resulting in very high resistance to pitting and crevice corrosion. Intended applications are in aggressive, for example seawater, environments that can exist in heat exchangers and for umbilicals.

12.3. Current (modern) DSS grades

With the rapid development of new alloys of duplex grades there is a difficulty to get a practical overview of all existing grades. For example, in ASTM, 17 different duplex grades are listed, whereas in Euronorm the number of listed grades is nine. Certainly more grades will appear in the future. As many grades exist with

quite different alloy contents and property profiles, it is relevant to divide them into different groups. A frequent way is to subdivide the duplex grades into lean, standard, and superduplex grades and in Table 12.1 a number of current duplex grades are listed according to this grouping.

Type	Alloy	ASTM/EN	Cr	Ni	Mo	Cu	N	Other	PRE[1)]
Lean	2101	S32101/1.4162	21.5	1.5	0.3	0.3	0.22	5Mn	26
	2202	S32202/	22	2	0.3	-	0.2		26
	2304	S32304/1.4362	24	4	0.3	-	0.1		27
Standard	3RE60	/1.4424	19	5	2.7	-	0.1	1.7Si	30
	329	S32900/1.4460	25	5	1.5	-	0.1		32
	2003	S32003	22	3,5	1.5	-	0.16		30
	2205	S31803/1.4462	22	5	3	-	0.17		35
	255	S32550	25	5	3	2	0.15		37
Super	2507	S32750/1.4410	25	7	4	-	0.28		43
	Z100	S32760/1.4501	25	7	3.5	0,7	0.24	0.7W	42
	52N+	S32520/1.4507	25	7	3.5	1	0.25		41
	2906	S32906	29	6	2	-	0.35		41

[1]Pitting resistance equivalent PRE = Cr+3.3Mo+1.65W+16N.

Table 12.1. *List of some duplex stainless steels with typical compositions (for convenience full trade names have not been used)*

12.4. Modern applications

In the following, applications where DSS is used will be described. For clarity the applications will be grouped in different industry segments as far as possible. There are clearly many different applications, which are used in several industry branches, where DSS is an excellent choice. Among these are, for example, heat exchangers, distillation equipment, and storage tanks.

It is not possible to describe all applications where duplex steels can or have been used in this chapter; however, some important uses of duplex stainless will be described for each industry, giving an overall picture of the versatility of the material.

12.4.1. *Oil and gas*

As is mentioned above, one of the real commercial breakthroughs for DSS came within the oil and gas industry. Thereby it is logical to start with the use of duplex stainless in this industry.

Even though oil itself is normally not very corrosive, the natural surroundings around production sites and the extraction process itself can create corrosive environments. Untreated oil and gas contain various levels of CO_2 and H_2S affecting the corrosiveness significantly. For the offshore industry, seawater handling is necessary and requires corrosion-resistant materials. The extraction of natural resources, such as oil and gas, often involves deep-sea sources and transport over long distances, which explains why a large part of the stainless steel requirement in this sector consists of tubular products. The most corrosive environments exist in deep sour wells with high temperatures and high pressures. For most of these situations different duplex alloys have offered attractive solutions and some examples are described below.

12.4.1.1. *Flowlines*

An important application of DSS in the oil and gas industry is flowlines for transport of oil and natural gas. There is probably today more than 1,000 km of welded duplex flowlines installed globally and with very good service performance. The main grade that has been employed for these flowlines is 2205 with some use of super DSSs for higher levels of H_2S. Pipe diameters in flowlines range from 4-36 inches. A large portion of the pipelines is used in offshore installations [SMI 00].

Flowlines and risers are used to recover the oil and connect the sub-sea equipment with surface production units. These transport lines for the extracted oil are often constructed as flexible tubes. They consist of layers of different materials and the stainless steel layer is built up from many small sections attached to each other, forming a tube that is bendable to a certain extent; hence the name flexible tube. This can be seen in Figure 12.5 below.

Reduced pressure in these flowlines causes water to condensate and in combination with the presence of chlorides and hydrogen sulfide (H_2S) this creates an environment where corrosion is a real risk. The working temperature and the high

flow rates in the transport lines further increase the need for a tough and corrosion-resistant material. Thanks to its superior mechanical strength and high corrosion resistance DSS is used by all the big manufacturers of flexible tubing for risers and flowlines.

Figure 12.5. *The layer build-up of a flexible tube with stainless steel as the innermost part*

12.4.1.2. *Umbilicals*

In order to control the offshore extraction of oil, sub-sea wellheads are connected to platforms by tubing, often referred to as umbilicals. As the name suggests, the necessities that are required in the extraction process are provided through these umbilicals. This includes power supply for sub-sea pumps, lubrication for these pumps, hydraulic pressure to operate valve actuators, chemicals for adjusting the process fluids, and the necessary control of functions installed at the wellhead.

As the umbilicals work in very harsh environments, where it is expensive and complicated to perform repairs, reliability is a very important aspect when choosing construction material; therefore DSS, with its mechanical strength and corrosion resistance, is an excellent choice. Depending on the working conditions, there are several duplex grades with different corrosion resistance to choose between. Superduplex grades, such as 2507, have proven to be a good choice where the environment demands a material with especially good corrosion properties. Most duplex umbilicals are provided as seamless tubing. However, longitudinally welded tubes can be a more cost-efficient option as they are provided in greater length than the seamless alternative. Longitudinally welded lean DSSs are an alternative if used in the zinc-clad condition [JOR 05].

12.4.1.3. *Blast walls*

Stainless steel is ideal for topside construction of oil rigs. Around living quarters and other important areas, protective walls are erected in order to safeguard personnel in case of accidents. These barriers are called “blast walls” and must be able to absorb as much energy as possible if an explosion occurs. It is also desirable that the protective walls show good resistance to buckling to stay as intact as possible. A lean DSS, for example 2304, possesses these properties, and is subsequently often chosen for the manufacturing of blast walls [ERB 93].

12.4.2. *Pulp and paper*

12.4.2.1. *Pulp digesters*

Being one of the first application areas for DSS, the pulp and paper industry is still a very important end-user for this family of steels. Applications can be found in most stages, from the chip preparation to papermaking. Developments in pulp processing and in material utilization have shown that DSS constitute the optimum materials choice, due to its competitive price:performance ratio. In the sulfate (Kraft) process, pulp digesters typically work under highly alkaline conditions, at temperatures between 150 and 180°C. The hot alkaline environment induces an increased risk of caustic SCC and general corrosion. Due to its microstructure, DSS has a high resistance to SCC and in the construction of pressurized vessels the high mechanical strength can be utilized with great advantage. In these hot alkaline environments high chromium and low molybdenum levels in the steel are beneficial to the corrosion resistance and this is a typical feature for most DSSs. To date type 2205 has mainly been selected for both batch and continuous digesters. However, low molybdenum alloys, such as 2304 and LDX 2101®, are viable alternatives for the future.

Other important duplex applications associated with the cooking process are chip pre-steaming vessels, black and white liquor tanks, and circulation systems including heat exchangers, piping, pumps and valves.

Different filter washers are used in many stages of the pulp and paper mill. These are mainly constructed of large rotating drums, and there is a great need for materials with high corrosion fatigue resistance. As DSSs have shown very good corrosion fatigue strength and high resistance to abrasion they are utilized favorably in this application.

12.4.2.2. *Bleaching*

In the bleaching process the pulp is exposed to various bleaching chemicals in large reactors. The early processes of chlorine and chlorine dioxide bleaching were very aggressive to both steels and the environment and are being phased out. However, DSS has been used in less harsh conditions prevailing in, for example, washers replacing austenitic alternatives. In the oxygen delignification process, the working conditions include elevated temperatures (~120°C) and a pressurized atmosphere. There are cases where external moisture on the reactors has caused problems with external SCC in austenitic stainless steels. The duplex grades provide a remedy to this problem and similar to the case with the digesters, the mechanical strength of duplex can be used to diminish the total weight, and thereby cost, of the vessels.

The process to transform pulp to paper includes several bleaching steps, from chlorine bleaching to "totally chlorine free" (TCF) bleaching processes. In the latter case, pressurized peroxide reactors are often used and the high-strength DSS handles the conditions of high temperature, a pressurized atmosphere, and alkaline environment perfectly. The rather newly developed lean duplex grade, LDX 2101®, is a good candidate for this type of application. Figure 12.6 presents a photo of a reactor vessel where this lean duplex grade has been used.

Figure 12.6. *Hydrogen peroxide reactor in LDX 2101®, constructed in 2006*

12.4.2.3. *Chemical recovery, evaporators*

In the final evaporator stage, prior to the recovery boiler, there is a trend towards higher temperature and higher concentrations of dry solids. These developments place greater demands on the construction materials. As in the applications described above, the high resistance to SCC of the duplex grades is also beneficial for the evaporator phase in the pulp mill. Grades, such as 2205 and 2304, have been successfully used.

12.4.2.4. *Suction roll shells*

The task of the suction rolls is to remove the water from the fibers in paper machines. To do this, the rolls are perforated with a multitude of small holes, through which the liquid is forced during rolling of the paper with the help of a vacuum system. The material for the suction roll shells is carefully chosen with respect to the forces affecting the shell and the chemical environment. High corrosion fatigue strength is crucial for the performance of a suction roll shell and the combination of good corrosion resistance and high mechanical strength make DSS superior in this respect. Another important aspect of the DSS grades is their high resistance to thermal fatigue, which can diminish the cost for maintenance. Thermal fatigue can occur when the rolls are not sufficiently lubricated during operation. This causes local heating and cooling, which can give rise to thermal fatigue in the material. These areas of local thermal fatigue can, in turn, result in small cracks. DSSs, both centrifugally cast and in wrought form, are used for this application. One wrought duplex alloy, 3RE60 SRG, has been used extensively for suction roll shells and has shown excellent performance.

12.4.3. *Desalination*

The supply of freshwater through desalination processes is expected to develop strongly as the growing global population needs more and more water. In the desalination industry there are basically three different types of plants, which are used for production of freshwater on a larger scale; the two thermal processes multi-effect distillation (MED) and multistage flash (MSF), as well as the reverse osmosis (RO) procedure. DSS is used in most stages of these three types of plants. A couple of which are given below.

12.4.3.1. *Flash chamber shells (MSF)*

The heart of an MSF plant is the flash chamber where the feed, normally deaerated seawater or brine, through evaporation is transformed into the product, the distillate. Flash chambers were originally made of plain carbon steel as the feed, according to the textbooks, should be free of oxygen and thus harmless to carbon

steel. Service experience showed, however, that the conditions inside these chambers were more severe than anticipated. This was mainly due to leakage of oxygen into the system during shutdown periods, and corrosion rates in the order of millimeters per year have been reported. This option requires a material resisting not only the internal, but also the external environment, which can involve wet saline deposits on a hot stainless steel surface. The use of solid stainless steel for the evaporator vessels can be a very cost-effective choice. If the right duplex grade is chosen there is no need to introduce a corrosion allowance, so this permits the use of much thinner gauges than would be the case with mild steel. In the flash chambers, the corrosive conditions are more hostile in the lower parts than in the upper ones. This means that in order to limit the material costs the use of several grades for the shells could be appropriate. The use of a more corrosion-resistant duplex grade, such as 2205, can be restricted to the lower part of the shell, while a less expensive grade with lower corrosion resistance, such as 2304, would be adequate for the upper part of the shells. This type of construction using these two different duplex grades is referred to as the Dual Duplex^{TM} concept [SNI 07].

In Figure 12.7 an example of an installation using 2205 is shown. The evaporator shells work in a similar environment for the MED process, and a comparable reasoning is valid for them.

Figure 12.7. *Series of evaporator shells in 2205 designed for an MSF plant*

12.4.3.2. *Vent systems (MED, MSF)*

In the vent systems, the vacuum needed for each boiling stage is created. A decreased pressure permits lower evaporation temperatures and, as a consequence, the working conditions for the materials are less hostile. The most common steel grade used for this application is ASTM 316L/EN 1.4404, but this grade has, on several occasions, suffered from pitting and SCC. Thanks to their good resistance to pitting and SCC, DSSs, such as 2205 and 2507, are often more reliable for equipment in the vent system.

12.4.3.3. *High-pressure pumps and piping (RO)*

If the flash chambers are the heart of an MSF plant, the high-pressure (HP) piping constitutes the arteries of an RO plant. The high pressure, normally in the range of 60 to 80 bars, requires the strength and toughness of metallic materials. Stainless steel is the most commonly used material and several different grades can be used depending on the salt content of the water. Given the high pressures involved, DSS with its superior strength is normally a cost-effective choice.

12.4.4. *Transport*

12.4.4.1. *Chemical tankers*

For longer transports of chemical products on the world's seas, chemical tankers are often employed. The liquid chemicals are held in cargo containers, constructed as separated compartments in the cargo space. It is normal practice to transport various chemicals using the same cargo container, with intermediary washing. Even though the chemical tankers are not themselves all stainless steel, the cargo containers holding the transported products must be corrosion resistant. The good corrosion resistance and the high strength of DSS make them a suitable and widely used choice today. Compared to the earlier employed austenitic grades, such as the frequently used 316LN with minimum 2.5 or 2.75% molybdenum, grade 2205 shows superior resistance in many of the important chemicals, such as phosphoric acid. Since the 1980s very large tonnages of DSS have been installed in chemical carriers. One example is shown in Figure 12.8.

Figure 12.8. *Cargo container made from 2205 in a parcel tanker*

The weight saving in selecting a duplex grade instead of an austenitic material in this application is about 10%, equating to a couple of hundred tons for a single ship. This means a great increase in loading capacity of the chemical to be transported by the carrier.

12.4.4.2. *Mobile tank containers*

Tank containers for road or rail transport often use stainless steel as a construction material. Depending on regulations and the requirements for the transported goods, there are different designs and material choices for the tank container.

Due to the increasing brittleness of DSS at lower temperatures, the inner shell, which is in contact with the transported goods, may not be constructed in duplex for the purpose of transporting liquids at cryogenic temperatures. Apart from this, there are no technical restrictions on using duplex grades for mobile tank containers. Especially for tanks designed to operate under elevated pressures, duplex might be a very interesting alternative. In Figure 12.9 a mobile container for road transport in LDX 2101® is shown.

Figure 12.9. *A mobile container for road transport in LDX 2101®*

12.4.5. *Storage tanks*

Cylindrical storage tanks are probably one of the more important applications for DSS. This is partly because of the sheer number of these constructions throughout the world, and partly because the properties of DSS lend themselves perfectly to saving large amounts of weight compared to austenitic material. Depending on the volume of the storage tank, as well as the stored liquid, the total weight of the tank shell could be as much as 25-30% lower when using duplex compared to standard austenitic stainless steel.

Figure 12.10. *Storage tanks built in LDX 2101®*

As the duplex family offers several grades, different choices can be made in accordance with the aggressiveness of the stored liquid. As in many other applications, the advantage of stainless steel is that the maintenance costs for the storage tanks can be greatly reduced. Figure 12.10 shows storage tanks built in grade LDX 2101®.

12.4.6. *Hydrometallurgy*

Hydrometallurgy is the technique of extracting metals from ore through leaching. The environmental conditions in this process are different depending on the metal to be processed, but generally the conditions can be rather hostile in some part of the plants due to a combination of elevated temperatures, acids, and the presence of chloride ions. As the conditions can vary appreciably between plants and the different stages in the plant, no grade can be generally said to always be a good choice for one distinct application. The application within this industry that uses the largest quantities of DSS is likely to be cylindrical vessels, such as leach tanks, thickeners, separation tanks, mixers, and settler tanks.

12.4.6.1. *Leach tanks*

The leach tank is the section in the hydrometallurgical leaching process where the ore is partially dissolved with the help of different leaching reagents, acid, or alkali.

Figure 12.11. *Embedded leach tanks in a zinc plant, installed in duplex 2507*

The environments in the leach tanks vary from plant to plant, and can be so aggressive that stainless steel is not an option. However, there are examples where leaching tanks for hot acid leaching in zinc plants using the Jarosite process have been constructed with success in the superduplex grade 2507. An example of this is shown in Figure 12.11.

12.4.6.2. *Thickeners*

The term “thickener” is used for equipment that separates residual solid material from the leach solution containing the desired metal. Thickeners can be used in series and thereby provide a method for washing the leached material, in order to diminish the loss of soluble material and increase the yield in the process. The material choice will depend mainly on the amount of chlorides present in the process fluid. Thickeners have been built in lean duplex material, as well as in super DSS.

12.4.6.3. *Cathode plates*

Metal from leach solutions is recovered through a method called electro-winning, which is actually an electrolysis process. To accomplish this it is necessary to have a cathode upon which the metal in solution can precipitate. One material option for these cathode plates is stainless steel and in the case of copper refining, the most common grade for this purpose is probably 316L/1.4404. However, this is a rather interesting application where DSS has recently been shown to perform well [EAS 07].

12.4.7. *Pollution control/flue gas cleaning*

Flue gas desulfurization (FGD) equipment is installed in power plants fired with different fuels in order to clean the flue gas from polluting elements, such as sulfur oxide compounds. The FGD systems include highly aggressive environments and

the materials are selected on the basis of corrosive media, operating conditions and plant design. The severity of the corrosiveness decreases from the gas inlet to the outlet area, and there is a range of different materials that could be used for different parts of the scrubber. The aggressiveness in the scrubber is specific for each plant, much depending on which type of fuel is used [BEC 07]. This means that the material choice is a quite complicated one.

For the less hostile environments in an FGD plant the more corrosive-resistant duplex grades (standard and superduplex) find their place in demisters and spray lances in the upper part of the absorber.

12.4.8. *Construction*

12.4.8.1. *Bridges*

A fairly new area where DSSs are used is the construction of bridges. The choice of materials is based on the high strength and low maintenance and life-cycle cost (LCC), but strong reasons are also environmental concerns and aesthetic values. The traditional material of choice in bridge building is painted carbon steel. However, a construction like a bridge is normally built to last for a long time. For this reason, the LCC has gained more and more significance. Using DSS in bridges will extend their lifetime and at the same time substantially diminish the need for maintenance and repairs during this lifetime. An example where the aesthetic side of stainless steel as a material has been utilized in a new design, with DSS as load-carrying structural material, is shown in Figure 12.12.

Figure 12.12. *The Apaté bridge in Stockholm uses duplex 2205*

12.4.8.2. *Reinforcement bars (rebars)*

Stainless steel can be used to improve the service life of a concrete structure supported with steel-reinforcement bars. This is especially beneficial in environments where an elevated concentration of chlorides can be expected. One example is the tidal zone on bridge columns erected in salt water. In these environments chloride-containing moisture penetrates through the concrete to initiate corrosion at the steel-concrete interface. With its superior corrosion resistance, DSS is an ideal material and Figure 12.13 shows some rebar samples.

Figure 12.13. *An assortment of reinforcement bars*

Additionally, it is often possible to decrease the thickness of the concrete cover layer around the duplex reinforcement bars, which further saves construction material.

12.4.9. *Hot-water boilers*

Another interesting application for DSS is domestic boilers. Most commonly, domestic hot-water systems include a hot-water tank. These water tanks could be carbon steel tanks, with an internal enamel coating or copper lining for corrosion protection, or they can be solid stainless steel tanks. With the entirely stainless solution, one single material provides the combined function of load bearing and corrosion protection. Stainless steel grades that have traditionally been used in hot-water tanks are 316L, 316Ti and ferritic 444 (EN 1.4521). The main corrosion risks for stainless steel used in hot-water tanks are pitting, crevice corrosion and SCC. The risk of SCC increases with higher metal skin temperature. The largest SCC risk thus occurs in those kinds of hot water tanks, which are externally heated by either a heating jacket or a gas flame.

DSS for domestic water heaters was introduced more than 15 years ago. The grade 2304 came to replace 444 due to a combination of better weldability and availability. Lately, many manufacturers of hot-water tanks have also chosen LDX 2101®. The degree of corrosion resistance required depends mainly on the chloride content of the water to be heated. All the duplex grades are much more resistant than the austenitic type 316 grades to SCC.

In general, one advantage of stainless steel water tanks is their lower weight compared to carbon steel tanks with corrosion protection. Due to the higher yield strength, DSS grades offer the possibility of further weight reduction compared to austenitic and ferritic stainless steels. Less weight to handle per tank is an advantage during transport, manufacturing, and final assembly.

12.5. Conclusions

DSS has existed for many years and is an established family of steels in many application areas. Their unique combination of high corrosion resistance and mechanical strength has made them a competitive alternative to both austenitic stainless steels and even to painted carbon steel. Progress in user segments and in material development has created new challenges where DSSs have been very successful choices of material. A wide range of duplex alloys exists and can meet different requirements in terms of corrosion performance. Therefore, DSSs are used with success in a growing number of applications in many different industries. The examples shown in this paper represent some of the major uses, but there are several more areas, such as the petrochemical and chemical industries, that are not covered here. The DSSs can be utilized under most conditions typical for stainless steel and can often replace austenitic grades with great benefits. When the LCC is considered there are a number of applications where DSS can compete economically with carbon steel. Today DSS constitutes a relatively small steel family, but thanks to their good corrosion resistance, their excellent price: performance ratio, and their high mechanical strength, this type of stainless steel is fast growing in popularity.

12.6. References

[AVE 50] *Avesta Jernverk Product Catalogue*, 1950.

[BEC 07] BECKERS B., SNIS M., OLSSON C., OLSSON J., “Stainless steels for flue gas cleaning – laboratory trials, field tests and service experience” in *Conf. Proceedings*, NACE International Airpol, Louisville, Kentucky, 2007.

[BER 83] BERNHARDSSON S., OREDSSON J., MÅRTENSON C., *Duplex Stainless Steels*, ASM, 1983.

[EAS 07] EASTWOOD K.L., WHEBELL G.W., "Electrorefining and electrowinning", in *Proceedings of the 6th International Copper-Cobre Conference 2007*, p.35, 2007.

[ERB 93] ERBING M-L, GROTH H., "Duplex stainless steels – weight saving in structural applications", *Proceedings of New Steel Construction*, June 1993, p. 30.

[FRE 36] French patent, Nouveaux alliages inoxydables, no. 803361, 1936.

[HOC 65] HOCHMAN J., *Revue du Nickel*, July-August-September, 1950, p. 53.

[JOH 00] JOHANSSON K., "Duplex stainless steels, past present and future", *6th World Duplex 2000 Conference*, AIM, p. 13, 2000.

[JOR 05] JORDAN L.C., MCENERNEY J.W., MACMANUS J.W., "The introduction of alloy 2101 for use as zinc-clad umbilical tubing for deepwater subsea oil and gas developments", *Stainless Steel World 2005*, P0 5056, 2005.

[OLS 94] OLSSON J., LILJAS M., "60 years of duplex stainless stell applications", *Corrosion/94*, NACE, paper no. 395, 1994.

[SMI 00] SMITH L., CELANT M., "A guideline to the successful use of duplex stainless steels for flowlines, *Proceedings of Duplex America 2000*, p. 17, 2000.

[SNI 07] SNIS M., OLSSON J., "Reduce costs for storage and distribution of desalted water – use duplex stainless steel", *Proceedings of Desalination and the Environment*, European Desalination Society, 22-25 April, Halkidiki, Greece, 2007.

[SWE 65] Swedish patent, Corrosion resistant steel alloy, Föremål bestående av en ferrit-aistenitisk stållegering med mycket hög beständighet mot korrosion, no. 312240, 1965.

Appendix

UNS	EN	DIN	AFNOR	AISI	Common[TM]	C(max)	Cr	Ni	Mo	N	Cu	W
Wrought duplex stainless steels												
First-generation duplex grades												
S32900	1.4460	X3 CrNiMo N27-5-2	Z5 CND 2705 Az	329	10RE51	0.10	25.00-28.00	4.50-6.50	1.30-2.00	0.05-0.20	–	–
S32404	–	–	–	–	UR 50	0.08	20.5-22.5	5.5-8.5	2.0-3.0	0.05-0.20	1.00-2.00	–
S31500	1.4417	X2 CrNiMo Si 19-5	–	–	3RE60 A903	0.03	18.0-19.0	4.3-5.2	2.50-3.00	0.05-0.10	–	–
Lean grades												
S32304	1.4362	X2 CrN N 23-4	Z3 CN23.04 Az	–	SAF 2304 UR 35N	0.03	21.5-24.5	3.0-5.5	0.05-0.60	0.05-0.20	–	–
S32101	1.4162	–	–	–	LDX2101		21.5	1.5	0.3	0.22	0.3	
S32003	–	–	–	–	AL2003	0.03	19.5-22.5	3.0-4.0	1.50-2.00	0.14-0.20	–	–
Standard grades: 22Cr DSS												
S31803	1.4462	X2 CrNiMo N22-5-3	Z3 CND 22.05 Az	329LN	SAF 2205 UR 45N	0.03	21.0-23.0	4.5-6.5	2.5-3.5	0.10-0.22	–	–
S32205	1.4462	X2 CrNiMo N22-5-3	Z3 CND 22.05 Az	–	SAF 2205	0.03	22.0-23.0	4.5-6.5	3.0-3.5	0.14-0.20	–	–

Duplex Stainless Steels Edited by Iris Alvarez-Armas and Suzanne Degallaix-Moreuil

UNS	EN	DIN	AFNOR	AISI	Common™	C	Cr	Ni	Mo	N	Cu	W
High-alloyed grades: 25 Cr DSS												
S31200	–	X 2 Cr Ni Mo N 25-6	Z3 CND 25.07 Az	–	UR 47N 44LN	0.03	24.0-26.0	5.5-6.5	1.20-2.00	0.14-0.20	–	–
S31260	–	X 2 Cr Ni Mo N 25-6-3	Z3 CND 25.07 AZ	–	DP-3-25-Cr	0.03	24.0-26.0	5.5-7.5	2.5-3.5	0.10-0.30	0.20-0.80	0.10-0.50
S32550	1.4507	X 2 Cr Ni Mo Cu N 25-6-3	Z3 CNDU 25.07 Az	–	UR52 N Ferralium 255	0.03	24.0-27.0	4.5-6.5	2.9-3.9	0.10-0.25	1.00-2.50	–
Superduplex grades												
S39274	–	–	–	–	DP-3W Zeron 100	0.03	24.0-26.0	6.8-8.0	2.5-3.5	0.24-0.32	0.20-0.80	1.50-2.50
S32750	1.4410	X 2 Cr Ni Mo N 25-7-4	Z 3 CND 25.06 Az	–	SAF2507 UR47N+ Atlas 958	0.03	24.0-26.0	6.0-8.0	3.0-5.0	0.24-0.32	0.50	–
S32760	1.4501	X 2 Cr Ni Mo Cu W N 25-7-4	Z3 CNDUW 25.06 Az	–	Zeron 100 UR52N+ 4501	0.03	24.0-26.0	6.0-8.0	3.0-4.0	0.20-0.30	0.50-1.00	0.50-1.00
S32520	1.4507	X 2 Cr Ni Mo Cu N 25-6-3	Z3 CNDU 25.07 Az	—	UR52N+	0.03	24.0-26.0	5.5-8.0	3.0-5.0	0.20-0.35	0.5-3.0	–
Hyperduplex												
S32707	–	–	–	–	SAF 2707	0.03	27	6.5	5	0.4		

Cast duplex stainless steels											
UNS *cast*	**ASTM**	**ACI**	**UNS wrought equivalent**	**Common**™	**C***(max)*	**Cr**	**Ni**	**Mo**	**Mn**	**N**	**Cu**
Standard grades 22% Cr											
J92205	A890-4A	CD3MN	S32205 / 31803	2205 UR45N	0.03	21.0- 23.5	4.5- 6.5	2.5- 3.5	1.50	0.10- 0.30	1.00
High-alloyed grades											
J93345	A351/A890 A995-2A	CE8MN	S32750	Escoloy 45D	0.08	20.0- 27.0	8.0- 11.0	3.0- 4.5	1.00	0.10- 0.30	–
J93370	A351/A890 A995-1A	CD4MCu	S32550	Atlas 957	0.04	24.5- 26.5	4.75- 6.00	1.75- 2.25	1.00	–	2.75- 3.25
J93371	A890-3A	CD6MN	–	Atlas 963	0.04	24.0- 27.0	4.0- 6.0	1.75- 2.50	1.00	0.15- 0.25	1.75- 2.50
J93372	A890-1B	CD4MCuN	S32550	Ferralium255 Atlas 957	0.04	24.5- 26.5	4.7- 6.0	1.7- 2.3	1.00	0.10- 0.25	2.7- 3.3
Superduplex grades											
J93404	A890-5A	CE3MN	S32750	2507 Atlas 958	0.03	24.0- 26.0	6.0- 8.0	4.0- 5.0	1.50	0.10- 0.30	–
J93380	A890/A351 6A	CD3MWCuN	S32760	Zeron 100 Atlas 962	0.03	24.0- 26.0	6.5- 8.5	3.0- 4.0	1.00	0.20- 0.30	0.5- 1.0

Cast austenitic stainless steels (predominantly austenite with 10-20% ferrite)										
UNS	**ASTM**	**ACI**	**UNS /AISI** *wrought equivalent*	**C**	**Cr**	**Ni**	**Mo**	**Mn**	**Si**	
J92500	A351/A743	CF3	S30403 / AISI 304L	0.03	17.0-21.0	8.0-12.0	–	1.5	2.00	
J92600	A743	CF8	S30400 / AISI 304	0.08	18.0-21.0	8.0-11.0	–	1.5	2.00	
J92602		CF20	S30200 / AISI 302	0.20	18.0-21.0	8.0-11.0	–	1.5	2.00	
		CF30		0.30	26.0-30.0	8.0-11.0	–	1.5	2.00	
J92800	A351/A743	CF3M	S31603 / AISI 316L	0.03	17.0-21.0	9.0-13.0	2.0-3.0	1.5	1.50	
J92900	A351/A743	CF8M	S31600 / AISI 316	0.08	18.0-21.0	9.0-21.0	2.0-3.0	1.5	2.00	

Chemical composition (wt%) of wrought and cast duplex stainless steels listed in the Unified Numbering System (UNS) and the equivalent in European (EN), German (DIN), French (AFNOR) and American (AISI) coding.

List of Authors

Iris ALVAREZ-ARMAS
Instituto de Física Rosario – CONICET
Universidad Nacional de Rosario
Rosario
Argentina

Nuri AKDUT
Belgium

Alberto F. ARMAS
Instituto de Física Rosario – CONICET
Universidad Nacional de Rosario
Rosario
Argentina

Véronique AUBIN
Laboratoire de Mécanique de Lille
LML, UMR CNRS 8107
Ecole Centrale de Lille
France

Jacques BESSON
Centre des Matériaux P-M. Fourt
Mines ParisTech Paris France
France

Duplex Stainless Steels Edited by Iris Alvarez-Armas and Suzanne Degallaix-Moreuil

Franco BONOLLO
Dipartimento di Tecnica e Gestione dei Sistemi Industriali (DTG)
Università di Padova
Vicenza
Italy

Jacques CHARLES
ArcelorMittal GM R&D
Stainless, Electrical steels, Plates, HRC and Tubular products
France

Suzanne DEGALLAIX-MOREUIL
Laboratoire de Mécanique de Lille
LML, UMR CNRS 8107
Ecole Centrale de Lille
France

Pierre EVRARD
Laboratoire de Mécanique de Lille
LML, UMR CNRS 8107
Ecole Centrale de Lille
France

Paolo FERRO
Dipartimento di Tecnica e Gestione dei Sistemi Industriali (DTG)
Università di Padova,
Vicenza
Italy

Isabel GUTIERREZ
CEIT and TECNUN
University of Navarre
San Sebastián
Spain

Amaia IZA-MENDIA
CEIT and TECNUN
University of Navarre
San Sebastián
Spain

Mats LILJAS
Avesta Research Centre
Outokumpu Stainless
Avesta
Sweden

Angelo Fernando PADILHA
Departamento de Engenharia Metalúrgica e de Materiais (PMT)
Escola Politécnica da Universidade de São Paulo (EP-USP)
São Paulo
Brazil

Ronald Lesley PLAUT
Departamento de Engenharia Metalúrgica e de Materiais (PMT)
Escola Politécnica da Universidade de São Paulo (EP-USP)
São Paulo
Brazil

André PINEAU
Centre des Matériaux P-M. Fourt
Mines ParisTech
Paris
France

Ingrid PRORIOL SERRE
Laboratoire de Métallurgie Physique et Génie des Matériaux
ENSCL/USTL (UMR CNRS 8517)
Université des Sciences et Technologies de Lille,
France

Daniel SALAZAR
Laboratoire de Métallurgie Physique et Génie des Matériaux
ENSCL/USTL (UMR CNRS 8517)
Université des Sciences et Technologies de Lille
France

Fredrik SJÖHOLM,
Special Coil & Plate
Outokumpu Stainless
Avesta
Sweden

Alberto TIZIANI
Dipartimento di Tecnica e Gestione dei Sistemi Industriali (DTG)
Università di Padova
Vicenza
Italy

Jean-Bernard VOGT
Laboratoire de Métallurgie Physique et Génie des Matériaux
ENSCL/USTL (UMR CNRS 8517)
Université des Sciences et Technologies de Lille
France

Index

Duplex Stainless Steels Edited by Iris Alvarez-Armas and Suzanne Degallaix-Moreuil

D

E

F

G, H

I, K

L

M

N, O

P, R

S

T

U-Y